ONR GRANT N00014-95-1-0539
A DoD Multidisciplinary Research Program
of the University Research Initiative (M-URI)

FINAL REPORT

INTEGRATED DIAGNOSTICS

March 1995 - August 2000

FOR
Office of Naval Research
800 N. Quincy Street
Arlington, VA 22217-5660

PREPARED BY
Richard S. Cowan, Program Manager
Ward O. Winer, Principal Investigator
Georgia Institute of Technology
MULTIUNIVERSITY CENTER FOR INTEGRATED DIAGNOSTICS
Woodruff School of Mechanical Engineering
Atlanta, GA 30332-0405
Ph: 404-894-3200

SUBGRANTEES
Northwestern University
Jan D. Achenbach, Director
Center for Quality Engineering and Failure Prevention
Ph: 847-491-5527

University of Minnesota
S. Ramalingam, Professor
Department of Mechanical Engineering
Ph: 612-625-4017
William Robbins, Professor
Department of Electrical Engineering
Ph: 612-625-8014

DISTRIBUTION STATEMENT A
Approved for Public Release
Distribution Unlimited

20000905 099

DTIC QUALITY INSPECTED 4

TABLE OF CONTENTS

Title Page i

Table of Contents iii

EXECUTIVE SUMMARY 1

1. **INTRODUCTION** 3
   - 1.1 Mission 3
   - 1.2 Organization 4

2. **RESEARCH ACCOMPLISHMENTS** 7
   - 2.1 Failure Detection and Identification (NDE) 12
     - 2.1.1 Flaw Detection and Characterization using Ultrasonics 13
     - 2.1.2 Crack Detection by Ultrasonic Guided Waves 18
     - 2.1.3 Eddy Current Microsensors for Integrated Diagnostics 28
     - 2.1.4 Sensing Acoustic Emission and Transmission 43
   - 2.2 Failure Characterization and Prediction Methodology 49
     - 2.2.1 Structural Fatigue Investigation 50
       - 2.2.1.1 Models for Small Fatigue Crack Growth Behavior 54
       - 2.2.1.2 Stress and Flaw Analysis of Components 75
       - 2.2.1.3 Fatigue Crack Initiation and Growth Mechanisms 86
       - 2.2.1.4 Fatigue Crack Growth: Microstructure, Load Sequence, Corrosion 111
       - 2.2.1.5 Algorithms for Remaining Life Prediction 125
       - 2.2.1.6 Advances in Understanding Structural Fatigue Life 132
     - 2.2.2 Fatigue Prediction Methodology/Fatigue Reliability 134
     - 2.2.3 Study of Acoustic Emission and Transmission from Incipient Fatigue Failure 143
     - 2.2.4 Acoustic Emission Modeling for Integrated Diagnostics 149
   - 2.3 Machinery Health Monitoring (Sensing, Analysis, Real-time Diagnosis) 157
     - 2.3.1 Detection of the Precursor to Mechanical Seal Failure in Turbomachinery 158
     - 2.3.2 Real-time Monitoring & Controlling of the Dynamic Behavior of Seals 167
     - 2.3.3 Dynamic Metrology as a Bearing Wear Diagnostic 192
     - 2.3.4 Integrated Microsensors for Aircraft Fatigue and Failure Warning 199
       - 2.3.4.1 Wideband Integrated Acoustic Emission Microsensors 200
       - 2.3.4.2 Vibration Sensors 203
       - 2.3.4.3 Multi-Sensor Coupon 206
       - 2.3.4.4 Signal Processing for the Detection & Classification of AE 209
     - 2.3.5 Modal Parameter Extraction from Structural Diagnostic Signals 237

3. **TECHNOLOGY TRANSFER** 267
   - 3.1 Publications 267
   - 3.2 Presentations 278

EXECUTIVE SUMMARY

Faculty and staff from the Georgia Institute of Technology, Northwestern University, and the University of Minnesota are pleased to submit this document, summarizing the results of Office of Naval Research (ONR) Grant N00014-95-1-0539, *Integrated Diagnostics*. Supported through the Department of Defense (DoD) Multidisciplinary Research Program of the University Research Initiative (M-URI), this program was initiated to promote basic research in the technologies and methodologies of use in determining how mechanical failures occur, and how they can be detected, predicted, and diagnosed in real-time.

To accomplish the objectives set forth by the M-URI program, the MULTIUNIVERSITY CENTER FOR INTEGRATED DIAGNOSTICS was formed. Under the direction of Principal Investigator Ward Winer, Regents' Professor and Chair of the Woodruff School of Mechanical Engineering at Georgia Tech, research has been conducted by twenty (20) faculty associated with four schools from the Georgia Tech College of Engineering, three (3) faculty from Northwestern University, and eight (8) from the University of Minnesota. Dr. S. Ramalingam and Dr. William Robbins of the University of Minnesota, and Dr. Jan Achenbach of Northwestern University are the Subgrant Principal Investigators for their respective schools. Georgia Tech's Richard Cowan serves as the Center's Program Manager.

Using material, load, and vibration information from critical rotorcraft components, experiments have been designed and conducted so as to collect information of relevance in understanding the mechanisms of failure for use in developing failure models. These models can serve as a guide in the selection and development of sensors to detect faults and pending failures. Effort has been placed on micro-sensor development, and achieving the means to analyze and correlate reliable sensor output for remaining life estimation and operator use. Organizationally, this activity is being accomplished through thirteen (13) projects, categorized by three (3) thrust areas:

- Failure Detection and Identification (Nondestructive Evaluation).
- Failure Characterization and Prediction Methodology
- Machinery Health Monitoring (Direct Sensing, Analysis, Real-time Diagnosis).

The broad range of cross-disciplinary research topics addressed by the Integrated Diagnostics program has necessitated an effective communication network encompassing both the faculties and sponsors. A number of activities have been engaged to facilitate the flow of information including traditional publication channels, meeting presentations, monthly updates, partnerships, and electronic reporting (http://www.me.gatech.edu/diagnostics/). Of course, the primary mode of transfer is through students, who upon entering an engineering profession, will be trained in an aspect of integrated predictive diagnostics. During the past year, the program accommodated five (5) post-doctoral researchers, four (4) visiting researchers, thirty-eight (38) graduate students and six (6) undergraduate students.

1. INTRODUCTION

Office of Naval Research (ONR) Grant N00014-95-1-0539, *Integrated Diagnostics*, was initiated on March 1, 1995, following approval of a research proposal submitted to the Department of Defense Multidisciplinary Research Program of the University Research Initiative (M-URI). To accomplish the objectives set forth by the M-URI program, the MULTIUNIVERSITY CENTER FOR INTEGRATED DIAGNOSTICS was formed, supported by faculty and staff from the Georgia Institute of Technology, University of Minnesota, and Northwestern University.

1.1 MISSION

America's military machines (e.g., ships, aircraft, and land vehicles) are growing old. Many of the systems that are confidently relied upon today were designed and built twenty and thirty years ago. Given the present economic climate, replacement with next generation equipment can no longer be taken for granted. As a result, an expectation of keeping aging machines in service well beyond their intended design life has emerged, which has elevated concern that poor performance, inadequate safety, and increasingly expensive maintenance will result.

To respond to this technological challenge, pending failures must be identified before disastrous consequences occur. Incipient failures, however, are hard to locate, and current maintenance systems have limited capabilities to do so. Today's systems rely mainly on time-based inspection, which requires that parts be inspected at specified intervals, and be replaced when deemed unfit for service. A more effective and efficient alternative to time-based inspection is to continuously monitor critical components. This necessitates an understanding of *Integrated Diagnostics*, a term associated with the technologies and methodologies used to determine how mechanical failures occur, and how they can be detected, predicted, and diagnosed in real-time.

As shown in Fig. 1, a systematic approach has been implemented to enable innovative ideas to reach maturity with respect to mechanical system diagnostics and prognostics. Provided funding through the Department of Defense M-URI, a technical organization has been built to facilitate and combine the various disciplines required to generate the payoff of a system capable of being installed on a commercial or defense service vehicle. Researchers, representing a variety of engineering disciplines at the Georgia Institute of Technology, Northwestern University, and the University of Minnesota have been assembled, offering expertise with respect to material fatigue, fracture, nondestructive testing, sensors, and signal processing. To gain first-hand knowledge of the problems that maintenance personnel face, engineering support has been obtained through the Cherry Point Naval Aviation Depot. Additional experience has been made available through industrial partnerships.

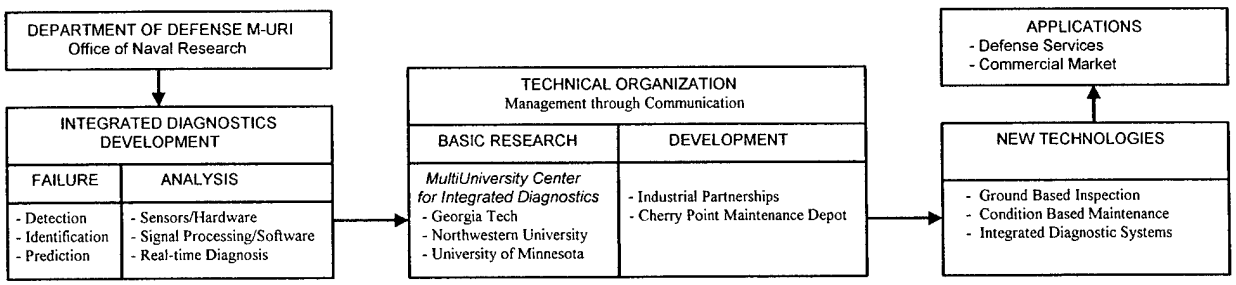

Figure 1. Technology Delivery

The MultiUniversity Center for Integrated Diagnostics is committed to perform studies associated with three major Integrated Diagnostic needs: the need to detect and identify incipient failures, the need to reliably predict the occurrence of failures, and the need to monitor the condition of a component or system in real-time. Organizationally, this has led to the formation of three research thrust areas, the objectives of which are defined below.

I. **Failure Detection and Identification (Nondestructive Evaluation)**: perform studies pertaining to deterioration mechanisms and techniques for detecting the initiation of fractures or other failures.

II. **Failure Characterization and Prediction Methodology**: perform studies pertaining to the methodology for failure prediction in real-time, including modeling fault initiation and failure signatures, and observing the propagation and fracture phases of fatigue-based failure.

III. **Machinery Health Monitoring (Direct Sensing, Analysis, Real-time Diagnosis)**: perform studies with respect to the responses of signals early in fault inception, including research on sensors that can be placed at critical sites on mechanical systems for responses to change in variables of state or vibration.

1.2 ORGANIZATION

To provide an overview of what is needed for developing the new technologies associated with integrated diagnostics, Fig. 2 is offered. This basic research "delivery system" begins through the understanding of Department of Defense *(DoD) needs* and is ultimately cultivated to produce payoffs in *decision technology*. The MultiUniversity Center for Integrated Diagnostics has focused attention on *sensor development*, the results of which are of use in accomplishing the Center's mission in furthering the understanding of failure mechanisms through *fatigue characterization* and the ability to reliably address *flaw detection*. It is anticipated that such knowledge will further the development of the two major components needed for the advancement of diagnostic/prognostic technologies: *life estimation* and *real-time diagnosis*.

A technical organization built on effective management and efficient communication has been formed to facilitate and combine the various disciplines required to develop the needed scientific and engineering foundation outlined above. The participating faculty and staff, representing the Georgia Institute of Technology, Northwestern University, and the University of Minnesota, are recognized for their significant contributions with respect to structural fatigue, fracture, nondestructive testing, acoustics, ultrasonics, sensors, and signal processing. Integrated Diagnostics research has been carried out by twenty (20) faculty associated with four schools from the Georgia Tech College of Engineering, three (3) faculty from Northwestern University, and eight (8) from the University of Minnesota.

Studies were performed for the purpose of developing an understanding of the mechanisms of failure (through detection, identification, and prediction) and the means to detect, identify and analyze them (through sensors/hardware, signal processing/software, and real-time diagnosis). Sections 2 and 3 of this report summarize the accomplishments obtained by the financial commitment made through the M-URI Program.

Program Organization Diagram

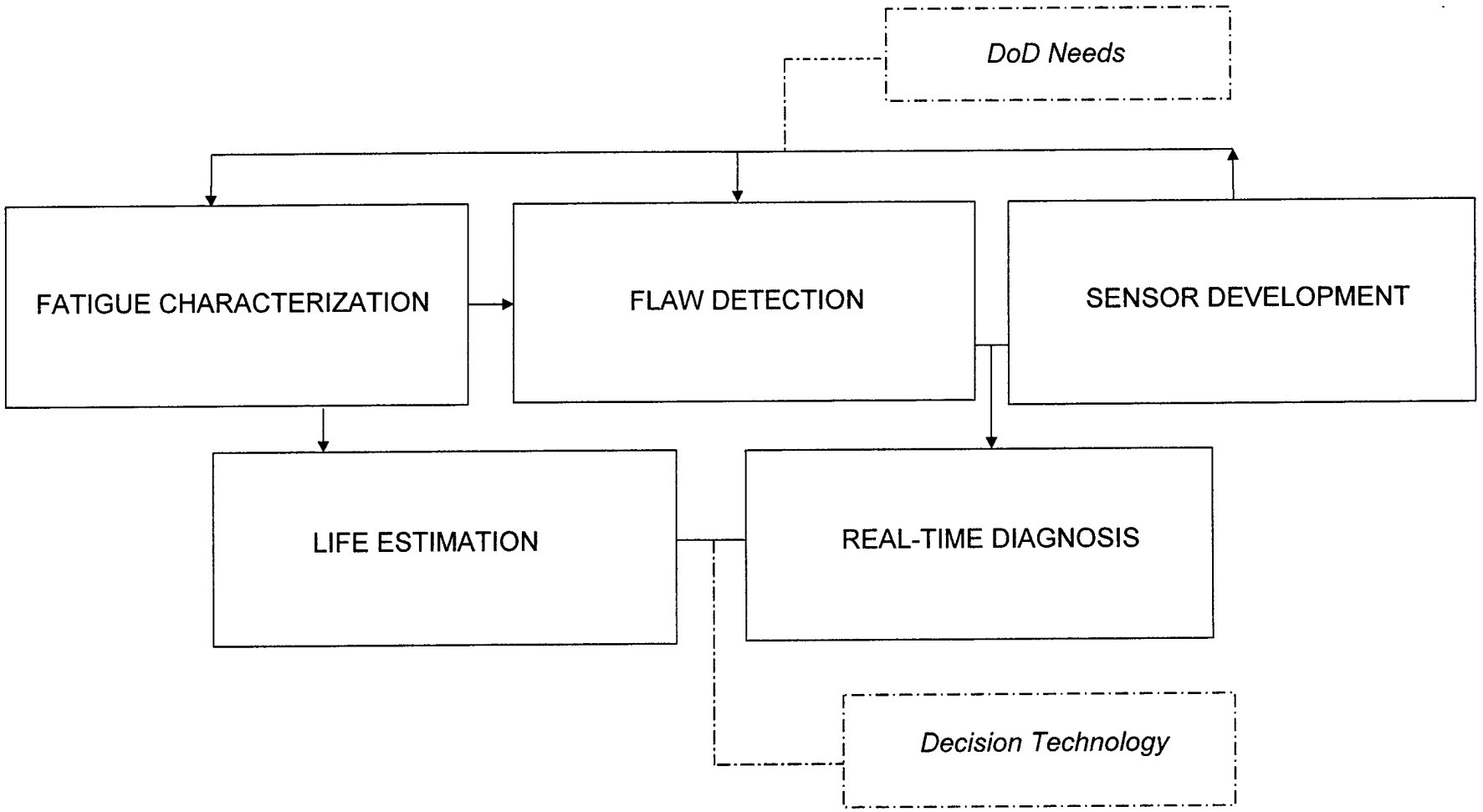

Figure 2

2. RESEARCH ACCOMPLISHMENTS

The MultiUniversity Center for Integrated Diagnostics is focused on providing a meaningful program of research for use in developing technologies to minimize the impact and or occurrence of *critical failures* in mechanical systems, including vehicle platforms and machinery. In the predictive maintenance community, a failure is identified as critical when it results in serious injury, loss of life, and or significant financial burden.

As discussed in Section 1, a cross-discipline team has addressed an assortment of projects, organized according to thrust areas that overlap in responsibility. This enabled the faculty and staff to focus on a particular predictive diagnostic need, while maintaining an awareness of the progress achieved through the overall program.

Experiments based on material, load, and vibration information from critical rotorcraft components were designed and conducted so as to collect data of relevance in understanding the mechanisms of failure for use in developing failure models. These models can serve as a guide in the selection and development of sensors to detect faults and pending failures. Effort has been placed on micro-sensor development, and achieving the means to analyze and correlate reliable sensor output for operator use.

The following pages summarize the achievements made in advancing the state-of the-art through predictive diagnostic research. Project titles, associated with a particular thrust area, are identified below with a list of significant milestones. These projects are similarly grouped by focus with their respective report section number in the organization diagram of Fig. 3.

Thrust I. Failure Detection and Identification (NDE)

1.1 Flaw Detection and Characterization using Ultrasonics

- Developed a compact fiberized laser-based system for remote nondestructive inspection. It was successfully applied to the detection of various surface-breaking and subsurface defects.
- Developed a Scanning Laser Source (SLS) technique for defect detection, offering (i) enhanced signal-to-noise performance when compared to the conventional pitch-catch mode of operation, (ii) a process that can be used with either a laser interferometer or a conventional PZT sensor, (iii) the ability to detect small defects of various orientations with respect to the scanning direction, and (iv) the ability to inspect surfaces of complex geometry.

1.2 Crack Detection by Guided Waves

- Demonstrated the detection of small crack growth (80 microns) in a notched specimen using 5 MHz guided Rayleigh surface waves and wavelet-based signal analysis.
- Developed and applied finite element models with visualization software to study the influence of radial cracks in a cylindrical component on a guided ultrasonic wavefield.
- Developed, validated and applied dispersion relationships (steady-state) that govern the propagation of guided circumferential waves, of use in determining which modes are effective in locating and sizing cracks that develop at the interfaces of layered cylinders.
- Developed two methodologies for sizing cracks in plates and cylinders. One uses Auld's Formula to relate scattered energy to crack length. The second uses dispersion curves developed with time-frequency representations.
- Developed a crack location scheme based on the reassigned spectrogram, shown to effectively characterize multimode Lamb waves.

1.3 Eddy Current Microsensors for Integrated Diagnostics

- Developed and applied eddy current microsensors mounted in "pencil-probes" using a 3-axis CNC machine to inspect a model part. The path control algorithm was derived directly from CAD software used for part description (Pro-E software).
- Fabricated flexible, disposable sensors (16 mm sq. and 4 mm sq.) used in producing cylindrical mesh coil sensors for internal surface inspection (e.g., blade slot inspection in turbine discs and rotors).
- Verified performance of large diameter (5.5 mm) mesh coil sensors and small diameter cylindrical sensors (constructed as partial cylindrical sensors). Configured these mesh coil sensors for rapid, single-pass, eddy current inspection of narrow slots as in turbine rotors (blade root, X-mas tree slots).
- Achieved separation of flaw localization and flaw imaging tasks with novel sensors to reduce total eddy-current inspection time.

1.4 Sensing Acoustic Emission and Transmission

- Manufactured and tested high-fidelity PZT sensors that enable point detection and generation of acoustic signals on curved surfaces and at locations of limited space.
- Designed, assembled and tested a system for measuring ultrasonic transmission through bearing balls for the purpose of detecting sub-surface cracks.
- Developed an optical fiber sensor designed to measure in-plane (tangential) surface motion using acoustic emission signals.

Thrust II. Failure Characterization and Prediction Methodology

2.1 Structural Fatigue Investigation

Stress Analysis and Stress Intensity Factor Solutions for Cracks

- Developed a numerical simulation post-processor for the visualization of stress fields in complex 3D components (e.g., helicopter rotorhub).
- Developed and validated an algorithm (AutoCrack) as an add-on tool for commercially-available finite element codes that modifies model geometry for each increment of crack growth.

Experiments and Modeling of Crack Growth

- Developed a unique multiaxial fatigue model based on the propagation of small cracks spanning the low & high cycle fatigue regimes. The model includes interaction with the strongest microstructure barrier (fatigue limit), amplitude and stress state sequence effects, and normal stress to crack plane effects. Conducted axial-torsional fatigue experiments on AISI 304 stainless and 1045 steel to validate the sequence effect capabilities of the model.
- Performed novel computational cyclic crystal plasticity calculations for determining the distribution of driving force parameters in a polycrystal under high cycle fatigue, and the mixed-mode behavior of cracks with length on the order of grain size as a function of stress amplitude and stress state.
- Characterized the crack nucleation and early crack growth of PH 13-8 Mo stainless and 4340 steel subjected to fretting fatigue. Linked acoustic emission signals with specific damage accumulation mechanisms.
- Evaluated a number of critical plane theories in light of fretting fatigue test results, and determined which are applicable to the rotorcraft steels under investigation. Determined that the influence that contact geometry has on crack growth may not be as significant as the influence that other fretting fatigue parameters have.
- Developed a database for evaluating the growth of small cracks in PH 13-8 Mo stainless steel. Investigated the influence of varying loads and salt water (as experienced in service) on small crack growth.

Damage Characterization and Remaining Life Estimation

- Demonstrated through nanoindentation measurements that crack growth of 4340 steel subjected to low-cycle fatigue (representative of helicopter components) is heavily influenced by microstructure.
- Identified the mechanism by which fatigue damage evolves in PH 13-8 Mo stainless steel through observations using atomic force microscopy (AFM). Results show a direct correlation between fatigue surface damage and microstructure, viz., from the early formation of surface streaks to the development of extrusions and the eventual nucleation of a fatal crack.
- Completed critical assessment of detection technologies and probabilistic prognostic tools for determining remaining life, proposing a first generation approach to be implemented by MATLAB.

2.2 Fatigue Reliability

- Determined that accurate fatigue reliability calculations for problems in three-dimensional fracture (with multiple random variables) can be addressed using the developed Limit State Surface Element method.
- Developed techniques for mixed-mode stress intensity factor evaluation along non-planar 3-D crack fronts.
- Developed an extended finite element method (X-FEM) for 3-D crack simulation using level set and fast marching techniques.

2.3 Study of Acoustic Emission and Transmission from Incipient Fatigue Failure

- Developed a robust, quantitative, waveform-based testing procedure to quantify acoustic emission signals from test samples experiencing torsion fatigue and fretting fatigue. Interpreted these signals with a combination of mechanics-based methodologies (e.g., finite element analysis) and advanced laser-based signal processing techniques.
- Developed and applied transfer functions to remove the effects of specimen geometry and transducer response (e.g., ringing) on acoustic emission waveforms.
- Related waveform characteristics from measured acoustic emission signals to specific deformation and damage phenomena in steel samples under investigation.

2.4 Acoustic Emission Modeling for Integrated Diagnostics

- Identified that the phase of loading amplitude is a key parameter in analyzing acoustic emission data as a function of the state of damage or age of a material subjected to fatigue.
- Developed a technique for categorizing acoustic emission data based on covariance processing.

Thrust III. Machinery Health Monitoring (Direct Sensing, Analysis, Real-time Diagnosis)

3.1 Detection of the Precursor to Mechanical Seal Failure in Turbomachinery

- Developed a novel, ultrasonic method for the condition monitoring of mechanical seals.
- Demonstrated that actively generated ultrasonic waves can effectively detect the onset of seal face contact and indicate the degree of contact in a) gas seals, through steady state and transient tests on a demonstration gas seal, and in b) liquid seals, through bench tests and transient tests on a commercial seal (John Crane Type I) approved by the Navy for general shipboard use.

3.2 Real-time Monitoring and Controlling of the Dynamic Behavior of Mechanical Face Seals

- Demonstrated a means to detect face seal contact, as evidenced by high harmonic oscillations, using eddy-current proximity probes, on-line signal processing and the real-time display of orbit plots.
- Developed and experimentally validated a method to correct and augment the dynamic behavior of failing seals using closed-loop adaptive control without human intervention.
- Demonstrated that the developed seal monitoring system could be used to detect the presence of a cracked shaft upon which a seal is riding.

3.3 Dynamic Metrology as a Bearing Wear Diagnostic

- Established a web-based dynamic method for diagnosing bearing condition and predicting remaining life using self-tuning estimation techniques on data obtained from multiple sensors (including contact potential difference probes, electromagnetic probes, acoustic emission sensors and accelerometers), statistical analysis of prognostic error margin, and signal source modeling of bearing defect vibration.

3.4 Integrated Microsensors for Aircraft Fatigue and Failure Warning

Microsensors

- Developed a miniature acoustic emission sensor with on-board amplification. The overall package size is 5-mm thick, with a 6-mm square footprint. The sensor bandwidth is about 50 kHz to 1 MHz.
- Designed, fabricated and tested a vibration monitoring microcantilever beam using piezoelectric thin films using PZT. The sensor is about 2-mm square with a sensitivity of 100 microvolts per G. The frequency response is flat to approximately 3 kHz.
- Designed a multi-sensor coupon (approximately 1.5 cm square and 6-mm thick) containing a temperature sensor, vibration sensor and acoustic emission sensor with on-board electronics for combining the sensor signals into one channel for transmission via a single, miniature coax cable.

Signal Processing

- Improved upon the understanding of differentiating acoustic emission (AE) signals and steady state/transient noise. Developed a number of algorithms for a) the detection of small transient signals in noise, when only approximate signal and noise characteristics are known, b) the mitigation of the distortion of acoustic emission signals due to their propagation and sensing, and c) the classification and dynamic characterization of detected events measured by multiple sensors.
- Tested, tuned and refined developed data reduction and classification algorithms using principal component analysis, self-organizing map neural networks, and vector quantitization.
- Applied algorithms using data obtained from controlled nano-indentation experiments, on-ground and in-flight helicopter trials provided by Honeywell, Inc., and fatigue experiments performed at Georgia Tech and Northwestern University to study fatigue crack initiation and growth.

3.5 Modal Parameter Extraction from Structural Diagnostic Signals

- Developed a mode isolation algorithm and automated methodology for modal parameter extraction of use in detecting changes in the dynamic characteristics of a component prior to failure. The algorithm is a state space modal formulation, which accounts for systems that contain arbitrary damping and gyroscopic effects.
- Demonstrated that the mode isolation method provides more accurate modal parameter estimations with noisy data than the Eigensystem Realization Algorithm (ERA) and Enhanced ERA.

Program Organization Diagram

Section number identified in parentheses

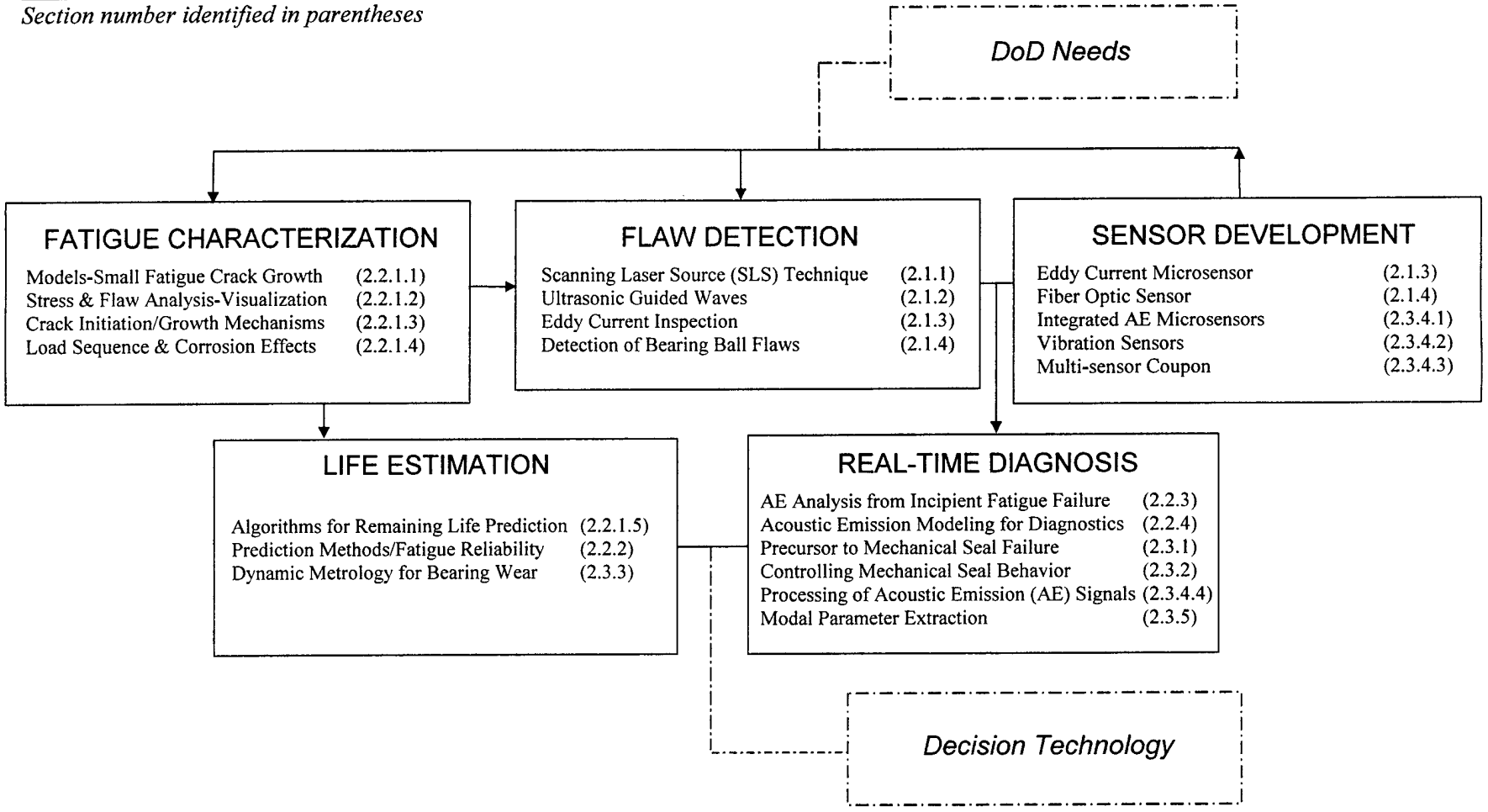

Figure 3

Thrust Area I

2.1 FAILURE DETECTION AND IDENTIFICATION (Nondestructive Evaluation)

Perform studies pertaining to deterioration mechanisms and techniques for detecting the initiation of fractures or other failures.

2.1.1 FLAW DETECTION AND CHARACTERIZATION USING ULTRASONICS 13
Overview 13
Objectives 13
Achievements 13
Future Research 16
M-URI Publications 16

2.1.2 CRACK DETECTION BY ULTRASONIC GUIDED WAVES 18
Overview 18
Objectives 18
Achievements 18
Future Research 22
M-URI Publications 26

2.1.3 EDDY CURRENT MICROSENSORS FOR INTEGRATED DIAGNOSTICS 28
Overview 28
Objectives 28
Achievements 28
Summary 41
M-URI Publications 42

2.1.4 SENSING ACOUSTIC EMISSION AND TRANSMISSION 43
Overview 43
Objectives 43
Achievements 43
Future Work 48
M-URI Publications 48

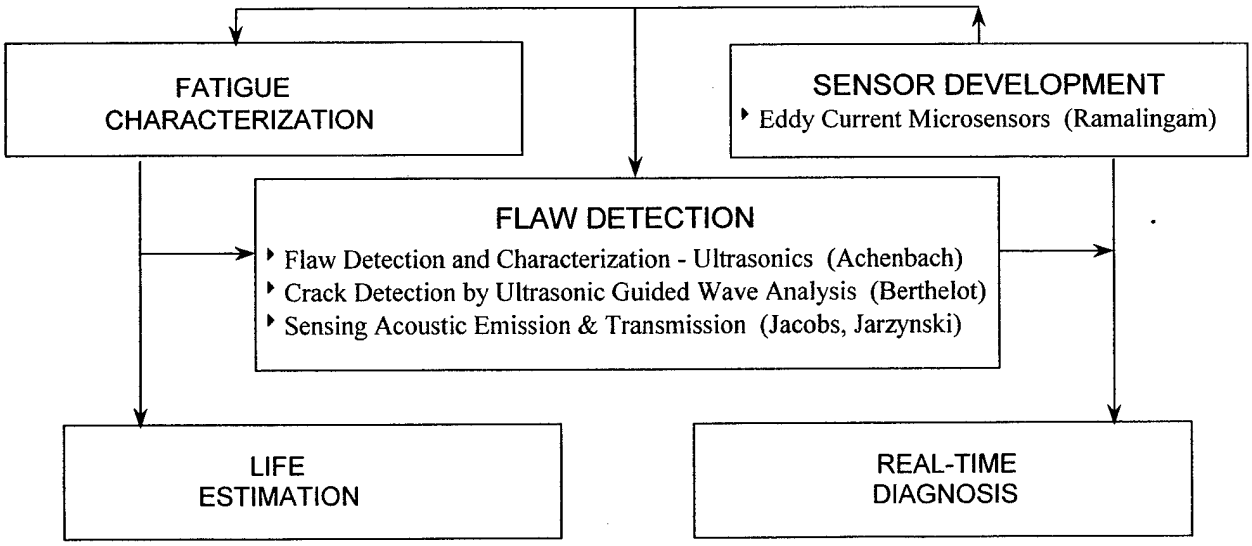

2.1.1 FLAW DETECTION AND CHARACTERIZATION USING ULTRASONICS

Co-investigators: Jan D. Achenbach and Alexei Kromine (Northwestern University)

OVERVIEW

Laser-based ultrasonic (LBU) methods provide a number of advantages over conventional ultrasonic techniques (non-contact, higher spatial resolution, curved surfaces applications, hard-to-access areas, ability to generate both narrowband and broadband ultrasound, scanning ease, ability to operate at high temperatures and in a hostile environment). Fiber delivery is the most attractive feature of LBU for practical use. Fiber delivery allows access even to internal components, requiring only the space of a few millimeters in diameter for the passage of optical cables.

When this project was initiated, there was a need for equipment to generate and detect ultrasound in locations of limited access such as small diameter holes in components or notches with high curvatures. The laser-based ultrasonic system developed in this project, and the related techniques of signal generation and detection are providing suitable methods for cracks detection in small holes and notches.

OBJECTIVES

- to design portable, reliable and completely fiberized non-contact ultrasonic devices for field applications;
- to develop an ultrasonic technique for the in-situ detection and characterization of flaws in components of complicated structures without disassembling or physically touching the component.

ACHIEVEMENTS

A laser system for ultrasound generation and detection with a flexible fiber delivery using a Big Sky Laser and employing a Sagnac interferometer or conventional piezoelectric transducers (PZT) for detection was designed, manufactured and tested. The combined system is compact and portable, and can be used for field applications.

A new approach for detection of surface-breaking and internal defects has been invented and applied. The approach is called the scanning laser source (SLS) technique. It does not monitor the interaction of a well-established ultrasonic wave with a defect, as in the case of traditional pitch-catch or pulse-echo methods, but rather monitors the changes in the generated ultrasonic signal as the laser source passes over the area of inspection. Changes in amplitude and frequency of the generated ultrasound are observed which result from the changed conditions under which the ultrasound is generated when the source passes over a small crack. These changes are quite readily detectable using laser interferometers or conventional PZT transducers.

The main advantages of the proposed SLS technique are (i) enhanced signal-to-noise performance compared to the conventional pitch-catch mode of operation, (ii) ability to detect defects smaller than the ultrasonic wavelength, (iii) ability to detect defects of various orientations with respect to the scanning direction, (iv) the procedure can be used with either a laser interferometer or a conventional PZT for measurement of the generated ultrasonic signals, and (v) ability to inspect surfaces of complex geometry such as bore holes and turbine disk slots.

A scanning laser source technique has been applied and evaluated for detection of various small surface-breaking and sub-surface defects. The technique provides distinct flaw signatures for small defects on flat and curved surfaces, and thin plates.

An ultra-compact and low cost YAG:Nd laser had been used as an ultrasonic source for a number of applications. The use of this laser provides a significant increase of the efficiency of inspection.

Scanning Laser Source Technique

The SLS technique has been successfully applied to a turbine disk specimen (provided by Allied Signal, Inc.) containing small EDM notches (0.75 mm length, 0.38 mm depth and only 0.05 mm in width). The turbine disk, made from titanium alloy Ti6Al4V, has a complicated surface geometry and allows only limited access to the inspection surface (see Figure 1a). Ultrasound generation was provided by a 200 μm fiber mounted in a cylindrical holder, which was rotated with an angular step of 1° to scan the laser point source over the investigated area. In a separate experiment, a fiber with a 45^{0} angled tip was used to deliver a laser beam to the area of inspection inside the slot. The advantage of the latter is an ability to reach places through extremely small (less than 0.3 mm) holes or other spaces. The detection of ultrasound was carried out by a PZT attached to the easy-to-access surface of the specimen.

It was found, that cracks can be detected by monitoring the amplitude of the measured ultrasonic signal. The amplitude shows a typical variation when the SLS approaches the crack due to: (i) the interference of the incident ultrasonic wave with an ultrasonic wave reflected from the defect when the laser source is close to the crack and (ii) the change of conditions of generation when the laser source is moving over the crack. A typical view of the scan curve is shown in Figure 1b.

A miniature and low-cost laser source (called Nanolase®) was also successfully used for detection of surface-breaking EDM notches in turbine disks (see Figure 2). A special rotary mount was used to hold a 50 μm core fiber. A positioning system allows scanning in the area of inspection with at least 5-10 μm resolution.

It was found that small sub-surface defects (a hole of 0.3 mm diameter at a depth of 0.25 mm from the surface of inspection) can not be detected in pulse-echo or pitch-catch modes of operation using standard 5 MHz PZT transducers. It was found, however, that the measured ultrasonic amplitude is significantly higher for the case when the SLS is just above a sub-surface defect, in comparison with the case of no defect. The main disadvantages of the earlier developed SLS technique are a low repetition rate, a long pulse duration and a high energy of the Big Sky Laser®, which is a more expensive, large and sophisticated device.

In recent experiments, a 50 μm core multimode fiber was used to deliver 3 μJ energy pulses from a NanoLase® to the inspected surface of a flat specimen with a sub-surface defect (see Figure 3a). A 5 MHz PZT mounted on a 90° wedge was attached to the specimen in order to measure changes of the laser ultrasonic generation, when the SLS passes over the defect.

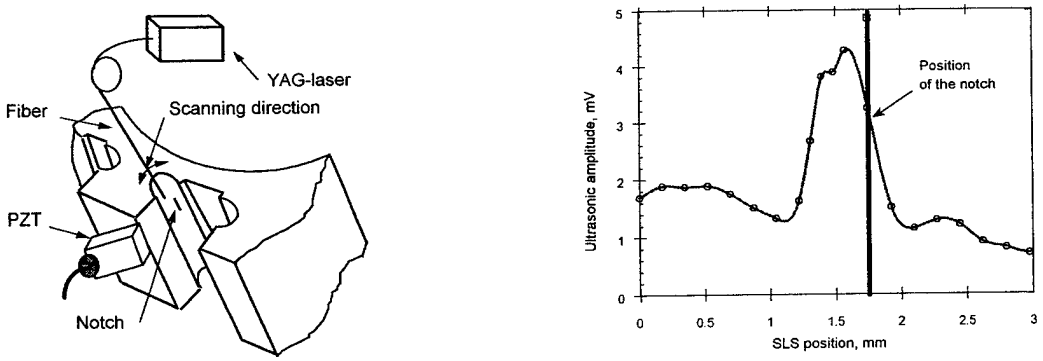

(a) (b)

Figure 1. **(a)** Schematic illustration of the SLS approach applied to the detection of a flaw on the curved surface of a turbine disk slot, **(b)** a typical scan curve for the amplitude of the ultrasonic signal.

A typical amplitude curve for the scan across the small sub-surface defect is shown in Figure 3b. Note that in addition to the central area over the defect, where the laser-generated ultrasonic amplitude is significantly higher than for the case of no defect, there are two side regions, where the amplitude is lower. It is expected that this behavior of the scanning curve can be explained by constructive and destructive interference of ultrasonic waves, when the source is above and at some distance from the defect axis, respectively.

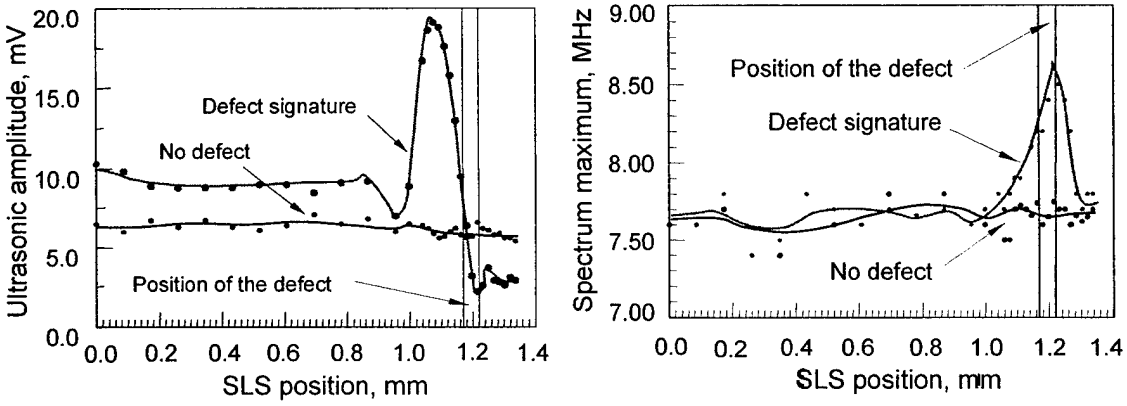

(a) (b)

Figure 2. Flaw signatures for an EDM notch of 0.75 mm length, 0.05 mm width and 0.375 mm depth: **(a)** amplitude curves, and **(b)** spectrum maximum curves.

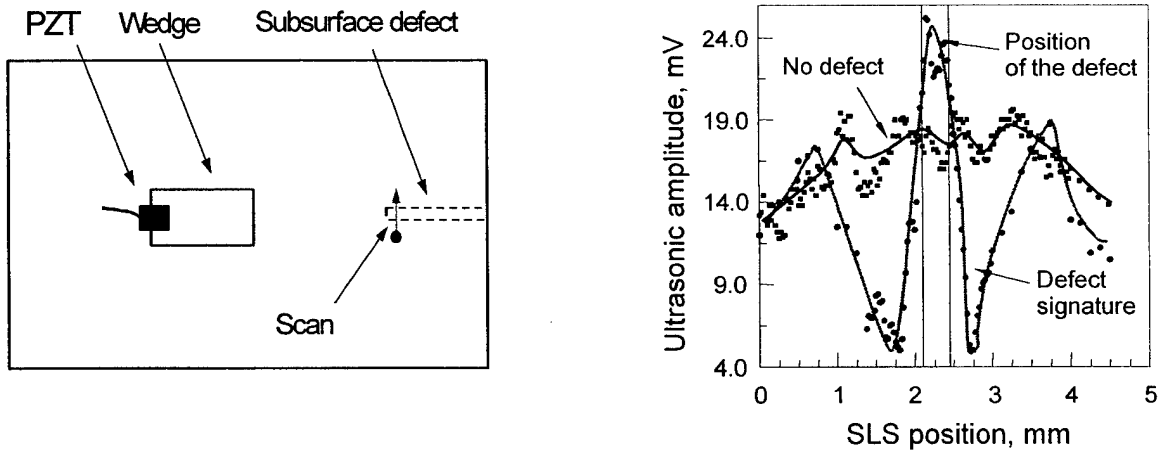

(a) (b)

Figure 3. (a) Schematic of the experiment, and (b) typical amplitude curves for the scan across a small sub-surface defect, and for the case of no defect.

FUTURE RESEARCH

- to develop a theory of interaction of the SLS generated signal with various surface-breaking and subsurface defects;
- to manufacture and test an automatic scanning system employing the SLS technique;
- to explore further applications of the laser-based ultrasonic system for the detection of flaws in limited-access locations and surfaces of high curvature, for various structures of interest.

M-URI PUBLICATIONS

1. L.S.Wang, J.S.Steckenrider, and J.D.Achenbach, "A Fiber-Based Laser Ultrasonic System for Remote Inspection of Limited Access Components", in *Review of Progress in Quantitative Nondestructive Evaluation*, (D.O.Thompson and D.E.Chimenti edition), Plenum Press, New York, Vol. 16A, 1996, pp.507-514.
2. P.Fomitchov, S.Krishnaswamy, and J.D.Achenbach, "Sagnac Interferometer for Ultrasound Detection on Rough Surfaces", in *Proceedings of 8th International Symposium on Nondestructive Characterization of Materials*, Boulder, CO, June 15-20, 1997.
3. L.S.Wang, P.Fomitchov, A.Kromine, S.Krishnaswamy, and J.D.Achenbach, "A Portable Laser-Based Ultrasonic System for the Inspection of Aging Aircraft Structures", in *Proceedings of the 1st DOD/FAA/NASA Joint Conference on Aging Aircraft*, Ogden, UT, July 8-10, 1997.
4. P.A.Fomitchov, A.K.Kromine, S.Krishnaswamy, and J.D. Achenbach, "Application of a Sagnac Interferometer for the Characterization of Scattered Ultrasonic Fields", in *IEEE Ultrasonics Symposium Proceedings*, Vol.1, 1997, pp. 609-612.
5. P.A.Fomitchov, A.K.Kromine, S.Krishnaswamy, and J.D.Achenbach, "Characterization of Laser Ultrasonic Sources Using a Sagnac Interferometer", in *Review of Progress in Quantitative Nondestructive Evaluation*, (D.O.Thompson and D.E.Chimenti edition), Plenum Press, New York, Vol. 17A, 1998, pp.675-681.
6. J.D.Achenbach, B.Moran, and A.Zulfiqar, "Techniques and Instrumentation In Structural Diagnostics", in *Structural Health Monitoring: Current Status and Perspectives,* edited by F.-K.Chang, Technomic Publishing Co., Inc., 1997, pp. 179-190.
7. A.K.Kromine, P.A.Fomitchov, S.Krishnaswamy, and J.D.Achenbach, "Scanning Laser Source Technique and Its Applications to Turbine Disk Inspection", in *Proceedings of the 25th Annual Review of Progress in Quantitative Nondestructive Evaluation*, (D.O.Thompson and D.E.Chimenti edition), Kluwer Academic/ Plenum Publishers, New York, Vol. 18A, 1999, pp.381-386.
8. P.A.Fomitchov, S.Krishnaswamy, and J.D. Achenbach, "Intrinsic Fiber Optic Sagnac Ultrasound Sensor for Process Monitoring in Composite Structures", in *Proceedings of SPIE*, Vol. 3589, pp. 156-159, 1999.
9. A.K.Kromine, P.A.Fomitchov, S.Krishnaswamy, and J.D.Achenbach. "Laser Ultrasonic Detection of Surface-Breaking Defects: Scanning Laser Source Technique ", in *Materials Evaluation*, Vol. 58, N°2, February 2000, pp.173-177.
10. P.A. Fomitchov, A.K. Kromine, S.Krishnaswamy, and J.D. Achenbach, "Sagnac-Type Fiber-Optic Array Sensor For Detection Of Bulk Ultrasonic Waves", in *IEEE Transactions on Ultrasonics, Ferroelectrics, and Frequency Control, UFFC-33*, Vol. 47, No. 3, 2000, pp. 584-590.

11. A.K.Kromine, P.A.Fomitchov, S.Krishnaswamy, and J.D.Achenbach. "Scanning Laser Source Technique for Detection of Surface-Breaking and Sub-Surface Cracks", in *Proceedings of the 26th Annual Review of Progress in Quantitative Nondestructive Evaluation*, (D.O.Thompson and D.E.Chimenti edition), American Institute of Physics Publishing, Melville, NY, Vol. 19A, 2000, pp.335-342.

12. A.K.Kromine, P.A.Fomitchov, S.Krishnaswamy, and J.D.Achenbach. "Applications of Scanning Laser Source Technique for Detection of Surface Breaking Defects", in Proceedings of The EOS/SPIE Symposium on Applied Photonics, May 22-24, 2000, Glasgow, Scotland, UK, *Proceedings of SPIE*, Vol. 4076, 34 (to appear in 2000).

13. P.A.Fomitchov, S.Krishnaswamy, and J.D.Achenbach, "Extrinsic and Intrinsic Fiber-Optic Sagnac Sensors for Ultrasound Detection", in *Optical Engineering*, Vol. 39, No. 7 (to appear in 2000).

14. A.K.Kromine, P.A.Fomitchov, S.Krishnaswamy, and J.D.Achenbach. "Detection of Sub-Surface Defects Using Laser Based Technique", in *Proceedings of the 26th Annual Review of Progress in Quantitative Nondestructive Evaluation*, (D.O.Thompson and D.E.Chimenti edition), American Institute of Physics Publishing, Melville, NY, Vol. 20A (to appear in 2001).

2.1.2 CRACK DETECTION BY ULTRASONIC GUIDED WAVES

Co-investigators: Yves Berthelot, Jianmin Qu, and Laurence Jacobs (Georgia Tech)
Postdoctoral Fellow: Guoli Liu
Graduate students: C. Valle, Z. Li, D. Cook, M. Niethammer, C. Eisenhardt, M. Kley, F. Moser

OVERVIEW

Inspection for fatigue cracks in a cylindrically shaped component, such as a helicopter rotor hub, is of prime importance. Such a component usually consists of (at least) an inner and outer cylinder, where fatigue cracks usually form at the interface between these two layers before growing in the radial direction. Currently, detection of such radial cracks relies mostly on visual inspection. Ultrasonic testing is one of the most widely used nondestructive evaluation (NDE) techniques in engineering practice. However, traditional ultrasonic techniques (such as pulse-echo) cannot be used to interrogate such parts because of problems associated with the curvature, the complicated nature of the reflected waveforms and difficult accessibility. Therefore, it is desirable to develop more reliable, accurate, and robust ultrasonic nondestructive methods to detect these cracks before catastrophic failure occurs. This is a critical missing link in determining remaining life and structural integrity of a component.

This research effort concentrates on using ultrasonic guided waves to inspect annular parts. Ultrasonic guided wave inspection is an *active* technique whereby an ultrasonic pulse is sent to interrogate a long path through the structure. A guided wave propagates in the axial direction of a layer, while behaving as a standing wave through the thickness of the layer. Guided wave ultrasonic methodologies have the advantages of being remote, of using the geometry of the layered cylinder to their advantage, and of being well suited to real-time analysis. Guided waves have been commonly used to interrogate simple geometries such as beams and plates. Unfortunately, guided *circumferential* waves in thick annular structures have received very little attention, so there is limited understanding concerning the mechanics of their propagation.

OBJECTIVES

The goals of this research are as follow: 1) to develop a quantitative understanding of the underlying principles of the propagation of guided circumferential waves in cylinders; 2) to optimize the generation of ultrasonic guided waves signals so they carry the maximum information about the integrity of the structure; 3) to concentrate wave energy on the interface to determine information about the wavefield scattered by radial fatigue cracks; 4) to develop a quantitative procedure capable of locating and sizing these radial cracks; and 5) to use guided surface waves to detect and size in real-time crack growth on a "hot spot" during high-cycle fatigue tests on steel samples and to compare ultrasonic estimates with optical measurements.

Prior to when this M-URI project was initiated in 1995, there was no literature on a reliable method to detect cracks in thick annular components. Ultrasonic guided waves had been successfully used for crack detection in plates, or in the axial direction of thin cylinders, but not in the circumferential direction of short, thick cylinders. The dispersion relationship for circumferential guided waves was unknown. The use of ultrasonic surface waves to detect surface-breaking fatigue crack growth at early stages in steel specimens under tensile cyclic loading had not been reported in the literature.

ACHIEVEMENTS

An analytical model that uses two-dimensional linear elasticity has been developed to construct the dispersion relationship for time harmonic, circumferential waves in (infinitely long) two-layered cylinders. This work uses potential functions that represent guided waves propagating in the circumferential direction, which is a natural extension of Lamb waves in a flat plate. The potentials are written in terms of Bessel functions of the first and second kind. The resulting system of six

homogeneous equations is written in matrix form, and the condition that the determinant of this matrix must vanish yields a characteristic equation that is solved numerically. The numerical solution involves selecting a specific (non-dimensional) wavenumber, and using a bisection root-finding scheme to solve the characteristic equation for the corresponding (non-dimensional) frequency. This procedure is used to develop the dispersion curves for the first several modes, as well as the displacement profiles in the radial and tangential directions. These results show that, at higher frequencies, the first mode asymptotically tends to a Rayleigh wave on a flat surface, while the second mode approaches a Rayleigh wave propagating along the interface. For example, Figure 1 shows the normalized radial displacement distribution along the radial direction. Journal articles [3-4] and [10] provide technical details of this procedure.

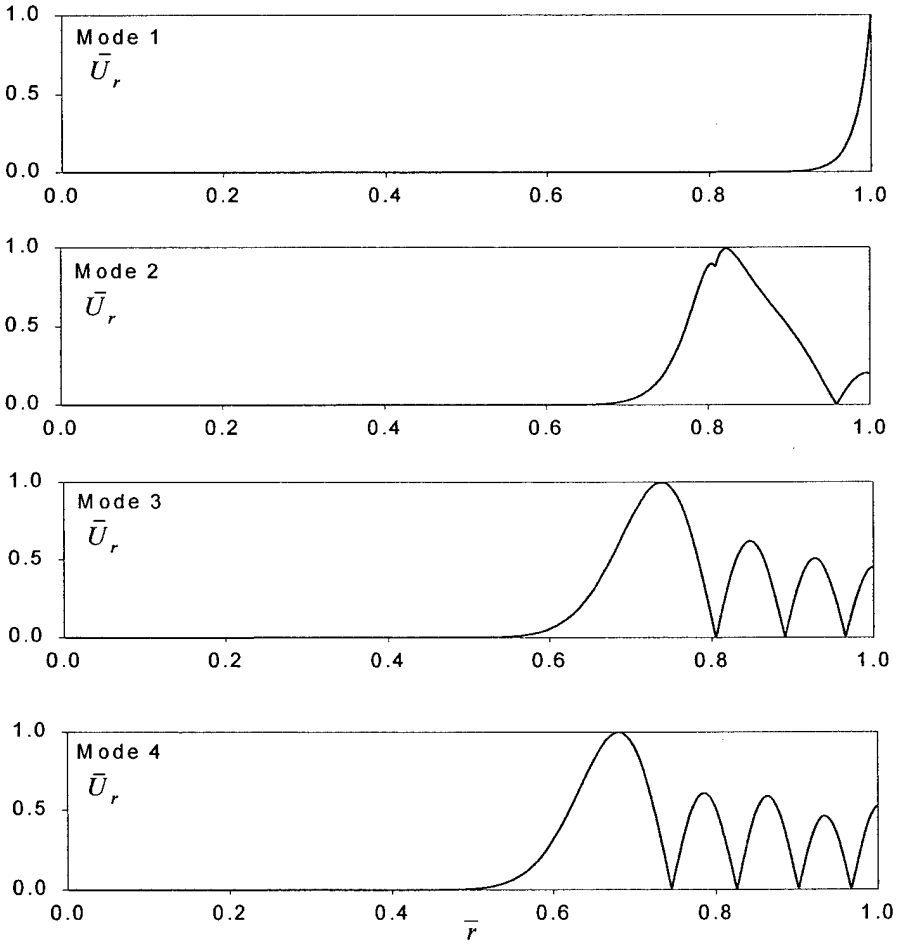

Figure 1. Normalized radial displacement distribution along the radial direction.

A time-domain solution has also been formulated for the transient excitation and propagation of circumferential ultrasound in a thick annulus, for the realistic case of generation and detection of ultrasound with angle-beam wedge transducers. The solution provides valuable information on the modal content of the detected signals and the radial dependence of the ultrasonic field within the waveguide. The model can be used to select the best possible parameters (transducer wedge angle, frequency, source-receiver positions) to detect cracks on the inner surface of the waveguide. Experimental results confirm the trends predicted by the model. In addition, mode identification and crack detection have been greatly facilitated by the use of the time-windowed, frequency band-limited, amplitude of the wavelet transform of the received signal. The technique has been used successfully to detect hidden cracks (3 mm machine made notches that would not be detectable by conventional ultrasonic technique) on a partially annular component of the pitch shaft of the H-46 helicopter. Figure 2 shows the signals received on such a part by a 2.25 MHz transducer in the send-receive mode, when the transducer was placed on a 30° wedge, at a distance of about 15 cm from the hidden crack. Wave propagation in a shaft/bearing assembly has also been investigated. The analytical/numerical model assumes that the interface is ideally lubricated. Under this assumption, it was found that waveforms are significantly affected by the presence of the shaft, a trend that was confirmed experimentally. Technical details can be found in journal article [25].

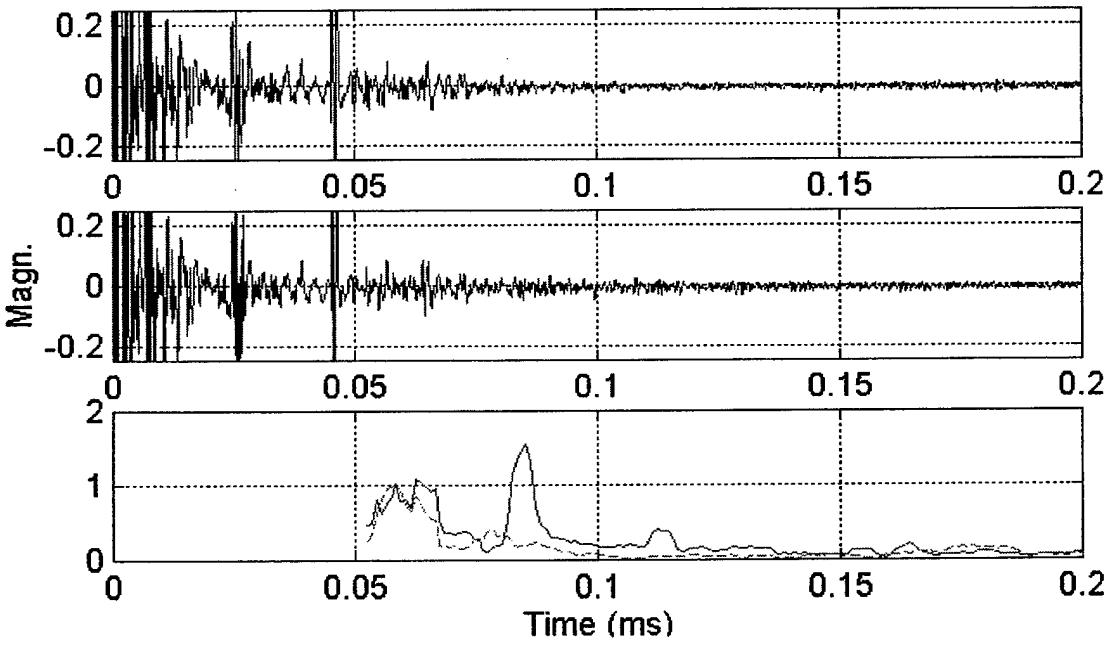

Figure 2. Received signals (arbitrary units) with a pulsed transducer (2.25 MHz)in the send-receive mode in the pitch-shaft of the H-46 helicopter. (a) without a crack, (b) with a 3 mm notch hidden on the inner surface of the cylinder at a distance of 150 mm from the transducer which is placed on a 30° wedge. The presence of the notch is clearly seen in (c) when plotting the squared wavelet transform of the signals, integrated between 2.0 and 2.5 MHz, over a sliding time-window of 0.01 ms.

A commercial finite element method (FEM) code, ABAQUS, has been used to model transient wave propagation in cylindrical components. This computational mechanics tool has been used to study the propagation characteristics of guided waves in annular structures. The effectiveness of using FEM methods has been clearly demonstrated for the case of guided wave propagation problems where an analytical solution is not possible because of complicated component geometry. Visualization software has been developed to demonstrate the robustness of FEM models and to understand guided wave propagation. The FEM code has been used to determine the optimum inclination angle for transducer wedge assembly to generate guided waves along the inner surface of a cylindrical component. Journal article [8] provides technical details of this procedure.

The theoretical and numerical predictions have been validated with experiments in which laser ultrasonic techniques were combined with the two-dimensional Fourier transform (2D-FFT) analysis to develop dispersion curves for Lamb waves propagating in an aluminum plate. This application demonstrates that, by combining the high fidelity, broad bandwidth, point source/receiver and the non-contact nature of laser ultrasonics with the robustness and accuracy of the 2D-FFT, it is possible to develop dispersion curves that contain more modes (through a broader bandwidth) than previously possible (see Figure 3). Journal article [13] provides technical details of this procedure.

Laser ultrasonic techniques were then used to develop a quantitative understanding of the underlying principles of the propagation of guided circumferential waves in two-layered cylindrical components. The high fidelity, broad bandwidth, point source/receiver and non-contact nature of these optical techniques were critical elements to the success of this work. The experimental procedure consisted of measuring a series of transient, circumferentially propagating waves in a cylindrical waveguide and then operating on these transient waveforms with signal processing techniques to develop the dispersion

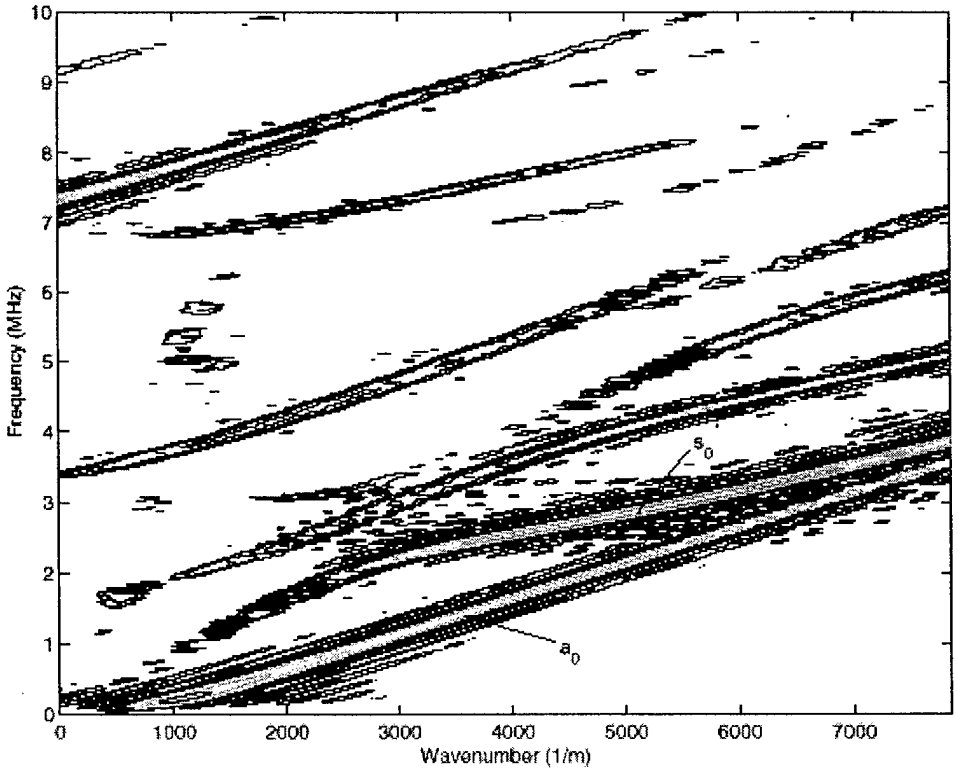

Figure 3. Dispersion curves for guided plate waves obtained with the 2D-FFT.

relationship for that waveguide. In this procedure, the steady-state behavior is found from a series of transient measurements. These dispersion curves are compared to theoretical values. There is good agreement between the experimental and theoretical results, thus demonstrating the accuracy and effectiveness of using laser ultrasonic techniques to study the propagation of guided circumferential waves. Journal article [11] provides technical details of this procedure.

The effectiveness of four different time-frequency representations (TFRs) to characterize guided ultrasonic waves were compared. The objective of this study was to compare four different TFRs (the reassigned spectrogram, the reassigned scalogram, the smoothed Wigner-Ville distribution and the Hilbert spectrum), in terms of their ability to resolve the dispersion relationships for guided plate waves generated and detected with optical techniques. This study illustrates the utility of using TFRs to quantitatively resolve changes in the frequency content of these nonstationary signals as a function of time. While each technique has certain strengths and weaknesses, the reassigned spectrogram is the best choice to characterize multimode guided ultrasonic waves. For example, Figure 4(a-b) compares the un-reassigned and the reassigned spectrogram for a 0.93 mm thick plate. Journal articles [18] and [20] provide technical details of this procedure.

The propagation of guided circumferential waves in a hollow isotropic cylinder that contains a crack was examined numerically with the goal of using these guided waves to both locate and size the crack. The crack is sized using a modified Auld's formula, which relates the crack's length to a reflected energy coefficient. The crack is then located by operating on the backscattered signal with a TFR digital signal processing (DSP) technique, and then by comparing these results to those obtained if the cylinder contained no crack. The guided circumferential waves are simulated with a commercial finite element method (FEM) code. One objective of this work is to demonstrate the effectiveness of using sophisticated DSP techniques to describe the effect of scattering on dispersive waves, showing it is possible to characterize cracks systematically and accurately by quantifying this scattering effect. The results show that the need for high frequency signals to detect small cracks is significantly decreased by using these techniques. Figure 5 shows the application of the reassigned spectrogram to locate a radial crack in a ring. Journal article [21] provides technical details of this procedure.

Finally, ultrasonic surface waves were successfully used to detect surface-breaking, fatigue crack growth at early stages (as small as about 40 microns in radius) in steel specimens under tensile cyclic loading with a pair of miniature 5 MHz transducers (Figure 6a). It was found that, for single cracks, the amplitude of the back-scattered signal is proportional to the square of the crack radius (Figure 6b). The short-time Fourier Transform (STFT) was successfully used to determine whether the back-scattered signal emanated from a single crack (high cycle fatigue) or from a distribution of small cracks (low cycle fatigue). In the experiment, the ultrasonic detection always preceded the optical detection with a long focal length microscope indicating the usefulness of the ultrasonic inspection technique. Technical detail can be found in a journal article [26]. The technique has been fully automated (using Labview and Matlab) to provide information on remaining life during a fatigue test.

FUTURE RESEARCH

- Refine methodologies capable of identifying multiple cracks
- Understand the effects of crack face roughness and contact, including nonlinear effects

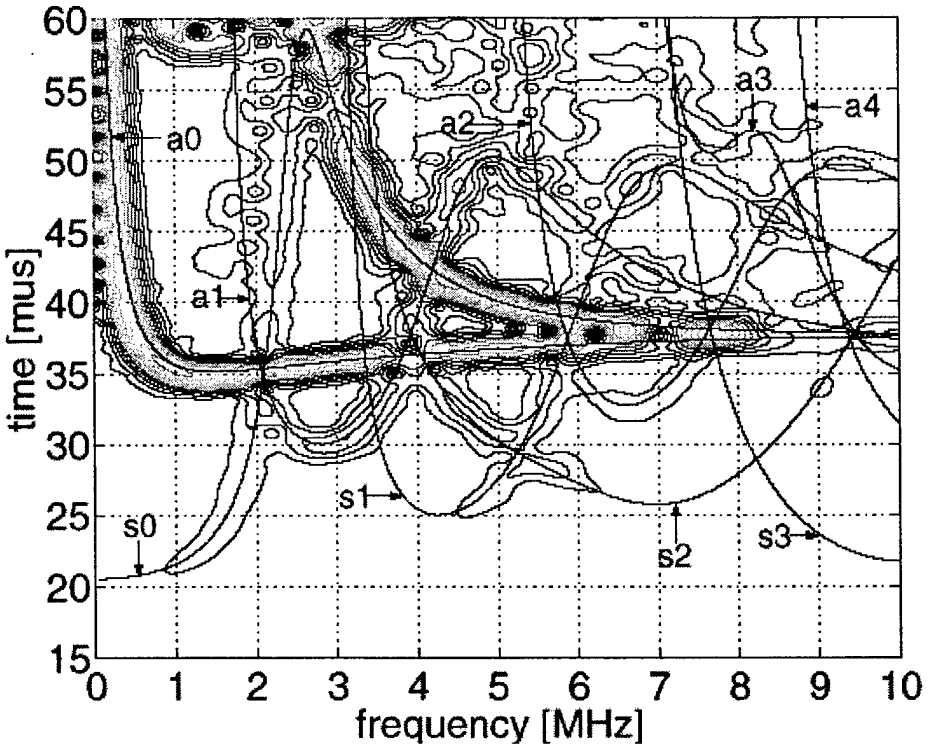

Figure 4a. Un-reassigned spectrogram for a 0.93 mm plate.

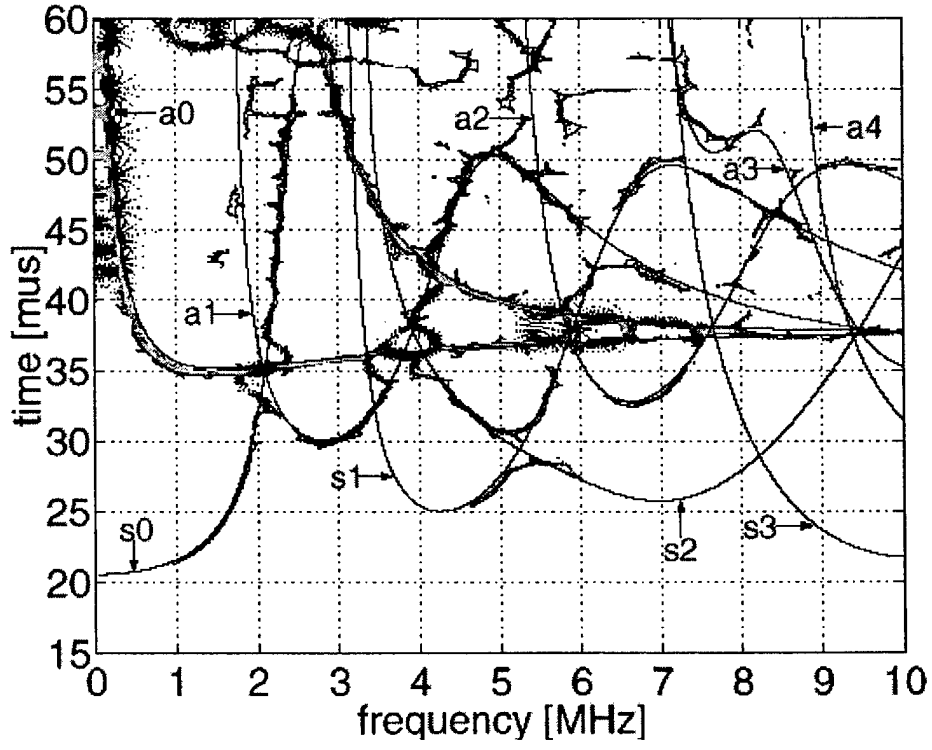

Figure 4b. Reassigned spectrogram, with improved time-frequency resolution.

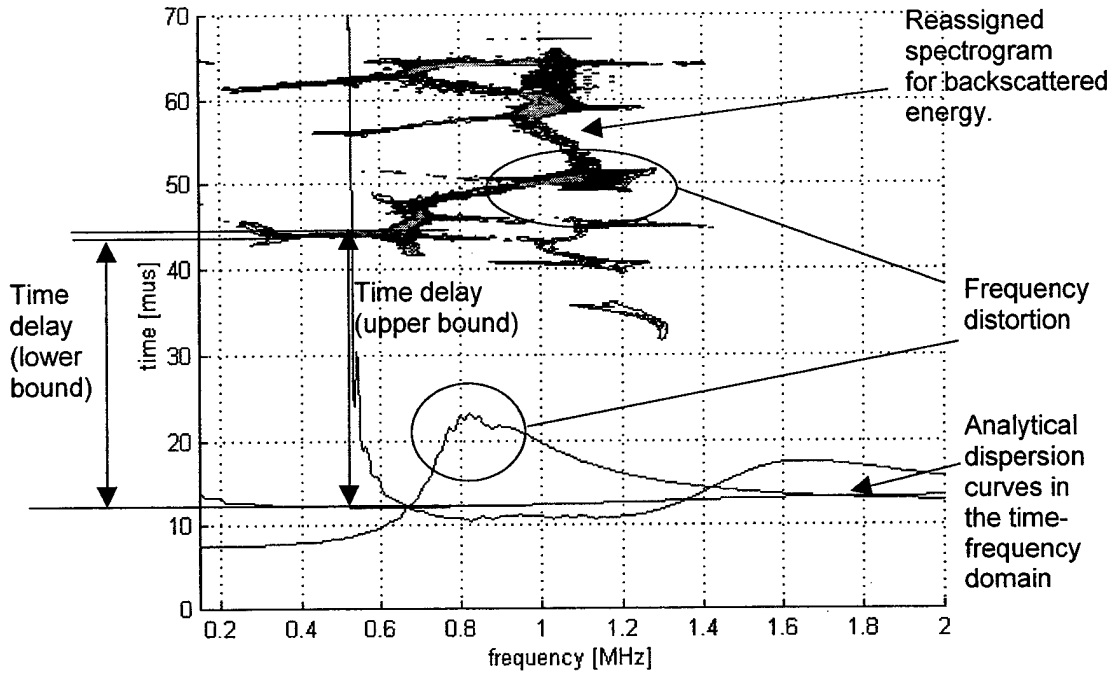

Figure 5. Methodology to locate the crack. Comparison between the reassigned spectrogram for the backscattered energy and the analytical dispersion curves in the time-frequency domain.

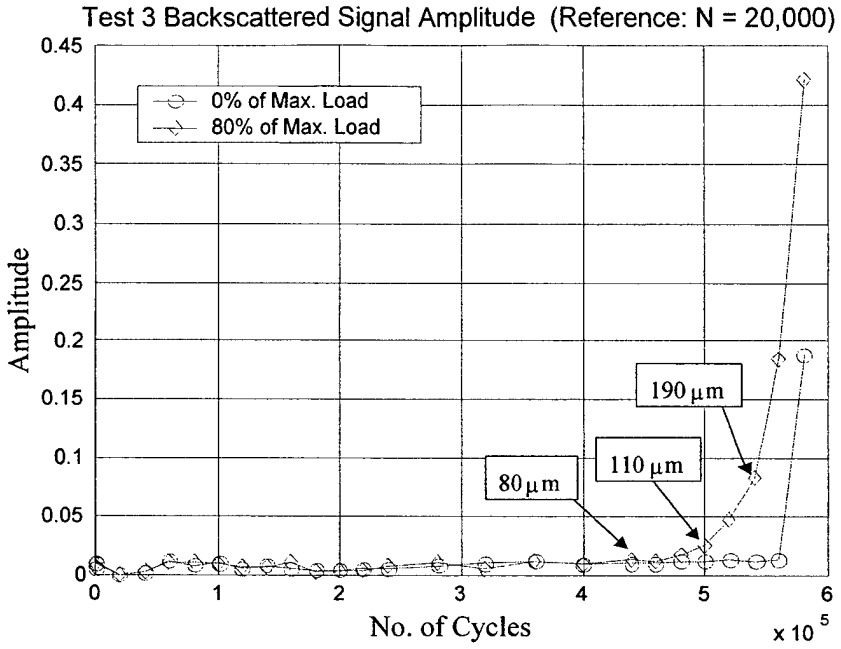

Figure 6a. Crack detection during a high-cycle fatigue test of AISI 4130 steel (flat bars 200 mm x 30 mm x 3 mm). Maximum stress amplitude 356 MPa, stress ratio of 0.1. Normalized backscattered signal as a function of elapsed cycles. The boxed numbers indicate the crack length (diameter) measured optically. The diamonds represent data taken at 80% of maximum load (open crack condition). The circles represent data taken at 0% load (closed crack condition).

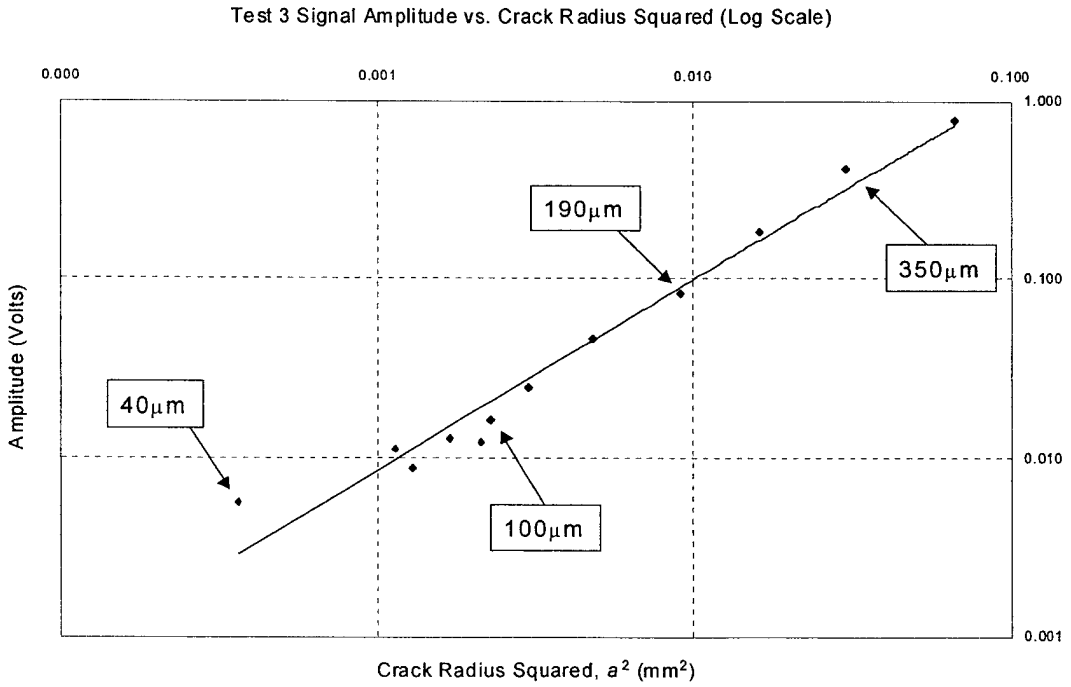

Figure 6b. RMS amplitude of the backscattered pulse as a function of the square of the crack radius.

M-URI PUBLICATIONS

[1] Qu, J., Berthelot, Y., and Li, Z., "Dispersion of Guided Circumferential Waves in a Circular Annulus," *Review of Progress in QNDE*, Vol. 15A, pp. 169-176, 1996.

[2] Li, Z. and Berthelot, Y. H. "Mode control of ultrasonic guided waves in thick cylinders for crack detection," J. Acoust. Soc. Am. 99, No 4, Pt 2, 2534 (1996). Presented at the 131th meeting of the Acoustical Society of America, Indianapolis, IN, May 1996.

[3] Liu, G. and Qu, J., "Guided Circumferential Waves in a Circular Annulus," *Journal of Applied Mechanics*, Vol. 65, pp. 424-430, 1998.

[4] Liu, G. and Qu, J., "Transient Wave Propagation in a Circular Annulus Subjected To Impulse Excitation on Its Outer Surface,", *J. Acoust. Soc. Am.*,Vol. 103, pp.1210-1220, 1998.

[5] Moser, F., Valle, C., Jacobs, L.J., and Qu, J., "Application of Finite Element Methods to Study Transient Wave Propagation in Elastic Waveguides," *Review of Progress in Quantitative NDE, Review of Progress in QNDE*, Vol. 17A, pp.161-167, 1998.

[6] Liu, G. and Qu, J., "Guided Transient Waves in a Circular Annulus," *Review of Progress in QNDE*, Vol. 17A, pp.153-160, 1998.

[7] Li, Z, and Berthelot, Y. H., " Propagation of transient ultrasound in a thick annulus: modeling, experiments, and applications to crack detection." *J. Acoust. Soc. Am.* 104, No 3, Pt 2, 1790 (1998). Presented at the 136th meeting of the Acoustical Society of America, Norfolk, VA (October 1998).

[8] Moser, F., Jacobs, L.J. and Qu, J, "Modeling of Elastic Wave Propagation in Waveguides with the Finite Element Method," *NDT&E International*, Vol. 32, pp. 225-234, 1999.

[9] Valle, C., Qu, J., and Jacobs, L., "On The Dispersion And Displacement Distribution of Circumferential Waves In a Composite Circular Cylinder," *Review of Progress in QNDE*, Vol. 18A, pp.247-254, 1999.

[10] Valle, C., Qu, J. and Jacobs, L.J., "Guided Circumferential Waves in Layered Cylinders," *International Journal of Engineering Science,* Vol. 37, pp. 1369-1387, 1999.

[11] Kley, M., Valle, C., Jacobs, L.J., Qu, J. and Jarzynski, J. "Development of Dispersion Curves for Two-Layered Cylinders using Laser Ultrasonics," *Journal of the Acoustical Society of America,* Vol. 106, No. 2, pp. 582-588, 1999.

[12] Qu, Jianmin, Berthelot, Y.H. and Jacobs, L.J., "Crack Detection in Thick Annular Components using Ultrasonic Guided Waves," *IMechE Journal of Mechanical Engineering Sciences,* accepted for publication, 1999.

[13] Eisenhardt, C., Jacobs, L.J. and Qu, Jianmin "Application of Laser Ultrasonics to Develop Dispersion Curves for Elastic Plates," *Journal of Applied Mechanics,* Vol. 66, No. 4, pp. 1043-1045, 1999.

[14] Valle, C., Qu, J. and Jacobs, L.J., "On the Dispersion and Displacement Distribution of Circumferential Waves in a Composite Circular Cylinder," *Review of Progress in QNDE,* Vol. 18A, pp. 247-254, 1999.

[15] Cook D. A.., and Berthelot, Y. H., "Detection of fatigue crack initiation and growth in steel specimens from Rayleigh scattering of 5 MHz Rayleigh waves," *J. Acoust. Soc. Am.* 106, No 4, Pt 2, 2168 (1999). Presented at the 138th meeting of the Acoustical Society of America, Columbus, OH (November 1999).

[16] Li, Z. and Berthelot, Y. H., "Modeling and experiments on the propagation of transient ultrasound in a thick annulus," *Review of Progress in QNDE,* Vol. 18A, pp. 231-238, 1999.

[17] Kley, M., Valle, C., Jacobs, L.J. and Qu, J., "Development of Dispersion Relationships for Layered Cylinders using Laser Ultrasonics," *Review of Progress in QNDE,* Vol. 18A, pp. 263-268, 1999.

[18] Niethammer, M., Jacobs, L.J., Qu, Jianmin, and Jarzynski, J., "Time-Frequency Representation of Lamb Waves using the Reassigned Spectrogram," *Journal of the Acoustical Society of America,* (Acoustics Research Letters Online) Vol. 107, No. 5, pp. L19-L24 (http://ojps.aip.org/jasa/), 2000.

[19] Valle, C., Niethammer, M., Qu, J. and Jacobs, L.J., "Crack Characterization using Guided Circumferential Waves," *Journal of the Acoustical Society of America,* submitted 2000.

[20] Niethammer, M., Jacobs, L.J., Qu, Jianmin, and Jarzynski, J., "Time-Frequency Representation of Lamb Waves," *Journal of the Acoustical Society of America,* submitted, 2000.

[21] Eisenhardt, C., Valle, C., Niethammer, M., Jacobs, L.J. and Qu, Jianmin "Effect of crack length on Laser-generated and detected Lamb waves," *Journal of Nondestructive Evaluation,* submitted, 2000.

[22] Niethammer, M., Jacobs, L.J. and Qu, J., "Application of STFT Techniques to Interpret Ultrasonic Signals," *Review of Progress in QNDE*, Vol. 19A, pp. 703-708, 2000.

[23] Valle, C., Qu, J. and Jacobs, L.J., "Scattering of Circumferential Waves in a Cracked Annulus," *Review of Progress in QNDE*, Vol. 19A, pp. 217-224, 2000.

[24] Eisenhardt, C., Jacobs, L.J. and Qu, J., "Experimental Lamb Wave Spectra of Cracked Plates," *Review of Progress in QNDE*, Vol. 19A, pp. 343-349, 2000.

[25] Li, Z. and Berthelot, Y. H., "Propagation of transient ultrasound in thick annular waveguides: modeling, experiments, and application to crack detection," *NDT&E International*, Vol. 33, pp. 225-232, 2000.

[26] Cook, D. and Berthelot, Y. H., "Detection of small surface-breaking fatigue cracks in steel specimens using 5 MHz Rayleigh scattering of Rayleigh waves," submitted to *NDT&E International*, August 2000.

2.1.3 EDDY CURRENT MICRO SENSORS FOR INTEGRATED DIAGNOSTICS

Co-investigator: S. Ramalingam (University of Minnesota)
Graduate Research Assistant: Zheng Shi

OVERVIEW

Flaw initiation and growth in a critical component of fixed and rotary wing flight systems can lead to catastrophic failure when a flaw within it reaches a critical size which depends on the stresses imposed during operation and the fracture toughness of the material used to make the part. On-board sensors may be used to monitor flaw initiation and growth in real-time from the energy release accompanying flaw growth. But, when such sensors are not available, critical components will require off-line inspection and condition monitoring for continued use.

A number of methods are available to detect larger flaws that can be readily repaired when detected. But, a major part of a critical component's life resides in the flaw initiation phase. Flaw length in this phase is several tens of microns in size. Skill and time-intensive inspection processes requiring highly trained operators are needed to reliably detect such small flaws when a flaw detection method is available. Flaws of this size typically lie below the detection limit of commercial eddy-current (EC) inspection systems.

Developing and implementing EC sensors compatible with eddy-current imaging and the automation of EC inspection can greatly lower the cost and the manpower requirements for off-line inspection of critical components. Inspection reliability may also be improved.

OBJECTIVES

A major goal of this project is to develop and demonstrate eddy current (EC) micro sensors with greatly improved spatial resolution so that EC inspection can extended to the flaw initiation phase of a component's life. Spatial resolution sought is 100 μm and less. A subsidiary goal is to make EC inspection objective to reduce the skill and training requirements for flaw detection, i.e., to eliminate subjective flaw identification methods now in use. Imaging techniques were sought so that the eddy current inspection practice can also be automated.

ACHIEVEMENTS

At the beginning of the M-URI program in Integrated Diagnostics, EC flaw detection/inspection relied on subjective interpretation of impedance plot measurements by skilled/well-trained inspection personnel. Reliable flaw detection was restricted to the flaw propagation phase of a component's life. Flaw detection in the initiation phase was not feasible.

The EC micro sensors developed have achieved sub-millimeter spatial resolution. Better than 100 μm resolution has been demonstrated with flux focusing Pencil Probes. Measurement methods devised have led to flaw imaging that has rendered the EC inspection objective. Pencil Probes have been developed that are compatible with EC inspection in 3-axis CNC systems, paving the way for robotic inspection. Path control algorithms needed for automated inspection are derived from the CAD software used for part design. All these make the need for highly trained manpower for off-line EC inspection much less critical.

a. Micro-Sensors for Eddy Current Flaw Imaging

As the flux available to detect changes in the AC magnetic field due to the presence of a flaw in a test object decreases with decrease in sensor dimensions, and since the excitation coil current used for EC inspection directly add to the sensor signals, flux focusing methods were developed to shield and enhance the flaw signals sensed by EC micro sensors.

Flux focusing concepts were verified in the early part of the ONR/M-URI program using manually wound macro sensors. Geometry of the flux focusing EC sensor used for finite-element modeling is

shown in Figure 1. Digital flaw imaging methods were developed so that subjective flaw detection based on impedance measurements is replaced with 3-dimensional flaw imaging. A computer-driven, scanning stage for automated data acquisition was developed and commercially available, software was used to display the EC signals acquired for objective flaw imaging. Model flaws, created with electrical discharge machining (EDM) and drilling (cylindrical holes, slots and keyhole defects) were used to determine flaw resolution capabilities. The wound core (macro) sensors used were satisfactory for flux focusing and flaw imaging but the flaw resolution sought could not be obtained.

Photolithography techniques were then used to build single element and 4 x 4 array micro sensors. Single element EC micro-sensors, 1300 μm x 1300 μm in size, implemented in Silicon, showed that a flaw resolution of 100 μm is feasible. Spatial resolution of 100 μm was achieved and 3-D flaw images were constructed by scanning the test sample using the scanning stage referred to in the last paragraph. Following this, smaller (320 μm x 320 μm single element and 4 x 4 array sensors) and disposable sensors were implemented in Kapton substrates. The geometry of the micro-sensors developed for objective EC inspection is shown in Figures 1a and 1b of last year's (1999) Annual Report. Images of a model flaw, a keyhole flaw extended with a narrow slot, in a steel test sample obtained with the 320 μm x 320 μm EC micro-sensor was also shown in the 1999 Annual Report. It is reproduced here as Figure 2 for the reader's convenience.

Following sub-millimeter flaw resolution demonstration with disposable Kapton EC micro sensors, the development of a Pencil Probe (with EC micro sensors) compatible with automated EC imaging for multi-axis CNC/robotic inspection using motion control drive signals from the CAD database of the component was sought. A rugged "Pencil Probe" was developed using the 320 μm x 320 μm single element EC micro sensor. The same model keyhole flaw made in a steel test object (Refer to Figure 2), was scanned and a resolution limit better than 100 μm was demonstrated with the "Pencil Probe".

There is no certainty that a highly stressed component will fail by the nucleation and growth of an isolated crack. Many closely spaced flaws may well be initiated at "hot spots" with catastrophic failure resulting from the competition among competing flaws. Crack branching may also occur. These considerations suggest that the EC inspection method should have high spatial resolution and an ability to detect closely spaced flaws. Test samples containing closely spaced 250 μm wide slots (model flaws) with a flaw spacing of 250 μm were made and inspected. A Pencil Probe with the 320 μm x 320 μm EC micro-sensor was used for flaw imaging. It was shown that EC micro-sensors can be used to identify one crack in a field of many cracks as well as branching cracks.

b. Sub-surface Flaw Detection

Most hot spots in many highly stressed components are close to an external surface. However, flaws leading to catastrophic failure need not always be surface-breaking cracks. For the EC sensor to be useful, they need to demonstrate a capacity to detect flaws that are not necessarily surface-breaking. Test objects with subsurface model flaws in the form of 2 mm diameter blind holes of variable depth were made in a block of aluminum, 6.5 mm in thickness. Eddy current inspection was made to demonstrate that the subsurface flaws can be detected. To detect sub-surface flaws lying well below the surface, eddy current 'skin depth' will have to be large. Larger skin depths are obtained with lower EC excitation frequencies (Note: The skin depth δ is a function of frequency and resistivity ρ of the material). Penetration depth of the excitation field also depends on the size of the flux-focusing pole piece.
The 1020 μm x 1020 μm EC micro sensor was used to demonstrate sub-surface flaw detection capabilities (20 kHz and 30 kHz excitation frequencies). Line scan test data obtained, showed that EC micro sensors can detect subsurface flaws at a depth of about 60% of the pole piece dimension below the inspection surface.

c. Untended Flaw Detection

To determine the off-line, untended inspection capability of EC micro sensors implemented as pencil probes (using path control data derived from CAD software used to generate part geometry), model flaws in the form of drill holes were made in the two aluminum test samples. The CL file (Center-Line file)

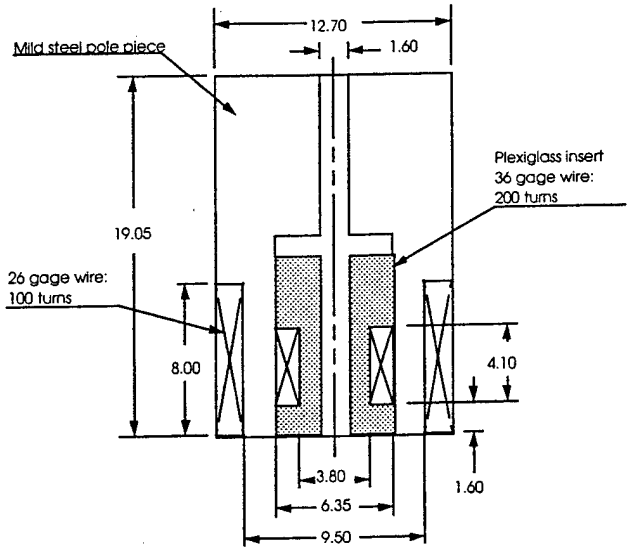

Figure 1. Geometry of the flux focusing eddy current sensor used for FEM modeling in the 5th year effort.

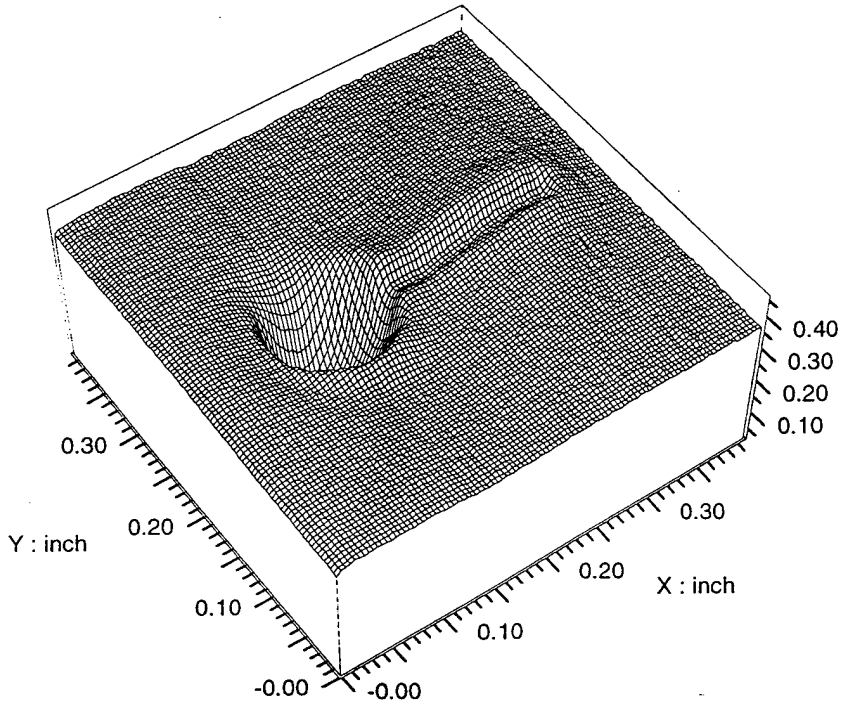

Figure 2. Reconstructed eddy current image of a model keyhole flaw - 2 mm drilled hole extended with an EDM slot, 5 mm in length, created with 0.004" diameter brass wire.

used to machine the test part in a 3-axis Cincinnati-Milacron CNC milling machine was used for EC inspection. The pencil probe with EC micro sensor replaced the milling tool during EC inspection. The 'flawed' test sample surface was scanned in a moving bed-type Cincinnati-Milacron CNC milling machine and the EC signal acquired was used to reconstruct the test part image with its model flaw.

Reconstructed images (c.f., Figure 4 of Annual Report for 1999) demonstrated that automated EC inspection is feasible. For improved signal-to-noise ratio (SNR), a DSP-lock-in amplifier was used which allowed continuous EC measurement at table speeds of several ten mm/minute. Slow EC inspection speeds and large inspection times may be compensated for by using untended robotic systems.

When parts with complex part geometries are inspected, probe normality condition is violated during EC flaw inspection. While the larger model flaws are unambiguously imaged, the SNR is significantly worse for some part geometries. Non-planar EC surface inspection for flaws were found to require EC inspection systems that meet the probe normality requirement. This makes it necessary to have more than 3-axis for untended EC inspection, i.e., a robotic system with 4 or more controlled axes will be necessary. It is also necessary to minimize stand-off distance sensitivity that implies a need for large stand-off distances during EC inspection.

d. Fluxset Probes

Square loop magnetic cores offered a means of rendering stand-off distance variation less significant during automated EC inspection of parts with complex geometry. To achieve reduced sensitivity to stand-off distance, Fluxset probes were made with an excitation and a (concentric) sensor coil, and a Metglass core within the concentric solenoidal coil assembly. In flux set probes, AC excitation of the primary (outer) coil leads to saturation of the square loop magnetic core. Field flipping in the core (AC-excited primary) is sensed by the inner solenoidal (sensor coil). In the presence of an external magnetic field, if the AC excitation current is maintained constant, the sensor coil voltage signal is time-shifted in saturation (forward saturation occurs sooner and reverse saturation is retarded). Measuring the time-shift with respect to the reference excitation current enables measurement of magnetic fields with high precision.

Fluxset probes were made and tested (Year 5 of program) with commercially available Metglass cores and found to function as anticipated. Test samples with model flaws were fabricated with drilled through-holes 3.25 mm and 4.76 mm in dia., and a 0.34 mm wide slot perpendicular to the hole axis (in aluminum, copper and stainless steel samples). The cylindrical flux set probe used, 2.5 mm in diameter x 8.00 mm in length, was able to detect larger model flaws. However, the spatial resolution of the flux set probe was unsatisfactory. Computational analyses, using numerical simulation underpinning the Fluxset probe, were made. A number of Fluxset probes/sensors were also empirically designed and tested in fifth year's effort to evaluate automated EC inspection with less sensitivity to variations in stand-off distance using the Fluxset probe. As the EC field perturbations accompanying the presence of a flaw with a small transverse dimension only extends a correspondingly small distance away from the surface containing the flaw, Fluxset probes with large stand-off distances can not be used for fine-scale flaw inspection. This part of the effort was fruitless and some other measurement scheme/principle will have to be developed to minimize the stand-off distance sensitivity during automated EC inspection.

e. Mesh Coil Sensors

Spatial resolution better than 100 μm displayed by the EC micro sensors and the pencil probes require fairly large inspection/scanning times. Data acquisition time for the keyhole flaw shown in Figure 2 was 15 minutes. This may not be appropriate for geometrically complex, large components even in untended EC inspection systems. Micro sensor arrays may be used to reduce scanning times. However, they will require signal multiplexing for data acquisition from each of the micro sensors raising measurement system complexity. There is also the need for probe normality during EC inspection. A two stage EC inspection scheme where the first scan serves primarily for flaw detection and the second scan for detailed flaw imaging is therefore more appropriate. Modified mesh coil sensors in which electrical drives replace mechanical rotation can be useful for two-stage flaw detection.

Planar mesh coil sensors may be wound around a mandrel to build cylindrical sensors needed for inner as well as external surface flaw detection. Mesh coil sensors of this type can also be miniaturized. Slots with complex geometry will require a partial cylinder sensor with a small tip radius. A mesh coil sensor with a tip radius as small as 600 μm was developed in the Year 4 effort for the single-pass inspection of the flawed (model flaw) blade root.

Mesh coil sensor performance demonstrated in the Year 4 effort was powered with an off-the-shelf function generator (excitation coil drive). A DSP Lock-in Amplifier, Stanford Research System Model 830, was used to obtain the flaw signal from the mesh coil sensor. Measured flaw signals are typically of the order of micro-Volts.

f. Modeling Mesh Coil Sensors

The mesh-coil sensor is modeled using the Maxwell's Equations given by:

$$\nabla \times H = J_s + J_e \qquad \nabla \times E = -\frac{\partial B}{\partial t} \qquad \nabla \cdot B = 0 \qquad (1)$$

Where H = magnetic field intensity vector; J_S = applied source current density vector; J_e = induced eddy current density vector; E = electric field intensity vector; B = magnetic flux density vector

Constitutive equations for the test material, the material with the real or model flaw, are:

$$B = \mu_r \mu_o H \quad \text{and} \quad J_s + J_e = \sigma E \qquad (2)$$

Where μ_r = relative permeability; μ_o = permeability of free space; σ = electrical conductivity

Maxwell's equations may be solved using the magnetic vector potential A and a scalar electric potential V.

$$B = \nabla \times A \qquad E = -\frac{\partial A}{\partial t} - \nabla V \qquad \nabla^2 V = 0 \qquad (3)$$

Then, the induced eddy current density vector J_e can be expressed in terms of the magnetic vector potential A as:

$$J_e = -\sigma \frac{\partial A}{\partial t} \qquad (4)$$

A commercial grade FEM Package, ANSYS, was used to solve the sensor modeling problem with the magnetic vector potential A as the primary unknown.

Problem geometry, shown in Figure 3a, has 16 mm x 16 mm drive and sensing coils with wire thickness and width of 0.2 mm and 0.6 mm respectively. The drive and sensor coils are made of copper (resistivity $\rho = 1.7 \times 10^{-8}$ Ωm) with the test sample made of 6 mm thick aluminum ($\rho = 2.8 \times 10^{-8}$ Ωm). Air elements were taken to represent the insulating layers between the aluminum block and the drive coil, and between the drive and sensor coils. Drive coil current was taken to be 20 mA at 80 kHz. The entire modeling region is 80 mm x 60 mm x 80 mm in size (x:y:z) containing a total of 14,850 8-node magnetic elements. Only a part of it is shown schematically in Figure 3. All fields outside the modeling region were taken to be zero.

The calculated, total eddy current density distribution in the aluminum test block (test sample) in 3-D and in the plan view are shown in Figure 3b and 3d respectively. Magnetic flux density (B_y) on the

sensing plane is shown in Figure 3c. Test block of Figure 3 is the reference sample containing no flaw but the block shown in Figure 4a contains surface-breaking flaws - cuts 5 mm long x 1 mm wide x 2 mm deep. The surface breaking flaws are more readily seen in Figure 4b showing the perturbations in eddy current density distributions due to the presence of model flaws. The y-component of the magnetic flux density, B_y, induced in the test block with the two surface breaking flaws are shown in Figure 4c.

Presence of surface flaws lead to changes in eddy current distribution within the block and thus to changes in the y-component of the magnetic flux density B_y. Voltage signal detected with the sensing coil is due to the perturbations in B_y resulting from the presence of surface flaws or cuts.

Voltage signal generated in the sensor coil is determined by calculating the change in magnetic flux within each 3/4 turn sensing loop caused by the surface-breaking cuts, i.e., by comparing the magnetic flux in test blocks with and without surface-breaking flaws. Magnetic flux passing through the sensing coil loop is calculated as shown below:

$$\begin{aligned} B_y^i &= B_{oy}^i\left[\cos(\omega t + \Phi_i) + j\sin(\omega t + \Phi_i)\right] = Re\left[B_y^i\right] + jIm\left[B_y^i\right] \\ \varphi_y^i &= S_i B_y^i \\ \varphi_m &= \sum_{i=1}^{n} S_i B_y^i \end{aligned} \tag{5}$$

Where B_y^i = magnetic field density in the *ith* element of the sensing coil loop

ω = $2\pi f$, where f is the drive current frequency

Φ_i = phase shift in the *ith* element with respect to the drive current

S_i = area of the *ith* element of the sensing coil loop

φ_y^i = magnetic flux along y direction in the *ith* element of the sensing coil loop

φ_m = total magnetic flux passing through the sensing coil

The real, $Re\left[B_y^i\right]$, and imaginary, $Im\left[B_y^i\right]$, parts of magnetic field density in the *ith* element of the sensing coil loop can be obtained directly from the FEM calculations.

The voltage or the electromotive force, *Emf* generated is given by:

$$\begin{aligned} Emf &= \frac{d\varphi_m}{dt} = \sum_{i=1}^{n} S_i \frac{dB_y^i}{dt} = j\omega \sum_{i=1}^{n} S_i \left\{Re\left[B_y^i\right] + jIm\left[B_y^i\right]\right\} \\ &= Re[Emf] + jIm[Emf] \end{aligned} \tag{6}$$

The sensing signal measured is:

$$\Delta Emf = \{Emf(\text{sample.with.flaw}) - Emf(\text{sample.without.flaw})\} \tag{7}$$

Calculated sensor output, in Volts, for the assumed problem geometry and flaw geometries are shown in Figure 5. Calculated *EMF* sensor signal as a function of mesh coil sensor position with respect to a stationary test block (one containing a flaw - Figure 4 and one containing no flaw - Figure 3) allows numerical simulation of the scanning process used for EC inspection. The x-axis in Figure 4 thus represents the position of the mesh coil sensor with respect to the flaw in the test block. Upper and lower figures represent the two flaw orientations and the associated sensor coil scanning directions. Experimentally measured signals are presented in Figure 6. Measured signals, in the absence of Metglass shields, are found to lie in the voltage range of 1.0×10^{-6} to 1.5×10^{-6} Volts. The relatively close

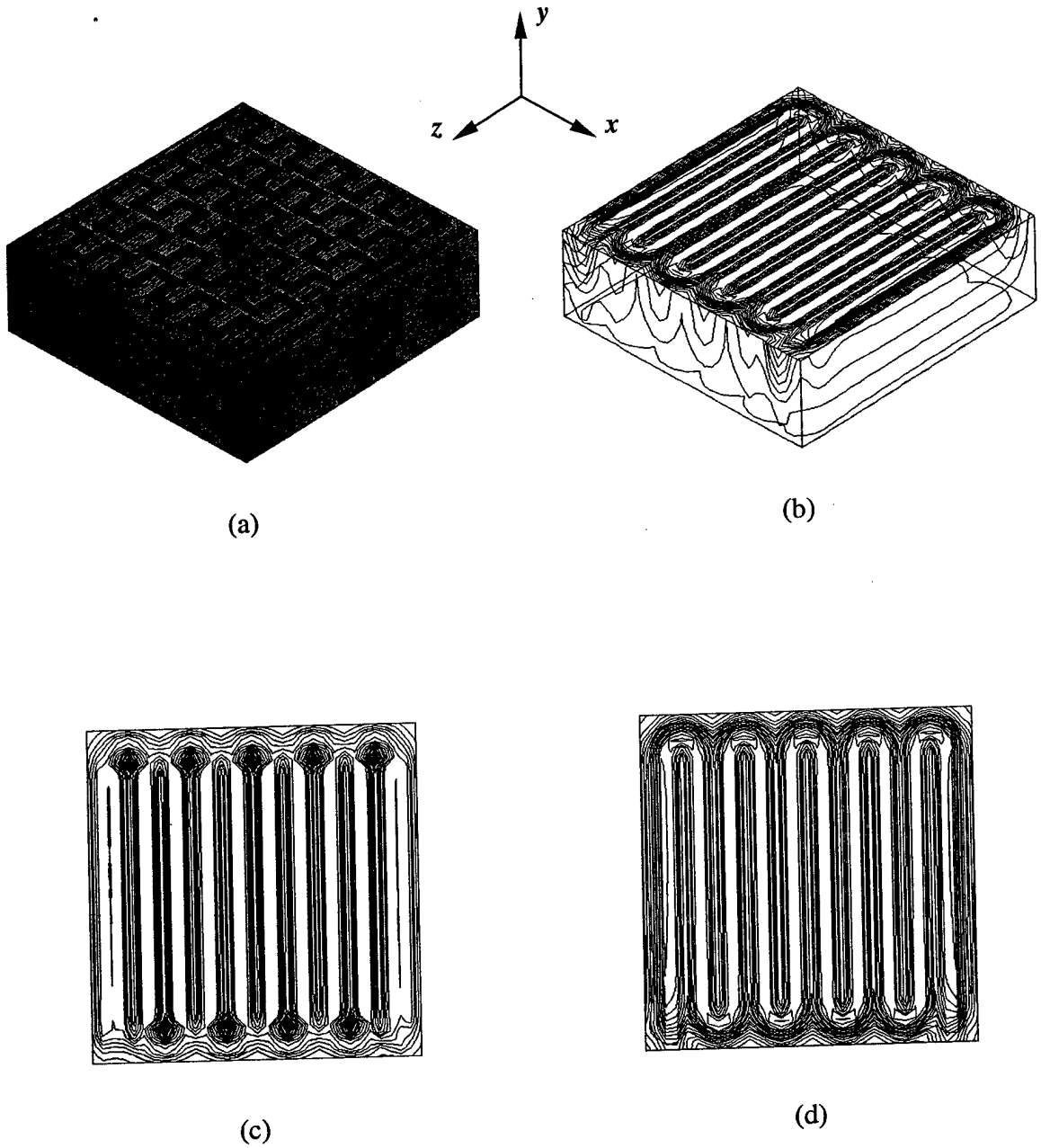

Figure 3. FEM modeling of the mesh coil sensor in a flaw-free test block. (a) Excitation and sensor coils. (b) Eddy current density in the test sample. (c) Magnetic flux density (B_y) in the sensing plane. (d) Eddy current density in plan view of test sample. Drive current is 20 mA and drive frequency is 80 kHz.

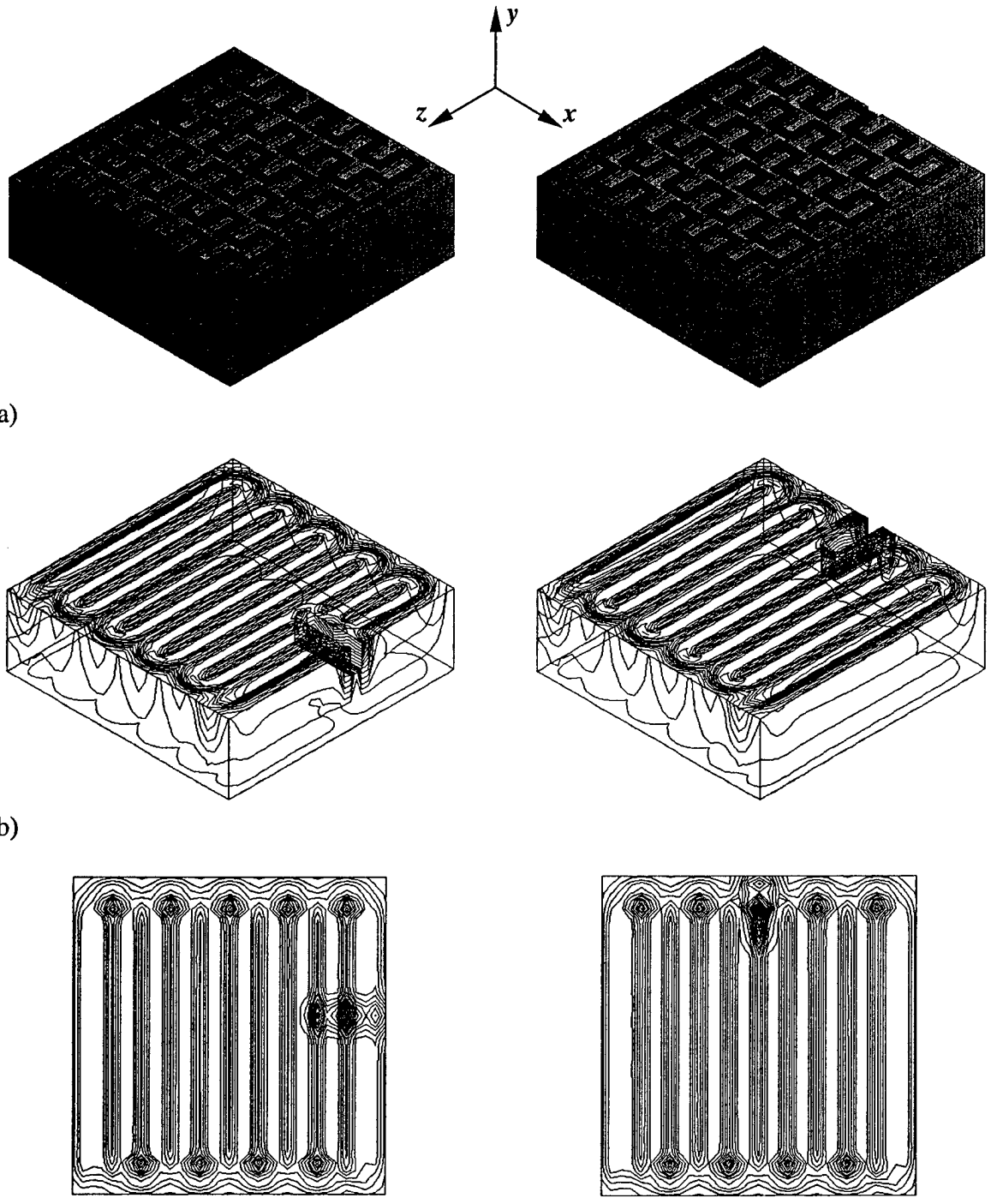

Figure 4. FEM modeling of the mesh coil sensor in a flawed test block. (a) Excitation and sensor coils. (b) Eddy current density in the test sample with flaws in two different orientations. (c) Magnetic flux density (B_y) in the sensing plane. Drive current is 20 mA and drive frequency is 80 kHz. Flaw size is 5.0 mm x 1.0 mm x 2.0 mm.

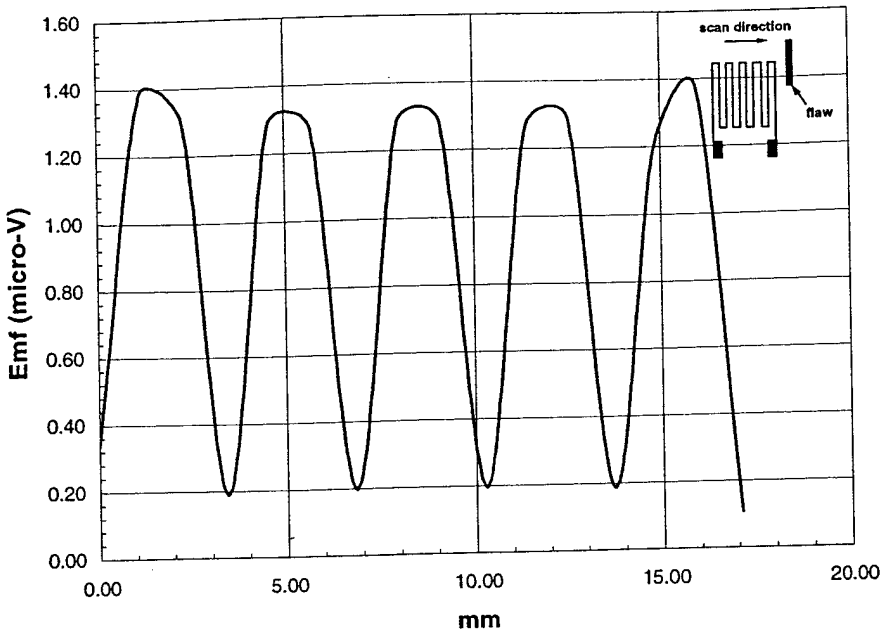

(a)

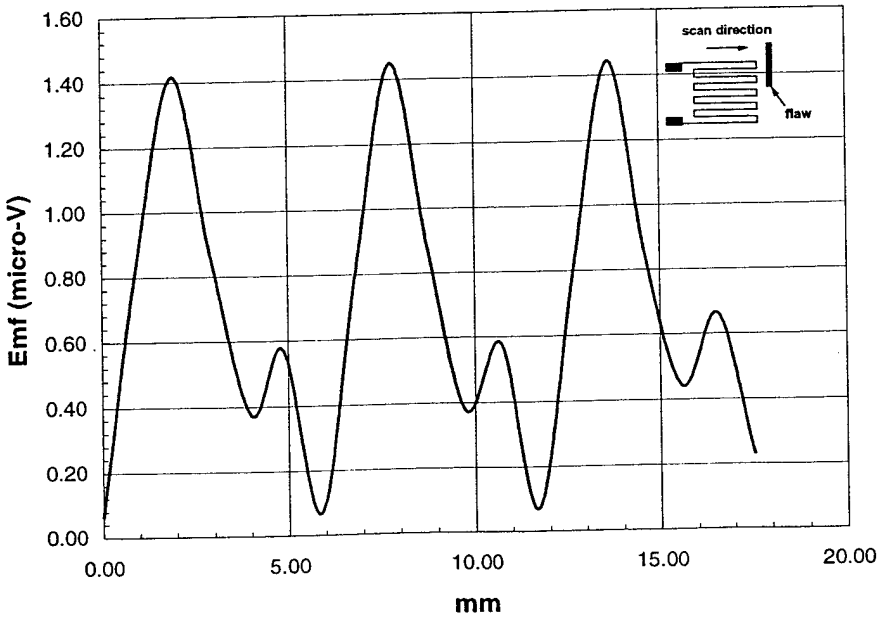

(b)

Figure 5. Calculated (FEM) mesh coil sensor signals as a function of sensor position with respect to the flaw - calculated "scanning" test results. Drive current is 20 mA and drive frequency is 80 kHz. Flaw size is 5.0 mm x 1.0 mm x 2.0 mm.

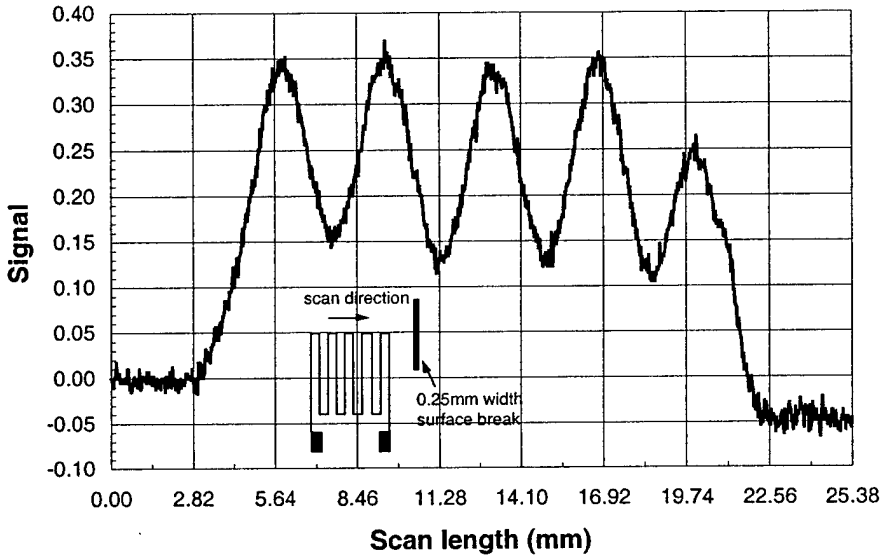

(a)

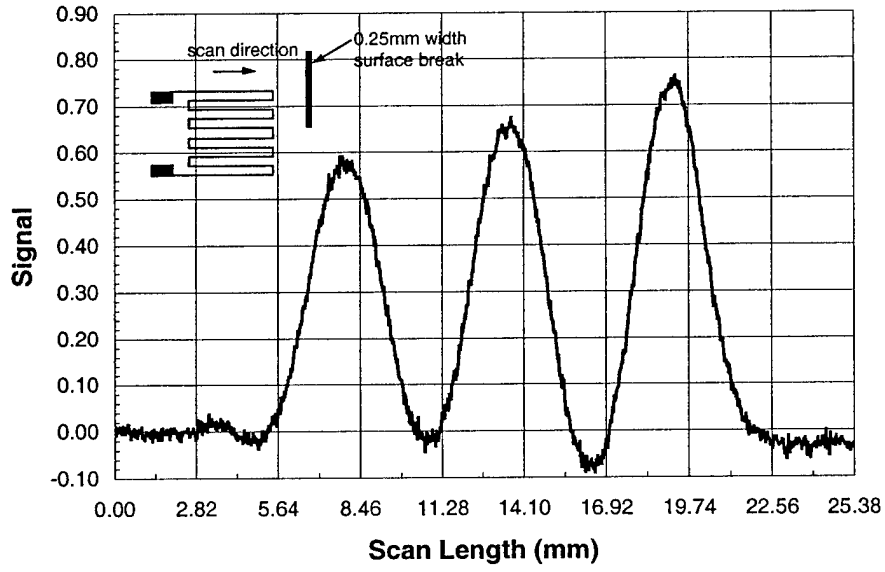

(b)

Figure 6. Measured mesh coil sensor signals as a function of sensor position with respect to the flaw - scanning test results. Drive current is 20 mA and drive frequency is 80 kHz.
Flaw size is 10.0 mm x 0.25 mm x 2.0 mm.

agreement observed between the calculated (Figure 5) and measured signals (Figure 6) suggests that a sound physical basis underpins mesh coil (Hoshi) sensor for Eddy current flaw inspection.

It appears that the mesh coil sensor can be reduced to a pair of closely spaced lines for eddy current excitation and a single, 3/4 turn, meander coil for flaw sensing. This enables the design and use of inexpensive, flexible, disposable small area (as well as large area) flaw sensors for any EC inspection task. Commercially available NOVAFLEX® films (polyimide sheets with two-sided copper plating) enable disposable, mesh coil sensors for rapid (single pass) inspection of turbine engine rotor discs and other intricate parts.

g. Electrically Rotated Mesh Coil Sensors

Calculations and experimental measurements show that the flaw signal varies with flaw orientation with respect to the axes of the mesh coil sensors. Flaws not aligned with the principal directions of the mesh coil sensors pose problems in flaw identification during rapid scanning for flaw localization. To avoid this, the sensor can be rotated through 360° after each incremental positioning during scanning along the two primary directions. As this defeats the purpose of rapid scanning incorporating an additional identical drive or excitation coil at 90° to the first excitation coil and driving it at the same frequency but with a drive current 180° out-of-phase with the first excitation coil offers a means of electrically rotating the mesh coil sensor.

Feasibility of electrically rotated mesh coil sensor was evaluated by building and testing a 16 mm x 16 mm mesh coil sensor containing two excitation coils and a single sensor coil. Dual drive mesh coil sensor was fabricated in NOVAFLEX film with copper plating on both sides. The sensor geometry implemented is shown in Figure 7. An aluminum test sample containing a model flaw, surface break 10 mm x 0.25 mm x 2 mm was scanned with the two-excitation coil mesh sensor. Scanning signal obtained as a function of flaw orientation is shown in Figure 8. A detectable flaw signal is obtained for all flaw orientations with maximum signal amplitude for the flaw aligned with one principal axis of the excitation coil. Once a flaw is identified, one has an option to excite drive coil 1 or drive coil 2 as the object is scanned to identify the flaw orientation.

h. Analytical Modeling of the Flux Focusing EC Sensor

Ability to analytically calculate EC signals during test object scanning with the mesh coil (Hoshi) sensor using the Maxwell equations raised the feasibility of calculating the EC signals when flux-focusing EC sensors are used. To test this approach, preliminary calculations were made using the large flux focusing pole piece shown in Figure 1. An aluminum test block with the flaw geometry shown in Figure 9 was modeled using the available FEM tool (ANSYS code). Flux focusing pole piece is stationary while the flaw position is systematically altered (two discrete flaw positions are shown schematically). EC excitation is achieved with the 26-gage, 100-turn external coil. EC signal is sensed with the 200-turn (36 gage) concentric inner coil. Calculated EC scanning signal, shown in Figure 10 suggests that EC sensors of this form can also be successfully modeled.

i. Flaw Growth Monitoring In Real-Time with Mesh Coil Sensors

The 16 mm square, mesh coil sensors may also be suitable for real-time flaw growth monitoring during fatigue tests. A set of four 16 mm Sq. mesh coil sensors have been made available to Co-investigators at Georgia Tech to evaluate the suitability of mesh coil sensors for this task. If the suitability of mesh coil sensors for fatigue monitoring can be confirmed, newer mesh coil sensors can be made with better spatial resolution to track flaw growth under load with greater precision.

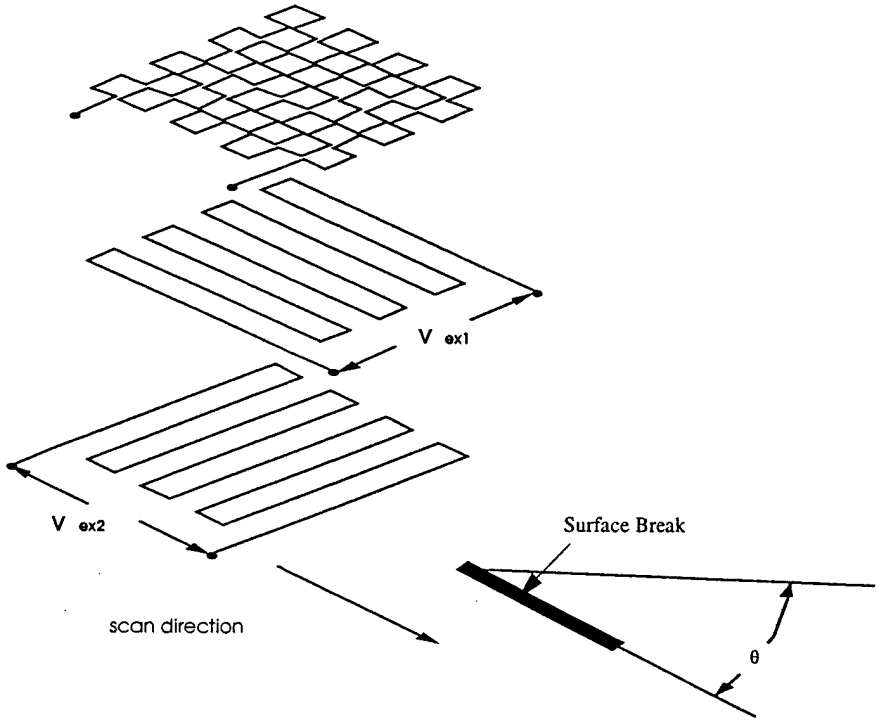

Figure 7. Electrically rotated mesh coil sensor with two excitation (drive) coils and a single sensor coil. Drive/excitation currents V_{ex1} and V_{ex2} are 180 deg. apart. Surface break in test sample is 10 mm x 0.25 mm x 0.25 mm. Initially, the flaw is aligned with the scanning direction ($\theta = 0$). Sample is rotated by 10 deg. following each linear scan.

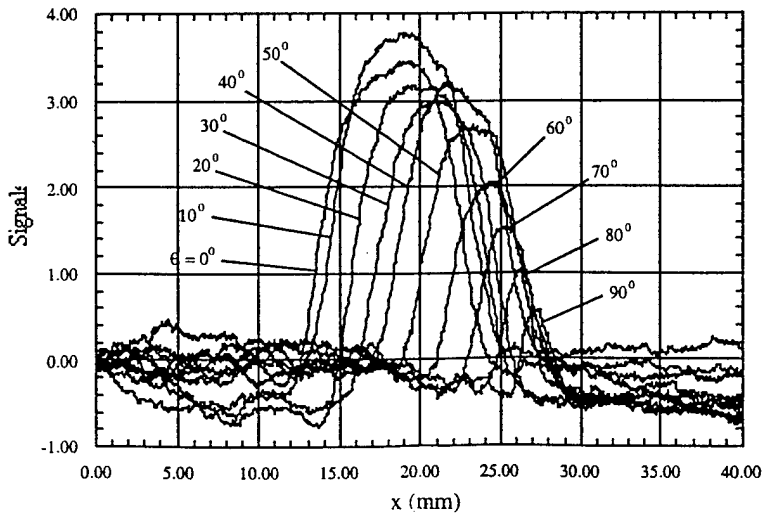

Figure 8. Measured signals from the electrically rotated mesh coil sensor with two excitation (drive) coils. Initially, the flaw is aligned with the scanning direction ($\theta = 0$). Sample is rotated by 10 deg. following each linear scan.

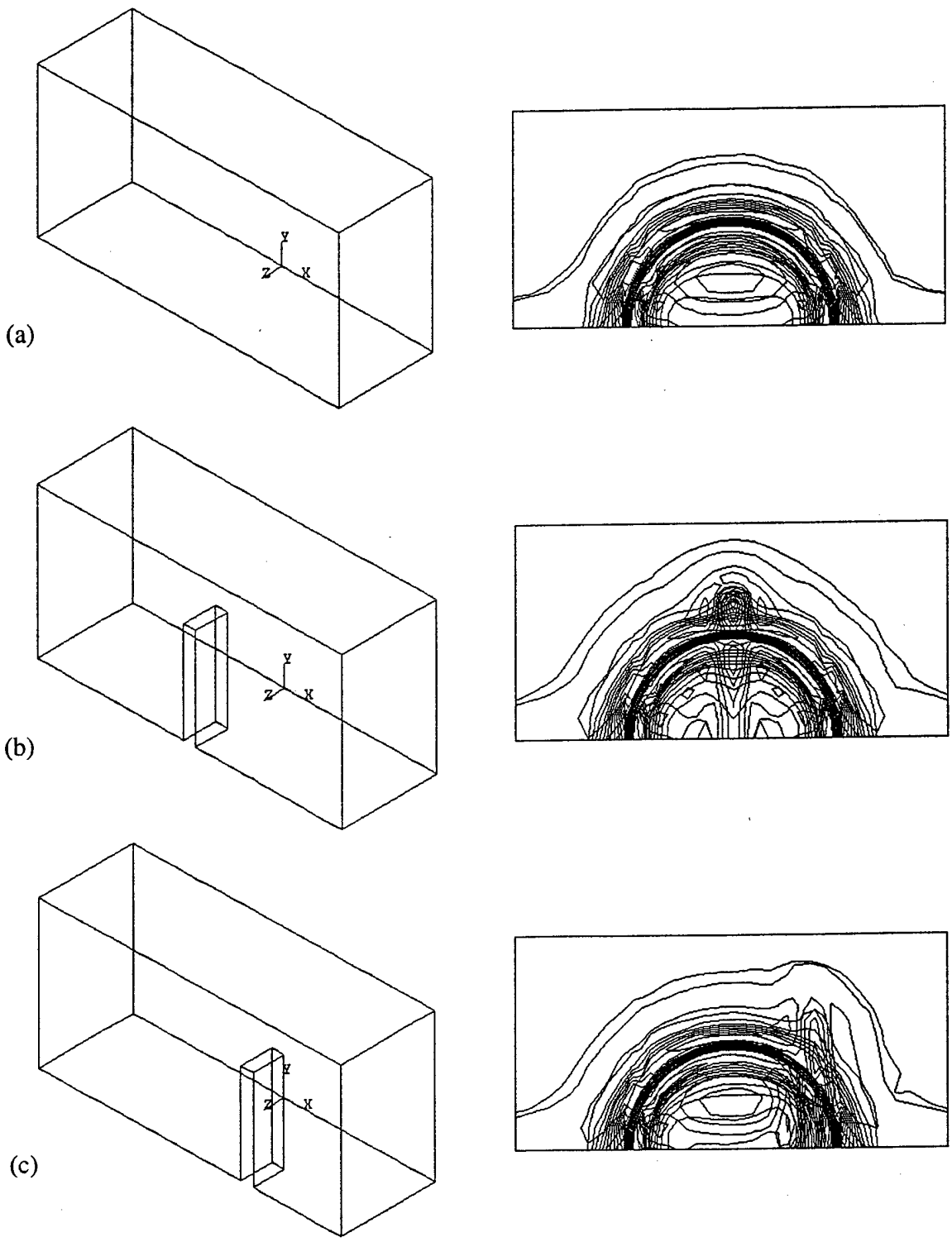

Figure 9. FEM modeling of the flux focusing eddy current sensor. Induced magnetic flux density (B_y) on the sensing plane is shown at right in a model, Aluminum test block with (a) no flaw and test blocks with model flaws (b) and (c). Drive current is 20 mA and drive frequency is 80 kHz.
Flaw size is 16 mm x 1 mm x 2 mm.

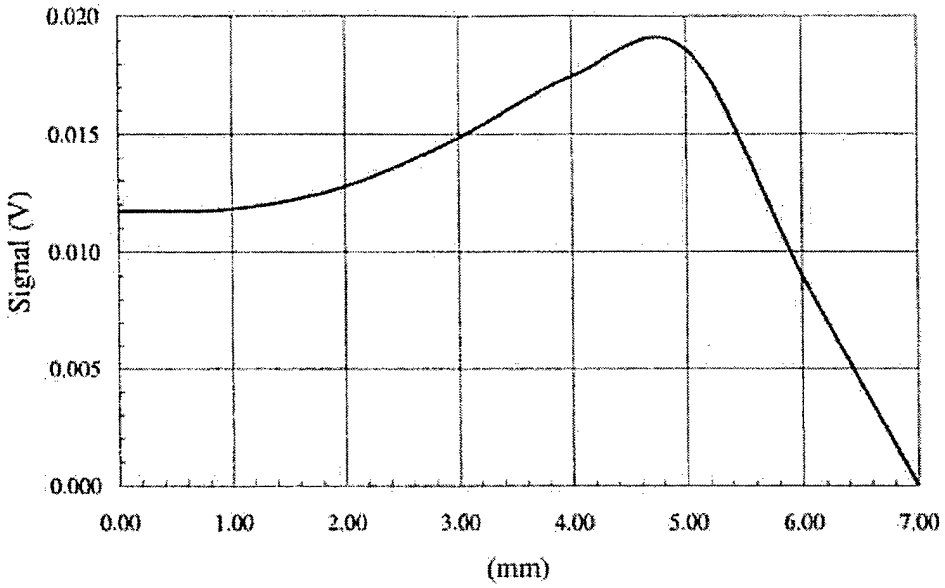

Figure 10. Calculated eddy current signal as an Aluminum test block with the model flaw shown in Fig. 9 is scanned with the flux focusing EC sensor shown in Fig. 1.

SUMMARY

1. Eddy current micro sensors have been developed and shown to have spatial resolution sufficient to detect 100 μm flaws. High spatial resolution is achieved with flux focusing pole pieces for EC excitation and a single, multi-turn (10-turn) sensor coil implemented on Silicon with 5 μm technology. It has been shown that less expensive, disposable micro sensors can be made by implementing the same 5 μm technology on copper-coated Kapton substrates. Smallest single-element sensor implemented is 300 μm x 300 μm in size. Sensors of the same size can also be implemented as 4 x 4 micro sensor arrays to reduce the total inspection time (raster scan) as long as the test object is largely flat.
2. Micro sensors developed can also be implemented as "Pencil Probes" without loss of flux focusing functionality. High resolution flaw sensing is time-intensive. Implementing digitally driven, untended inspection systems equipped with "Pencil Probes" can reduce inspection costs. Multi axis, paths control algorithms for digital drive can be derived from the same commercial CAD software. Simple part geometries can be accommodated with 3-axis drive systems but complex part geometries will require 4 to 6 axis direct numerical control systems (DNC) since probe normality conditions will have to be met during EC inspection. Use of Lock-In amplifiers (phase-locked loops) facilitates high-speed data acquisition with minimal measurement complexity.
3. Micro sensors, implemented as Pencil Probes, can detect a single flaw in a field of closely spaced flaws and can also detect sub-surface flaws. Detection depth is limited by the AC field 'skin depth' and the dimensions of the flux focusing pole piece used.
4. Imaging techniques have been developed to make EC flaw inspection objective. Reliance on qualitative interpretation of measured data by highly trained operators is no longer necessary. EC inspection is automatable and can be implemented in untended systems without losses in flaw detection reliability.
5. Untended EC inspection with micro sensor - equipped Pencil Probes will require fairly large times for flaw imaging. Separating flaw detection from flaw imaging can reduce the total EC inspection time and manpower needs. A mesh coil (Hoshi) sensor is appropriate for flaw detection. The defect, once localized, can be imaged with Pencil Probes (micro sensors).

6. Planar mesh coil sensors have been designed and demonstrated for flaw detection applications. Flexible, disposable sensors have also been made and their flaw detection capability verified. Flexible mesh coil sensors can be wound to make cylindrical sensors suitable for great many internal surface inspection applications. Performance of large diameter and small diameter cylindrical sensors has been verified.
7. Mesh coil sensors can also be configured for rapid, single-pass, EC inspection of narrow slots as in turbine rotors (blade root, Christmas tree slots). Mesh coil sensors may be enhanced with electrical drives using two excitation coils at 90^{o} to each other. This can eliminate the orientation-dependence of the mesh coil sensor signal.
8. Numerical simulation has been used to verify the functionality of the of the mesh coil sensor. Calculated results demonstrate that the mesh coil sensors are suitable for real-time flaw growth monitoring under well-controlled test conditions. To evaluate feasibility for such tasks, mesh coil sensors have been made available to ONR/M-URI Program Co-investigators.
9. Stand-off distance variation during untended inspection with EC micro sensors can introduce geometric artifacts in flaw images. Reducing the stand-off distance sensitivity of EC sensors can offset this problem. Flux set probes, with their inherently much greater magnetic field measurement sensitivity, offer an opportunity to reduce stand-off sensitivity of EC probes. Although the feasibility of flux set sensors has been verified, practical implementation could not be achieved for micro-flaws as the perturbation fields associated with discontinuities have a limited range. Ability to reduce stand off distance sensitivity during EC inspections continues to be a major challenge.

M-URI PUBLICATIONS

L. Zheng, J. Xue and S. Ramalingam, "Eddy-Current Micro-Sensors For Flaw Imaging: Numerical Simulation And Experimental Evaluation," ASME/STLE Joint Conference, October 1996, San Francisco, CA.

J. Xue, S. Ramalingam and Z. Shi, "Modeling Eddy Current Imaging with Thin Film Micro-Sensors," International Mechanical Engineering Congress, November 1997, Dallas, TX.

J. Xue, S. Ramalingam and Z. Shi, "Eddy Current Flaw Imaging using Micro-Sensor Arrays," International Mechanical Engineering Congress, November 1997, Dallas, TX

J. Xue, "Nondestructive Inspection with electromagnetic induction approach and eddy current micro-sensors," M. S. Thesis, Department of Mechanical Engineering, University of Minnesota, October 1998.

2.1.4 SENSING ACOUSTIC EMISSION AND TRANSMISSION

Co-investigators: Laurence Jacobs and Jacek Jarzynski (Georgia Tech)
Graduate students: Zhiqiang Shi, Brad Beadle, and Stefan Hurlebaus

OVERVIEW

Catastrophic failure of an in-service, structural component can be prevented if small cracks can be identified and arrested before they propagate into large cracks. As a result, it is necessary to develop a technique that can accurately detect and characterize any small cracks that may exist in complex, in-service components; such ability is a critical step towards developing a methodology for quantitatively predicting remaining service life. Acoustic emission (AE) testing offers a distinct advantage over more conventional nondestructive testing techniques because it allows for the real time monitoring of in-service structures.

Successful implementation of an acoustic detection technique requires the development of ultrasonic sensors that are capable of improved discrimination against environmental noise and reverberation. One need is for sensors that measure the tangential (in-plane) component of surface displacement, since such a sensor should provide better discrimination against environmental vibration noise, particularly in plate and shell structures. In these structures, the dominant source of vibration noise is bending waves with a large out-of-plane surface displacement component. A second need is for robust, inexpensive point sensors.

To assure maximum lifetime performance, an active acoustic wave technique to detect and characterize flaws in components, e.g., bearing balls, offers promise. The application of point source/receiver acoustic techniques enables the generation and detection of elastic waves capable of characterizing sub-surface flaws.

OBJECTIVES

(a) The objective of this investigation is to develop ultrasonic receiving transducer designs: (1) point piezoactive ceramic (PZT) elements, and (2) an optical fiber sensor designed to measure tangential (in-plane) surface strains at ultrasonic frequencies. The advantages of the fiber sensor are high sensitivity and immunity to electromagnetic noise.

(b) Internal cracks can develop in bearing balls during manufacture. These cracks are difficult to detect, so a second objective of this research is to develop an ultrasonic technique for nondestructive detection of such cracks.

ACHIEVEMENTS

a. Sensor Development

The initial fiber optic sensor designed and developed in this program is shown in Fig. 1a. It consists of 20 to 50 turns of fiber, where a short length of each turn is bonded to a thin metal base. This base is then coupled, with a shear-wave couplant, to the sample. In-plane strains at the surface of the sample are transmitted through the metal base to the fiber segments bonded to the base. These strains modulate the phase of the light propagating through the fiber and the phase modulation is detected by interference with a reference beam.

The sensor was tested by detecting transient extensional ultrasonic waves; a typical sensor output voltage is shown in Fig. 1b. The efficiency of this sensor was measured by comparison with signals measured with a laser Doppler vibrometer (LDV). The measured sensor outputs were then compared with the output estimated for complete transmission of strains from the sample to the fiber. This comparison showed, surprisingly, that the sensor's efficiency is very low, on the order of 3%. To understand this result, a finite element model for the response of the sensor was developed, and this model showed that at any instant, the strains in the regions of the fiber adjacent to the segment bonded to

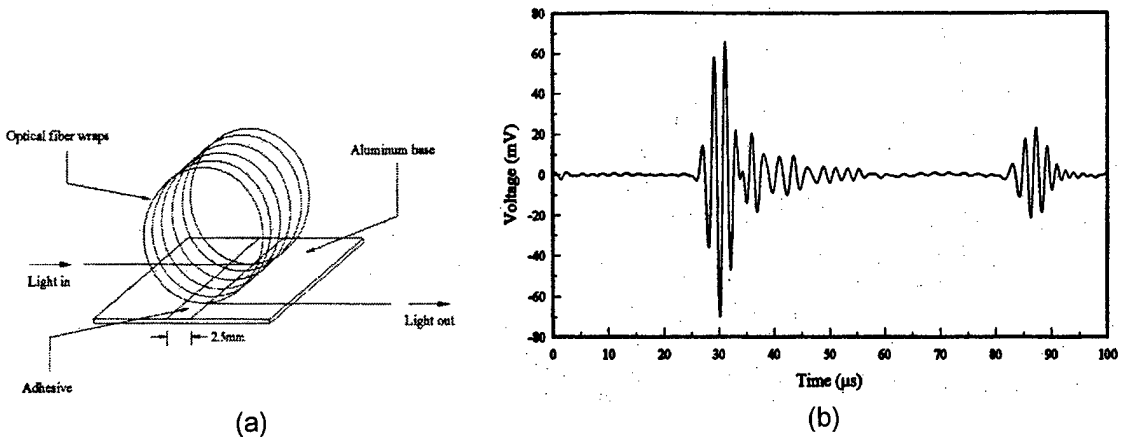

Figure 1. (a) Schematic of the fiber-optic sensor; (b): A signal generated from the sensor (Inefficient, initial design)

the base plate are of opposite sign to the strain in the bonded segment. Therefore, the integrated strain in each fiber loop, which determines the optical phase shift, is small compared to the strain in the bonded segment.

The finite element model led to a much more efficient sensor configuration, shown in Figure 2a. In this configuration, each loop of the fiber sensor is bonded over its entire length to the base plate. A typical output from this sensor is shown in Figure 2b. Calibration of this sensor, using the LDV, showed an efficiency of around 40%. This sensor can be designed for frequencies up to 200 kHz. This upper limit for the operational frequency is determined by the smallest allowed bend radius for the optical fiber. The minimum in-plane surface strain that can be detected with the above sensor is ~ $4x10^{-10}$, for a 100 kHz bandwidth of the receiving electronics. Publication [1] provides technical details of this sensor.

Small piezoactive ceramic (PZT) elements were purchased and assembled into AE sensors. The assembly involved mounting of the PZT elements and making electrical connections. In addition to their small size, an advantage of these point sensors is that they are relatively inexpensive. The PZT elements are 6mm long, 2 mm wide and 0.5 mm thick and are poled to respond to displacements or stresses in the thickness direction. The fundamental thickness resonance of these PZT elements is 4 MHz — this is above the frequency spectrum of AE signals (in the 50 kHz to 2 MHz range). Therefore, in the frequency

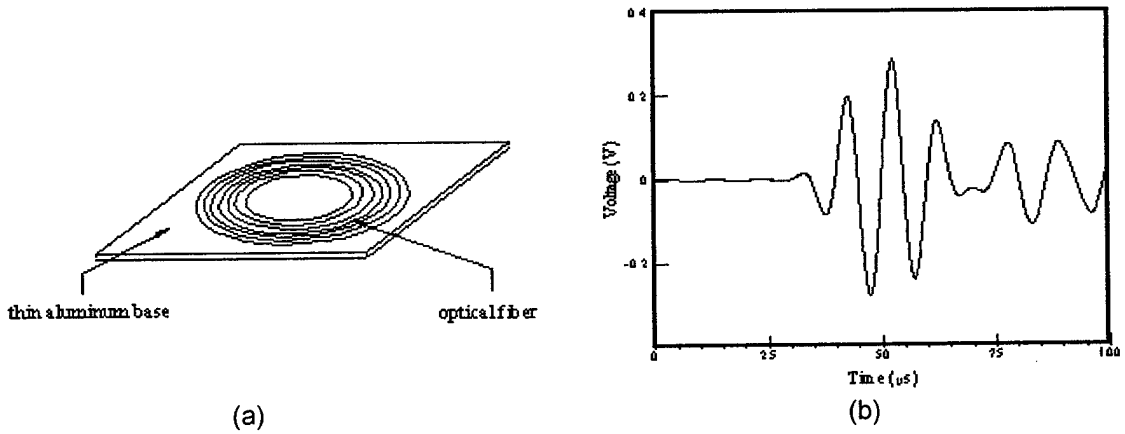

Figure 2. (a) Final sensor configuration (good efficiency) and (b) typical sensor output.

range of AE signals, the response of these sensors is approximately flat. Laser ultrasonic techniques were used for the broadband calibration of these AE sensors, as well as commercially available, broadband AE sensors. A pulse laser is used to generate a broadband (0-8 MHz) ultrasonic test signal in a metal block. The frequency spectrum of the test signal is then measured with a broadband LDV. The transducer to be calibrated is bonded to the metal block, at the same location as the LDV measurement, and the output voltage from this transducer is recorded. The frequency response of the transducer is the ratio of the frequency spectrum of the transducer output to the frequency spectrum of the LDV output. This study showed that the commercial sensor has a flat response up to 4 MHz, while the Georgia Tech PZT sensor is not as flat, but it is adequate for detection of broadband AE signals.

The development of transducer arrays is a promising area of research for improving the capability to detect low level AE signals. An array can be designed to focus on any designated region of the sample. In practice this would be a region of high stress, where fatigue crack initiation is expected. The simplest way to achieve focussing is by appropriate positioning of the transducers on the sample. A more sophisticated method, which is now possible with fast digital processing electronics, is to acquire the outputs from individual sensors and electronically insert appropriate time delays to achieve focussing. Some initial measurements were made using an array of three compact PZT sensors, and the results are shown in Fig. 3. The outputs of the individual sensors were acquired and array operation was simulated by post-processing the sensor outputs using MATLAB software. The fourth waveform in Fig. 3 is the array output obtained by adjusting the delay time for the output from each sensor so that the initial portions of the outputs are in phase. The fourth waveform clearly shows the increase in amplitude for the initial portion of the signal due to the array effect.

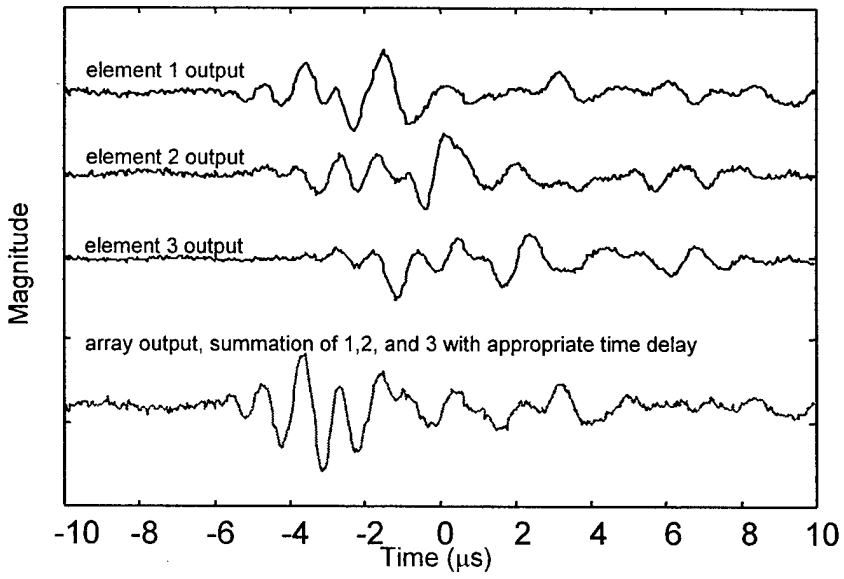

Figure 3. Response of a sensor array with three elements

b. Detection of flaws in bearing balls

A fixture was designed and assembled for mounting bearing balls between two ceramic PZT transducers. One transducer transmits a burst of ultrasound (several cycles at megahertz frequencies) that travels through, and reverberates in, the ball. The second transducer receives the ultrasound.

Three steel bearing balls, 1-inch diameter, were subjected to different degrees of heat treatment designed to produce internal cracks. Measurements of the time-of-flight and attenuation of ultrasound in the above balls were made, using 2 MHz, transient ultrasonic signals. The experimental data did not show any significant differences in ultrasonic propagation in the three balls. By going to a higher frequency, the resolution of the measurements increased.

A known surface crack was simulated in one of the bearing balls by cutting a groove, 0.001inches wide, 0.4inches long and 0.04inches deep (at the point of maximum depth). Commercial 5 MHz transducers were used, with the transmitting and receiving transducers placed at diametrically opposite ends of the ball, as shown in Fig. 4a. The transmitting transducer was driven with a one-cycle, 5 MHz electrical voltage signal. A typical received waveform is shown in Fig. 4b. The various signals in this waveform can be identified from their time of arrival at the receiving transducer, as follows.

The first signal is the direct longitudinal wave, the second signal is a shear wave and the third signal is a combination of the direct surface wave and a longitudinal echo. For this transmitter-receiver configuration, the echo from the groove is small and is masked by the above signals. It is possible that the echo from the groove can be detected using appropriate signal processing techniques, such as, for example, time-frequency analysis.

Stronger echoes from the groove are obtained with the configuration shown in Figure 5a. Here, the ultrasonic wave is transmitted into the bearing ball through a plastic wedge. This generates a surface wave in the ball that is directional and has higher amplitude. Fig. 5b shows a typical received waveform for the case when the ball is oriented so that the groove is in the path of this surface wave. It can be seen that the second signal in this waveform is a new signal, which arrives between the longitudinal and shear waves. This signal is attributed to scattering of the surface wave by the groove and conversion to a scattered longitudinal wave.

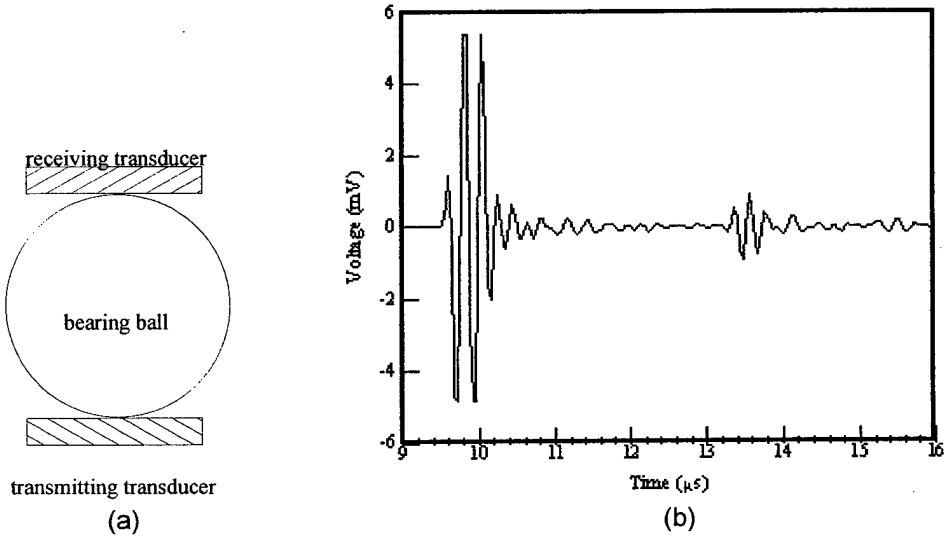

Figure 4. Configuration for measurements of ultrasonic propagation in bearing balls. (a) Transducer configuration. (b) Ultrasonic signals at 5 MHz in bearing ball with simulated surface crack.

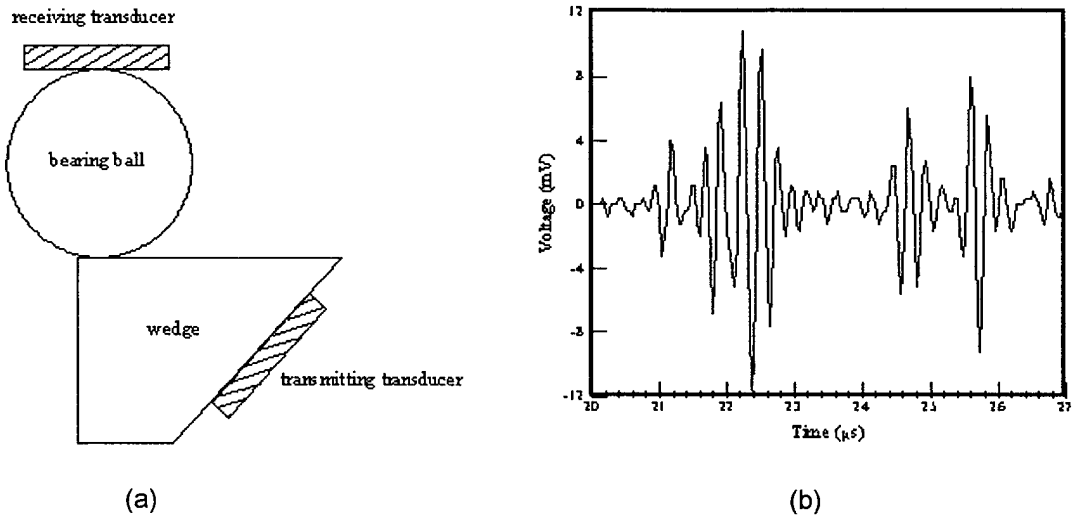

Figure 5. Alternate configuration for measurements of ultrasonic propagation in bearing balls. (a) Transducer configuration. (b) Ultrasonic signals at 5 MHz in bearing ball with simulated surface crack.

For the on-line inspection of bearing balls, it may be necessary to develop a system with non-contact generation and detection of ultrasound. Such systems are possible. Figure 6 shows a configuration (and a typical waveform) where a high power, pulsed neodymium-YAG laser is used for non-contact generation of ultrasound, and a conventional PZT transducer is used as a receiver. A non-contact laser Doppler vibrometer can replace the PZT receiver. Also, air-borne ultrasound can be used, instead of the YAG laser, to excite vibrations of the ball.

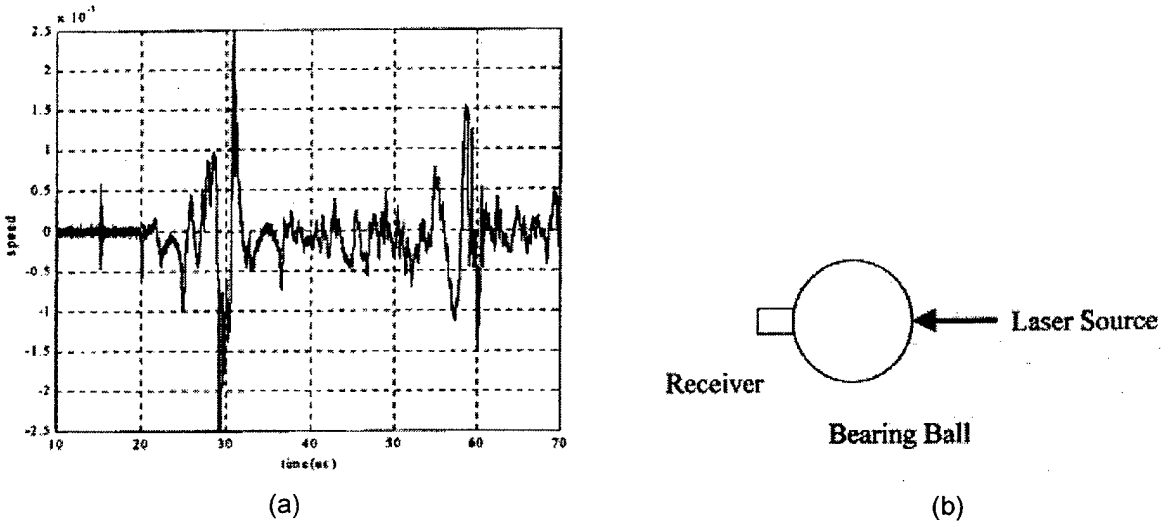

Figure 6. (a) Signal detected from a point sensor; (b) experimental setup.

FUTURE WORK

- Develop a compact, portable design of the fiber optic sensor for field measurements.
- Continue measurements on bearing balls with simulated surface cracks, as a function of crack size, frequency and transducer configuration. Concurrent with the measurements, a theoretical model should be developed. A finite element model is good for this application since it can handle cracks, both external and internal, of different size and shape.

M-URI PUBLICATIONS

1. Beadle B. M. and Jarzynski J., "Measurement of speed and attenuation of longitudinal elastic waves in optical fibers," submitted to SPIE for publication in *Optical Engineering.*

Thrust Area II

2.2 FAILURE CHARACTERIZATION AND PREDICTION METHODOLOGY

Perform studies pertaining to the methodology for failure prediction in real-time, including modeling fault initiation and failure signatures, and observing the propagation and fracture phases of fatigue-based failure.

2.2.1 STRUCTURAL FATIGUE INVESTIGATION 50
Project Overview 50
Introduction 50
2.2.1.1 Models for Small Fatigue Crack Growth Behavior 54
a. Robust Engineering Models for Integrated Prognostics 54
b. Microstructure-Dependent Small Crack Propagation from Notches 59
c. Computational Micromechanics of Fatigue of Polycrystalline Metals 60
d. Fretting Fatigue Damage 69
2.2.1.2 Stress and Flaw Analysis of Components 75
2.2.1.3 Fatigue Crack Initiation and Growth Mechanisms 86
2.2.1.4 Small Fatigue Crack Growth: Microstructure, Load Sequence, Corrosion Effects 111
2.2.1.5 Algorithms for Remaining Life Prediction 125
2.2.1.6 Advances in Understanding Structural Fatigue Life 132
Summary 132
Future Work 133

2.2.2 FAILURE PREDICTION METHODOLOGY/FATIGUE RELIABILITY 134
Overview 134
Objective 134
Achievements 136
Future Work 142
M-URI Publications 142

2.2.3 STUDY OF ACOUSTIC EMISSION AND TRANSMISSION FROM INCIPIENT FATIGUE FAILURE 143
Overview 143
Objective 143
Achievements 143
Future Work 147
M-URI Publications 147

2.2.4 ACOUSTIC EMISSION MODELING FOR INTEGRATED DIAGNOSTICS 149
Overview 149
Objective 149
Achievements 149
M-URI Publications 156

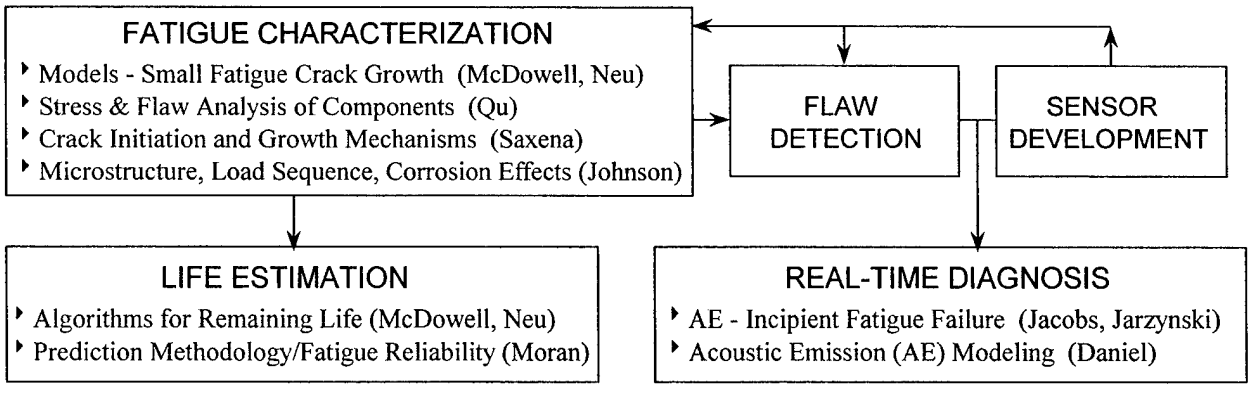

2.2.1 STRUCTURAL FATIGUE INVESTIGATION

PROGNOSTIC TOOLS FOR CONDITION BASED MAINTENANCE

Co-investigators: David McDowell (Lead), W. Steven Johnson, Richard Neu, Jianmin Qu, Ashok Saxena
Graduate Research Assistants: A. Bell, V. Bennett, L. Cretegny, B. Gardner, R. Hamm, O. Jin, J.A. Pape, A.M. Patel, C. Rosen, D.R. Swalla, F. Yang
Postdoctoral Fellow: Fan Yang
Collaborators: Rosario Gerhardt (Georgia Tech), Brian Moran (Northwestern University)

PROJECT OVERVIEW

An integrated system for diagnosing the "health" of a structural component subjected to high cycle fatigue (HCF) consists of sets of embedded or emplaced sensors at various locations, extracting information related to the generation of material defects, presence of crack-like discontinuities and their progression, and changes of system dynamics that may relate to this progression. Conceptually, signals from these sensors are fed into a processing environment that can ascertain deleterious conditions related to the onset of loss of function or propagation of cracks to critical dimensions. Since the idea is to monitor the gradual changes of component performance and various local related indices before catastrophic failure to enable the operator to respond with a maintenance hold, it is essential to couple the diagnostics with prognostic capability; this facilitates a prediction of how much time remains within the window of viable servicing or repair.

In the HCF regime, the dominant fraction of total fatigue life may be spent at crack lengths on the order of 20 to 500 μm. The detection of longer cracks near the end of component life is critical since component failure may lead to failure of the overall structure. This necessitates the identification of (i) finite-element algorithms for identifying component "hot spots" where failure is likely to occur, (ii) development of appropriate crack growth laws for cracks of different length scales, ranging from on the order of grain size to on the order of component dimensions, including consideration of contacting components (fretting fatigue) and environmental effects, and (iii) development of algorithms for identifying the progression of component degradation based on multiple sensor inputs at different time and length scales, providing feedback to support cause for maintenance shutdown. This report discusses the accomplishments made at Georgia Tech over the past five years in addressing these needs through the Structural Fatigue Task within the Department of Defense M-URI on Integrated Diagnostics.

INTRODUCTION: APPROACH TO INTEGRATED PROGNOSTICS

One of the key issues in current procedures for maintenance of high-speed machinery and transportation vehicles is the ability to accurately estimate the remaining life and to set safe inspection intervals for the critical structural parts of complex systems. With on-board diagnostics and high-speed digital signal processing, an effective maintenance strategy relies on periodic assessment of the degradation of components during service and specification of conditions for shutdown and/or maintenance. The detection refresh rate (inspection interval), the nature and interpretation of the sensor signal (choice of inspection technique(s)) and the updated projection of remaining life must be specified as part of an overall strategy which provides the basis for making decisions such as continuation of operation, retirement, replacement at present or replacement at a future date (possibly during a scheduled maintenance outage). Such a strategy must address the risk due to the uncertainties in the predicted component life which are related to:

- detection difficulties for small cracks in actual components,
- non-classical characteristics of propagation of small cracks and long 3-D cracks under fatigue loading, and
- complex service loading conditions.

In many cases, the cracks may be essentially undetectable by optical methods, due either to small length or lack of accessibility. This is particularly true of metallic components subjected to high

frequency, relatively low amplitude fatigue loading such as rotor and drive components of helicopters. Under such conditions, fatigue cracks may remain very small (e.g. 20 to 500 μm) for over 90% of the life, amenable to optical detection only near the very end of component life. Moreover, the three-dimensional shape of typical components often leads to fairly complex shaped crack fronts and crack face contact during fatigue.

In components, the determination of whether or not a crack is on the verge of catastrophic propagation depends on the rate of change of the driving force for crack growth as a function of crack length (e.g. dK/da), which varies among possible crack initiation sites in components. Consequently, the operator may be faced with the relatively rapid in-flight onset of deleterious structural performance, including loss of control, landing capabilities, etc. Accordingly, it is prudent to assess the evolving state of damage at hot spots (stress concentrations) or sites of enhanced contact fatigue using micro sensors and/or acoustical methods with resolution necessary to track the development of fatigue cracks and to estimate when these cracks may become long enough to warrant maintenance decisions.

In some cases, fretting fatigue, foreign object impact damage or surface defects introduced through component assembly or material processing serve as the initiation sites for fatigue cracks, leading to the need for a robust diagnostic capability which can detect such cracks over the entire component volume, outside the envelope of cataloged hot spots. These "rogue" cracks fall outside the regular categorization of pre-defined hot spots, and demand an enhanced degree of robustness for both detection and remaining life estimation. The detection of rogue flaws that are uncorrelated with hot-spot detection may give rise to the need for component inspection or adaptive, multi-sensor, multi-spectral signal analysis at multiple length scales combined with an artificially intelligent algorithm for estimation of the crack propagation rate and remaining life. However, it is important to recognize that the gist of the problem lies in real-time characterization of the hot-spot behavior, since field observations corroborate computational results, as pointed out in the next section.

A schematic showing the overall philosophy of an integrated, multi-scale diagnostic/prognostic system for component fatigue response appears below:

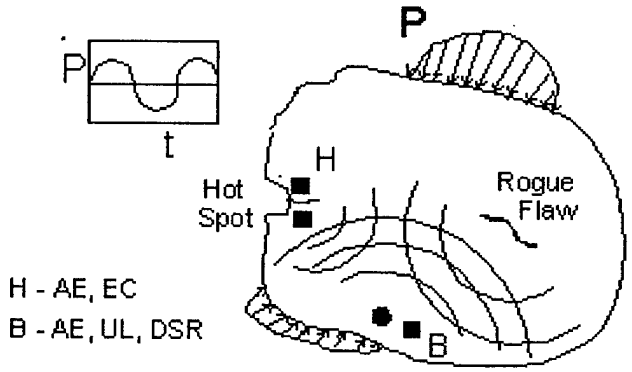

Figure 1. Integrated diagnostic/prognostic schematic for a component subjected to generalized cyclic loading, P, showing hot spot and associated focused micro-sensors (H) and a rogue flaw with broad area scanning detection (B). Legend: Acoustic emission (AE), eddy current (EC), active ultrasound (UL), and changes of dynamical system- component response (DSR).

TRACKING PROGRESSION OF DAMAGE

Once a set of hot spots in each component are identified, dedicated sensors may be applied to monitor the occurrence and progression of cracking during service. Under HCF conditions, the processes of crack nucleation and small crack propagation are of great importance at these hot spots.

The proximity of small HCF cracks to free or contacting surfaces and interaction with microstructural barriers vastly alter the crack tip stress and strain fields and the rate of crack propagation. Heterogeneity of cyclic plastic deformation under low amplitude loading conditions is also an important consideration, as are associated near-surface residual stress fields.

Small cracks in polycrystalline metals often display lower apparent threshold stress intensities and much higher propagation rates than long crack data when interpreted within the framework of either linear elastic fracture mechanics (LEFM) or elastic plastic fracture mechanics (EPFM) solutions for long cracks in homogeneous, isotropic materials. Small cracks in single crystals show little or no evidence of a threshold, particularly in predominantly mode II loading conditions. At locations where cracks occur in components, the stress state is often of multiaxial character due to changes of the mixity of applied loading (e.g. excitation of multiple dynamical modes), structural constraints (e.g. change of geometry) or local contact with adjacent structures (e.g. joints). Hence, modeling concepts that address only uniaxial and/or Mode I loading conditions are not sufficiently general to meet diagnostic requirements.

Use of classical fatigue crack initiation approaches for HCF (S-N curves, Goodman diagrams) is not effective in supporting the estimation of remaining component life since they do not predict the rate of propagation of detected cracks. Moreover, use of LEFM solutions based on long cracks in homogeneous, isotropic materials does not match the fatigue crack growth rate observed for cracks on the order of a few grain sizes in dimension, in general. Ample evidence exists to confirm that for cracks with length at the scale of repeating microstructure, the propagation behavior is quite distinct from that of mechanically long cracks which exceed this scale by over an order of magnitude. Therefore, a major technical challenge in support of integrated, near real time diagnostics is to develop new models for microstructurally and physically small fatigue crack growth that can be deployed in a manner analogous to conventional fracture mechanics methods. In this section, we discuss some of the considerations for modeling the behavior of small crack development and growth at sites of stress concentration.

Fatigue Crack Nucleation

Cracks in critical locations in components subjected to nominally HCF conditions may form from pre-existing machining- or process-induced defects, precursory events such as fretting fatigue (relative microslip of contacting components), impact of foreign objects, or from periodic overload cycles which induce fracture of inclusions or interfaces and enhance cyclic slip. A large fraction of the HCF lifetime is typically spent in the formation and growth of small cracks. Hence, there is a potentially strong dependence upon surface conditions, pre-existing or service-induced defects, and microstructure. The nucleation or incubation period required to form sharp cracks either from intrinsic or extrinsic defects typically comprises a very significant fraction of total fatigue life, often in excess of 90%. In this case, total fatigue life is defined as the combination of formation of cracks and their subsequent propagation to dimensions where either rapid crack advance and catastrophic failure occurs, or to the point where component response is unacceptably degraded. From a design perspective, initiation models may be used to estimate the number of cycles to formation of cracks, while fracture mechanics approaches then apply to their propagation (cf. Socie, 1977). Various schemes have been proposed along these lines. In the context of an integrated diagnostic/prognostic system for components, however, it is the propagation of crack-like defects that is most relevant to component evaluation. It may be useful to monitor, for example, local acoustic emission events that correspond to the development of localized inelastic deformation or "pop-in" of cracks, but each microsensor is generally limited in its resolution of such microscale events. Above a certain limit of resolution, crack length can be reliably monitored, and its progression compared to that estimated by a life estimation scheme correlated to a specific material, for a specific range of crack length and for the stress intensity (driving force) appropriate to that hot spot location.

Standard fracture mechanics approaches for long cracks cannot be applied to very small cracks in a direct manner to address the relevant mechanisms. Crack propagation analyses have relied heavily upon a fracture mechanics-based description of crack tip stress fields that assume the material is homogeneous and isotropic. The notion of self-similar crack growth for these small cracks is known to be a leap of faith in many respects. Furthermore, there are processes that may consume a significant fraction of total fatigue life that involve the formation of cracks from pre-existing defects such as foreign object damage (FOD) or precursor events such as periodic LCF or fretting that are well beyond the scope of conventional fracture mechanics and are also outside the domain of intended applications of the local stress approach to

fatigue crack initiation.

Novel experimental and analytical or computational mechanics approaches, which focus on formation and growth of small cracks under HCF conditions, are necessary to resolve these issues from a basic perspective. Development of improved concepts for fatigue crack driving and material resisting forces are necessary, including appropriate extensions of fracture mechanics as well as new approaches that recognize key physical aspects of the HCF problem, such as the influence of local cyclic plasticity, free surfaces and attendant gradients of dislocation density, and fretting fatigue in promoting the propagation/opening of small cracks, orientation and spatial distribution of microplasticity among grains in polycrystals, local mode mixity, interaction of small cracks with microstructure, crystallographic propagation across grain boundaries into misoriented grains, stochastic and probabilistic aspects of HCF crack propagation.

Crack Propagation Mechanics

Current models for HCF have been divided largely into two classes: (1) initiation approaches for endurance/fatigue limit concepts based on S-N curves or local stress-life approaches, and (2) application of LEFM for suitably long cracks in components. Much of fatigue design for rotating/reciprocating machinery is based on the former, while damage tolerance concepts for airframes, which make use of periodic inspections, are employed in the latter. Here, we focus first on the development of models for propagation of small cracks in fatigue. Then, we will point to some complexities associated with modeling the growth of longer cracks in three-dimensional components.

The growth of small cracks in polycrystalline metals is subject to several characteristic regimes (Miller, 1993; Tanaka, 1987). Microstructurally small cracks within the first surface grain are relatively less constrained than long cracks, resulting in increased crack tip opening and sliding displacements. As discussed by Miller (1993), microstructurally small cracks are subject to strong interactions with microstructural barriers. Microstructurally small crack growth is characterized by a series of periodic activation of slip in adjacent grains of different orientation, followed by dislocation blockage by grain boundaries and associated deceleration of da/dN (Hussain et al., 1993). Oscillatory da/dN behavior is commonly observed for microstructurally small cracks (Nisitani, 1987; Tanaka and Akiniwa, 1989; Wang and Miller, 1992). Typically, the experimentally observed crack length for the minimum da/dN, d, is somewhat higher than the characteristic grain size, δ, assumed in slip transfer models. Other mechanisms, which slow the growth of small cracks, include development of plasticity- and roughness-induced closure, and both may contribute to the observed minimum da/dN. The relative balance of these mechanisms is highly dependent upon slip mechanisms and microstructure. If the applied stress is insufficient to nucleate cyclic slip in adjacent grains, small cracks will decelerate and arrest at this length scale ($a \approx d$), giving rise to a fatigue limit. In general, d depends on the particular composition and arrangement of microstructure, and does not correspond simply to optical identification (Wang and Miller, 1992). If cracks propagate past the strongest barrier (minimum da/dN), they continue to be subject to a diminishing influence of microstructure for several multiples of this length scale ($a < kd$, $k \approx 2$ to 7) (Tanaka, 1987; Tanaka and Akiniwa, 1989; Hussain et al., 1993). Comprehensive reviews of the mechanics challenges in developing fatigue crack growth laws for small cracks are available in the literature (Leis et al., 1986; McDowell, 1996).

Extensions of Existing Small Fatigue Crack Growth Relations

The models considered in this study were specifically formulated for either mechanically small cracks or microstructurally small cracks or both. When a crack is considered small, local stress gradients due to geometry are negligible. However, as a crack extends beyond the small crack regime, stress gradients and constraint caused by geometry cannot be ignored. The stresses that a crack feels decays from the local stresses to the nominal applied stresses. A fracture mechanics treatment of these cracks must be able to integrate Microstructural Fracture Mechanics (MFM), Elastic-Plastic Fracture Mechanics (EPFM), and Linear-Elastic Fracture Mechanics (LEFM), as appropriate to the length relative to microstructure.

2.2.1.1 MODELS FOR SMALL FATIGUE CRACK GROWTH BEHAVIOR

a. Robust Engineering Models for Integrated Prognostics

Co-investigator: David L. McDowell (Georgia Tech)
Graduate Student: Valerie Bennett

In this section, novel developments are explained within the program of robust, approximate multistage model framework for the growth of microstructurally and physically small fatigue cracks which is inspired by observed cyclic crack tip displacement correlations with the FCP rate. Several phenomena should be recognized in development of a realistic small crack propagation model:

(i) Arrest threshold for propagation of microstructurally small cracks (fatigue limit) and less microstructure-sensitive threshold for physically small cracks (LEFM threshold).
(ii) Adherence to the cyclic stress-strain and strain-life relations for loading above the fatigue limit.
(iii) Concurrence with the format of critical plane models for Stage I cracks in multiaxial fatigue which provide excellent correlation of the characteristic mixed mode propagation behavior of small cracks under various stress states.

The critical plane-based multiaxial small fatigue crack growth law developed by McDowell and Berard (1992) with later refinements by McDowell and Bennett (1996) satisfies (ii)-(iii) above and serves as the starting point for addressing (I) above. We introduce a generalization of the small crack propagation approximation based on slip transfer (Hobson, 1985; Hobson et al., 1986; Miller, 1993; Hussain et al., 1993) within the context of the multiaxial critical plane approach set forth by McDowell and Bennett (1996), assuming completely reversed loading. We define Regimes I, II and III as the microstructurally small crack regime (MSC), transition from microstructure sensitivity to relative insensitivity, and the physically or mechanically small crack regime (PSC), respectively. The equations of the model appear in Table 1 for each of the three Regimes. The MSC regime model is observed to be a generalized form of the Hobson model (Hobson, 1985; Hobson et al., 1986; Miller, 1993) for deceleration of microstructurally small cracks, primarily associated with the primary barrier(s). In these equations, a is crack length with a_i as its initial value, d is the primary microstructure barrier spacing, kd is the transition crack length into the PSC regime, $\Delta\gamma_{max}$ and $\Delta\gamma_{max}^e$ are the maximum shear strain range and its elastic component, σ_n and τ_n are the normal and shear stresses, respectively, on the plane of maximum range of shear strain, ρ is a constraint factor for biaxial or triaxial stress states (μ is a proportionality constant), and ψ is the driving force parameter for fatigue crack propagation. The ψ parameter has previously been shown (McDowell and Berard, 1992) to provide accurate correlation of the full range of stress states. Constants C_e, C_p, m, M and parameters β_e and β_p have been thoroughly described, along with definitions of R_n, R_e, j_e, j_p, μ and ρ in earlier work (McDowell and Berard, 1992; McDowell and Bennett, 1996).

The form of D_{aN} in Table 1.1 is introduced to normalize the solution of the system of propagation relations to the strain life relations for uniaxial and torsional fatigue above the smooth specimen fatigue limit in each case, taken independently, assuming an initial crack length, $a_i < d$, and a final crack length, $a_f > kd$. Below a value of ψ slightly above the fatigue limit, ($\psi < \xi(\psi_{th})_I$, $\xi > 1$), D_{aN} is assumed to be fixed at the value corresponding to $\psi = \xi(\psi_{th})_I$. The crossover crack length between growth rates in Regimes I and II (i.e. minimum da/dN) occurs at $a^* < d$, in general.

It is also noted that if a > d due to prior loading above the fatigue limit, then the nonpropagating crack threshold is decreased from the smooth specimen fatigue limit, in accordance with the Kitagawa diagram (Tanaka, 1987; Tanaka and Akiniwa, 1989; Miller, 1993). The mechanisms for the fatigue limit in Regime I and the mechanical threshold in Regime III differ. In Regime I, small cracks are arrested by microstructure blockage, while in Regime III they arrest if the mechanical state at the crack tip is

Table 1.1 Equations of multiaxial small crack growth law.

$$\left(\frac{da}{dN}\right)_I = D_{aN}\psi A\psi^B\left(1-\frac{a}{d}\right)$$

$$\left(\frac{da}{dN}\right)_{II} = D_{aN}\psi\left\{\psi^r\left(\frac{a}{kd}\right)-D\right\}$$

$$\left(\frac{da}{dN}\right)_{III} = D_{aN}\psi\left\{\psi^r\left(\frac{a}{kd}\right)-D\left(\frac{a}{kd}\right)^{1-Mr}\right\}$$

$$\frac{da}{dN} = \max\left\{\left(\frac{da}{dN}\right)_I,\left(\frac{da}{dN}\right)_{II}\right\} \quad \text{for } a < kd$$

$$\frac{da}{dN} = \max\left\{\left(\frac{da}{dN}\right)_{III},\left(\frac{da}{dN}\right)_{FM}\right\} \quad \text{for } a \geq kd$$

with <g> = g if $g \geq 0$; <g> = 0 otherwise. Here, $(da/dN)_{FM}$ is the long crack FCGR based on either EPFM (ΔJ_{eff}) or LEFM (ΔK_{eff}).

$$\psi = R_e\, C_e\, (\Psi_e)^M + (1 - R_e)\, C_p\, (\Psi_p)^m$$

$$\Psi_\alpha = (1 + \mu n \rho)(\beta_\alpha R_n + 1)\,(\Delta\tau_n/2)(\Delta\gamma_{max}{}^\alpha/2)\,,\ \alpha = e, p$$

$R_e = \Delta\gamma_{max}{}^e/\Delta\gamma_{max}$ ($0 < R_e < 1$), $R_n = (\Delta\sigma_n/2)/(\Delta\tau_n/2)$, and with $\rho = (\Delta\sigma_{kk})/(2\Delta\tau_n) - R_n$ for $\psi \geq \xi(\psi_{th})_I$; $D_{aN} = D_{aN}$ evaluated at $\xi(\psi_{th})_I$ for $\psi < \xi(\psi_{th})_I$, where $(\psi_{th})_I$ is the MSC threshold value of ψ (corresponding to the smooth specimen fatigue limit) and ξ is a constant, $\xi > 1$.

insufficient to drive them. The former is considerably more sensitive to microstructure than the latter, and indeed is not subject to the same similitude and other LEFM requirements. General threshold conditions for nonpropagating cracks in each of the three regimes have been derived from these relations (McDowell, 1997), along with the specialized expressions for the completely reversed stress amplitude in the uniaxial case; here, σ_{FL} is the uniaxial fatigue limit. The Regime III threshold conforms to the LEFM threshold for mechanically small cracks. The model makes liberal use of standard constants based on fatigue tests above threshold, where a_i and a_f correspond to the initial and final crack length conditions which apply to these experiments. Most of the other parameters can be assessed from small crack observations (minima of FCGR and typical Kitagawa trajectories in Regime II) as well as the long crack threshold ΔK_{th}, as shown in Table 1.2.

Table 1.2 Identification of constants.

Long crack LEFM threshold, ΔK_{th}	
Smooth specimen fatigue limit amplitude, σ_{FL}	
r	b/r is the slope of the transition regime in the uniaxial Kitagawa diagram, with typical values of r in the range of 0.2 to 0.5 for typical values of fatigue strength exponent $b \approx -0.1$.
d	Discerned from minima of FCGR data for microstructurally small cracks (Wang and Miller 1992).
k, D	Established by intersection points on Kitagawa diagram for completely reversed uniaxial loading, i.e.

$$k = \left(\frac{\Delta K_{th}}{\sigma_{FL}} \frac{1}{\sqrt{\pi d}} \right)^{\frac{2Mr}{Mr-1}} \quad , \quad D = \left(\frac{\Delta K_{th}}{\sigma_f} \frac{1}{\sqrt{\pi k d}} \right)^{2Mr}$$

Constants A and B are selected to fit experimental data for crack growth rate in the MSC Regime I. Figure 1.1 shows the Kitagawa diagram (logarithmic plot of stress amplitude versus crack length for threshold conditions) computed from the theory for completely reversed uniaxial loading, with branches corresponding to the threshold conditions in each Regime. The threshold curves for $a < d$ and stresses below the fatigue limit σ_{FL} are computed using the MSC regime growth law with constant D_{aN} as specified in Table 1. This plot is very much characteristic of similar alloys as reported by Tanaka (1987) and Tanaka and Akiniwa (1989). Below these threshold stress amplitudes, cracks will arrest.

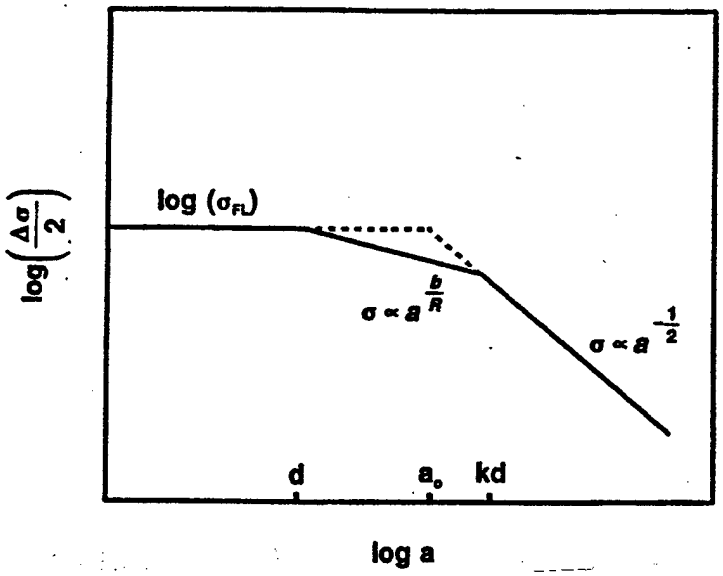

Figure 1.1 Computed Kitagawa diagram for HCF thresholds, with multiple contours for cracks in MSC regime, corresponding to 10^8, 10^9 and 10^{10} cycles. Material: 1045 steel (McDowell, 1997).

In Figure 1.2 we plot the predicted FCGR under completely reversed uniaxial loading for cracks growing from 10μm initial length up to 1 mm in a manner that will be familiar to practitioners of LEFM and EPFM. An equivalent stress intensity factor range, ΔK_J, may be defined based on the ΔJ-integral (Dowling, 1977). As distinguished from $\Delta K = Y\Delta\sigma(\pi a)^{1/2}$, ΔK_J includes a contribution from plasticity which may be very significant in the case of small cracks subjected to moderate to high remote stress

amplitudes in the LCF regime. The calculated values of ΔK_J are based on only the fraction of the stress range which is tensile, since closure effects are not explicitly considered. The characteristic dip in da/dN is evident in these calculations, as are a wide range of MSC Regime da/dN levels for different amplitudes; this dip is characteristic of experiments, and has also been predicted by plasticity-induced closure models which consider initially fully open small cracks growing from initial defects (Newman, 1994), analogous to short cracks growing from notches. The predicted da/dN versus ΔK_J trajectories generally approach the long crack R = 0 data (Hua and Socie, 1985) from the left, forming an asymptotic envelope. The minimum in da/dN is associated with the transition from Regime I to Regime II. Of course, for $\psi < (\psi_{th})_I$ the cracks would arrest at a = d, as shown for the lowest stress amplitude on the plot. The typical scatter for small crack behavior observed for moderate amplitudes to HCF can therefore be understood, at least some extent, to arise from deterministic amplitude dependence in addition to material microstructure variation, as pointed out in the plasticity-induced closure modeling of Newman (1994). The non-uniqueness of growth behavior in Figure 1.2 illustrates the apparent anomalies that can arise when interpreting small crack behavior in terms of standard long crack fracture mechanics, and the utility of the present framework.

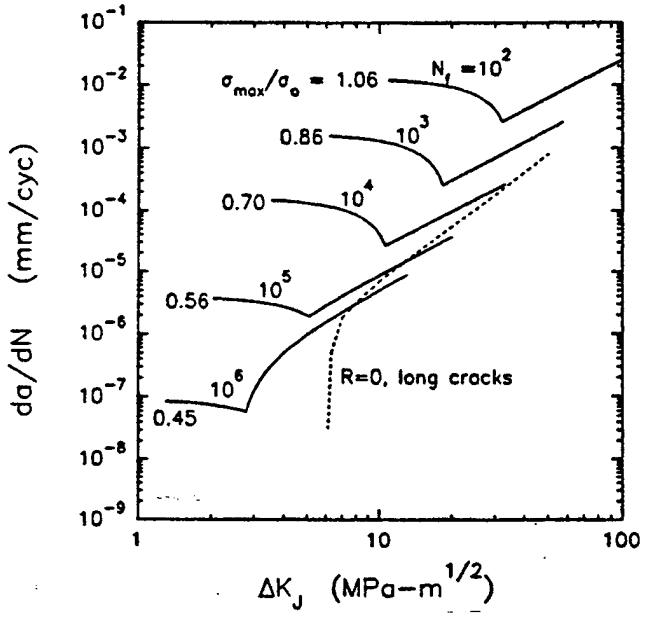

Figure 1.2 Predicted da/dN versus ΔK_J for small cracks in 1045 steel for a range of completely reversed uniaxial stress amplitudes; σ_o = 548 MPa is the mean cyclic plastic flow stress (McDowell, 1997).

It is important to note that the framework presented here is more correlative than predictive in nature, but covers a broad range of crack lengths (including the MSC regime) and stress states that might be encountered in hot spot regions. This robustness, along with its its capacity for nonlinear amplitude and stress state sequence effects, closed form integrability for constant amplitude loading (efficient for block loading integration), and compatibility with the format of crack growth required for consistency with the diagnostic inspection scheme based on distributed microsensors, renders such a framework particularly suitable for this particular class of applications. We have conducted axial-torsional fatigue experiments on AISI 304 SS, 1045 steel and PH 13-8 Mo SS to evaluate sequence effect capabilities of the model.

Once a crack propagates past the microstructurally small regime, it generally moves into Stage II propagation (mode I-dominated), but may still be under the influence of notch root gradients associated with the hot spot location. Hence, it is necessary to invoke the specific solution(s) obtained for each

stress concentration to properly capture the change of fatigue crack driving force with crack extension. In some cases, the driving force falls off below threshold conditions to continue propagation, and crack arrest may occur. In other cases, the crack growth rate may accelerate, i.e. dK/da increases as the crack lengthens.

As the crack extends beyond the influence of the notch, the crack front often takes on a complex, tortuous path in response to the three-dimensional shape of the component. Complications arise for such mechanically long cracks due to phenomena such as premature crack face contact that reduces the driving force or wedging action that may enhance it, variation of crack driving force along the crack front and tunneling, complex changes of specimen compliance and associated dynamical response, etc. These are the principal technical challenges associated with the modeling the growth of long cracks in components. In most cases, the occurrence of long cracks represents a potential envelope condition for continued safe operation and therefore must be evaluated for impending criticality and associated component distress. It is the formation and early growth of such cracks that is of most practical interest to an integrated on-board diagnostic/prognostic system in terms of estimating service life well into the future.

References for Section 2.2.1.1a

Dowling, N.E., 1977, "Crack Growth During Low-Cycle Fatigue of Smooth Axial Specimens," *Cyclic Stress-Strain and Plastic Deformation Aspects of Fatigue Crack Growth*, ASTM STP 63, pp. 97-121. Philadelphia: ASTM.

Hobson, P.D., 1985, "The Growth of Short Fatigue Cracks in a Medium Carbon Steel," PhD Thesis, University of Sheffield, Sheffield, UK.

Hobson, P.D., Brown, M.W. and de los Rios, E.R., 1986, "Two Phases of Short Crack Growth in a Medium Carbon Steel," in *The Behaviour of Short Fatigue Cracks*, K.J. Miller and E.R. de los Rios (eds), EGF Publ. 1, Inst. Mech. Engrs, London, pp. 441-459.

Hua, C.T. and Socie, D.F., 1985, "Fatigue Damage in 1045 Steel Under Variable Amplitude Biaxial Loading," *Fatigue Fract. Engng. Mater. Struct.*, Vol. 8, No. 2, pp. 101-114.

Hussain, K., de los Rios, E.R. and Navarro, A., 1993, "A Two-Stage Micromechanics Model for Short Fatigue Cracks," *Engng. Fract. Mech.*, Vol. 44, No. 3, pp. 425-436.

McDowell, D.L., 1996, "Basic Issues in the Mechanics of High Cycle Fatigue," *Int. J. Fracture*, Vol. 80, pp. 103-145.

McDowell, D.L. and Berard, J.-Y., 1992, "A ΔJ-based approach to biaxial fatigue," *Fatigue Fract. Engng. Mater. Struct.*, Vol. 15, No. 8, pp. 719-741.

McDowell, D.L. and Bennett, V.P., 1996, "A Microcrack Growth Law for Multiaxial Fatigue," *Fatigue Fract. Engng. Mater. Struct.* Vol. 19, No. 7, pp. 821-837.

McDowell, D.L., 1997, "Multiaxial Small Fatigue Crack Growth in Metals," to appear in *Int. J. Fatigue*.
Miller, K.J., 1993, "The Two Thresholds of Fatigue Behaviour," *Fatigue Fract. Engng. Mater. Struct.*, Vol. 16, No. 9, pp. 931-939.

Newman, J.C., Jr., 1994, "A Review of Modelling Small-Crack Behavior and Fatigue-Life Predictions for Aluminum Alloys," *Fatigue Fract. Engng. Mater. Struct.*, Vol. 17, No. 4, pp. 429-439.

Nisitani, H., 1987, "Behavior of Small Cracks in Fatigue and Relating Phenomena," in *Current Research on Fatigue Cracks*, T. Tanaka, M. Jono and K. Komai (eds), Current Japanese Materials Research, Elsevier, Vol 1, pp. 1-26.

Nisitani, H., Kawagoishi, N. and Goto, M., "Growth Behavior of Small Fatigue Cracks and Relating Problems," Handbook of Fatigue Crack Propagation in Metallic Structures, Andrea Carpinteri, Ed., 1994, pp. 733-778.

Patel, A., 1997, "Growth of Small Fatigue Cracks in PH 13-8 Mo Stainless Steel ," M.S. Thesis, Georgia Instititute of Technology, Atlanta, GA.

Socie, D.F., 1993, "Critical Plane Approaches for Multiaxial Fatigue Damage Assessment," in *Advances in Multiaxial Fatigue*, ASTM STP 1191, D.L. McDowell and R. Ellis (eds), pp. 7-36. Philadelphia: ASTM.

Tanaka, K., 1987, "Short-Crack Fracture Mechanics in Fatigue Conditions," in *Current Research on Fatigue Cracks*, T. Tanaka, M. Jono and K. Komai (eds), Current Japanese Materials Research, Elsevier, Vol 1, pp. 93-117.

Tanaka, K. and Akiniwa, Y., 1989, "Propagation and Non-Propagation of Small Fatigue Cracks," in Advances in Fracture Research, Proc. ICF7, Houston, TX, March 20-24, Vol. 2, pp. 869-887.

Wang, C.H. and Miller, K.J., 1992, "The Effects of Mean and Alternating Shear Stresses on Short Fatigue Crack Growth Rates," *Fatigue Fract. Engng. Mater. Struct.*, Vol. 15, No. 12, pp. 1223-1236.

Wang, C.H., 1996, "Effect of Stress Ratio on Short Fatigue Crack Growth," *ASME J. Engng. Mater. Techn.*, Vol. 118, pp. 362-366.

b. Microstructure-Dependent Small Crack Propagation from Notches

Co-investigator: Richard W. Neu (Georgia Tech)
Graduate Student: Akshay Patel

Figure 1.3 compares experimental measurements in our laboratory (Patel, 1997) for microstructurally small crack growth in PH 13-8 Mo stainless steel, a corrosion-resistant alloy for use in the next generation rotor hubs, with predictions using a sequential grain boundary blockage model (Wang, 1996). Most of this study focused on the small crack growth behavior to determine the limit of the applicability of conventional fracture mechanics which is often used in remaining life prediction methodologies. Constants for long crack growth models were also determined for this material. The experimental details are given in Patel et al. (1999). Much of the data needed for the remaining life prediction schemes is provided in the paper. In addition, two fatigue crack growth models (Newman, 1981; Wang, 1996) for predicting the growth of small cracks were evaluated. The details are given in Patel (1997).

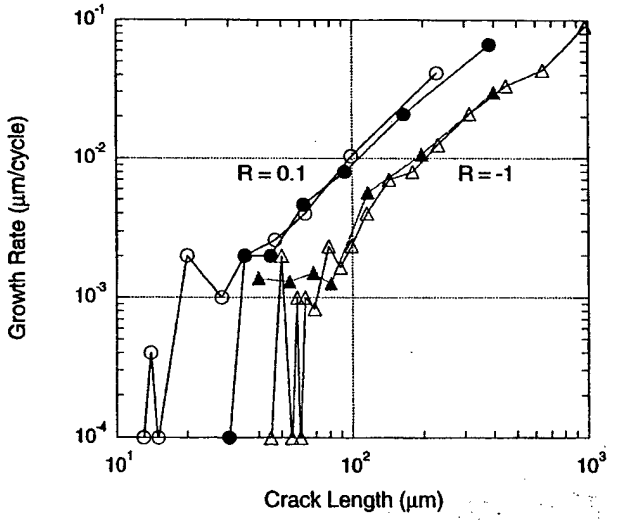

Figure 1.3 Comparison of predicted and experimentally measured crack length versus cycles in 13-8 PH Mo stainless steel at room temperature (Patel, 1997).

c. Computational Micromechanics of Fatigue of Polycrystalline Metals

Co-investigator: David L. McDowell (Georgia Tech)
Graduate Student: Valerie Bennett

To improve our understanding of the role of microstructure in small crack propagation, we have employed computational cyclic planar double slip crystal plasticity to develop an understanding of:

(i) the role of heterogeneity of grain orientation distribution on the cyclic microplasticity and other relevant candidate fatigue crack initiation parameters for polycrystals under nominally HCF loading conditions, and
(ii) crack tip opening and sliding displacements for microstructurally small surface cracks in polycrystals subjected to monotonic and cyclic loading as a function of crack length relative to grain size and applied stress state.

Understanding gained from these calculations is of value in developing improved, "next generation" multi-stage small crack propagation laws. There are two sources of mode mixity - on a *macro* level (combined loading situation), and on the *micro* level - which affect the propagation of small crystallographic cracks. This work explores mode mixity on the micro level by utilizing a computational model to simulate microstructural influences on driving forces for the formation and growth of small cracks.

Two-dimensional computational cyclic crystal plasticity calculations have been conducted to study the distribution of cyclic slip and critical plane-type fatigue parameters in a material with nominal stress-strain characteristics of 4340 steel. Cases of applied cyclic tension-compression and cyclic shear have been analyzed at strain amplitudes below macroscopic yielding. Emphasis is placed on stress state and amplitude dependence of the distribution of these parameters among grains. The role of anisotropic plasticity is isolated by assuming the elastic behavior of grains to obey homogeneous, isotropic linear elasticity. All grains are of equal dimension and are assigned a random orientation distribution. It is found that the distribution of the Fatemi-Socie critical plane fatigue parameter among grains is Weibull-distributed, and it is argued that it forms an improved linkage to cyclic crack tip displacement for microstructurally small cracks.

We have also computed crack tip opening and sliding displacements as a function of maximum applied tensile strain (from well below to just above nominal yielding) for small cracks within surface grains surrounded by a nearly random orientation distribution of grains subject to both monotonic and cyclic remote loading conditions. Multiple realizations of the local microstructure are examined for each crack length for sub-grain size cracks, with results normalized to the ratio of crack length to grain size. Key results include a very strong role of the free surface on crack tip displacement, with opening displacement being much greater than the sliding for suitably small crystallographic cracks in the surface grains. There is also a strong effect of the orientation of the next grain ahead of the crack on local mode mixity of the crack tip displacements, which plays an increasingly influential role as the crack tip approaches the first grain boundary, with a lessened role for successive encounters with grain boundaries, analogous to previous idealized solutions based on pile-ups represented by continuously distributed dislocations, but different in detail. In effect, this work is the **first-ever** exploration of crack tip behavior in relative large scale polycrystal realizations.

Finite Element Models Based on Crystal Plasticity

A planar double slip idealization of cyclic crystal plasticity was implemented in ABAQUS [1] through the User MATerial subroutine, UMAT. Crystal plasticity models relate applied stress to the microscopic crystallographic slip response of the material. These models provide a phenomenological description of crystallographic slip and dislocation interactions at the grain level and offer insight into the nature of heterogeneous cyclic plasticity and driving forces for small crack growth due to intergranular misorientation. This micromechanical model is useful to (1) study the distribution of cyclic

microslip amongst a set of grains in a polycrystal, (2) investigate the character of crack tip fields for small cracks in the presence of crystallographic anisotropy and heterogeneity, and (3) better understand the interaction of a crack with microstructural barriers. Naturally, the 2-D nature of planar double slip gives these calculations more qualitative value when assessing the influence of microstructure. Moreover, the effect of shear localization within slip bands is not explicitly treated with this model without the introduction of bands of preferred plastic flow or crystallographic systems with less resistance to flow. None-the-less, it offers a more direct treatment of crystallographic dislocation glide than most previous ad hoc models.

For a FCC crystal, there are 12 crystallographic slip systems in 3-D. For 2-D planar slip in a {110} plane, the deformation can be represented by a pair of effective slip systems [2]. These effective slip systems (plane-strain assumption) maintain a fixed orientation with respect to each other and rotate with respect to the continuum. Figure 1.4a shows the geometry for the two effective slip systems. The bisector angle, θ, orients the slip system pair relative to the fixed specimen axis. The angle ϕ defines the crystallographic close-packed planes in relation to the bisector angle, where $\phi = 35.1^\circ$ for a FCC crystal.

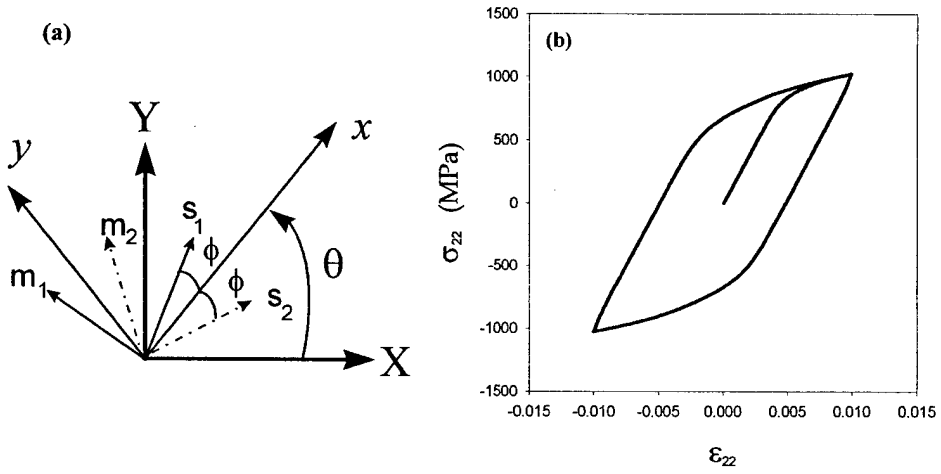

Figure 1.4 Simulation using planar double slip approximation: **(a)** assignment of bisector angle, and **(b)** cyclic stress-strain behavior of a 100 grain polycrystal subjected to cyclic tension-compression.

The slip system level constitutive framework essentially follows that of Cailletaud *et al.* [3] and Jordan and Walker [4]. Pure nonlinear kinematic hardening was used to describe the cyclically stable response. To represent cyclically stable behavior, pure nonlinear kinematic hardening is employed according to the Armstrong-Frederick form. The backstress relates to long range interactions due, for example, to dislocation walls produced by cyclic loading and acts in the opposite direction of loading to resist deformation. Since the finest scale of resolution considered in the present model is the crystallographic slip system (CSS), it is assumed that all phenomena which are related to lengths scales below the grain level (e.g., atoms and lattice defects) are modeled at the CSS level using this phenomenological approach. The local resolved shear stress on each slip system is the driving force for the rate of dislocation shearing on each slip system. A backward Euler, fully implicit integration scheme was employed for the numerical integration. An incremental line search algorithm and a time step subincrementation scheme were both used to assist the rate of convergence [5]. The plane strain tension-compression hysteresis loops were assigned a behavior typical of uniaxial behavior of 4340 steel for illustrative purposes, as shown in Fig. 1.4b for a 100 grain polycrystal. Elastic behavior in all calculations reported here is assumed to be isotropic and linear elastic. For certain metals such as Al and its alloys, the degree of elastic anisotropy is very mild, while for others it plays an important role.

Polycrystal Distribution of Small Crack Formation and Growth Parameters

As discussed earlier, the extent and distribution of plasticity among grains is an important factor in fatigue crack formation and early Stage I growth. A direct measure of the cyclic microplasticity is the maximum cyclic plastic shear strain on a slip system normalized by the global cyclic plastic strain, defined here as the maximum cyclic plastic shear strain amplitude in individual grains normalized by the applied macroscopic cyclic plastic strain (N-CM parameter). Further, we consider similar distributions of two other prominent multiaxial fatigue correlation parameters, the Fatemi-Socie parameter (F-S)

$$(\Delta\gamma_{max}{}^{p} / 2)\ \{1 + k^{*}\ (\sigma_n{}^{max}/\sigma_y)\} = C_3$$

where C_3 is a constant for a given life, and the Mohr-Coulomb parameter (MC)

$$(\Delta\tau_{max}{}^{\alpha} / 2) + k\, P_{hyd} = C_2\ .$$

A series of 2-D (plane strain) finite element analyses were conducted to assess polycrystal distributions. The grains were modeled as 8-noded quadrilateral, biquadratic elements. A total of 576 grains were employed in the analyses. In each realization, grain orientations were randomly assigned to describe an initially isotropic effective medium. The strain amplitude levels for tension and shear ranged from well below to just above the total strain at the 0.2% offset plastic strain cyclic yield point (values are $\varepsilon_y = 0.006$ and $\gamma_y = 0.0063$, respectively) of the polycrystal. Strain was applied at an effective strain rate of $1.5\text{x}10^{-3}\ s^{-1}$. Peak strain levels considered were fractions (0.3, 0.5, 0.7, 0.9, 1.0) of the cyclic total yield strain in order to investigate the cyclic microstrain distributions under predominately HCF conditions. A total of two completely reversed macroscopic strain cycles were applied to ensure a cyclically stable hysteresis loop in the simulation. The distribution of parameters among grains arising from microstructural inhomogeneity are assessed by the fitting of Probability Distribution Functions (PDFs). While details of each PDF is of little importance, the overall shape of these distributions may reveal useful information regarding the stress state and amplitude dependence of the driving forces for fatigue crack formation and microstructurally small crack propagation. They should not be confused with PDFs for fatigue strength per se, as it is only our intent to consider the distribution of various driving force parameters as a function of stress amplitude and stress state. For each strain level, the probability distribution among grains for normalized forms of the N-CM, F-S and MC parameters are shown in Fig. 1.5. With increasing strain, plots are skewed to the left. Error bars denote the range of the distribution obtained from several realizations of orientation distribution of grains; there is little variation among the simulations. Clearly, only a limited number of grains experience cyclic plastic strains that considerably exceed the macroscopic plastic strain; these grains are expected to control fatigue crack formation and early Stage I growth. For all strain levels considered here, the overall shapes of the distributions are very similar. In addition to such plots, we are also considering plots of distributions of the differences of these parameters among nearest neighbor grains and for different stress states.

CTOD and CTSD Studies

For the propagation of small fatigue cracks in polycrystals, it is evident from both experimental observations and previous micromechanical calculations, based on slip band impingement, that grains, phases, and other high angle boundaries play a key role in at least temporarily retarding the advance of the crack front. The internal stress fields, which arise from pile-ups of dislocations emitted from the fatigue crack at such boundaries and local constraint conditions on slip at the crack tip, conspire to substantially reduce the fatigue crack growth rate prior to boundary impingement. According to the approach of Navarro and de los Rios [6], the stress concentration in the adjacent misoriented grain must reach the threshold level to initiate slip in that grain in order to nucleate new cracks and coalesce the cracks across the boundary. If the stress concentration in the next grain is insufficient, the crack will be

arrested by the boundary interaction. They employ the Bilby-Cottrell-Swinden (BCS) model of continuously distributed dislocations for a freely slipping crack of length 2a embedded in a grain of diameter D and assume that the crack tip plastic zone extends to the boundary; dislocations are blocked at the grain boundary, giving rise to a backstress necessary to achieve equilibrium under a given applied stress. Propagation is assumed to follow in proportion to the CTSD. This model describes several key phenomena, including periodic retardation/acceleration behavior of microstructurally small cracks, an explicit relation for the fatigue limit, a prediction of the Kitagawa diagram for the threshold stress intensity factor for cracks beyond the first grain, and the transition to long crack behavior, which is assumed to occur when the size of the cyclic plastic zone just reaches the grain size (crack length on the order of 7-10 grains). This finding agrees with experiments [7] that show that the sensitivity to microstructure barriers is far more evident for small cracks growing over the first few grains in many cases. Similar observations are prevalent for other polycrystals. Long crack behavior corresponds to a condition where the plastic zone size is suitably small compared to crack length for SSY conditions to apply.

Calculations for the driving forces for growth of microstructurally small cracks in a heterogeneous polycrystal using computational crystal plasticity have been very limited. It behooves us to consider first the case of mixed mode crack tip displacements for surface cracks in a polycrystal subjected to monotonic loading to understand microstructure-level shielding and redistribution effects in the absence of slip band considerations in fatigue. In this section we report computational results for crack tip opening and sliding displacements as a function of applied average stress ranging from well below to slightly above nominal yielding for tensile loading of small crystallographic cracks in a surface grain which is surrounded by a range of nearest neighbor grain orientations, all grains being the same size. The grain ahead of the crack tip along the slip plane is assigned each of two orientations: either identical to that of the surface grain with the crack, or in a conjugate slip orientation with significant misorientation relative to the surface grain. The former assignment is to some extent analogous to a crack in a large surface grain and promotes shear localization or slip transfer to the next grain to the greatest extent, while the latter is expected to produce maximum blockage of the driving force (CTD) for growth. Results for the CTSD and CTOD are reported at 2μm and 25 μm behind the crack tip. For the smallest crack analyzed, a/d = 0.25, we report the CTSD and CTOD at a distance 18 μm behind the crack tip. We might consider the values at 25μm to be CSD and COD, rather than crack tip values, but we do not make that distinction in the nomenclature here so as to facilitate presentation.

The crack is assumed to reside within a surface grain which is favorably oriented for single slip, with one of the two available slip systems aligned with the macroscopic maximum shear plane orientation. For the case of tensile loading, the surface crack is oriented at 45° to the tensile axis. The geometry used in the finite element analyses is a two-dimensional, plane strain specimen with a height of 0.9 mm and width of 1 mm. The grains are rectangular with the dimensions of 0.1 mm (= d) by 0.15 mm. The finite element program ABAQUS [1] is used to perform the analyses with the UMAT formulation for crystal plasticity described in a previous section. Two-dimensional, 8-noded quadrilateral, biquadratic (CPE8R) and 6-noded quadratic (CPE6) solid elements were used throughout the mesh. Considerable mesh refinement is employed in the surface grain and nearest neighbors; the elements surrounding the crack tip are 0.5 μm in dimension to resolve the near tip CTSD and CTOD properly. The CTSD and CTOD are determined by resolving the relative displacements of two nodes along the initial crack surface into components along and normal to the original crack plane, respectively. Crack surfaces are assumed to be initially perfectly planar. Three a/d ratios (a = crack length) are analyzed in this study (0.25, 0.5, and 0.97). All cracks are stationary, i.e. introduced without prior effects of growth history. In the grain adjacent to the cracked surface grain and diagonally in the path of the crack plane, labeled as grain A, two different orientations of the slip systems are considered. These include an aligned orientation that promotes extended single slip on the plane of the crack and the conjugate slip case, where both systems are oriented equally with respect to the favored slip system in the surface grain. The remaining grains are

constrained to have a minimum misorientation within 15 degrees of their nearest neighboring grain, but are otherwise randomly oriented. It should be recognized that while Grain A provides the most influence due to misorientation, the adjacent grains also contribute; their influence affects the solution differently from that of a crack interacting with a bicrystal grain boundary, as reported in Ref. [8]. The present study considers a range of peak applied strain levels as fractions (0.3, 0.5, 0.7, 0.9, 1.0) of the total strain at yield, $\varepsilon_y = 0.006$, corresponding to the cyclic stress-strain curve. Figure 1.6 also shows the contour plots of the plastic zones at the crack tip for a/d = 0.5, illustrating the role of the orientation of the next grain ahead of the crack tip in blocking slip and affecting the local mode mixity at the crack tip.

Reference elastic solutions were performed in each case using *precisely* the same mesh and boundary conditions, but suppressing the plasticity. Effects of the free surface are reflected in the elastic solutions as well. The elastic behavior in both sets of simulations is linear, isotropic and homogeneous; hence, there are no weak elastic singularities at junctions of grains. Of course, this is an approximation for crystals, but the intent here is to isolate the effects of plastic anisotropy.

Figure 1.7 shows plots of CTOD and CTSD from the calculations for monotonic loading, along with the elastic reference solutions. For both orientations of the adjacent grain considered in this work, the CTOD 2μm behind the crack tip is on the order of three to six times greater than the elastic solution as general yielding is reached. At 18 μm behind the crack tip, the opening displacements are two to three times greater than the elastic solution. For both distances behind the crack tip, the CTOD in the single slip case significantly exceeds that for the conjugate slip orientation of Grain A for an applied strain less than $0.5\varepsilon_y$. The CTSD, on the other hand, lies below the elastic solution for an applied strain below half the macroscopic yield strain for both distances behind the crack tip. Above $0.5\varepsilon_y$, the CTSD for the single slip case increases significantly above the elastic solution, while it diminishes to small values as general yielding is approached for the conjugate slip orientation of Grain A. The largest difference between the elastic and the elastic-plastic solutions occurs for an aligned orientation of the adjacent Grain A. This might be representative of the case of a large, favorably oriented surface grain, for example, and suggests why the growth rates might be considerably higher than for cracks in smaller surface grains. Misorientation of the next grain ahead of the crack path does, however, cause the sliding displacements near the crack tip to be significantly less than for the favorable orientation of Grain A for single slip at the largest applied strain level of $0.9\varepsilon_y$.

These CTOD findings differ markedly from those calculated based on slip band impingement on a grain boundary ahead of the crack as in distributed dislocation [6-7, 9-10] or finite element solutions that use some type of constraint argument to represent slip bands [8]. Of course, Fig. 1.7 clearly shows that the CTOD dominates the CTSD even in the reference elastic solutions that do not depend in any way on the arrangement of grains or their orientation (due to elastic homogeneity), but does depend on the geometry and boundary conditions we impose. In particular, the CTOD near the tip departs significantly form the elastic solution well below $0.5\varepsilon_y$, and then continues to intensify relative to the elastic solution as general yielding is approached. The increase of the CTOD is at least that of the CTSD with an increase of applied strain for both realizations of the adjacent grain orientation. This illustrates why application of the elastic solution to the analysis of small cracks can produce anomalous results, even in the HCF regime. We also note that the ratio of CTOD/CTSD for both cases differs substantially at 2 μm and 18μm behind the crack tip, suggesting those surface measurements might not reflect crack tip mode mixity very well.

The CTOD solutions appear to be strongly influenced by the interaction of the crack tip with the free surface, and also by the full set of nearest neighbor grains surrounding the cracked grain. This is a feature that has not been provided by previous analyses. The capacity for multislip in the cracked surface grain is activated by stress redistribution associated with neighboring grains. Plots of von Mises stress contours and contours of equivalent plastic strain support this assertion.

Finally, Fig. 1.8 presents results of CTOD and CTSD calculations for three cycles of tension-compression loading for both cases where the next grain is favorably oriented for slip or arranged in a

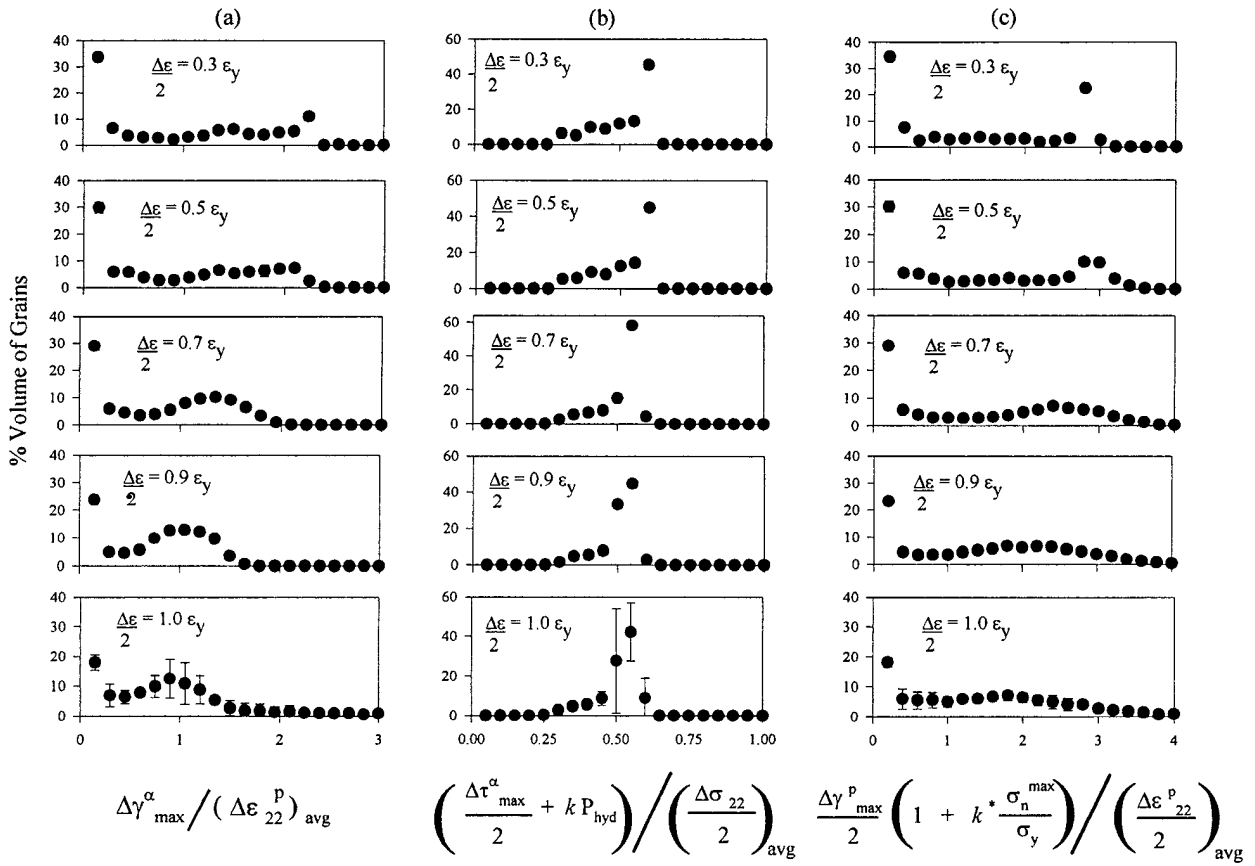

Figure 1.5 Distribution functions for the volume fraction of grains subjected to cyclic tension-compression loading for (a) the N-CM parameter, (b) the MC parameter and (c) the F-S parameter as a function of applied strain amplitude.

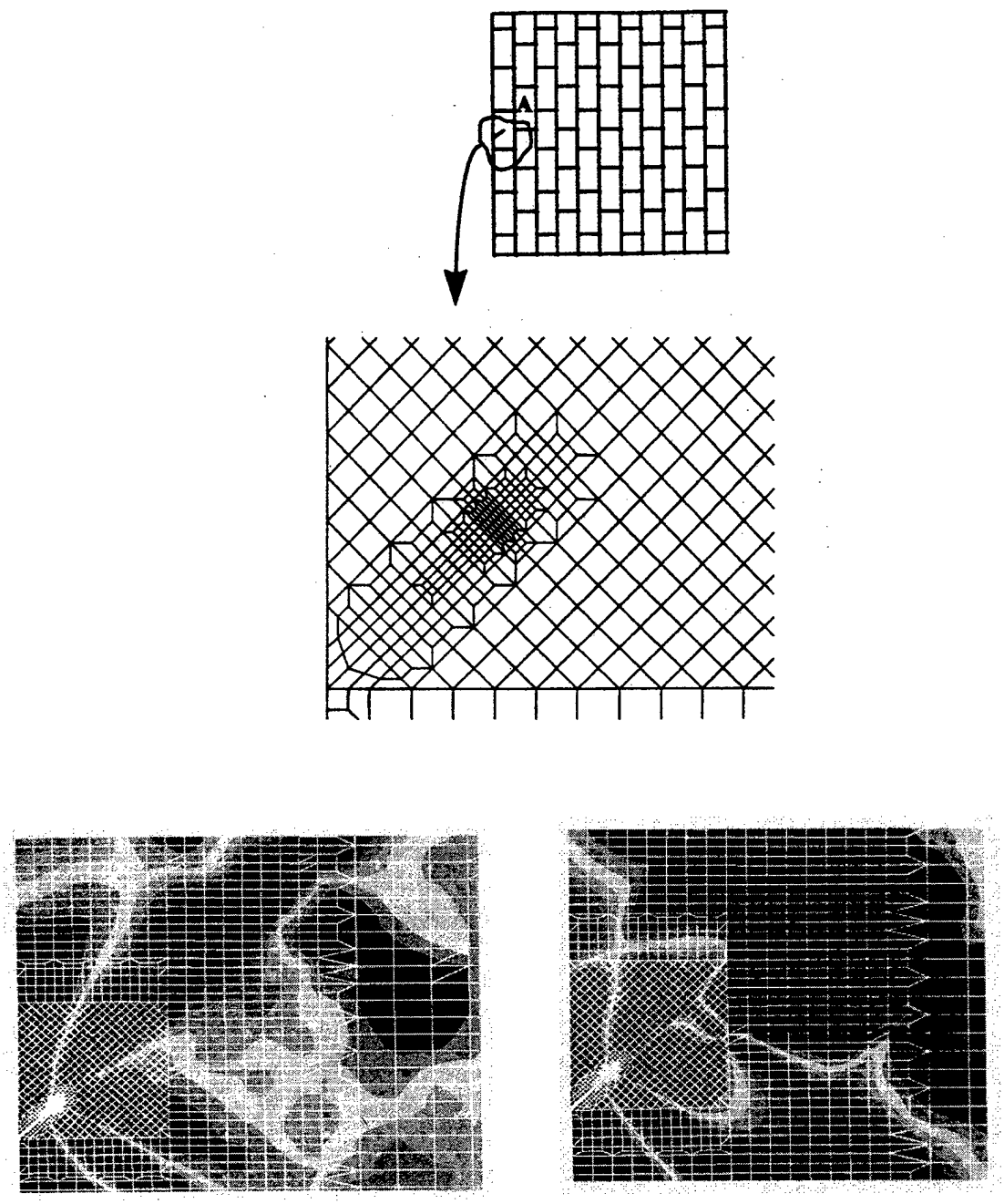

(a) (b)

Figure 1.6 Typical FE mesh with the highly refined crack tip region within the surface grain (see inset), and contour plots of effective plastic strain for an applied tensile strain of $0.7\varepsilon_y$ for **(a)** single slip and **(b)** conjugate slip orientation of the next grain for a/d = 0.25; the peak strain intensity has a threshold of 1% plastic strain.

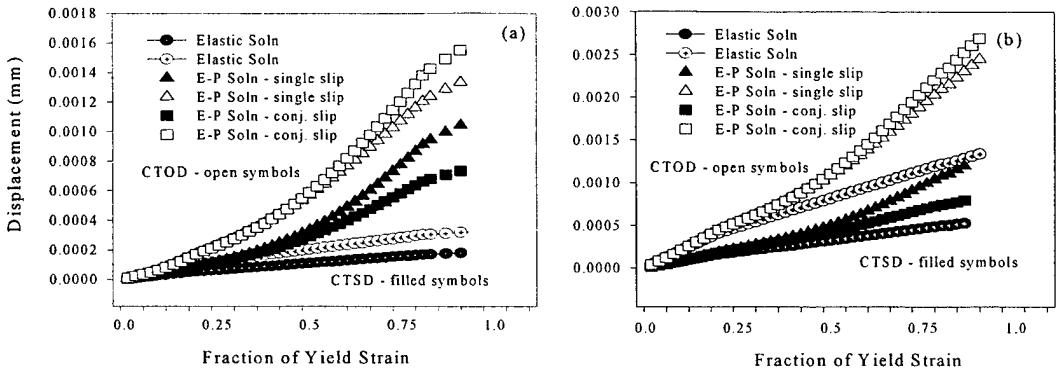

Figure 1.7 CTSD and CTOD as a function of applied polycrystal tensile strain for a surface crack (a/d = 0.5) in a favorably oriented grain with a range of nearest neighbor grain (Grain A) orientations, evaluated (a) 2 μm and (b) 25 μm behind the crack tip.

"hard" orientation which tends to block slip from transferring from the surface grain. Interpenetrating of crack surfaces is prevented by use of a contact algorithm in the finite element code (contacts assumed frictionless here), which is very time-consuming computationally.

The cyclic crack tip opening and sliding displacements stabilize somewhat after several cycles. It is very interesting to note that a phase angle develops between the CTOD and CTSD as the degree of crack tip cyclic plasticity increases. There is a marked ratchetting behavior evident in the sliding – the mean sliding progressively increases with cycles; further, the amplitude of sliding decreases, while the opening amplitude increases at a decreasing rate with cycles.

References for Section 2.2.1.1c

[1] ABAQUS, Ver. 5.7, Hibbitt, Karlsson & Sorensen, Inc., Pawtucket, RI, 1998.

[2] Rashid, M. M., "Texture Evolution and Plastic Response of Two-Dimensional Polycrystals," *Journal of the Mechanics and Physics and Solids*, Vol. 40, No. 5, 1992, pp. 1009-1029.

[3] Cailletaud, G., Doquet, V., and Pineau, A., "Cyclic Multiaxial Behavior of an Austenitic Stainless Steel: Microstructural Observations and Micromechanical Modeling," in *Fatigue under Biaxial and Multiaxial Loading*, ESIS10, K. Kussmaul, S. McDiarmid, and D. Socie, Eds., Mechanical Engineering Publications, London, 1991, pp. 131,-149.

[4] Jordan, E. H. and Walker, K. P., "A Viscoplastic Model for Single Crystals," *ASME Journal of Engineering Materials and Technology*, Vol. 114, 1992, pp. 19-26.

[5] Cuitiño, A. M. and Ortiz, M., "Computational Modeling of Single Crystals," *Modelling and Simulation in Materials Science and Engineering*, Vol. 1, 1992, pp. 225-263.

[6] Navarro, A. and de los Rios, E.R., "A Model for Short Fatigue Crack Propagation With an Interpretation of the Short-Long Crack Transition," *Fatigue and Fracture of Engineering Materials and Structures,* Vol. 10, No. 2, 1987, pp. 169-186.

[7] Tanaka, K., "Short-Crack Fracture Mechanics in Fatigue Conditions," *Current Research on Fatigue Cracks*, eds. T. Tanaka, M. Jono and K. Komai, Current Japanese Materials Research, Elsevier, 1, 1987, pp. 93-117.

[8] Li, C., "On the Interaction among Stage I Short Crack, Slip Band and Grain Boundary: A FEM Analysis," *International Journal of Fracture*, Vol. 43, 1990, pp. 227-239.

[9] de los Rios, E. R., Mohamed, H. J., and Miller K. J., *Fatigue and Fracture of Engineering Materials and Structures,* Vol. 8, 1985, pp. 49-63.

[10] Tanaka, K., Akinawa, Y., Nakai, Y., and Wei, R. P., "Modeling of Small Fatigue Crack Growth Interacting with Grain Boundary," *Engineering Fracture Mechanics*, Vol. 24, 1986, pp. 803-819.

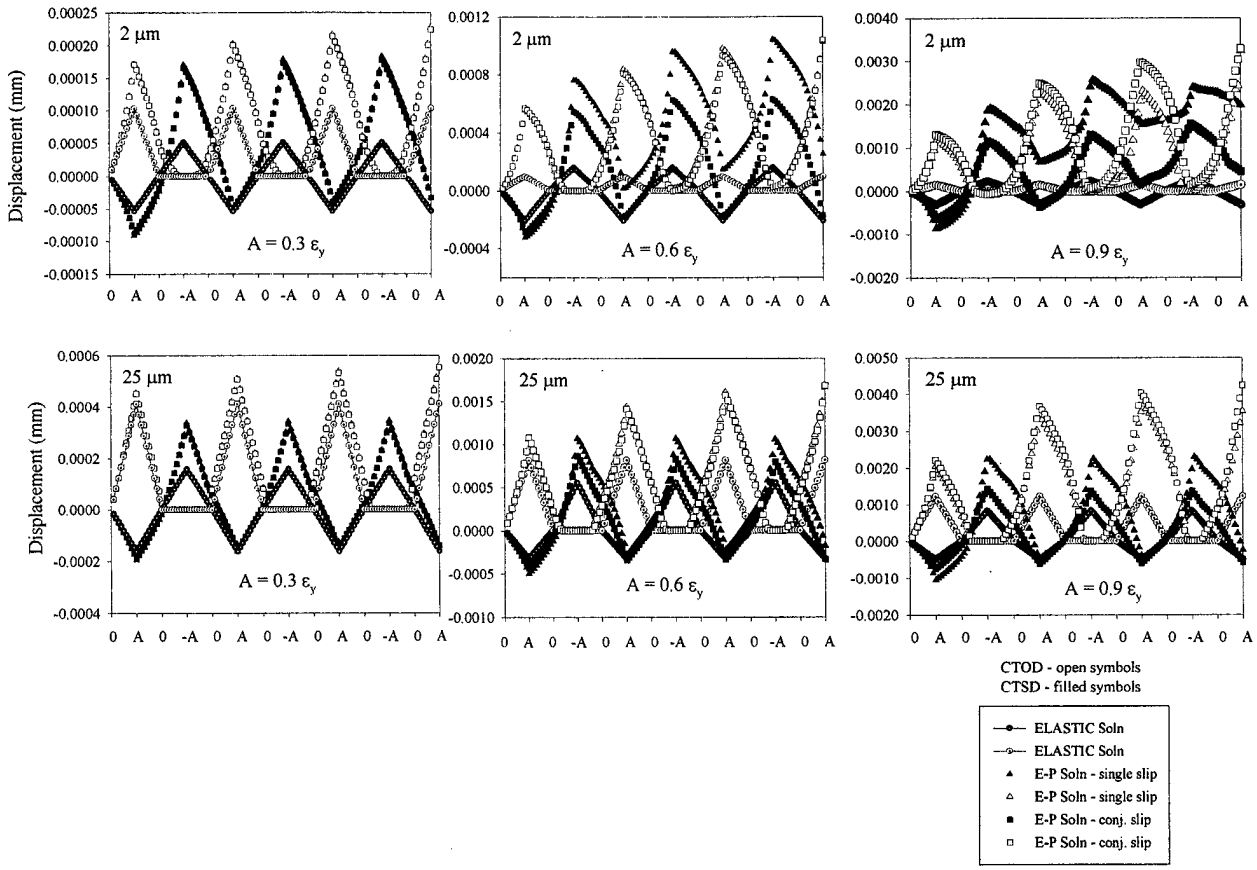

Figure 1.8 Cyclic CTOD and CTSD for cyclic tension-compression loading for crack oriented at 45° with a/d = 0.5 for strain amplitudes of 0.3 ε_y, 0.6 ε_y and 0.9 ε_y at distances of 2 and 25 μm behind the crack tip.

d. Fretting Fatigue Damage

Co-investigator: Richard W. Neu (Georgia Tech)
Graduate Students: John Pape, Dana Swalla

Fretting fatigue is a widespread phenomenon that occurs in a vast number of engineering components where two bodies are in contact and undergo a small oscillatory slip and at least one of the bodies is experiencing a bulk cyclic loading. Fretting fatigue is a widespread problem in navel structural components and is often the root cause of fatigue crack nucleation. Some examples include fasteners such as bolted, riveted, and clamped joints; press-fit components; keyways, splines, and dovetails; steel ropes and springs. Since it is often not feasible to eliminate fretting fatigue as a failure mode, the use of sensors at critical locations ("hot spots") where fretting fatigue cracks will grow is a viable option. However, to interpret the sensor signals under these conditions requires a better fundamental understanding of the stages of fretting fatigue and how they relate the sensor signals. A model that describes this damage evolution that includes crack nucleation and the growth of small cracks is needed for prognostics.

Fretting fatigue crack nucleation and early crack growth is characterized using both destructive and non-destructive methods to determine the stages of the fretting fatigue process. This research involves understanding the growth of small cracks under both plain (i.e., absence of fretting) and fretting fatigue conditions. These well-controlled tests are used as a test bed for emerging sensor technologies in both determining minimum damage size that can be detected as well as separation of damage from fretting and plain fatigue. This information is used to develop the next generation life prediction models for fretting fatigue crack nucleation and early crack growth. The materials investigated in this program include PH 13-8 Mo stainless steel and 4340 steel used in critical aerospace components (specifically in CH-46 helicopter).

An extensive literature survey of modeling methodologies that can be used to predict fretting fatigue crack nucleation and crack growth was conducted to determine the state of the art and directions for the next generation in modeling. Nucleation involves all the processes leading to the formation of a crack, typically of the order of 10 μm. The crack growth process describes the additional crack driving forces under fretting fatigue. The Fretting Fatigue Damage Parameter (Ruiz et al., 1984) is currently the most widely used model to predict fretting fatigue crack nucleation (see Fig. 1.9a). It is an empirical model that has been shown to accurately predict the location of fretting fatigue cracks along a contact interface, but cannot account for differences in fretting fatigue behavior for different materials because of its lack of a physical basis. The mechanisms of fretting fatigue crack nucleation appear to be closely related to those of multiaxial low cycle fatigue, although occurring in a relatively smaller process volume (Neu et al., 1999). Next generation nucleation models may be based on multiaxial fatigue criteria, such as a critical plane approach (Socie, 1993), which can predict the direction of early crack growth as well as the nucleation location (see Fig. 1.9b). These critical plane approaches can potentially bridge nucleation and fracture mechanics approaches. Detailed discussion is given in McDowell et al. (1997) and Neu et al. (1999).

Our work has focused on validating and refining these next generation approaches to make them useful in engineering prognostic tools. This includes testing various hypotheses in applying different multiaxial fatigue criteria to clarify and validate this methodology. The idea is good but there has been no validation especially with respect to physical damage. This validation includes determining the local cyclic stress-strain response along the interface and using this response to evaluate a number of multiaxial fatigue criteria. The prediction modeling is then compared to its capability for predicting the fatigue damage observed experimentally.

The development and validation of computational methods to determine the time-varying local stress-strain response for any fretting contact situation was needed before the multiaxial criteria could be evaluated. Considering that the interfacial contact geometry between engineering components is usually complex, the finite element method (FEM) was used. It was also chosen because of widespread

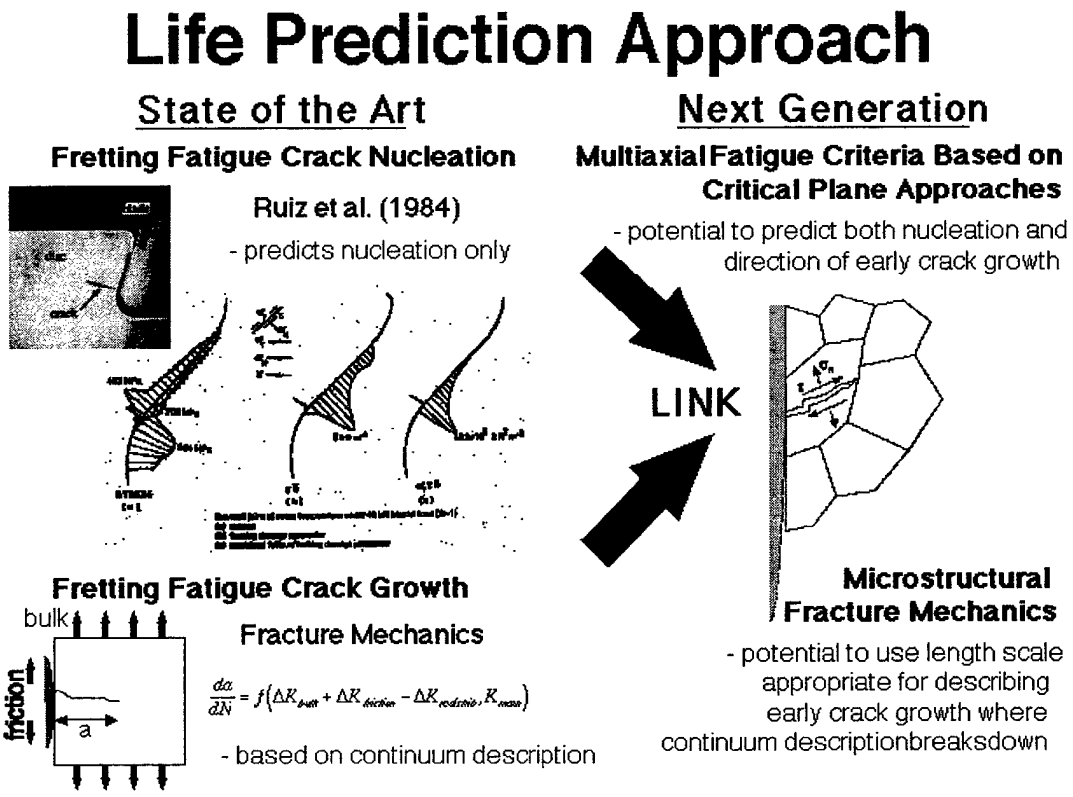

Figure 1.9 Life prediction approach.

acceptability in industry. However, a number of issues and challenges in using FEM in this application had to be resolved. For example, how fine does the mesh need to be near the interface? Or in other words, how small is the fatigue process volume that needs to be considered? What type of contact elements work best for this application? With simple geometries such as cylindrical on flat and linear material behavior, does the solution reduce to the analytical Mindlin result? Initially, ANSYS, a general purpose commercial FEM code, was used. However, we soon realized that the contact elements in ANSYS were not ideal for the fretting problem especially in determining the local stress and strain near the contact interface. So we switched to ABAQUS, another commercial code. After exploring a couple different contact element options, converged solutions were obtained for all our loading and contact conditions. Each fretting fatigue analysis is run to shakedown. The stress-strain response in the last cycle along the interface in the fatigue specimen is used as input to evaluate the various predictions of theories. Details on the FEM modeling are reported in Swalla-Michaud (1999).

Our fatigue specimen was modeled closely with FEM so that we could have direct experimental validation for the prognostic modeling. Elastic-plastic (using multiple linear fits to the cyclic stress-strain curve) 2-D finite element analyses of our fretting fatigue specimen configuration have been conducted to determine the local time-varying stress and strain fields in the region of fretting. The effects of mesh refinement and contact element stiffness have been explored. Near the contact, the mesh must be very fine (of the order of 10 μm) to reach converged solution. In addition, parametric studies exploring the effects of stress amplitude, mean stress, friction coefficient (e.g., 0.75, 1.0, 1.25, 1.5), relative slip (different pad spans), and geometry of interface (e.g., radii of 1.5 mm, 15 mm, and 150 mm) have been performed (Swalla-Michaud, 1999) and continue to be conducted.

Using the results of the FEM modeling, various multiaxial crack nucleation criteria were evaluated. These included the current state of the art (the maximum tangential stress and the Ruiz criterion) as well as those based on critical plane theories (in particular, Fatemi-Socie and Smith-Watson-Topper (see Socie, 1993)). A maximum shear strain range criteria was also considered. All of these nucleation criteria were critically examined in light of our new experimental results (Neu et al., 1999). Neither of the state-of-the-art nucleation criteria predict the observed oblique crack direction and early crack growth behavior. Shear-based multiaxial fatigue criteria based on critical plane theories (in particular, the Fatemi-Socie parameter) were shown to predict not only the nucleation site but also the plane of maximum damage which corresponded to the physically observed orientation of the crack nucleus.

The development of the modeling methodology also makes it possible to explore other effects that may be important to the fretting fatigue problem. For example, (1) the evolution of the *local* friction along the interface, (2) the influence of the microstructure through modeling grains with different crystallographic orientations, and (3) the size of the representative volume element (i.e., the fatigue process zone).

Experimental Program in Fretting Fatigue

The fretting fatigue test apparatus developed for this investigation is unique in that it addresses the needs of both life prediction modeling and integrated diagnostics. The fretting fatigue test method was developed (1) to validate and refine the next generation prognostic models and (2) to be used as a test bed for detecting real fatigue damage with sensors. The new fretting fatigue apparatus designed and developed for this program was based on ones previously used to study fretting fatigue behavior of materials (Attia and Waterhouse, 1992). However, our apparatus contains a number of design changes, both to improve upon the previous designs as well as for easily accepting the application of sensors. Fretting fatigue tests are performed using a flat dog-bone shaped specimen with bridge-type fretting pads attached to the edge of the specimen (see Fig. 1.10). The fatigue specimen with fretting apparatus attached is gripped and tested in a 90 kN servohydraulic fatigue test system. The frictional force is determined using a strain gage measure located on the bottom of the fretting pad.

The fretting fatigue test set-up is ideally suited for evaluating sensors and other crack growth monitoring techniques, due to the large area on the fatigue specimen where sensors can be attached. Sensors are attached to either the flat side or edge of the specimen, typically after studies to determine their optimal placement. Many parameters which influence fretting fatigue behavior can be controlled, including the fatigue stress amplitude, mean fatigue stress, nominal relative slip amplitude, contact pressure distribution, normal contact load, and frequency of oscillation. Thus, this test set-up provides all of the experimental information required to evaluate current state-of-the-art life prediction methods for crack nucleation and propagation under fretting fatigue. It is also anticipated that the methods developed in this investigation will impact an ASTM standard for fretting fatigue testing currently under development.

A study of the fretting fatigue behavior of PH 13-8 Mo stainless steel has been conducted. The design and implementation of a fretting fatigue testing apparatus proved quite successful in nucleating and propagating fretting fatigue cracks. The fretting fatigue tests performed at stress levels of 40% to 50% of the fatigue limit exhibited extremely short lives. Many interesting and significant observations have been made (Pape, 1997; Pape and Neu, 1999) which will continue to stimulate further research in year 5. For example, the evolution of the frictional force between the fretting pads and the fatigue specimen was monitored throughout the fretting fatigue tests. The general trend of a relatively quick increase during the first few hundred cycles (bedding-in), followed by a gradual decrease throughout the remainder of the test, was seen in most of the tests (Fig.1.11). Furthermore, a sharp drop in the range of frictional force was observed near the end of the test. This drop has been correlated with the presence of a well-defined fatigue crack in the specimen. It seems to be possible, based on the observations made, to use the frictional force evolution as a measure of the size of the fatigue cracks.

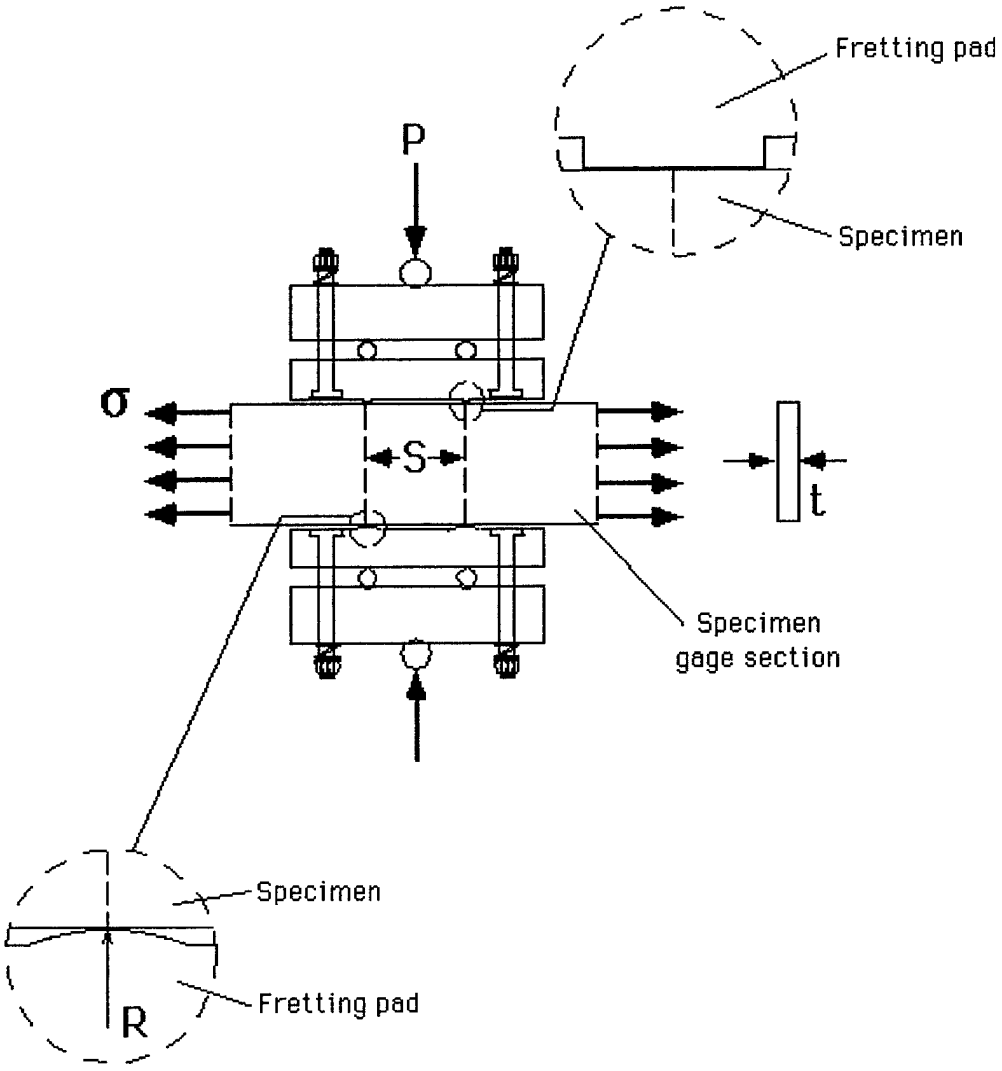

Figure 1.10 Fretting fatigue apparatus.

A great deal can be learned by monitoring the progression of fretting damage with sensors. Due to the extensive plastic deformation and numerous crack nuclei generated in the early stages of fretting fatigue, it may be difficult to detect the growth of very small cracks with sensors. Fortunately, the evolutionary nature of the fretting fatigue damage may be more easily detected than cracks initiating naturally under plain fatigue. A preliminary comparison of the evolution of frictional force/displacement hysteresis with the frequency of acoustic emission events (in collaboration with Jacobs/Jarzynski (GT)) suggests it is possible to detect the characteristic changes during this evolution even when the fretting fatigue damage is not very extensive such as during the early stages of fretting fatigue damage accumulation. One of the motivations for developing a fretting fatigue method is the likely capability for sensors to pick up information as to the evolution of the interface damage. Further validation continues through a series of interrupted tests where changes in the sensor signals are directly correlated with the physical damage state.

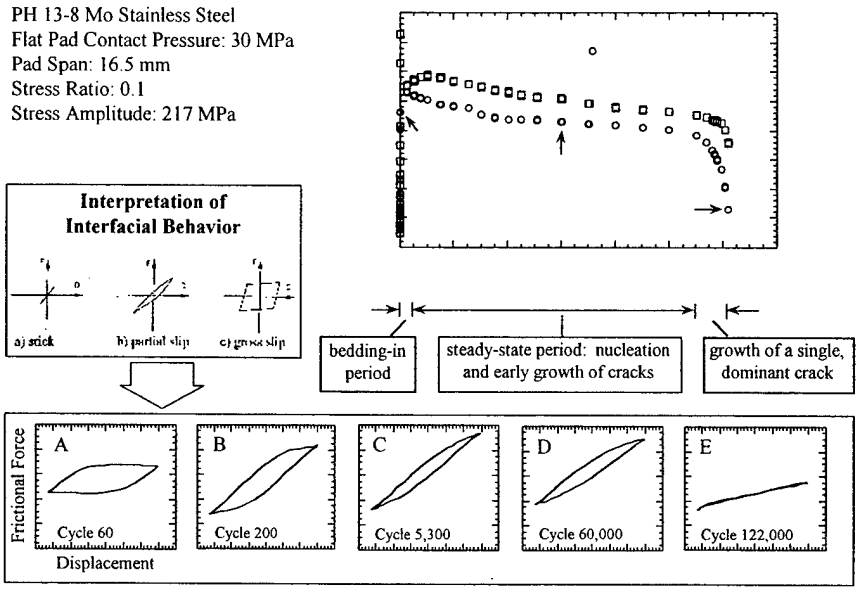

Figure 1.11 Stages of fretting fatigue.

One of our most significant contributions to the fretting fatigue testing community has been the use of different initial contact geometries in the same test (Pape and Neu, 1999). This was to address a current controversy as to the importance of the contact geometry on fretting fatigue crack nucleation. Unique tests using "flat" pads on one side of the fatigue specimen and cylindrical pads on the other side were used to assure all other parameters (e.g., fatigue loading, normal load, relative slip) were the same (see Fig. 1.10). Even though the maximum contact pressure at the cylindrical fretting pad was much higher than the average pressure at the flat pad, there was not a large difference (less than a factor of 2) in fatigue life between the two configurations. Clearly, this is relevant to dealing with contacts between components that may have more complex contact geometries and assuring that the new prognostic models can handle these geometric differences and be applied to components with confidence. In addition, in year 5 we plan to investigate the role of the cylindrical pressure distribution by using pads with different radii of curvature (e.g., 1.5 mm, 15 mm, and 150 mm).

The effect of the fatigue mean stress (i.e., stress ratio) on the evolution of damage leading to fatigue crack nucleation has been found to be small (Neu et al., 1999). The increase in remaining life at lower mean stress appears to be associated with the delay in the onset of crack propagation. Various fretting fatigue crack nucleation criteria have been critically examined in light of these experimental results investigating the mean stress effect (Neu et al., 1999).

A number of fretting fatigue specimens have been sectioned and cracks lengths and angles have been measured. A typical example taken from Neu et al. (1999) is shown in Fig. 1.12. Here, the initial crack angle is about 57° measured from a line perpendicular to the fretted surface. At about 50 μm below the surface, the angle changes to about 27°. From between 200 μm and 800 μm below the surface, the angle gradually changes from 27° to 0°, which is a crack growing normal to the remote fatigue loading. The fatigue mean stress does not seem to significantly influence these angles. These physical crack growth observations are critical for determining at what length the crack growth can be predicted using fracture mechanics methods and for evaluating different crack growth criteria for predicting the growth rate and direction for this material. Based on our small crack growth work specifically on PH 13-8 Mo stainless steel (Patel et al., 1999), when the fatigue crack is 50 μm or larger, its growth rate can be predicted fairly well using long crack growth models even though the crack is still physically small.

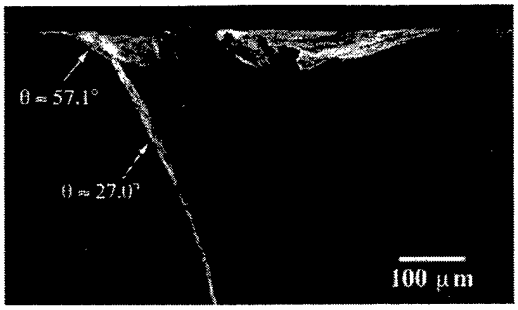

Figure 1.12 Fretting fatigue crack.

References for Section 2.2.1.1d

Attia, M.H. and Waterhouse, R.B. (eds.), *Standardization of Fretting Fatigue Test Methods and Equipment, ASTM STP 1159*, American Society for Testing and Materials, Philadelphia, 1992.

Newman, J.C., 1981, "A Crack Closure Model for Predicting Fatigue Crack Growth Under Aircraft Spectrum Loading," *Methods and Models for Predicting Fatigue Crack Growth Under Random Loading*, ASTM STP 748, pp. 53-84.

Ruiz, C., Boddington, P.H.B., and Chen, K.C., 1984, "An Investigation of Fatigue and Fretting in a Dovetail Joint," *Experimental Mechanics*, Vol. 24, No. 3, pp. 208-217.

Socie, D.F., 1993, "Critical Plane Approaches for Multiaxial Fatigue Damage Assessment," *Advances in Multiaxial Fatigue*, ASTM STP 1191, D.L. McDowell and R. Ellis, eds., pp. 7-36.

Wang, C.H., 1996, "Effect of Stress Ratio on Short Fatigue Crack Growth," *Journal of Engineering Materials and Technology*, Vol. 118, pp. 362-366.

2.2.1.2 STRESS AND FLAW ANALYSIS OF COMPONENTS

Co-investigator: Jianmin Qu (Georgia Tech)
Graduate Student: Brian Gardner

OVERVIEW

The stress analysis can provide detailed stress distribution on critical components in naval structures. Knowledge of the stress distribution is critical to identify "hot" spots on those components where failure is most likely to occur. The fracture mechanics studies can provide a predictive tool to estimate the crack growth rate that is essential to estimate the remaining life of such components.

PROPOSED OBJECTIVES

The specific objects of this project are to conduct:

- Stress analysis of critical components.
- Fracture mechanics analysis of 3-D crack growth under complex loading conditions.
- Computer Simulation and Visualization of stress distribution and crack growth.

ACHIEVEMENTS

A visualization program was developed to enable improved understanding of component behavior under various loading conditions. The visualization program allows the user the ability to look inside the finite element model of a complex structure and see how the field quantities of interest develop. In particular, the visualization program provides for a more complete assessment of the stress field, providing insight to the driving force behind crack initiation and the growth of small cracks. A complete stress analysis was performed on the H-46 rotorhub. The visualization program was utilized to predict probable failure locations and planes of possible crack growth on the rotorhub.

An automatic crack growth algorithm (Autocrack) was developed and implemented as an add-on tool for ABAQUS. Autocrack allows for the fully automatic growth of arbitrary 3-D cracks in finite element models without any user intervention. Autocrack reduces the amount of time required to predict crack growth behavior in a component. Additionally, Autocrack can be used to develop or tune crack growth laws for particular materials. This feature is important for a better understanding of 3-D crack growth. Currently, 3-D crack growth is based on approximations using well-know 2-D crack growth laws.

a. Finding the "Hot-spots"

A visualization program was developed to enable improved understanding of component behavior under various loading conditions. The visualization program allows the user the ability to look inside the finite element model of a complex structure and see how the field quantity of interest develops. In particular, the visualization program provides for a more complete assessment of the stress field, providing insight to the driving force behind crack initiation and the growth of small cracks. To demonstrate the effectiveness of the visualization program, a thorough stress analysis was performed on the H-46 rotor hub.

The H-46 rotor hub was chosen as the sample component due to its complex geometry. Assuming the rotor blades exert identical forces on the rotor hub independent of time, periodicity can be used to reduce the rotor hub to a one-third model (Fig. 2.1). Loading of the rotor hub was idealized into three components: lift, centrifugal, and drag. Assuming low speed conditions, drag can be neglected (Fig.2.2). The final finite element model contained 32,296 tetrahedral elements (Fig. 2.3). Two finite element models were solved, one with a unit lifting load and one with a unit centrifugal load. From the two finite element models, component behavior under various loading conditions can be simulated using the principal of superposition.

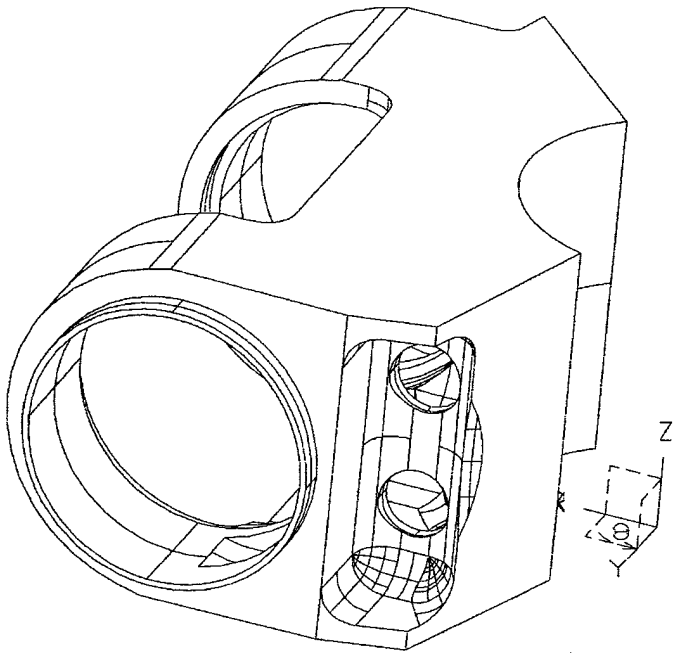

Figure 2.1 Rotor Hub (One-Third) Solid Model (Right View)

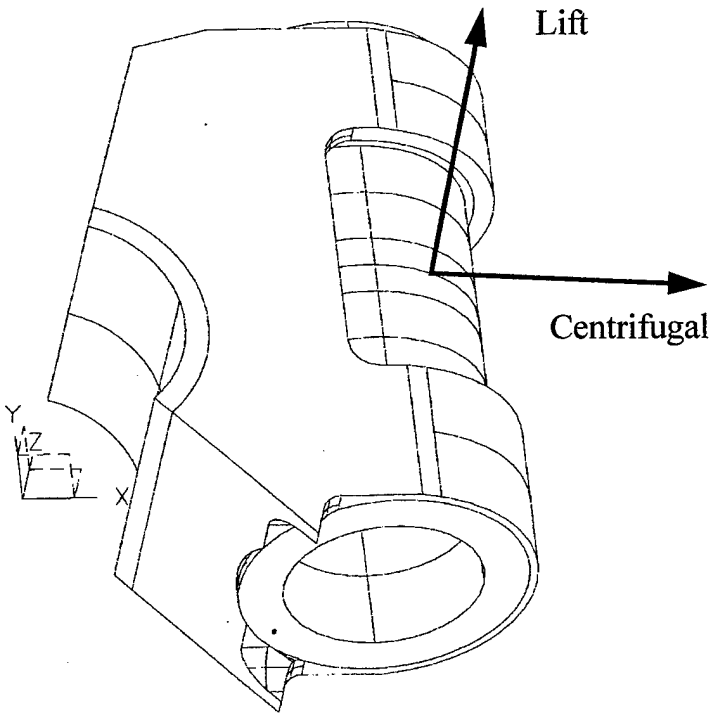

Figure 2.2 Rotor Hub Loading Components

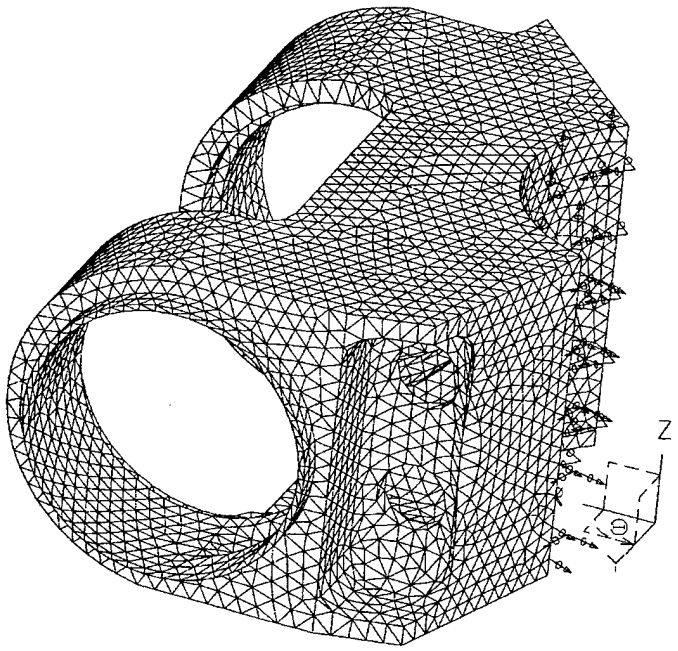

Figure 2.3 Mesh of Rotor Hub Model (Right View)

A parametric study was performed in order to determine the relationship between the maximum normal stress and the maximum von Mises stress versus combination of centrifugal and lifting loads. Table 2.1 details the results of the parametric study. These results are also shown in graphical form (Fig. 2.4 – 2.5).

Using the results of the finite element analysis, predictions of possible failure locations were made based on two criteria: Maximum Principal Stress and Maximum von Mises Stress. The maximum principal stress criterion assumes a crack will initiate at a point with the largest maximum principal stress and propagate perpendicular to the maximum principal direction (Mode I growth). The von Mises Stress Criterion assumes a crack will initiate at a point with the largest von Mises stress. Fatigue crack initiation site are predicted to occur in elements with both large maximum principal stress and large von Mises stress. Case 24 of the parametric study (Table 2.1) provided the most severe loading of the rotor hub and is used to predict possible failure sites. Four locations were established as potential failure site (Fig. 2.6). One important observation is that the four predicted sites are all located near through holes in the rotor hub. Additionally, element one coincided with an actual failure recorded at Cherry Point.

Table 2.1 Results From Parametric Study

Case	Centrifugal	Lift	Φ_1	Φ_e
	(lbf/blade)	(lbf/blade)	(kPa)	(kPa)
1	0.00	0.25	1.5189	1.6141
2	0.00	0.50	3.0378	3.2274
3	0.00	0.75	4.5574	4.8415
4	0.00	1.00	6.0764	6.4556
5	0.25	0.00	1.1838	1.0611
6	0.25	0.25	2.1146	1.8044
7	0.25	0.50	3.1895	3.3088
8	0.25	0.75	4.3327	4.8994
9	0.25	1.00	6.2225	6.5011
10	0.50	0.00	2.3739	2.1215
11	0.50	0.25	3.1957	2.7400
12	0.50	0.50	4.2299	3.6087
13	0.50	0.75	5.2952	5.0490
14	0.50	1.00	6.3797	6.6169
15	0.75	0.00	3.5508	3.1826
16	0.75	0.25	4.2975	3.6956
17	0.75	0.50	5.3021	4.5368
18	0.75	0.75	6.3446	5.4131
19	0.75	1.00	7.4070	6.7996
20	1.00	0.00	4.7339	4.2430
21	1.00	0.25	5.4082	4.6581
22	1.00	0.50	6.3908	5.1704
23	1.00	0.75	7.4139	6.3377
24	1.00	1.00	8.4599	7.2167

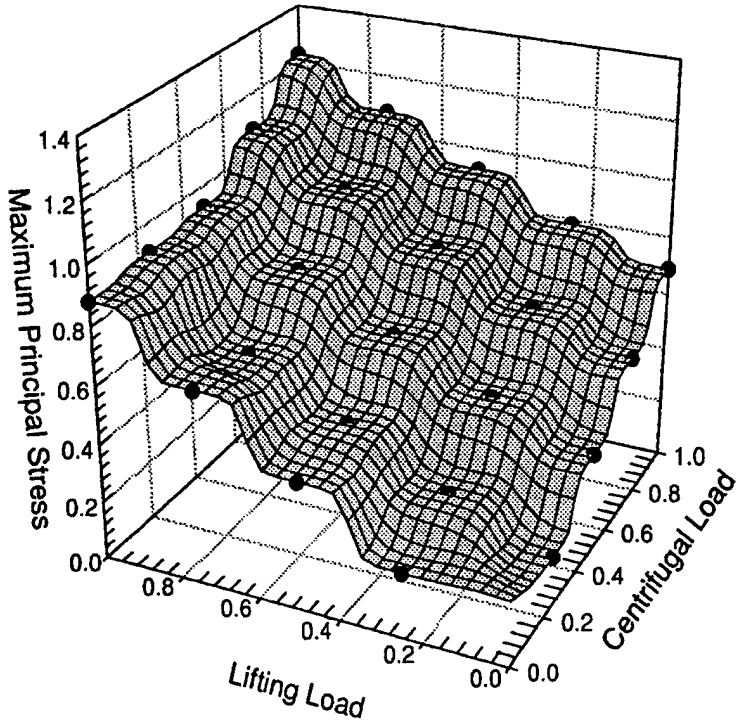

Figure 2.4 Plot of Maximum Principal Stress Results (From Table 2.1)

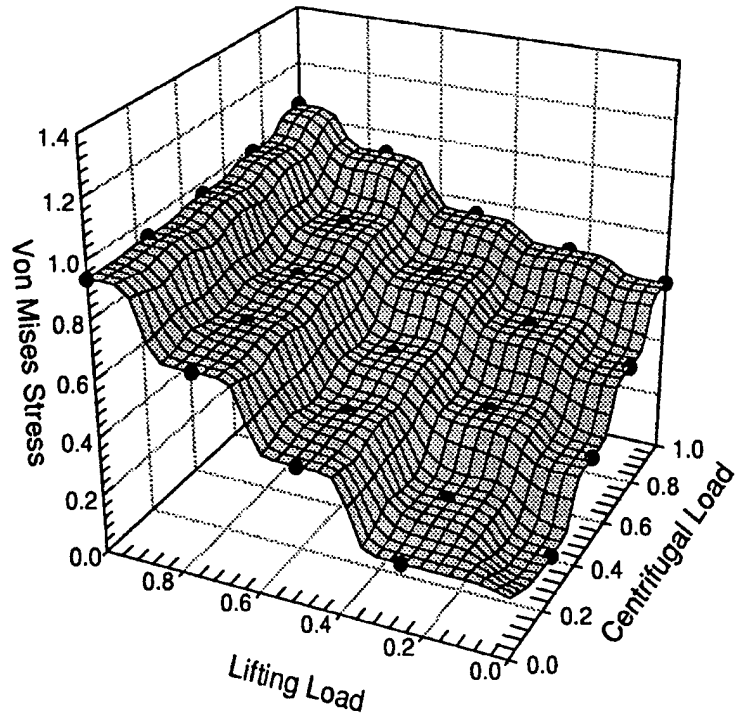

Figure 2.5 Plot von Mises Stress Results (From Table 2.1)

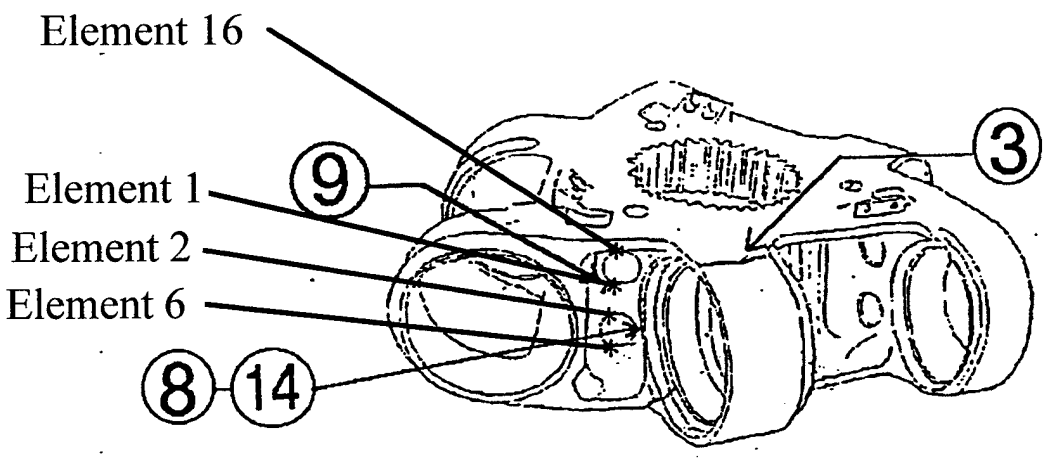

Figure 2.6 Rotor Hub Predicted Failure Locations

b. Modeling Long Fatigue Crack Propagation in 3-D Components

The next step in the research is to develop a method to allow prediction of crack growth behavior in a component in order to determine the safe life of the component. This portion of the research was split into to areas: calculation of crack tip parameters (Northwestern) and development of automatic crack growth algorithm for finite element analysis (Georgia Tech).

Geometry, loading, and material properties influence crack growth in structures; these factors can lead to crack geometry that is non-planar and impossible to model with 2-D approximations. Therefore, the ability to model 3-D crack propagation is an important tool in predicting the remaining safe life of a structural component. Many commercially available finite element codes support the inclusions of cracks in the model geometry, but they do not support the fully automatic crack propagation required to perform efficient analysis of 3-D crack growth behavior. An automated crack growth algorithm (Autocrack) has been developed as an add-on tool for commercially available finite element codes that modifies the model geometry for each increment of crack growth.

The complexity of creating finite element models of complex geometric structures has been greatly reduced due to continuous improvements in mesh generators. The vast majority of commercially available finite element pre-processors have advanced tetrahedral mesh generators capable of creating a high quality mesh on a solid model with little input from the user. Recently, there is a large amount of ongoing research into improving brick mesh generators to provide the same level of mesh quality and ease of use as tetrahedral mesh generators [1-3]. At this point in time, the majority of complex geometry models are still created with an underlying tetrahedral. Therefore, the implementation of the Autocrack algorithm was developed for tetrahedral meshes, although the concepts described within translate equally well independent of the underlying mesh.

The Autocrack crack growth algorithm can be divided into five major components: model input, calculation of crack growth increment and direction, remeshing, reassembly, and calculation. A flowchart outlining the main routines within Autocrack is shown in Fig. 2.7. Each component will be described below.

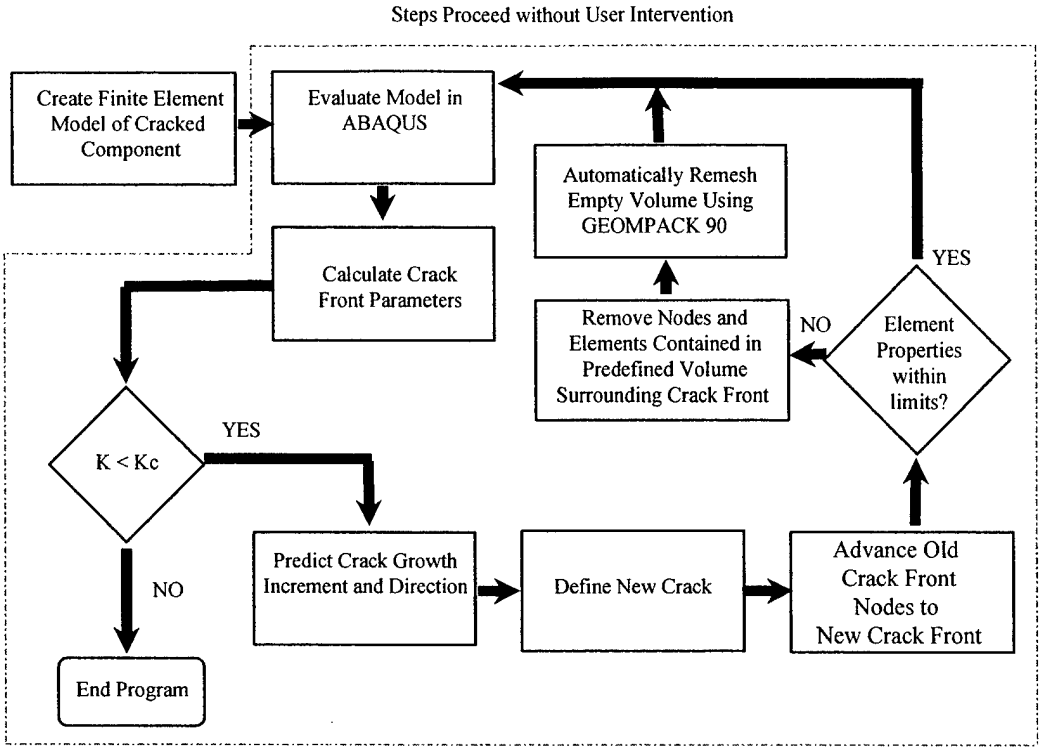

Figure 2.7 Autocrack Flowchart

Model Input

One of the main considerations in the development of the crack growth algorithm was to minimize to amount of time required for a user to integrate the algorithm with the pre-processing and analysis software currently in place. Therefore, this algorithm is constructed as an add-on for current pre-processor and analysis software used by the end user. A solid model of the structure with an initial crack is created and meshed in a pre-processor that supports the particular analysis code of interest. The only required additions to the model file are two nodes sets for each crack in the solid model: one node set for the nodes on upper crack surface nodes and one node set for the nodes on the lower crack surface. Each of the crack surface node sets contains the nodes that lie on the crack front. Autocrack requires that the nodes on the upper and lower crack surfaces are coincident, this will be further explained in the remeshing section.

The input for Autocrack is the model and results file from a finite element simulation of the structure with an initial flaw. The model file contains all the geometric (extracted from the mesh data) and boundary condition information for the structure and the results file contains the stress/displacement results from the finite element solution of the boundary value problem. The model file includes two node sets for each crack being considered: one for the upper crack surface and one for the lower crack surface. The crack growth algorithm reads the model file and creates a database of nodal positions, connectivity (element) information, boundary condition information, and initial crack surface information. Using the information from the model file, the crack growth algorithm determines the outer boundary of the modeled structure, which, of course, defines the boundary of crack growth. The crack front is defined as the union of the upper and lower crack surface node sets.

Computation of Crack Growth Increment and Direction

The prediction of crack growth increment and direction depend on two factors: accurate calculation of crack tip parameters and crack growth laws applicable to the material and loading conditions under consideration.

Over the past decade, there has been much research into calculating crack tip parameters from three-dimensional finite element solutions [4,5,6,7]. The domain integral approaches appear to be the most promising methods to use with tetrahedral meshes. One of the challenges with a tetrahedral mesh is accurately representing the $1/\sqrt{r}$ singularity in the case of LEFM. In the case of a brick mesh, it has been shown that moving the mid-side nodes, behind the crack tip nodes, to the quarter-point position replicates $1/\sqrt{r}$ singularity. But, no similar approach exists with the use of tetrahedral elements. The domain integral approach overcomes the singularity modeling problem by calculating crack tip parameters from a volume (domain) of elements surrounding the crack front, not just results near the crack front as displacement extrapolation or virtual crack closure. Both the displacement extrapolation and virtual crack closure techniques have shown excellent accuracy in calculating crack tip parameters using brick meshes. Recently, Rajaram et al. [8] showed that accurate values of the energy release rate, J, along the crack front of a planar crack surface could be obtained from finite element mesh with irregular tetrahedral meshes. Additionally, Moran et al. [9] have completed a formulation to allow the extraction of stress intensity factors along the crack front of a non-planar crack surface from an interaction energy approach.

The development of three-dimensional crack growth laws will be an area of heavy research over the next decade. Currently, the majority of three-dimensional crack growth is based on the application of 2-D theories. This is one area where an automated crack growth routine can have an enormous impact. In conjunction with experimental programs to determine crack growth behavior in candidate materials, the automated crack growth routine could be tuned to develop or refine current crack growth laws. New crack growth laws can be evaluated by comparing the experimental results to the numerical prediction and performing parametric studies to determine which crack tip parameters have the greatest impact on crack growth behavior.

After the finite element solution is complete, the appropriate crack tip parameters are computed along the crack front. Applying the crack tip parameters to the crack growth law chosen to model the crack behavior, the crack growth increment and direction at each crack front node are computed and passed to the remeshing algorithm.

Remeshing

Remeshing occurs in four steps: remove a volume of elements surrounding the original crack front, move the crack front to the new position, create a surface mesh on the new crack surface created by the crack increment, and finally mesh the solid region surrounding the crack front.

The first step in the remeshing procedure is to remove a volume of elements surrounding the original crack front (local region). In this algorithm, the volume of elements is defined by a number of element rings surrounding the original crack front. It is important to consider to the size of the crack increment, the size of the solid elements used to remesh the local region, and the size of the elements in the global mesh bounding the local region when determining the number of element ring used to define the local region. All of these parameters will have an impact of the mesh quality in the local region after remeshing. The elements are removed from the connectivity database. Also, nodes not connected to the global mesh or crack surfaces are also removed from the nodal database.

In typical finite element models of cracked structures, the region immediately surrounding the crack contains the fine mesh required to accurately capture the high gradients seen surrounding the crack tip. But as one moves away from the crack front, the mesh becomes coarser in order to optimize the balance between computational resources (e.g. run time, disk space) with solution accuracy. Therefore, it is important to realize that as the crack front propagates away from it's original position, it will enter

regions with an increasingly coarse mesh density. This will require a larger volume of elements surrounding the original crack front in order to create an appropriate crack tip mesh and allow for an adequate transition region from finer crack tip elements to a coarser global mesh boundary.

Next, the crack is incremented based on the results of the crack growth law used to define the behavior of the crack. The original crack front nodes are placed in the lower crack surface node set. A set of nodes coincident to the original crack front nodes is placed in the upper crack surface node set. A new set of crack front nodes is created based on the increment length and direction prescribed by the crack growth law used. The position of each new crack front node is determined by adding the appropriate increment length and direction to the position of the original crack front node. Therefore, the new crack front has the same number of nodes as the original crack front. After the increment, nodal spacing between crack front nodes are evaluated. If the spacing between crack front nodes falls outside a predetermined range, new nodes are added on the crack front to insure an appropriate crack front spacing is maintained.

A surface mesh is created on the new crack area created during the crack increment. Since there is no restriction on the crack growth increment, the resulting new crack surface can be non-planar. The new crack surface is modeled as a NURBS surface. Using a NURBS surface representation allows both planar and non-planar surfaces to represented in a similar fashion, simplifying the overall remeshing routine. The surface mesh is created using GEOMPACK90 [10]. The surface mesh is defined so the normal of the elements on the surface correspond to the normal of the lower crack surface, this will be further explained during the discussion of the solid meshing.

The final step in the remeshing algorithm is to create a solid mesh in the local region. The solid mesh is subject to two constraints: the crack surface within the local region and the boundary between the local region and the global mesh. The solid tetrahedron mesh is created using GEOMPACK90. GEOMPACK90 allows a solid mesh to be generated given the surface mesh of the boundary of the volume. In this case, the surface mesh of the boundary of the volume corresponds to the element faces from the global mesh which border the local region. Using these element faces will allow the remeshed region to fit seamlessly back into the global mesh. During the solid meshing, the crack surface within the local region is modeled as an element face constraint. The surface mesh created on the new crack area along with the element faces which correspond to the original crack surface are used to create the element face constraint. The element face constraint requires tetrahedrons to be created in the volume with a face corresponding to the constraint. After the local region is meshed, it is necessary to split the faces of the tetrahedrons on the element face constraint to create the upper and lower crack surfaces. Using the normal of the lower crack surface, it is possible to determine which of the coincident tetrahedron faces correspond to the upper and lower crack surfaces. The upper crack surface is created by creating new nodes coincident to the nodes on the element face constraint and updating the connectivity database such that the tetrahedrons connected to the upper crack surface utilize the new nodes. Now, the remeshing of the local region is complete.

Reassembly

Now that the local region has been remeshed, it must be reassembled back into the global mesh. The nodal and connectivity databases of the remeshed local region are modified to allow the reintroduction back into the global mesh. The nodes on the element faces forming the outer boundary of the remeshed region are renumbered to correspond to the node on the coincident element faces of the global mesh. The tetrahedrons in the remeshed region containing these element faces are modified to reflect the global node numbers. Now, the remeshed region has been reassembled into the global mesh and the next increment is ready to be evaluated in the analysis code.

Simulations

The algorithm has been used to model crack growth from a corner crack in a square bar (Fig 2.8a) and a circular crack within a square bar (Fig 2.9a). For these simulations, the crack front displacement and direction were input to the crack growth routine, they were not computed based on the crack tip parameters. Also, the crack growth and subsequent finite element analysis proceeded without any user intervention. Figures 2.8b and 2.9b show the crack surface after several crack growth increments.

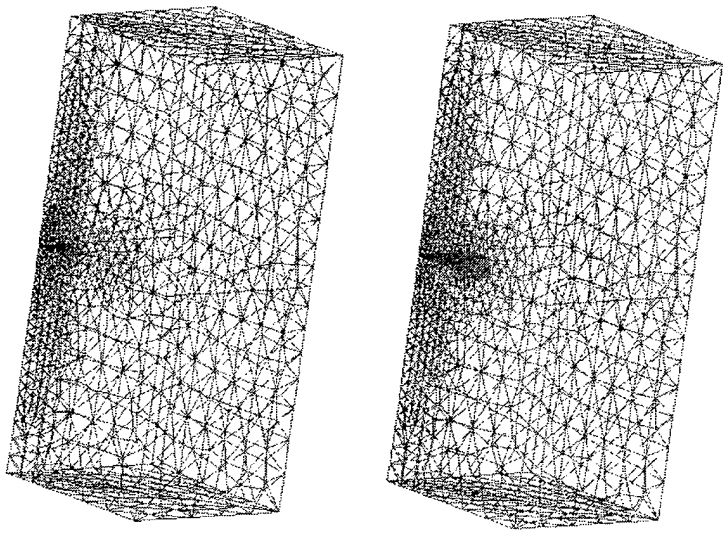

(a) (b)

Figure 2.8 Corner crack in a square bar – **(a)** Initial Crack, **(b)** Crack after 5 increments

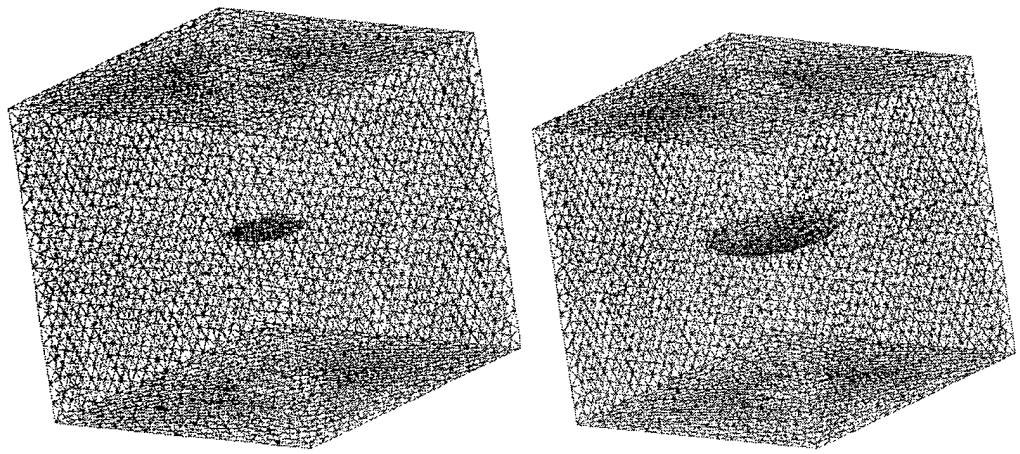

(a) (b)

Figure 2.9 Corner crack in a square bar – **(a)** Initial Crack, **(b)** Crack after 5 increments

M-URI PUBLICATIONS

Gardner, B.M., "Visualization and Stress Analysis of Complex Three-Dimensional Solids," Master's Thesis, Georgia Institute of Technology, 1996.

References for Section 2.2.1.2

[1] Schneiders, R. and R. Bunten ,"Automatic Generation of Hexahedral Finite Element Meshes", Computer Aided Geometric Design, Vol 12, pp.693-707, 1995

[2] Shephard, M.S. "Update to: Approaches to the automatic generation and control of finite element meshes", Appl Mech Rev, ASME, Vol 49, Num 10, pp.S5-S14, October 1996

[3] Owen, S. J. and S. Saigal, "H-Morph: An Indirect Approach to Advancing Front Hex Meshing", 2nd Symposium on Trends in Unstructured Mesh Generation, University of Colorado, Boulder, August 1999

[4] Claydon, P.W., "Maximum Energy Release Rate Distribution From a Generalized 3-D Virtual Crack Extension Method," Engineering Fracture Mechanics, Vol. 42, No. 6, pp 961-969, 1992

[5] DeLorenzi, H.G., "On the Energy Release Rate and the J-Integral for 3D Crack Configurations," Int. J. Fracture, Vol. 19, pp. 183-193, 1982

[6] Nikishkov, G.P. and S.N. Atluri, "Calculation of Fracture Mechanics Parameters for and Arbitrary Three Dimensional Crack, by the 'Equivalent Domain Integral' Method," Int. J. Num. Meth. Eng., Vol. 24, pp 1801-1821, 1987.

[7] Cervenka, J. and V.E. Saouma, "Numerical Evaluation of 3-D SIF for Arbitrary Finite Element Meshes," International Journal of Fracture, Vol. 57, pp. 541-563, 1997.

[8] Rajaram, H., Socrate, S., and D.M. Parks, " Application of Domain Integral Methods using Tetrahedral Elements to the Determination of Stress Intensity Factors," Engineering Fracture Mechanics, Vol. 66, pp 455-482, 2000

[9] Moran, B., and Z. Ali, Private Communication.

[10] Joe, B., Geompack90, 1999.

2.2.1.3 FATIGUE CRACK INITIATION AND GROWTH MECHANISMS IN HELICOPTER ROTOR MATERIALS

Co-investigator: Ashok Saxena (Georgia Tech)
Graduate Students: Fan Yang (3/95 – 6/96); Laurent Cretegny (7/98 – 8/00)
Post-doctoral Fellow: Fan Yang (7/96 – 8/97)
Collaborators: Dr. David L. McDowell (ME) and Dr. Rosario A. Gerhardt (MSE)

OVERVIEW

In this study, atomic force microscopy (AFM) was used to study the mechanisms of fatigue crack initiation in helicopter rotor steels, AISI 4340 and PH 13-8 stainless steel, and a model material which was copper. AFM allows the observation and quantitative measurement of surface roughness features on fatigued specimens with a resolution of few nm. In addition, nanoindentation hardness was used to characterize the cyclic deformation characteristics ahead of growing fatigue cracks and impedance spectroscopy was used to detect damage as a function of fatigue cycles.

AFM observations have identified the mechanisms by which fatigue damage evolves in 13-8 PH stainless steel specimens and has also revealed the location of crack nucleation in both high cycle fatigue (HCF) and low cycle fatigue (LCF). In the low strain amplitude tests in the HCF range, fatigue surface damage occurred in the shape of narrow streaks at the interface between martensite laths where reverted austenite was present. On average, the streaks were measured to be 4 nm deep and between 1 and 2 μm long. The streaks increased in density with the increase in the number of cycles, and they eventually coalesced to form crack nuclei. In high strain amplitude tests, extrusions formed with lengths that averaged between 2 and 5 μm with a maximum of 15 μm, and heights between 10 and 200 nm. The results showed a direct correlation between fatigue surface damage and microstructure throughout the fatigue life, from the early formation of surface streaks to the development of extrusions and eventually the nucleation of a fatal crack. AFM has also provided a tool to characterize the distribution of surface upset on fatigue specimens and from these results define the onset of crack nucleation by using a criterion that corresponds to the magnitude of irreversible surface strain of a region where a crack nucleus has developed. In the high strain amplitude tests, a high level of irreversibility of slip (irreversibility factor $f \approx 0.0025$) was maintained throughout the fatigue life. However, at low strain amplitude, a low initial irreversibility of slip ($f < 0.001$) was observed which then increased in the last ten percent of the life to reach value of f larger than 0.001. The application of the crack nucleation criterion to the tests performed in this study showed that crack initiation occurred in most cases when about thirty percent of the surface had reached a critical level of irreversible surface strain. In AISI 4340 steel, such surface characterization led to a direct correlation between surface roughness and the fatigue life fraction spent.

Nanoindentation measurements have shown the importance of microstructure in the growth of fatigue crack growth of 4340 steel, especially in the low crack growth rate regime that is most important for helicopter rotors. Due to its coarser microstructure, the crack growth resistance of the annealed steel was consistently better than that of the quenched and tempered steel.

The use of impedance spectroscopy for the detection of structural changes in the materials due to cyclic loading has shown promising results in copper specimens, where the impedance spectra changed significantly with fatigue life fraction, N/N_f. However, the complex microstructure of 13-8 PH stainless steel and its high initial dislocation density intervene with the collection of repeatable data. Additional research should be conducted to explore the utility of this technique as a tool for nondestructive fatigue damage detection.

BACKGROUND

Fatigue crack initiation usually accounts for a significant fraction of the lives of engineering components such as helicopter rotors subjected to cyclic loading. Also, critical helicopter components are designed for damage tolerance because nondestructive techniques can reliably only detect cracks that are

on the order of few millimeters. Therefore, a detailed understanding of both fatigue crack initiation and growth is essential for predicting remaining life, for improving the total fatigue life, and for reliably detecting cracks in order to take corrective actions to avoid catastrophic failures in critical components. Fatigue crack initiation usually occurs at locations where discontinuities are present or where plastic strain accumulates preferentially in the form of slip bands. For components free of significant internal defects, free surface is frequently the site for fatigue crack initiation. When the cyclic strain range reaches the levels required for plastic deformation, long-range dislocation motion takes place. Since some fraction of dislocations continuously emerge at the surface while the others pile-up against internal obstacles, slip bands on the surface evolve in the form of intrusions and extrusions, subsequently acting as stress concentrators and facilitating the nucleation of fatigue cracks. The growth of fatigue cracks, especially ones that are small in relation to the microstructural features, interact extensively with the microstructure which can alter their path away from the direction normal to the loading and can significantly influence their growth kinetics.

Several new and novel techniques, such as atomic force microscopy (AFM), nanoindentation hardness testing and impedance spectroscopy have been employed to observe and quantify early damage development, fatigue crack initiation and crack growth in two helicopter rotor materials and a model material. The AFM technique has been used to study fatigue damage in prior studies [1,2] but the latter two are being used for the first time. For comparison and for assessment of the new techniques, established techniques such as scanning electron microscopy and optical microscopy are also employed.

TEST MATERIALS

The mechanisms of fatigue crack initiation and growth were investigated as part of this project in three different materials including (a) American Iron and Steel Institute (AISI) 4340 steel in quenched and tempered as well as in annealed condition (b) 13-8 PH stainless steel and (c) C101 high purity grade copper. While the first two materials are of direct interest for helicopter rotor applications, copper is a model material and is very well suited for developing techniques such as atomic force microscopy (AFM) and impedance spectroscopy (IS) for studying fatigue mechanisms and then transferring the concepts and techniques to other microstructurally more complex materials such as 4340 and 13-8 PH steels. The results section mainly covers the tests performed on steel specimens, but a selection of results on impedance spectroscopy of copper are also included. The remainder of this section describes the materials characteristics and their properties.

The 4340 steel used in this research was acquired in the form of 50.8mm diameter bar. The generic chemical composition of 4340 steel is listed in Table 3.1. To study the influence of various microstructures, two heat treatments were applied to the steel used in our research. The annealed steel consists of coarse pearlite domains and some proeutectoid ferrite, while the quenched and tempered steel consists of tempered martensite. Microstructural analyses along different orientations and at different locations of the bulk steel show that the microstructures are homogeneous for both heat treatment conditions. Table 3.2 provides the tensile properties of the steel under the two conditions. The fatigue crack growth behavior of the test material in the two conditions is reported in a recent paper [3].

PH 13-8 Mo steel is a martensitic precipitation-hardening stainless steel with low carbon content used in applications that require corrosion resistance, high strength, high fracture toughness and oxidation resistance to temperatures of up to 425°C [4]. Table 3.3 shows the chemical composition of the alloy and the tensile properties are given in Table 3.2. The resistance to corrosion is mainly provided by a surface passivation layer of chrome-oxide, which is further reinforced by the presence of molybdenum which reduces the tendency for pitting in salt water environment [5]. The material was obtained in the form of solution treated bar 14.5 mm in diameter. It was subsequently aged in-house for 4 hours at 566°C in Argon environment. The resulting microstructure consists of essentially martensite lathes that also contain spherical intermetallic β-NiAl precipitates of less than 7 nm size that are coherent with the matrix [6]. In addition to precipitation, the aging process, when performed at temperatures above 566°C, also

Table 3.1 Chemical composition of the 4340 steel bar (in weight %).

C	Cr	Mn	Mo	Ni	Si
.390	.82	.70	.26	1.70	.17

Table 3.2 Tensile Properties of the 4340 steel bar, 13-8 PH stainless steel and annealed C101 copper.

Material	σ_{uts} (MPa)	σ_{ys} (MPa)	RA (%)	Hardness
Annealed 4340	731	414	42.5	32 RC
Quenched + Tempered 4340	1124	1035	46.8	44 RC
13-8 PH Stainless Steel	1325	1286		42 RC
Annealed C101 Copper	210	33.3		10 RB

Table 3.3 Chemical composition of 13-8 PH stainless steel (in weight %).

Cr	Ni	Mo	Al	Si	C	Cu	Other Elements
12.41	8.28	2.2	1.02	.04	.033	.02	S, Mn, Co, Ti, Zr, P, Cb, W, V, N ≤ .01

forms measurable amounts of reverted austenite that is not transformed back to martensite upon cooling [6,7]. The amount of austenite can reach as high as 15vol% when aged 4 hours at 625°C [7]. Patel et al. report a volume fraction of 13.3% after aging for 4 hours at 566°C [8]. Hochanadel et al. determined that the reverted austenite is distributed along the martensite lath boundaries [7]. The important microstructural dimensions for the current study are the size of the prior austenite grains, the martensite packets and the martensite laths. From optical microscopy and SEM observations, Figures 3.1 and 3.2 respectively, grain size measurements between 10 and 30 μm were obtained. From the same micrographs, one can distinguish several packets of martensite in each grain, with sizes that vary between 5 and 15 μm. Martensite packets are clusters of laths with similar crystallographic orientations. Due to their distinct crystallographic orientations, separate packets appear with different contrasts on optical micrographs and are also apparent on SEM micrographs, which in addition show the orientation of the martensite laths, e.g. Figure 3.2. Transmission electron microscopy (TEM) observations made by Seetharaman et al. [6] showed that the packets are formed of nearly parallel laths of martensite about 0.25 μm wide, and that the misorientation between laths is low, similar to that of small angle grain boundaries.

The last material used in this study was high purity grade C101 copper, which was heat-treated for 1 hour at 500°C to obtain uniformly shaped grains. The size of the grains ranged from 10 to 100 μm in size with an average value of approximately 40 μm. The mechanical properties of the copper are provided in Table 3.2.

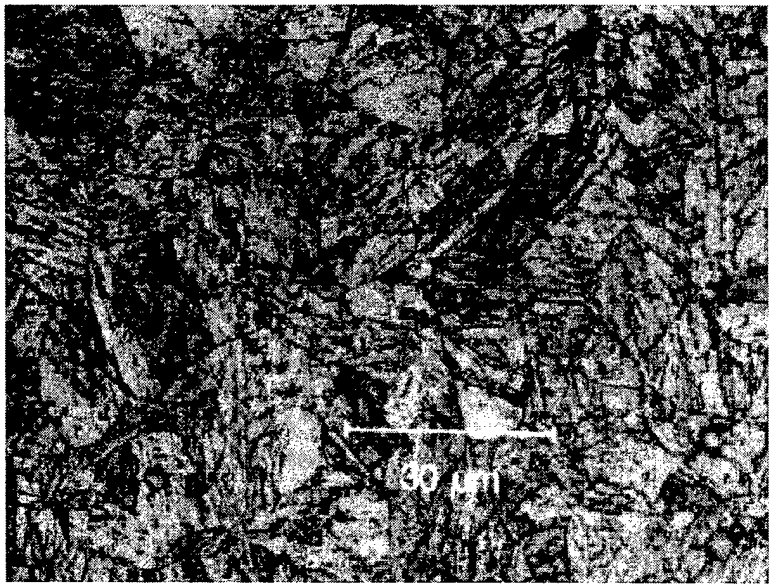

Figure 3.1 Optical micrograph showing the microstructure of 13-8 PH stainless steel.

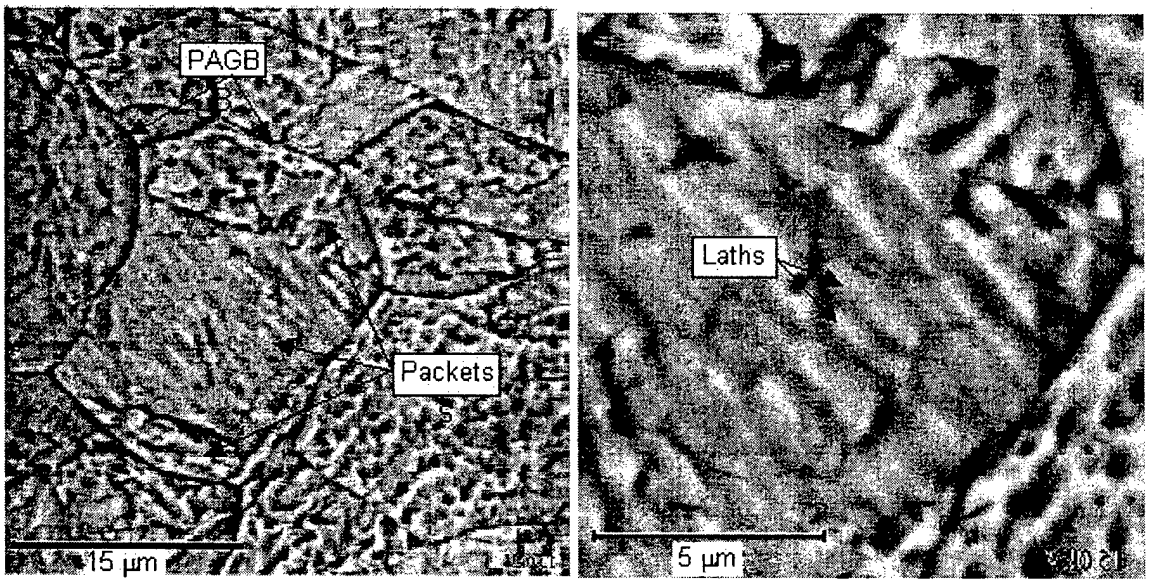

Figure 3.2 SEM micrographs of etched 13-8 PH stainless steel (Fry's reagent, 1 min.). The etchant has revealed prior austenite grain boundaries (PAGB), packets of martensite and outlined individual lathes.

ACHIEVEMENTS

In this section, results from the different analytical methods are presented in the following order. First, the surface topography of the cyclically loaded materials is described through observations by atomic force microscopy. Then, results from the nanoindentation measurements are provided and, finally, the use of impedance spectroscopy for monitoring accumulation of fatigue damage is discussed.

a. Atomic Force Microscopy

The quantitative understanding of fatigue crack initiation has been limited by the lack of techniques to accurately observe and obtain quantitative measurements of slip band evolution during different stages of fatigue. Most of the small-crack measurement techniques used in previous studies [9-12] lack the necessary resolution to measure slip band characteristics. Typically, the height and spacing of the slip bands can reach several microns in single crystals [13], but their sizes are expected to be in the submicron range in polycrystals and are expected to decrease as the grain size decreases [1]. Scanning electron microscopy (SEM) has a typical resolution of ≥100 A. Transmission electron microscopy (TEM) of thin films has a lateral resolution of ≥2 A, but is not suited for a surface topographic image. Although TEM analysis of thin replica films shadowed with heavy metal can provide surface topography information, the experimental difficulties and uncertainties associated with the replication process severely constrain the applicability of TEM replica in the investigation of nanometer scale features. Most importantly, both SEM and TEM cannot provide quantitative information about the vertical depths of surface features, which are key to the measurement of slip bands.

By scanning a sharp stylus over a surface, AFM is capable of imaging solid samples with the lateral resolution of 2 Å and the vertical resolution of 0.1 Å [14,15]. The contrast of an AFM image comes from the digital difference of vertical depths of the surface features. Consequently, the accurate depth and space of the surface features can be reliably obtained and interpreted with conventional data analysis software. As long as the slip bands on a specimen surface are larger than the surface roughness, AFM can perform the quantitative measurement of the surface topography. In this research, AFM technique is explored for observing surface upset produced by cyclic plastic deformation on the surface of 4340 steel in quenched and tempered condition and on 13-8 PH stainless steel. We have come across two previous studies on the use of AFM for observing slip bands produced by fatigue and aimed at the detection and modeling of fatigue crack nucleation [1,2]. In these studies, two different metals (a titanium alloy and a high strength low alloy steel) were fatigue tested under plastic strain ranges, and a characterization of the surface upset was performed using measurements of periodicity and height of the slip bands. The characterization method used in these studies applies only to materials that develop slip bands distributed periodically over the surface, as the spacing between them is an important parameter of the theory. This concept is however not applicable to the 13-8 PH stainless steel, because it develops surface damage in an irregular fashion, as it is shown later in this section. To achieve the characterization of the evolution of fatigue surface damage of this material, a different analytic procedure was developed which lead to the development of a criterion for crack nucleation that is based on physical evidence of damage at the surface.

This section first shows an assessment of the quality of AFM measurements, followed by the analysis of the evolution of the RMS surface roughness in 4340 steel and 13-8 PH stainless steel. Finally, a characterization of the surface features that appear in 13-8 PH stainless steel in high and low cycle fatigue is provided.

Assessment of AFM Measurements

To evaluate the potential of the AFM technique for characterizing surface features, a few specimens for which the microstructure is well established were subjected to AFM examination. Figure 3.3 shows the AFM image of a 35 x 35 μm^2 scanning area on an annealed steel sample and a cross-section analysis of the image. Clear image and digital information are provided. As the scanning area decreases, the AFM resolution improves as shown in Figure 3.4 for a 3.5 x 3.5 μm^2 pearlite colony on the same sample

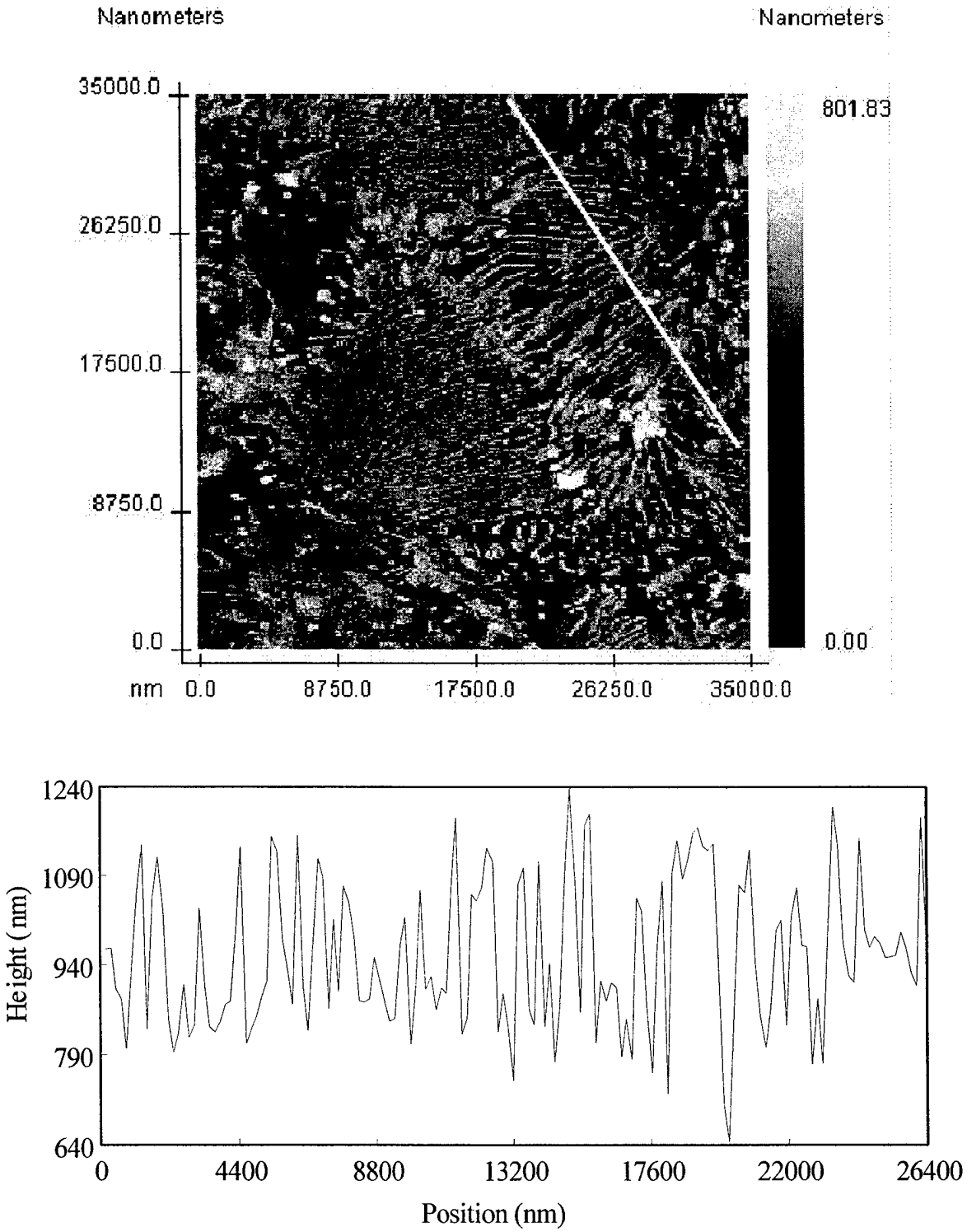

Figure 3.3 AFM image of a 35x35 μm area of a flat polished and etched sample of annealed 4340 steel and a cross-sectional profile.

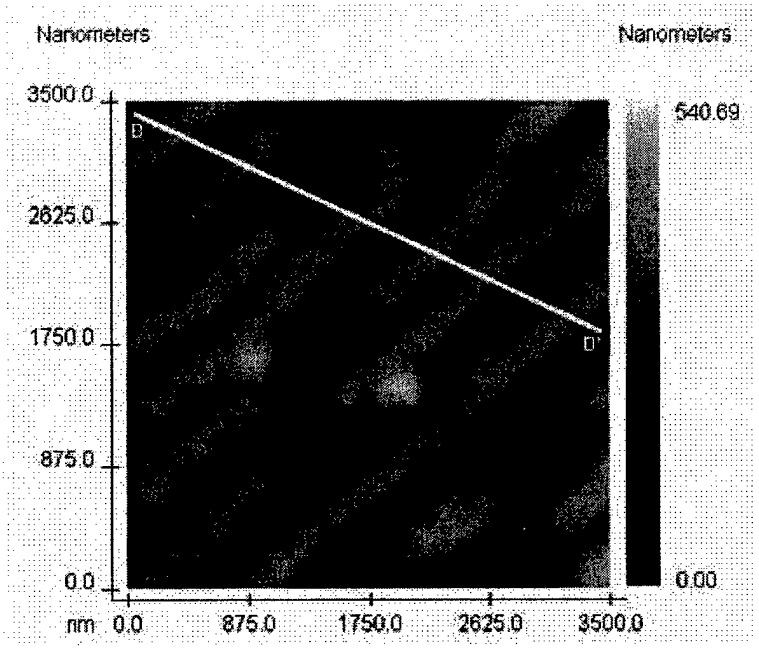

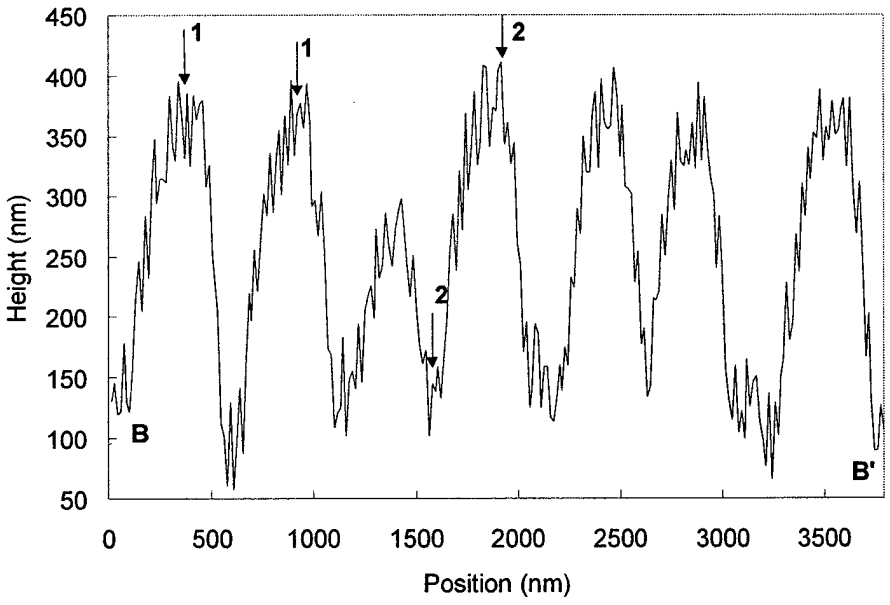

Figure 3.4 A higher resolution AFM image and cross-sectional profile of a selected region from the previous figure.

as in the previous image. The cross-section analysis of this image provides detailed information about the spacing and height of the cementite plates. For example, the first pair markers 1-1 show that the distance between the two adjacent cementite plates is approximately 550 nm, while the second pair markers 2-2 demonstrate that the corresponding cementite plate is approximately 300 nm high. The same test was performed on the martensite steel samples and the corresponding microstructure dimensions were obtained. Therefore, the AFM is suitable for producing high quality images and accurate quantitative surface topographic information on the steel samples.

RMS Roughness Results

As-polished flat metallographic samples were subjected to AFM examination to obtain the base-line surface roughness of 4340 steel. From a 7 x 7 μm^2 scanning area, the as-polished sample showed a root mean square (RMS) surface roughness of 9.76 nm, while the quenched and tempered sample shows a RMS roughness of 11.41 nm. With the scanning area of 35 x 35 μm^2, the RMS roughness becomes 11.50 nm and 14.40 nm for the annealed and the quenched and tempered steels, respectively. These roughness values suggest that the polishing process produces similar roughness for the two steels. For details of the tests performed and the results, see references [16,17].

Figure 3.5 shows the AFM image of a 35 x 35 μm^2 scanning area on the untested 4340 steel LCF specimen and the cross-section analysis in both transverse and axial directions. The transverse sectioning trace shows the specimen curvature, while the longitudinal sectioning trace shows a straight base line. The RMS roughness of this image is 55.15 nm which is significantly higher than that of the as-polished flat metallographic samples. The measured RMS roughness of the untested LCF specimens, with the scanning area of 7 x 7 μm^2, is about 11 and 8 nm for the annealed and the quenched and tempered steels, respectively. These roughness data agree well with the roughness of the flat metallographic samples showing insignificant influence of the specimen curvature. Therefore, 7 x 7 μm^2 was chosen as the optimum scanning area on all the 4340 steel LCF specimens. In 13-8 PH, the issue of curvature was avoided by machining four small 90° flats along the gauge area of the specimens. It was anticipated that the small angle created at the edges of the flats (160° instead of 180°) would not lead to significant corner stress concentrations, which was supported by SEM observations that showed a similar quantity of slip bands at the edges as in the center of the flats. In fact, base-line RMS roughness measurements were performed on 12 x 12 μm^2 scanning area and yielded RMS roughness of 9.97 nm for 13-8 PH stainless steel, which is very similar to the RMS values obtained for 4340 steel.

RMS surface roughness of the various LCF specimens tested from the annealed and quenched and tempered microstructures of 4340 steel and from 13-8 PH stainless steel specimens tested at 0.4% and 0.6% strain amplitude were characterized and recorded. Figure 3.6 shows the RMS roughness as a function of the number of cycles. In 4340 steel, the surface roughness clearly increases as fatigue cycles increase. Linear regressions of the two groups of the data shown in Figure 3.6(a) demonstrate that the trends of the roughness increase with fatigue cycles are similar for both annealed and the quenched and tempered steels. However, the annealed steel seems to have a larger scatter in the roughness data than the quenched and tempered steel. This may be due to the coarser microstructural features in the annealed steel consisting of pearlite and pro-eutectoid ferrite. The topographic changes due to plastic deformation are different in the two phases. Because the 7 x 7 μm^2 scanning area is smaller than some pearlite domains, the measured surface roughness is strongly affected by the scan location leading to more scatter. On the other hand, the quenched and tempered steel has fine martensite lathes, leading to less scatter in the measured roughness among various scanning locations.

RMS surface roughness measurement of 13-8 PH stainless steel, Figures 3.6b (1) and (2), do not show the same clear increase with the fatigue cycles. Two different sizes of AFM scans were used for the compilation of the results, because surface features of various sizes (described later in this section) appeared on the surface of the specimens and the optimum resolution for each was obtained at different magnifications. The comparison of magnitude of the RMS roughness of Figures 3.6b (1) and (2) shows that the larger images have a roughness that is about twice that obtained on the smaller images, because of

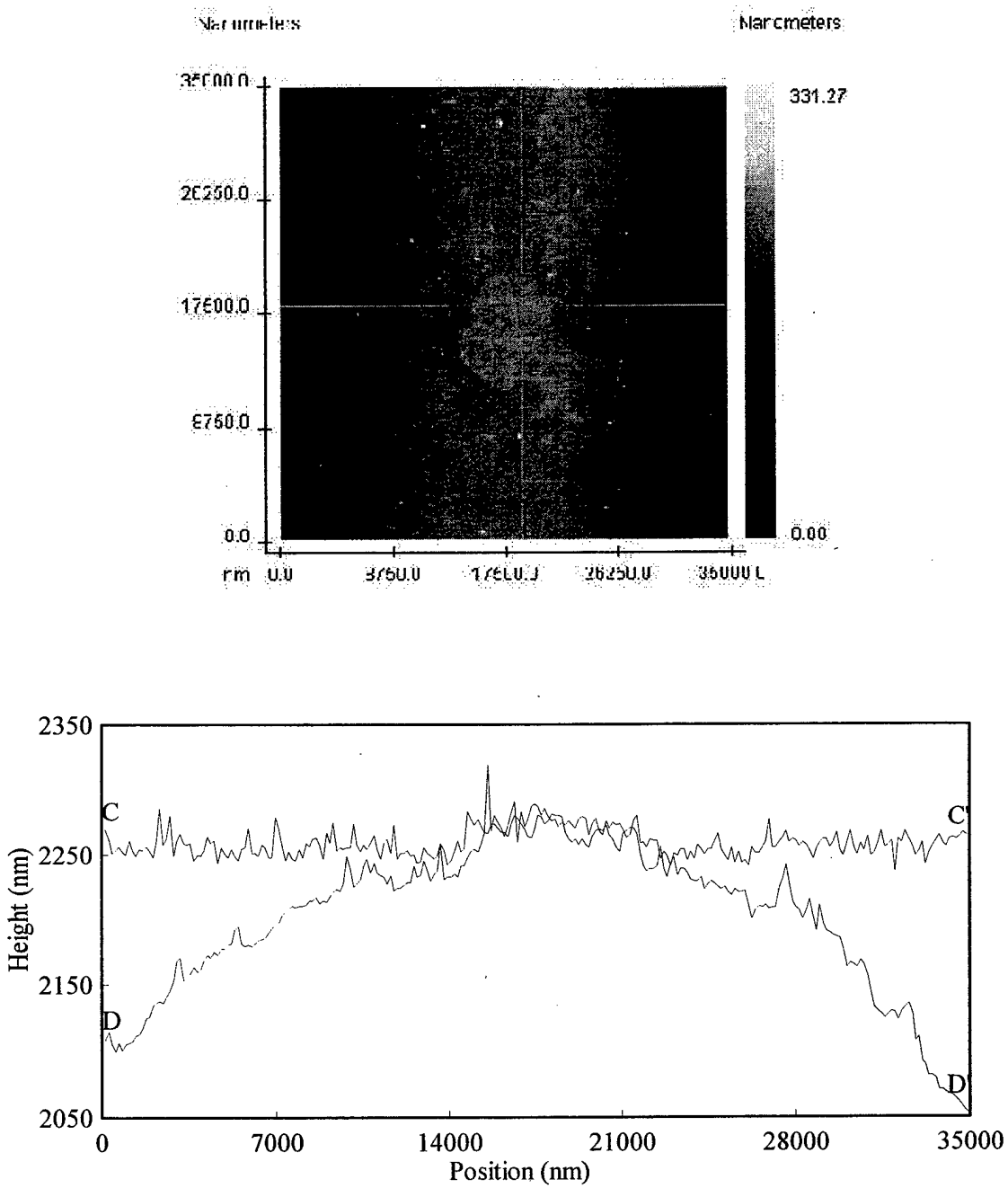

Figure 3.5 AFM image of an untested cylindrical fatigue specimen and cross-section profiles along the axial direction and the transverse direction. The latter direction shows the curvature of the specimen.

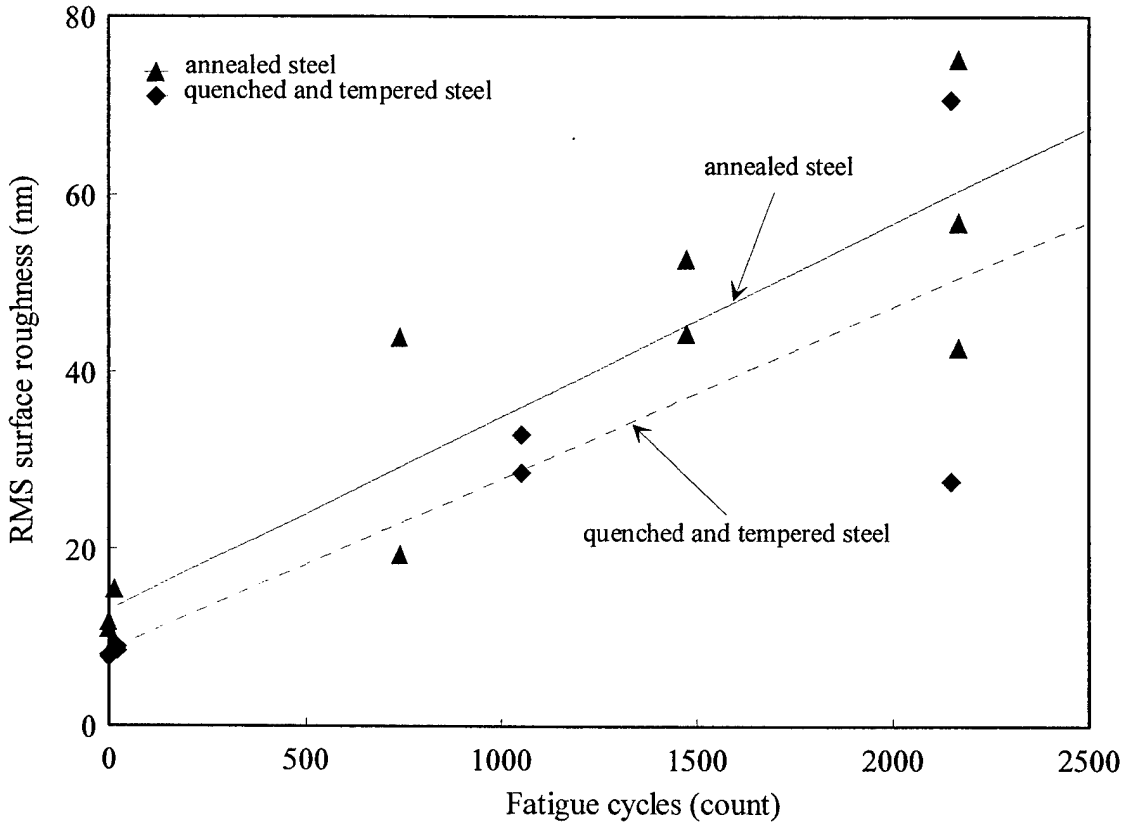

Figure 3.6a RMS surface roughness versus fatigue cycles in annealed and quenched and tempered 4340 steel.

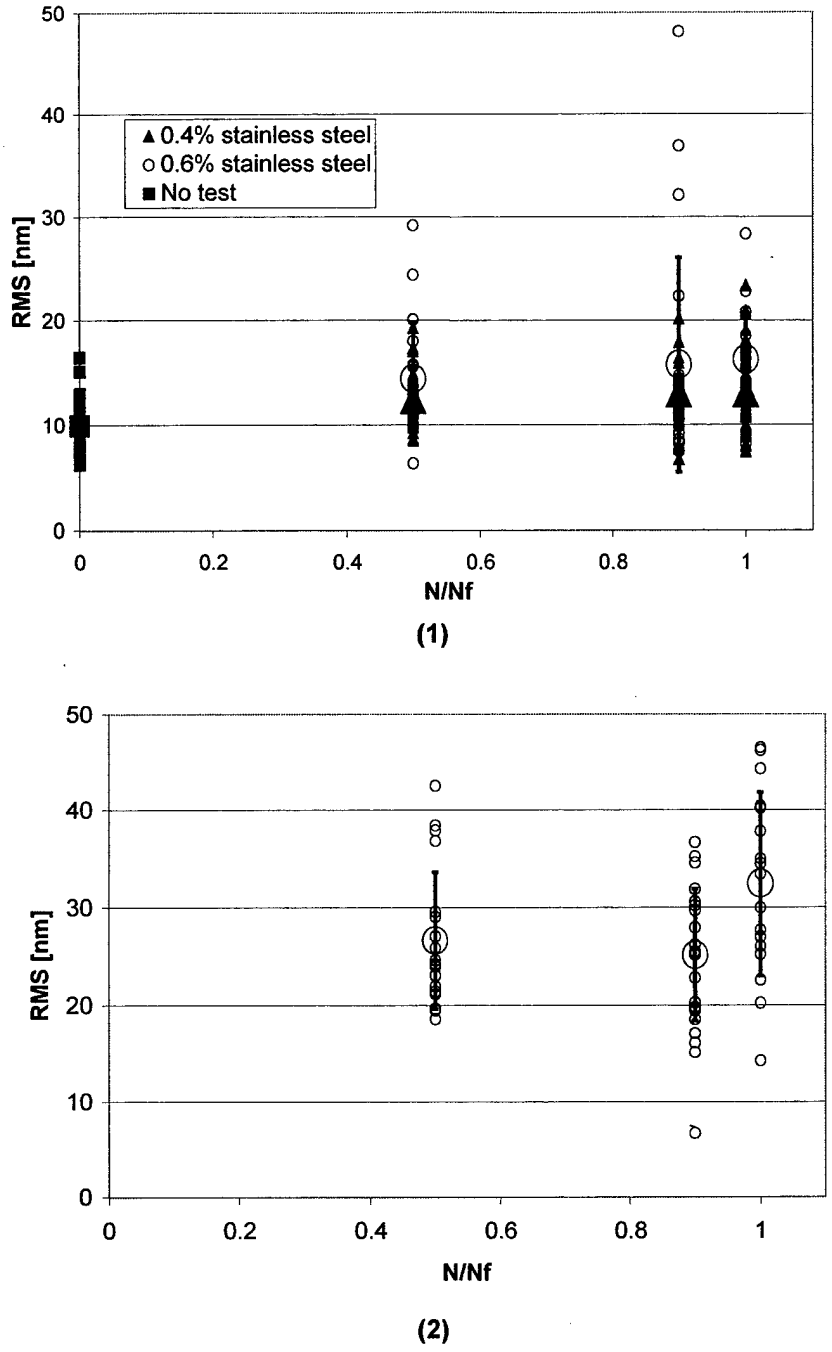

Figure 3.6b RMS surface roughness versus fatigue cycles in 13-8 PH stainless steel tested from **(1)** 12x12 μm^2 and **(2)** 30x30 μm^2 scanning areas.

the different surface features that appear in them. Also, the changes in RMS values due to the alteration of the surface topography after cyclic loading are small in comparison to the variations from one region to another, illustrated by the large scatter of the data of Figure 3.6b (1) and (2). Therefore, this method is not capable of providing an accurate quantitative characterization of the surface damage in this material, and another procedure is proposed later in this section to reach that objective.

Characterization of Surface Features in Fatigued Specimens

Figure 3.7 shows the AFM image and the surface profile of untested 4340 steel specimen LCFA1. Cementite platlets protrude from the ferrite base with heights ranging from 25 to 50 nm. In the specimen that was cycled for 1050 cycles at 1.5 % strain range, the slip bands show varying heights and widths, Figure 3.8. The surface profile of the image shows the height of one slip step at approximately 100 nm, as indicated by the marker pair 1-1. The 2-2 marker pair shows the distance between adjacent slip steps to be approximately 218 nm. In the case of quenched and tempered conditions, because the martensite has a fine lathe microstructure, it is difficult to distinguish the plastic slip steps within the small martensite lathes.

In 13-8 PH stainless steel tested at the high strain amplitude (0.6%), fatigue surface damage was essentially dominated by the formation of extrusions, e.g. Figure 3.9. They were on average between 2 and 5 μm long and 15 μm maximum, and between 10 and 200 nm high. The extrusions grow across multiple martensite laths, but generally remain within individual martensite packets because of the considerable mismatch between the crystallographic planes of two adjacent packets. Crack nucleation occurred at this strain amplitude at the edges of well-developed extrusions (at least 10 μm long and with sizeable height), and were thus of transgranular nature.

In both the low and the high strain amplitude tests, another type of surface deformation feature develops which, to the best of the authors' knowledge, has not been reported in any previous studies. It consists of narrow lines, referred to as "streaks" thereafter, about 1.5 micron long and 3.5 nm deep that are often clustered in a parallel fashion and form at crystal discontinuities (high and low angle grain boundaries), Figure 3.10. Streaks are not directly the result of a concentration of slip in a narrow band within a crystal (which defines a slip band) and, therefore, the term "slip band" does not apply to them. An extensive analysis of the streaks was conducted on numerous AFM fields of view at several points in the fatigue life, and it was shown that streaks are indeed the result of cyclic loading and the cause of fatigue failure in high cycle fatigue [18]. Their formation is explained by the presence of reverted austenite that precipitated during the aging process along the martensite lath boundaries. This newer phase has a much lower dislocation density than the neighboring martensite and, consequently, a concentration of plastic deformation takes place at the martensite lath boundaries upon cyclically loading the material, which results in the creation of streaks. The formation of fatigue cracks from streaks is illustrated in Figure 3.11, where SEM and AFM images show a series of streaks coalescing into deeper grooves approximately 20 microns long and 40 nm deep, which is about ten times the depth of regular streaks. Such features are precursors to fatigue cracks and were observed at various locations in the gauge area, including the vicinity of the major crack.

A procedure was developed in this study using AFM measurements to quantitatively characterize the amount of irreversible surface strain and assess the level of heterogeneity in the distribution of irreversible surface strain as a function of fatigue life fraction. For that purpose, the irreversible surface strain parameter, γ_{irrev}, was defined as

$$\gamma_{irrev} = \delta_{norm} / L_{tot} \tag{3.1}$$

where L_{tot} is the total length of the FOVs, equivalent to the gauge length, and δ_{norm} is the total normalized upset of all *i* surface features in all *j* FOVs, given by

$$\delta_{norm} = \Sigma[2 \Sigma (\delta_i a_i^{norm})]_j \tag{3.2}$$

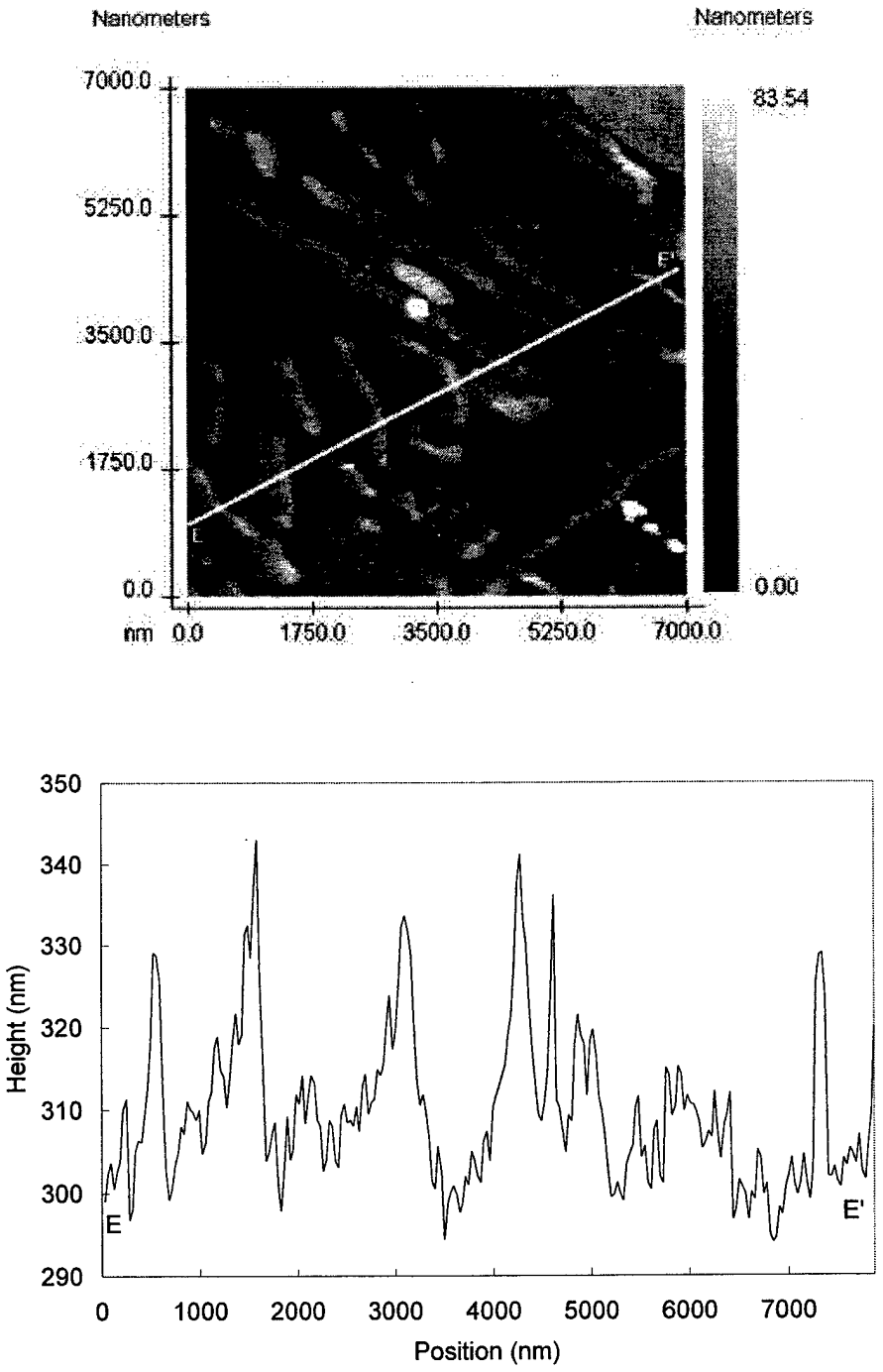

Figure 3.7 AFM image of an annealed untested 4340 steel LCF specimen and a cross-sectional profile.

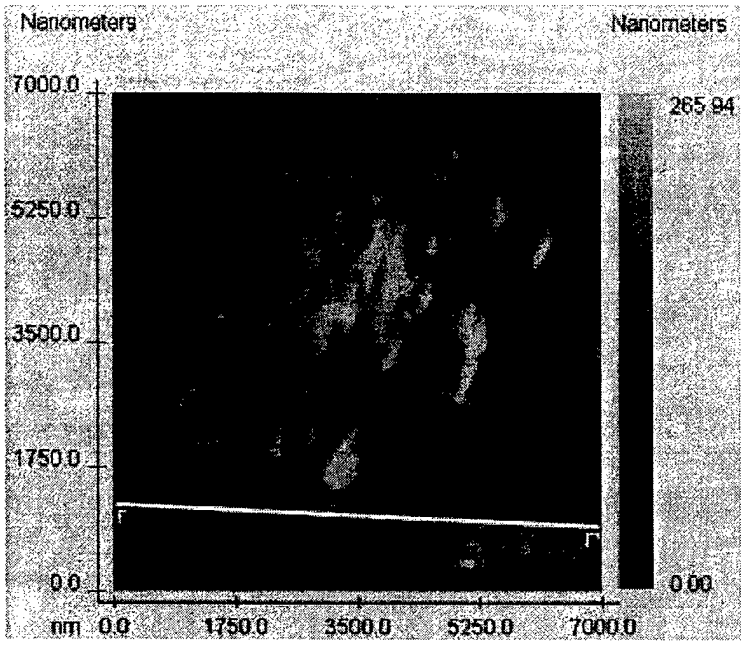

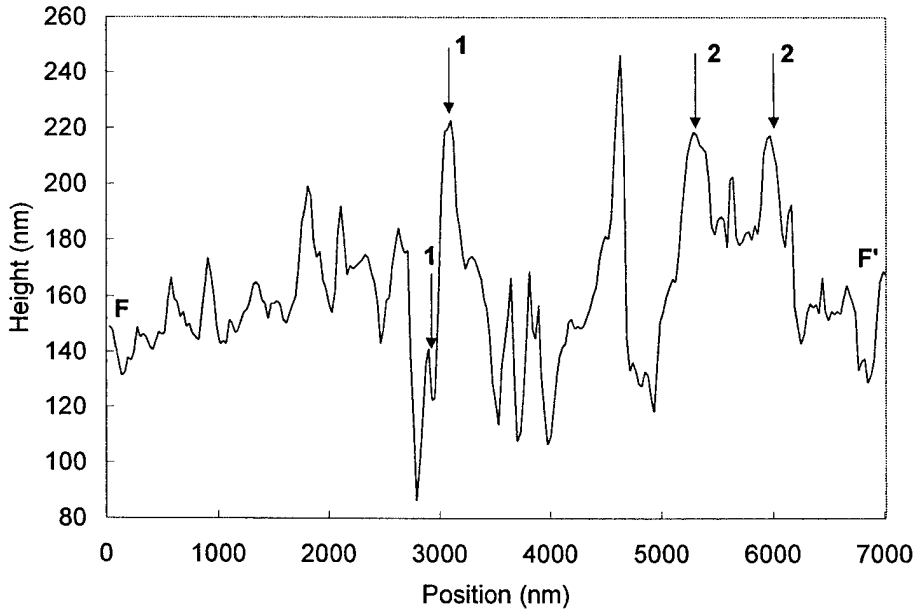

Figure 3.8 AFM image and the surface profile of annealed 4340 steel LCF specimen fatigued for 1050 cycles at a strain range of 1.5 percent.

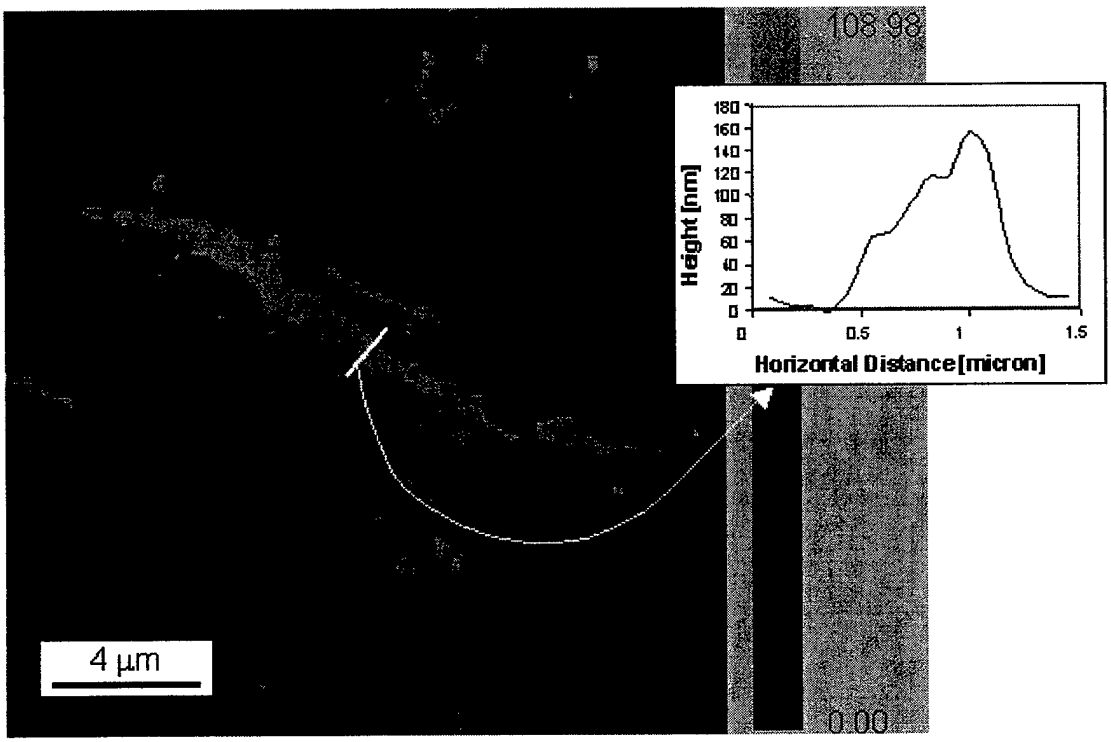

Figure 3.9 AFM scan of a large extrusion and several small adjacent ones in 13-8 PH stainless steel. The vertical scale is given on the right in nanometers. The inset shows a cross section of the extrusion along the white line.

Figure 3.10 Enhanced SEM image of streaks in tested 13-8 PH stainless steel.

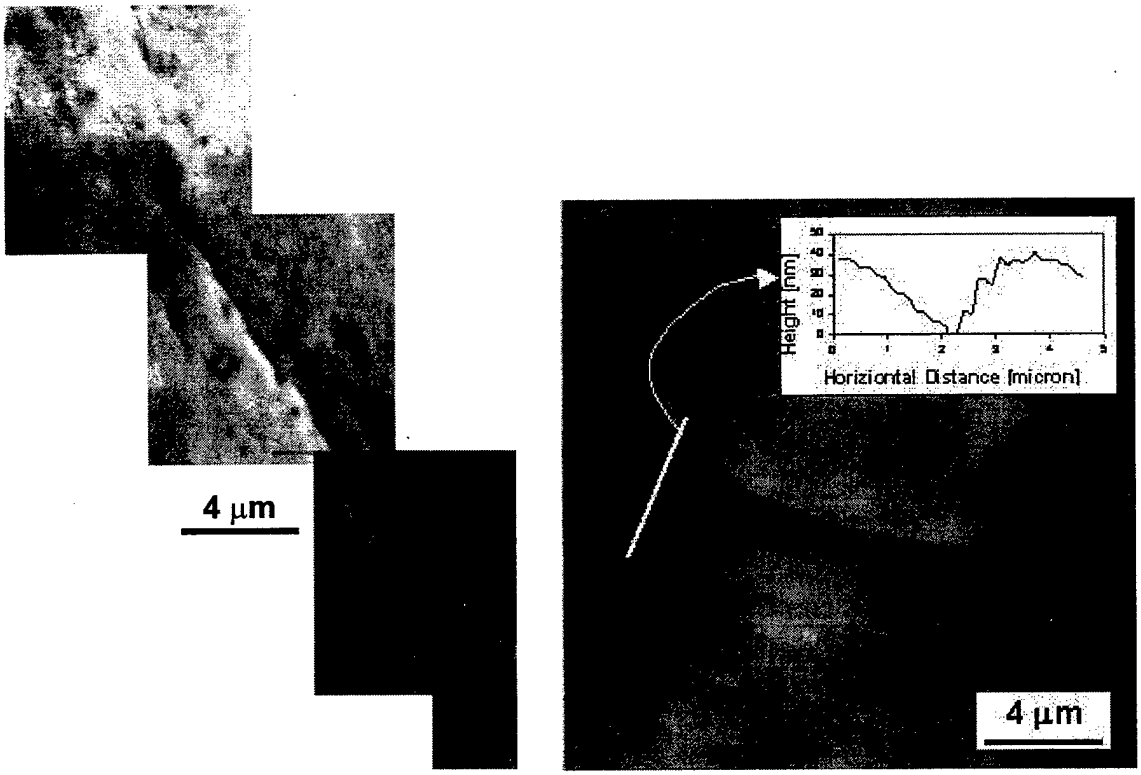

(a) (b)

Figure 3.11 **(a)** SEM and **(b)** AFM images of microcrack formation from the convergence of streaks, the inset of **(b)** shows the cross section along the white line.

and a^{norm} is the length of the surface features normalized by the width of the FOV in the direction parallel to the surface feature, Figure 3.12. This normalization is necessary to account for the fact that in polycrystals, surface features do not cover the entire width of the sample. The summary plot shown in Figure 3.13 clearly shows an increase of the irreversible surface strain with increasing cumulative plastic strain at both applied strain amplitudes. The detailed analysis of the distribution of irreversible surface strain has led to a measure of the irreversibility of slip and a criterion for crack nucleation that is applicable to any material, independent of the type of surface damage. This criterion was defined as the critical level of irreversible surface strain beyond which a material is likely to nucleate a crack, and was determined from AFM images that contained a crack nucleus. Irreversibility of slip is measured by the irreversibility factor, f, which corresponds to the rate of accumulation of irreversible surface strain, or

$$f = d\gamma_{irrev} / d\varepsilon_{pl}^{cum} \tag{3.3}$$

where ε_{pl}^{cum} is the cumulative applied plastic strain, $2N\Delta\varepsilon_{pl}$.

The results showed that, in the high strain amplitude tests, a high level of irreversibility of slip (irreversibility factor $f \approx 0.0025$) was maintained throughout the fatigue life. However, at low strain amplitude, a low initial irreversibility of slip ($f < 0.001$) was observed which then increased in the last ten percent of the life to reach value of f larger than 0.001. The application of the crack nucleation criterion to the tests performed in this study showed that crack initiation occurred in most cases when about thirty percent of the surface had reached a critical level of irreversible surface strain. Figure 3.14 is an example of the use of this criterion in the case of PH 13-8 Mo stainless steel tested at 0.6% strain amplitude. The plot in this figure corresponds to the inverse cumulative normal distribution plots that were fitted on the actual data of the distribution of irreversible surface strain on the surface of the various specimens. The vertical axis indicates the fraction of the surface that developed irreversible surface strain larger than the amount indicated on the horizontal axis. The vertical dotted line in the Figure corresponds to the criterion for crack nucleation, and its intersection with the different curves indicates the fraction of the surface that has reached the critical value of irreversible surface strain, which is equivalent to a measure of the probability of failure. The latter is thus directly read on the vertical axis, and is 0%, 36% and 32% for fractions of fatigue life of 0.5, 0.9 and 1, respectively.

b. Nanoindentation Hardness Technique

The objectives for this aspect of the research was to better understand the interactions among the growing fatigue cracks, the microstructure encountered by the crack and the cyclic plasticity that develops in a small zone ahead of the fatigue crack. While previous studies have attempted to relate microstructure to fatigue crack growth resistance, the role of crack tip plasticity in determining the microstructure/crack interactions has not been investigated. In this study, fatigue crack growth tests were performed in the pearlite-ferrite and the tempered martensite microstructures. The microstructure/crack interaction was characterized using optical microscopy and scanning electron microscopy. Subsequently, nanoindentation hardness tests were performed to characterize the crack tip plasticity in various specimens. The results are used to shed more light on ways to improve the fatigue resistance of helicopter rotor parts.

Under cyclic plastic deformation, a metal may harden, soften, or remain stable, depending on the microstructure and test conditions such as the strain amplitude of the fatigue cycle employed. Since hardness of a metal is directly correlated to its yield strength, the cyclic deformation zone may be delineated with precise hardness measurement around the crack tip. Nanoindentation hardness is a unique technique, which allows one to determine the mechanical properties down to the microstructural length scales. The definition and the calculation of the nanohardness are identical to the conventional Vickers hardness, but the former provides a much more accurate measure of hardness within smaller length scales.

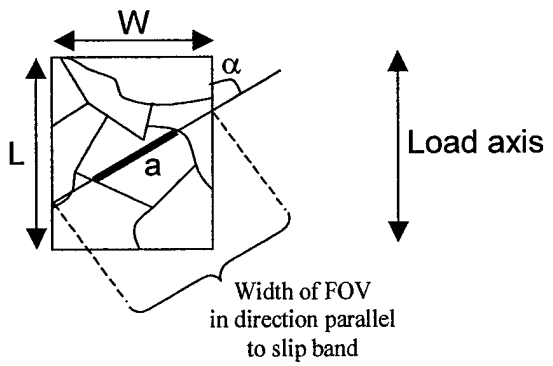

Figure 3.12 Example of a field of view (FOV) containing several grains and a single slip band of length *a*. The normalization of the slip band length is done relative to the width of the FOV in the direction parallel to the slip band, which can be determined from the angle α with the loading axis.

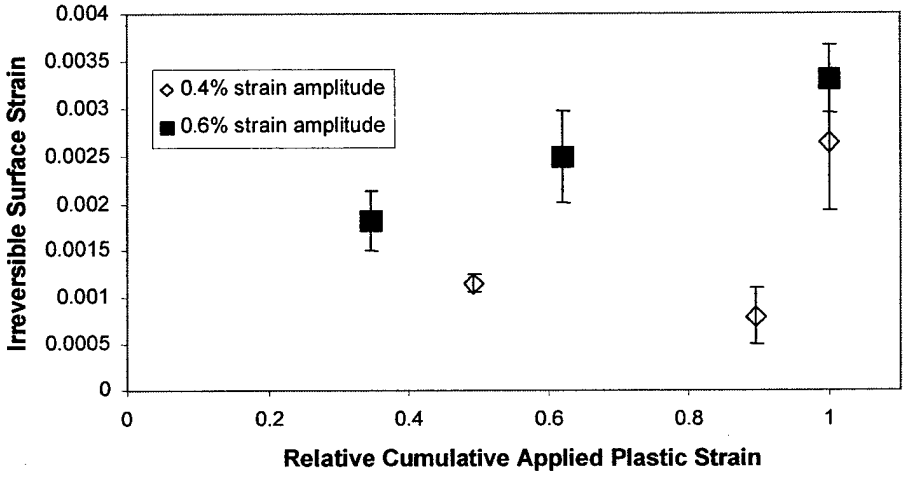

Figure 3.13 Irreversible surface strain of 13-8 PH stainless steel tested at 0.4% and 0.6% strain amplitude. The relative cumulative plastic strain, indicated on the horizontal axis, represents the cumulative plastic strain normalized by the cumulative plastic strain at failure.

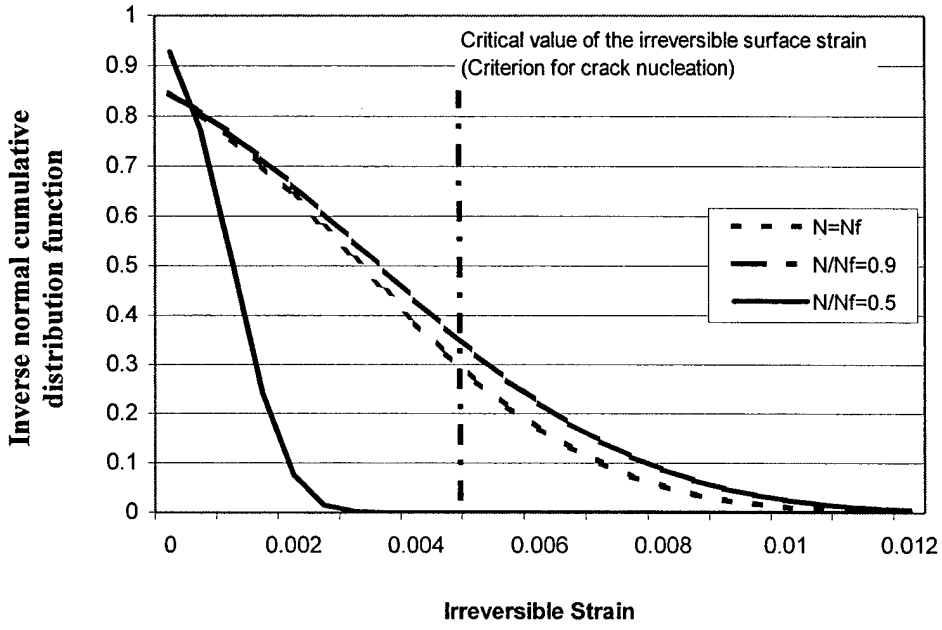

Figure 3.14 Inverse normal cumulative distribution of the irreversible surface strain for PH 13-8 Mo stainless steel tested at 0.6% strain amplitude. The criterion for crack nucleation is indicated by the vertical dotted line.

Figures 3.15 and 3.16 show the plots of resulting hardness versus distance from the crack tip for the two heat treatment conditions. Figure 3.15 shows that the hardness close to the crack tip is higher than the far-field hardness, indicating that the annealed steel tends to cyclically harden. On the other hand, Figure 3.16 shows that the hardness decreases as one approaches the crack tip in the quenched and tempered steel, confirming a cyclic softening trend for this steel. In Figure 3.15, hardening is seen to occur even at distances in excess of 6000 μm. Thus, the monotonic plastic zone boundary is located at least that far away from the crack tip. The analytically estimated plastic zone size was 5757 μm which is in good agreement with the measured value. The analytically estimated fatigue plastic zone size is 870 μm which is also marked on Figure 3.15. This is also in good agreement with the onset of the plateau region of the hardness plot, which is expected to coincide with the end of the fatigue plastic zone boundary. This result is extremely encouraging for nanoindentation hardness as a technique for studying microstructure/crack tip plasticity interactions. However, similar comparisons between the analytically estimated and measured fatigue and monotonic plastic zone sizes did not yield similar results for the quenched and tempered samples, Figure 3.16. In this instance, the measured zone sizes were considerably larger than the analytically calculated values. There are several possible reasons for this discrepancy, which have been discussed in reference [3].

This study of the mechanisms of fatigue crack growth in 4340 steels has led to the following conclusions. The microstructure plays an important role in determining the fatigue crack growth resistance of 4340 steel, especially in the low crack growth rate regime which is most important for helicopter rotors. The annealed steel, which has a coarser microstructure than the quenched and tempered steel, consistently has better fatigue crack growth resistance. The fatigue crack tends to grow within the ferrite base in the annealed steel, avoiding going through the cementite lamellae. In the quenched and tempered steel, the crack goes straight through the martensite lathes. The meandering of the cracks in the annealed steel to avoid going through cementite results in higher fatigue crack growth resistance. Nanoindentation technique has the potential for providing the data for understanding these microstructure/crack interactions. However, due to limited resources, this technique was not being pursued any further within this project.

c. Impedance Spectroscopy

Impedance spectroscopy (IS) is a non-destructive method of material characterization which has proven its effectiveness with various material systems. For instance, it has been used to determine corrosion rate and efficiency of corrosion inhibitors in metallic materials, to study the kinetics of electrochemical reaction (e.g. in batteries) and to investigate the bulk and surface properties of semi-conductor materials. In metals, the changes in the microstructure during fatigue consists of the multiplication and rearrangement of dislocations, development of surface roughness, increase in vacancy concentration and microcrack formation, and each one of these is likely to affect the electrical properties of the specimen. The purpose of this aspect of the project was to correlate changes in the IS response with evolution of fatigue damage in metals.

Because different crystal imperfections affect the electric signal at distinct frequencies, IS measurements are performed by applying an AC sinusoidal potential signal and monitoring the resulting current over a wide frequency range, typically 5 to 10^7 Hz. The impedance, Z^*, is a complex number representing the transfer function between the potential and the current. To better display the relaxation processes that occur in the metal, the results are then converted into another formalism, the complex admittance Y^*, which is the inverse of the impedance. The results presented below were obtained from two different materials, polycrystalline copper that showed positive results and 13-8 PH stainless steel for which IS measurements were inconclusive.

Figure 3.17 summarizes the IS measurements of a copper specimen tested at 0.255% strain amplitude up to 30% of the fatigue life. These plots show the imaginary versus real part of the admittance, and each data point corresponds to the magnitude of the admittance at a given frequency. The high frequencies are close to the origin and the low frequency are at the other end of the semi-circle, where the changes in polarity of the electric signal occurs at rates slow enough for the material's response to resemble that of a

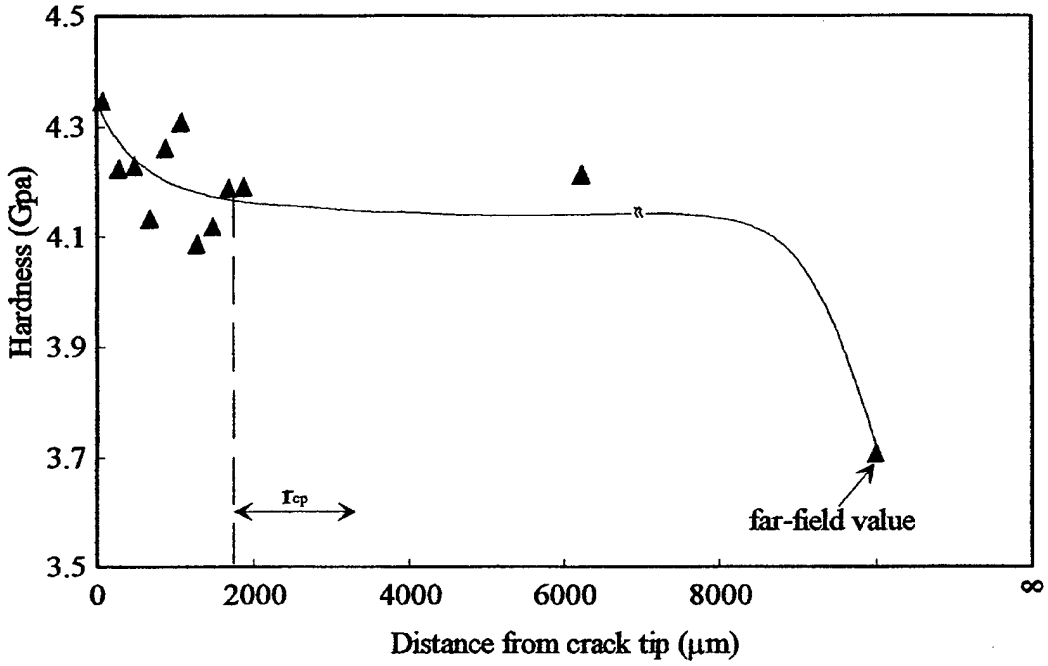

Figure 3.15 Nanoindentation hardness versus distance from the crack tip of a fatigue crack growth 4340 steel specimen in annealed condition.

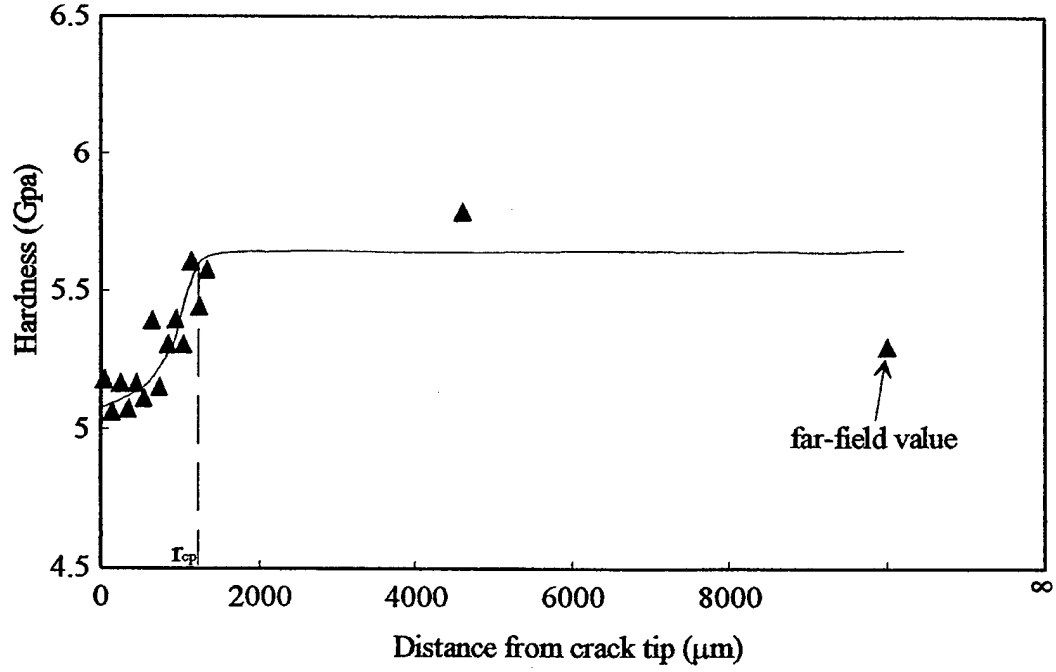

Figure 3.16 Nanoindentation hardness as a function of distance from the crack tip from a fatigue crack growth specimen from quenched and tempered 4340 steel.

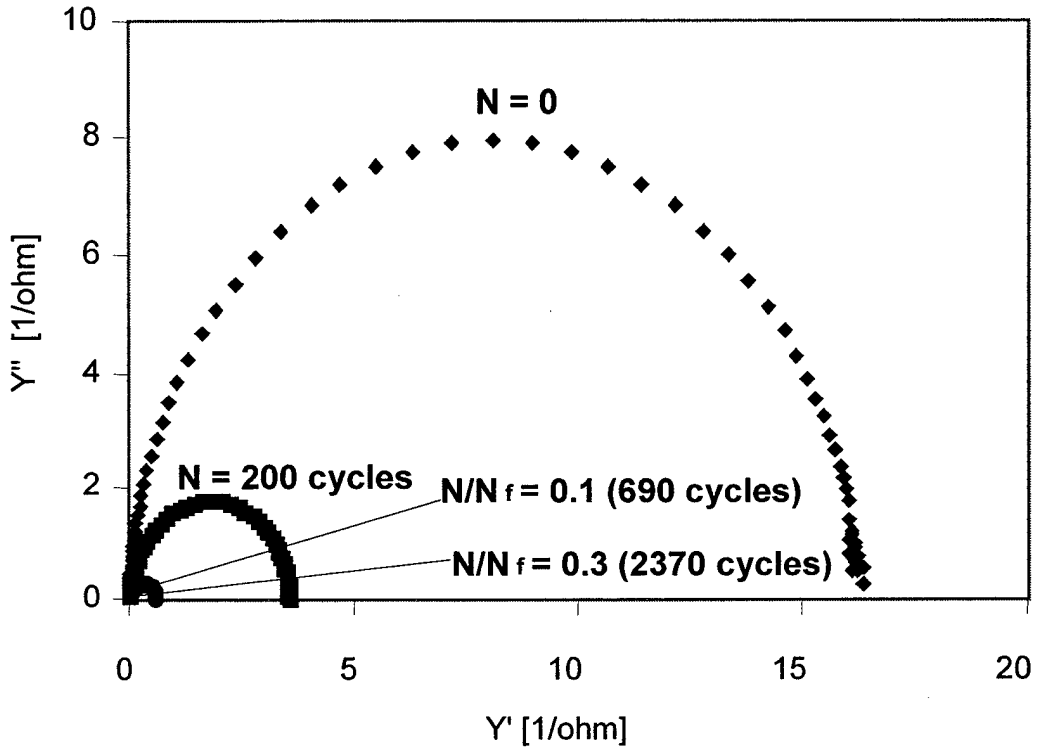

Figure 3.17 Complex representation (Nyquist plot) of the admittance results of copper tested at 0.255% strain amplitude (N_f=6896 cycles).

DC circuit. IS measurements were particularly sensitive to changes in the dislocation density that occurred during the primary cyclic hardening stage. However, IS measurements did not seem to be able to detect surface upset with the same level of sensitivity. Little change in IS response was observed beyond the initial cyclic hardening stage, as shown in Figure 3.18, which summarizes the results from all copper specimens by plotting the value of the imaginary part of the admittance at the peak of the semi-circle (see Figure 3.17) normalized by the corresponding value in the prior testing condition.

IS measurements were ineffective in 13-8 PH stainless steel, because the interaction between the numerous electrical domains that exist in the complex microstructure of the material inhibits the successful collection of repeatable measurements. Also, the sensitivity of the IS measurements performed on copper samples was attributed to the significant increase in dislocation density during the primary cyclic hardening phase, which does not take place in stainless steel due to its high initial dislocation density.

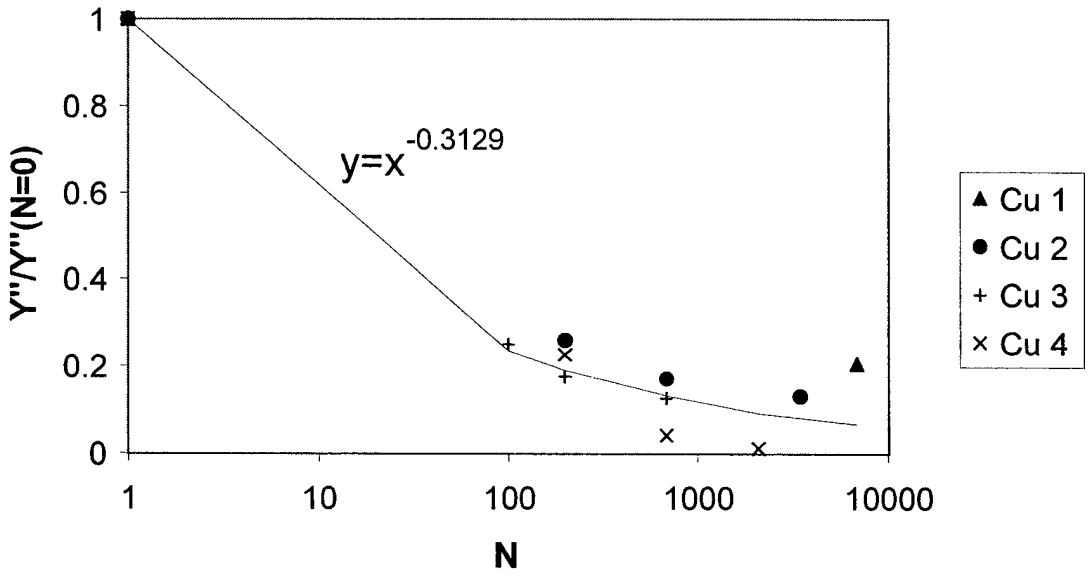

Figure 3.18 Normalized representation of the imaginary part of the admittance at the peak of the semi-circle versus the number of cycles for copper tested at 0.255% strain amplitude (N_f=6896 cycles). A power-law regression curve is fitted among the data from all specimens.

References for Section 2.2.1.3

1. Harvey, S.E., Marsh, P.G. and Gerberich W.W., "Atomic Force Microscopy and Modeling of Fatigue Crack Initiation in Metals", Acta Metallurgica Materials, Vol.42, No. 10, 1994, pp 3493-3502.
2. W.W. Gerberich, S.E. Harvey, D.E. Kramer, J.W. Hoehn, "Low and High Cycle Fatigue – A Continuum Supported by AFM Observations", *Acta Materialia*, Vol. 46, No. 14, 1998, pp. 5007-5021.
3. F.Yang, A.Saxena and L. Riester, "Use of Nanoindentation Technique for Studying Microstructure/Crack Interactions in Fatigue of 4340 Steel", Metallurgical and Materials Transactions A, Vol. 29A, 1998, pp 3029-3036.
4. Mil Handbook 5G, Nov.1, 1994, pp 2-147 – 2-156
5. Metals Handbook, ASM International, 1985.
6. V.Seetharaman, M. Sundaraman, R.Krishnan, "Precipitation Hardening in a PH 13-8 Mo Stainless Steels" Materials Science and Engineering, Vol. 47. 1981, pp 1-11.
7. P.W. Hochanadel, C.V. Robino, G.R. Edwards, M.J. Cieslak, "Heat Treatment of Investment Cast PH 13-8 Mo Stainless Steel: Part I. Mechanical Properties and Microstructure", *Metallurgical Transactions A*, Vol. 25A, 1994, pp. 789-798.
8. A.M. Patel, R.W. Neu, J.A. Pape, "Growth of Small Fatigue Cracks in PH 13-8 Stainless Steel", submitted to *Metallurgical and Materials Transactions A*, April 1998.
9. Swain, M.H., "Monitoring Small Crack Growth by Replication Method", Small-Crack Test Methods, ASTM STP 1149, American Society for Testing and Materials, 1992, pp 34-56.
10. Larsen, J.M., Jira, J.R. and Ravichandran, K.S., "Measurement of Small Cracks by Photomicroscopy: Experiments and Analysis", Small-Crack Test Methods, ASTM STP 1149, American Society for Testing and Materials, 1992, pp 57-80.
11. Sharpe, W.N., Jira, J.R. and Larsen, J.M. "Real-Time Measurement of Small Crack Opening Behavior Using an Interferometric Strain/Displacement Gage", ASTM STP 1149, American Society for Testing and Materials, 1992, pp 92-115.
12. Gangloff, R.P. Slavik, D.C., Piascik, R.S. and Vanstone, R.H. "Direct Current Electrical Potential Measurement of the Growth of Small Cracks", ASTM STP 1149, American Society of Testing and Materials, 1992, pp 116-168.
13. Fine, M.E.. and Chung, Y.W., "Fatigue Failure in Metals", ASM Handbook, Volume 19, Fatigue and Fracture, 1996, pp63-72.
14. Gould, S.A.C., Drake,B., Prater, C.B. et al., " The Atomic Force Microscope: A Tool for Science and Industry", Ultramicroscopy, Vol.33, 1990, pp 93-98.
15. "Metris-2000 Atomic Force Microscope", Operating Manual (Rev.E), Burleigh Instruments, Inc. Burleigh Park, Fishers, NY 14453-0755, 1997.
16. Saxena, A., Yang, F., Cretegny, L., "Use of Atomic Force Microscopy for Studying Fatigue Crack Initiation", *Proceedings of the Seventh International Fatigue Congress*, Editors: X.R. Wu, Z.G. Wang, Beijing, P.R. China, Vol. 4, 1999, pp. 777-2782.
17. Yang, F., Saxena, A., "Mechanisms of Fatigue Crack Initiation in Annealed and Quenched and Tempered 4340 Steel", *Special Issue on Integrated Diagnostics of the Journal of the Institution of Mechanical Engineers*, in press.
18. Cretegny, L., Doctoral Thesis, Georgia Institute of Technology, July 2000.

2.2.1.4 BEHAVIOR AND MODELS FOR SMALL FATIGUE CRACK GROWTH: MICROSTRUCTURE, LOAD SEQUENCE AND CORROSION EFFECTS

Co-investigator: W. Steven Johnson (Georgia Tech)
Graduate Assistants: Richard Hamm (6/96-6/98); Ohchang Jin (9/98-8/00)

OVERVIEW

This report includes research activities for the past five years of the program. First of all, a state-of-art small crack survey was conducted to determine the direction of the research. Secondly, extensive model comparison was performed on the growth behavior of small cracks in Ti-6Al-4V used on the CH-53 helicopter and a model enhancement was developed to account for small to large crack transition. Thirdly, the effect of microstructure on the small crack initiation and growth was investigated on Ti-6Al-4V. Fourthly, small crack growth behavior in PH 13-8 Mo stainless steel (SS) under various loading conditions was characterized. Corrosion fatigue behavior of PH 13-8 Mo SS was also evaluated at several frequencies in saltwater since PH 13-8 Mo SS will be used in a naval environment on the CH-46 helicopter.

ACHIEVEMENTS

a. Survey

An international survey was conducted by ASTM committee E08.06.04 and was executed by the investigators to determine the state of small-crack research and knowledge (see reference 1). The survey consisted of short answer questions regarding: the nature of the research, the materials studied, applications of the investigators' research, smallest crack size monitored, techniques used to monitor crack growth, testing environment, surface conditioning/preparation, and models used to predict crack growth. In addition, survey participants were asked to say what critical questions they were addressing with their research and what some important unresolved questions are in the area of small-cracks. Some results from the survey (50 responses from 12 countries) that apply to the project are as follows:

- Titanium alloys make up 41% of all the materials studied by the survey participants. But, only 8% of all replies indicated that small-crack research is being done on Ti-6Al-4V.
- Only 15% of all replies indicated that load interaction effects were being investigated on small-cracks. The most common type of loading was constant amplitude loading with different stress ratios, totaling 83% of how loading was characterized by survey participants.
- 50% of replies stated the smallest crack size being monitored was smaller than equal to ten microns in length.
- 70% of all small crack specimens are being mechanically polished with only 3% incurring no polish. Of the specimens that are mechanically polished, 26% are being electropolished as well. Specimens for the current research are mechanically polished and electropolished.

Some of the unresolved issues, noted by survey participants, included: what the load interaction effects are on small cracks, how are these effects modeled and how do metallurgical features influence small-crack growth. These are questions being addressed by the current research.

b. Model Enhancement

The models presented in this study were specifically formulated for either mechanically small cracks or microstructurally small cracks or both (see reference 2). When a crack is considered small, local stress gradients due to geometry are negligible. However, as a crack extends beyond the small crack regime, stress gradients and constraint caused by geometry cannot be ignored. The stresses that a crack feels decay from the local stresses to the nominal applied stresses. A fracture mechanics treatment of these cracks must be able to integrate Microstructural Fracture Mechanics (MFM), Elastic-Plastic Fracture

Mechanics (EPFM), and Linear-Elastic Fracture Mechanics (LEFM) seamlessly. The models presented in this study have not done so. Hence, an enhancement is proposed to unify MFM, EPFM and LEFM through a single growth law. The goal of the modeling is not to explore the possible forms of the equation or values in the equation, but rather to show the merit of the concept.

Formulation

The enhancement was inspired by the growth laws used in the Wang [3] and Nisitani [4] models, but modified to link small crack growth characteristics to large crack growth characteristics. The enhancement assumes a growth law of the form:

$$\frac{da}{dN} \propto \rho^{\lambda} \tag{4.1}$$

where ρ is the plastic zone and λ is the crack growth exponent. While a crack is small large stresses are required to propagate the crack. The large stresses may come from large far-field stresses or they may be due to a stress gradient caused by specimen geometry, such as notches. The proposed extension assumes the latter. At this point, the plastic zone may be the same order of magnitude as the crack. This can be considered an MFM or EPFM plastic zone size characteristic. As a crack grows beyond the first microstructural boundary into a large crack and out of the stress gradient, the stresses are generally low and the plastic zone size decays to a small fraction of the crack length, which are LEFM characteristics. The models used in this study with plastic zone formulations predict the plastic zone size stays on the same order as the crack length at all crack sizes. The proposed enhancement decays the plastic zone size from the same order of magnitude as the crack length to a small fraction of the crack length. The enhancement links the small crack MFM and EPFM behavior to the large crack LEFM behavior by the following:

$$\frac{\rho}{a} = \Theta\Psi + \Phi \tag{4.2}$$

where ρ is the plastic zone size, Θ is the MFM and/or EPFM behavior and Φ is the LEFM behavior. Ψ is a decaying function that is only dependent upon α and 2a/d where d represents the characteristic microstructural unit length and α is a multiple of 2a/d. The advantages of using Equation 4.2 are that it is general enough so as not to be model specific.

The role of λ in equation 1 is to provide a link between exponents of small crack formulations and large crack formulations. Consider:

$$\frac{da}{dN} \propto \rho_{MFM/EPFM}{}^{m} \qquad \text{for small cracks} \tag{4.3}$$

$$\frac{da}{dN} \propto \rho_{LEFM}{}^{z} \qquad \text{for large cracks in Paris regime} \tag{4.4}$$

where z equals 1/2 of the Paris exponent (n) since the LEFM plastic zone is $\rho_{LEFM}{}^{1/2} \propto \Delta K$.

Several models with plastic zone formulations use various values for the exponent, λ, in Equation 4.1. For example, the Wang model assumes a value of $\lambda = 1$ while the Nisitani model prescribes a value $\lambda >> 1$. The reason for the differences is due to the assumptions about which regime the small crack is in.

To generalize λ for different values of m and to link the small crack and large crack exponents, the following conditions must be satisfied:

$$\lambda = m \text{ for } 2a/d < 1$$

$$\lambda = n/2 \text{ for } 2a/d \geq \alpha$$

Between $1 < 2a/d < \alpha$, λ changes from m to n/2. A linear interpolating function is assumed for λ and is given by:

$$\lambda = \left(\frac{m - n/2}{1-\alpha}\right)\frac{2a}{d} + \left(\frac{n/2 - m\alpha}{1-\alpha}\right) \tag{4.5}$$

combining everything together:

$$\lambda = m \qquad \text{for } 2a/d < 1, \tag{4.6a}$$

$$\lambda = \left(\frac{m - n/2}{1-\alpha}\right)\frac{2a}{d} + \left(\frac{n/2 - m\alpha}{1-\alpha}\right) \qquad \text{for } 1 < 2a/d < \alpha, \text{ and} \tag{4.6b}$$

$$\lambda = n/2 \qquad \text{for } 2a/d \geq \alpha. \tag{4.6c}$$

Using Equations 4.1, 4.2, and 4.6, a single formulation can be used to describe crack growth at any size, under any geometry with known boundary correction factors, under any constraint. The only drawback is that the formulation prescribes one fitting factor; α, which can roughly be connected to the length scales that define the various small crack regimes. The final formulation gives:

$$\frac{da}{dN} \propto \rho^{\lambda} = f(\rho_{MFM/EPFM}, \rho_{LEFM}, m, n, \alpha, a, d)$$

So, as a crack grows from a small crack to a large crack, the unified growth law evolves smoothly:

$$\frac{da}{dN} \propto \rho_{MFM/EPFM}{}^{m} \Longrightarrow \frac{da}{dN} \propto \rho_{LEFM}{}^{n/2}$$

The enhanced model was applied to all the small crack data used in the study. Plane strain conditions were assumed ($\beta = 6$). The results are shown in Figs. 4.1 and 4.2 as they compare to the Wang model.

The enhanced Wang model predicted lower crack growth rates than the Wang model at R = 0.4 while predicting higher rates at R = 0 and -1. One aspect of the predictions that is noteworthy is that the slope of the enhanced model was nearly the same as the Wang model and the data at all stress levels, validating the growth exponent formulation. The enhanced model showed reduced oscillatory behavior compared to the Wang model, downplaying the microstructural interaction as the crack length increases.

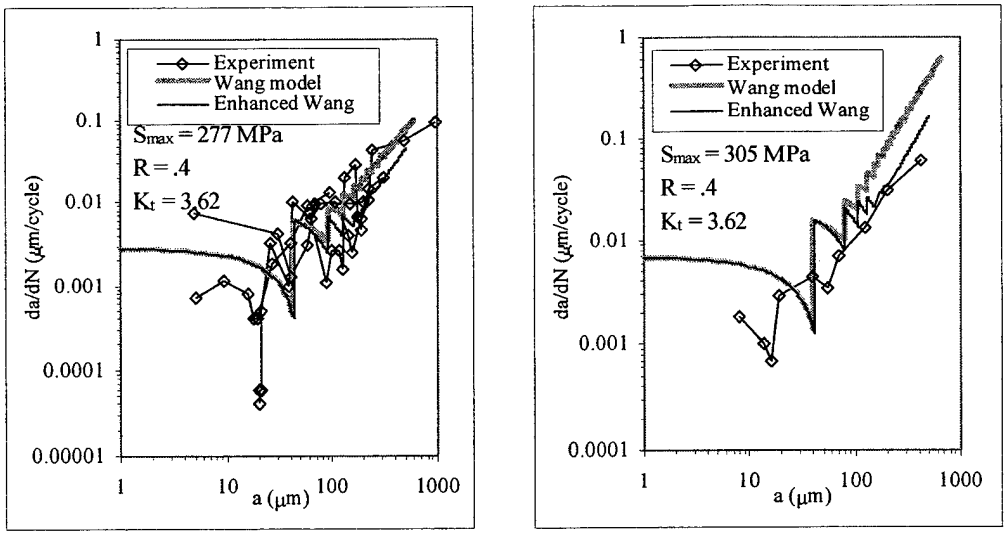

Figure 4.1 Enhanced Wang model crack growth predictions at R = 0.4.

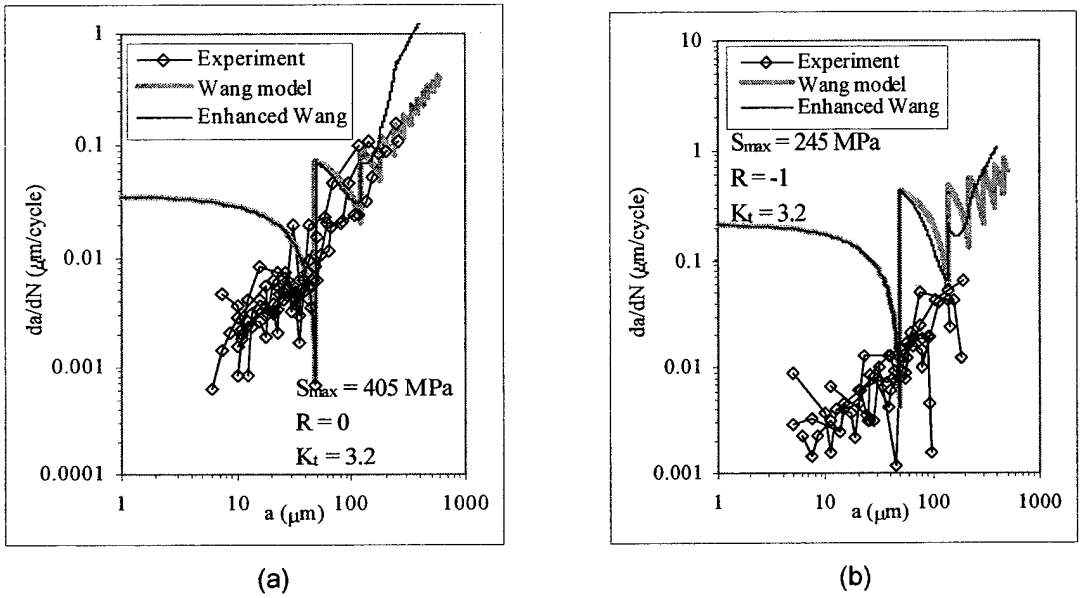

Figure 4.2 Enhanced Wang model crack growth predictions at a) R = 0 and b)R = -1.

c. Small Crack Growth Behavior in Ti-6Al-4V

The microstructure of a material plays a dominant role in many aspects of crack growth (reference 5). One such influence is the role that microstructure has in determining a crack's path through the material. In addition, the type of microstructure can have a significant effect on the material's crack growth rate characteristics.

Figure 4.3 shows a microstructure of Ti-6Al-4V that consists of lighter α grains with darker β grains. The microstructure exhibited textured bands of α-rich and β-rich material that ranged in width from approximately 20 to 100 μm with an average width of 41 μm and a standard deviation of 27 μm. The bands were oriented in the longitudinal direction, parallel with the material's loading axis. As such, the bands were perpendicular to the crack growth direction, so it was expected that they would have some effect on the small crack growth behavior of the material. The α grains had an average grain diameter in the crack growth direction of approximately 3-5 μm.

Bands of α grains clearly influences crack extension in Ti-6Al-4V. The dependence of crack growth rates on the bands of α grains is dependent upon the applied stress level. Specifically, a stronger dependence between growth rates and bands of α grains is noted as the maximum stress level increases. This microstructure promotes crack branching to absorb applied energy rather than impart resistance to an advancing crack. The size and orientation of α platelet colonies in α+β titanium alloys in relation to local stress fields were the chief parameters controlling the kinetics of fatigue crack propagation rather than the grains themselves.

Oscillations in the crack growth rates were found to occur with increasing crack length at all stress levels tested. This is shown in Figs. 4.4a and 4.4b. In the figures, a is equal to half the crack length as defined by Newman's stress intensity factor formulation for a SEN specimen. The oscillations seen in these figures have wavelengths between 50-100 μm. The wavelengths approximately correspond to the widths of the α-rich and β-rich bands exhibited by the microstructure. Hence, more evidence shows that the overriding characteristic microstructural length is defined by the microstructural band widths. As an example, consider the plot for a maximum stress at 305 MPa in Fig. 4.4. In the plot, the crack growth rate reaches a minimum at a crack length of 20 μm.

As the cracks extend beyond approximately 300 μm, the growth rates collapse into a narrow scatterband, representing the overall large crack behavior. Figure 4.5 shows the comparison between small crack and large crack growth data in terms of the stress intensity factor range at a stress ratio of R = 0.4. There was little small crack effect. This can be partly explained in terms of crack tip shielding. At higher stress ratios, the level of closure induced by roughness or plasticity does not play a significant roll in a crack's behavior, whether the crack is small or large. Hence, the average behavior of small and large cracks at higher stress ratios would be similar, as observed. The difference between the behavior of the two types of cracks is then seen in terms of scatter in the data.

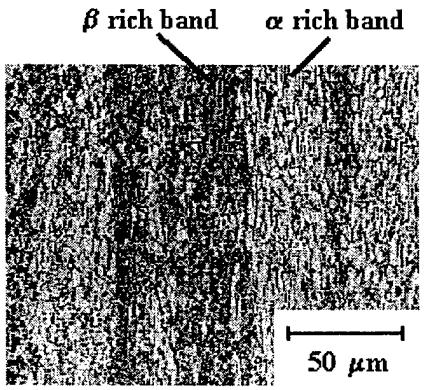

Figure 4.3 Bands of α and β rich material in the Ti-6Al-4V microstructure.

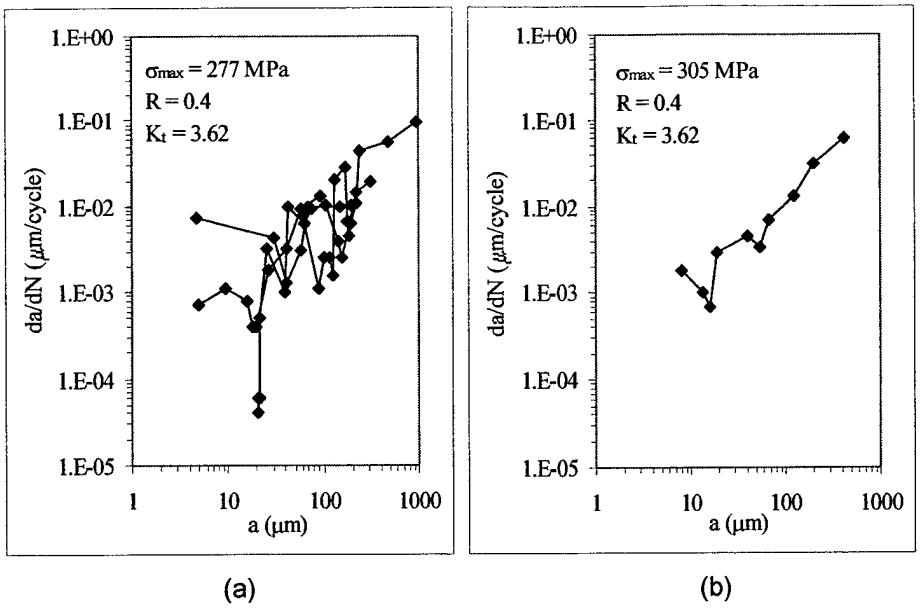

Figure 4.4 Crack growth rates verses crack lengths for small cracks at maximum stresses of **(a)** 277 MPa, and **(b)** 305 MPa at R = 0.4.

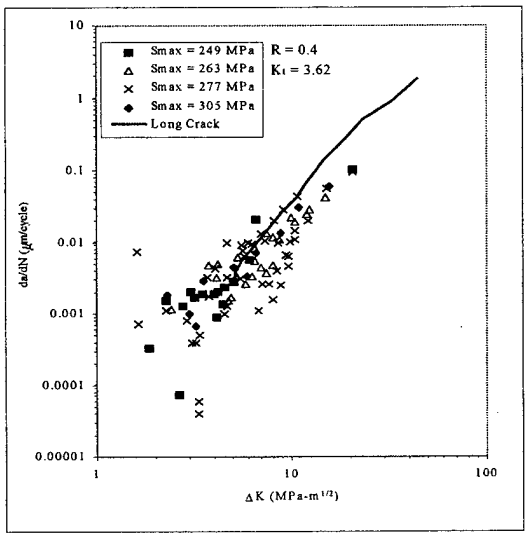

Figure 4.5 Comparison between large crack and small crack behavior at R = 0.4.

The scatter in the small crack data at lower ΔK levels is due to the inability of ΔK to characterize the crack tip stresses and the fact that there may be error in the measured crack growth rates because of the small measured crack growth increments. In addition, microstructural influences on crack aspect ratio variations may have played a role in the scatter.

It was shown in Fig. 4.5 that growth rates did not exactly fall in line with the large crack data, as the small cracks became larger. There is a possibility that the crack growth rate properties of the Ti-6Al-4V were different in the thickness direction (direction that the small cracks grew in) than in the width direction (direction that the large cracks grew in). This could be caused by microstructural influences in the two directions.

d. Small Crack Growth Behavior in PH 13-8 Mo Stainless Steel

The microstructure of PH 13-8 Mo stainless steel was examined to study its role in the small crack propagation. A double edge notch specimen and a compact tension specimen with a blunt notch were used for constant and variable amplitude loading and for corrosion fatigue, respectively.

Microstructure

PH 13-8 Mo SS has a complex microstructure. This is shown in Fig. 4.6 obtained using a scanning electron microscope (SEM): lath martensite, packets of martensites, and prior austenite grains. The lath martensites are shown to be less than 1 μm wide. Grain size measurement was done on 22 grains and resulted in an average grain size of 14 μm and a standard deviation of 2.72 μm. The average packet size was 7 μm±2.1 μm. Since the grain size is approximately 10-20 μm wide, one grain may have 2-4 packets depending on the grain size.

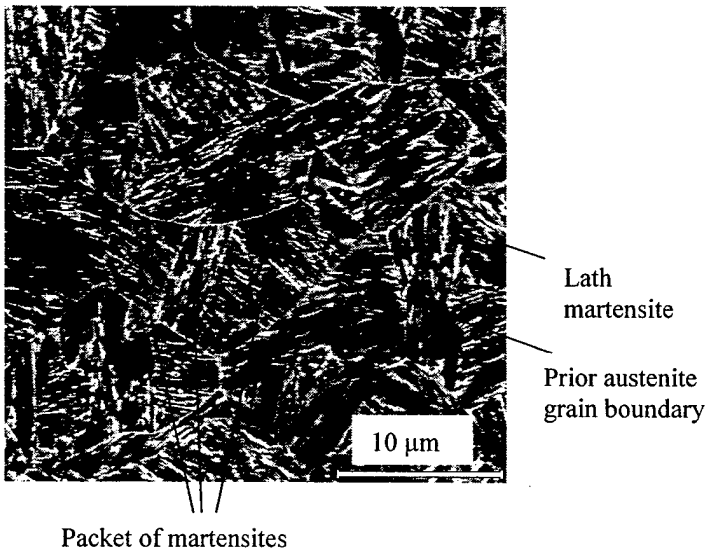

Figure 4.6 Microstructure of PH 13-8 Mo Stainless Steel: lath martensites, packets of martensite and prior austenite grain boundary

Constant Amplitude Loading

The constant amplitude loading was done at six stress levels of 455 MPa, 476 MPa, 482 MPa, 517 MPa, 552 MPa and 621 MPa, and two stress ratios of 0.1 and 0.4. Fig. 4.7 shows the small crack growth behavior at 476 MPa and a stress ratio of 0.1. The small crack in PH 13-8 Mo SS did not show the initial crack growth deceleration. However, the oscillation in crack growth rate was apparent and continued until the half crack length was approximately 100 μm. From the figure, the crack growth behavior can be divided into three different regions depending on the amount of crack extension. In Region I, crack growth oscillation corresponded to the crack increment of approximately 1 μm. This is the width of lath martensites. In Region II, the average crack increment (4.65 μm) between two local crack growth rate minimums was similar to the width of martensite packets (5~10 μm). The final stage of small crack growth was dependent upon the grain size.

The small crack growth behavior was not influenced by applied stress levels and stress ratios as shown in Fig. 4.8. These phenomena are different from large crack growth behavior and cannot be explained by a traditional fracture mechanics. It is noted that multiple cracks were found at the higher applied stresses (517 MPa and 552 MPa).

In order to compare the small crack growth with large crack growth, the large crack data were obtained from Damage Tolerant Handbook. The comparison is shown in Fig. 4.9. The small crack growth rate is a little slower than large crack growth rate at the stress ratios of 0.1 and 0.4. This means the small crack life could be estimated from large crack data although the prediction would be conservative.

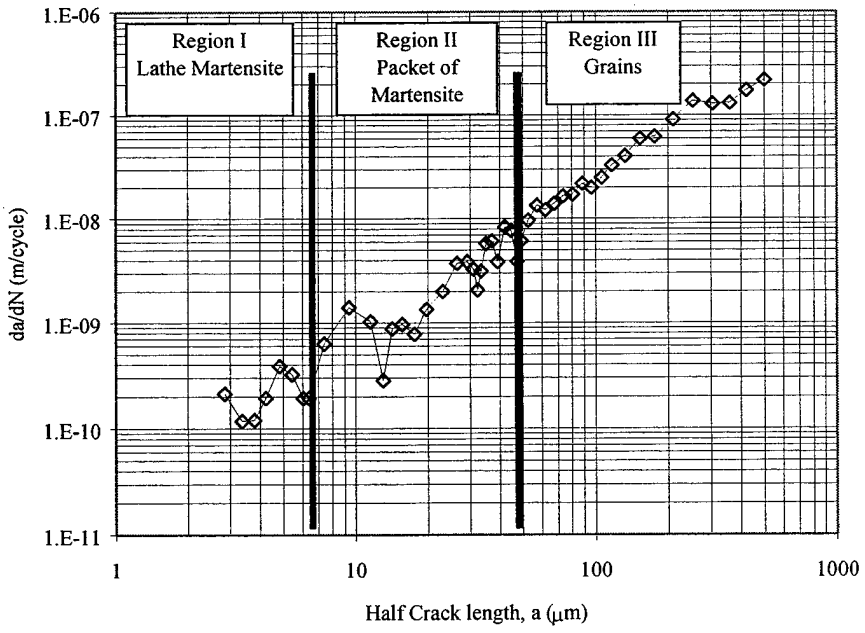

Figure 4.7 Microstructural effects on small crack growth behavior at 476 MPa and R=0.1: Region I-lath martensite; Region II-packets of martensites; Region III-prior austenite grains.

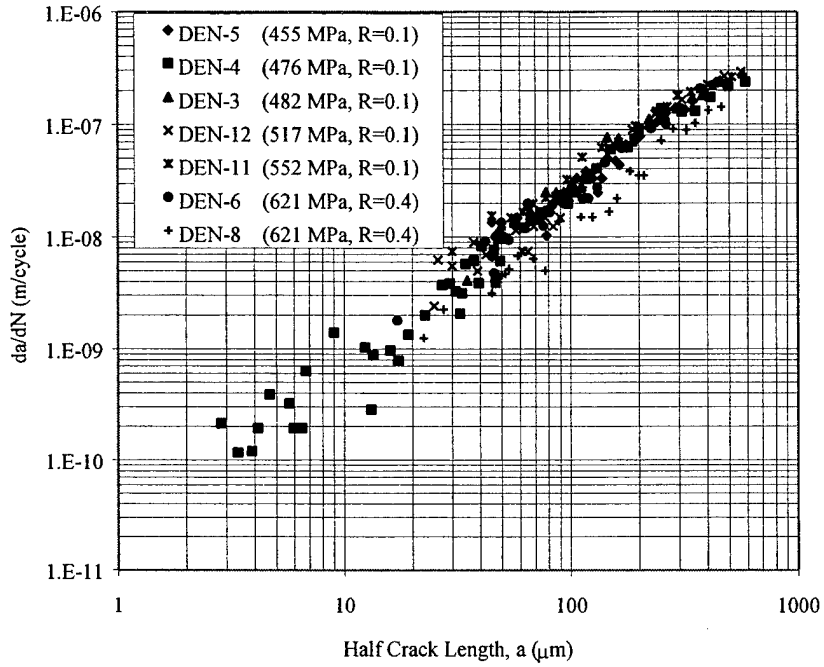

Figure 4.8 Small crack growth behavior at six different stress levels and two stress ratios.

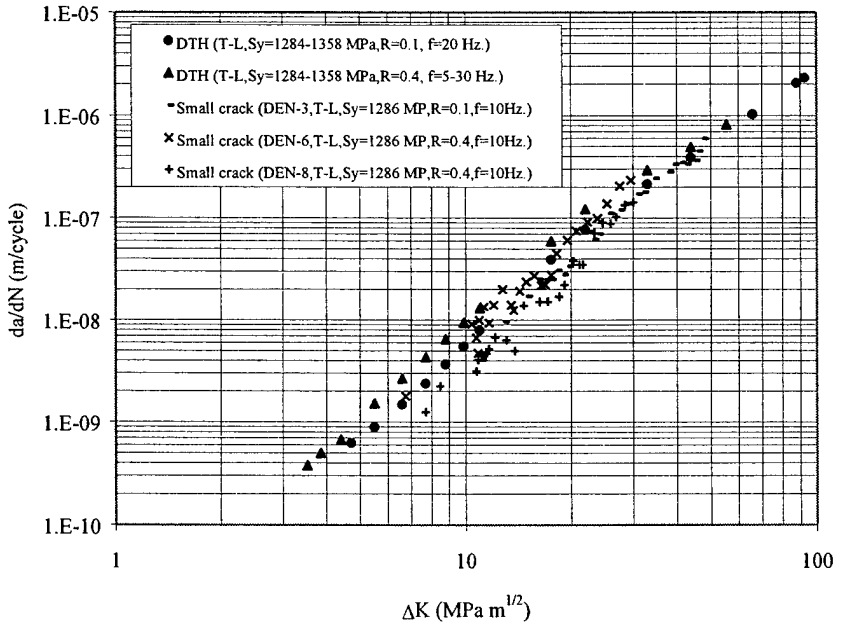

Figure 4.9 Comparison of the small crack growth in current study with the large crack growth obtained from Damage Tolerant Handbook.

Variable Amplitude Loading

To estimate accurate remaining lifetime of small crack growth it is necessary to know how one loading condition influences the crack growth behavior under different loading conditions. Generally, large cracks are retarded in some extent under variable amplitude loading although the load interaction effects do cause crack growth accelerations under some conditions. The amount of the retardation will depend upon the difference in stress levels and the order of the stress being applied. In this study, overload tests and simple block loading were conducted to characterize the load interaction behavior in PH 13-8 Mo SS. For both tests, the baseline stress was 476 MPa with the stress ratio of 0.1.

The overload stress levels were 517 MPa/R=0.1 and 621 MPa/R=0.4. Single overload was applied when the small crack was approximately 100 μm for each test. The results are shown in Fig. 4.10. The figure indicates that there was no crack growth retardation due to the overload. At the overload stress of 621 MPa/R=0.4 there was immediate crack extension after the overload cycle. However, the small crack growth immediately after the overload was not consistent. This may result from the relative location of crack tip in the microstructural unit (packets or austenite grains). The overall small crack growth was not affected by the overload(s) and similar to the crack growth behavior at the constant amplitude loading.

Simple block loading was used to examine the load interaction effect on small crack growth behavior. The baseline stress level was 476 MPa/R=0.1. The three different stress levels were used for the second load block. They were 517 MPa/R=0.1, 552 MPa/R=0.1 and 621 MPa/R=0.4. The crack initiation lives in the three simple block loadings were much longer than the constant amplitude loading at 476 MPa/R=0.1. This implies that the introduction of the second stress block induced some crack growth retardation. In order to compare the extent of load interaction between three different block loadings, the crack growth rate was plotted against half crack length in Fig. 4.11. It seems that the crack growth was slower at higher maximum stress (for the second block) than at lower maximum stress. The comparison of simple block loading tests with constant amplitude loading is shown in Fig. 4.12. It is apparent that the small crack growth in simple block loading was much slower than that in constant amplitude loading.

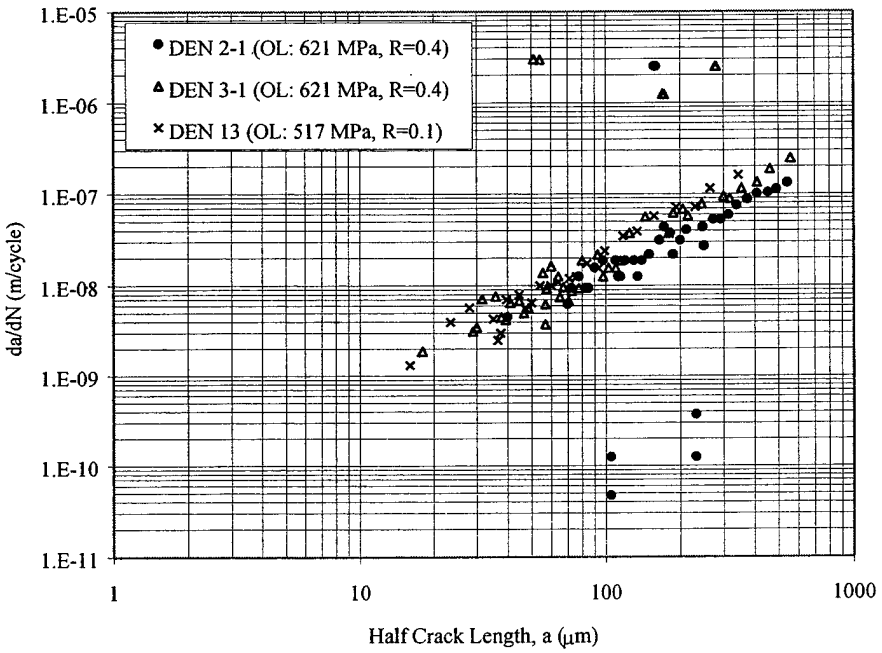

Figure 4.10 Results of overload at 517 MPa/R=0.1 and 621 MPa/R=0.4. The several data point above and below the band of crack growth data resulted from the crack extension and no growth immediately after the overload cycle.

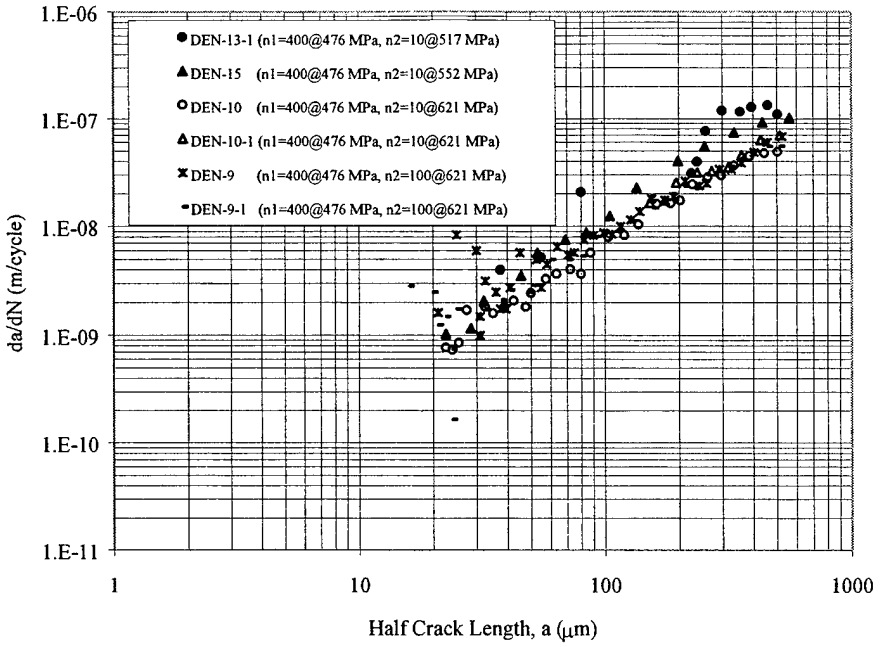

Figure 4.11 Results of simple block loading.

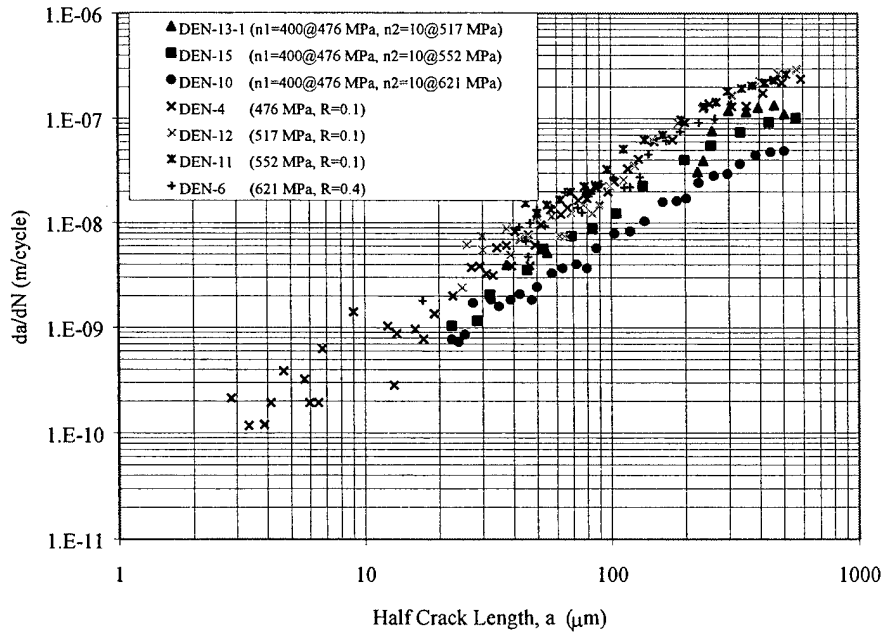

Figure 4.12 Comparison of the small crack growth under simple block loading with that at constant amplitude loading.

Corrosion Fatigue

Since PH 13-8 Mo stainless steel (SS) is expected to be used in a naval environments, it was necessary to perform corrosion fatigue in saltwater (ASTM D1141-90). A compact tension (CT) specimen with blunt notch (diameter of 0.82 cm) was used for corrosion tests, and the applied load was 3.34 kN. The specimens were completely immersed in circulating saltwater and cycled at three different frequencies of 0.1 Hz., 1 Hz. and 10 Hz.

Small crack growth in air (at 10 Hz.) was determined in advance to evaluate the influence of environment on the small crack growth. The comparison is made in Fig. 4.13. There is no difference in crack growth rate at a frequency of 10 Hz. between in air and saltwater environment. However, small crack growth in saltwater was a little different because initial crack growth deceleration was observed. To further study the effect of environment on the small crack growth, the test frequency was reduced to 1 Hz. and 0.1 Hz. Since current study did not intend to characterize the crack initiation, for slow cyclic frequencies of 1 Hz. and 0.1 Hz., specimens were cycled in air at a frequency of 10 Hz. until a small crack was initiated at the notch root. When a small crack was detected, the specimens were immersed in saltwater and cycled at 1 Hz and 0.1 Hz. The test results are shown in Fig. 4.14. The figure indicates that the small crack growth in saltwater did not dependent upon the cyclic frequency. It is noted that the small crack growth oscillation in early stage of growth increased with decreasing frequency. This suggests that the small crack growth had an interaction with microstructures and environment.

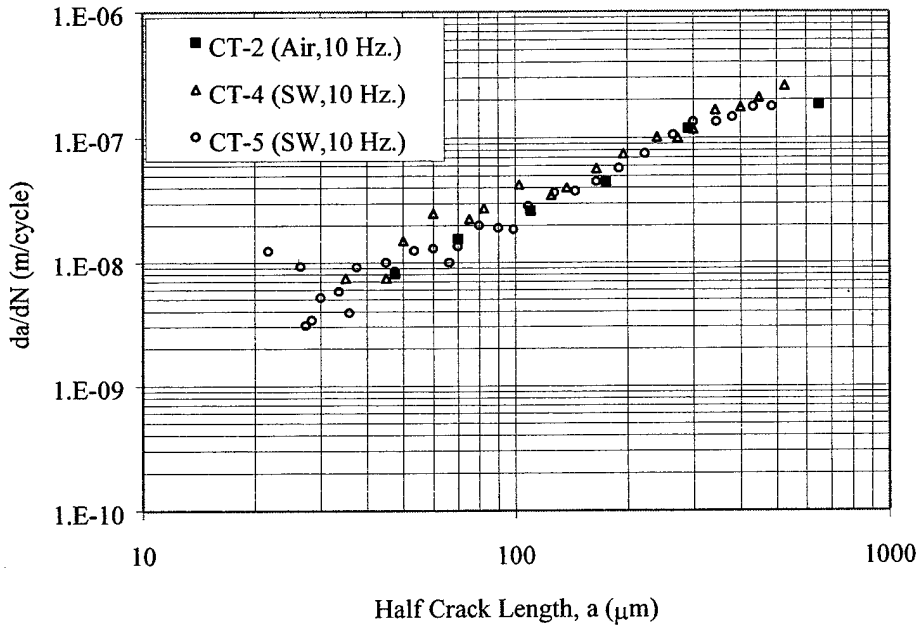

Figure 4.13 Comparison of small crack growth in air at 10 Hz. with that in saltwater at 10 Hz.

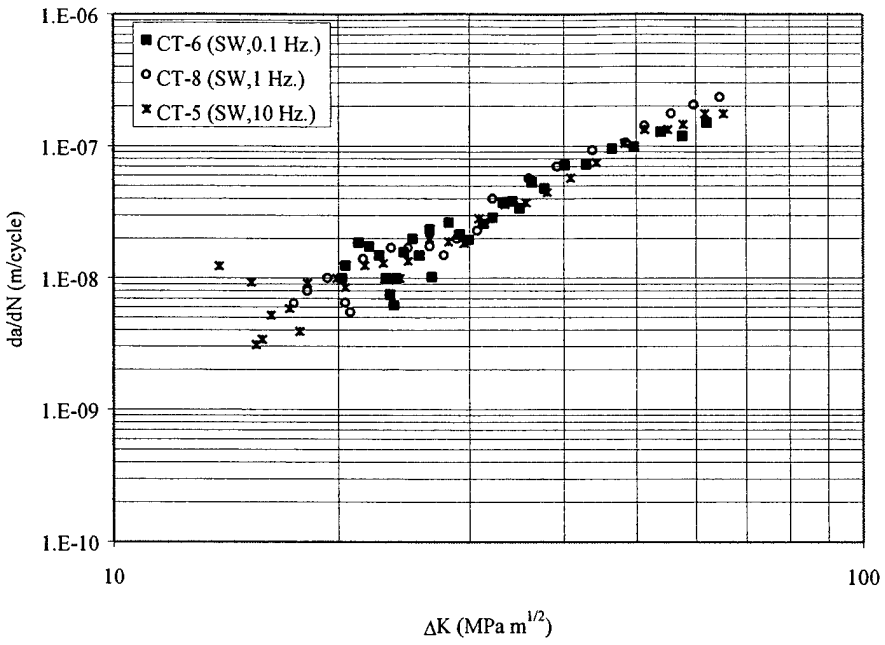

Figure 4.14 The small crack growth behavior in saltwater at three different cycle frequencies.

e. Conclusions

Several conclusions were made based on the observation made during the investigation and the analysis of the data obtained.

Constant Amplitude Loading

1. The small crack growth in Ti-6Al-V alloy and PH 13-8 Mo Stainless Steel (SS) was greatly influenced by the details of microstructure: bands of α phase and β phase in Ti-6Al-4V and packets of martensite in PH 13-8 Mo SS.
2. Small crack growth acceleration and deceleration were observed in most experiments. This oscillation was higher in early stage of crack growth and reduced as the crack grew, and continued until the half crack length was 100 μm. The crack increments between the oscillations (two minimum crack growth rates) were influenced by microstructures.
3. Small crack growth behavior in PH 13-8 Mo SS was not strongly influenced by the applied stress level over the range of levels tested. At all six stresses the small crack growth was similar each other. The only difference among these stresses was the crack initiation period: the higher the applied stress the shorter the initiation life was. In addition, the stress ratios did not affect the small crack growth behavior in PH 13-8 Mo SS. These observations indicate that a traditional linear elastic fracture mechanics cannot be used to explain the small crack behavior.
4. The small crack growth in Ti-6Al-4V alloy was faster than the large crack growth below the large crack threshold. On the other hand, the small crack growth in PH 13-8 Mo SS was a little slower than large crack growth at equivalent stress intensity range. This means that the remaining lifetime of small cracks in PH 13-8 Mo can be estimated based on the large crack data although it would be conservative.

Variable Amplitude Loading (PH 13-8 Mo stainless steel)

1. Overload tests indicated that there was inconsistent crack extension immediately after the overload cycle. In one case, the small crack grew due single overload. This inconsistent crack growth may result from the location of crack tip relative to microstructural barrier. In addition, the overload did not change the small crack growth behavior and resulted in similar crack growth to the constant amplitude loading.
2. It was found that the crack initiation and growth periods were longer in the simple block loading than in constant amplitude loading. As the maximum stress of the overload stress block increased the small crack growth rate decreased. This indicates that there is some load interaction between two load levels. This load interaction was not predicted from the result of constant amplitude loading.

Corrosion Fatigue (PH 13-8 Mo stainless steel)

1. At high frequency, a saltwater environment did not substantially influence the small crack growth in PH 13-8 Mo SS. The crack growth in both air and saltwater environment shows essentially identical behavior. However, the initial crack growth deceleration was observed in the test in saltwater unlike the crack growth under the constant and variable amplitude loading in air.
2. The crack growth oscillation was observed until the half crack length was 100 μm. It was rather higher oscillation than in air environment. The average crack growth deceleration increased as the test frequency increased. This may result from the interaction between small crack tips and environment and be complicated by the microstructure.
3. The small crack growth in saltwater did not depend significantly upon the frequency over the range tested. It is surmised that PH 13-8 Mo has excellent corrosion fatigue properties.

References for Section 2.2.1.4

[1] Hamm, R.W. and Johnson, W.S., "Survey of the State-of-the Art in Small crack Research," *Journal of Testing and Evaluation*, Vol. 26, No. 3, March 1998, pp. 168-175.

[2] Hamm, R.W. and Johnson, W.S., "A Unification of Small and Large Crack growth Laws," *Journal Fatigue and Fracture of Engineering Materials and Structures*, to be published.

[3] Wang, C.H., "Effect of Stress Ratio On Short Fatigue Crack Growth," *ASME Journal of Engineering Materials and Technology*, Vol. 118, 1996, pp. 362-366.

[4] Nisitani, H., Kawagoishi, N. and Goto, M., "Growth Behavior of Small Fatigue Cracks and Relating Problems," Handbook of Fatigue Crack Propagation in Metallic Structures, Andrea Carpinteri, Ed., 1994, pp. 733-778.

[5] Hamm, R.W., Jin, O. and Johnson, W.S., "Small Crack Growth Behavior in Ti-6Al-4V and the Microstructural Influence," submitted to *Journal Fatigue and Fracture of Engineering Materials and Structures*

[6] Patel, A.M., "Growth of Small Cracks in PH 13-8 Mo Stainless Steel," M.S. Thesis, Georgia Institute of Technology, 1997.

[7] Newman, J.C, Jr., Swain, M.H. and Phillips, "An Assessment of the Small-Crack Effect for 2024-T3 Aluminum Alloy," Small Fatigue Cracks, R.O. Ritchie and J. Lankford, Eds., 1986, pp. 427-452.

M-URI PUBLICATIONS

Hamm, W. R., "A Multi-Regime Model Comparison for Constant Amplitude Small Crack Behavior in Ti-6Al-4V," MS Thesis, Georgia Institute of Technology, 1998.

Jin, O., "The Characterization of Small Fatigue Crack Growth in PH 13-8 Mo Stainless Steel," Ph. D. Thesis, Georgia Institute of Technology, August 2000.

2.2.1.5 ALGORITHMS FOR REMAINING LIFE PREDICTION

Co-investigators: David L. McDowell and Richard W. Neu (Georgia Tech)
Graduate Students: Valerie Bennett, John Clayton, John Pape and Charles Rosen

OVERVIEW

A fracture mechanics-based methodology for predicting remaining life of structural components based on fatigue crack growth behavior is quite well developed [1]. The emphasis is on hot spot locations that are identified and quantified based on *a priori* finite element analyses of components. Such models for predicting fatigue crack growth have been primarily developed for long fatigue cracks, i.e. > 1mm. Due to the high frequency of loading in helicopter rotor components, majority of the lifetime is expected to be spent in the regime of "small" cracks with dimensions in the range of 30 to 50 μm.

Even though the basic methodology for near real time diagnostics/prognostics to support condition-based maintenance is similar to that of classical damage tolerance approaches, the models used must be able to address considerations such as (i) small crack behavior including effects of interactions between small cracks and the microstructure, (ii) crack propagation under mixed-mode loading, (iii) influence of surface residual stresses, (iv) interactions between multiple cracks (v) variable amplitude fatigue loading, and (vi) stochastic aspects of fatigue crack initiation and early growth. Moreover, the format for the "data-link" between on-board sensors and this remaining life estimation scheme is an important element of practical implementation of the scheme, which in practice would be resident in memory of an on-board processor charged with continuous updating of damage and comparison with growth rate estimates, along with evolving estimates of remaining life. Naturally, these estimates may be presented in terms of statistical bounds that reflect stochastic aspects of the crack growth behavior. A series of distributed microprocessors could be used to track hot spot damage for each critical component, or a single processor for each component could be applied with a sweeping algorithm across hot spot locations, using ROM-based look-up tables, for example, based on component-specific stress analysis for each hot spot.

For rogue flaws, the problem is fundamentally altered. Since these defects lie outside the envelope of hot spots or well-characterized critical locations, it is impractical (if not impossible) to achieve a rigorous description of their shape, driving forces for crack extension and effect on dynamical system response from an a priori analysis. By definition, these sorts of cracks occur in unanticipated locations. Accordingly, it is necessary to conceive a broader, more robust class of algorithms for estimating remaining life in this case. Input to this assessment is from a broad area array of sensors, likely involving sensors of various degrees of fidelity, resolution, and signal characteristics. Several options exist for treatment of rogue flaws, including (i) flagging for shutdown and static/manual inspection at first detection, followed by assignment of sensors for subsequent tracking, (ii) assessment of rate of degradation of dynamic component response in combination with other broad area sensor measurements to estimate rate of crack propagation and remaining life, or (iii) some combination of these. A training algorithm that employs, for example, artificial neural network technology may accomplish pattern recognition of system degradation. In this manner, equivalent flaw propagation characteristics may be established. It is emphasized that this technology is most useful for broad area damage or rogue flaws, and is complementary to the hot spot remaining life assessment algorithms.

METHODOLOGY

a. Processing and Classification of Sensor Data

The proposed diagnostic system includes sensors on two levels of detection: focused micro-sensors and broadband sensors. The focused sensors are embedded near "hot spot" locations where critical defects are expected to occur. These locations have been successfully identified in the H-46 rotor hub using finite element (FE) stress analysis [2]. The focused sensors include acoustic emission (AE) and eddy current (EC) devices. On the broadband level, the overall structure is monitored for "rogue flaws" using less-focused AE and EC sensors as well as dynamic system response (DSR) measurement devices.

Obviously, the uncertainty in the defect characteristics obtained from the broadband sensors will be greater than that from the focused micro-sensors (i.e., more information is available concerning cracks at hot spots than is available for rogue flaws). This paper focuses on utilizing signals from AE sensors, either from the focused or broadband devices. AE devices detect the elastic waves emitted from forming and progressing flaws as the material resists applied stress.

The sensors are expected to provide data that gives some measure of defect size (crack length) and location. Multiple sensors allow monitoring of numerous cracks' lengths and approximate growth rates at various locations in the structure throughout the life of the component. Local AE events corresponding to development of localized inelastic deformation or "pop-in" of cracks may be detectable using embedded sensors, and above a certain level of resolution crack length may be reliably monitored using AE data and incorporated into a life-prediction scheme based on crack propagation models [2-3]. A proposed model by McDowell [4] for use in the integrated diagnostic system divides small crack growth in polycrystalline metals into three characteristic regimes:

1. Regime I, the microstructurally small crack regime (MSC), for cracks on the order of the material grain size which are highly sensitive to microstructural features
2. Regime II, the transition region from microstructural sensitivity to relative insensitivity
3. Regime III, the physically or mechanically small (PSC) crack regime

For the system to use such a model, the crack length must be known to a limited degree in order to classify the defect into one of the three regimes. Then the estimated crack length, as well as material constants, microstructural dimensions, stress analysis results, and load histories, is incorporated by the model in order to calculate the crack growth rate, da/dN. This crack growth rate is then used, along with the loading frequency, to calculate the length of life remaining. Other models also calculate da/dN using similar information, and are valid only for certain crack lengths (e.g., conventional linear elastic fracture mechanics (LEFM) models are not valid for "small" cracks). Since the structural reliability algorithm may utilize multiple crack growth models, each of which is valid only for a certain crack length range, correct prediction of the remaining life depends on identifying the regime of crack growth of each flaw, if not its precise length, such that valid models may be selected for use in the algorithm. Due to the resolution of the AE sensors (especially the broad-band devices), precisely determining the numerical length of very small cracks (on the order of 50 μm) is probably not feasible. However, classification of the small crack into one of the three characteristic regimes may be possible using AE data, particularly that from focused micro-sensors at hot spots. Above a certain length, the cracks may be monitored more effectively using the AE sensors, enabling more accurate predictions for remaining life. However, the proper classification of small cracks is crucial, since the cracks typically remain small for up to 90% of the life of components under HCF.

The signal conditioning and classification stage of the reliability prediction involves removing noise from the AE signals and extracting all the useful information from the AE data. The processed data may then allow, in the case of small cracks, the classification of the growth rate into one of the three characteristic regimes. This information can then be used to select appropriate crack growth models for estimating remaining life. In the case of larger cracks that may be more accurately measured with AE data, the measured crack growth rates may be compared to predictions of da/dN made by the various crack growth models, and the error between the predictions and the actual growth rates may be used to continuously update the life prediction algorithm during service.

b. Proposed Method of Operation for the Integrated System

A methodology for use in the proposed diagnostic system for estimating the structural reliability for components under HCF conditions is now presented. The recommended approach is intended to take advantage of the useful signal processing tools and modeling strategies presented in this paper; it incorporates wavelet analysis, a neural network, and a combination of probability- and possibility-based methods for calculating reliability. Figure 5.1 shows the steps involved in the recommended methodology, with steps performed by the on-board processing unit surrounded by the dotted boundary.

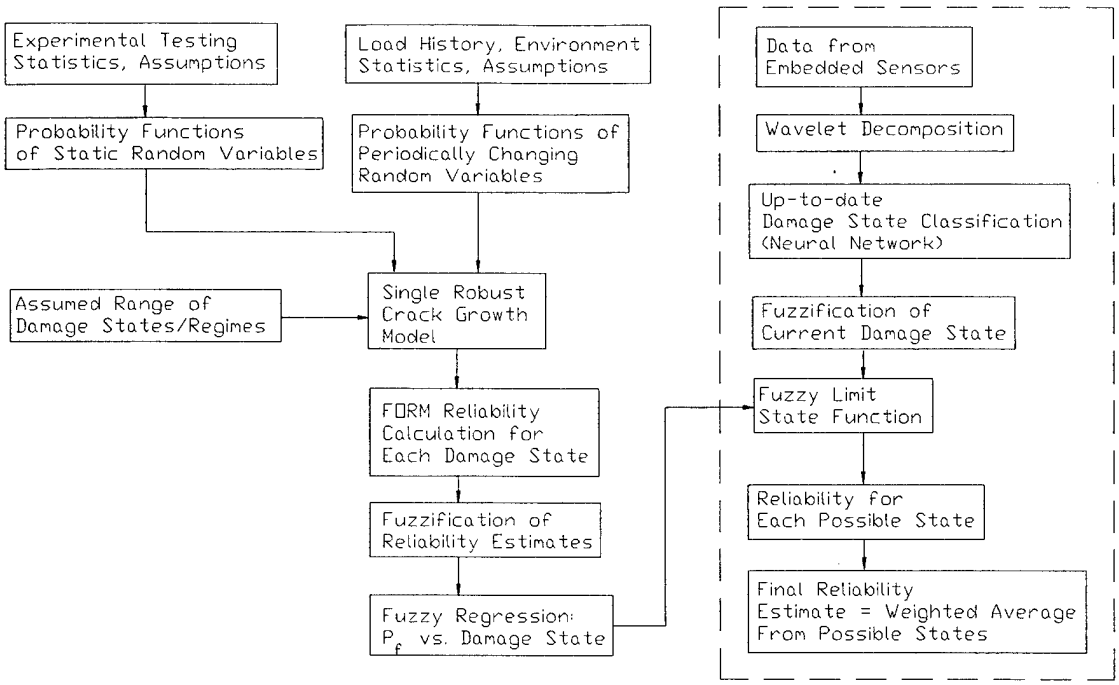

Figure 5.1 Proposed System Methodology

Features of Fig. 5.1 are now discussed in more detail, beginning with those steps outside the boundary (outside the box surrounding the right column in Fig. 5.1) which are not directly performed by the on-board processor. The proposed method uses a single robust crack growth model, which is actually a collection of individual models, each valid at a particular crack length scale or growth regime. A robust multi-length scale regime model for growth of small fatigue cracks was developed by McDowell [4]. Inputs to the crack growth model are the following:

- The probability density functions and descriptive parameters of the static governing random variables, such as material properties and empirical constants, which may be determined from laboratory test data or assumptions and heuristic knowledge
- The probability density functions and descriptive parameters of periodically changing governing random variables, such as load amplitude and phase, mean stress, and environmental conditions; these must be updated periodically as service conditions change
- A range of assumed damage states (crack lengths, numbers, directions, etc.)

Next, the first order reliability (FORM) method is proposed to be used in conjunction with the crack growth model to calculate the reliability of the structure at each increment of the assumed damage state. FORM is recommended because of its reduced cost when compared to MCS and LSSE; however, an alternative probabilistic computational method may be used if FORM yields inaccurate results. The reliability estimates calculated using the FORM method are then fuzzified in order to account for subjective uncertainty sources such as modeling errors. In this fuzzification process, each damage state value (each crack length, for example) is assigned membership in various reliability levels; the shapes of the membership functions are chosen to reflect the degree of uncertainty in the crack growth model. A fuzzy limit state function is then generated using fuzzy regression techniques, as discussed in [5-6]. A possible form of such a state function is shown in Fig. 5.2.

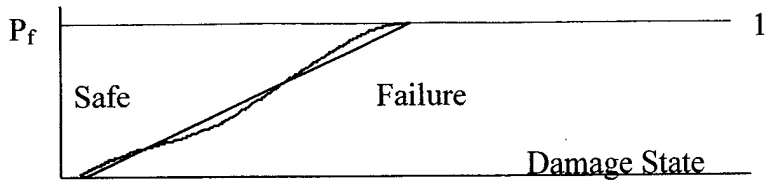

Figure 5.2 Fuzzy Limit State Function

Fuzzy regression is used to create a fuzzy relationship between damage state and the fuzzified reliability predictions calculated from the FORM method. Note that the boundary of the limit state surface is fuzzy; certain assumptions regarding the shape of this boundary may be required to employ the regression technique. The fuzzy regression procedure yields a direct relationship between the damage state and the reliability (or actually P_f in Fig. 5.2), accounting for statistically quantifiable uncertainties from the FORM calculations as well as subjective uncertainties such as modeling errors. This functional regression model, once determined, is later exported to and stored in the on-board processor for use in making real time reliability estimations. It may be updated periodically to account for changes in loading and environment, and its fuzzy membership functions may be tuned based on the performance of the system.

Now the proposed operations of the on-board components of the integrated diagnostic system are addressed. The embedded broad-band and focused sensors continuously send signals related to damage evolution to the processing unit. These signals are then decomposed using a wavelet transformation. Noise caused by fretting and other sources is filtered, while spikes in the signals corresponding to crack extension are preserved. Useful features regarding crack length, position, orientation, and growth rate are extracted from multiple sensor data. The decomposed, conditioned sensor data (perhaps in the form of wavelet coefficients at different frequencies) is then used as input to a neural network that classifies the current damage state of the material (e.g., data may be classified into crack length or growth regime). A backward-propagating neural network (BPNN) would be well-suited for this classification process. The network would have to be trained prior to use in the on-board processor via comparison of sensor data with experimentally measured crack growth data (the training set). The training, which could be lengthy, need not be done on-board; once trained, the BPNN could later classify sensor data very quickly for use in the reliability algorithm. The processor could also identify the critical flaw (perhaps the longest crack) at the current damage state.

Next, the damage state or crack length of the critical flaw is fuzzified to a degree based on the operator's confidence in the sensor data and in the neural network's performance. Membership functions for inclusion in various damage states or crack growth regimes are created based on subjective assumptions and heuristic knowledge, with broader membership functions used for more uncertain data, such as that for rogue flaws. As a simplified example, consider the membership functions shown in Figure 5.3.

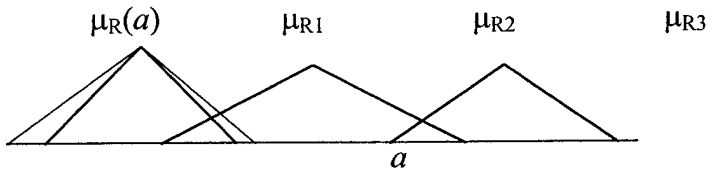

Figure 5.3 Example Membership Functions for Damage State

In Figure 5.3, a is the neural network's numerical prediction of crack length, and μ_{R1}, μ_{R2}, and μ_{R3} are membership functions in Regimes I, II, and III, respectively, of small crack growth. The triangle membership function shape is commonly used, but it is not required. Note that the overlap of the membership functions permits inclusion of a given crack dimension in more than one regime. The dotted membership function illustrates a means of increasing the fuzziness or uncertainty associated with classification of rogue flaws using signals from less-focused broad-band sensors. The proposed system may implement membership functions for inclusion in various regimes by considering more than just crack length; membership in a damage set or regime may be a function of crack number, orientation, and location, in addition to crack length a.

As a result of the fuzzification process, the current condition of the material becomes a fuzzy number having degrees of membership in one or more possible fuzzy damage states. Using the fuzzy regression model discussed previously, the reliability for each of these possible states is determined based on the functional relationship between P_f and the possible state, as indicated by the shape of the fuzzy limit state function. The current overall reliability of the component is then calculated as a weighted average of the reliabilities afforded by membership in each of the possible states. Larger weights are assigned to reliability values associated with more likely damage states (i.e., the degree of membership in each possible damage state determines the magnitude of the weight assigned to each reliability value.)

The proposed algorithm for estimating reliability has the following notable characteristics:

- Probabilities are used where available to quantify uncertainty in statistically measurable random variables.
- Possibility measures (fuzzy sets) are used to account for subjective uncertainty and modeling errors.
- Expensive, time-consuming computations (such as FORM, neural network training, fuzzy regression) need only be performed periodically to update the system, and need not be done on-board.
- Real-time reliability updates are available quickly, since all on-board operations are relatively fast: wavelet decomposition, BPNN classification, fuzzification of the damage state, and use of the pre-determined (by regression) limit state function.

c. Integration of Crack Propagation Methods & Sensor Output to Predict Remaining Life

There are several different ways to predict remaining life of a component. Some of these are based on modeling heuristics and some are based on acoustic data. A MATLAB platform was used in this study as a basis for providing an example interface between the sensor diagnostics and prognostic algorithms to estimate N_T, the remaining life of the specimen until a critical crack length is reached at one of the hot spots. The remaining life estimation modules employed in the MATLAB interface includes a traditional linear elastic fracture mechanics scheme, the Navarro-de los Rios model and the robust small crack growth model, all based on crack growth from a notch. Sensor inputs based on estimated probability distribution for crack length are interfaced with these schemes to provide the user a range of estimates of the component remaining life.

Figure 5.4 shows the flowchart for developing the algorithm. Figure 5.5 shows a schematic of a graphical user interface (GUI). It allows the user to communicate with the MATLAB program. It provides the user with an estimate of remaining life (cycles to failure) based on the probability of crack detection and length.

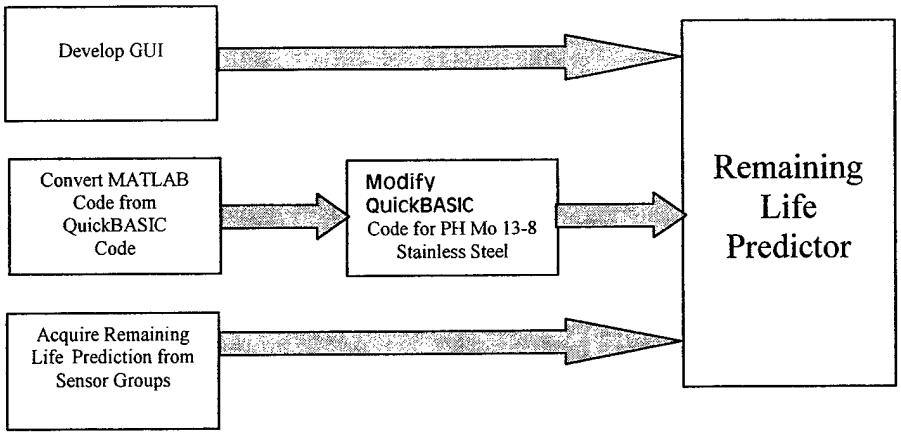

Figure 5.4 Flow chart for Remaining Life Algorithm.

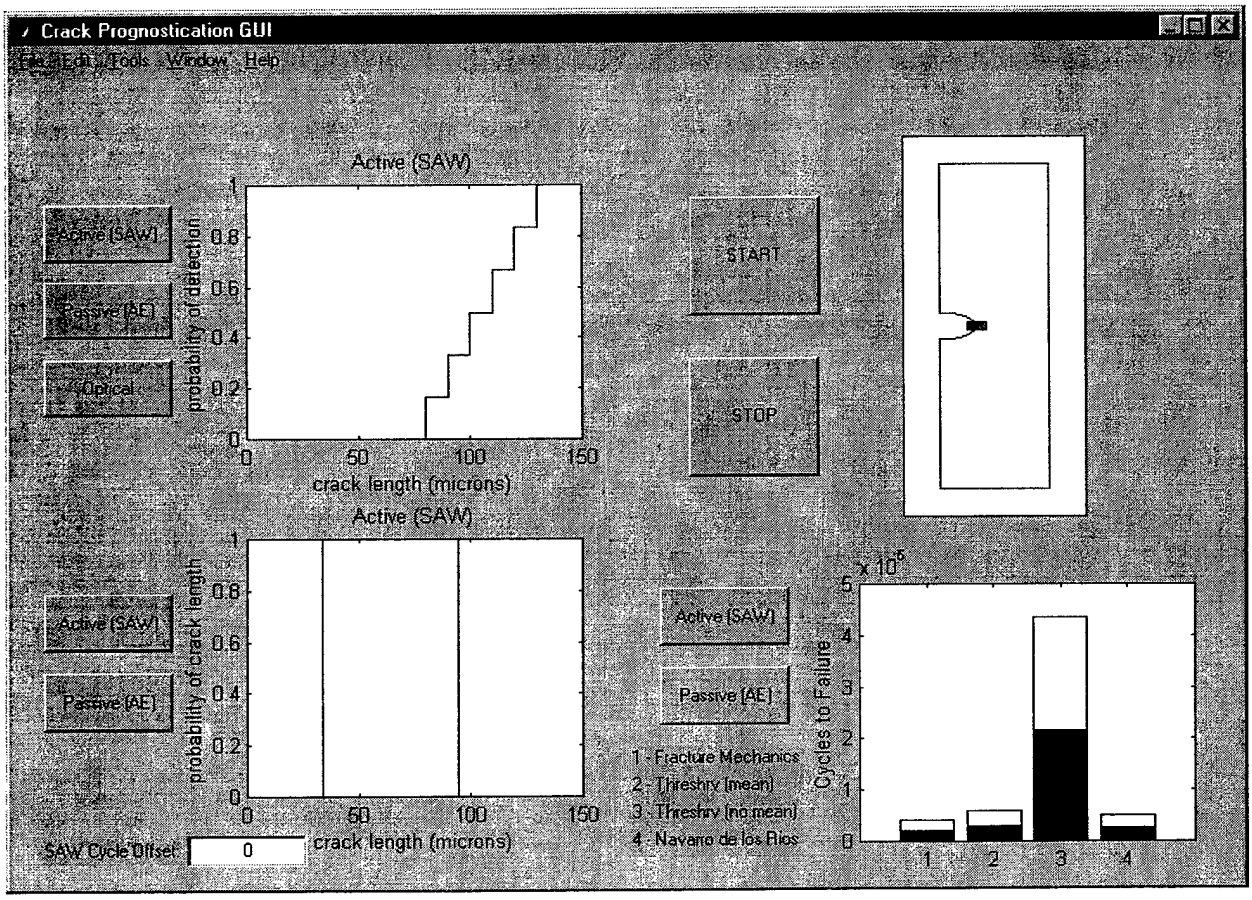

Figure 5.5 Schematic of a Graphical User Interface (GUI)

References for Section 2.2.1.5

[1] Liaw, P.K., Saxena, A. and Perrin, J., 1993, "Life Extension Technology from Steam Pipe Systems - Part I and II," Engineering Fracture Mechanics, Vol. 45, pp. 759 - 803.

[2] McDowell, D.L, Winer, W.O. and Cowan, R.S., "Developing an Integrated Diagnostic System," ASME IMECE Symp. On Quantitative Nondestructive Evaluation in Integrated Diagnostics, Dallas, TX, November 17, 1997.

[3] McDowell, D.L., Neu, R.W., Qu, J., and Saxena, A., "Prognostic Tools for Small Cracks in Structures," Emerging Technologies for Machinery Health Monitoring and Prognosis, TRIB-Vol. 7, R. Cowan, Ed., ASME, 1997, pp. 1-12.

[4] McDowell, D.L., "Multiaxial Small Fatigue Crack Growth in Metals," Int. J. Fatigue, Vol. 19, No. 1, 1997, pp. S127-S135.

[5] Ross, Fuzzy Logic with Engineering Applications, McGraw-Hill, 1995.

[6] Liu and Huang, "Fatigue Reliability of Structures Based on Probability and Possibility Measures," *Computers and Structures*, Vol. 45, 1992, pp. 361-368.

2.2.1.6 ADVANCES IN UNDERSTANDING STRUCTURAL FATIGUE LIFE

Co-investigators: D.L. McDowell (Lead), W. S. Johnson, R. Neu, J. Qu, and A. Saxena (Georgia Tech)

SUMMARY

A number of significant advances have been made at Georgia Tech in the Structural Fatigue Task of the M-URI program in Integrated Predictive Diagnostics for the development of prognostic tools to serve Condition-Based Maintenance requirements. The problem has been decomposed into treating a relatively small number of critical locations or "hot spots" in each component, requiring dedicated microsensors. These hot spots are defined as locations that are assigned high probability as failure sites based on preliminary component elastic stress analysis, which employs realistic loading conditions. Models for small fatigue crack propagation have been developed or enhanced as applicable to dedicated hot spot microsensor algorithms. Research is described in numerous supporting areas for understanding the formation and propagation of microstructurally small, mechanically small, and long fatigue cracks. Fretting fatigue is described as a potential failure mechanism and our related research is summarized. The structure of a component remaining life estimation scheme for hot spot locations is outlined, focusing on the near- real time prognostics. Principal innovations in integrated diagnostic and prognostic technology have been made as follows:

- Developed a finite-element based methodology for rapid identification of hot spot locations in components and verified for H-46 rotor hub by comparing to field data for failure locations.
- Clarified mechanics challenges and essential developments for next generation fatigue crack growth models for small cracks.
- Experimentally evaluated and modified existing micromechanical models for growth of microstructurally small cracks (based on dislocation pile-up at obstacles) for helicopter alloys and Ti-6Al-4V, and identified strong microstructure barrier features.
- Investigated the effects of varying loads and salt-water environment on PH 13-8 Mo Stainless Steel, as would be experienced in service, on the growth of the small cracks.
- Developed and enhanced multi-stage fatigue models for propagation of small cracks spanning the LCF and HCF regimes for remaining life estimates.
- Conducted novel fretting fatigue experiments and suggested improvements for models of fretting fatigue.
- Used nanoindentation, Atomic Force Microscopy (AFM) and Impedance Spectroscopy (IS) as tools to explore surface roughening during fatigue cycling, changes in local hardness near the crack tip for long cracks during fatigue, and understanding fatigue mechanisms.
- Conducted novel computational cyclic crystal plasticity calculations for distribution of driving force parameters for formation and growth of subgrain-scale fatigue cracks in a polycrystal under HCF, as well as first-ever calculations for mixed mode behavior of microstructurally small cracks in surface grains in polycrystals.
- Developed algorithms for evaluating driving forces of long cracks with complex 3-D crack fronts.
- Performed critical assessments of near real time algorithms/methodologies for remaining life estimation, and proposed most potentially fruitful algorithms.
- Interfaced with Georgia Tech acoustic emission team to instrument laboratory specimens in smooth specimen and fretting fatigue to demonstrate capabilities of sensor arrays to monitor stages of fatigue damage evolution in smooth specimen fatigue and fretting fatigue.

The task on investigating structural fatigue has involved 11 graduate students, 4 undergraduate students, and a post-doctoral fellow. It has produced two Ph.D. degrees, with four in-progress, and four M.S. degrees, with one in-progress.

Limited demonstration of the integrated technology has been undertaken, largely owing to the immaturity of sensor signal acquisition and signal processing. Reasonably good correlation of acoustic emission signals with evolving fatigue damage has been obtained for fretting fatigue as well as small crack formation and growth from notches based on acoustic emission and the use of surface waves to gain higher sensitivity for small crack sizes.

FUTURE WORK

An inevitable outcome of this kind of multi-investigator, multi-disciplinary investigation is a glimpse into what it takes to integrate physics-based prognostics models with signal processing of multiple transducers to achieve an integrated diagnostics-prognostics system. One of the significant challenges is the relaying of needs for information among groups with disparate backgrounds or views. The primary requirement of physics-based models to estimate remaining life, for example, is an estimate of the probability distribution of estimated crack sizes at hot spots from the diagnostics suites. This is a highly non-trivial task, because of (a) the complexities of variability of crack location within a notch, crack aspect ratio, etc., (b) limited data and correlations (often indirect) of sensor signals to evolving fatigue damage and crack systems at hot spots, and (c) the difficulty of assigning probability distributions to crack size in view of all the other sources of variability in the signal. For these reasons, we are convinced that artificial neural networks will likely not serve the function of pattern recognition for damage unless untenably large datasets on prototype components are available. This may be the case for high cost components with extreme reliability requirements, but is likely not applicable to standard components in the field. Hence, the strategy we have pursued is a practical one, based on an estimated "fuzzification" of the probability distribution made by the sensor diagnostician. It has become apparent to us that this process is nonstandard, and therefore future attention should be devoted to it.

Similarly, accounting for variability in the physics-based models is a tremendous challenge that has not been fully dealt with to date. This is an area of substantial scientific endeavor for future work, including effects of variation of microstructure and/or applied loading and effects of corrosion and wear.

Another important area of future research is the development of 3-D crack growth laws for component materials. Currently, applying 2-D crack growth laws on planes perpendicular to the crack front approximates the behavior of 3-D cracks. The development of truly 3-D crack growth laws will enhance the predictive capability of the crack growth algorithm.

2.2.2 FAILURE PREDICTION METHODOLOGY/FATIGUE RELIABILITY

Co-investigator: Brian Moran (Northwestern University)
Graduate student: Ali Zulfiqar
Postdoctoral Fellow: Natarajan Sukumar
Collaborators: Yonglin Xu (Northwestern University), Jianmin Qu (Georgia Tech)

OVERVIEW

This report summarizes the research activities of the Office of Naval Research (ONR) Grant N00014-95-1-0539, *Integrated Diagnostics*, subgrant *Failure Prediction Methodology/Fatigue Reliability* to Northwestern University. The research was carried out during the period March 1, 1995 to August 31, 2000 under the direction of Professor Brian Moran, Department of Civil Engineering, Robert R. McCormick School of Engineering and Applied Science, Northwestern University, 2145 Sheridan Road, Evanston, IL 60208.

Throughout the research program collaboration with Professor Jianmin Qu, Georgia Institute of Technology was maintained to assure that the research activities were complementary. Professor Qu is the lead investigator for *Structural Fatigue Investigation Sub-task 1: Stress Analysis and Stress Intensity Factor Solutions* (Section 2.2.1.2).

The objectives of the research project were to develop a methodology for fatigue reliability and lifetime prediction of metallic structural components within the framework of condition based maintenance. This report highlights novel contributions and developments by the investigator and his students and collaborators during the course of the program. Specifically, new methods for fatigue reliability or risk assessment of safety critical structures were developed and new computational techniques were developed for modeling fatigue crack growth. These new developments overcome limitations of previous methodologies and help to make fatigue reliability assessment of safety critical structures and components feasible for complex three-dimensional components.

OBJECTIVE

The objective of the research program *Failure Prediction Methodology/Fatigue Reliability* was to develop a methodology for risk assessment (fatigue reliability) and lifetime prediction for safety critical metallic structural components. The civilian and civil infrastructure of this country and its transportation equipment are becoming old. It is expected that many of the systems that were built twenty or thirty years ago will not be replaced in the near future by next generation structures and equipment. Consequently, these aging systems will have to be kept in service for the next decade or more. This is feasible provided adequate measures are taken to prevent poor performance, inadequate safety and increasingly expensive maintenance. This need for extended life expectancy does raise substantial technical challenges, however. In the following, our response to these challenges is summarized and the key outcomes of the research are delineated.

INTRODUCTION

In the area of fatigue reliability, the key challenge is the assessment of the effect of (possibly undetected) flaws and defects on the structural integrity of a safety critical component. To meet this challenge, new computational tools are required in the areas of risk assessment and in simulation of fatigue crack propagation. Fatigue reliability (or risk assessment) methods provide an estimate (or probability) of failure over the course of the expected lifetime of the component. The effects of NDE inspections can be taken into account. Fatigue crack propagation is inherently a random process and probabilistic fracture mechanics methods are usually required. Typically, randomness in fatigue crack propagation parameters and in the detection of cracks is accounted for. The estimate of failure probability is obtained by carrying out fatigue crack propagation simulations for different values of the random variables. The well-known Monte Carlo methods require on the order of one million simulations for the low probabilities of failure in effect in safety critical structures. Because each simulation requires many

increments of three-dimensional crack growth (using the finite element method, for example) Monte Carlo methods become prohibitively expensive. The so-called direct integration method (which computes the evolution in time of the crack size probability density function) similarly requires extensive numbers of three-dimensional simulations.

The direct integration method developed in this program [1,2] alleviates the computational burden by use of an efficient discretization of the random variable space and a selective integration scheme. This led to an approximate tenfold increase in speed over our original version of the code. This procedure works well when the number of random variables is relatively small and the processing time for each realization (fatigue crack propagation simulation) is small. When this is not the case, alternative methods such as the first order reliability method (FORM) are required. Unfortunately, FORM techniques are inaccurate when the failure surface has high curvature near the so-called most probable failure point, as is sometimes the case with crack problems. To circumvent this drawback, we developed a new reliability method called the limit state surface element (LSSE) wherein the failure surface is discretized into a number of finite elements near the most probable failure point. For a single element, the method reduces to FORM. In [3] we introduced the LSSE method and demonstrated its accuracy for a wide variety of problems exhibiting large curvature and abrupt transitions in the failure surfaces. The utility of the method for fatigue crack propagation problems incorporating NDE inspections is also demonstrated.

In the simulation of fatigue crack propagation, stress intensity factors are required for use in the crack growth law. The computation of stress intensity factors along the three-dimensional (often non-planar) crack front remains a challenging problem. We have developed a method for the extraction of mixed-mode stress intensity factors along non-planar crack fronts [4]. The method is based on the domain integral representation of crack tip interaction energy integrals. The contribution due to the curvature of the crack front emerges in the domain integral method.

In finite element methods, representation of the crack surface and assuring adequate refinement in the vicinity of the crack tip can make mesh generation extremely cumbersome and time consuming. The problem is exacerbated when propagation of the crack is involved. In [5], we developed an extended finite element method (X-FEM, also called the generalized finite element method) for three-dimensional crack modeling. In the method, no finite element discretization of the crack surfaces is required. A discontinuous function and two-dimensional asymptotic crack-tip displacement fields are added to the finite element approximation using the concept of partition of unity. Thus the crack can be "placed" anywhere in the finite element mesh for the un-cracked body. Numerical examples illustrate the accuracy of the method.

As mentioned above, remeshing associated with crack growth is cumbersome and time-consuming, often requiring user intervention. In [6] we develop a new procedure for three-dimensional crack growth using level sets and the fast marching method in conjunction with the extended finite element method. The level sets are used in locating the crack front, in specifying the partition of unity enrichments for the representation of the crack and in the evaluation of stress intensity factors using the domain integral. By exploiting the power of level set methods in this fashion, we have developed a method for simulating crack growth (restricted to planar cracks at the present time) without meshing the crack and without user intervention. Numerical examples indicate that the method is extremely accurate.

The principal accomplishments of the program are summarized below:

a. Developed an efficient direct integration scheme for fatigue reliability
b. Developed a new reliability method called the Limit State Surface Element Method that alleviates difficulties associated with curvature of the failure surface.
c. Introduced a domain integral method for extracting mixed mode stress intensity factors along non-planar crack fronts.
d. Developed the extended finite element method for three-dimensional crack modeling. No meshing of the crack required.
e. Implemented a level set and fast marching method for crack growth in three-dimensions in conjunction with X-FEM. No meshing of the crack and no user intervention required during crack growth simulation.

ACHIEVEMENTS

a. Direct Integration Method

The computation of fatigue life expectancy is an integral part of the design and analysis of structural components that experience cyclic loading. It is well known that considerable scatter occurs in fatigue lives even under carefully controlled laboratory conditions. Hence a deterministic approach to fatigue life prediction may not be appropriate for safety critical structural components such as in airplanes, helicopters, rotating machinery and bridges. One of the most common methods for computing fatigue reliability is the direct integration method. The method can be computationally intensive however and is usually restricted to as few as three random variables. In this program, we developed an efficient direct integration method [1,2] (numbers in brackets refer to publications under this grant listed in section 3.1) which achieved a tenfold increase in speed over our original version of the code. The direct integration method involves the evolution in time of the crack size probability density function. Using concepts from mass conservation, the probability density function is computed by evolving discrete probability mass elements in time. The speed up was obtained by invoking an efficient discretization of the probability mass and using a selective integration procedure. The service life is mapped onto the initial joint probability distribution for crack length. Only those discretizations are considered for computation, which lead to failure during the service life of the component. In a comparison of the method with the first order reliability method for a fatigue reliability problem with NDE inspections, excellent agreement was obtained.

One of the advantages of the direct integration method is that it gives accurate results in situations where the first order reliability method does not give good results due to the high curvature of the failure surface (the failure surface separates the space of random variables into safe and unsafe parts, i.e., the sets of random variables which do not or do cause failure, respectively).

b. New Limit State Surface Element Method for Fatigue Reliability

A new method, termed the Limit State Surface Element (LSSE) method, for problems in structural reliability has been developed. The first order reliability method (FORM) is a popular method for problems in fatigue reliability because the number of realizations or trials of the problem being simulated is vastly reduced over traditional Monte Carlo methods for example. This is especially true for cases where each trial involves computationally intensive simulations in three dimensions such as fatigue crack growth in complex components. A limitation of the method, however, is that it is inaccurate when the curvature of the limit state surface is large and this is often the case in fatigue reliability problems. In contrast, the LSSE method [3] developed in this project, which is based on the discretization of the limit state surface into a number of elements in the vicinity of the most probable failure point, allows for a better representation of the limit state surface in regions of high curvature leading to more accurate risk assessments (or reliability). The method is aimed at retaining the advantages of first order reliability methods while alleviating disadvantages associated with high curvature of the limit state surface. This is accomplished through discretization of the limit-state surface into a finite number of elements. This allows for better representations of the failure surface in regions of high curvature than is possible with standard first and second order reliability methods. The reliability is estimated as a sum of integrals over subdomains in the space of standard normal variables associated with the surface elements. Several benchmark problems are presented to demonstrate the accuracy and utility of the method and a problem in fatigue reliability is presented as a practical application of the method and a demonstration of the potential interrelations between QNDE and reliability assessment.

In Figure 1, the reliability for an elliptical safe domain, obtained by the LSSE method is given. For a fixed unit value of the semi-minor axis, the reliability increase with increasing aspect ratio as expected and asymptotes to a value of 0.6826, which is the value obtained by FORM. Thus, unlike FORM, the LSSE method captures the variation in reliability associated with an increase in size and aspect ratio of the safe domain.

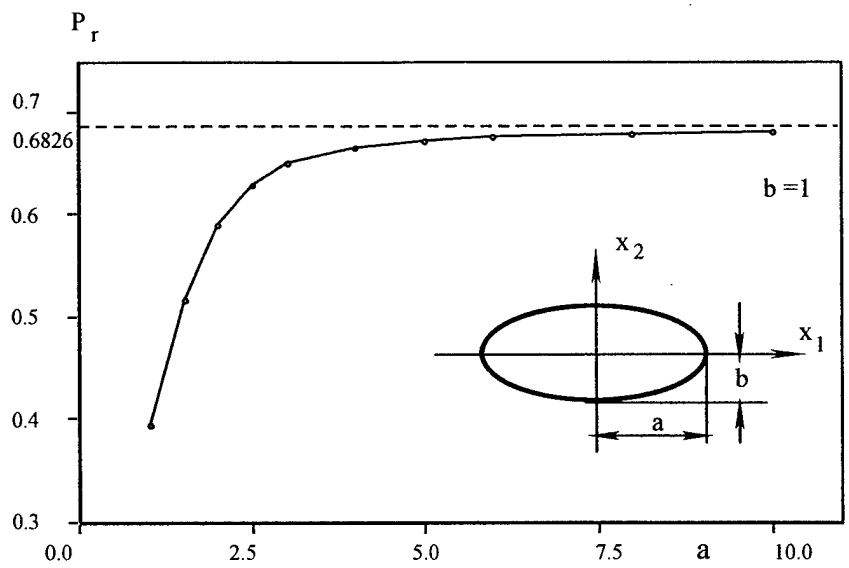

Figure 1. Reliability for an elliptical safe domain

In Figure 2, nodal points used in the LSSE discretization of the failure surface are indicated. The single line approximation of the failure surface by FORM is also indicated. Inaccuracies in FORM are due to the discrepancy between the straight-line approximation and the more accurate representation achieved with the LSSE method.

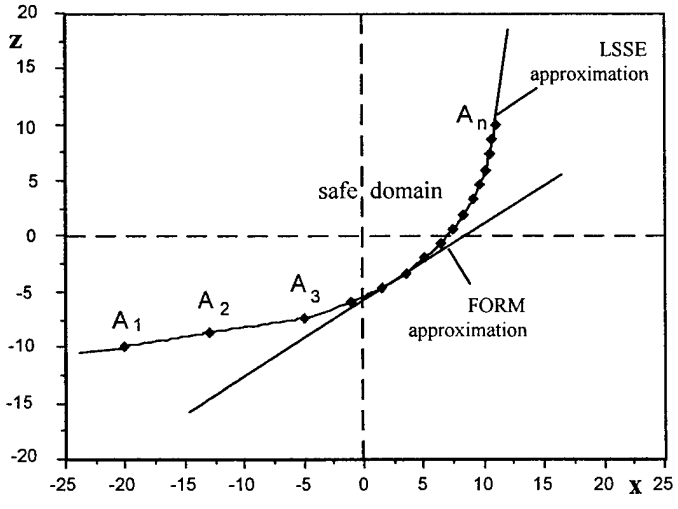

Figure 2. Representation of Limit State Surface by LSSE method and by FORM

In Figure 3, the probability of failure for a fatigue reliability problem consisting of an edge crack under cyclic tension is given. The LSSE and FORM results are in good agreement for this relatively straightforward problem and this demonstrates the accuracy of the LSSE method for crack problems. When the failure surface exhibits high curvature near the most probable failure point, the LSSE method retains the accuracy shown in the figure whereas the FORM method deteriorates.

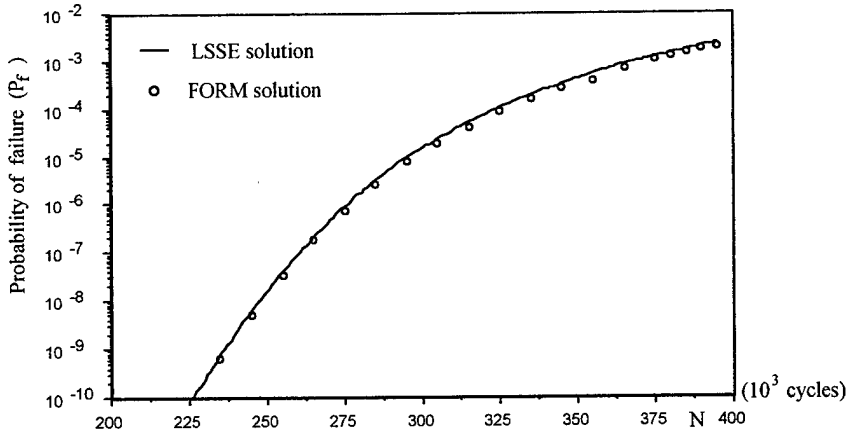

Figure 3. Comparison of Failure Probabilities for Edge Crack Problem.

c. Domain Integrals for Mixed Mode Stress Intensity Factors of Non-Planar Crack Fronts

The computation of stress intensity factors along a general curvilinear crack front remains a challenging problem in computational mechanics. Stress intensity factors are required for use in fatigue crack propagation relations such as the Paris Law and need to be computed accurately to avoid accumulating errors in fatigue crack growth simulations in reliability calculations. Mixed-mode stress intensity factors are expressed in terms of a crack tip interaction energy contour integral at a point *s* on the crack front as shown in Figure 4 below. By suitable choice of auxiliary fields the individual stress intensity factors can be computed. Because of a mathematical limit in the definition of the crack tip contour integral, it can not be computed directly in finite element methods. To overcome this, domain integral methods have been developed in which the crack tip contour integral is expressed as a domain (volume in 3D) integral surrounding the point *s* on the crack front.

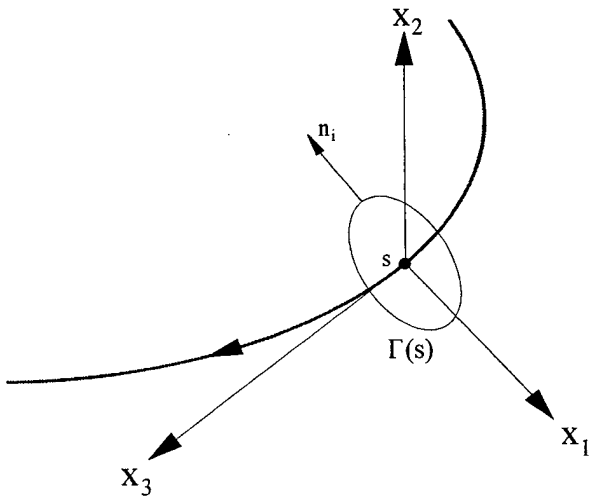

Figure 4. Curvilinear Crack Front in 3D.

The correct implementation of the interaction energy domain integral requires the incorporation of crack front curvature terms. The curvature terms do not appear in domain forms of the energy release rate (J-integral), however mixed-mode stress intensity factors can not be obtained from the J-integral. In [4], we have developed the domain integral formulation for the extraction of mixed-mode stress intensity factors along a non-planar crack front. Field quantities are expressed in terms of an orthogonal curvilinear coordinate system based on the crack front and the local tangent and normal planes to the crack front. By expressing the auxiliary fields in the curvilinear coordinate system, the curvature terms emerge naturally in expressions for gradients. Several benchmark problems are solved in [4] to illustrate the accuracy and utility of the method. For example, in Fig. 5 the finite element mesh for an arc crack problem is shown.

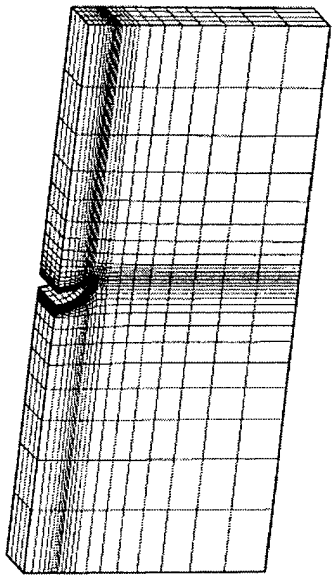

Figure 5. Mesh for arc crack problem

In Table 1, results obtained using the newly developed domain integral procedure are compared to the analytical result and the agreement is seen to be excellent with errors of less than about 1% in stress intensity factors.

Table 1. Comparison of numerical and analytical results for arc crack problem

	$\frac{K_I}{\sigma\sqrt{\pi a}}$	$\frac{K_{II}}{\sigma\sqrt{\pi a}}$	$\frac{G}{\frac{1-\nu^2}{E}(K_I^2+K_{II}^2)}$
Analytical	0.806	0.334	1.000
Numerical	0.807	0.317	0.996

d. Extended Finite Element Method for 3D Crack Analysis

The modeling of cracks in three-dimensional finite bodies remains a challenge in computational mechanics. Assuring that finite elements conform to the crack and that adequate refinement of the mesh is achieved in the vicinity of the crack can be cumbersome and time-consuming. The extended finite element method (X-FEM) alleviates the shortcomings associated with meshing the crack in traditional finite element methods. In [5], the extended finite element method is used for modeling cracks in three dimensions. In the X-FEM, the finite element method is used as the building block. The component is first meshed without the crack. The crack surfaces are then represented by a discontinuous function and accuracy in the crack tip region is achieved by using the two-dimensional asymptotic displacement fields (suitably referred to the curvilinear crack front). These enrichment functions are then incorporated in the finite element approximation using the concept of partition of unity. No finite element meshing of the crack is required. Obviously a mathematical or computational geometry representation of the crack surface is required for specification of the crack size, shape and location in the underlying finite element mesh and for specifying the enrichment functions.

In Figure 6, a three-dimensional finite element mesh (cubic) is shown along with the location of a penny shaped crack which is not meshed. In Figure 7, results for an elliptical crack centrally located in the cube are shown and are seen to be in excellent agreement with the analytical solution.

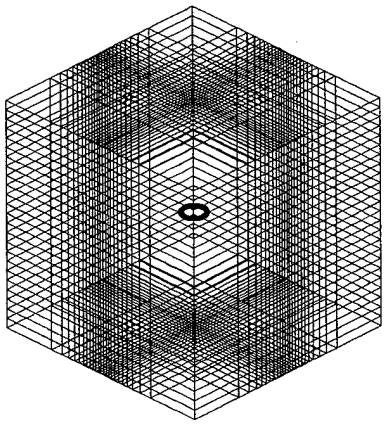

Figure 6. Finite element mesh with penny shaped crack location indicated.

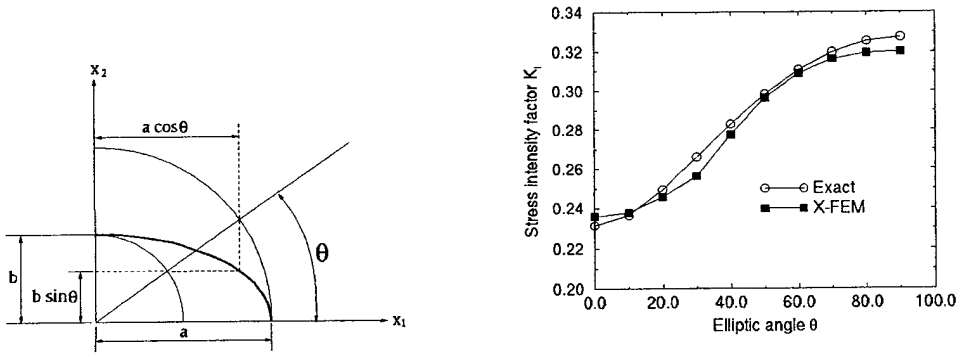

Figure 7. Stress intensity factors for elliptical crack.

e. Fast Marching and Level Set Method for Crack Growth

To alleviate difficulties associated with simulating crack growth via traditional finite element methods, a new numerical technique which couples the extended finite element method and level set and fast marching methods was developed [6]. The crack is represented in the X-FEM as discussed in subsection **d.** above. This enables the domain to be modeled by finite elements with no explicit meshing of the crack surfaces. The initial crack topology is represented by a signed distance (level set) function and signed distance functions are used to compute the enrichment functions that appear in the displacement based finite element approximation. A fast marching method in conjunction with the Paris crack growth law is used to advance the crack front. The signed distance functions are shown in Figure 8.

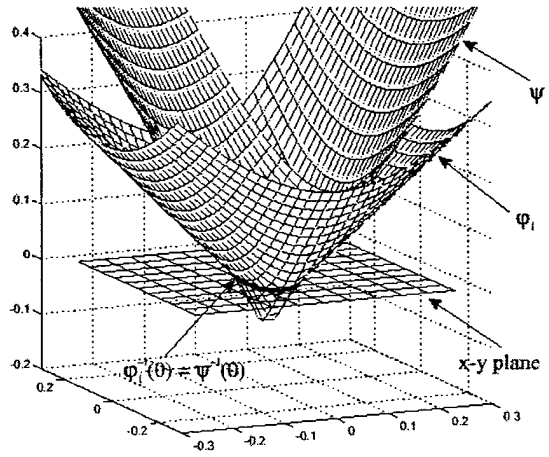

Figure 8. Signed distance functions for planar elliptical crack.

In Figure 9, the evolution of an elliptical crack (via the fast marching method) is shown (the mesh used is similar to that of Figure 6). As expected, the elliptical crack evolves into a circular shape. It is worth noting that in the simulation, there was no explicit meshing of the crack and no user intervention involved in the evolution of the front. In addition, the underlying finite element mesh is cubic and the crack growth increments are substantially smaller than the prevailing element dimensions. For additional details see [6].

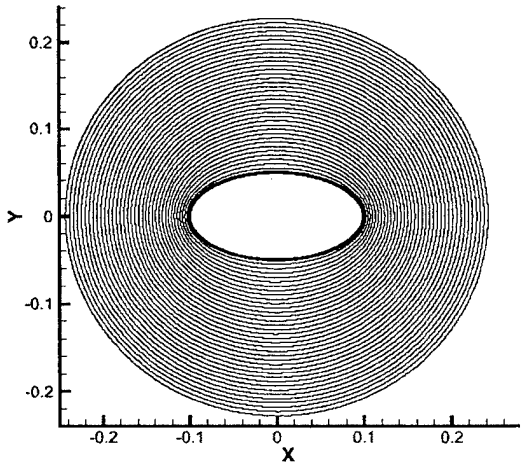

Figure 9. Fatigue crack growth simulation by fast marching method for an elliptical crack.

FUTURE WORK

The limit state surface element method will be further developed as a robust computational tool for fatigue reliability. The finite element techniques for stress intensity factor determination and fatigue crack growth modeling provide a foundation for computational simulation of crack growth in life-cycle engineering design. An area of significant promise and which would be of immense help in the practical application of these methods would be the development of the level set and fast marching methods for out of plane crack growth and the implementation of these procedures in commercial finite element codes.

M-URI PUBLICATIONS

[1] Moran, B., Zulfiqar, A, and Sukumar, N. (1996), "On the Direct Integration Method for Fatigue Reliability Calculations" MURI Integrated Diagnostics Report, Department of Civil Engineering, Northwestern University, Evanston, Il 60208

[2] Achenbach, J., Moran, B., and Zulfiqar, A. (1997), "Techniques and instrumentation for structural diagnostics, " in *Proceedings of the International Workshop on Structural Health Monitoring*, Edited by Fu-Kuo Chang, pp.179-190.

[3] Moran, B. and Xu, Y., and Achenbach, J.D. (2000) "Limit State Surface Element Method: Application to Fatigue Reliability with NDE Inspections" *ASCE Journal of Engineering Mechanics*, 126, No. 7, 684-692.

[4] Gosz, M. and Moran, B. (2000) "An Interaction Energy Integral Method for Computation of Mixed-Mode Stress Intensity Factors along Non-Planar Crack Fronts" submitted to *Engineering Fracture Mechanics*

[5] Sukumar, N., Moes, N., Moran, B., and Belytschko, T. B. (2000) "Extended Finite Element Method for Three-Dimensional Crack Modeling" *International Journal for Numerical Methods in Engineering*, 48, No. 11, 1549-1570.

[6] Sukumar, N., Chopp, D., and Moran, B. (2000) "Extended Finite Element Method and Fast Marching Method for Three-Dimensional Fatigue Crack Propagation" submitted to *Journal of the Mechanics and Physics of solids*

[7] Zulfiqar, A. and Moran, B. "Domain Integral Method for Mixed-Mode Stress Intensity Factors for Arbitrary Cracks in 3D," manuscript in preparation.

[8] Zulfiqar, A.and Moran, B. "Domain Integral Method for Unstructured Meshes," in preparation.

EDUCATION

During the course of this project, a graduate student Ali Zulfiqar was supported for his Ph.D. studies. Mr. Zulfiqar is currently writing his Ph.D. thesis in absentia and is employed as a research engineer in a consulting branch of Ford Motor Co. Mr. Zulfiqar developed the improved direct integration method and is completing work on unstructured meshes and domain integral methods for finite element modeling of cracks and crack growth in three-dimensions.

Dr. Yonglin Xu was supported as an assistant research professor. Dr. Xu was principally involved with the developed of the LSSE method. He will join the faculty at SUNY Buffalo in Fall 2000.

Dr. Natarajan Sukumar was supported as a post-doctoral research fellow on this project. Dr. Sukumar assisted with the development of the extended finite element method and the level set and fast marching methods for crack growth. He is currently a research associate at Princeton University and will join the faculty of the Department of Civil Engineering at the University of California at Davis in January 2001 as an assistant professor.

2.2.3 STUDY OF ACOUSTIC EMISSION AND TRANSMISSION FROM INCIPIENT FATIGUE FAILURE

Co-investigators: Laurence Jacobs, Jacek Jarzynski and Scott Bair (Georgia Tech)
Graduate students: Zhiqiang Shi, Brad Beadle, and Stefan Hurlebaus

OVERVIEW

Catastrophic failure of an in-service, structural component can be prevented if small cracks can be identified and arrested before they propagate into large cracks. As a result, it is necessary to develop a technique that can accurately detect and characterize any small cracks that may exist in complex, in-service components; such ability is a critical step towards developing a methodology for quantitatively predicting remaining service life.

Acoustic emission (AE) testing offers a distinct advantage over more conventional nondestructive testing techniques because it allows for the real time monitoring of in-service structures. To be effective, AE testing must be able to identify the location of an arbitrary defect (such as a fatigue crack) and to characterize the severity of that defect. The difficulty in the application of AE techniques to locate and detect these damage events from a source within a body is in interpreting and categorizing the large quantity of data and in rejecting the spurious information. Of fundamental importance for the advancement of the current state of AE technology is the isolation and identification of the signal from a fatigue crack.

OBJECTIVE

The goal of this research project is to develop quantitative, waveform based acoustic emission (AE) techniques that can locate and characterize small cracks in complex engineering components.

ACHIEVEMENTS

a. Transfer Function Development

Laser ultrasonic techniques were applied to develop a transfer function that quantifies and removes geometric effects from a measured acoustic emission signal. The geometry of a specimen changes the original acoustic emission signal as it propagates from its source to a receiving sensor. These changes, which are caused by reflection, transmission and mode conversion at interfaces and boundaries, have a significant impact on the acoustic emission waveform that is measured by the receiving sensor. The geometry effects (which do not contain any useful information for acoustic emission testing) tend to swamp and mask the initial signal, making it difficult to uniquely identify the original source of the acoustic emission.

The transfer function is developed as follows: First, a broad band, repeatable acoustic emission signal is generated in the specimen whose geometry is being characterized (e.g., a fatigue crack specimen). This experiment is repeated in a "geometry-less specimen" that only contains the effect of the source; it has no geometric features. Next, both the specimen and "geometry-less" signals are transformed into the frequency domain using a fast Fourier transform (FFT), and the transfer function, is obtained by dividing the FFT of the half-space signal by the FFT of the specimen signal (point-by-point). Once a transfer function has been developed for a particular specimen, it can be used with other sources.

The objective of this study is to establish the validity of using transfer functions to quantify and remove geometric effects from measured acoustic emission waveforms. The results of this study show that a transfer function is most effectual when the unknown source is similar to the original source (the source that is used to make the transfer function). Publication [1] provides technical details of this procedure.

b. Signal Feature Identification

Artificial AE signals, emanating from fatigue crack specimens, were examined to identify signal features by the determination of non-dispersive modes. This was accomplished by clustering the scalogram (energy density function) of the wavelet transform.

A synthetic laser source generates an ultrasonic signal that is detected with four commercially available PZT transducers. The finite size of the transducers and the geometry of the fatigue crack specimen (reflections at the boundaries) complicate this wave propagation problem. The theoretical arrival times of the waveforms (direct, reflected, mode-converted) are calculated and compared to the scalogram. The identification of multiple nondispersive waveforms (first arrival of the longitudinal, the transverse and the Rayleigh wave) will enable a more exact source location.

This study determines the applicability of the wavelet transform to more systematically quantify arrival times in experimentally measured passive ultrasonic signals. One could consider using a contour plot (or a three-dimensional mesh) of a scalogram to determine the arrival times of certain signal features, but this proves to be unwieldy because it is very complicated and it is difficult to implement. Instead, an automatic procedure is developed that reduces the complexity of the representation. The goal is to find the nondispersive modes, and to plot the different arrival times in the time-domain.

The fact that straight, horizontal lines (above approximately 0.3 MHz) represent all of the modes, as shown in Figure 1, shows that the complicated, multiply reflected wave arrivals are effectively nondispersive. The proposed procedure provides insight into the strength of individual features within the signal, and the non-dispersive assumption is verified by examining the intermediate scalogram. The technical details will be published in a journal article that is in preparation.

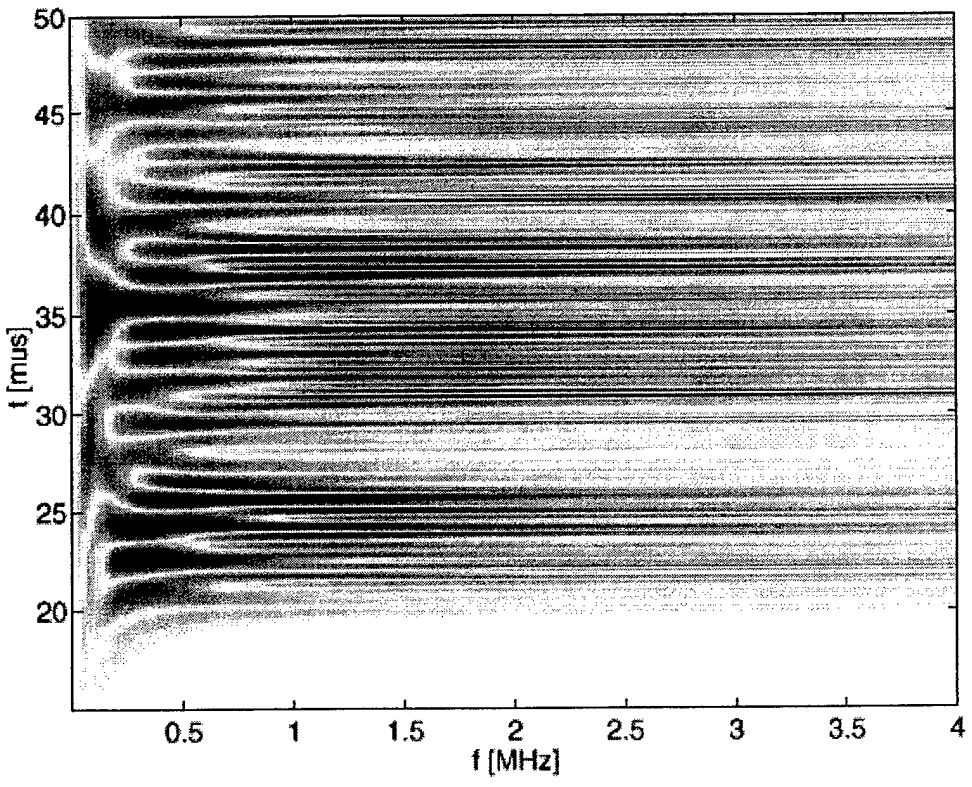

Figure 1. Scalogram of a signal generated by a laser source in the notch.

c. Fatigue Studies

A cylindrical stainless steel specimen under torsional fatigue loading was studied by monitoring acoustic emission with a two-channel system that digitizes the complete AE event waveform. By examining the cumulative AE event counts versus number of fatigue cycles curve, three "event growth" zones are observed.

It is found that specific characteristics of the measured AE waveforms (such as amplitude, energy distribution and frequency content) change significantly as the fatigue test progresses. In addition, these AE waveform changes are correlated with the damage mechanisms that occur during the different stages of the fatigue test. The three distinct stages of fatigue damage are 1) the uniform growth and distribution of small, sub-grain sized cracks; 2) the growth of micro-cracks across the grain boundaries; 3) and the coalescence of micro-cracks into localized cracks. These stages are confirmed by the microscopy of surface replicas taken at regular loading cycle intervals. Figure 2 shows a typical waveform from stage 2, plus its associated frequency spectrum. Publication [2] provides technical details of this procedure.

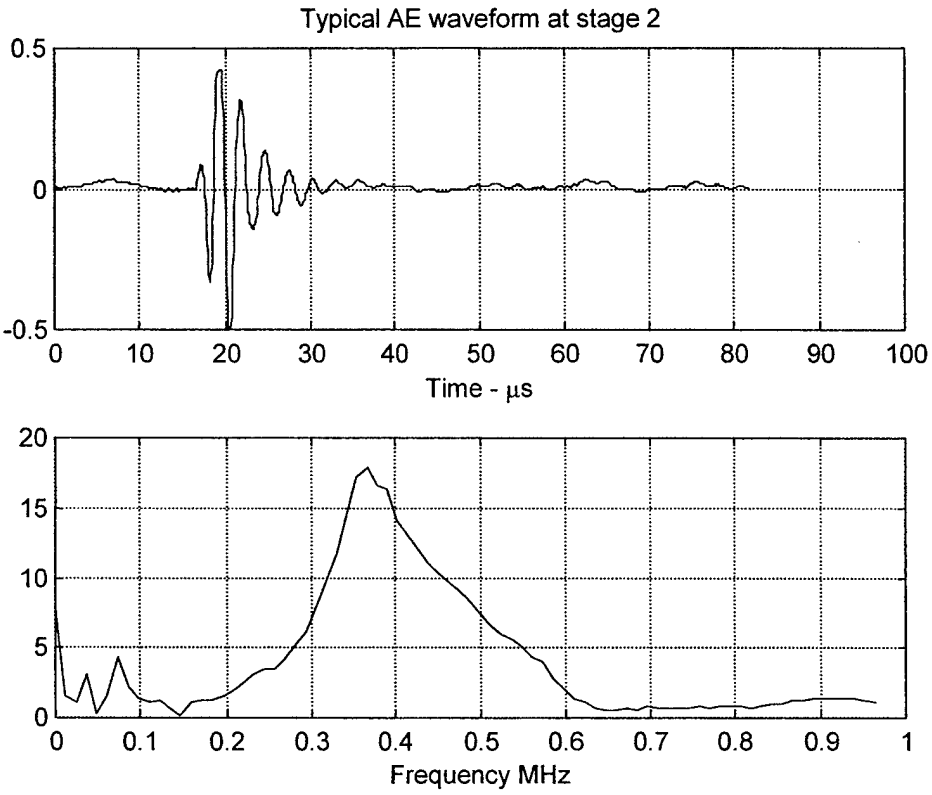

Figure 2. A typical waveform from Stage 2 (growth of micro-cracks across the grain boundaries) with its associated frequency spectrum.

Multiple AE fatigue tests were conducted on "hot spot" demonstration fatigue specimens using both lab-developed PZT sensors and broadband digital wave sensors, and obtained comparable results. The following stages of AE activities were identified: (1) noise activities (similar to AE) in the initial stage of fatigue, 20-35% of the fatigue life; (2) isolated AE signals during the middle stage of fatigue, 40-80% of the fatigue life, with waveforms (barely) discernable above the noise levels; (3) significant AE activity in the final stage of fatigue, 10-20%, with distinctive AE signals that originate from the notch crack (sub-mm range). Figure 3 shows a schematic of the specimen, plus a plot of AE activity versus number of fatigue cycles and typical AE waveforms that occur during the initial and final stages of fatigue.

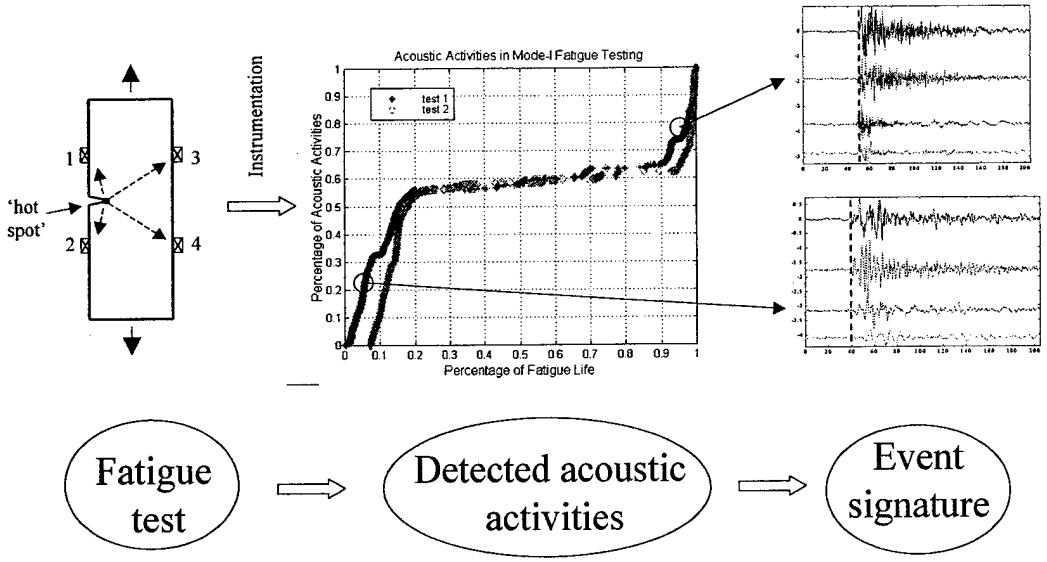

Figure 3. Schematic of acoustically studying fatigue.

Development highlights include:

- Devised a system for rejection of noise from authentic AE (this is a post processing procedure) using time of arrival and a cross-correlation function; calculated a time window for the "hot spot" to eliminate signal originated from out-of-region of interest.
- Analyzed AE waveforms (Post Processing). Applied window and filter to enhance the waveform frequency spectrum and identification procedure.
- Adopted detailed testing procedures to ensure accurate and repeatable AE testing. Procedures include: reciprocity check of sensor bonding during the fatigue test; and sensor location to maximize the ability to pickup AE's from the "hot spot" while reducing noise source triggering.
- Performed sensor calibrations of compact PZT sensor, commercial broadband sensor and sensor from University of Minnesota (Section 2.3.4). Calibration procedure includes sensitivity and frequency response function.
- Provided acoustic emission signals to the Signal Processing group at University Minnesota for analysis using recently developed pattern recognition algorithms (Section 2.3.4.4).

These technical details will be published in a journal article that is in preparation.

The fretting fatigue of PH13-8 stainless steel was studied using AE techniques, capturing AE events emanating from localized sources during the fatigue process. The AE phenomena observed are correlated to the material's fatigue behavior, and confirmed by SEM observation of the fracture surface. Specifically, the occurrence of AE correlates with the frictional force evolution during the fretting fatigue. A time window, based on the time-of-flight criteria, is computed to differentiate between authentic AE events from the spurious noise events. The features of typical AE events from the different stages are determined, and related to their respective fracture process. Publication [6] provides technical details of this procedure.

d. Elastic Wave Propagation

A finite element method (FEM) approach was combined with laser ultrasonics to investigate AE source and geometry effects on elastic wave propagation in 3-dimensional "plate-like" structures. The FEM has the flexibility to model a variety of sources (including finite rise-time and orientation), 3-dimensional geometric effects, and finite sensor size effect. Laser ultrasonic measurements are used to verify the FEM results. For example, Figure 4 is a comparison of the AE signals due to a vertical point force source measured with the laser ultrasonics set-up, compared to the FEM prediction. Publication [7] provides technical details of this procedure.

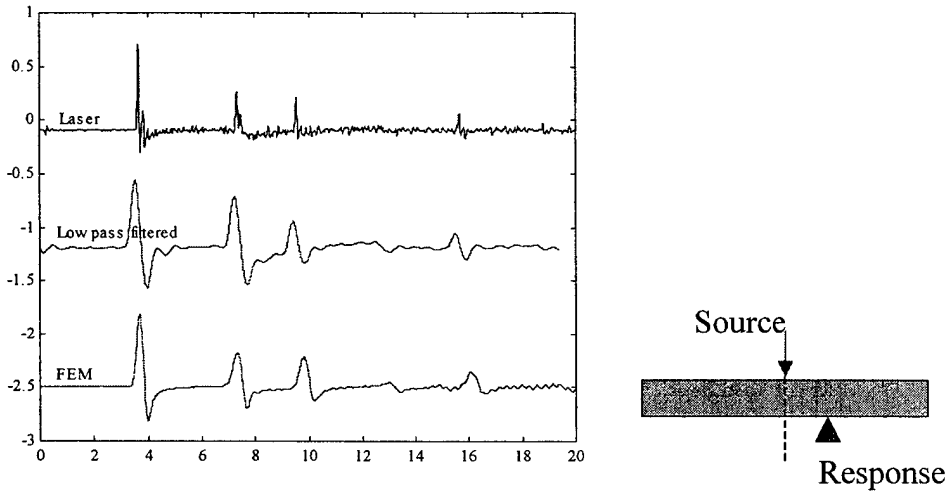

Figure 4. A comparison of AE signals due to a vertical point force source measured with the laser ultrasonics set-up, compared to the FEM prediction.

FUTURE WORK

- Examine fracture phenomena in more complex structural components as a more realistic test of the robustness of the proposed technique.
- Develop real-time analysis, including noise discrimination/rejection and source location, enhanced triggering to enable rejection of noise and extraneous signals.
- Develop a compact, portable design of the fiber optic sensor for field measurements.
- Apply signal processing techniques to detect echoes from cracks in the presence of a reverberant ultrasonic field. Promising signal processing techniques have been identified in Section 2.1.2.

M-URI PUBLICATIONS

1. Hurlebaus, S., Jacobs, L.J. and Jarzynski, J., "Laser Techniques to Characterize the Effect of Geometry on Acoustic Emission Signals," *Nondestructive Testing and Evaluation*, Vol. 14, pp. 21-37, 1998.

2. Shi, Zhiqiang, Jarzynski, J., Bair, S., Hurlebaus, S. and Jacobs, L.J., "Characterization of Acoustic Emission Signals from Fatigue Fracture," *Journal of Mechanical Engineering Sciences,* accepted for publication, 1999.

3. Hurlebaus, S., Jacobs, L.J. and Jarzynski, J., "Optical Techniques to Develop Transfer Functions to Remove Geometric Features in Acoustic Emission Signals," *Review of Progress in QNDE*, Vol. 16A, pp. 421-426, 1997.

4. Shi, Z., Koutsak, M., Bair, S., Jarzynski, J. and Jacobs, L.J., "Characterization of Acoustic Emission Signals from Fracture Events," *Review of Progress in QNDE*, Vol. 17A, pp. 565-570, 1998.

5. Shi, Z., Bair, S., Jarzynski, J. and Jacobs, L.J., "Study of Acoustic Emission from Incipient Fatigue Failure," *Review of Progress in QNDE*, Vol. 18A, pp. 395-401, 1999.

6. Shi, Z., Jarzynski, J. and Jacobs, L.J., "Quantitative Acoustic Emission from Localized Sources in Material Fatigue Processes," *Review of Progress in QNDE*, Vol. 19A, pp. 367-373, 2000.

7. Shi, Z., Jarzynski, J. and Jacobs, L.J., "Study of Acoustic Emission in a Plate using the finite element Method and Laser-Ultrasonics," *Review of Progress in QNDE*, Vol. 20, to appear.

2.2.4 ACOUSTIC EMISSION MODELING FOR INTEGRATED DIAGNOSTICS

Co-investigator: Isaac M. Daniel (Northwestern University)
Research Assistants: J.-J. Luo, J. Choi
Postdoctoral Fellows: H. J. Chun, C. G. Sifniotopoulos, J. -J. Luo

OVERVIEW

This project addresses the need to monitor in real time the condition of key components of naval systems, to detect and characterize critical flaws, monitor damage growth and provide input to life prediction modeling.

Results obtained in this task represent breakthroughs in the application of acoustic emission methods for damage detection and characterization. Specifically, the introduction of loading phase as a relevant parameter, the development of an anthropomorphic (user friendly) interface for probing data and the introduction of covariance processing and categorization of data, are novel and significant advancements of the technology.

OBJECTIVE

The objective of this project is to investigate and develop/adapt acoustic emission methods for the detection and characterization of fatigue damage growth in metallic components. This research applies to components whose failure results from the initiation and propagation of a major crack at a known location of stress concentration.

ACHIEVEMENTS

The primary accomplishments of this task since its inception include techniques for acoustic emission (AE) data acquisition, methods for simultaneous measurement of physical damage and innovative approaches for processing, analysis and correlation of acquired data with physical damage [1-3].

Techniques were developed or adapted for monitoring AE output during cyclic loading of notched metallic specimens. Two materials were investigated, 2024-T3 aluminum and 4340 steel. Three types of specimens were used, edge notch and center notch tensile specimens and a compact tension specimen. The AE output was monitored with a pair of resonant transducers equally spaced from the specimen notch. Crack propagation was monitored independently and concurrently with AE output using crack propagation gages.

The latest specimens were 4340 steel bars of 2 x 0.5 in. cross section and 14 in. in length with a 0.8 in. long central through crack machined by EDM (Fig. 1). After machining the specimens were heat treated to a hardness of 38-40 RC. Acoustic emission was recorded by two 150 kHz resonant transducers placed on either side of the crack at a distance of 1.5 in. Crack propagation gages were mounted on the face of the specimen near the crack tips.

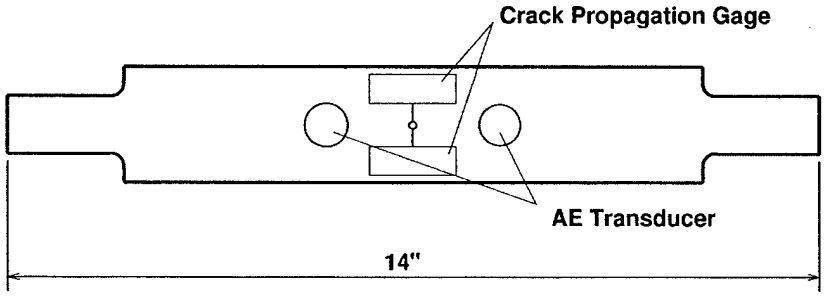

Figure 1. Specimen geometry and AE transducer location for fatigue testing.

The MISTRAS Acoustic Emission (AE) data acquisition system (Physical Acoustics) was used to acquire the data. AE Waveforms were acquired at 1 MHz sampling rate during fatigue tests. The AE threshold was set at 47 dB which is above the background noise of the test environment. The load level signal from the servo hydraulic machine (Instron) was fed to and recorded by the MISTRAS system. Traditional AE parameters as well as AE waveforms were recorded for later analysis. A typical fatigue test generated between 50-100 thousand waveforms, and required more than 1 GB of hard drive space. Fatigue tests were conducted at 2 Hz frequency under tension-tension loading with an R-ratio of 0.1.

It was found that crack growth plotted versus normalized fatigue cycles was independent of loading amplitude, i.e., fatigue lifetime [3]. The crack growth rate (da/dn) follows a power law relationship with the stress intensity range ΔK, i.e., it follows Paris law as shown in Fig. 2.

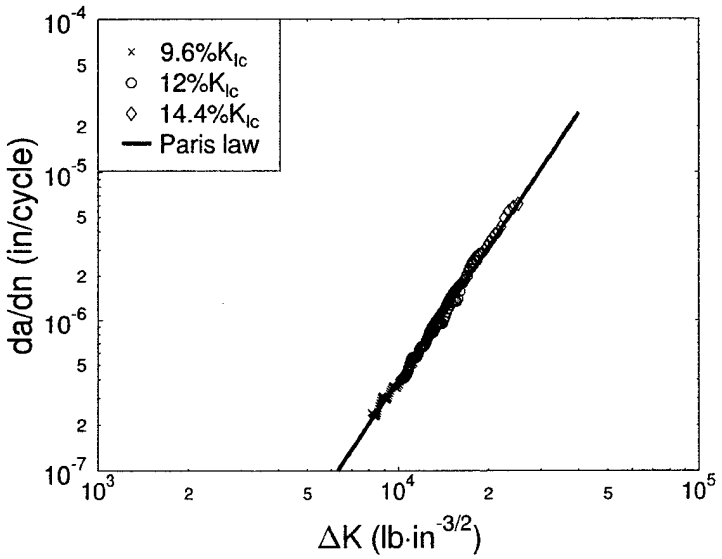

Figure 2. Crack growth rate versus range of stress intensity factor for fatigue testing of 4340 steel.

The phase of the loading cycle was identified as an important parameter in further filtering and analysis of AE data [1,2]. The AE output was separated into three groups or regions according to the phase of the loading cycle in which it occurs (Fig. 3) The origin of the AE signals of the various groups was also investigated by comparing amplitude distributions of the differential time of arrival at the symmetrically located transducers and of the signal duration. AE signals in group A, corresponding to the end of the unloading cycle are primarily associated with noise. AE activity in group B, occurring during the loading part of the cycles, corresponds to crack opening and crack propagation. AE signals in group C, occurring near the end of the fatigue lifetime near the peak of the loading cycle, correspond to rapid crack propagation in the final stage.

One puzzling observation was that, whereas crack growth was smooth, AE activity, especially near the middle of the fatigue lifetime included jumps as seen in Fig. 3. Examination of signal waveforms showed that waveforms corresponding to jumps in AE activity are distincly different from those corresponding to a normal AE rate (Fig. 4). These signals have relatively high amplitudes and cannot be filtered out by raising the threshold. Since these jumps obviously cannot be correlated with crack growth, a major effort was directed and focused on a better algorithm for processing and categorizing AE signals. The sheer size of waveform data, however, poses big obstacles to this approach. In a typical AE experiment the data size collected is between 0.5 and 3 gigabytes. Most existing waveform analysis algorithms would take from a few hours to several months to process the data.

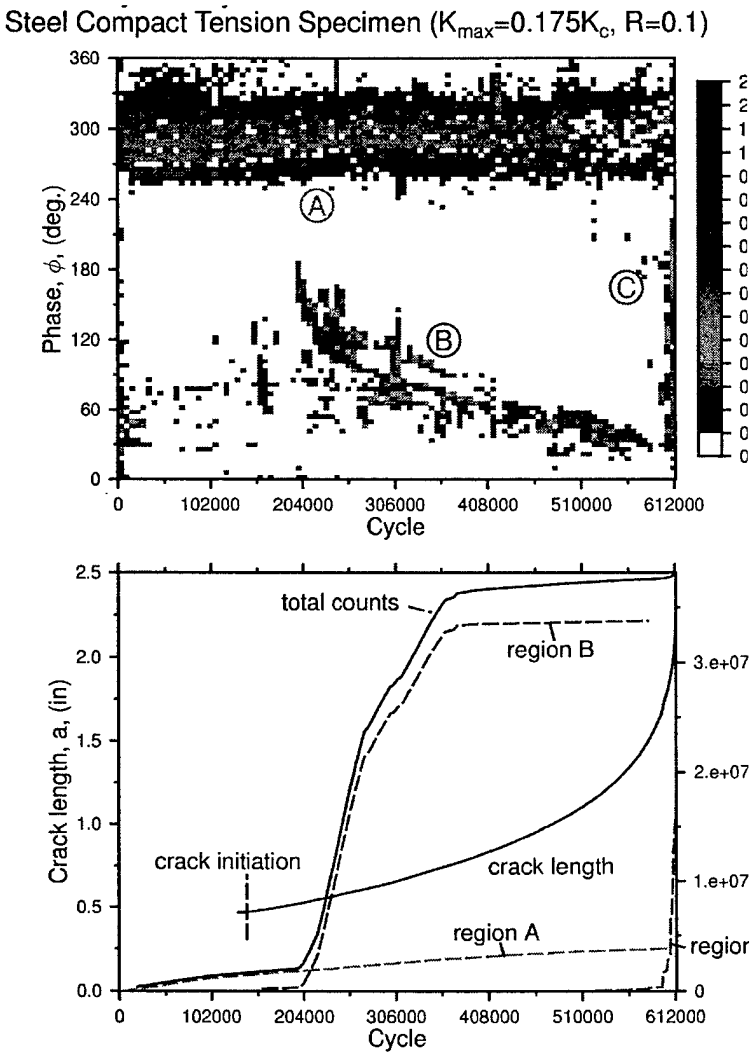

Figure 3. AE count distribution and cumulative counts versus fatigue cycles of compact tension 4340 steel specimen under fatigue loading.

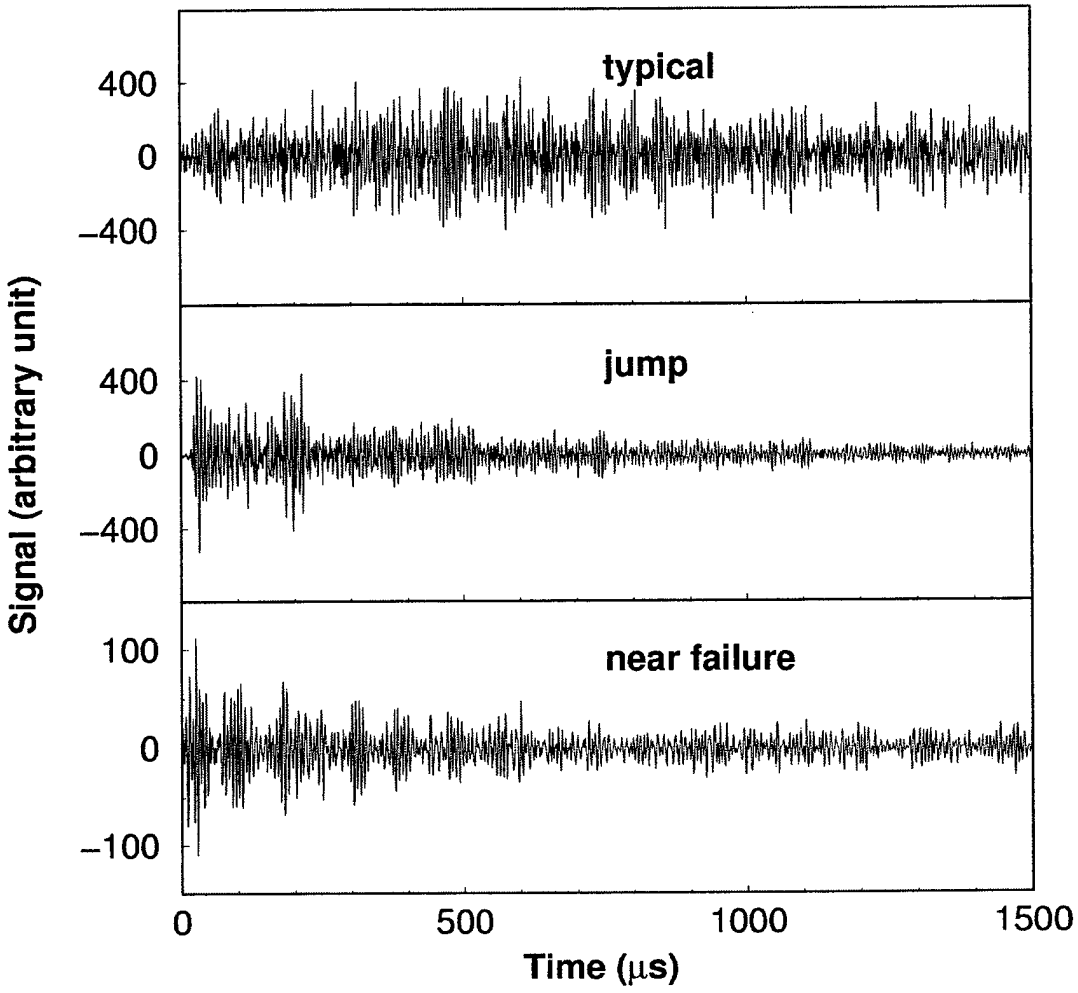

Figure 4. Acoustic Emission Waveforms

A scientific visualization software package (DtaReader and DtaProbe) was written. This software allows the user to explore gigabytes of AE waveform data from an intuitive user interface of cumulative hit count graph. The user can click on any part of the graph with a mouse, then the following information is displayed (Fig. 5).

1. A red arrow pointing to the data point in question.
2. The waveform data. It can be scaled (enlarged) by using the slide bar on the side in case the amplitude is too low to appear on the current scale.
3. Fourier transform data. FFT (Fast Fourier Transform) is calculated on the fly and displayed for frequency component analysis.
4. Parametric data. All conventional parametric data are displayed both numerically as well as graphically.

DtaProbe is interactive software for the user to probe into the large waveform data intuitively and effectively. DtaProbe works on a set of data files that another pre-processing software package, named DtaReader, created. The creation of DtaReader and DtaProbe by itself was a major achievement because they provide a tool with which all researchers can visualize and analyze the waveform data interactively and intuitively. The software was written in C++ for the Windows environment. Any Windows 95, 98 or NT4 environment can run this software.

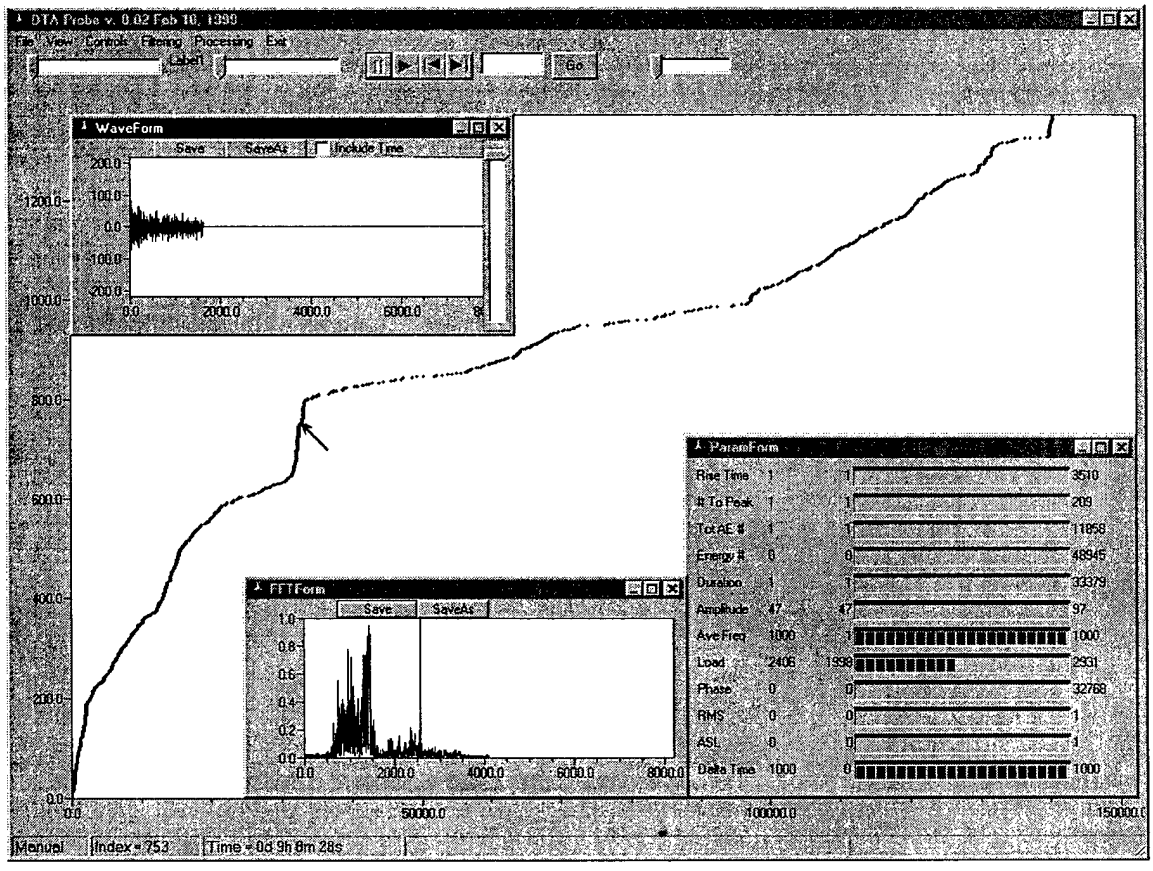

Figure 5. DtaProbe user Interface

A second major development in the data processing task was the study of covariance of the waveform signals, i.e., correlation of waveforms among themselves. Each data set, or waveform, is compared with itself and all other data sets by sliding it over the other until a good matching point is found. The degree of match is called covariance value and is normalized so that a perfect match corresponds to a covariance value of 1.0. The covariance value is represented graphically on a gray scale, with black corresponding to 1.0 and white to 0 covariance.

Covariance of a number of signals can be represented graphically in the form of a covariance matrix, where waveforms are arranged initially according to their order of occurrence along two axes. For example, if ten signals representing only three different types of waveforms A, B and C are obtained in the sequence ABCBACCABB, their covariance matrix can be represented as in Fig. 6a. Black squares represent maximum covariance value (1.0) and white squares zero (or low) covariance value. Given such a matrix, the challenge is to find and sort out the different types of waveforms that are represented in this matrix. An algorithm was developed to perform this task. This algorithm rearranges the matrix in such a way that most similar signals (resulting in the darkest black squares) will be placed next to each other. The result of rearranging is shown in Fig. 6b. It becomes clear that three different types of signals were present in the matrix. This rearranging (sorting) of the matrix is important because certain types of waveforms or signals should correlate with specific physical events during the material or structure lifetime.

The number of signals for a typical AE test can be of the order of 50-100 thousand which require Gigabytes of storage space to acquire and record all the waveforms. To save on computation time, a set of one thousand waveforms was sampled randomly and sorted by the same algorithm. Figure 7 shows gray scale covariance matrices of AE data from an actual fatigue test. The first matrix corresponds to the chronologically acquired sequence of data sets (waveforms) starting from the upper left corner. The second matrix was obtained after rearrangement by the sorting algorithm starting again from the upper left corner but in an arbitrary sequence. By observing the number of black squares, it is possible to estimate the number of signal types that are present in the data set. To verify that the randomly selected waveforms form a legitimate polling base of all AE events, several random sets of the same number (1000) of waveforms were selected and results were found to be similar.

A new software interface, called *Classify*, was written to re-map the sorted groups back into the original covariance matrix. This interface allows the user to draw a rectangular box around a group of the sorted matrix, paint it with a selected color and repaint the corresponding points in the original covariance matrix with the same color. The results at such an operation is shown in Fig. 8, where the colors are represented as gray scales.

The correspondence between the color coded (or gray scale coded) groups or classes of waveforms and the actual physical crack propagation process is examined by superimposing the cumulative AE count graph and/or the crack propagation graph on the original covariance matrix (Fig. 8a). Thus, it was observed that waveforms of a certain group appear only near failure, regions of high and low AE rates are associated with distinct groups of waveforms. Investigation on the appearance and progression of individual groups of waveforms during the entire fatigue life of the specimen will help in the correlation of sorted AE events with physical damage.

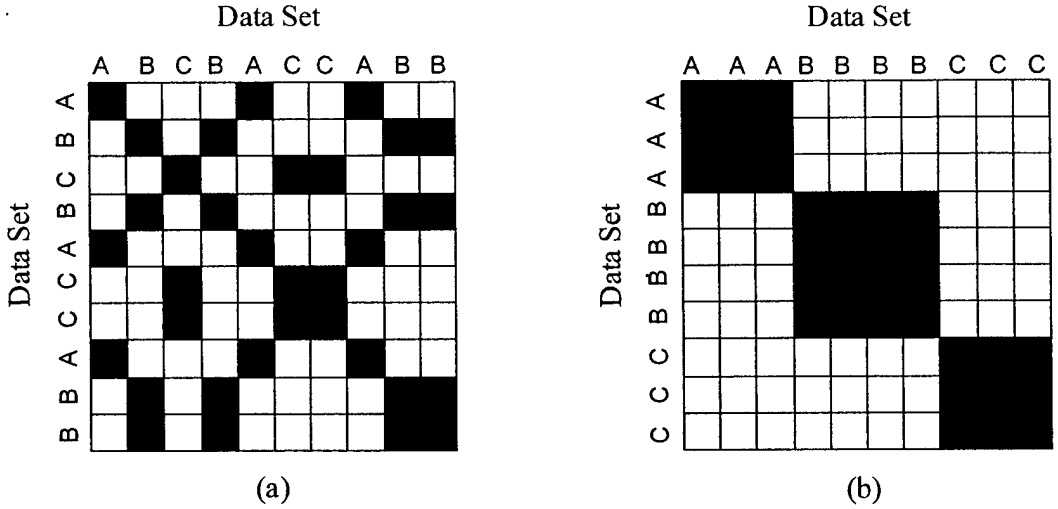

Figure 6. Covariance matrix of ten data sets representing three types of signals A, B and C. (a) as acquired sequence (b) rearranged sequence.

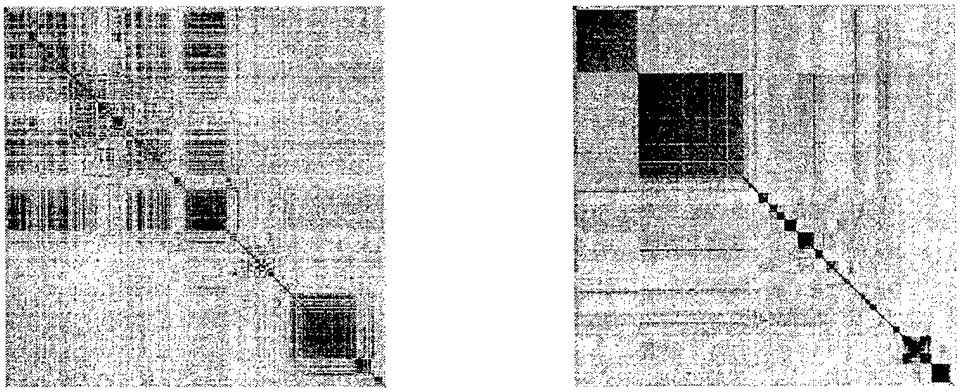

Figure 7. Covariance matrices of AE data from a fatigue test before and after sorting.

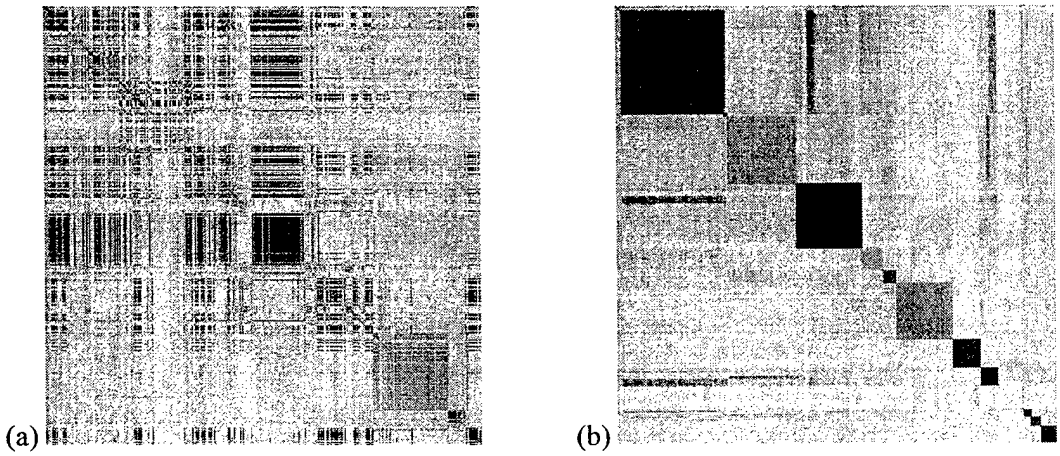

Figure 8. Repainting of the original matrix (a) based on the specified colors in the sorted matrix (b).

M-URI PUBLICATIONS (REFERENCES)

1. I. M. Daniel, J.-J. Luo, C. G. Sifniotopoulos and H.-J. Chun, "Acoustic Emission Monitoring of Fatigue Damage in Metals," *Review of Progress in Quantitative Nondestructive Evaluation,* Vol. 16, ed. by D. O. Thompson and D. E. Chimenti, Plenum Press, New York, 1997, pp. 451-458.

2. I. M. Daniel, J.-J. Luo, C. G. Sifniotopoulos and H.-J. Chun, "Acoustic Emission Monitoring of Fatigue Damage in Metals," *Nondestr. Test Eval.*, 1997, pp. 1-15.

3. I. M. Daniel, C. G. Sifniotopoulos and J.-J. Luo, "Analysis of Acoustic Emission Output from Propagating Crack," Review of QNDE, Vol. 17, ed. by D. O. Thompson and D. E. Chimenti, Plenum Press, New York, 1998, pp. 1331-1338.

4. J. Choi, J.-J. Luo and I. M. Daniel, "Analysis of AE Waveforms from Propagating Fatigue Cracks," Review of Progress in QNDE, Vol. 19, ed. by D. O. Thompson and D. E. Chimenti, Plenum Press, New York, 2000, pp. 351-358.

5. I. M. Daniel, J.-J. Luo and C. G. Sifniotopoulos, "Monitoring of Fatigue Crack Growth in Metals with Acoustic Emission," in *Eng. Scie. of Structures*, special volume honoring Sidney A. Gurelnick, ed. by Jay Shen, Illinois Institute of Technology, 2000.

Thrust Area III

2.3 MACHINERY HEALTH MONITORING (Sensing, Analysis, Real-time Diagnosis)

Perform studies with respect to the responses of signals early in fault inception, including research on sensors that can be placed at critical sites on mechanical systems for responses to changes in variables of state or vibration.

2.3.1 DETECTION OF THE PRECURSOR TO MECHANICAL SEAL FAILURE IN TURBOMACHINERY 158
Overview 158
Objective 158
Achievements 158
Future Research and Development 165
M-URI Publications 166

2.3.2 REAL-TIME MONITORING & CONTROLLING OF THE DYNAMIC BEHAVIOR OF MECHANICAL FACE SEALS 167
Overview 167
Objectives 167
Achievements 171
M-URI Publications 191

2.3.3 DYNAMIC METROLOGY AS A BEARING WEAR DIAGNOSTIC 192
Overview 192
Objectives 192
Achievements 193
M-URI Publications 197

2.3.4 INTEGRATED MICROSENSORS FOR AIRCRAFT FATIGUE AND FAILURE WARNING 199
Project Overview 199
2.3.4.1 Wideband Integrated Acoustic Emission Microsensors 200
2.3.4.2 Vibration Sensors 203
2.3.4.3 Multi-Sensor Coupon 206
M-URI Publications 208
2.3.4.4 Signal Processing for the Detection and Classification of Acoustic Emissions 209
a. Signal Modeling 210
b. Noise and Interference Models 217
c. Channel Effects and Blind Deconvolution 218
d. Transient Signal Detection 219
e. Classification 223
M-URI Publications (References) 235

2.3.5 MODAL PARAMETER EXTRACTION FROM STRUCTURAL DIAGNOSTIC SIGNALS 237
Overview 237
Objectives 237
Achievements 241
Summary and Conclusions 262
Future Research 262
M-URI Publications and References 263

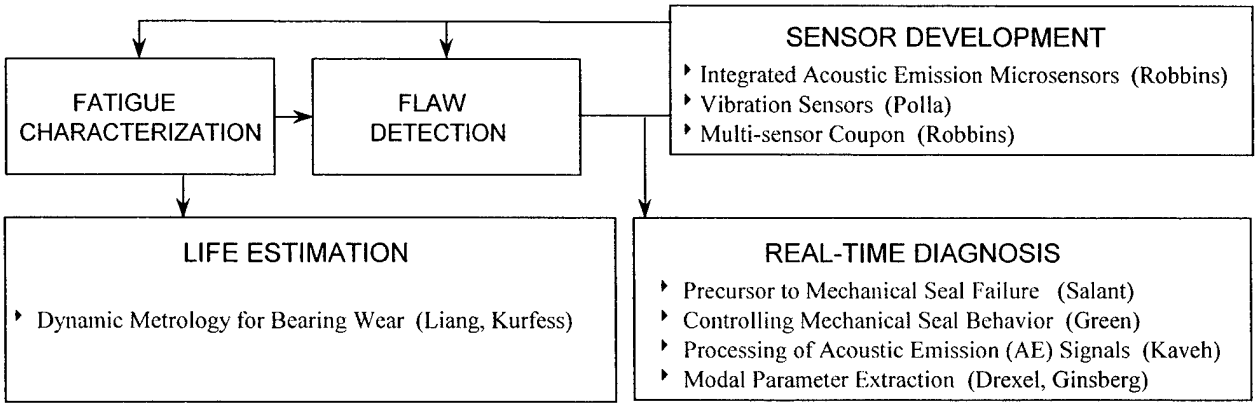

2.3.1 DETECTION OF THE PRECURSOR TO MECHANICAL SEAL FAILURE IN TURBOMACHINERY

Co-investigators: Richard F. Salant and Jacek Jarzynski (Georgia Tech)
Graduate research assistant: William Anderson

OVERVIEW

The U.S. Navy uses a large number of mechanical seals in such turbomachines as centrifugal pumps, compressors, turbines, turbopumps, propeller shaft assemblies, and gas turbine engines. Mechanical seal failure is one of the principal causes of breakdown of these machines. The use of a monitor to detect a precursor to seal failure will allow preventive action to be taken to avoid failure. Such a monitor will eliminate the need for scheduled preventive maintenance, thereby reducing costs, and will minimize the possibilities of catastrophic failure and the disruption of naval operations due to seal failure.

In this project, a monitor to detect the collapse of the lubricating film between the two faces of a mechanical seal has been developed. Such collapse is a precursor to seal failure. The monitor detects both the occurrence of mechanical contact between the seal faces and the severity of contact. The latter is important because many seals are designed to operate normally with partial contact between the faces.

Two versions of the monitor have been developed, one for gas seals and one for liquid seals. Both use the same general principal of operation: detection of actively generated ultrasonic waves reflected at the interface between the seal faces. In the gas seal system, compressive waves are used, while in the liquid seal system, shear waves are used.

Both monitoring systems have been tested in the laboratory. The gas seal system has undergone bench tests and tests on a demonstration prototype seal for a NASA turbopump. The liquid seal system has undergone bench tests and tests on a commercial seal that is extensively used in naval applications. These tests have demonstrated that the systems are feasible.

Additional research and development will be required before these systems can be put into commercial use. These activities include exploration of higher frequency systems (4 MHz) to obtain cleaner signals, extension of the theoretical models of both the gas and liquid systems to partial contact conditions, development of failure criteria and development of commercial versions of the hardware and software.

OBJECTIVE

Mechanical seals generally fail as the result of the collapse of the lubricating film between the two seal faces. The goal of the present project is to develop a real-time monitoring system that will detect the collapse of the lubricating film before mechanical and thermal damage to the seal is sustained.

Prior to this project, the only sensor for monitoring mechanical seals that had been investigated is the acoustic emission (AE) sensor. Several efforts to use this sensor had yielded mixed results (refs. 1-6). While significant results could be obtained under controlled laboratory conditions, the method was not successfully implemented in the field. The major problem is the difficulty in distinguishing mechanical seal AE emissions from those produced by other sources. This is compounded by changes in AE characteristics from seal to seal, and with changing operating conditions, making it extremely difficult to develop a universal AE system for seal monitoring.

ACHIEVEMENTS

In the first three years of this project, a monitoring system has been built, analyzed, and successfully tested on a seal in a laboratory environment, under steady-state and transient conditions. The monitoring system utilizes actively generated ultrasonic waves to determine if the two seal faces make contact and, if so, the degree of contact. A piezoelectric transducer is placed behind one of the seal faces and is used as a source, generating a train of ultrasonic wave packets that propagate toward the interface between the seal faces. A second piezoelectric transducer is placed behind the other seal face, and is used to detect the

waves that are transmitted across the interface. On the basis of theoretical work and work by other investigators (refs. 7-9), it had been expected that the transmitted signal would be virtually zero when the film is intact and nonzero when the film has collapsed, with an amplitude indicative of the degree of contact between the seal faces.

The monitoring system has been installed on the double mechanical seal shown in Fig. 1. This seal, originally designed for a turbopump, seals air and is electronically controlled so that the separation between the seal faces can be varied at will. In the first stage of testing, a large number of steady-state tests have been run, in which the spacing between the seal faces was varied. Typical results are shown in Fig. 2. The transmitted signal strength, at the driving frequency, is plotted against the leakage rate. The latter is a measure of the spacing between the seal faces. As the leakage rate is reduced from approximately 12.4 l/min to approximately 1.7 l/min (by reducing the spacing), the signal strength remains substantially constant at the noise level (0.25 V). The leakage rate of 1.7 l/min corresponds to the seal faces making contact (there is leakage bypassing the seal). At this contacting condition, the signal strength takes on values ranging from the noise level to approximately nine times the noise level.

To interpret these results, two series of bench tests were performed. In the first series, the shaft with the rotating tungsten carbide face and the two floating carbon face assemblies were placed in a jig, with the same relative positions as in the seal tester. The film thicknesses between the tungsten carbide and carbon faces were set using Mylar spacers of known thickness. Ultrasonic waves were generated and detected as in the seal tester. These tests showed that for all non-zero film thicknesses, the transmitted signal is essentially zero; it is non-zero only when there is mechanical contact between the faces, in agreement with the results of our analytic model. In the second series of bench tests, the seal components were stacked vertically, and ultrasonic measurements were made with various weights placed on the assembly to vary the contact pressure between the faces. These tests showed that as the contact pressure is increased, the transmitted signal strength increases. This is due to an increase in the real area of contact, and is in agreement with the work of other investigators (refs. 1-3).

It is therefore clear, from Fig. 2, that the strength of the transmitted signal indicates whether or not face contact occurs. If the signal strength is equal to the noise level, there is no contact. If the signal strength is greater than the noise level, there is contact, and the magnitude of the signal strength is a measure of the contact pressure between the faces. This is a very favorable characteristic for a seal monitor, because it allows assessment of the severity of the contact.

In the second stage of testing, ultrasonic measurements were made on the seal under transient conditions in real time. Two types of transients were investigated. In the first, the coning was decreased rapidly to induce face contact, and then increased to resume normal operation. Typical results are shown in Fig. 3. It is seen that each instance of face contact results in a sudden increase in the detected signal strength. In the second type of transient, face contact was induced by suddenly reducing the sealed pressure. Typical results, contained in Fig. 4, show that each time the faces make contact, there is again a sudden increase in detected signal strength. These results, together with those of the steady state tests, confirm the effectiveness of this monitoring system.

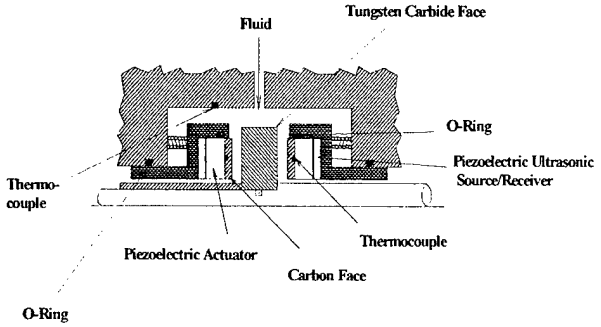

Figure 1. Apparatus

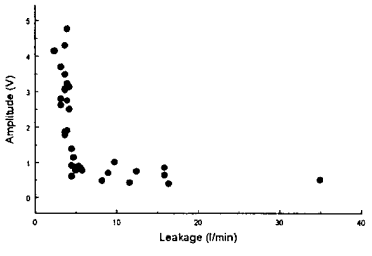

Figure 2. Transmitted Signal Strength

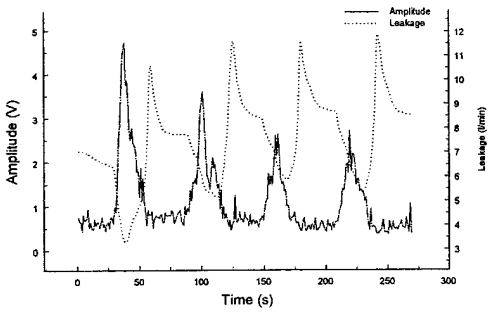

Figure 3. Transient Coning (Transmission)

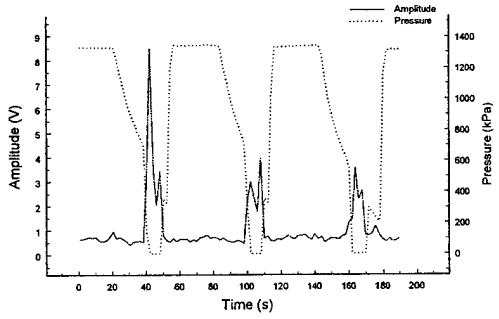

Figure 4. Transient Pressure (Transmission)

During year 4 of this project, initial work was done on developing a similar monitoring system for a seal used in an actual Navy application. Since most Navy applications require single seals, rather than the double seal arrangement of Fig. 1, it was necessary to modify the general scheme described above. That scheme, in which ultrasonic waves transmitted across the sealing interface are detected, requires two transducers, one behind each of the seal faces. Therefore, with a single seal, a transducer must be placed behind both the non-rotating and rotating face. It would then be necessary to use either slip rings or telemetry to transfer signals between the rotating transducer and ground. To eliminate such a complication, a method using only a single transducer, placed behind the non-rotating seal face, has been developed. In this method, the waves reflected from the sealing interface (rather than the transmitted waves) are monitored. When the lubricating film is intact, the reflected wave amplitude will be a maximum. When there is contact between the seal faces, the amplitude will be reduced; the greater the degree of contact, the lower the amplitude. The apparatus of Fig. 1 has been used for this work, but with only one of the transducers activated. That transducer is used as both a source and a receiver. It is driven to produce a continuous train of ultrasonic wave packets, each packet containing three or four waves (at 2 MHz) with 1 ms between consecutive packets. The transducer is gated, so that during times when the reflected wave packets are received, the received signal is transmitted to a processing system.

As in the case of the transmitted wave system, two series of bench tests were performed: one with calibrated film thicknesses using Mylar spacers, and one with face contact and calibrated contact pressures using weights. These tests showed that for finite film thicknesses, the reflected wave amplitude is substantially independent of film thickness, but when the film thickness is zero there is a substantial drop in amplitude. Furthermore, the higher the contact pressure (the greater the degree of contact), the lower the reflected wave amplitude.

Figure 5 shows some typical steady state tests, in which the film thickness (and leakage rate) was varied through electronic control. This is the complement of Fig. 2. It is seen that at large film thicknesses (and leakage rates), the reflected signal is relatively large and independent of film thickness. However, once the film thickness (and leakage rate) is reduced to the point where face contact occurs, the signal amplitude decreases substantially, with the amount of decrease depending on the degree of contact.

The results of transient tests are shown in figures 6 and 7. Figure 6 (the complement of Fig. 3) contains the results of a test in which the coning was decreased to induce face contact, and then increased to resume normal operation. It is seen that each instance of face contact results in a significant increase in the detected signal strength. Figure 7 (the complement of Fig. 4), shows the results of a test in which face contact was induced by suddenly reducing the sealed pressure. Each time the faces make contact, there is again a significant decrease in detected signal strength. These results, together with those of the steady state tests, confirm the effectiveness of this single transducer monitoring system. In its present form, it could be used on virtually any single gas seal.

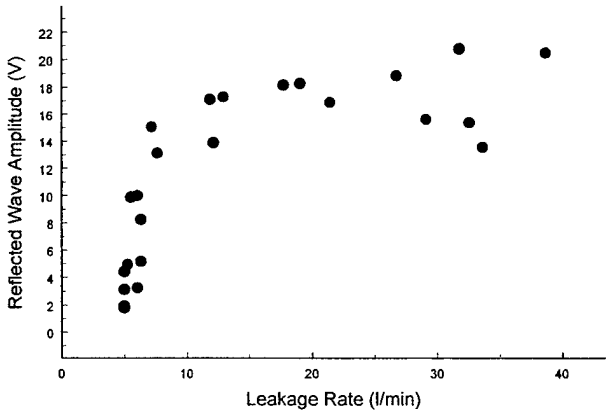

Figure 5. Reflected Signal Strength

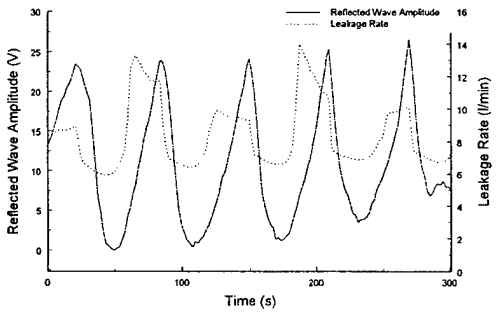

Figure 6. Transient Coning (Reflection)

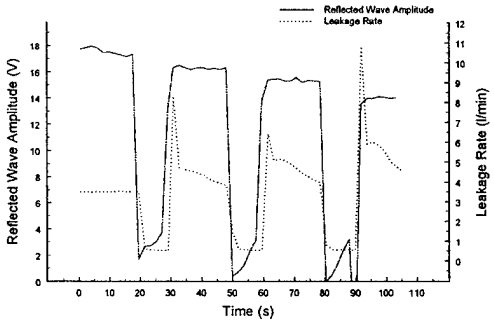

Figure 7. Transient Pressure (Reflection)

While the system is suitable for gas seals, it was decided to develop a similar monitoring system for a particular liquid seal used in naval applications: the John Crane type 1 seal, used for general shipboard service. A number of such seals were acquired for testing. A schematic of the seal is shown in Fig. 8.

It should be noted that in the gas seal tests, described above, ultrasonic compressive waves were used. However, for the John Crane liquid seals, ultrasonic shear waves must be used instead, due to the higher acoustic impedance of liquid as compared to gas. It was found that the most effective performance is achieved when separate transducers are used for the source and the receiver. They are shown in Fig. 9, which schematically illustrates the mounting arrangement on the silicon carbide seal face.

Each transducer pair consists of two square PZT-5A piezoelectric transducers, mounted on steel wedges, as shown in Fig. 9. These transducers are poled to operate in the transverse mode. One is used as a source of ultrasonic shear waves, while the other is used as a receiver. The angle between each transducer and the seal face (9 degrees) was chosen to account for the spacing between the transducers and the change in shear wave propagation speed between the steel and the silicon carbide. As in the gas seal experiments, the source transducers are driven at 2 MHz by a function generator and amplifier, producing a continuous train of wave packets. Each packet consists of 2 waves, with a repetition rate of 100 Hz. The received signal was processed in a similar manner as with the gas seal system, except no gating was necessary and the signal was compensated for temperature effects.

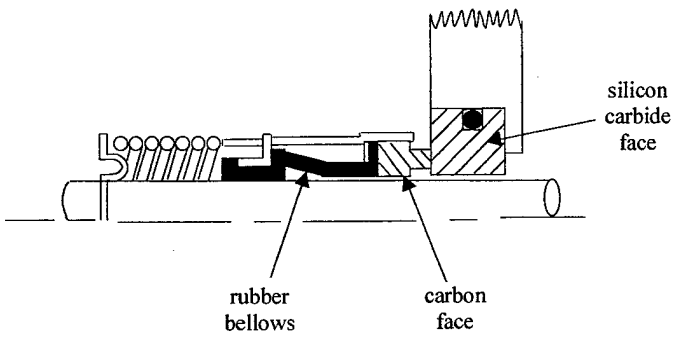

Figure 8. Schematic of John Crane Type 1 Seal

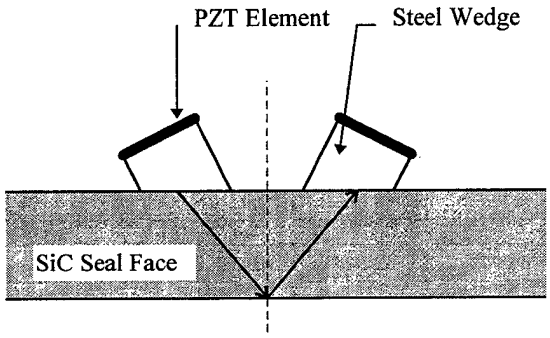

Figure 9. Schematic of Transducer Mounting

A theoretical model of the propagation and reflection of the shear waves was constructed, based on the finite interfacial stiffness technique. Figure 10 contains the model predictions. It is seen that with perfect contact between the seal faces, the predicted reflection coefficient is 0.68. As soon as the film thickness is a small fraction of a micron, the reflection coefficients jumps to 1.0 and remains at that value as the film thickness is increased further. This behavior is very similar to that predicted for the gas seal system, and indicates that the reflected shear waves can be successfully used for monitoring the liquid seal. Also shown in Fig. 10 is a curve for longitudinal waves. It shows that there is virtually no change in the reflection coefficient of longitudinal waves when contact occurs, which is why shear waves must be used with the liquid seal.

As with the gas seal, two types of bench tests were performed. In the first test, the two seal faces were separated by PET shims of various thicknesses to set the film thickness, and placed on a mandrel. They were partially immersed in water such that the interface between the two faces was filled with water, and the reflected ultrasonic wave amplitude was measured at each film thickness. Figure 11 shows the results, in the form of a plot of reflected wave amplitude versus film thickness. When the film thickness is increased from zero to 1.5 microns, the reflected wave amplitude jumps by approximately 0.9 volts, and then remains substantially constant as the film thickness is increased to 4.5 microns. This result is consistent with the theoretical predictions, and provides additional evidence that the reflected shear wave approach will be successful in detecting contact. The plot on Fig. 11, for shear waves in the liquid seal system, is qualitatively very similar to the corresponding result for longitudinal waves in the gas seal system.

In the second bench test, the shims were removed, and calibrated weights were placed on top of one of the seal faces to vary the contact force between the faces. Figure 12 shows that as the load was increased over a range of approximately 11.5 kg., the reflected wave amplitude drops by approximately

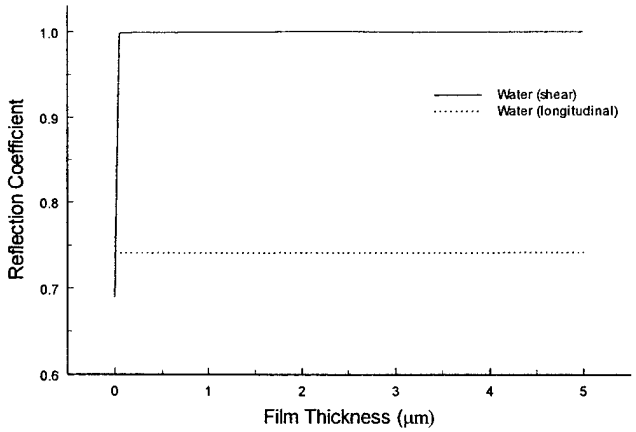

Figure 10. Liquid Seal Model Predictions

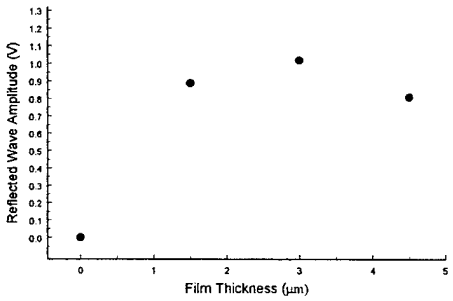

Figure 11. Bench Test, Variable Film Thickness

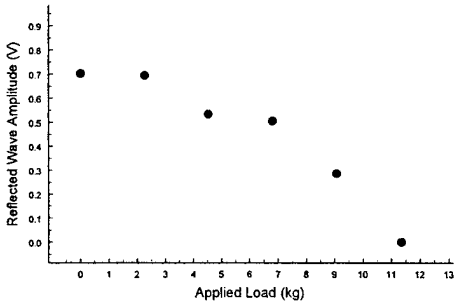

Figure 12. Bench Test, Variable Load

0.7 volts. This result is qualitatively similar to that obtained in the corresponding gas seal test, and shows that the reflected shear wave amplitude indicates the severity of contact. This is especially important for the John Crane seal, because that seal is unbalanced, and always runs with partial contact. It is when the contact becomes too severe that failure is imminent.

Dynamic tests were performed using the tester, acquired from John Crane, shown in Fig. 13. A series of tests at a speed of 377 rad/s (3600 rpm) involved subjecting the seal to transient pressure loading. Figure 14 shows the results of a test in which the seal, initially at a sealed pressure of 1.04 MPa gage (150 psig), is subjected to a series of 10 second pressure pulses, which momentarily raise the sealed pressure to 1.66 MPa gage (240 psig). Each pressure pulse produces a momentary drop in the reflected wave amplitude, indicating an increase in the severity of contact between the faces. This is what is expected for the John Crane Type 1 seal, which is unbalanced. It is the opposite of the behavior of the balanced gas seal, in which a drop in pressure produces face contact (Figs. 4 and 7).

The results of a test in which the sealed pressure is momentarily dropped from 1.04 MPa gage (150 psig) to 0 MPa gage are shown in Fig. 15. Each pressure depression produces a momentary increase in the reflected wave amplitude, indicating a decrease in the severity of contact. This behavior is just the opposite of that of the previous test, and is expected of an unbalanced seal.

Figure 16 shows the results of a test in which the sealed pressure varies in a stepwise manner between 0.35 MPa gage (50 psig) and 1.04 MPa gage (150 psig). As in the previous tests, the results show a decrease in the reflected wave amplitude each time the pressure and severity of contact increase, and an increase in the reflected wave amplitude each time the pressure and severity of contact decrease. They also show a small low frequency oscillation of the contact at the low pressure.

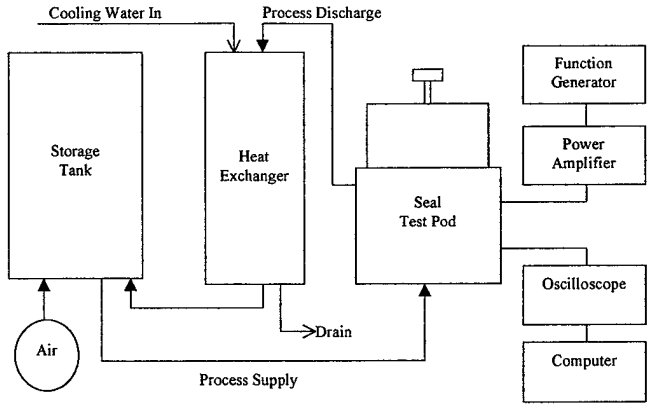

Figure 13. Liquid Seal Tester

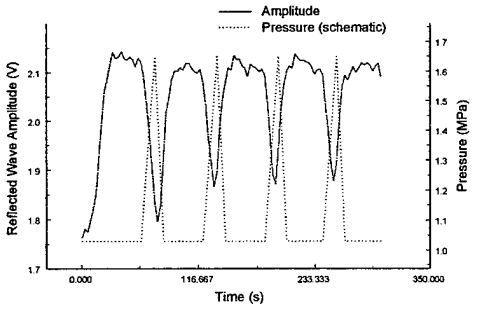

Figure 14. Liquid transient test, pressure pulses.

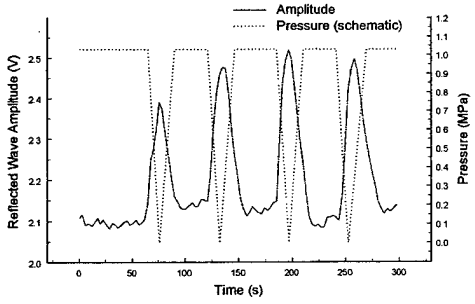

Figure 15. Liquid transient test, pressure drops.

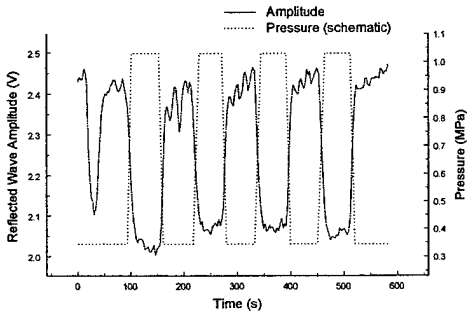

Figure 16. Liquid transient test, stepwise pressure variation.

References

1. Orcutt, F. K., 1969, "An Investigation of the Operation and Failure of Mechanical Face Seals," *BHRA 4th International Conference on Fluid Sealing*, p. 205-217.
2. Kataoka, T., Yamashina, C. and Komatsu, M., 1987, "Development of an Incipient Failure Detection Technique for Mechanical Seals," Proceedings *of the Fourth International Pump Symposium*, Texas A & M University, pp. 121-129.
3. Miettinen, J. and Siekkienen, V., 1995, "Acoustic Emission in Monitoring Sliding Contact Behavior," *Wear*, Vol. 181-183, pp. 897-900.
4. Miettinen, J., Siekkienen, V. and Tornqvist, P-E, 1996, "A New Way to Use Mechanical Face Seal In Centrifugal Pump," *7th Nordic Symposium on Tribology*, Bergen, Norway.
5. Williams, M. and Barnes, N. D., 1993, "The Use of Acoustic Emissions for Monitoring Mechanical Seals," 13th *BPMA Pump Technical Conference*.
6. Holstein, A. P., 1996, "Diagnosis of Mechanical Seals in Large Pumps,"*Sealing Technology*, N. 33, pp. 9-12.
7. Drinkwater, B. W., Dwyer-Joyce, R. S. and Cawley, P., 1995, "A Study of the Transmission of Ultrasound Across Real Rough Solid-Solid Interfaces," *Rev. Prog. Quantitative Non Destructive Evaluation*, Vol. 14, Plenum, New York.
8. Drinkwater, B. W., Dwyer-Joyce, R. S. and Cawley, P., 1996a, "A Study of the Interaction Between Ultrasound and a Partially Contacting Solid-Solid Interface," *Proceedings, Royal Society of London A*, Vol. 452, pp. 2613-2628.
9. Drinkwater, B. W., Dwyer-Joyce, R. S. and Cawley, P., 1996b, "The Interaction of Ultrasound with a Partially Contacting Solid-Solid Interface in the Low Frequency Regime," *Review of Progress in Quantitative Non Destructive Testing*, Vol. 15, Plenum, New York.

FUTURE RESEARCH AND DEVELOPMENT

While the completed research program has demonstrated the feasibility of the gas and liquid monitoring systems, additional research and development will be required before these systems can be put into commercial use. These activities include:

1. exploration of higher frequency systems (4 MHz) to obtain cleaner signals
2. extension of the theoretical models of both the gas and liquid systems to partial contact conditions
3. development of failure criteria
4. development of commercial versions of the hardware and software.

M-URI PUBLICATIONS

Anderson, W. B., Salant, R. F. and Jarzynski, J., 1997, "Detection of Lubricating Film Breakdown in Mechanical Seals," ASME Public. TRIB-7, Emerging Technologies for Machinery Health Monitoring and Prognosis, 1997 ASME Mechanical Engineering Congress and Exposition, Dallas, November 16-21, 1997.

Anderson, W. B., 1997, "Detection of Lubricating Film Breakdown in Mechanical Seals," M. S. Thesis, Georgia Institute of Technology.

Anderson, W., Salant, R. F. and Jarzynski, J., 1999 "Ultrasonic Detection of Lubricating Film Collapse in Mechanical Seals," *STLE Tribology Transactions*, vol. 42, pp. 801-806 and 54th Annual Meeting, STLE, pp. 99-AM-1, 1999.

Anderson, W., Jarzynski, J, and Salant, R. F., 1999, "Condition Monitoring of Mechanical Seals: Detection of Film Collapse Using Reflected Ultrasonic Waves, *IMechE Journal of Mechanical Engineering Sciences*, accepted for publication.

Salant, R. F., Anderson, W. and Jarzynski, J., 2000, "Condition Monitoring of Mechanical Seals Using Actively Generated Acoustic Waves," *16th International Conference on Fluid Sealing*, BHRG, Brugge, Belgium, accepted for presentation and publication.

Jarzynski, Y., Salant, R. F., Anderson, W. B., "Condition Monitor for a Liquid Mechanical Seal," U.S. Provisional Patent Application, Georgia Tech # 2137PR, November 1, 1999.

Jarzynski, Y., Salant, R. F., Anderson, W. B., "Condition Monitor for a Mechanical Seal, U.S. Provisional Patent Application, Georgia Tech # 2206PR, November 1, 1999.

2.3.2 REAL-TIME MONITORING AND CONTROL OF MECHANICAL FACE SEAL DYNAMIC BEHAVIOR

Co-investigator: Itzhak Green (Georgia Tech)
Visiting Professor: Joshua Dayan (Technion – Israel Institute of Technology)
Graduate Research Assistants: Min Zou (PhD), Cody Casey (M.S.)

OVERVIEW

Noncontacting mechanical face seals are extensively used in centrifugal pumps, compressors, powered vessels, and other high performance rotating machinery. Unpredictable mechanical face seal failure in critical applications may have severe implications. Added maintenance cost attributed to mechanical seal failure is much higher than the cost of just the seal itself. At the inception of this work the exact cause of seal failure as exhibited by higher harmonic oscillations (HHO) was not well understood.

This research has determined that HHO are caused by the intermittent contact between the rotor and the stator (i.e., caused by an excessive relative face misalignment), leading to this harmful failure mode. Then, once such failure has been detected corrective measure have been implemented via active control to alter the system dynamics and eliminate the damaging behavior. Particularly, the techniques of monitoring, identification, and control developed in this research can be applied to water seals in Naval chillers, as well as other application that critically need to be monitored to increase their reliability and reduce maintenance cost. It is emphasized that since contact is determined ad hoc (i.e., phenomenologically) the technology developed here can be applied equally well to mechanical seals for compressible (gas/air) or incompressible (liquid) fluids.

In addition, the existing mechanical face seal monitoring system has been utilized as a multi-fault monitoring system to also detect the presence of a transverse crack in the shaft upon which the seal is riding. A monitoring system that has the ability to detect multiple types of system failure has significant advantages including lower cost and simplification of the overall system.

OBJECTIVES

This research consisted of two objectives:

(1) A Mechanical Seal Monitor

The objective here is to monitor and control the dynamic behavior of a noncontacting mechanical face seal having a flexibly mounted rotor in a seal test rig (see Figure 1). In particular, the research focuses on detecting and controlling the contact between the rotor and stator that may cause severe face wear and imminent seal failure. The condition monitoring system consists of three eddy current proximity probes and a universal controller board connected to a personal computer. The dynamic behavior of the noncontacting mechanical seal is monitored on-line. The monitoring system can display the orbit of the rotor angular misalignment in real-time where the shape of the orbit gives an indication of the seal dynamic behavior. Key dynamic parameters, such as seal clearance and relative angular misalignment between the rotor and the stator have been chosen to be monitored. Contact between the rotor and stator is detected by a combination of relative angular misalignment and seal clearance. A dominant indication of contact is the presence of higher harmonics oscillations, which are integer multiples of the rotating shaft speed. The monitoring system can detect seal contact during operation using orbit plots and signal processing, and suppress contact by incorporating an active control strategy. The control strategy is to eliminate contact between the rotor and the stator by adjusting the seal clearance. This is achieved by controlling a pneumatic air pressure in the rotor chamber, which governs the closing force. The fluid film stiffness and damping coefficients change with the clearance, thus a change in the clearance causes changes in the rotordynamic responses in both angular and axial modes.

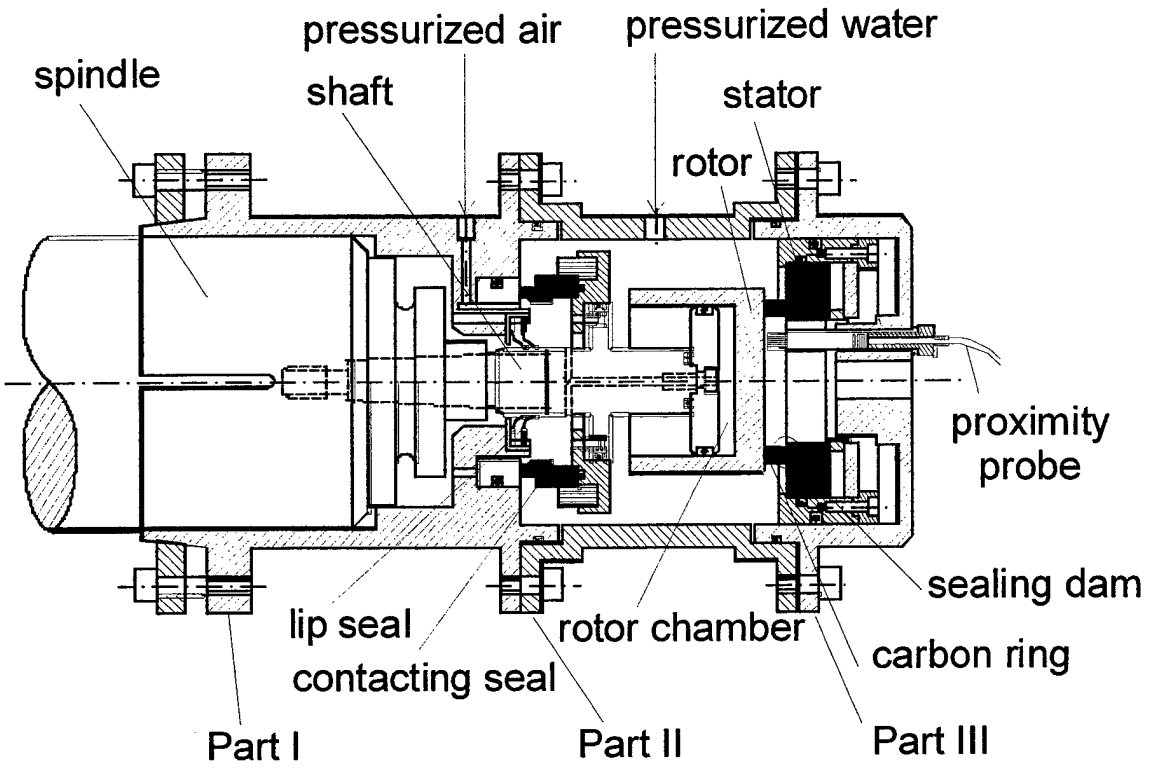

Figure 1. Schematic of the FMR noncontacting mechanical seal assembly

The seal clearance and the instantaneous rotor response are determined from signals of three eddy-current proximity probes. Contact is determined phenomenologically from pattern recognition of probe signals and their power spectrum densities as well as angular misalignment orbit plots, all calculated and displayed in real-time. The contact elimination strategy is experimentally investigated for various values of stator misalignment and initial rotor misalignment. Contrary to intuition, but compliant with the results of a parametric study, the experimental results show that for the seal under consideration contact can be eliminated through clearance reduction.

An experimental test rig has been built to study the dynamic response of a flexibly mounted rotor (FMR) mechanical face seal. This rig is being used to study higher harmonic oscillations because they have been detected under various operation conditions. Mechanical face seal designed to operate in a noncontacting mode, may experience abnormal HHO, thus indicating the presence of rubbing contact between the rotor and stator. It is this contact that leads to face wear which obviously must be avoided. The seal system operates under the balance of the opening force and the closing force. The seal pressure drop provides the opening force across the sealing interface, while the sealed hydraulic pressure, the initial spring compression, and the air pressure in the rotor chamber provide the closing force. Initially the air pressure was set manually by a pressure regulator and was not automatically controlled. Subsequently an electro-pneumatic transducer automatically adjusted the pneumatic pressure in the rotor chamber, and thus adjusted the closing force acting on the flexibly mounted rotor. The monitoring system based on the eddy-current proximity probes and a flow meter has been used to monitor the rotordynamic behavior and detect the presence of HHO. The flow meter outputs a voltage that is proportional to the flow rate. Ultimately a control algorithm on the closing force was incorporated. Once contact was detected the control system altered the system dynamics to reduce the relative misalignment between rotor and stator for maximum reduction of HHO.

(2) Crack Detection in Seal Driving Shaft[1]

As rotating machinery is designed to operate at higher mechanical efficiency, operating speeds, power, and loads are increased as weight and dimensional tolerances are decreased. The result is a significantly increased level of operating stress in modern rotating machinery. As a consequence of this increased stress level, many practical rotor dynamic systems contain shaft/rotor elements that are highly susceptible to transverse cross-sectional cracks due to fatigue. Vibration monitoring of rotating machinery has become common practice in many industries involving turbines, generators, pumps, and other types of rotating systems. Various types of transducers and monitoring systems are utilized by operators to measure, monitor, and diagnose system faults such as shaft out-of-balance or misalignment, damaged roller bearings, loose bearings, oil film whirl, damaged gear or belt drives, etc.

Early detection of mechanical malfunction is essential. Not only can a catastrophic failure be avoided, given adequate warning of plant failure, arrangements for equipment repair or replacement can be made and efficiently carried out to minimize the amount of time the machine is off-line. Vibration monitoring also has the significant advantage of usually requiring no disassembling of the system components. On-line methods can be implemented without even taking the system out of use. A monitoring system that has the ability to detect multiple types of system failure has significant advantages including lower cost and simplification of the overall system. This work explores the feasibility of utilizing an existing seal monitoring system to detect an additional type of system fault, in particular the presence of a crack in the seal-driving shaft.

The existing monitoring system has the ability to detect seal face contact in a flexibly mounted rotor (FMR) mechanical face seal, by directly monitoring the dynamic response of the rotor, and eliminate or reduce the severity of the contact with real-time active control. The primary objective of here is to explore the feasibility of utilizing the existing mechanical face seal monitoring system to detect a transverse crack in the shaft of the test rig. This research has focused on developing a fundamental understanding of and detecting a shaft crack in the system using the existing seal monitoring system. Ultimately, crack detection results could be used in conjunction with the seal face contact detection results to develop a multi-fault detection system.

To accurately predict the response of a system to the presence of a transverse crack, an appropriate crack model is essential. Once the crack is included in the system model, unique characteristics of the system response can be identified and attributed directly to the presence of the crack. These predicted indicators then serve as target observations for the monitoring system.

This research utilizes a global asymmetry crack model in a continuous representation of the system as well as a gaping crack model in a discrete representation of the system. The theoretical analyses focus on the prediction of the behavior of an induced 2X component in the system response. The global asymmetry crack model analysis approximates the stiffness of the cracked shaft with the stiffness of a shaft whose cross-section, for the entire length of the shaft, is identical to the uncracked cross-section at the location of the crack. The local asymmetry crack model utilizes a transfer matrix method to discretize the system so that the additional flexibility introduced by the presence of the crack is localized along the axis of the shaft. Free and forced response analyses were used to identify characteristics of the system response that can be directly attributed to the presence of a crack in the shaft of the system.

The free response analyses yield plots of the natural (whirl) frequencies of the system as a function of shaft speed for various crack depths. Plots obtained for both crack models show the natural frequencies of the system as a function of the shaft speed for crack depths up to 40% of its diameter. Shaft speeds at which a resonance type behavior in the 2X harmonic component of the system response can be predicted from these free response analyses. The decrease in the 2X resonance shaft speeds for an increasing crack depth indicates a decrease in the natural frequencies of the system, and can serve as a first indicator of a crack in the shaft of a system.

---

[1] This second objective was not part of the original proposal. It was added to the work upon accomplishing the objectives stated in objective (1) towards end of year 4.

Then the forced response analyses provide a prediction of the behavior of the magnitude of the 2X component of the response of the system. Analysis reveals a decrease in 2X resonance speeds for increasing crack depth, as well as an increase in the magnitude of the 2X component at resonance. These behaviors of the system forced responses are predicted to serve as second indicators of a shaft crack in the system.

In the seal experiments the shaft was made particularly stiff to monitor the behavior of the flexibly mounted seal alone. Here experiments were performed utilizing a modified test rig and a manufactured crack to verify the predicted behavior of the 2X harmonic component of the system response. The shaft was made slender (i.e., flexible) but the rotor was rigidly attached to the shaft. Since higher harmonic components of the system response are always present in a realistic system, the behavior of the 2X component of the system response is experimentally obtained for uncracked and various cracked cases so that relative changes in system response components can be observed. A single shaft was used in the experiments. The crack was incrementally deepened incrementally (using EDM at width of 0.3 mm) for each data set up to 40% of the shaft diameter.

The experimental results qualitatively confirm the behavior of a meaningful 2X harmonic component of the response of the cracked system that was predicted in the theoretical analyses. The decrease in 2X resonance speeds for increasing crack depth, as well as an increase in the magnitude of the 2X component at resonance could clearly be observed.

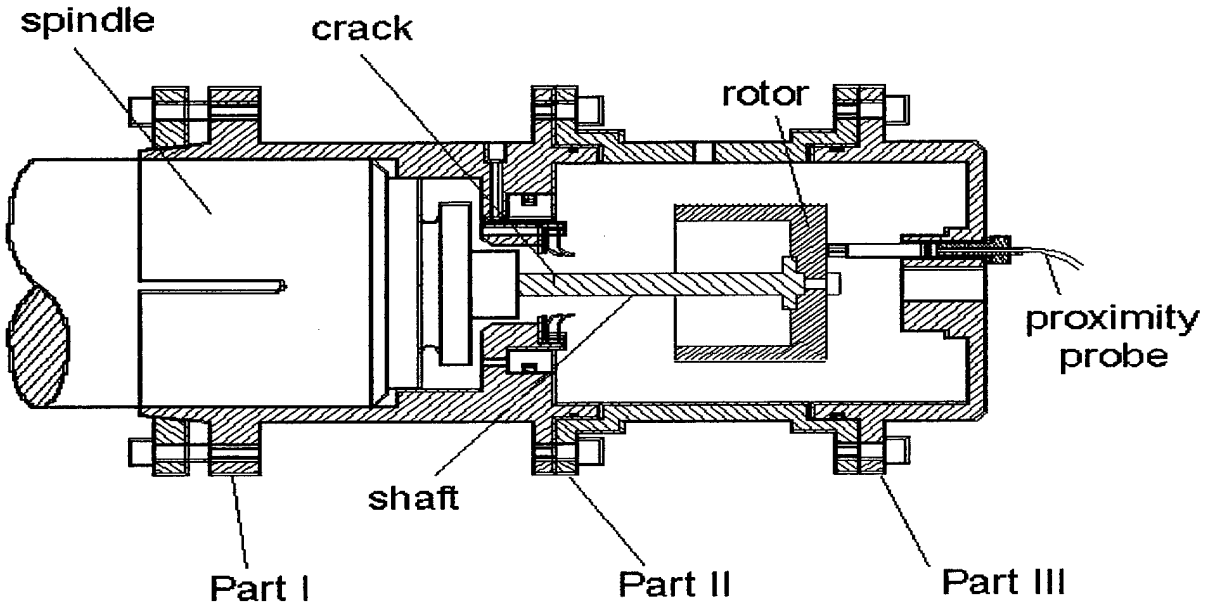

Figure 2. Schematic of a cracked shaft in the same mechanical seal assembly.

ACHIEVEMENTS

a. Dynamic Simulation and Monitoring of a Flexibly Mounted Rotor Face Seal

The rotordynamics has been investigated through both, simulation and real-time monitoring. Dynamic simulation has been performed to investigate the seal rotor angular response to the stator misalignment, the stator angle, the initial rotor misalignment, and clearance. Rotor angular response orbit has been introduced, capable of characterizing the rotor dynamic response. A real-time monitoring system has been constructed in the test rig to monitor the instantaneous dynamic behavior of the seal rotor including its angular response, precession angle, and angular response orbit. Experimental results agree well with those of the dynamic simulation.

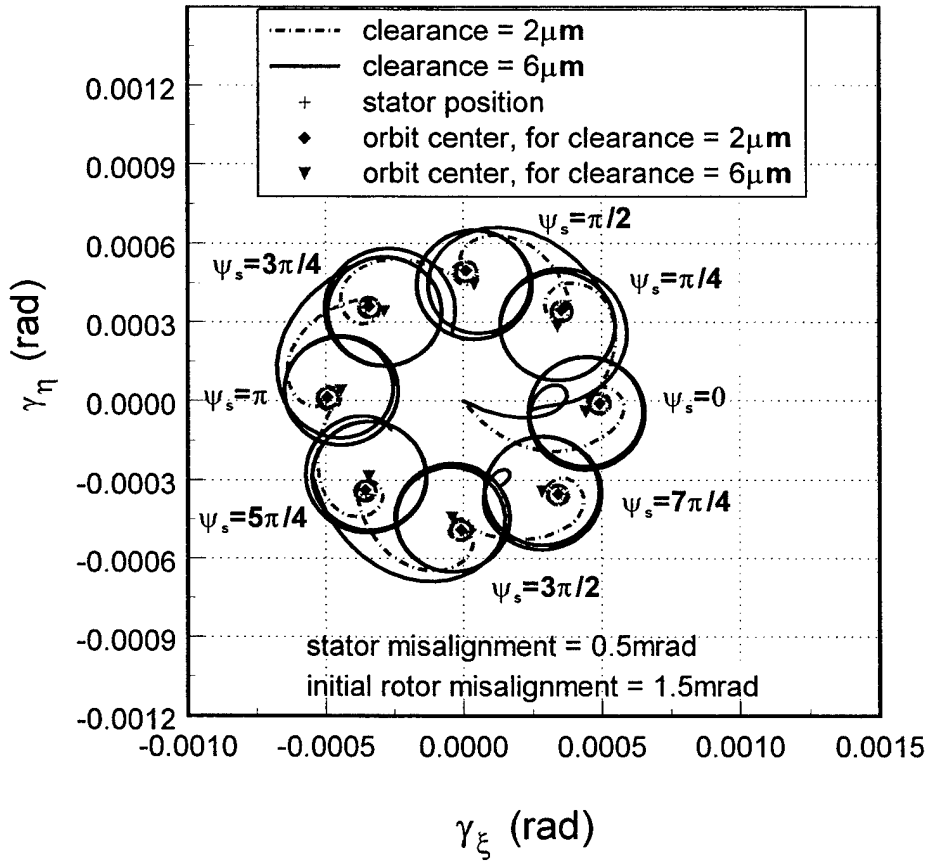

Figure 3: Simulated rotor angular response orbits at various stator angles, for two seal clearances.

The ability for the rotor to track the stator misalignment, γ_s, and stator angle, ψ_s is investigated. The stator misalignment (in this example) is set to 0.5 mrad. The initial rotor misalignment is arbitrarily set to 1.5 mrad, a value that is different from stator misalignment. These values are typical for real seal applications. In reality the stator angle is fixed but it can assume any value between 0 and 2π. Therefore, in the simulation the stator angle is checked for different values between 0 and 2π, at $\pi/4$ steps, every 0.2 s intervals, and for two different clearances, 2 μm and 6 μm. The simulation results are plotted in Figs. 3, which shows the rotor angular response orbit as it changes with various stator angles and two clearances. The simulation starts at the origin, $\gamma_\xi = \gamma_\eta = 0$. The steady-state rotor angular response orbit is a circle

centered at the point whose polar coordinates are the mean value of the rotor misalignment (the magnitude) and the mean value of rotor precession (the angle). This point, for the parameters investigated here, is close to another point whose polar coordinates are the stator misalignment and the stator angle, ψ_s. The distance between the two points depends on various seal parameters, such as, clearance, the smaller the clearance the smaller the distance. The mean value of the rotor misalignment is γ_{rs}. The variation of the rotor misalignment about its mean value is γ_{rl}. The simulation is shown as a continuous plot, however, each orbit represents a specific condition. This will now be shown to correlate well with the monitoring results from specific experiments.

Because clearance is a very important parameter in seal operation, its effect on rotor response is further investigated. Figs. 4a – 4c show the simulation results for stator misalignment of γ_s=0.5 mrad, while Figs. 5a –5c show the simulation results for γ_s=1.5 mrad. The chosen values of ψ_s for the simulation match those of the experimental results, which follow later. The simulation results are plotted for two different initial rotor misalignments, 0.5 mrad and 1.5 mrad, at six clearances ranging from 1 μm to 6 μm. The clearance is changed at time intervals of 0.2 s, in a scheme that can be implemented physically in the test rig for the purpose of clearance control (accomplished and described subsequently).

It can be seen from Figures 4a and 5a that the ability of the rotor precession angle, ψ_r, to follow the stator angle, ψ_s, varies with clearance. The precession angle better adapts to the stator angle and results in smaller oscillation amplitude as the clearance decreases. The precession angle amplitude also depends on the initial rotor misalignment, the smaller the initial misalignment the smaller the amplitude. By comparison it can be seen that when the stator misalignment is smaller (Fig. 4a), the rotor precession angle tracks the stator angle closer but with a larger amplitude.

Similar conclusions can be drawn from Fig. 4b and Fig. 5b for the rotor misalignment, γ_r. This misalignment better adjusts itself to the stator corresponding misalignment of γ_s = 0.5 mrad or 1.5 mrad, when γ_s is smaller. The oscillation amplitudes decrease with the clearance. The amplitudes also depend on the initial rotor misalignment, γ_{ri}, where the smaller the initial misalignment the smaller the amplitude. Comparison of Fig. 4b and Fig. 5b also shows that when the stator misalignment is smaller (Fig. 4b), the rotor misalignment tracks the stator misalignment more closely. The amplitude of the rotor misalignment is essentially the same for both values of stator misalignment.

Fig. 4c and Fig. 5c show the rotor angular response orbits for the two stator misalignments of 0.5 mrad and 1.5 mrad, respectively, at two different initial rotor misalignments, 0.5 mrad and 1.5 mrad, and six clearances. For both initial rotor misalignments cases shown, the radius of the orbit decreases when the clearance decreases. While the loci of orbit centers is not shown in the figures, the results are such that when the clearance decreases the center of the orbit also moves towards the point whose polar coordinates are the stator misalignment and the stator angle. An interesting phenomenon is that when the initial rotor misalignment is equal to (or close to) the stator misalignment, i.e., γ_{ri} = 0.5 mrad in Fig. 4c, and γ_{ri} = 1.5 mrad in Fig. 5c, the rotor response orbits for different clearances pass through a common point. Therefore, for practical monitoring purposes dynamic responses that pass through the same point indicate that the stator and initial rotor misalignment are close to each other.

The monitoring system

Three eddy current proximity probes mounted on the end of the housing are used to detect the instantaneous dynamic response of the rotor. These proximity probes have a bandwidth of about 10 kHz. They can measure the static and dynamic distances between their tips and the rotor end surface. A low pass filter with a cut-off frequency of 1 kHz is used to eliminate high frequency cross-talk noises among the probes and also to serve as an anti-aliasing filter. The maximum output of each proximity probe is -24 V. A voltage divider is used to drop the maximum amplified voltages of the proximity probes outputs from -24 V to -10 V. The reduced voltages are then sent into a universal board that is mounted in a personal computer. The board has a floating-point Digital Signal Processor (DSP). The DSP has been supplemented by a set of on-board peripherals, such as analog to digital (A/D) and digital to analog

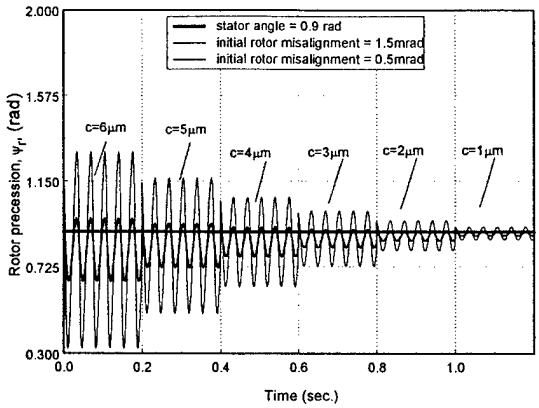

Figure 4a. Simulated rotor precession vs. time for changes in seal clearance.
Stator misalignment= 0.5 mrad, stator angle = 0.9 rad, initial rotor misalignment = 0.5 mrad and 1.5 mrad.

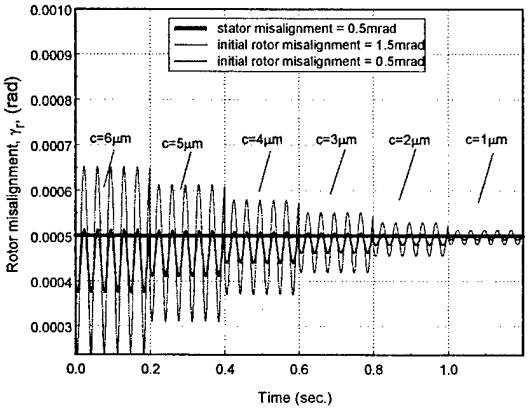

Figure 4b. Simulated rotor misalignment vs. time for changes in seal clearance.
Stator misalignment = 0.5 mrad, stator angle = 0.9 rad, initial rotor misalignment = 0.5 mrad & 1.5 mrad.

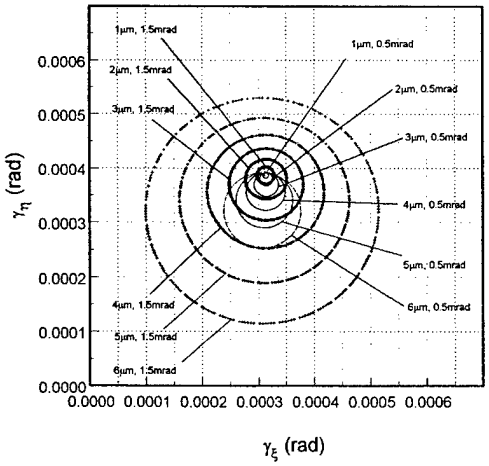

Figure 4c. Simulated rotor angular orbit plot for changes in seal clearances.
Stator misalignment = 0.5 mrad, stator angle = 0.9 rad, initial rotor misalignment = 0.5 mrad & 1.5 mrad.

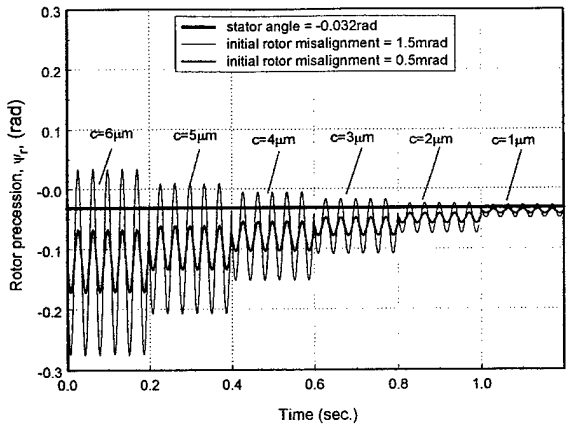

Figure 5a. Simulated rotor precession vs. time for changes in seal clearance. (Stator misalignment = 1.5 mrad, stator angle = -0.032 rad, initial rotor misalignment = 0.5 mrad & 1.5 mrad)

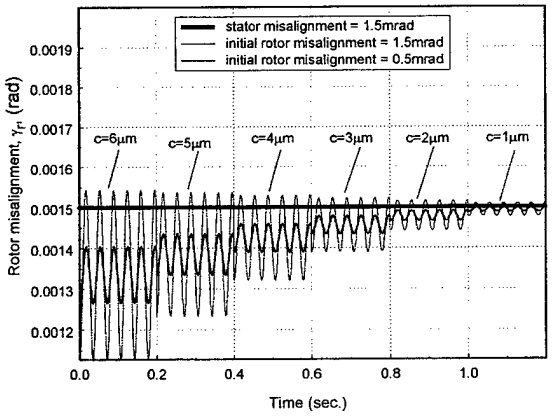

Figure 5b. Simulated rotor misalignment vs. time for changes in seal clearance (stator misalignment = 1.5 mrad, stator angle = -0.032 rad, initial rotor misalignment = 0.5 mrad and 1.5 mrad)

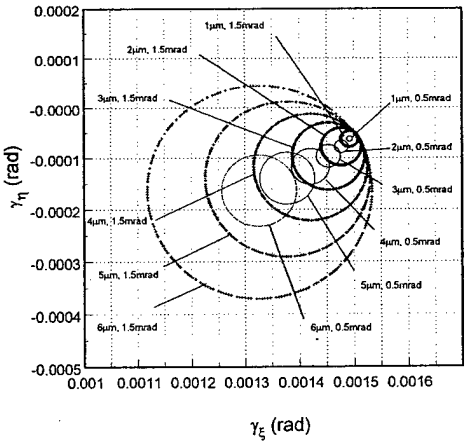

Figure 5c. Simulated rotor angular orbit plot for changes in seal clearances (stator misalignment = 1.5 mrad, stator angle = -0.032 rad, initial rotor misalignment = 0.5 mrad and 1.5 mrad)

(D/A) converters. The proximity probe signals are obtained through the A/D converter of the board. A flow meter is also used to measure the leakage of the seal. The proximity probe signals and leakage measurement are then processed by the on-board DSP and the results are sent to the computer in real-time for on-line display or for data recording. Key dynamic parameters, such as the rotor misalignment, the rotor precession angle, the rotor angular response orbit, and the clearance are monitored.

Real-time Monitoring

The sealed water pressure is set to 345 kPa, and the shaft speed is 28 Hz. The graphite stator in the stator assembly is deformed to provide a coning angle of 1 mrad. The monitored parameters are the same as those in the dynamic simulations, i.e., the rotor misalignment, the rotor precession angle, and the rotor angular response orbit. Two sets of experimental results are described in Figures 6 and 7. These are then compared qualitatively with the simulations of Figures 4 and 5, respectively.

The first set of experimental results for four different clearances are presented in Fig. 6. The procedure for taking experimental data is: setting the air pressure in the rotor chamber to 27.6 kPa, running the shaft at 28 Hz and recording the monitored data; repeating this procedure by incrementing the air pressure (by approximately 14 kPa) to 41.4kPa, then 55.2 kPa, and lastly 69.0kPa. From the leakage measurement (see Fig. 6e) the clearances are calculated to be 6μm, 2.8μm, 1.5μm, and 0.5μm, respectively. Also, from the three proximity probe signals (Fig. 6d) the stator misalignment and angle are calculated to be 0.5 mrad, and 0.9 rad, respectively. The second set of experimental results is obtained by the same procedure (Fig. 7). This time, however, tests are conducted for six decreasing clearances from 6μm to 1μm, in increments of 1μm. Again, Fig. 7e depicts the clearances as calculated from the leakage measurement. Fig. 7d shows the three proximity probe signals from which the stator misalignment of 1.5 mrad and the stator angle of –0.032 rad (cyclically equivalent to 6.251 rad) are calculated.

As stated, the rotor response is a function of the initial rotor misalignment as well as the stator misalignment. The simulations in Section 2 pertain to the four combinations of stator and initial rotor misalignments of 0.5 and 1.5 mrad. The purpose of the physical testing is to verify the seal dynamic behavior experimentally under similar conditions. However, it should be noted that the initial rotor misalignment is set only once, at the beginning of each set. In the execution of the successive runs for the different clearances the initial rotor misalignment assumes some value affected by both the previous run and the amount of relaxation present in the two O-rings, which form the flexible rotor support. Therefore, the rotor gradually adjusts itself to the stator misalignment and the initial rotor misalignment is not fixed as theoretically assumed, but varies each time the system runs and stops (i.e., between clearance changes). Consequently, only the first run in each set of experiments nearly corresponds to the assumed initial rotor misalignment used in the simulation (γ_{rI}=1.5 mrad for C=6 μm in Fig. 6 and γ_{rI}=0.5 mrad for C=6 μm in Fig. 7). All the other experimental results fit only qualitatively to the simulated ones, exhibiting better dynamic responses because of an effectively decreasing initial rotor misalignment at the beginning of each test. The outcome of which are smaller final rotor misalignments, displaying tighter rotor response orbits.

Figures 6a and 6b depict, respectively, the changes in the rotor precession angle and the rotor misalignment with the clearance. Both the rotor precession angle and the rotor misalignment vary periodically and their amplitude decreases as the seal clearance decreases. A similar behavior is displayed by Fig. 4a and 4b for initial rotor misalignment of 1.5 mrad. The large peak to peak amplitude at the beginning of the operation is due to the large initial rotor misalignment with respect to the stator misalignment (0.5 mrad). As explained, the rotor gradually adjusts itself to the stator misalignment as the clearance decreases and both the rotor precession angle and misalignment amplitudes are also reduced. The mean value of the rotor precession angle approaches the stator angle and the rotor misalignment approaches that of the stator (its behavior becomes similar to Fig. 4b for initial rotor misalignment of 0.5 mrad). The same phenomenon is observed by comparing Fig. 6c with Fig. 4c. They show the rotor angular response orbits for different clearances in both experiments and in simulation. As expected the

orbits approach circular shapes. The smaller the clearance the smaller the orbit size, and the orbit centers approach the point whose polar coordinates are the stator misalignment and the stator angle. At the beginning of the experiment, for the clearance of 6μm, the initial rotor misalignment (presumably 1.5 mrad) is not close to the stator misalignment (0.5 mrad). With the decrease of the clearance at the beginning of each test, the initial rotor misalignment reduces as well. Therefore, the experimental orbits (Fig. 6c) are intersecting having a behavior between the two extremes of the simulated orbits of Fig. 4c. It should be pointed out that the center of the orbit has polar coordinates defined by the average of the maximum and minimum of the rotor misalignment, and the average of the maximum and minimum of the rotor precession angle. These averages eventually approach the point defined by the stator misalignment and stator angle.

Results obtained from the second set of experiments (Fig. 7) are similar in nature, although the stator and initial rotor misalignments are reversed (γ_s=1.5 mrad and γ_{rI}=0.5 mrad for C=6 μm). Again, the rotor precession angle is cyclic and its amplitude decreases as the seal clearance decreases (Fig. 7a). This behavior is qualitatively similar to Fig. 5a for initial rotor misalignment of 0.5 mrad. Likewise, the rotor misalignment is also periodic and its amplitude decreases as the seal clearance decreases (Fig. 7b). Since its behavior is similar to Fig. 5b (for initial rotor misalignment of 0.5 mrad) it may suggest that the initial rotor misalignment is indeed about 0.5 mrad and effectively remains constant between tests (even for smaller clearances). Comparing Fig. 7c and Fig. 5c, shows the resemblance between the experimental orbits and those of the simulation for initial rotor misalignment of 0.5 mrad. Similarly, the clearances calculated from the proximity probe signals (Fig. 7d) match very well (within a few percents) the clearances calculated from the leakage (flow rate) measurements (Fig 7e).

FFT analyses performed on both experimental sets (Figs. 6d and 7d) reveal very minor second higher harmonic components in the eddy current proximity probe signals for all the tested clearances, indicating that there is no contact between the seal faces. Also the similarity between the experimentally obtained orbits and the numerically simulated orbits (the latter are based upon a noncontacting analytical model) further support the conclusion that the seal operates in a noncontacting mode.

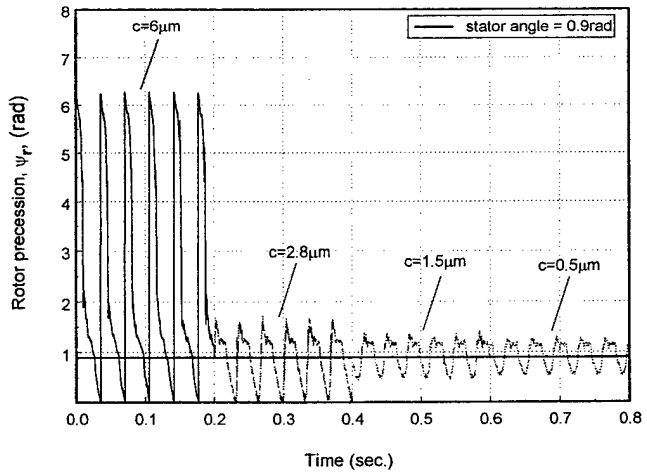

Figure 6a. Experimental rotor precession for changes in seal clearance.
(Stator misalignment = 0.5 mrad, stator angle = 0.9 rad)

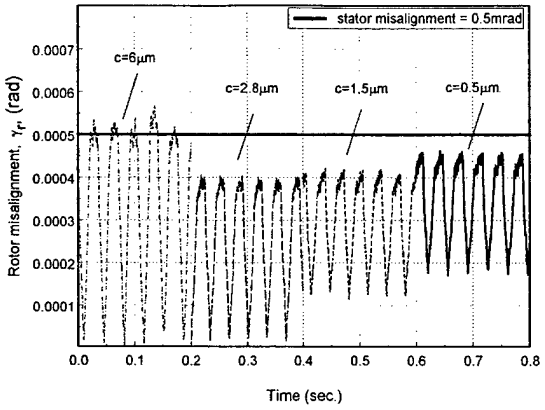

Figure 6b. Experimental rotor misalignment vs. time for changes in seal clearance (Stator misalignment = 0.5 mrad, stator angle = 0.9 rad)

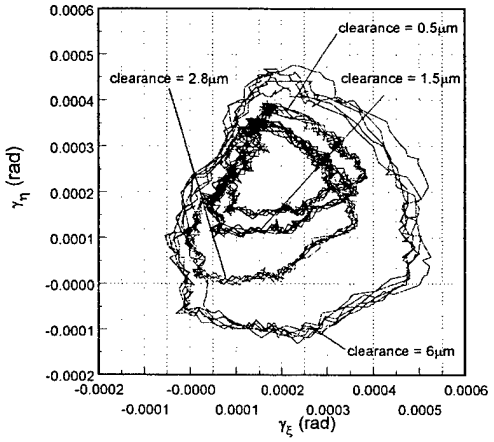

Figure 6c. Rotor angular misalignment orbit changes with seal clearance. (Stator misalignment = 0.5 mrad, stator angle = 0.9 rad)

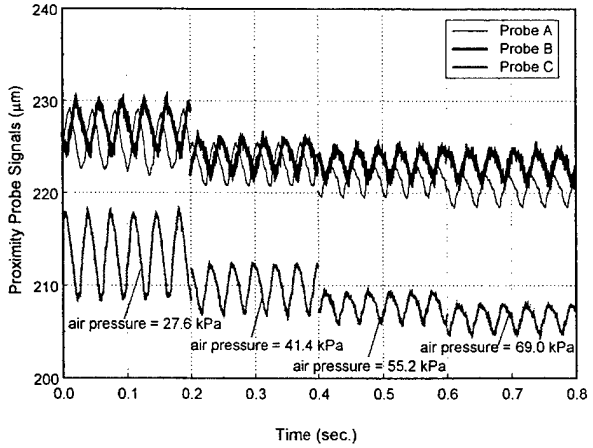

Figure 6d. Proximity Probe signals vs. time (stator misalignment = 0.5 mrad, stator angle = 0.9 rad)

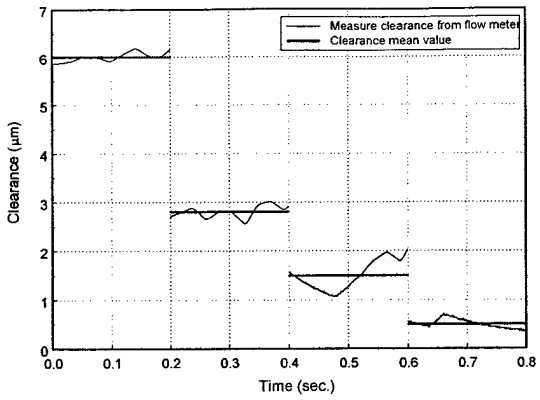

Figure 6e. Clearance measured by flow meter vs. time
(Stator misalignment = 0.5 mrad, stator angle = 0.9 rad)

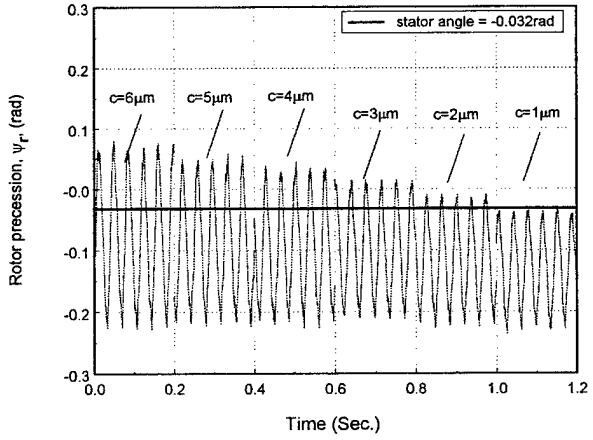

Figure 7a. Experimental rotor precession vs. time for changes in seal clearance.
(Stator misalignment = 1.5 mrad, stator angle = -0.032 rad)

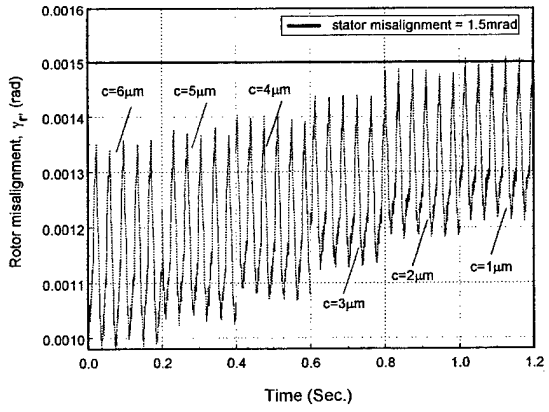

Figure 7b. Experimental rotor misalignment vs. time for changes in seal clearance.
(Stator misalignment = 1.5 mrad, stator angle = -0.032 rad)

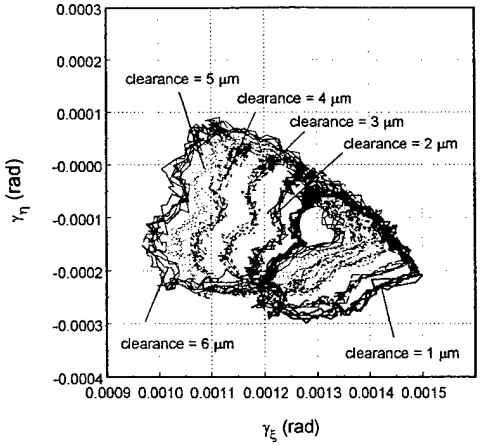

Figure 7c. Rotor angular misalignment orbit changes with seal clearance.
(Stator misalignment = 1.5 mrad, stator angle = -0.032 rad)

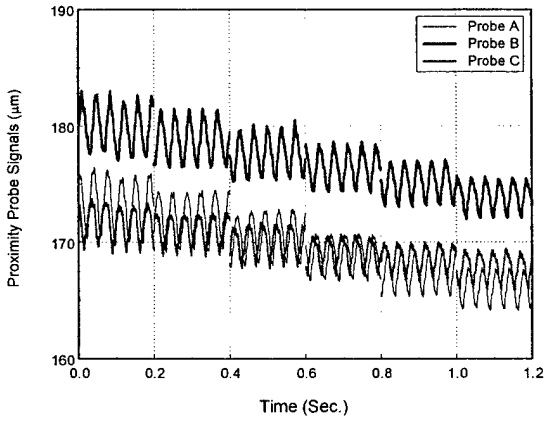

Figure 7d. Proximity Probe signals vs. time (stator misalignment = 1.5 mrad, stator angle = -0.032 rad).

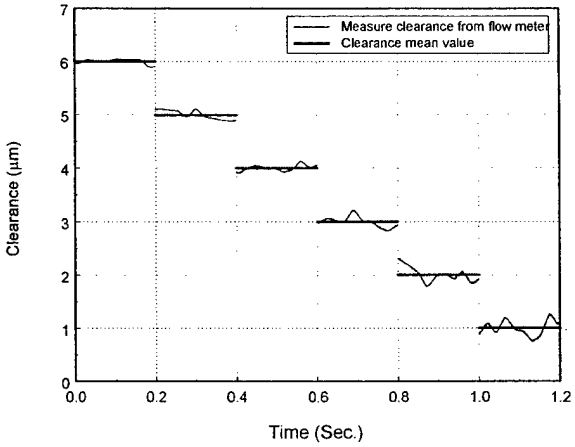

Figure 7e. Clearance measured by flow meter vs. time.
(Stator misalignment = 1.5 mrad, stator angle = -0.032 rad)

Dynamic simulation is performed using the parameters of a noncontacting FMR mechanical face seal test rig. A monitoring system is constructed to monitor the dynamic behavior of the seal in real-time. The similarities between the simulation and monitoring results clearly indicate that the seal dynamic model established captured the major dynamic behavior of the seal. Any subtle differences between the simulation and the monitoring results could have been caused by unavoidable experimental uncertainties, or by the small perturbation assumption made in the development of the analytical model. The fact that the experimental results cover a large range of clearances, which is beyond the small perturbation range, gives more confidence in applying this model to a larger clearance range. The rotor angular misalignment orbit is found to contain information related to the rotor angular response, rotor precession angle, and the stator misalignment and stator angle.

When a seal operates in noncontacting mode the seal rotor dynamic behavior could be better understood by comparing the dynamic monitoring and the simulation results. If contact occurs the monitored rotor response would be visibly different from the simulated response because the simulation is based upon a noncontacting analytical model. It is expected that the sensors signal will be corrupted by noise and vibration generated by the face contact and the misalignment orbit will deviate substantially from the smooth circular one predicted by the simulation for the noncontacting case. Therefore, the monitoring system can potentially function also as a detection system of seal face contact.

A more advanced and proactive step in face seal dynamics is to control the seal rotordynamic behavior and prolong its life. A control system that can take meaningful action based on the real-time dynamic monitoring and contact detection results is now being described.

b. Clearance Control

Seal clearance control is an advancement in noncontacting mechanical face seal operation because seal clearance variation caused by process disturbances may cause either severe face contact or excessive leakage, each of which is regarded as seal failure. The objective of controlling the seal clearance at a desired value overcoming operation disturbances, including variations in shaft speed and sealed fluid pressure, has been accomplished. The clearance control concept is to adjust the closing force that acts upon the flexibly mounted rotor. The seal axial dynamic model has experimentally been determined for the design of a proportional-integral (PI) controller with anti-windup. The controller has been then applied to the test seal. Results have shown that the controlled seal maintains or follows set-point clearance changes with and without disturbances in sealed water pressure and shaft speed (Figure 8). The controlled seal has been shown to respond quickly (having a small time constant) with a small control effort.

c. Feasibility of Contact Elimination through Clearance Adjustment

The feasibility of eliminating contact in a noncontacting flexibly mounted rotor (FMR) mechanical face seal has been studied. The approach for contact elimination is based on a parametric study using FMR seal dynamics. Through clearance adjustment it is possible to reduce the maximum normalized relative misalignment between seal faces and, therefore, eliminate seal face contact. Contact has been determined phenomenologically from pattern recognition of probe signals and their power spectrum densities as well as angular misalignment orbit plots, all calculated and displayed in real-time. The contact elimination strategy has experimentally been investigated for various values of stator misalignment and initial rotor misalignment. Contrary to intuition but compliant with the parametric study, the experimental results have shown that for the seal under consideration contact can be eliminated through clearance reduction. In Figures 9a-9c the time signals and PSD are shown for decreasing values of clearance. It is clear that the synchronous 1X PSD component is increasing, while the HHO (2X, 3X, etc.) are decreasing with the clearance. Such a behavior is desirable because a stronger synchronous 1X component and weaker HHO indicate superior tracking in the noncontacting mode of seal operation.

The orbit plot (Figure 10) is also becoming more organized and closer to circular with a decrease in clearance. This is consistent with a dynamic analysis discussed above.

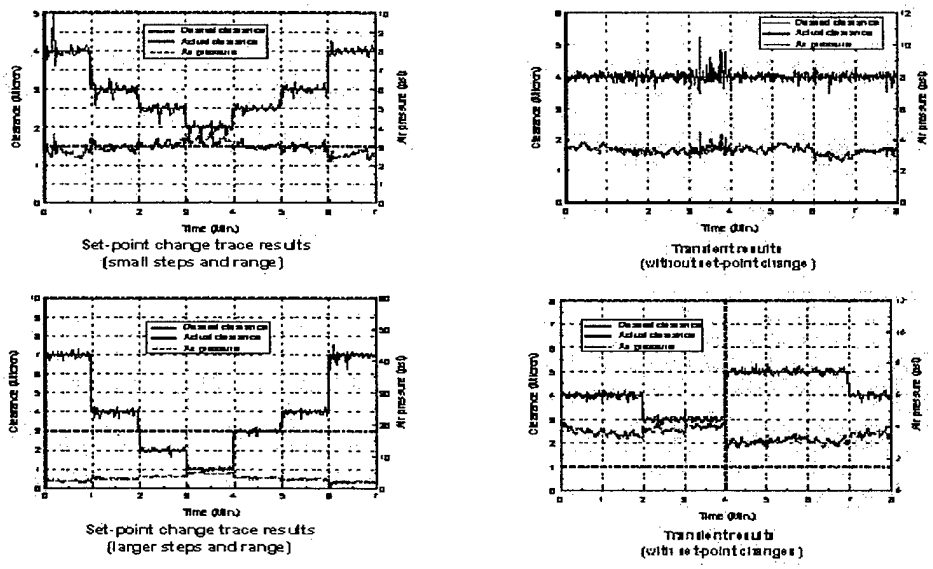

Figure 8. Seal clearance control results.

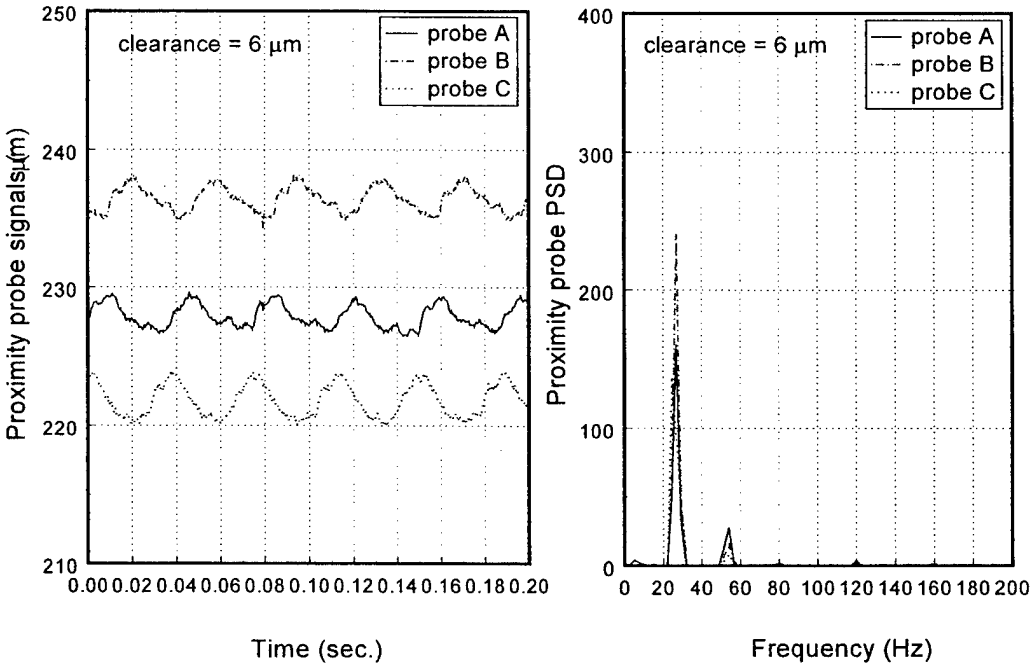

Figure 9a. Proximity probe signals and their PSDs for clearance = 6 μm

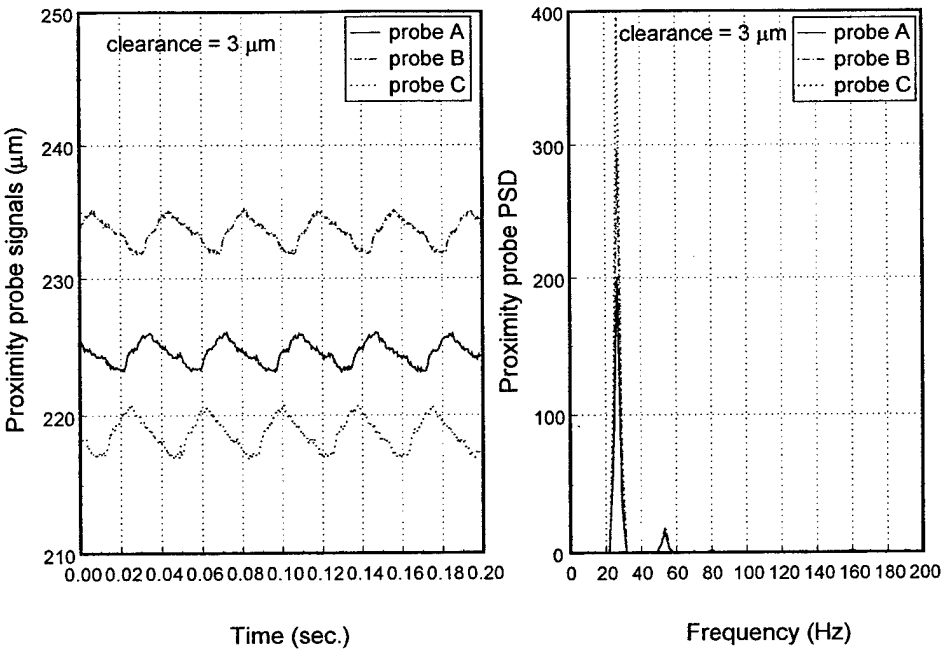

Figure 9b. Proximity probe signals and their PSDs for clearance = 3 μm

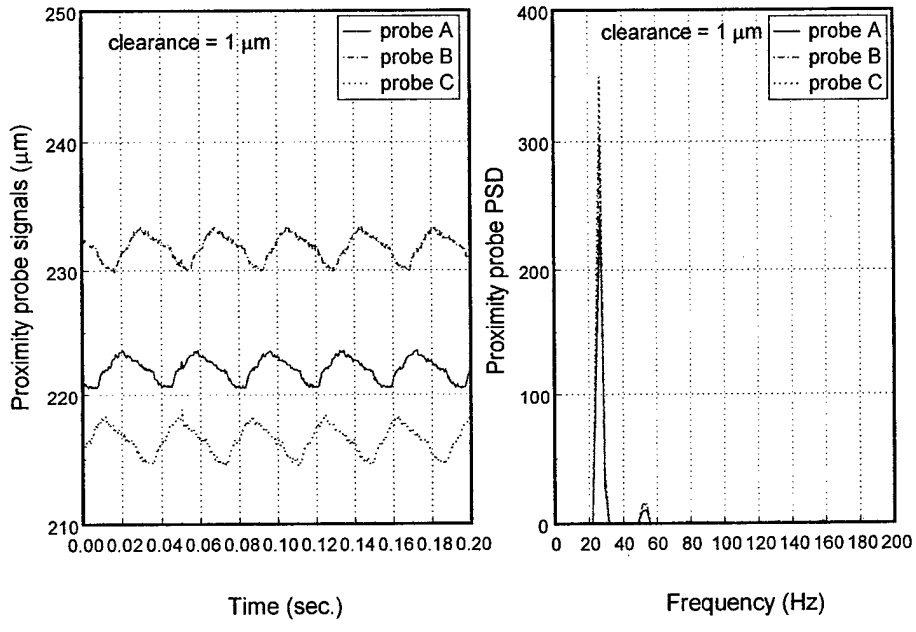

Figure 9c. Proximity probe signals and their PSDs for clearance = 1 μm.

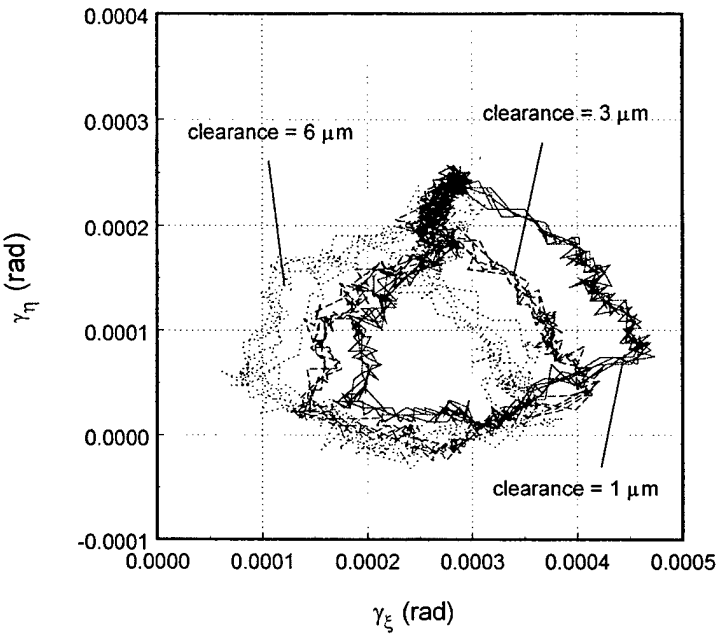

Figure 10. Rotor angular misalignment orbit for different clearances

d. Contact Elimination

The large relative misalignment between seal faces causes the intermittent seal face contact. Controlling seal clearance is the most versatile way of eliminating damaging face contact. A cascade controller that includes two PI feedback control loops has been used. The inner loop is a clearance control loop that maintains a desired clearance set point. Eddy current proximity probes are used to directly measure the seal clearance. Clearance control is accomplished through adjusting the air pressure in the rotor chamber of the seal. The outer loop adjusts desired clearance when contact is detected, i.e., when the variances of the probe signals are different. Experiments have been conducted to test the cascade controller. Results below show that, when coning angle is small (and contrary to intuition) reducing seal clearance can eliminate contact.

Contact elimination results

Experiments are conducted under different stator coning angles, shaft speeds and sealed water pressures, testing if the entire cascade controller is able to eliminate face contact. The results of one of the experiments, where coning angle is 1 mrad, water pressure is 344.8 kPa, shaft speed is 28 Hz, and stator misalignment 2 mrad are plotted in the following set of figures (11-15).

Figure 11 depicts the changes in probe displacement signals obtained when the control is switched on and off. Clearly, the shape and peak-to-peak values of the signals are different for the three probes when control is off but they are almost identical when the control is on.

It is easier to see these differences from the PSDs of the three probes as plotted in Fig.12, for the respective control on and control off cases. The relative misalignment between the rotor and the stator is smaller when the control is on (Fig. 13).

The rotor misalignment orbit, indicating the magnitude of the rotor misalignment positioned at its instantaneous precession angle, is plotted in Fig. 14. The orbit becomes more circular for the 'control on' case, and its center moves towards the point that is defined by the stator misalignment and stator angle.

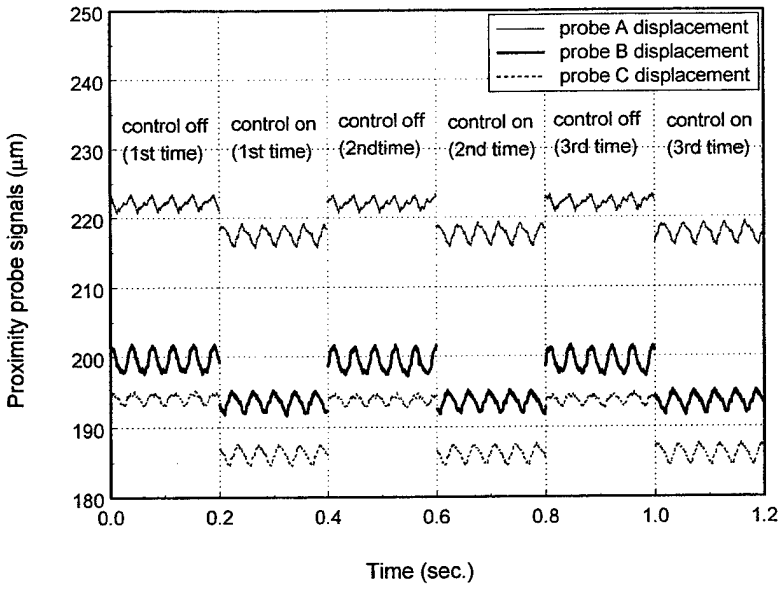

Figure 11. Proximity probe signals when the control is on and off.

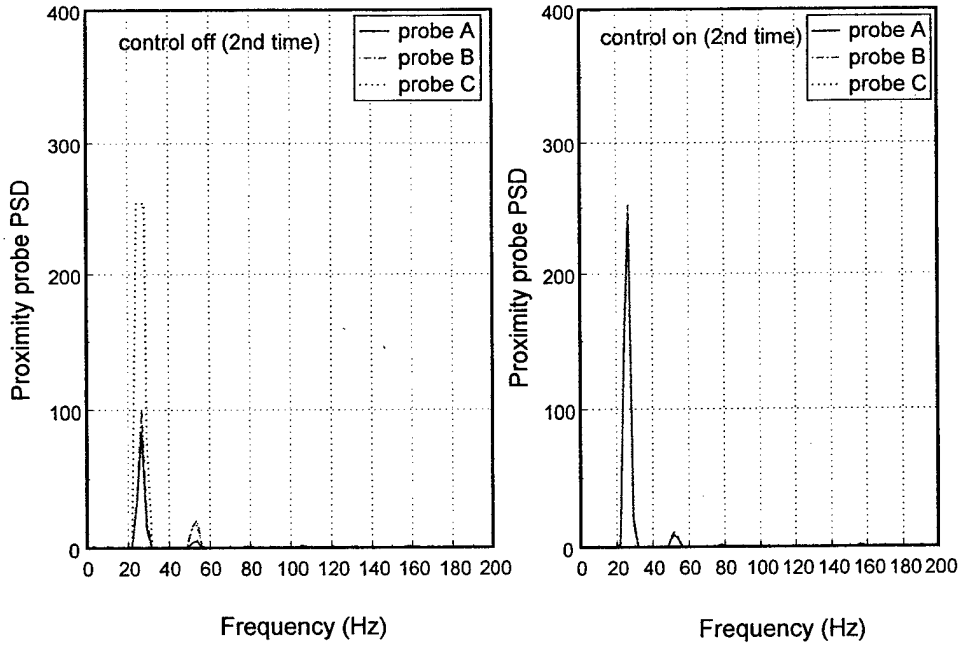

Figure 12. Proximity probe PSDs when the control is on and off.

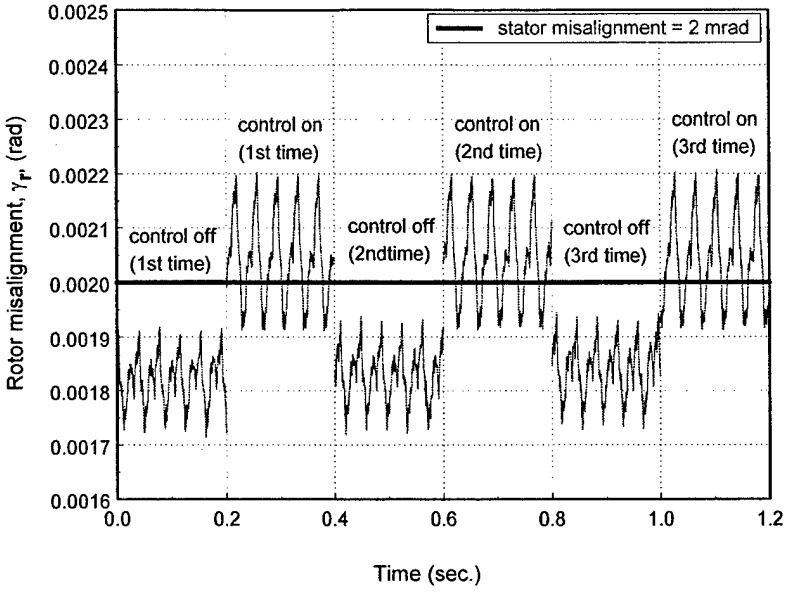

Figure 13. Rotor misalignment when the control is on and off.

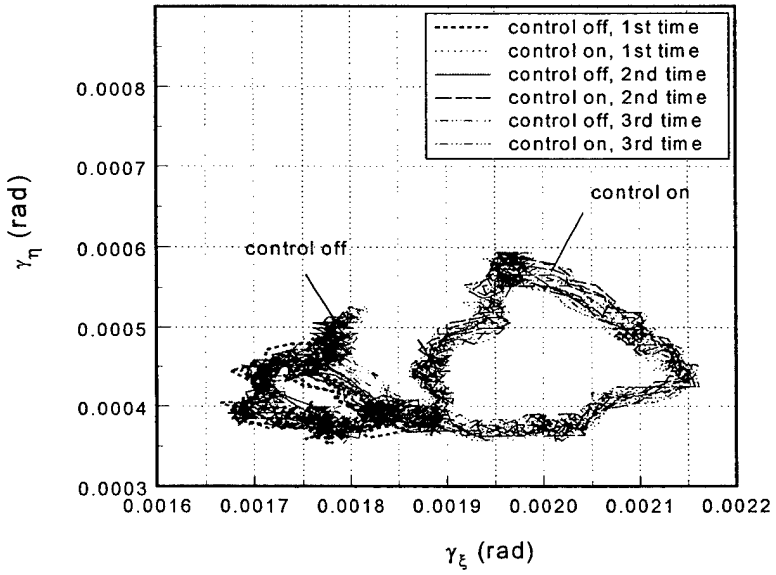

Figure 14. Rotor angular misalignment orbit for control on and off cases.

When the cascade control is 'on' the variance loop drives the system toward better alignment (eliminating the contact), and as can be seen from Fig. 15 it is automatically reduces the clearance. This is an indication that under the tested conditions reducing the clearance does indeed reduce the relative misalignment, as was shown analytically. Figure 15 also shows that clearances calculated from the probe measurements are well correlated and in good agreement with clearances calculated from leakage measurements (assuring that both methods are adequate). The changes in the controller output required (air pressure in the rotor chamber) are very small, demonstrating that the control is well tuned and quite effective.

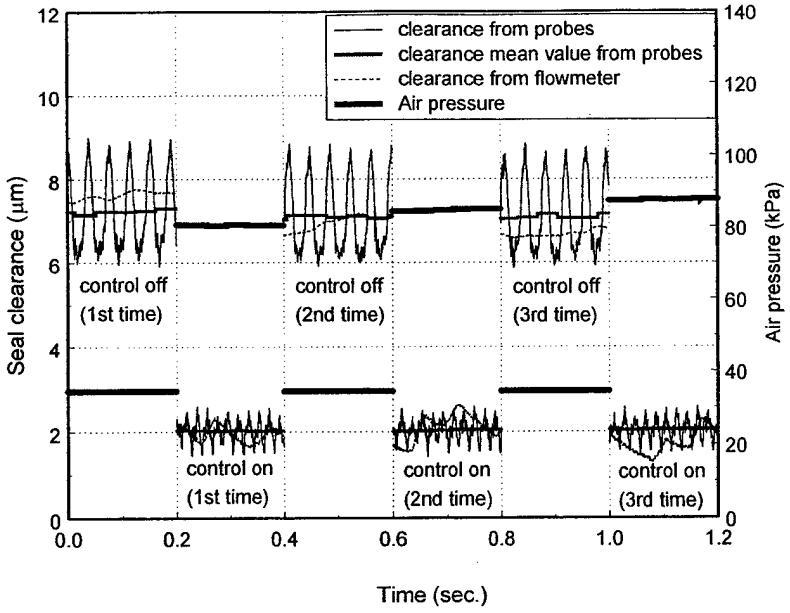

Figure 15. Seal clearance and air pressure when the control is on and off.

The active control is realized by a cascade scheme using two PI control loops. The inner control loop maintains the desired clearance, while the outer loop calculates and dictates the setpoint, based on the contact detecting result. The contact is determined by the appearance of abnormal HHO in the signal of the measured clearance (the output of eddy current proximity probes). These HHO are detected by parameters of the DSP and misalignment orbit for the seal. Once detected, a feedback control loop measuring the probe signal variance differences determines the new target gap, which will eliminate the contact and resume normal noncontacting operations. Also because the leakage is proportional to the clearance cubed, when the control is on the leakage is significantly reduced as well.

In summary, using the proximity probes measurements as feedback in a cascade control loop, interpreting the existence of high harmonics or non-circular orbits as contact, and applying the necessary closing force on the FMR to adjust the clearance, eliminates that contact.

e. Crack Detection

To develop a truly local crack model it is necessary to determine the additional flexibility due to the presence of the crack alone. The additional flexibility can then be represented by its own lumped parameter element. A section of a shaft containing a crack of depth a is shown, under general loading, in Figure 16.

Utilizing the Paris equation and Castigliano's theorem the additional flexibility due to a crack of depth a, can be obtained from the strain energy density function. Using a unique complex extended transfer matrix the forced response is computed as a function of shaft speed. The magnitudes plotted in Figure 17 are the radii of the predicted circular 2X tilt responses. It is clear that for an arbitrary shaft speed, the amplitude of the 2X response is predicted to increase as the crack depth increases.

To generate experimental plots of the magnitude of the 2X component of the system response as a function of shaft speed, within the selected shaft speed ranges, the following methodology was utilized. The shaft speed was incrementally adjusted via the manual motor control. The DS1102 board took a time sample of the probe data. The power spectral density (PSD) of the time data was computed

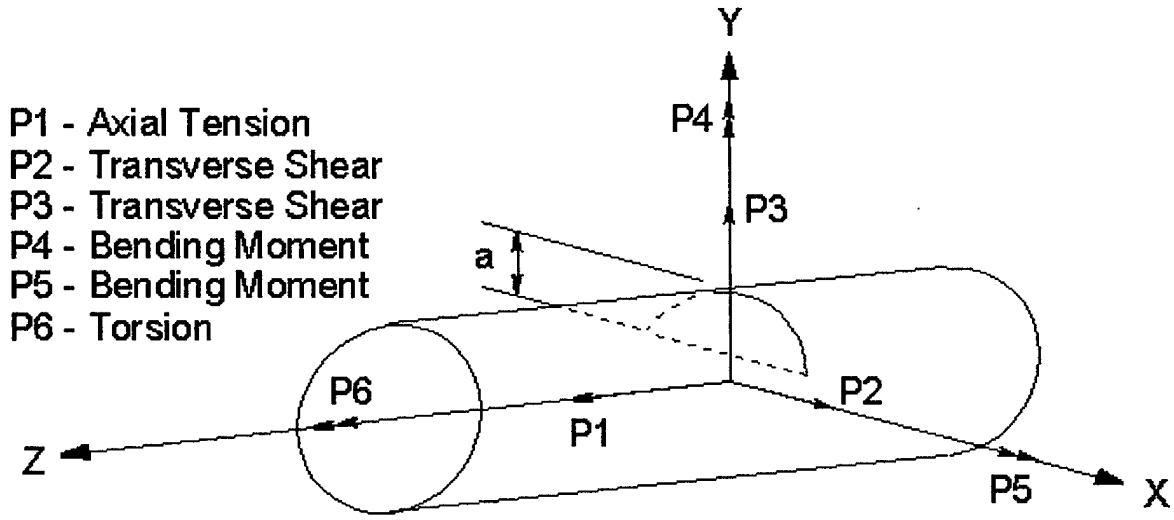

Figure 16. Shaft section containing a crack

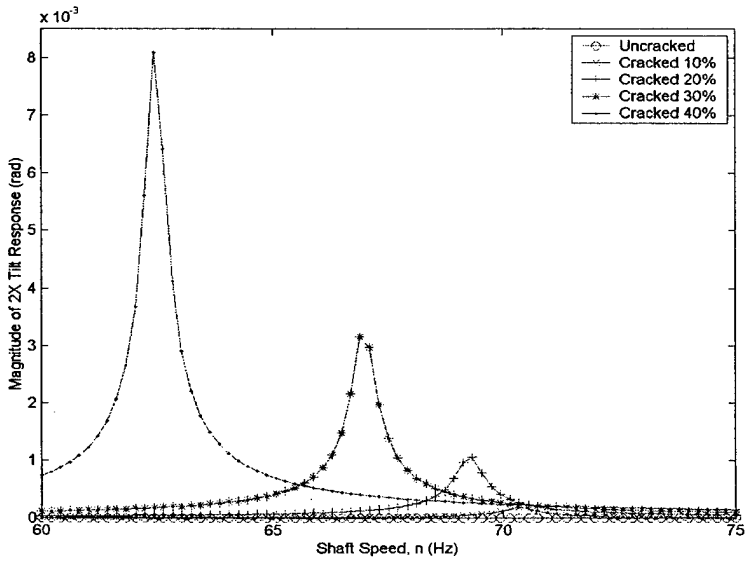

Figure 17. Local asymmetry model forced 2X response.

using Matlab, and the 1X and 2X magnitudes were obtained and stored. This process was repeated over the range of desired shaft speeds for crack depths ranging from 0%-40% of the shaft diameter. A single shaft specimen was utilized in these experiments. The crack depth was incrementally increased for each set of experiments. Figure 18 shows the 2X PSD amplitude of the response provided by one of the probes as a function of shaft speed, for the low and high speed ranges respectively, for crack depths ranging from 0%-40% of the shaft diameter. It is clear from Figure 17 and 18 that the experimental results agree qualitatively quite well with the theoretical model, particularly with the local asymmetry model. Hence, this 2X behavior may provide a strong indication for the presence of a crack.

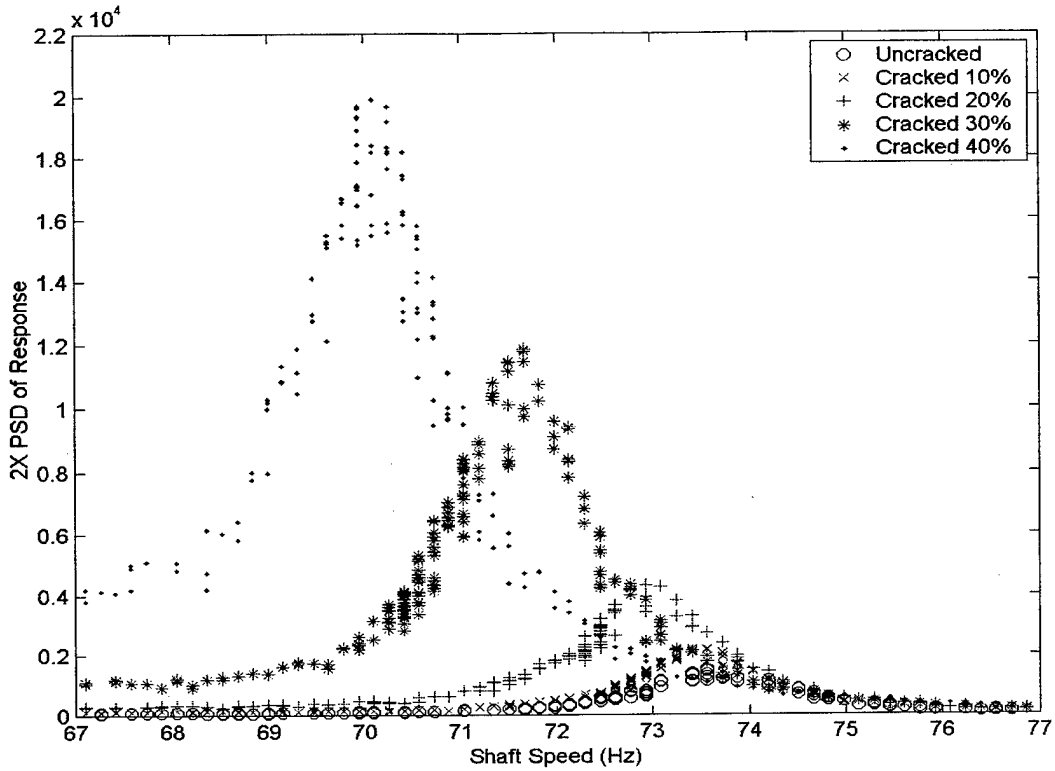

Figure 18. Experimental 2X response.

Tilt Orbit Monitoring

As described above the FMR mechanical face seal monitoring system has the unique capability of obtaining the instantaneous rotor angular response orbit from the signals of the three proximity probes. The predicted behavior of the magnitude of the 2X component of the system response is likewise expected to be experimentally observed. To experimentally observe the effects of the introduction and propagation of the open crack in the crack detection test rig on the 2X component of the time response of the tilt orbit obtained from the monitoring system, the signals are passed through a high pass filter, in the time domain, which removes 1X and lower frequency content. Since, in the absence of contact (the FMR seal is absent), the harmonic components of the signal that are greater than 2X are relatively small, the resulting signal is primarily the 2X harmonic component of the response orbit. Figure 19 shows the 2X content of the tilt orbit, for four depths of the crack near 2X resonance.

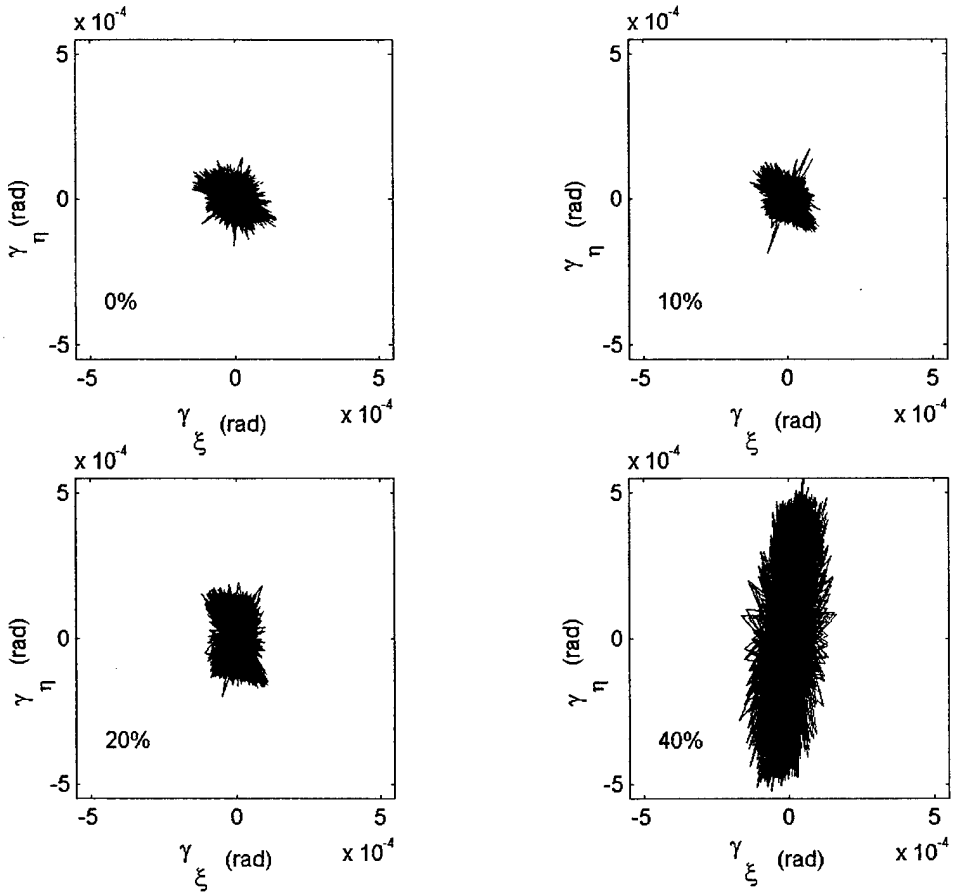

Figure 19. Experimental 2X content of tilt orbit at 71 Hz

In the figure the depth of the crack is indicated, as a percentage of the shaft diameter, in the lower left corner of the axes. It is clear that the increasing crack depth increases the magnitude of the 2X component of the tilt orbit response. The increase in the magnitude of the 2X component of the tilt orbit response is more significant for increasing shaft speeds. The shapes of the 2X component of the tilt orbit responses are not exactly circular.

Since this research is focused on exploring the feasibility of utilizing an existing monitoring system to detect an additional type of system fault, it is important to, at least preliminarily, consider the type of issues that could arise if the monitoring system was used to detect both types of failure simultaneously. The most direct interference that could occur between the two types of fault detection is a scenario in which one type of fault induces a system response characteristic that influences the response characteristic upon which the monitoring system diagnoses the other type of fault. The seal face contact detection system diagnoses contact based on the relative variance between the three proximity probe signals. Any relative variance in the probe signals will manifest itself in the angular response orbit as a non-circular shape. To observe the characteristics of the orbit shape due to the introduction of the crack into the test rig system, the unfiltered angular response orbits of the system are shown in Figure 20 for shaft speeds which are near the respective 2X resonance shaft speeds, and crack depths ranging from 0%-40%. The orbit shapes at these near 2X resonance speeds demonstrate the most significant influence of the presence of the crack on the system.

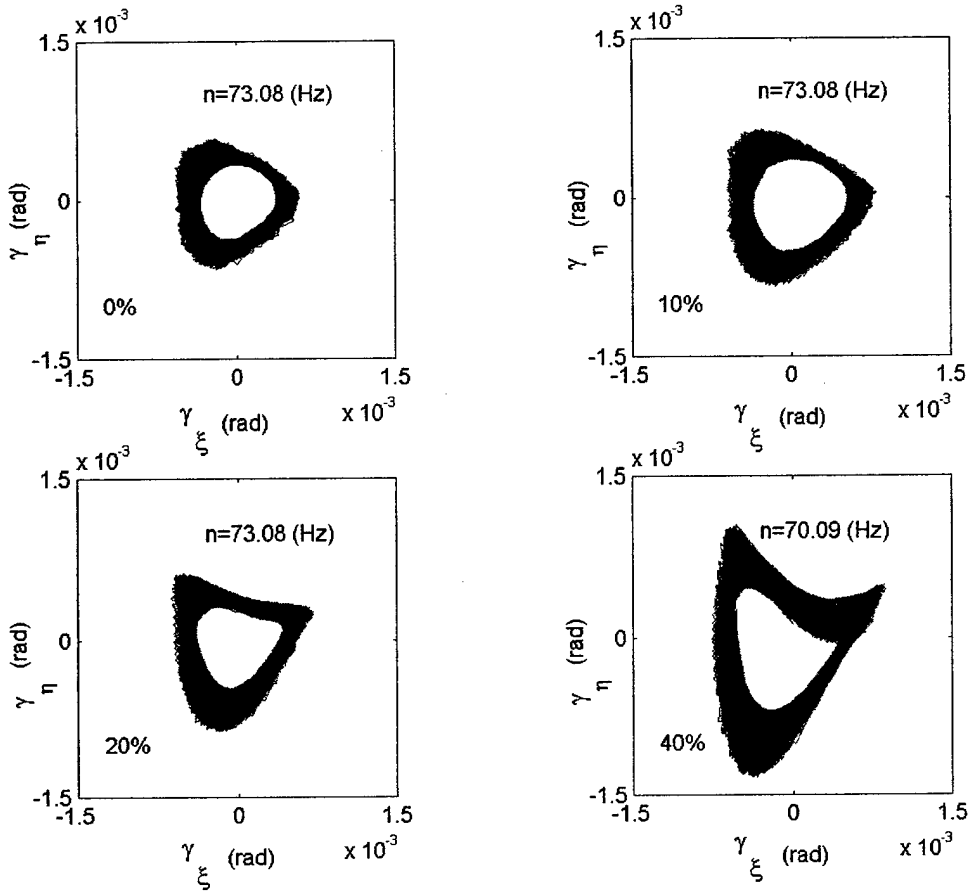

Figure 20. Unfiltered experimental tilt orbit new 2X resonance.

These 2X resonance tilt orbits clearly deviate increasingly from a circular shape, which becomes more non-circular for increasing crack depths. The shapes of the tilt orbits for the sealing system when contact is occurring are mostly circular. By observation (e.g., Figure 10), these orbits are distinctly different than the non-circular tilt orbits for the cracked shaft (Figure 20). The non-circular shape of the 2X resonance tilt orbits indicate that relative variance in the probe signals, which is a target observation of the seal face contact detection system, is induced by the presence of a shaft crack. It has also been shown that higher harmonics, one of which (2X) is a target observation for the shaft crack detection system, are induced by seal face contact. This potential interaction, between a shaft crack and seal face contact detection system, raises some questions regarding interference in a simultaneous multi-fault detection system. However, the relative variance in the probe signals induced by the shaft crack is much less significant at shaft speeds that are not near 2X resonance speeds. Also, the higher harmonic responses induced by seal face contact occur for all integer harmonics, not only at the 2X. Furthermore, the clearly non-circular shape of the angular response orbits at 2X resonance speeds may be useful in differentiating between seal contact and a shaft crack. The specific capabilities of the monitoring system to detect either type of failure, or to discriminate between the two, depends almost entirely on the unique characteristics of the specific system which is under observation.

FUTURE RESEARCH

In this research, a seal monitoring system was used to study both the detection of seal face contact, and the detection of the presence of a crack in a driving shaft. Each phenomenon was investigated separately to isolate the behavior, and understand better the physical processes that occur. It is desirable to install the flexibly mounted rotor seal back into the test rig, where now it would ride upon a cracked shaft. The analysis of this coupled problem will have to be developed, and then experimentally investigated. Monitoring of other machine elements, such as failing gears or bearings, could also be added to such an investigation.

M-URI PUBLICATIONS (REFERENCES)

Zou, M., and Green, I., "Real-time Condition Monitoring of Mechanical Face Seal," Proceedings of the 24th Leeds-Lyon Symposium on Tribology, London, Imperial College, (Sept. 4-6, 1997) 423-430.

Zou, M., and Green, I., "Clearance Control of a Mechanical Face Seal," *STLE Tribology Transactions, STLE Tribology Transactions,* Vol. 42, No. 3 (July 1999) 535-540, (presented at the ASME-STLE Tribology Conference, Toronto, 1998).

Zou, M., Dayan, J., and Green, I., "Parametric Analysis for Contact Control of a Noncontacting Mechanical Face Seal," *Proceedings of Vibration, Noise & Structural Dynamics, 1999*, Venice, Italy, (28-30 April, 1999) 493-499.

Zou, M., Dayan, J., and Green, I., "Dynamic Simulation and Monitoring of a Noncontacting Flexibly Mounted Rotor Mechanical Face Seal," Accepted for publication in the *Journal of Mechanical Engineering Science (IMechE).*

Dayan, J., Zou, M., and Green, I., "Sensitivity Analysis for the Design and Operation of a Noncontacting Mechanical Face Seal," Accepted for publication in the *Journal of Mechanical Engineering Science (IMechE).*

Zou, M., Dayan, J., and Green, I., "Feasibility of Contact Elimination of a Mechanical Face Seal through Clearance Adjustment," accepted for publication is *ASME Transactions*, Preprint 99-GT-147, presented at the ASME Turbo Expo 99' (ASME INTERNATIONAL GAS TURBINE INSTITUTE).

Dayan, J., Zou, M., and Green, I., "Contact Elimination in Mechanical Face Seals Using Active Control" Accepted pending revisions, *IEEE Transactions on Control Systems Technology*, August 2000.

M-URI THESES

Min Zou, "Higher Harmonic Oscillations of Triboelements," Ph.D. Dissertation, Georgia Tech, March 1999 (currently Senior Advisory Development Engineer with Seagate Inc.).

Cody Casey, "Crack Detection in Rotor Dynamic System by Vibration Monitoring," M.S. Thesis, Georgia Tech, June 2000 (accepted position with Schlumberger Inc.).

2.3.3 DYNAMIC METROLOGY AS A BEARING WEAR DIAGNOSTIC

Co-investigators: Steven Liang, Thomas Kurfess, Steven Danyluk (Georgia Tech)

OVERVIEW

Rolling element bearings are of paramount importance to almost all forms of rotating machinery, and are among the most common machine elements. The largest bearing manufacturers, with 26% of the market, sell approximately $3 billion worth of bearings each year. Meanwhile, in order to address the design demands related to miniaturization, decrease of weight, high speed and load in modern industry, bearing service conditions are becoming more severe resulting in a higher probability of failure. Therefore, as a consequence of their extensive use and importance, bearing failures account for a large percentage of breakdowns in rotating machinery. Such bearing failure can be catastrophic.

From the day a rolling element bearing leaves the factory, events take place that reduce its designed running time to as low as tens of hours. There are several reasons that a bearing fails, such as improper storage, improper installation, poor lubrication, harsh operating environment, overload, overspeed etc. Even under normal operating conditions, a bearing will eventually fail due to fatigue. Complete elimination of bearing failure is not possible in practice.

Currently there are two basic methods for bearing maintenance. One is the statistical method of bearing life estimation and the other is bearing condition monitoring. Owing to the fact that rolling contact fatigue is probabilistic, the statistical method, while widely applied by industry, is not necessarily the best practice. This approach has two obvious deficiencies. First, the procedure results in costly machine shutdown and perfectly good bearing replacement. This approach can damage machine components during re-assembly, and perhaps, exchange a bearing with the potential for long life by a new one yielding a shorter life. Second, an abrupt malfunction can occur outside scheduled maintenance hours.

Alternatively, bearing condition monitoring has received considerable attention since the 1980's. The propagation of a rolling contact fatigue spall beyond its initial appearance is a highly variable process. The variation to reach the final failure size, which is commonly defined to be 6.45 mm^2 (0.01 in^2) by industrial standards, from the point where a defect can be detected may be more than the L_{10} life of the bearing. When a defect is detected, it is common to stop the bearing as soon as possible to avoid a catastrophic consequence and perform maintenance. This can be at an inconvenient time. Therefore, it is critical that the remaining life of a bearing be predicted so that bearing replacement can be optimally scheduled. Unfortunately, bearing remaining life prediction techniques with a physical understanding have not been well developed. This is mainly due to a lack of a reliable diagnostic methodology in terms of the probabilistic characteristics of bearing life and the highly variable propagation process of bearing fatigue.

Bearing failure life testing is a valuable way to investigate the mechanism of bearing fatigue from crack initiation, crack propagation to flake or spall. However, like most modern products, bearings are designed to operate without failure for years, tens of years, or more. Thus, life testing at designed conditions is impractical. For this reason, accelerated life tests (ALT) are used widely in manufacturing industries to obtain timely information on the reliability of product components and materials. Data from tests at high stress levels (e.g., temperature, voltage, pressure, corrosive media, etc.) are extrapolated through a physically reasonable statistical model to obtain life estimates at lower, normal stress levels.

OBJECTIVES

The overall objective of this proposed work is to develop a scientific, systematic, and reliable methodology to optimize schedules of bearing maintenance and prevent catastrophic failure of rolling element bearings. The major challenges of this optimization hinge on the capability to reliably assess bearing defect severity under practical operating conditions, on-line, and subsequently predict remaining life in real-time. As stated in the project overview, bearings are characterized by high reliability when their mean time to failure (MTBF) is high, in comparison to other bearings. It is obvious that the

observation of life data within a reasonable time is impractical. Rather, accelerated life tests (ALT) are used widely in manufacturing industries to obtain timely information on the reliability of product components and materials. Therefore, development of an approach to predict or evaluate the life probability of bearings based on accelerated testing data is another important objective. In order to achieve the above objectives, the proposed study includes: 1.) development of new signal processing methods for initial bearing defect detection; 2.) development of effective diagnostic methods to evaluate on-line a defect severity based on signal features of vibration with signal processing techniques; 3.) development of techniques to predict, in real-time, the bearing life in practical operating conditions; and 4.) development of approaches to predict or evaluate the life probability of a bearing based on accelerated test data.

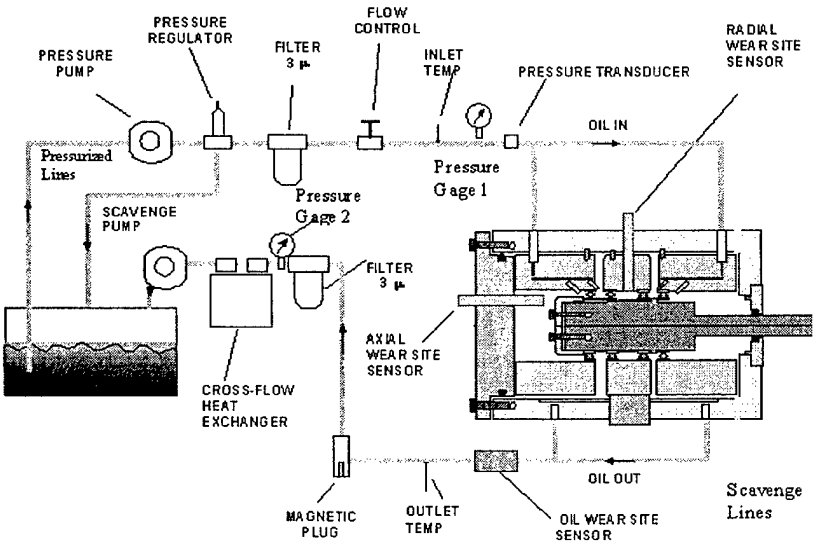

Figure 1. Bearing Test Housing Schematic

ACHIEVEMENTS

a. Techniques of Bearing Defect Detection

HFRT and ALE for Bearing Defect Detection

In the area of initial defect detection of rolling element bearings, the utility of a new signal processing combination of the High Frequency Resonance Technique (HFRT) and Adaptive Line Enhancer (ALE) was investigated. Most difficulties posed in bearing fault detection stem from the presence of a variety of noises and the wide spectrum of a bearing defect signal. Hence, the success of a bearing fault detection method usually hinges on its ability to increase the defect signal to noise ratio. It is known that the energy generated by a defect impacting another surface in a bearing manifests itself in the system resonance. The HFRT takes advantage of the large amplitudes of these defect signals in the range of a high resonant frequency, and provides a demodulated signal with a high defect signal to noise ratio. This also aids in reducing the presence of low frequency mechanical noise. Next, the ALE routine was applied to the demodulated signal. It utilized the signal itself and a delayed version of the signal as a reference input to the adaptive filter. An error sequence was then generated and fed back to adjust the filter weights. This filter, when applied to the signal, enhanced the repetitive characteristic defect frequencies while reducing broadband noise. Experimental results have been obtained for four types of defects: outer race, inner race, roller, and debris denting. Results confirmed the effectiveness of the signal processing technique to determine both the severity and location of a defect.

CPD Probe for Bearing Defect Detection

The use of a CPD (contact potential difference) probe to detect bearing defects is another particular interest in this project. The CPD probe works on the basic principle that there is always a potential difference between two surfaces. Such a potential difference can be used to generate an electrical current if the proper steps are taken. As a surface passes by the stationary CPD probe, a current is generated that is measured by the probe. The current is then sent through a linear pre-amplifier, converting it to a voltage. With an analytical model, this voltage output can then be applied to the detection of the bearing defect. To demonstrate the capability of the CPD probe, a series of tests have been done to examine its functionality. The experimental investigation demonstrates two important points. First the CPD probe is capable of detecting surface anomalies on the order of microns with little difficulty. Second, by analyzing the periodicity of the signal, the CPD probe also provides rotational frequency information. Recent experiments with a CPD probe mounted in the outside race of a roller bearing have demonstrated its utility in identifying roller damage in real-time, as well. Experimental investigation also shows that this probe is sensitive to and effective on the bearing failure modes of adhesive wear, corrosive wear, stress concentration, and peeling. In the future, the contact potential difference (CPD) probe, will be integrated into the whole diagnostic system for bearing defect detection.

b. Investigation of Sensor and Machine Condition Effects in Bearing Monitoring

An objective of this investigation is to evaluate the effects on vibration and acoustics emission signal metrics due to changes in sensor type, sensor location, signal processing method, bearing loading, and rotational speed. The signal processing techniques used in this research were based on band-pass filtering raw signals around systems resonance. Peak indicators of the demodulated signals were used to quantify the magnitude of defect frequencies. RMS of the band-pass signals was also used to quantify defect magnitude. Experimental results show that RMS indicators increased linearly with increasing speed as a result of a proportionally increasing number of defect impulses in a sensor signal. The relationship of both RMS and peak indicators to radial load is greatly dependent on sensor type and location. Dynamic models suggest a cause for this relationship. Peak indicators are also shown to decrease at high rotational speeds despite an increase in RMS. A model relating system damping and impulse decay to the speed was also proposed. Both the accelerometer and acoustic emission sensors showed similar capability in detection of different bearing damage levels from different sensor locations.

c. Techniques of Bearing Defect On-line Evaluation (Diagnostics)

Minimizing the Influence of Operating Condition Variations in Bearing Diagnostics

Currently available diagnostic methods primarily focus on determining the presence of a fault by comparing measured signals with pre-calibrated baseline signals at specific operating conditions. Their application is limited to previously tested operating conditions, and usually cannot be reliably extended to untested conditions. Techniques have not been developed to relate data to the defect severity of a bearing under operating conditions different than those originally tested. Hence, the success of defect severity evaluation depends on how to minimize the influence of operating condition variations. A diagnostic model based on the hypothesis testing procedure was developed, permitting defects to be assessed under bearing operating conditions that have not been previously assessed. In this work an accelerometer mounted on the bearing housing provided vibration signals under a range of shaft speeds, lateral loads, and bearing out-race defect sizes. A full factorial experimental design and a statistical analysis method were used to identify the optimal diagnostic model structure and parameters that estimate defect severity while minimizing the effects of shaft speed and lateral loads. The experimental results indicate that this defect diagnostic model has the capability to provide more accurate predictions of defect widths by minimizing the operating condition effects.

Impact Dynamics Modeling of Bearing Vibration for Defect Size Estimation

A challenge to diagnosing a bearing defect is in relating the dynamic modeling of vibration signals under practical operating conditions to a fundamental understanding of bearing physics. To provide a better understanding of the basic physics involved in the generation of sensor signals from a defective bearing, a rigid body dynamic model was developed to describe the relationship between measurable vibration signals and the surface defect size on the bearing outer race. Based on the modeling of impact interactions between rolling components, a rigid body dynamic model was developed that describes a dynamic relationship between the measurable vibration signals, the geometrical structure of tapered roller bearings, the rotational speed of the system and the defect width on the outer-race. Finite-element (FEM) techniques were also employed to analyze the elastic impact deformation of rolling element and outer-race containing a surface defect The FEM analysis provided the contribution of elastic strain energy to the overall impact energy. To validate this analytical model, a series of experiments were performed by acquiring the accelerometer signal from a bearing operating under a range of rotational speeds, lateral loads, and surface defect widths on the outer-race. The experimental results confirmed that the analytical model could effectively interpret the bearing vibration level to infer the defect condition under various operating conditions.

d. Techniques of Bearing Life Prognostics

Deterministic Defect Propagation Model and Adaptive Prognostics

A deterministic bearing defect propagation model and a formulation of an adaptive bearing prognostic methodology was developed. In this research, an artificially induced initial crack served as the origin for spall generation due to high stress concentration. Spalls occurred primarily in the rolling direction in the experiment. Defect severity in terms of defect area size was modeled as a linear function of acceleration RMS and acoustic emission (AE) RMS. Although there was a large variance in the diagnostics for defect area estimations, the proposed adaptive scheme still effectively predicted the general defect propagation trend. Based on the deterministic defect propagation model, an adaptive algorithm was used to fine-tune the rate of defect propagation in a real-time manner via vibration signal analysis. The variable nature of defect propagation was addressed by time-varying parameters. The adaptive alteration of the model parameters offered the best estimation, in the least square error sense, of a given diagnostic model. Numerical simulations were included to illustrate the implementation principles and an experimental study was conducted to verify its effectiveness.

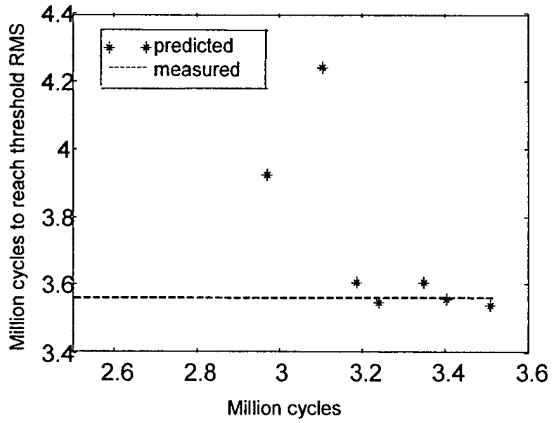

Figure 2. Adaptive RLS Algorithm Prediction Converges as Bearing Test Proceeds[1]

[1] Both axes are in millions of cycles. The dashed line indicates the time for the actual bearing to reach a signal threshold. The stars represent the prognostic algorithm's prediction for bearing lifetime as the test proceeds forward (x-axis). The algorithm converges to show a prediction for reaching a signal threshold roughly 0.4 million cycles in advance.

Stochastic Modeling of Defect Propagation

In terms of experimental observations, fatigue crack growth is a nonlinear stochastic process. Variations in the fatigue crack growths are due to uncertainties inherent in the crack growth process and material characteristics. The deterministic defect growth model cannot address the stochastic nature of the process. Consequently, a stochastic defect propagation model was developed by introducing a lognormal random variable to the deterministic defect propagation rate given in the deterministic propagation model. The stochastic model is calibrated, on-line, by a recursive least square (RLS) approach. This approach does not require a priori knowledge. An augmented stochastic differential equation vector is established with the consideration of model uncertainties, parameter estimation errors, and diagnostic model inaccuracies. It evolves to two ordinary differential equations for the first and second moments of its random variables through the second order approximation of a Taylor expansion. This approach allows the predictions of the mean path of defect propagation and its dispersion at any instance. Therefore, it is suitable for on-line monitoring, remaining life prediction and decision making for optimal maintenance scheduling. Simulations and a bearing life test in terms of prediction of vibration level were performed to verify this method.

Damage Mechanics Approach for the Prognostics of Bearing Life

A stiffness-based life-signal prognostic model of a bearing system based on vibration response analysis and damage mechanics was also developed. This methodology overcomes the shortcomings from both deterministic and stochastic defect propagation models that induced artificial initial cracks and arbitrary threshold of defect size with the lack of analytical explanation. It is found that the natural frequency of the system is proportional to the system stiffness, and the amplitude of acceleration response (i.e., vibration signals from an accelerometer), at the natural frequency is opposite to the system stiffness. On the other hand, based on the rules of accumulating damage of structure and material, the relationship among failure lifetime, running time (or million cycles) of a bearing system and variations of stiffness of a bearing system can be established. Then, with the combination of these two relationships, the amplitude of acceleration response (vibration signals from an accelerometer) at the natural frequency can be related to the bearing running time and failure lifetime. The only information needed by this prognostic model is a time series of vibration acceleration signature. This methodology was verified by both simulation and experimental.

e. Techniques of Bearing Life Prediction Based on Accelerated Life Testing

An objective of this research is to develop a methodology that can evaluate or predict the life probability of bearings based on accelerated testing data with condition monitoring techniques. This technique offers the attractive benefit of requiring relatively short investment in time and resources. If implemented correctly, ALT can save 80~90% of the testing time while providing satisfactory prediction of mechanical component life probability. The design of the accelerated life testing in this study is based on a step-stress scheme. The main test parameter is the salt content of water. The primary attributes of the life prediction model consist of the model structure and the model parameters. To determine the model structure, a power inverse law was applied in this research. Based on accelerated life testing data, the law provided the life distribution for the bearing to fail at a life of T under a particular stress. In this study, the testing results from a series of life testing experiments were utilized to identify the model parameters based on the maximum likelihood principle. Then, the accelerated factor (AF) was calculated and the relationship between accelerated stress condition and the use stress condition was established. By extrapolating this information, the failure rate of bearings under any operating conditions can then be evaluated.

f. Techniques of Off Site Monitoring

A distributed Visual Basic platform was developed to facilitate the automation of the testing process. A networking scheme was also developed to add remote monitoring capabilities. Data can be analyzed and displayed using computers on the network, remote from the test stand. Graphical test results,

including current results from experiments in progress, are then made available to a wider audience via the Internet. This automation and networking increase the versatility of the experimental setup.

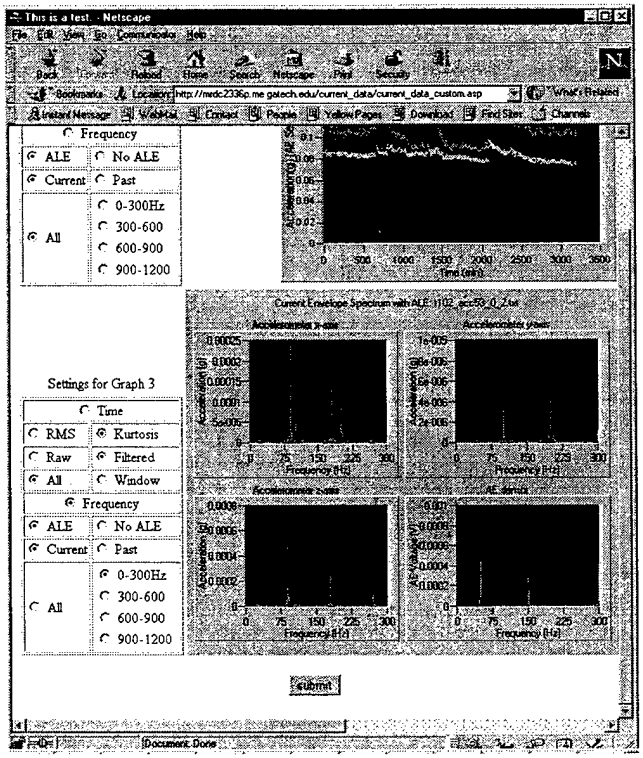

Figure 3. Screen Shot of Web Based Diagnostics

M-URI PUBLICATIONS

Shiroishi, J., Li, Y., Liang, S., Kurfess, T., Danyluk, S., "Bearing Condition Diagnostics via Multiple Sensors," *Mechanical Systems and Signal Processing*, Vol. 11, No. 5, September 1997, pp. 693-705.

Shiroishi, J., Li, Y., Liang, S., Danyluk, S., Kurfess, T.R., "Vibration Signal Analysis for Bearing Race Damage Diagnostics," Keynote paper for the *7th International Conference on Dynamic Problems in Mechanics*, Brazil, March 1997, pp. 187-190.

Billington, S.A., Li, Y., Kurfess, T.R., Liang, S.Y., Danyluk, S., "Roller Bearing Defect Detection with Multiple Sensors," *1997 ASME International Mechanical Engineering Congress and Exposition*, TRIB Vol. 7, Dallas, TX, November 1997, pp. 31-36.

Shiroishi, J., Li, Y., Liang, S., Kurfess, T., Danyluk, S., "Vibration Analysis for Bearing Outer Race Condition Diagnostics," *Journal of the Brazilian Society of Mechanical Sciences* (in press).

Li, Y., Shiroishi, J., Danyluk, S., Kurfess, T., Liang, S.Y., 1997a, "Diagnostics of Roller Bearing Defects Based on Vibration and Acoustic Emission," *COMADEM 97, 10th International Congress & Exhibition on Condition Monitoring & Diagnostic Engineering Management,* Vol. 2, pp. 256-267.

Li, Y., Shiroishi, J., Danyluk, S., Kurfess, T., Liang, S.Y., 1997b, "Bearing Fault Detection via High Frequency Resonance Technique and Adaptive Line Enhancer," *21st Biennial Conference on Reliability, Stress Analysis and Failure Prevention (RSAFP),* Virginia Beach, Virginia, pp. 763-772.

Li, Y., Billington, S. A., Kurfess, T. R., Danyluk, S., Liang, S.Y., "Dynamic Prognostics of Rolling Element Bearing Condition," *Proceedings of 52nd Meeting of the Society for Machinery Failure Prevention Technology*, , Virginia Beach, March 30-April 3, 1998, pp. 429-430.

Li, Y., Kurfess, T. R., Danyluk, S., and Liang, S. Y., "Bearing Prognostics Based on Adaptation of Stochastic Defect Growth Model," accepted by *Proceedings of 53rd Meeting of the Society for Machinery Failure Prevention Technology*, April 19-22, 1999 (in press).

Billington, S. A., Li, Y., Kurfess, T. R., Danyluk, S., "Operating Condition Effects on Rolling Element Bearing," *Proceedings of 52nd Meeting of the Society for Machinery Failure Prevention Technology*, Virginia Beach, March 30-April 3, 1998, pp. 313-322.

Li, Y., Billington, S., Zhang, C., Kurfess, T., Danyluk, S., Liang, S.Y, "Adaptive Prognostics for Rolling Element Bearing Condition," *Mechanical Systems and Signal Processing,* 1998, Vol. 12, No. 4, pp. 345-357.

Li, Y., Billington, S., Zhang, C., Kurfess, T., Danyluk, S., Liang, S.Y., "Dynamic Prognostic Prediction of Defect Propagation on Rolling Element Bearing," *ASME/STLE Tribology Conference*, Toronto, Ontario, Canada, October 26-28, 1998.

Zhang, C., Li, Y., Kurfess, T.R., Danyluk, S., Liang, S.Y., "Minimizing the Influence of Operating Condition Variations in Bearing Diagnostics," *International Journal of COMADEM*, Vol. 2, No. 1, 1999, pp. 23-29.

Zhang, C., Qiu, J., Kurfess, T.R., Danyluk, S., Liang, S.Y., "Impact Dynamics Modeling of Bearing Vibration for Defect Size Estimation," *International Journal of COMADEM*, 2000 (to appear).

Zhang, C., Kurfess, T.R., Danyluk, S., Liang, S.Y., "Dynamic Modeling of Vibration Signals for Bearing Condition Monitoring," *The Second International Workshop on Structural Health Monitoring*, Stanford, 1999, pp. 926-935.

Qiu, J., Zhang, C., Seth, B.B., Liang, S.Y., "A Damage Mechanics Approach for the Prognostics of Bearing Lifetime," *Journal of Mechanical Systems and Signal Processing*, 2000 (submitted).

Qiu, J., Zhang, C., Seth, B.B., Liang, S.Y., "Failure Lifetime Prognostic of Bearing Based on Vibration Response and Damage Mechanics," *Japan-USA Symposium on Flexible Automation*, 2000, (accepted).

Yang, Y., Kurfess, T. R., Liang, S. Y., Danyluk, S., "Application of A Specialized Capacitance Probe in Bearing Diagnosis," *Wear*, 1998 (in press).

Yang, Y., Kurfess, T. R., Liang, S. Y., Danyluk, S., "Application of A Specialized Capacitance Probe in Bearing Diagnosis," *Proceedings of the 12th International Conference on Wear of Materials*, Atlanta, April 25-29, 1999 (in press).

2.3.4 INTEGRATED MICROSENSORS FOR AIRCRAFT FATIGUE FAILURE AND FAILURE WARNING

Lead Investigator: William P. Robbins (University of Minnesota)

PROJECT OVERVIEW

Four principal activities have taken place with the goal of developing miniature structural health monitoring systems and their related signal processing. These include 1) wideband acoustic emission sensors, 2) vibration monitors, 3) sensor interface circuits, and 4) signal processing methods.

The technical approach taken in this work is largely based on the use of piezoelectric materials and MEMS processing methods. As early as 1992, it was believed that piezoelectric (PZT) MEMS would be attractive for integrated diagnostic monitoring devices due to its inherent high sensitivity, low electrical noise, and low power dissipation. The main technical challenges however of microfabrication complexity, reproducibility, and integration with electronics represent the challenges of PZT MEMS. Prior to the start of this program, no structural health monitoring devices had been made. Some preliminary data on microphones and related pressure sensors did however did indicate promise for integrated diagnostics applications. While other technologies have been developed since 1992, the use of piezoelectric MEMS is still compelling for structural health monitoring applications.

The main accomplishments for each of these activities are briefly summarized below:

- Integrated acoustic emission microsensors and associated packaging methods have been developed and demonstrated for the detection of fatigue-induced microcracking.
- Piezoelectric microcantilever vibration monitors have been designed and fabricated for the detection of abnormal mechanical vibration signatures in rotating machinery.
- Custom integrated circuits have been developed for interfacing multiple sensors combined in one package to the outside world.
- A design for a multi-sensor coupon has been developed.
- Signal processing methods have been developed for analyzing crack signatures.

The overall goal of this project is to realize a smart structural health-monitoring coupon consisting of sensors, electronics, and signal processing methods. Figure 1 shows the overall systems objective of this project.

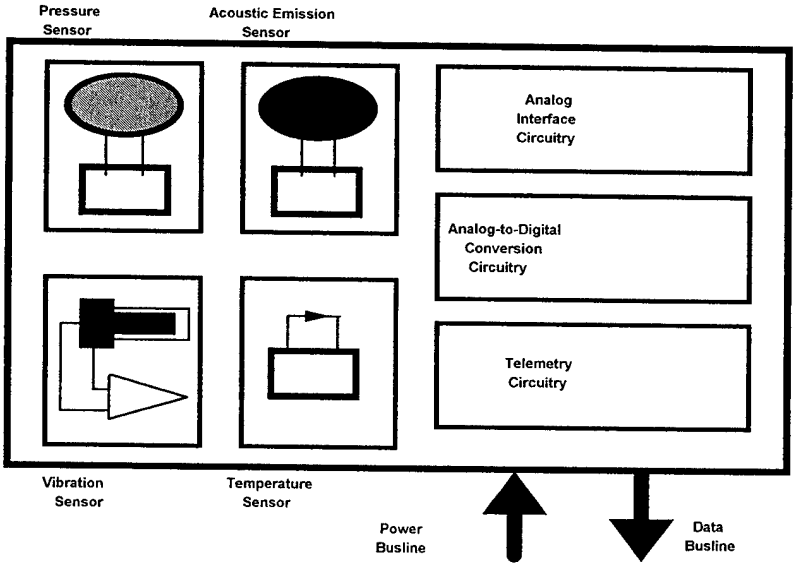

Figure 1. Smart structural monitoring coupon systems concept.

2.3.4.1 WIDEBAND INTEGRATED ACOUSTIC EMISSION MICROSENSORS

Co-investigators: W. P. Robbins and R. Harjani (University of Minnesota)
Students: J. Plummer, Baris Kazar and K. Nair

OVERVIEW

The real-time detection of the precursor signatures leading to material failure is critical to a variety of defense needs. This is particularly relevant to helicopters were fatigue related crack formation can lead to catastrophic component failure. Real-time detection of crack formation is also important in routine maintenance of aircraft components and ship machinery where materials are often unnecessarily replaced or serviced even though they are structurally healthy.

OBJECTIVE

One of the major goals of the Integrated Diagnostics effort has been the use AE sensors mounted on critical components in a system such as a helicopter to provide monitoring for microcrack development while the component was in service. The system would be taken out of service only when the development of microcracks reached a predetermined threshold and maintenance time and expense would be minimized. This would maximize the availability of the system for mission assignments.

However the AE microsensors available in 1995 at project inception were unsuitable for this application. Commercially available wideband (50 kHz - 1MHz) acoustic emission sensors were too large (typically 1-2 cm in diameter and 2 cm tall), too heavy (tens of grams), too expensive ($200-$400 each), and required 40-60 db of external amplification.

The integrated AE microsensor project was initiated to overcome these limitations. The goal of the project was to develop a microsensor having a small size (packaged sensor dimensions having a lateral footprint of a few mm on a side and a few mm vertical height) and capable of wideband (50 kHz to 1 MHz) operation. An amplifier made as in integrated circuit chip was to be included in the packaged sensor to achieve good sensitivity.

ACHIEVEMENTS

During the first three years of the project, several generations of hybrid AE sensors have been fabricated and tested. The term hybrid refers to the on-board charge amplifier being fabricated with discrete surface mount components and positioned on a circuit board. The hybrid sensors had a twofold purpose: 1) to demonstrate that reductions in the PZT sensor sensitivity because of PZT size reductions could be compensated for by means of onboard amplification and 2) to develop an optimum circuit design for the onboard amplification. The details of the hybrid AE sensor were reported in the Year 3 Annual Report. During Year 4, efforts concentrated on developing an integrated AE sensor.

During the past year (Year 5), a number of integrated AE sensor have been fabricated and undergone preliminary testing. Photographs of the completed sensor shown in Fig. 1.1 and a detailed sketch of the interior are shown in Fig. 1.2. The coax cable from the AE sensor package connects to a small electronics unit that provides the dc power to the AE sensor, separates the dc power from AE signal, and provides additional amplification. The overall AE sensor package size is 6 mm by 6-mm lateral footprint and 5 mm tall. Four of the sensors and their external electronics units were provided to team members at Georgia Tech for evaluation in their crack fatigue experiments.

Sample pencil lead break test results comparing the integrated AE sensor with a wideband commercial sensor are shown in Fig. 1.3. Both the time domain waveforms generated by a pencil lead break and detected by the integrated AE sensor and commercial sensor simultaneously are shown as well as FFTs of the waveforms. The figure illustrates that the integrated AE sensor detects significantly more high frequency information than the commercial sensor.

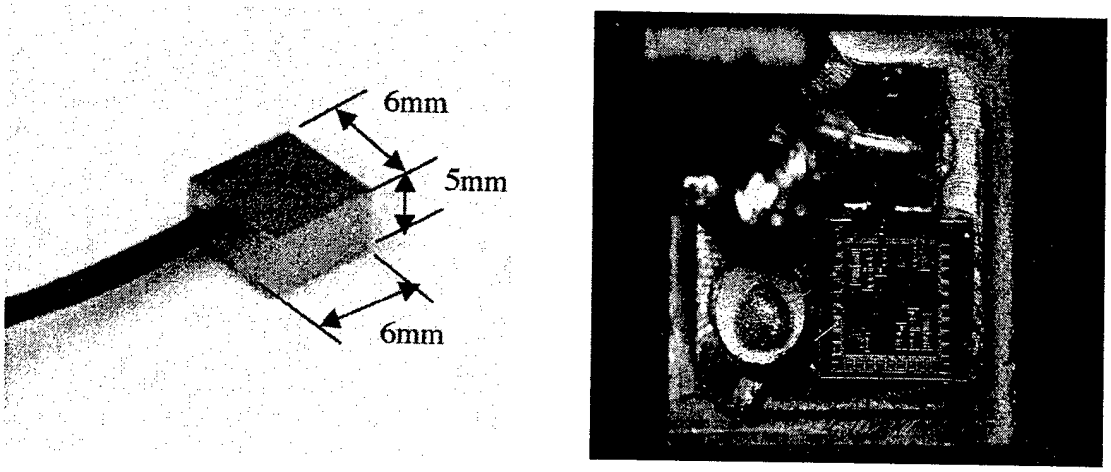

Figure 1.1 Photographs of integrated AE sensor showing both an exterior view of the assembled sensor and a view with the cover removed to show the interior layout.

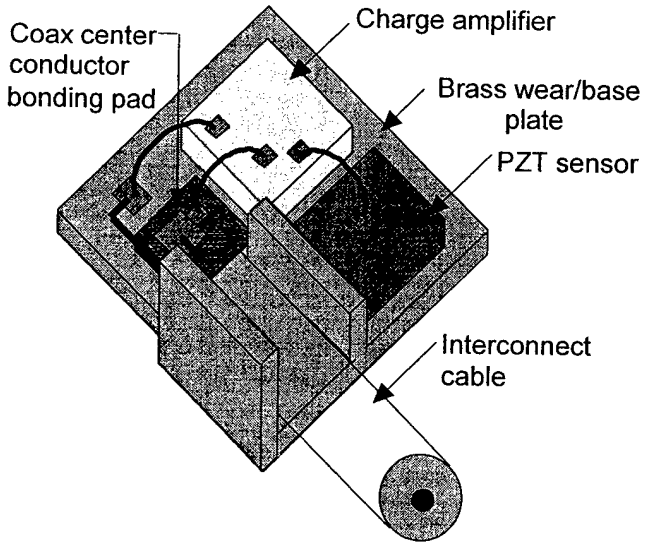

Figure 1.2 Details of the interior of the integrated AE sensor.

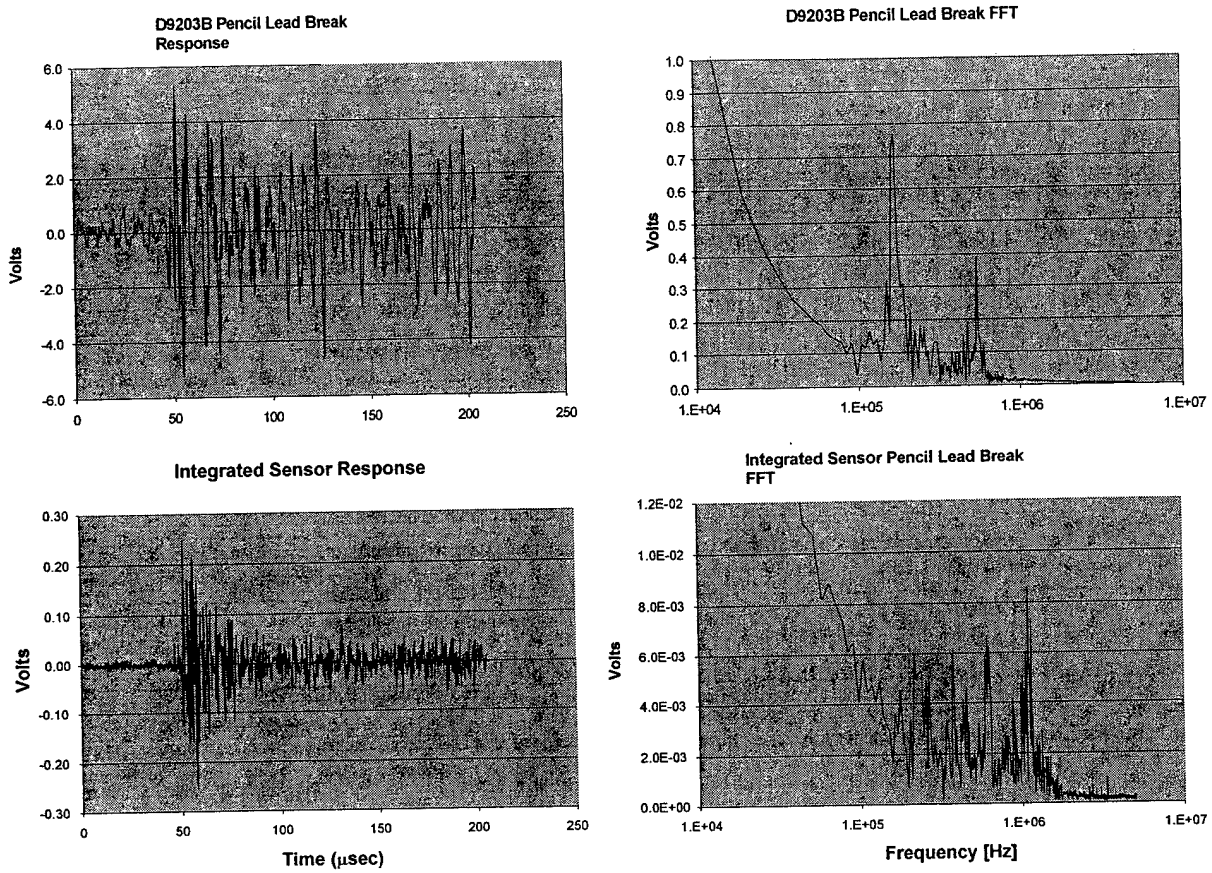

Figure 1.3 Pencil lead break tests between the integrated AE sensor and a wideband commercial AE sensor, the Physical Acoustics D9203B. The time response is shown as well as the FFT of the time responses.

The integrated AE sensor with onboard amplification represents a significant advance in the state of the art of AE sensors. The integrated sensor is smaller than commercially available AE sensors that do not have internal amplification and has a bandwidth that exceeds that of most AE sensors. The cost of the integrated sensor is expected to be considerably less than present commercially available sensors if the integrated sensor is designed for mass production.

FUTURE RESEARCH

1. Improve packaging for integrated AE sensor.
2. Investigate effect of damping materials combined with stacking amplifier chip on top of piezoelectric sensor.
3. Compare use of voltage amplification versus charge amplifiers.

2.3.4.2 VIBRATION SENSORS

Co-investigator: Dennis Polla (University of Minnesota)
Students: L. Zhang

OVERVIEW

One of the goals of structural health monitoring is to detect the onset of unusual vibration characteristics prior to component failure; e.g., bearings. This is desirable for reasons of both preventing major systems damage and providing timely information in regularly scheduled maintenance. Most mechanical vibrations present on either helicopters or ships have fundamental movements at frequencies below 10 kHz. This presents a challenge for both silicon microsensors and signal processing due to the high 1/f electrical noise and parasitic signal losses.

OBJECTIVE

At the inception of this program, MEMS-based vibration sensors for structural health monitoring had not been reported in the technical literature. A variety of solid-state accelerometers had been commercially realized using either piezoresistive or capacitive sensing principles. These approaches however had significant barriers of high electrical power dissipation and need for precision micromachining methods with on-chip electronics.

Given the selection of piezoelectric sensors for AE sensing, the primary approach taken in this project is to apply similar microfabrication processing and electronics integration methods for both the vibration sensor and AE sensor with the goal of possibly merging these functions on common chipsets.

ACHIEVEMENTS

Preliminary success in the development of microfabrication methods for piezoelectric thin film microsensors based on 0.5 μm-thick PZT was achieved in Year 3 of this program. While basic functionality was demonstrated, microsensor response characteristics (sensitivity and frequency response) were non-optimal. Activity during Year 4 included process refinement and microfabrication, electrical characterization, and hybrid amplifier integration. A secondary back-up approach for the vibration sensor was realized using Analog Devices dual-axis MEMS comb-drive oscillators. These oscillators consist of two right-angle MEMS microfabricated electrostatic combs. An electronic circuit approach has been developed to simultaneously process changes in these oscillator characteristics in the presence of mechanical vibrations.

During Year 5, more microfabrication runs were carried out to further optimize the processing and improve the responsivity of the piezoelectric vibration monitors. A photomicrograph of the thin-film PZT cantilever vibration sensor is shown in Fig. 2.1. The overall chip size, including the relatively large bonding pads for wire bonds is approximately 2 mm square. The details of the fabrication process including cross-sectional diagrams of the layers that make up the sensor are described in previous reports. The cantilever beam vibration sensors are ready for use in a multi-sensor coupon.

As shown in Fig. 2.2, the cantilever beam vibration sensor has a flat response only to about 1 kHz because of a fundamental-mode resonance at approximately 2 kHz. The bridge structure shown in Fig. 2.3 (a beam clamped at both ends) was investigated as a way of increasing the fundamental resonance to frequencies to above 10 kHz so that the response would be flat to 10 kHz. Simulations indicate that the fundamental mode resonance of the bridge structure is about 9 kHz while a cantilever of the same dimensions has a fundamental mode resonance of 2 kHz. Initial testing of the bridge structure was just beginning at the end of the grant period.

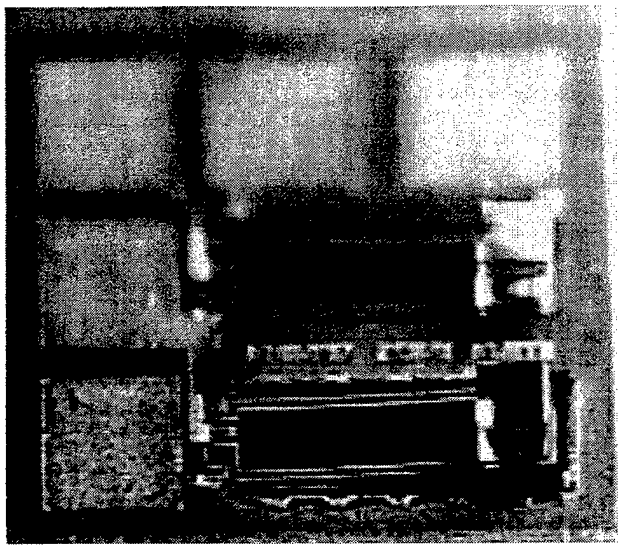

Figure 2.1 Photomicrograph of the cantilever beam vibration sensor. The cubic-shaped objects at the free end of the beam are made of photoresist and act as proof masses. The upper part of the photo is out of focus so that the free end of the cantilever at the bottom of the picture could be in focus.

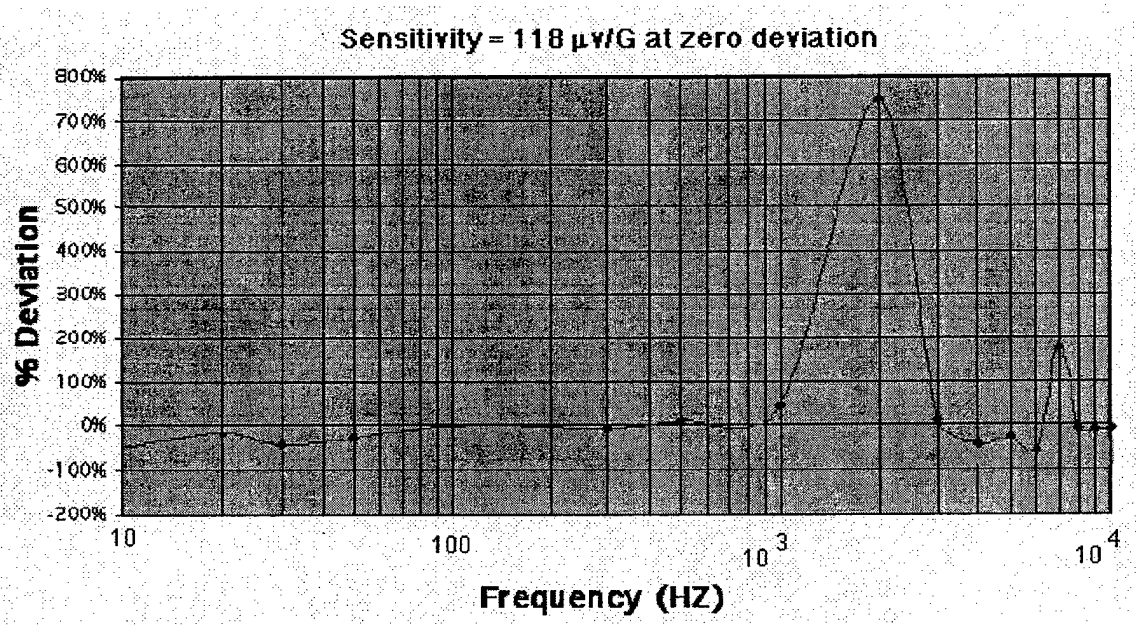

Figure 2.2 Deviation of the cantilever beam sensitivity from a nominal sensitivity of 118 µV per G versus frequency. The information was obtained from a calibrated mechanical shaker table.

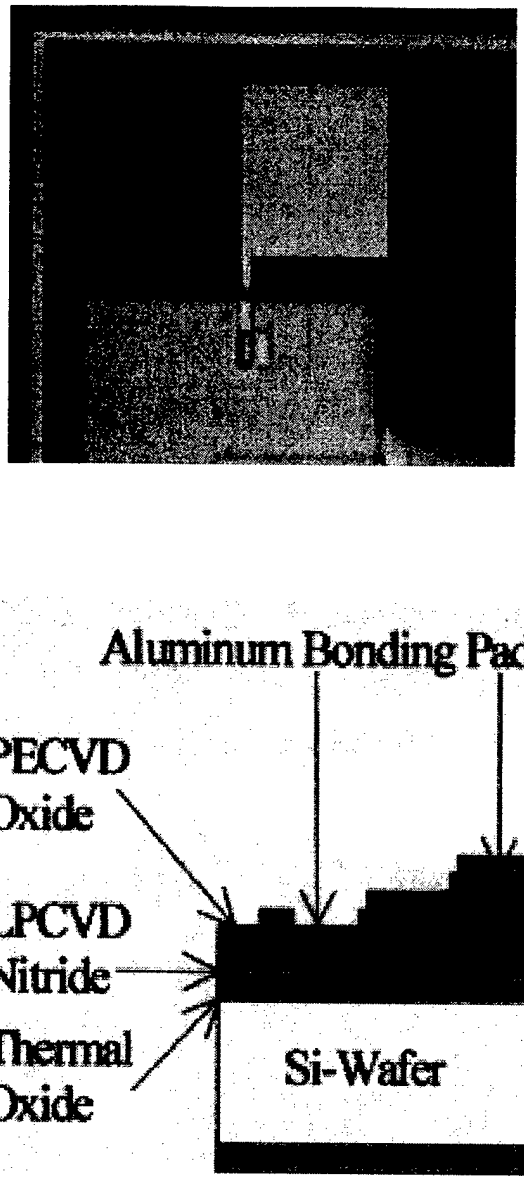

Figure 2.3 Photomicrograph and diagram of a bridge or double-clamped beam geometry for thin-film PZT vibration sensor. The bridge is 300 μm wide, 1000 μm long, and 2.5 μm thick. The chip is approximately 2.5 mm square.

FUTURE RESEARCH

1. Complete characterization of bridge geometry vibration sensor.
2. Design package for vibration sensor with on-board amplification.
3. Evaluate use of vibration sensor, first in test situations and then in field tests.

2.3.4.3 MULTI-SENSOR COUPON

Co-investigators: William Robbins, Dennis Polla and Ramesh Harjani
Postdoctoral Fellow: Raed Riqz
Student: K. Nair

OVERVIEW

The placement of a variety of sensors including AE sensors, vibration sensors, and temperature sensors on platforms including helicopters, aircraft, and ships for the real-time detection of precursor signatures to material failure is important for a variety of defense needs. However if the sensors are individually packaged components, it becomes increasingly expensive to place them on platforms as the sensor quantity and variety grows. In addition the complexity of the interconnection network grows even more and can significantly degrade the ability to maintain real-time surveillance of sensor outputs. Some means is needed for combining multiple sensors into an inexpensive package with as few separate outputs as possible.

OBJECTIVE

A major goal of the Integrated Predictive Diagnostics effort is to combine the AE sensors, vibration sensors, and temperature sensors into a single package termed a multi-sensor coupon. The number of interconnects between the coupon and the outside world was to be minimized with the theoretical minimum being a two conductor interconnect.

ACHIEVEMENTS

During the first four years of the program, our efforts centered on developing well-characterized and miniaturized sensors, including acoustic emission (AE) sensors and vibration sensors. Until the sensors reached sizes of a fraction of a square centimeter in area, the size of a multi-sensor coupon that included the sensors and on-board electronics would have been impracticably large. By the end of Year 4, our sensors had reached the necessary state of development and we then began the detailed design of the multi-sensor coupon.

The basic design of the multi-sensor coupon is shown in Fig. 3.1. The outputs of each of the three sensors in the coupon occupies a different frequency range, so it was possible to combine all three outputs on a single interconnect line which also carries the dc power from an external source to the on-board amplifiers. An on-board voltage regulator separates the dc power from the ac sensor outputs thus preventing undesirable feedback. A filter bank in the external signal separation electronics divides combined output signal into separate signal channels.

The multi-sensor has a total of seven chips including three sensor chips and four identical amplifier chips. The AE sensor is a disk of PZT 1.5 mm in diameter and 250 microns thick, identical to that used in the integrated AE sensor. The vibration sensor chip was described in the previous section, 2.3.4.2. The temperature sensor is a commercial chip about 3 mm square which outputs an ac waveform whose frequency varies about 10 kHz in proportion to the temperature. The amplifier chips are a modified version of the chip designed for the integrated AE sensor. This chip was described in detail in the Year 4 report. The circuit fragment composed of the Sum op amp with resistors R1, R2,R3 and Rf were added to the chip with connections to R1, R2, R3, and the output of the Sum op amp brought to bonding pads for possible external connections.

The package for the multi-sensor coupon will be similar to that for the integrated AE sensor. A layout of the sensor and amplifier chips on the multi-sensor base plate is shown in Fig. 3.2. Each chip is drawn as 3 mm square with a spacing between chips of 1 mm. The wire-bonded interconnections for signals and dc power are indicated on the diagram.

The modified amplifier chips were only received from the silicon foundry (MOSIS) in late July 2000. Hence, no assembly of the multi-sensor has been possible.

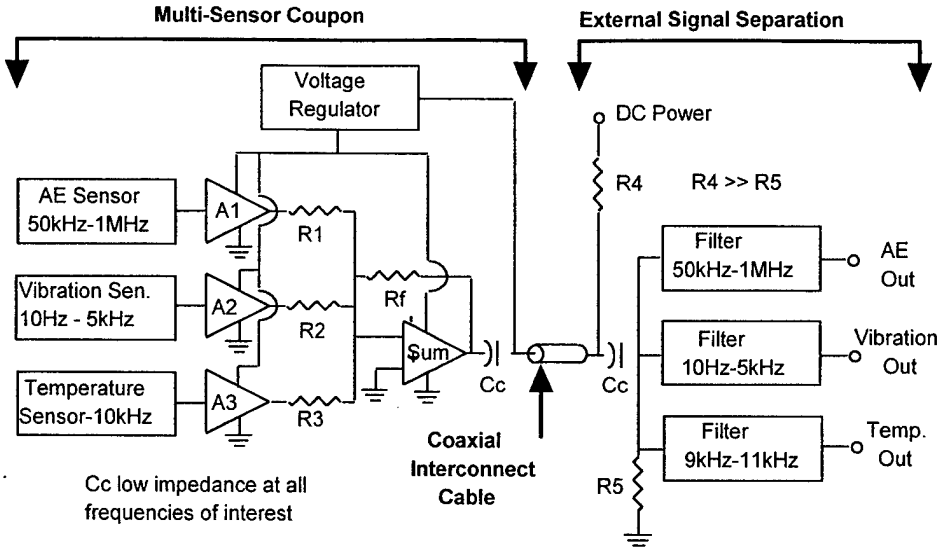

Figure 3.1 Design of the multi-sensor coupon. The temperature sensor is a commercial chip which provides a variable frequency output (centered at 10 kHz) that is proportional to temperature.

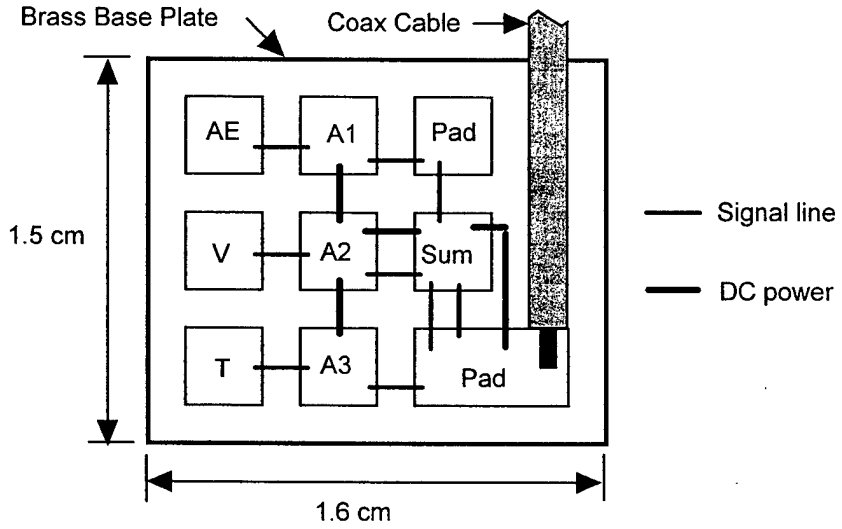

Figure 3.2 Chip layout on the multi-sensor base plate. Electrical interconnections between the chips are also indicated. The blocks marked Pad serve as wire-bonding pads.

FUTURE RESEARCH

1. Complete assembly of coupon and external electronics.
2. Test coupon for functionality and characterize performance relative to specifications.
3. Trial coupon in crack fatigue and vibration experiments and in field-tests.
4. Develop coupon with on-board power (battery) and wireless telemetry link.

M-URI PUBLICATIONS (for Sections 2.3.4.1 - 2.3.4.3)

1. Ming Zang, Shayne M. Zurn, Dennis L. Polla, Bradley J. Nelson, and William P. Robbins, "Design, Simulation, and Fabrication of a Bridge Structure Microtransducer," Modeling and Simulation of Microsystems, 3rd International Conference, San Diego, CA, March 27-29, 2000.

2. Dennis L. Polla, David T. Markus, William P. Robbins, and Hui Tao, "Piezoelectric Devices and MEMS," International Symposium on Integrated Ferroelectrics, Aachen, Germany, March 12-15, 2000.

3. D. L. Polla and L. F. Francis, "Processing and Characterization of Piezoelectric Materials and Integration into Microelectromechanical Systems," *Ann. Rev. Mater. Sci.,* V. 28, 1998, pp. 563-597.

4. C. R. Cho, L. F. Francis, and D. L. Polla, "Ferroelectric Properties of Sol-Gel Deposited $Pb(Zr,Ti)O_3/LaNiO_3$ Thin Films on Single Crystal and Platinized-Si Substrates," *Materials Letters*, V. 38, 1999, pp. 125-130.

5. D. L. Polla, L. F. Francis, D. Drinkwater, W. P. Robbins, R. Harjani, L. Zhang, K. Nair, J. Plummer, Y. Nam, and P. Schiller, "Piezoelectric MEMS for Integrated Diagnostics," Materials Research Society, San Francisco, CA, March 1999 (invited).

6. K. Nair and R. Harjani, "An Ultra Low Power Transconductance Cell." ISCAS 1996.

7. K. Nair, C. Zillmer, R. Harjani, and D. Polla, "Data Acquisition and Conversion," *Encyclopedia of Electrical and Electronics Engineering*, John Wiley and Sons Inc.

8. D. F. Bahr, J.S. Wright, L.F. Francis, N.R. Moody, and W.W. Gerberich, "Mechanical Behavior of a MEMs Acoustic Emission Sensor," Mat. Res. Soc. Symp. Proc., 444, pp. 209-214 (1997).

9. K. Nair and R. Harjani, "A Telemetry and Interface Circuit for Piezoelectric Sensors," IEEE Int'l Symposium on Circuits and Systems, May 30-June 2, 1999.

2.3.4.4 SIGNAL PROCESSING FOR THE DETECTION AND CLASSIFICATION OF ACOUSTIC EMISSIONS IN INTEGRATED DIAGNOSTICS

Co-investigators: Mos Kaveh, Ahmed H. Tewfik, Kevin M. Buckley (University of Minnesota)
Graduate students: V. Emamian, H. Sun, G. Venkatesan, D. Zhang, and D. West
Visiting student: P. Andersson

OVERVIEW

Failure of machine components in industrial and aeronautical applications during operation can have costly and dangerous consequences. A traditional approach to avoiding such failure is based on planned obsolescence and replacement along with a judicious mix of regular machinery inspection and preventive maintenance. This approach is becoming impractical due to financial reasons and substantial down time constraints. Automatic fault monitoring techniques that gauge the "health" of the components as the machine is in operation are attractive for safely relaxing and simplifying inspection schedules.

An early indicator of the onset of component or material failure is the appearance of micro-cracks. The formation and growth of such cracks creates ultrasonic waves, called acoustic emissions (AEs), that can be recorded by strategic placement of piezo-electric sensors on the surface of the component. These AE signals are transient with high frequency components. The detection and classification of these signals during machine operation can thus provide a possible avenue for automatic monitoring of crack generation, growth and propagation. It is important to note that this transient signal measured at the surface of the component is a distorted version of the signal generated at the location of the crack. This distortion arises due to propagation of the wave through the component and is a complex function of the component's material, size and geometry.

Though the characteristics of the generated AE signals had been extensively studied before the inception of this project, most of this work was carried out under controlled laboratory conditions at high signal to noise ratios (SNRs) and for specimens of simple geometries [1]. In operating machinery, such as a helicopter with deteriorating rotor assembly however, the AE signals are buried in a wide variety of strong interference and noise, which other than low frequency mechanical vibration, include high frequency fretting noise, electromagnetic interference and other high frequency mechanically-generated transients that may originate from fasteners and joints [2]. Accordingly, the detection and isolation of crack-generated AE events from the measured data is not an easy task and requires understanding of signal and noise characteristics and the development of intelligent multichannel space-time-frequency signal processing algorithms. The development of such analysis tools, algorithms, and systems formed the primary mission of the signal processing effort in this project.

The study of the feasibility of using AEs as a tool for automatic fault monitoring is by its very nature a multidisciplinary effort. We have interacted with and acquired a variety of data sets from a number of academic, industrial and government sources. Microcrack data from nano-indentation experiments were obtained in collaboration with Prof. W. Gerberich of the Department of Chemical Engineering and Material Science, Univ. of Minnesota, and his post-doc, Dr. Karl Yoder and student Dr. David Bahr. The Minnesota National Guard and the Cherry Point Naval Aviation Depot enabled the acquisition of mechanical noise data from on-ground helicopters. Mr. J. Schoess of Honeywell provided data from the Boeing testbed and from in-flight tests on a CH-46 Sea Knight helicopter from Cherry Point. Data on crack initiation and growth on several specimen were provided by Profs. L. Jacobs and J. Jarzynski and their student Mr. Z. Shi of Georgia Tech. Crack growth data from periodically loading of 4340 steel specimen were obtained from Prof. I. Daniel of Northwestern University and his student, Dr. J. Luo.

OBJECTIVES

The objectives of the signal processing effort, aimed at the development of algorithms and systems for the detection and classification of crack-generated AEs in presence of noise and interference, were to:

- Develop an understanding of the waveform characteristics associated with crack-generated acoustic emission signals of interest.
- Gain an understanding of the noise and interference expected in operational and fatigue test situations.
- Determine the evolution of signal characteristics associated with the dynamics of crack propagation and growth.
- Understand the effect of sensor placement on the properties of the measured AE signals (channel effect).
- Develop sensitive and robust methods for the detection of small transient signals of the type expected in crack-generated AEs in the presence of background noise.
- Develop space-time-frequency algorithms and systems to classify and discriminate between spectrally overlapping transient AE signals of interest and interference.

ACHIEVEMENTS

Following a considerable investigation of relevant AE signal and noise time and frequency characteristics, a number of algorithms have been developed for i) the detection of small transient signals in noise, when only approximate signal and noise characteristics are known, ii) the mitigation of the distortion of the AE signals due to their propagation and sensing, and iii) the classification and dynamic characterization of the detected events measured by multiple sensors. Data obtained from controlled nano-indentation experiments, on-ground and in-flight helicopter trials from Honeywell, the Georgia Tech fatigue experiments for crack initiation and growth and Northwestern crack growth experiments were used throughout the project to test and tune the algorithms and motivate the development of other techniques. The following gives a summary of the key results and of the project, with additional technical details provided in the associated publications.

A. Signal Modeling

A.1 Micro-crack models

The base model for the expected AE signals that are generated by micro-cracks were developed based on a series of nano-indentation experiments on Tantalum Nitride films. Using Prony's method, it was found that the signal generated at the location of the crack is well-modeled as a superposition of a few, typically no higher than 3, damped sinusoids (pole-zero model), with the component frequencies and damping constants dependent on the material, load and other physical conditions [3]. In one of the more revealing experiments, the nano-indenter set-up was modified to accommodate a bar of 4340 steel with 3 sensors mounted 2 inches apart to evaluate the effects of AE signal propagation. Figure 4.1 shows the samples and the sensors used in the experiment. The time-frequency distributions and the waveforms of the transients at the near (A), middle (B) and far (C) sensor is shown in Figures 4.2 to 4.4.

Several conclusions about the micro-crack transients were drawn from the experiment.

1. The energy of the transients declines fast with the distance from the source of the crack. The transients have almost no energy left in frequencies above 400 kHz at sensor B or C and the amplitude has dropped rapidly compared to sensor A.
2. Multimode propagation and reflections interfere with the measurements of the transients. This interference increases with the distance from the crack, as can be seen when comparing the time domain of the transients at sensor A with sensor B (Figures 4.3 and 4.4).

3. It is unlikely that signal components at several MHz can be present at the sensor outputs away from the source of the micro-crack. Hence, simple highpass filtering at very frequencies is not a viable option for eliminating many of the expected sources of interference. Most of the signal energy is expected to be below 1MHz and most likely in the 100kHz to 300kHz range.
4. The interfering reflected components depend on the geometry of the medium, making it almost impossible to create an exact, predefined model for the signal. However, the model of sum of decaying and delayed sinusoids is still a reasonable general model.

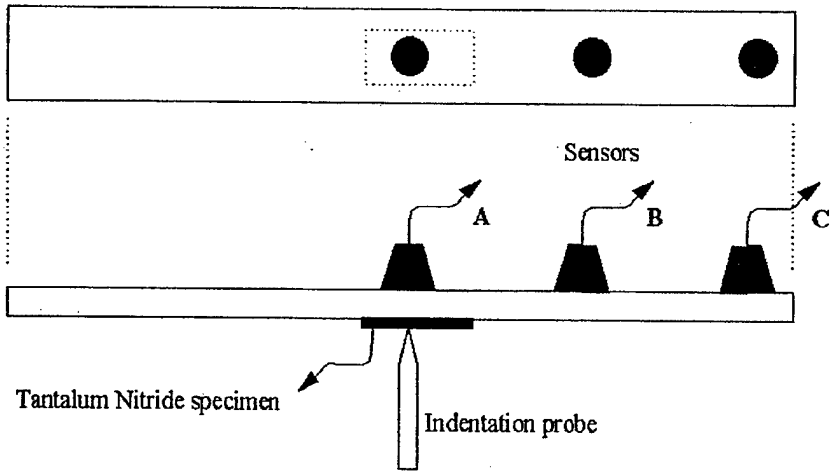

Figure 4.1 Nano-indentation experiment setup

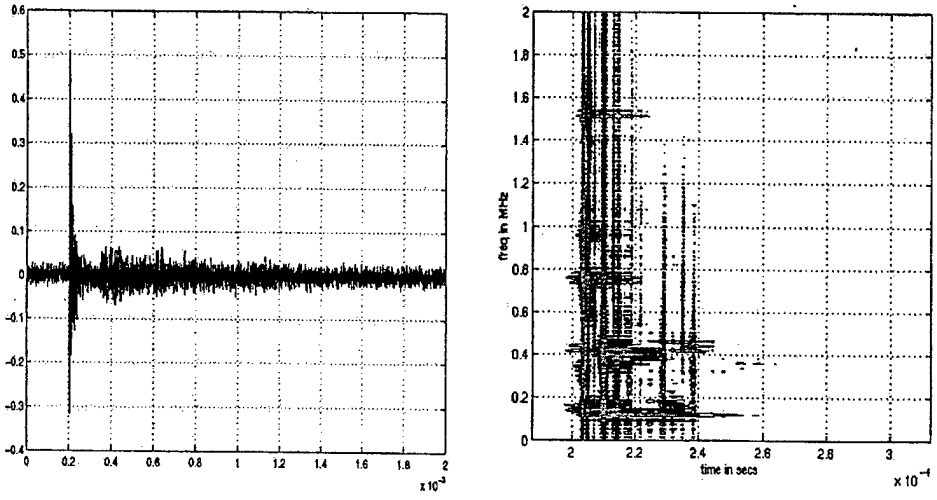

Figure 4.2 Time domain and time-frequency distribution at sensor A.

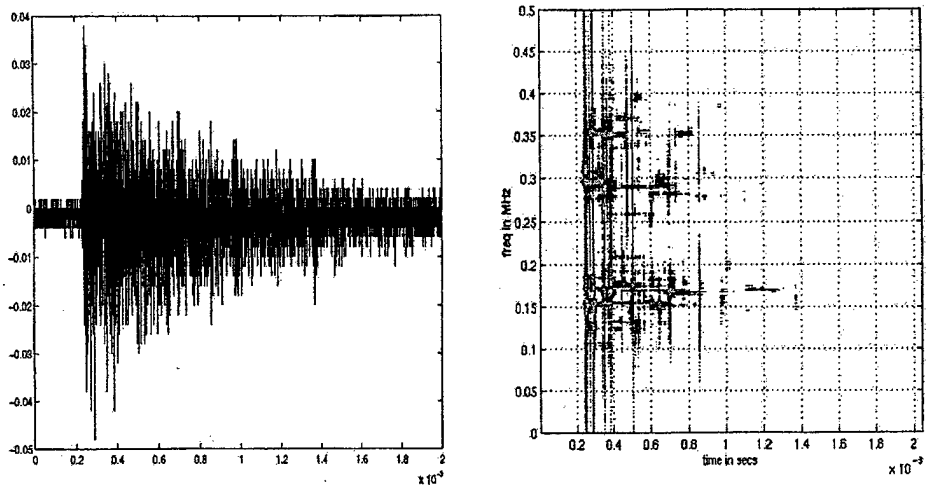

Figure 4.3 Time domain and time-frequency distribution at sensor B.

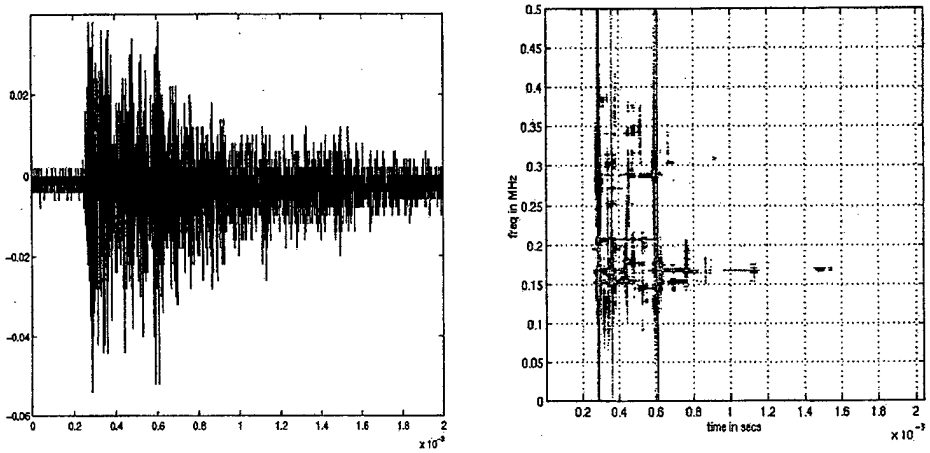

Figure 4.4 Time domain and time-frequency distribution at sensor C.

A.2 Signals from Crack Growth and Propagation

For diagnosis and prognosis purposes, in addition to the detection of the existence of cracks, characterization of signals at different stages of crack initiation and growth are desirable. Work by other members of the Integrated Diagnostics Research team has provided substantial information on the cumulative event counts and their relationship to the phases of loading during fatigue tests for crack growth and propagation. We have examined the waveform characteristics of these events based on data provided by Northwestern and Georgia Tech colleagues. Below, we will summarize some of the key features of these signals that may aid, for example, in the discrimination of crack-generated AE events from other sources of interference.

The spectral characteristics of the acquired event waveforms from the various fatigue tests did not provide us with substantial new information, other than the fact that there is no need for sampling at frequencies higher than 2-4 MHz, as the frequency contents of the measured signals for different material generally is below 1 MHz. Examples of the spectral peaks for AE event signals for several fatigue tests are shown in Figures 4.5 and 4.6. These figures show the existence of higher frequency components for the PH13-8 specimen compared to 4340 steel.

Another important characteristic of the measured signals from the fatigue tests concerns the cross-correlation of the events. There appear to be very high correlation between waveforms of adjacent events *during periods of rapid rise in the cumulative AE counts.* We have used the normalized maximum correlation between a waveform and the shifted version of another waveform, as a measure of the similarity of the two. Figure 4.7 shows the normalized peak cross-correlation of event 1000 from the test given in Fig. 4.5 with all other events in the test. Notice the high degree of correlation among events over much of the experiment. Only the waveforms in the earliest segment of the experiment and the final stage, before the breakage of the sample have low correlation with the majority of the events measured during a rapid rise in the cumulative number of events.

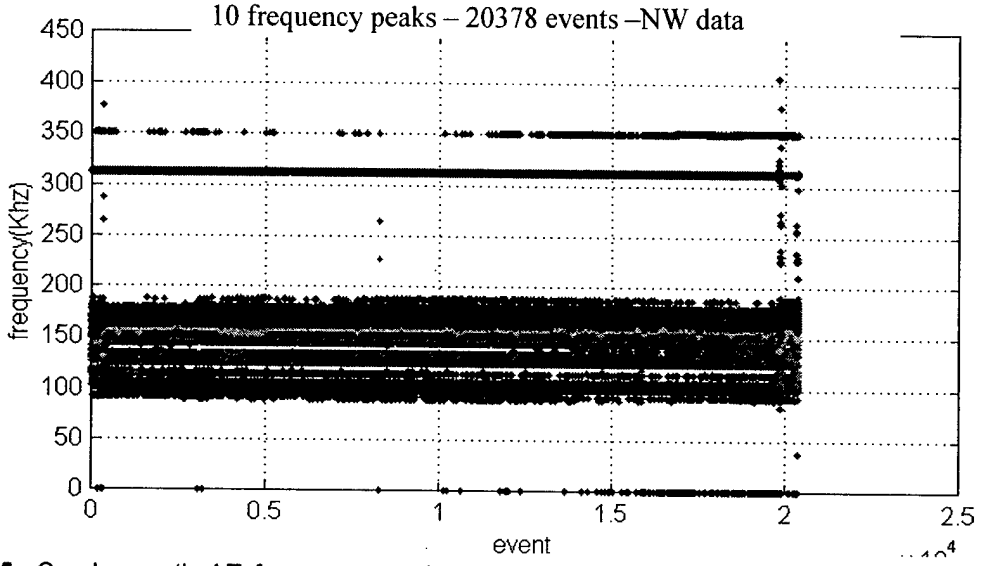

Figure 4.5 Crack growth AE frequency peaks versus event number for all 20378 events in the 4340 steel, NWU data (test B07).

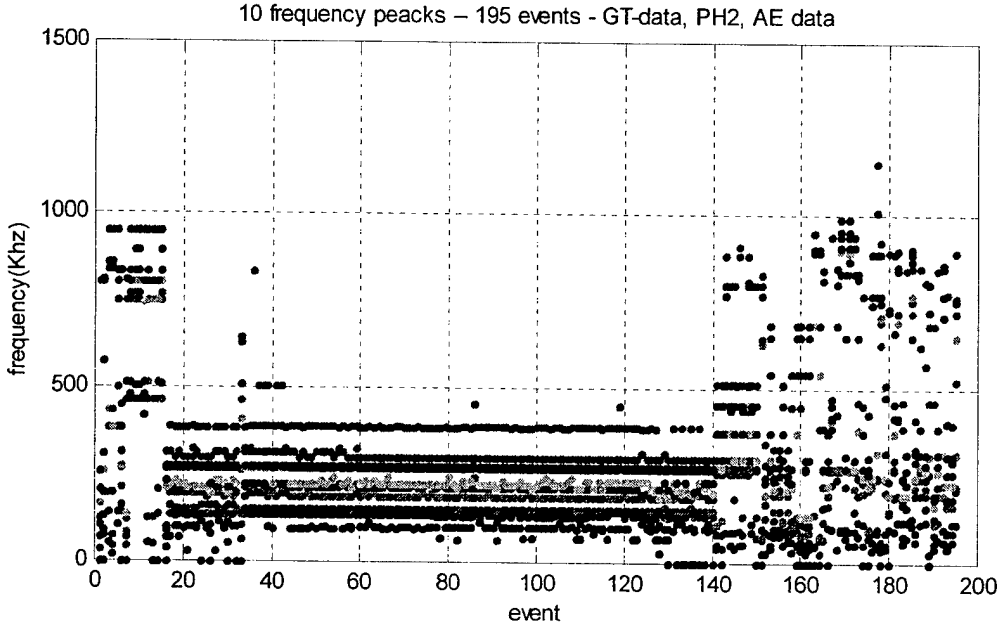

Figure 4.6 Crack growth AE frequency peaks versus event number for GA Tech data PH2, Sensor 1, PH13-8 specimen

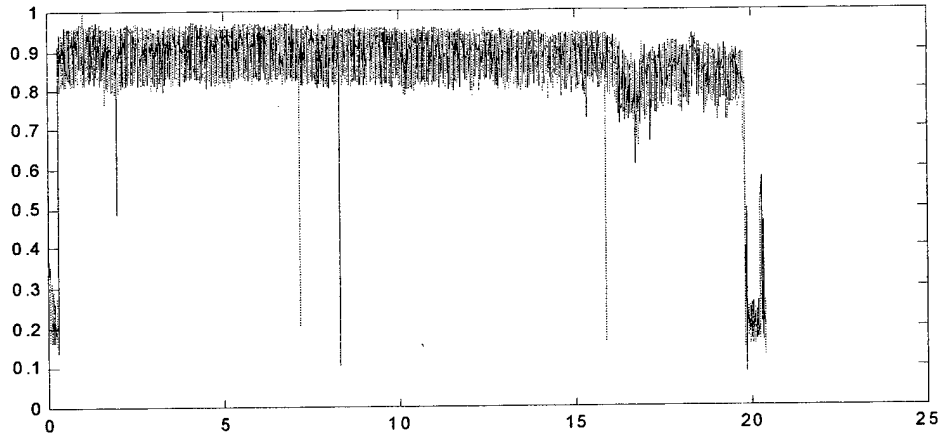

Figure 4.7 Maximum cross-correlation between the waveforms for event 1000 and other events for the test given in Figure 4.5.

Figure 4.8 shows the gray scale cross correlation matrix for the events in the experiment of Figure 4.6. Notice the generally banded structure of the matrix indicating significant correlation between adjacent waveforms in regions of rapid rise in the cumulative number of events.

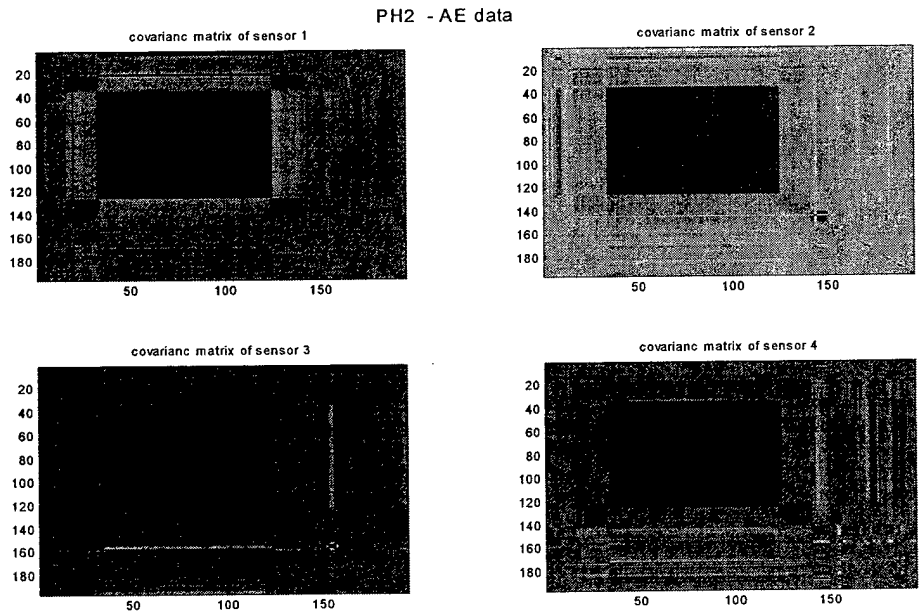

Figure 4.8 Cross-correlation matrix for the event waveforms of the experiment given in Fig. 4.6, Sensor 1 is the left top.

Figure 4.9 depicts over-plots of groups of waveforms associated with segments with high correlation. Notice the almost deterministic nature of some of these waveforms, which nearly overlap completely. It appears from these and other similar results that the potential exists for the use of cross-correlation between succeeding events, over a time window, as an indicator of the changes in the development and growth stage of a crack. This aspect requires careful studies of crack size association with waveform group correlation by experimentalists.

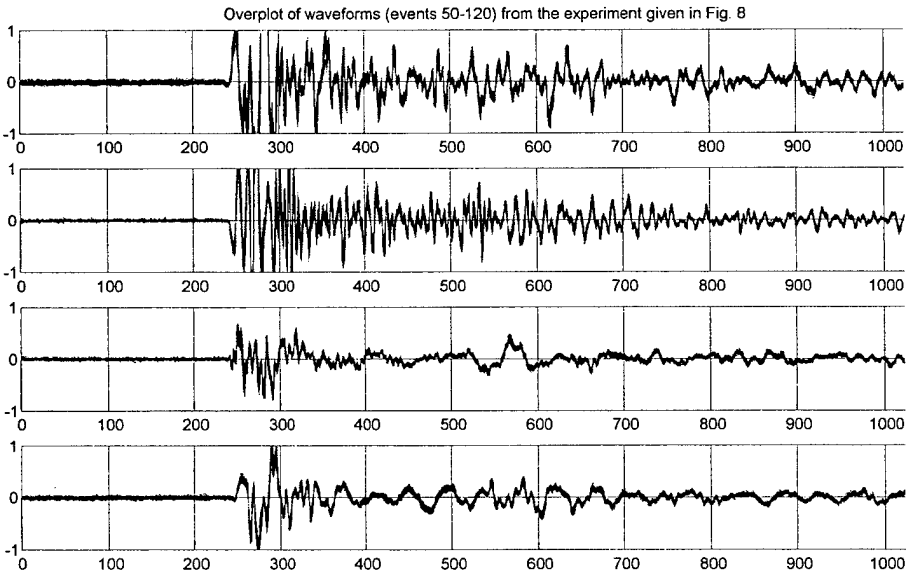

Figure 4.9 Over-plot of waveforms from the experiment given in Fig. 4.8., events 50-120, test PH2, AE data.

A.3 Principal Component Analysis (PCA)

Principal Components (PCs) are a convenient way of summarizing the significant statistical characteristics of a group of random signals in terms of an orthonormal basis set. This basis set will be called principal signals, or principal vectors for the case of discrete-time signal vectors. The principal vectors are simply the eigenvectors, with unit Euclidean norm (energy), of the sample covariance matrix of the N of signal vectors. These eigenvectors are arranged in order of decreasing eigenvalues, and the projection of a signal vector on the ith principal vector becomes the ith PC of that signal vector. The first few PCs can be a major source of data reduction, and the subspace spanned by the first few primary principal vectors can serve as a low-dimensional space for describing "signatures" of the signals of interest. Noise and other less significant components are also reduced or eliminated by the projections onto this lower dimensional signal subspace. In turn, clustering of PCs in an appropriate subspace may serve in the discrimination or classification different classes of signals.

Let $X=[X_1, X_2,\ldots,X_N]$ denote a matrix of N signal vectors from the group of crack-generated signals, with no dc components, during a fatigue experiment. The sample covariance matrix for this ensemble of signals is given by $\Sigma=XX^T$, where superscript T denotes matrix transpose. The eigendecomposition of is given by $\Sigma=\beta\Lambda\beta^T$, where β is the matrix of normalized eigenvectors and Λ is the diagonal matrix of eigenvalues of Σ with the eigenvalues $\lambda_1>\lambda_2>\ldots>\lambda_L$. The vector of PCs for the ith signal vector is then given by $P_i= \beta^T X_i$. In the following we present the PCA for an ensemble of N= 195 crack-generated AE signal vectors from the fatigue test PH2 from Georgia Tech. Each signal is contains L=1024 samples.

Figure 4.10 shows the distribution of the largest 10 eigenvalues of the sample covariance matrix. It is clear that the first principal vector dominates the description of the ensemble and that the first few

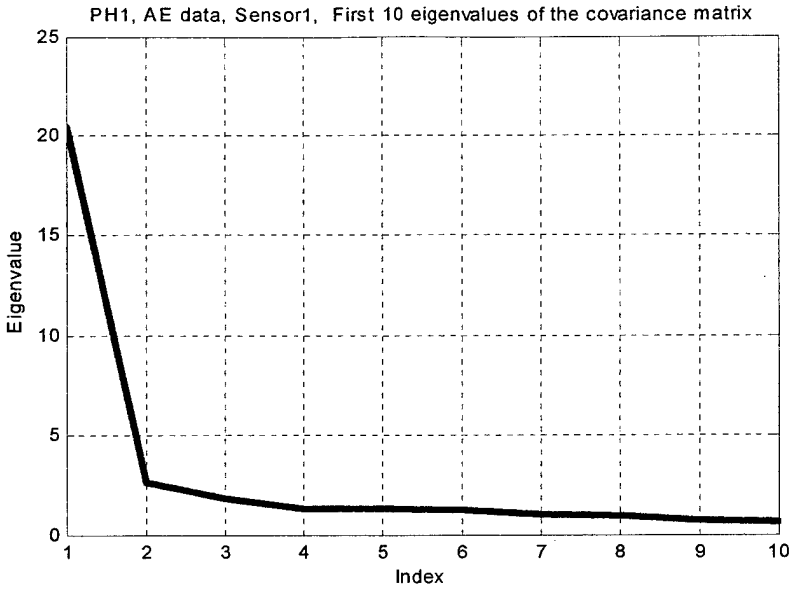

Figure 4.10 Distribution of ten largest eigenvalues of the signal covariance matrix for experiment PH2.

components are sufficient for the characterization of the signal subspace. The relatively large ratio of the first to second and third eigenvalues (effective rank near 1) is also an indicator of the high degree of similarity between the signal vectors in the ensemble. This seemingly indicates again that many of the AE waveforms generated from well-developed cracks are very similar (see also Figure 4.9). In the development of algorithms for classification of transients to be described later, we have used only the first two principal components as signatures for the signals and noise, although one can clearly increase this number without any problem other than an increase in the cost of computation.

Figure 4.11 shows plots of the first 5 eigenvectors describing this ensemble of signal samples. Notice that most of the energy is carried out in the lower frequency components of the transients (first eigenvector) with the higher dimensions characterizing the higher frequency details for the signal as well as the wideband noise present in th measurements.

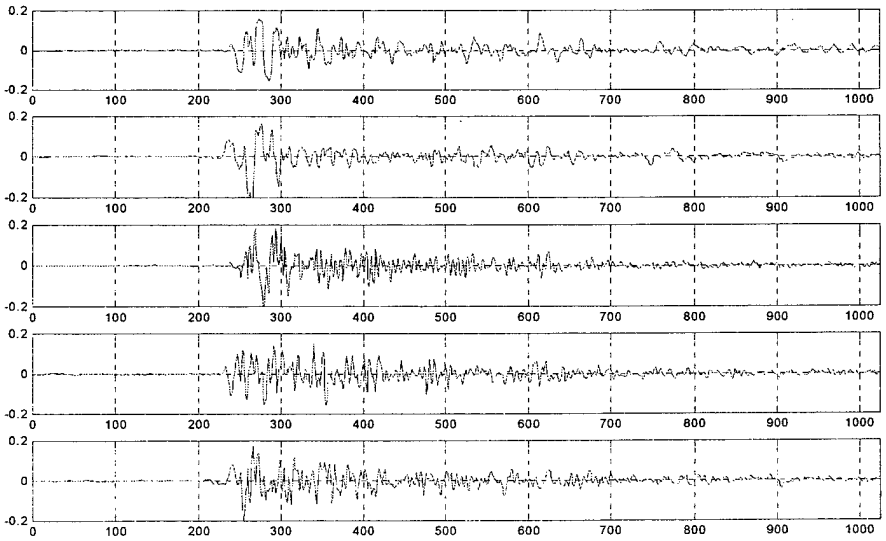

Figure 4.11 First five principal vectors for crack-generated AE signals of PH2.

B. Noise and Interference Models

As mentioned earlier, a number of measurements from on-ground and in-flight helicopter tests, as well as laboratory-based fatigue tests have produced information about the types of noise and interference one might expect in an operational AE based monitoring system. Not unexpectedly, the largest noise component is from mechanical vibrations. This noise, however, has low frequency content and is easily eliminated, for example, by an appropriate highpass filter, e.g. with 50KHz cut off. Other broadband noise observed from measurements on helicopters indicated the existence of nonstationary broadband noise in addition to the usual white electronic noise. A linear predictor may be useful as a data-adaptive whitening filter for this noise component.

The persistent type of noise, mentioned above, is ever-present in any signal acquisition systems and algorithms that are discussed later in this report, have been developed for the detection of AE and other transient signals buried in them. However, crack-generated AE signals are measured in the presence of a variety of other transient signals with significant spectral overlap. These interfering signals include AE signals generated, for example, by fretting, movement of fasteners and electromagnetic transient from switching mechanisms, relays and radar and communication sources. Accordingly, classification of the detected transients in a manner that isolates the crack-generated AE signals is key to the success of envisioned monitoring or diagnostic systems. Space-time processing using multiple sensors around hot spots provide the possibility of some filtering based on differential time of arrival. However, such arrival time may not be easily detected, resolvable, or in the case of electromagnetic interference be the same at all sensors.

A good source of mechanically-generated AE interfering signals was provided by the Georgia Tech fatigue experiments. Here we examine some of the characteristics of these interfering signals that are apparently generated by the grip mechanism at the two ends of the sample under test. Figures 4.12 and 4.13 provide the same characteristics, as given in Figs. 4.10 and 4.11 for the crack signals, for the grip-generated AE interferences. As can be observed from the slowly decaying eigenvalues, these signals appear to be much more random than the crack signals of Figs. 4.10 and 4.11. The difference between the characteristics of the principal eigenvectors is also evident in Figs. 4.11 and 4.13, providing the opportunity for signal- (or noise-) subspace processing for the selection of many of the crack signals even with a single sensor.

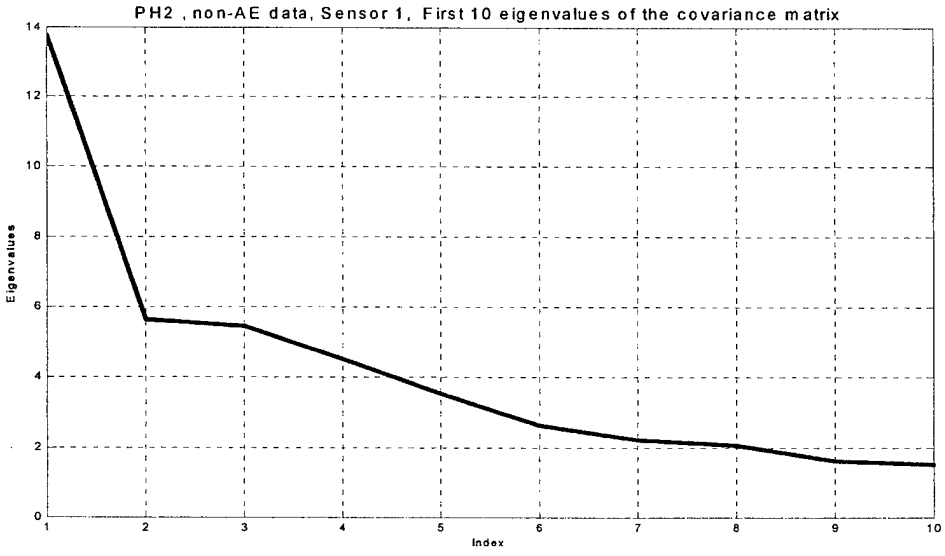

Figure 4.12 Distribution of the ten largest eigenvalues of the interference covariance matrix for experiment PH2.

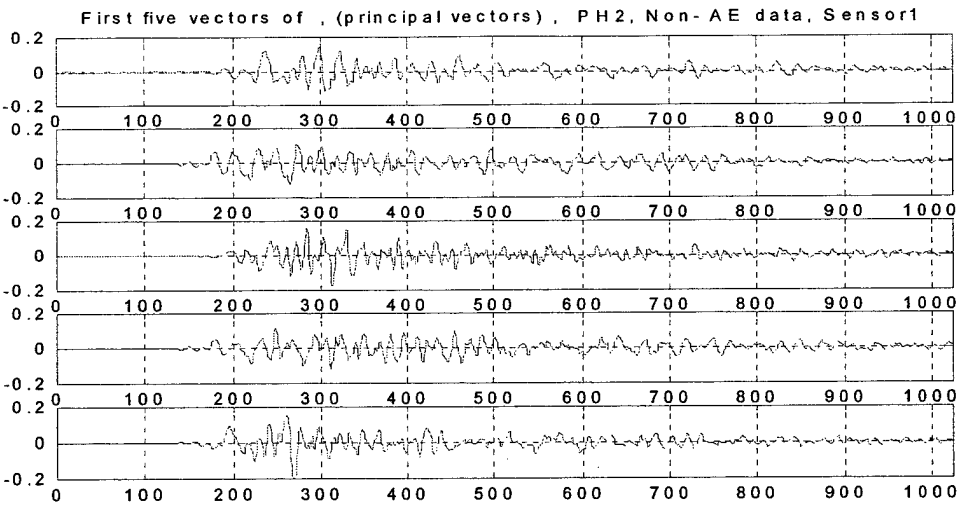

Figure 4.13 First five principal vectors for crack-generated AE signals of PH2.

C. Channel Effects and Blind Deconvolution

For small specimens of simple geometries the signal recorded by an ideal sensor placed on the surface of the specimen is a good approximation of the actual crack signal. But in cases where the machine component has a complex geometry and is large enough to exhibit significant dispersion characteristics due to wave propagation, the signal recorded by the sensor can be quite different from the AE signal that is generated at the location of the crack (source signal). In addition, sensor and electronic interface frequency responses may vary. This causes a wide variability in the characteristics of the AE signal recorded by the sensors depending on factors like the relative location of the crack with respect to the sensors. An example of these effects is demonstrated in subsection **A.1**. An understanding of the channel distortion thus becomes important. This becomes particularly critical for any multisensor space-time processing, other than a very simple processor such as differential time of arrival processor that is structured based on thresholding the received signal level-an approach that is only possible in a high signal to noise ratio situations. A more elaborate detector/classifier would require channel characterization to be used to extract spatial data from the detected transients as well as to construct estimates of the actual crack signals through deconvolution. Unfortunately, since the relative location of the crack may not be available a-priori, the channel characteristics must be obtained from the measured data. This places this approach in the blind equalization or unsupervised deconvolution category. When multiple sensors are used, the AE data acquisition can be represented equivalently as a single-input multiple-output (SIMO) system. The problem is then cast in the form of estimating the channel and source (crack signal) from the observed noisy outputs of the various channels.

The SIMO structure possesses certain properties that have been exploited in the last few years to provide blind solutions for the source in nonminimum phase systems using only second order statistics (SOS). Most of this work, however, has focused on communication systems where the underlying assumptions on the channel and source characteristics is not valid in the AE application. For example, the short finite impulse response (FIR) channel model is a realistic assumption in a wide variety of communication situations. In the AE context, based on the analysis of real AE data sets, we concluded that an infinite impulse response (IIR) channel model is more suitable. Using an FIR channel model for such a case is unrealistic as it contributes to a large model order. In the case of the complex geometries of machine components, minimal assumptions need to be made on the source characteristics due to the lack of information thereof. Therefore, we have treated the source as an unknown deterministic sequence. We

have provided blind solutions for the channel and source under respectively pole-zero and deterministic models.

Details of these results are provided in [5-7]. While these results have extended the state of the art in the general blind system identification and deconvolution, we have determined that their utility in a practical AE crack signal detection scenario is too complex and not very robust. Unfortunately, the implication of this is that techniques such as generalized cross-correlation may be limited for differential delay estimation. For example, while relatively high correlation levels, above 0.7 for the correlation coefficient, are found among groups of AE signals for the same sensor in the fatigue experiments, the cross-correlation between the waveforms of the same events measured by different sensors is relatively low. Accordingly, a low threshold level, around 0.4, must be used in the design of correlator-based differential time of arrival estimation. Figure 4.14 shows an example of the cross correlation between the signals for the same event received by sensors 1 and 2 from experiment PH2 for one of the events included in Figure 4.8.

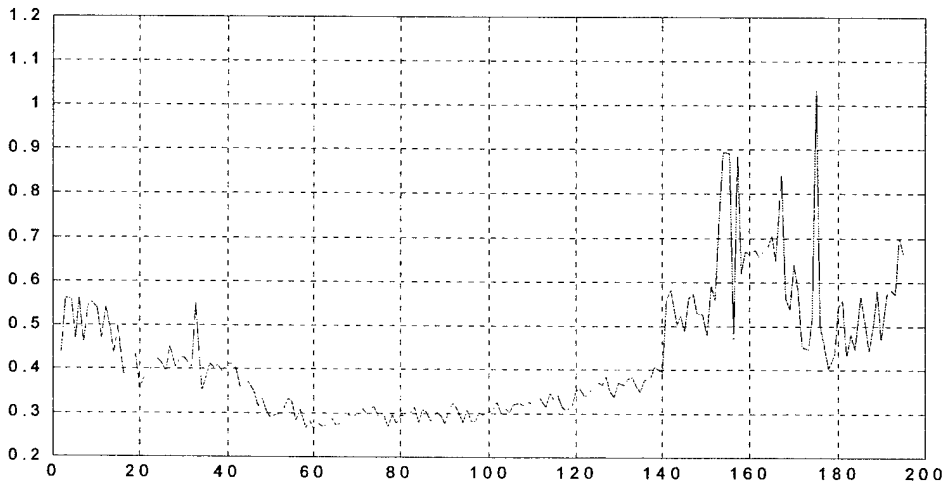

Figure 4.14 An example of the cross correlation between the signals for the same event received by sensors 1 and 2, as a function of delay, from experiment PH2, AE data.

D. Transient Signal Detection

As was mentioned earlier, the uncertainty in the precise characteristics of the signals and the propagation effects, present a challenge in the design of detectors of transient signals in noise, when signal parameters are only approximately known. Accordingly, traditional matched filtering is rarely an option. As part of this research, we have developed a suite of detectors in this category for use in low signal to noise ratio operations. Here we summarize two of these detectors. The signal model used is as was given in subsection **A.1**. In this model, the transients can be adequately represented as a sum of decaying sinusoids. This model assumption implies a specific type of pole-zero (ARMA) model for the observed transients, and the two specific detectors that are summarized below rely on such a parametric signal model. Details are given in references [4, 7-10].

When cracks are reasonably well-developed with sensors in close proximity of the cracks, experience seems to indicate that there is sufficient signal level that the detection can be performed on the basis of simple processors such as bandpass or multiband filter, followed by signal level thresholding. The follow up processors to be discussed, are then concerned with the classification of the detected transients into those that are generated by cracks and by sources of interference.

D.1 Eigenfilter Bank

For this method, in addition to the pole-zero model assumption, we assume prior knowledge of the range of frequencies and decay rates of the sinusoidal components that make up the AE transient. Note that as fault diagnosis is not solely based on detection, accurate knowledge of this range might not be critical. A rough estimate might serve as a preliminary sieve for rejecting some of the noise events in the detection stage itself.

In this method we construct a filter bank that divides the frequency range of interest into frequency bins. We have no complete prior knowledge of the frequency and decay rate of the AE signals, but a range of frequencies and decay rates that they might exhibit could be known. Optimal tapers for this case can be computed as a generalized eigenvector problem [7, 9]. The set of eigenvectors computed for each frequency bin are then used as the filter coefficients (with time index reversed) for the bank of filters corresponding to that frequency bin. The output of these eigenfilters are then combined as weighted sum using the corresponding eigenvalues. Using a set of these eigenfilter banks, each corresponding to a given frequency bin of interest, decomposes the original time series into several components. The collection of time series' of all the channels can be thought of as a decomposition of the original time series on a highly redundant frame. "Denoising" of the time series can then be accomplished by suitable thresholding of the frame coefficients. The denoised time series then contains, ideally, the ``detected" transients.

This method was applied to a set of nano-indentation AE signals recorded from Tantalum Nitride specimens, as discussed in subsection **A.1**. Using part of the data set, a suitable range for the decay rate was estimated. The optimal taper for frequency bins of 100 KHz width for this range of decay rates was then numerically computed. The AE signals that were not used in the above estimation were then used to synthetically construct a time series that consisted of a random cluster of AE signals buried in additive white Gaussian noise. The outputs were then denoised using the method proposed in [10].

To evaluate the performance of this technique in more realistic noise environment and with AE signals affected by propagation effects, the AE signal of sensor B in Fig. 4.3 was used in the presence of additive colored noise with the same spectral characteristics as the background noise measured in the Honeywell in-flight helicopter data. This noise was simulated by an autoregressive model that was fit to the noise in sensor 4 of the helicopter data [11]. Figure 4.15 shows the power spectrum of this noise. Figures 4.16 and 4.17 show the transients buried in the noise and the output of the eignfilter bank processor, respectively [11].

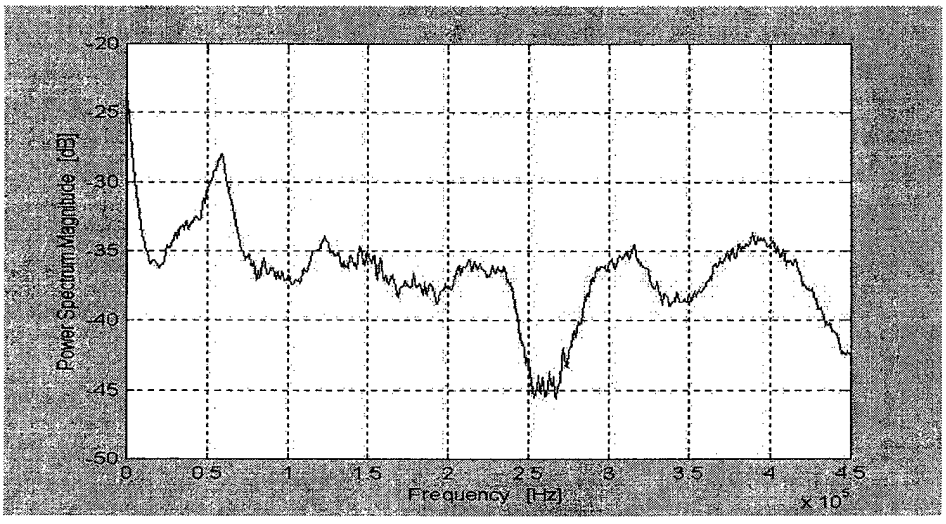

Figure 4.15 Helicopter noise spectrum.

The range of time bandwidth for the filter was taken to be between 1kHz and 10kHz, and the resonance frequency range was assumed to be between 100kHz and 200kHz. The filter had 50 taps. While the eignefilterbank is designed with a sense of optimality in terms of maximizing SNRs within the expected bands, a simpler bank of deterministic filters, e.g. tuned to the expected range of frequencies may, in practice suffice. Such a filter bank followed by a thresholding operation at the output of each filter may be sufficient for denoising. The threshold, must be adapted to the background noise. Reference [11] has examples of such a processor with results comparable to the eigenfilter bank, in the case of the data used in Figure 4.17.

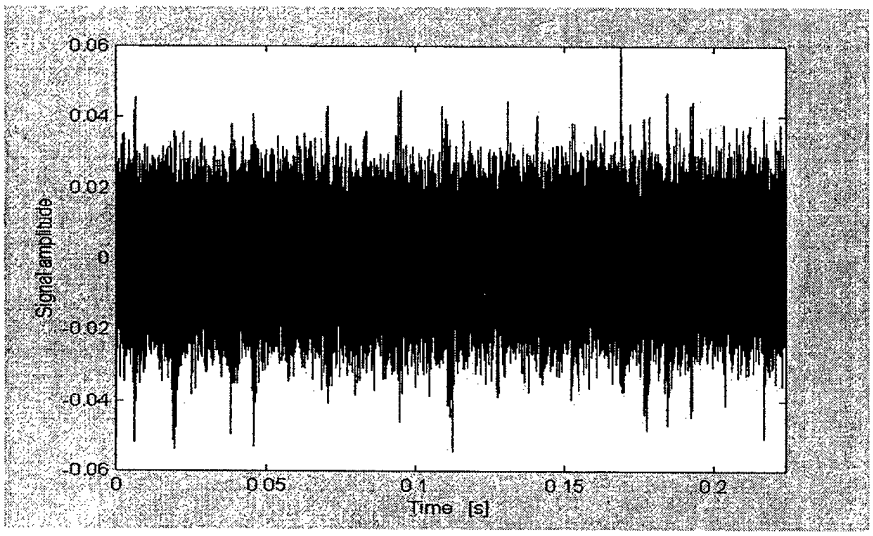

Figure 4.16 AE transients in the noise of Figure 4.15 at –2 dB SNR.

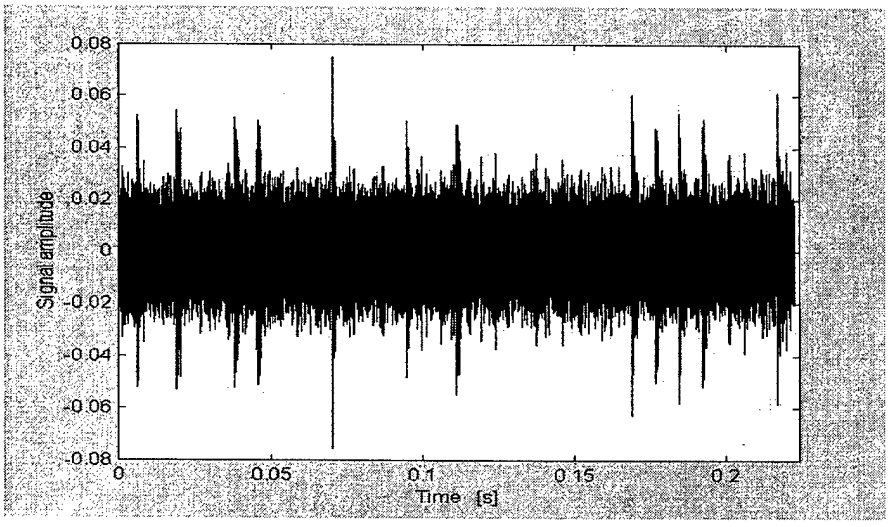

Figure 4.17 Output of the single-band eigenfilter to the input of Fig. 4.16.

D.2 Model Residual Detector

In this scheme, detection is based on thresholding the error associated with fitting the observed waveform with a parameterized model, specifically, a pole-zero (ARMA) model. The decision is made by the thresholding of the ratio of the residual energy in fitting the model to the total signal energy. Of course, the parameters of the model are not known a priori but are estimated from the recorded data. However, direct constraints can be placed on them if a priori information on their range is available [7-9].

Using the signal model as a combination of damped sinusoids, N samples of the signal can be represented by the linear parametric model $s=M(\theta)a$, where M is a matrix with columns giving the time samples of the modes (complex) of the signal involving the unknown frequencies and bandwidths represented by the parameter vector θ, and a is the relative amplitudes of the different modes (for other than dc, all the modes are in conjugate pairs). Define

$$\eta = \min_{\theta} \frac{Y^T Q_M Y}{Y^T Y} \qquad \text{with} \qquad Q_M = I - M(M^H M)^{-1} M^H$$

where Y is the measured noisy signal, and Q_M is the projector onto the left null space of M. η is compared with a threshold from below, for the detection of a transient modeled well by the estimated model parameters. In case a transient is present in the data the residual η will be smaller than if the data only consists of noise. The real residual curve generally has a large variance and must be smoothed to achieve clearly detectable transient dips. The drawback is a decrease of the resolution, i.e. two very closely-spaced transients may be interpreted as one. We have developed block-based and adaptive, low-complexity versions of the algorithm, with the block-based one with slightly better performance. Figure 4.18 shows an example of η for the same AE signals that are used in Figures 4.16 and 4.17 measured in the presence of white noise, using an LMS-type adaptive estimator for the parameters. Note that the minima in the figure are indicators of the transients. While, this approach works well for detection in white noise, it is not well suited to cases for which the noise is highly correlated. This is because at low SNRs, spectral peaks of the noise may dominate the modeling, with η tracking a model for the noise, rather than the signal. If there is substantial difference in the characteristics of the noise and the transients, a pre-whitening step on the noise may alleviate this problem.

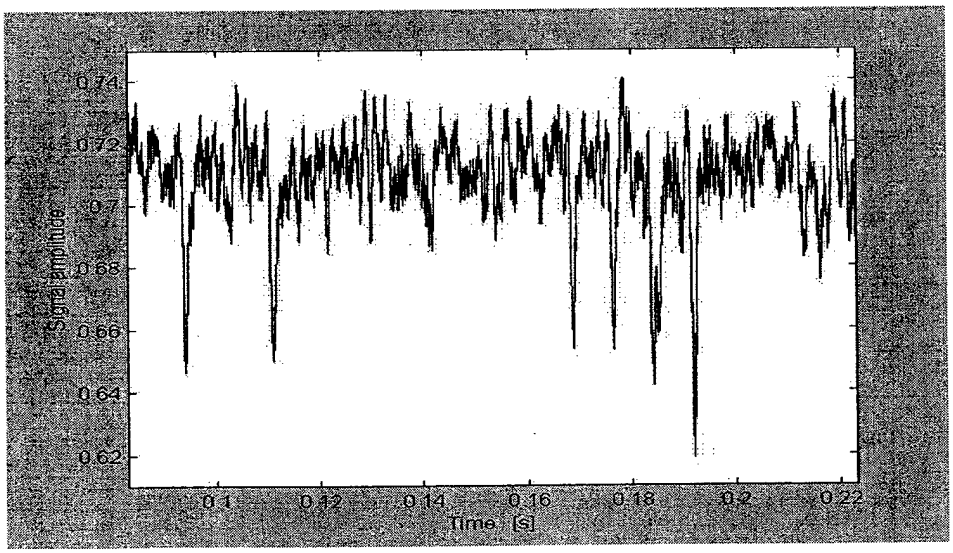

Figure 4.18 Residual curve for transients in white noise, SNR = -5 dB.

E. Classification

In this section, we summarize some of the results related to the classification and discrimination of transients that are detected. The data that was utilized for this development consisted of the in-flight single sensor helicopter data provided by Honeywell [12], and the four-sensor notch-based fatigue experiment provided by colleagues at Georgia Tech. [17]. The tools that were employed, in addition to normal filtering and correlation analysis and principal component analysis that was discussed earlier, included neural networks, particularly the Kohonen Self-Organizing Map network [13-15]. We will first summarize the structure and training approach that we have developed for improving the learning process of the SOM network for the types of signals under study.

E.1 The SOM Network

The Kohonen SOM network [16] is depicted in Figure 4.19.

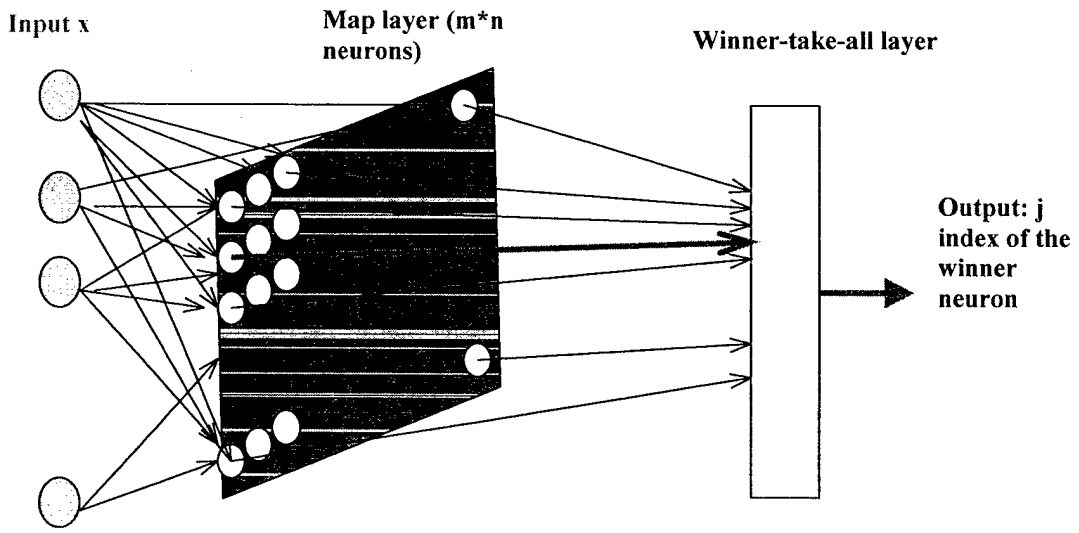

Figure 4.19 The SOM network structure.

Consider a k-input, M-by-N Kohonen network, where each neuron has a k-dimensional weight vector W_i, $i = 1,2,...,MN$. The training steps for the network are as follows:

1. Initialize the network by assigning small random values $\{m_1, m_2, ..., m_k\}$ to the weight vector of each neuron:
   $W_i(0) = [m_1\ m_2 \cdots\ m_k], \quad i = 1,2,\cdots,MN$,
   where $W_i(0)$ refers to the initial value of W_i. Let n=0, where n is the training step.
2. From the set of k-dimensional training vectors, choose a vector as the initial input vector $X(n) = [x_1\ x_2 \cdots\ x_k]$. Then calculate the Euclidean distance between the weight of all neurons and $X(n)$:
   $D_i(n) = \|X(n) - W_i(n)\|, \quad i = 1,2,\cdots,MN$.
3. Select the j^*-th neuron as the winner neuron if D_j is minimum among D_j's, i.e.:

$$j^* = \arg\min_j D_j, \quad j = 1,2,\cdots, MN.$$

4. Update the weight vectors of the winner neuron j^* and its neighboring neurons according to the following equations:

$$W_i(n+1) = W_i(n) + \eta(n)[X(n) - W_i(n)], \quad i \in S_{j^*}(n)$$

$$W_i(n+1) = W_i(n), \qquad i \notin S_{j^*}(n)$$

where $\eta(n)$ is the learning rate such that $0 < \eta(n) < 1$, and $S_{j^*}(n)$ is the neighborhood of the winner neuron j^*.

5. Repeat steps 2-4 for n=1, ..., N_T −1, where N_T is the total number of training vectors. This number should be at least 500 times the number of neurons MN in the Kohonen network.

In order to improve the performance of the Kohonen network for our purposes, we have developed the following strategies for the implementation of the learning process

1. For selecting appropriate values of M and N, start with a large number, for example, M=N=8. In the next step, change M and N such that MN is approximately equal to the number of the neurons which have been activated.
2. The norm of the initial weight vectors should be chosen to fall within the range of the norms the training vectors.
3. The initial $S_{j^*}(0)$ can be large enough to include all the MN neurons in the network. If after several hundred training steps, neurons show an ordered pattern, $S_{j^*}(n)$ may be pared down to contain only the winner neuron j^*. Let $M > N$. Several experiments have shown that the following $S_{j^*}(n)$ is the best:

$$| S_{j^*}(n) | = \begin{cases} g(n), & \text{if} \quad g(n) > 1 \\ 1, & \text{if} \quad g(n) \le 1 \end{cases},$$

where $| S_{j^*}(n) |$ is the size of the neighborhood and $g(n) = M(1/M)^{10n/N_T}$.

4. The learning rate $\eta(n)$, can be either a constant or a monotonically decreasing function. We suggest the following learning rate:

$$\eta(n) = \frac{1}{1+L}\left(\frac{5}{4+n} + L^n\right), \qquad L = \left(\frac{1}{N_T}\right)^{\frac{1}{\sqrt{1000\ N_T}}}.$$

5. Since random initial weight vectors are used, after repeating the training procedure with the same training set $\{X(0), X(1), ..., X(N_T)\}$, similar weight vectors will be assigned to different neurons. For repeatability of the training results with the same training vector, the final weight vectors after the training procedure should be sorted. Here the vectors are sorted based on the value of the first element in each vector.

In most cases, we use the time-frequency distribution of the data as input to the network. These features are encoded into the weight vectors of the Kohonen network. Each weight vector represents a particular type of input pattern. Thus, different locations of the neurons in the Kohonen map reflect different input spaces, which provide us with the information required for clustering the test data. During the clustering of the test data, each neuron or a group of neighboring neurons in the Kohonen map responds to a particular kind of input pattern. So, we expect different types of transient input signals to activate neurons (winning neurons) in different locations of the Kohonen map. Consequently, we can use the index sequence of active neurons to discriminate between crack-related AE's and other transient interferences. We now summarize the application of this tool in and others discussed earlier to the data from the Honeywell in-flight data and the Georgia Tech fatigue test data.

E.2 Honeywell In-Flight Data

In fall 1997, Honeywell performed 15 hours of flight tests on a CH-46 Sea Knight helicopter in order to assess the feasibility of detecting crack-generated AE signals at sensors placed on different locations of the helicopter [12]. Figure 4.20 shows a diagram of the rotor arm.

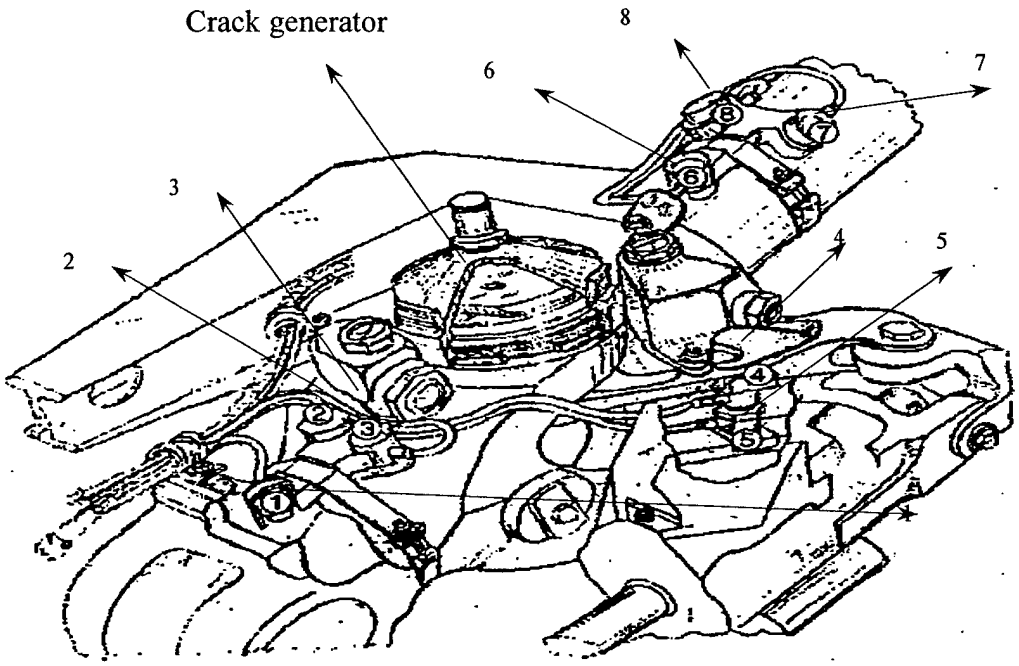

Figure 4.20 Rotor assembly (courtesy of Honeywell [13])

assembly that was instrumented with multiple sensors and a crack generation simulator. Eight piezo-electric sensors were mounted on one of the three rotor arms to monitor the rotor .The sensors were located at three different parts; #1, #2 and #3 on the connecting link, #4 and #5 on the pitch shaft and #6, #7 and #8 on the pitch housing. Crack-generated AE signals were simulated with a periodic pulse train applied to a pieazoelectric "pinger" at different signal strengths. The signals from the sensors were filtered with a variety of filters in an effort to evaluate the optimal filter type. The filters were all connected to a 16-1 MUX, i.e. only one sensor was recorded at a time. No multi-sensor data is available. The signal was amplified, frequency modulated and transmitted via a FM 2.3 GHz S-band telemetry link to a receiver inside the helicopter. After demodulation and filtering with a 1-pole low-pass filter, the signal was digitized with 8 bit accuracy and finally recorded

For the in-flight data, a 5×5 Kohonen network was considered. The training set was composed of 2000 five-dimensional principal component vectors of the short-time Fourier transforms (STFTs) of the first half of the signal recorded by sensor 2. In this case the window size and FFT size of the STFT are 1024. The test set consists of the second half of the signal of sensor 2, and all the signals of other sensors. Note that both the training and the test sets contain simulated cracks together with other interferences. Figure 4.21 shows a small portion of the input test signal in time-frequency space, and Figure 4.22 is the index of the corresponding activated neurons at the output of the Kohonen network. As can be inferred from these two figures, crack events (spikes in the time-frequency domain) activate neurons with high indices. This kind of behavior has been observed for other test signals, and shows the mechanism by which the Kohonen network identifies cracks from strong interferences.

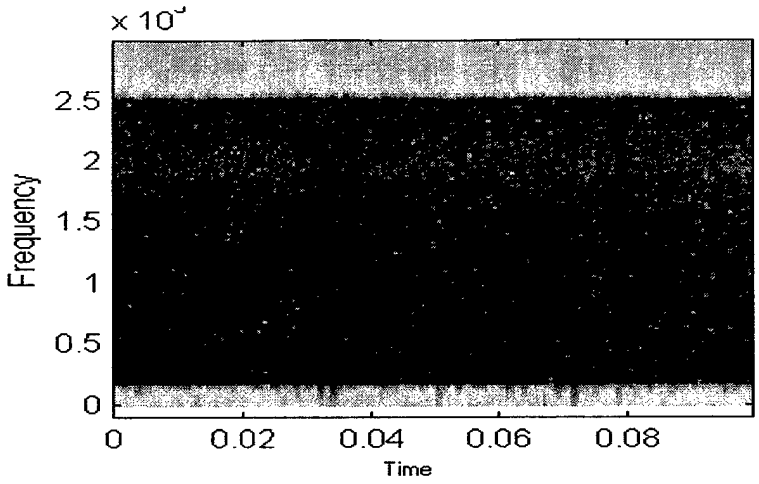

Figure 4.21 STFT of a segment of data from sensor 2.

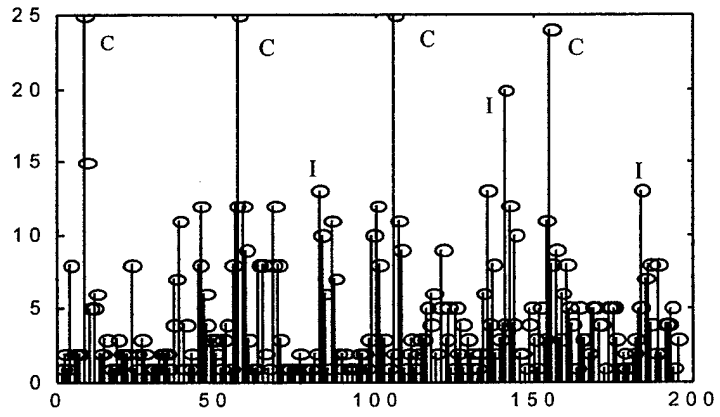

Figure 4.22 Indices of the activated neurons corresponding to the time-frequency components of the above segment.

For sensor 2, the probability of incorrect identification was less than 4%, i.e. more than 96% of simulated cracks were identified correctly. For other sensors (except sensor 3 which was highly corrupted), the probability of correct identification was in the range of 75%-85%.

E.3 Georgia Tech Multi-Sensor Fatigue Data

The experimental setup of the multi-sensor data is shown in Fig. 4.23 (see [17] for details of the experiment). During the fatigue experiment, the specimen was cyclically stretched to generate micro-cracks in the central notch and to grow resulting well-developed crack. The four sensors are placed in positions such that transient AE signals emitted from the generated at and propagated from the notch, propagate to the four sensors at nearly the same time. If the transients are clean and well-defined, spatial filtering should be able to eliminate interfering transients through differential time of arrival discrimination. Data was collected with different types of sensors, loading and mounting. We have analyzed the characteristics of several sets of the data on two different materials. Here, we only report on some of the results from two tests, denoted PH1 and PH2 [17]. The sampling frequency for these two tests is 5MHz, and the data length for each recorded event is 1024 samples.

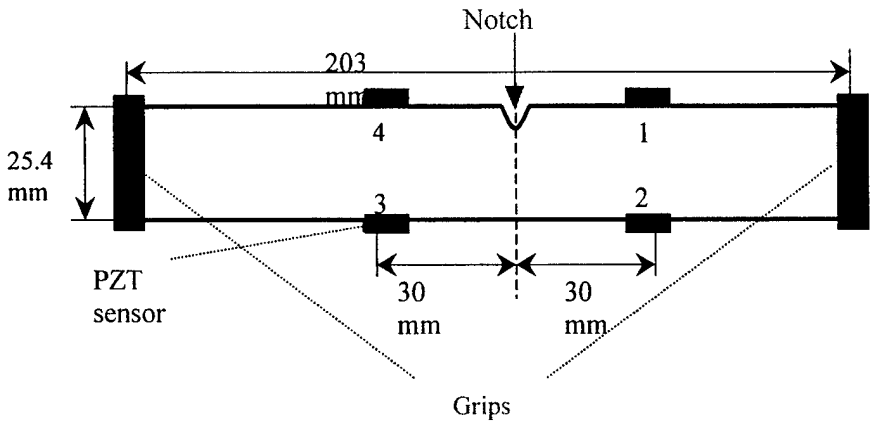

Figure 4.23 Fatigue test set-up for the PH13-8 Notch specimen

E.3.1 Multi-Sensor Acoustics Emission Signal Characteristics

The four-channel data acquisition system that was employed, utilized a voltage threshold stage for activating the simultaneous capture of the event transients by the four sensors. The threshold was set high enough that the made the capture of low-level micro-crack AE signals at the earliest stages of the crack generation highly unlikely. Therefore, all the captured events (signal and interference) were at relatively high signal to noise ratio, with clearly visible transient signal characteristics. During stretching, the grips that are located at both ends of the specimen generate, and/or couple to the sample many AE transient signals that are co-channel with the crack-related AE signals. We will denote these interfering events as "grip signals" or "non-AE" signals, and also refer to the crack-generated signals as "AE signals".

Grip signals provide a real case, in which crack-generated AE signals must be discriminated from unwanted interference. The estimated delays between pairs of sensors are clearly random. A threshold can be placed on this estimated delay, to discriminate between signals arriving from the region of the crack and those coming from, for example, the grip regions. Usually the waveforms of Sensors 1 and 2 look similar from a delay point of view, and the same observation holds for the other pair of sensors. This can be attributed to the fact that Sensors 1 and 2 are on one side and sensor 3 and 4 are on the other side of the specimen. Unfortunately, it is not possible to distinguish between the two types of "desired" and "undesired" signals, automatically, based *purely* on spatial processing. This is because threshold-based differential delay estimation has high variance for many of the lower signal-to-noise ratio events and for cases where the transient signals are not well structured (fast rise-time). As mentioned earlier, cross-correlation analysis between the sensors also is not an optimum estimator for the delays, since the signals received at different sensors suffer from channel effects that are more complex than a simple propagation delay. We will describe several approaches for successfully discriminating between the signals and interference by space-time processing, using differential delays, time-frequency information, and principal components. In the next section of the report, we will briefly examine the multi-sensor PH1 and PH2 signals with regard to frequency characteristics, and principal components.

E.3.1.1 Frequency Domain Features Of The Data

For some sensors, the crack-related AE events for the PH1 and PH2 tests appear to have more frequency components between 500KHz to 1MHz than the interfering events (see Figure 4.24). In addition, we found it necessary to bandpass filter all the signals within a passband of 20KHz - 1MHz to remove a number of noise-related signals of unknown origin.

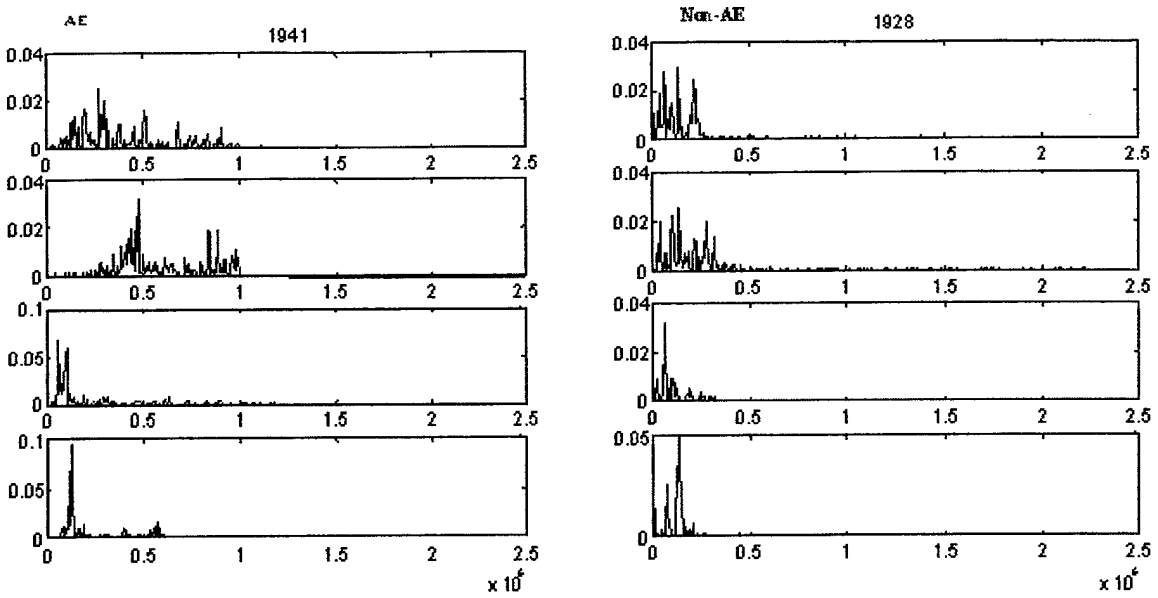

Figure 4.24 PSD of an AE (left) and non-AE (right) event. The four figures in each column represent signals from sensor 1 (top) to 4 (bottom). Horizontal axis is in Hz.

E.3.1.2 Principal Components Of The Data

In subsections **A.2** and **B**. we presented a characterization of the AE and non-AE signals for these fatigue experiments in terms of their respective first few principal components. A visual inspection of the principal vectors in Figs. 4.11 and 4.13 indicated the possibility of discrimination between the AE and non-AE events based on a separation of their respective "principal subspaces", that is the subspaces spanned by the first few principal vectors of the two classes of signals. We will call these two subspaces "signal subspace" and "interference subspace". For the type of data under consideration, the dimensions of each subspace will typically be less than 10, which is a significant reduction from the dimension of the covariance matrix, which is 1024. In a later section, we will summarize some results based on the discrimination between the signal and interference, based such on projections onto the signal subspace. Such an approach, however, requires a preliminary process, in which the signal subspace has been estimated. This may not be possible, in which case one is faced with the possible separation of the signals and interference based on the PCs of the *combined signal and interference data set*. This is discussed next. Figure 4.25 shows the distribution of the first two principal components associated with the output of the RBF network.

Figure 4.26 shows the second principal component vs. the first principal component (AE and non-AE) for each of the four sensors. This figure shows that the two principal components are mainly divided into four clusters (three blue regions and one red region). By plotting the waveforms of the events in four regions of Fig. 4.26 and analyzing their delay characteristics, we have determined that the blue clusters correspond to grip-related signals. This is not surprising, in that non-AE (grip) events are in substantially greater number than AE events in the complete data set. Accordingly, the first two PCs are heavily influenced by the statistical characteristics of the interference, resulting in a clustering of the AE PCs around the origin. One can use the clustering of the PCs, then to remove a large number of non-AE events, either based on single sensor data only, or by a validation or voting rule using the PCs of all the sensors. To separate the clusters, use a simple radial basis function (RBF) network. Here, the unsupervised RBF network, initiated with three random bases, will converge to the real location after several steps. However, there remain many grip-related events in region red of Fig. 4.26. In the next section we use other features to remove these.

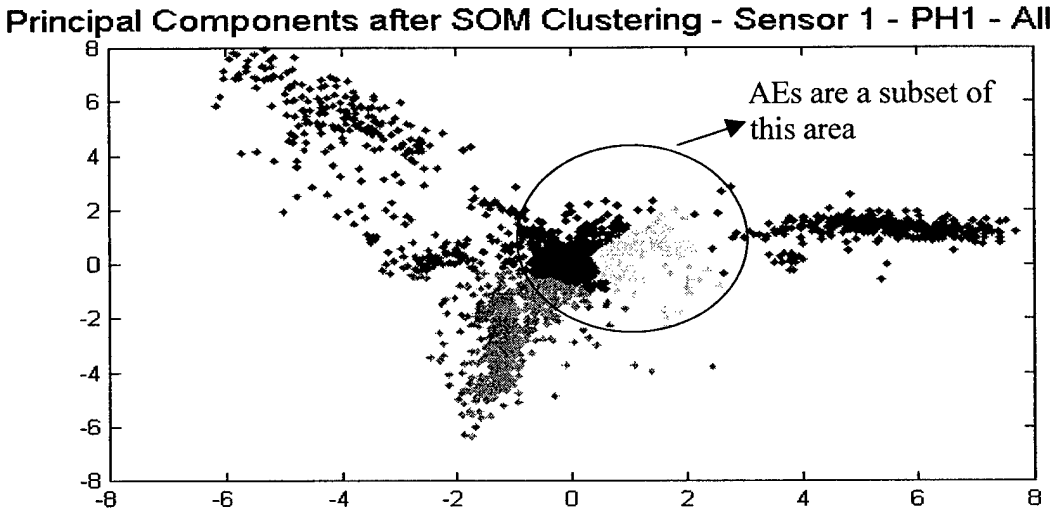

Figure 4.25 Second principal component vs. first principal component for sensor 1, PH1 data. Regions green, red and cyan are non-AE

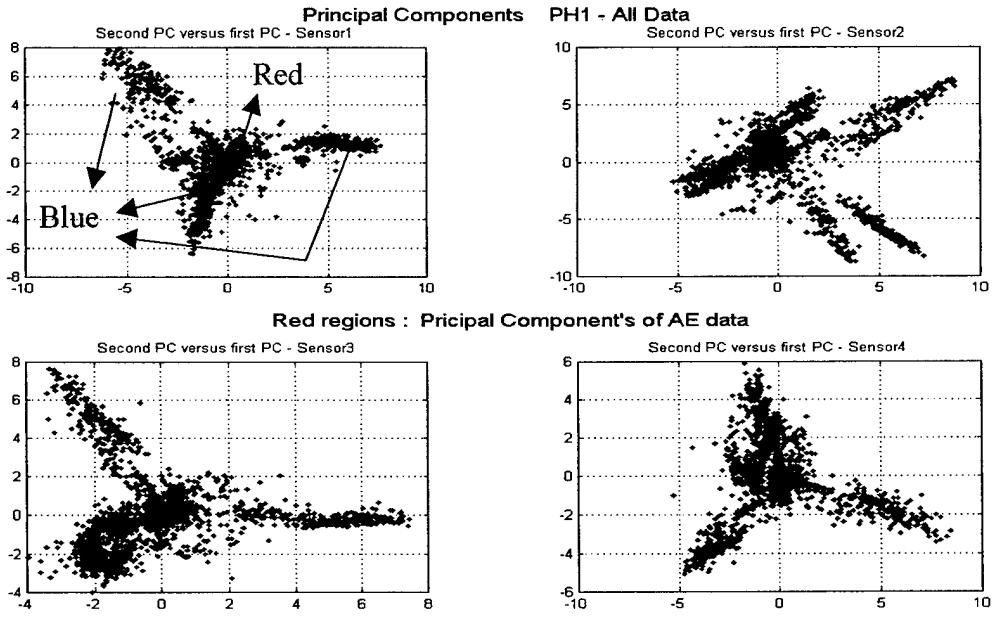

Figure 4.26 Second principal component vs. first principal component for all sensors.

E.3.2 Proposed System And Delay Analysis

In this section, we propose a system that removes the non-crack signals and applies a Kohonen network to cluster the potentially crack-related signals. Fig. 4.27 shows the proposed system for AE signal clustering. An explanation of the system blocks follows. The band-pass filter 20Kz - 1Mhz, is used to remove low frequency noise signals. This filter will remove a signal if the ratio of its output energy to the input energy is below a certain threshold. Using the first and second principal components (a larger number of PCs, e.g. 5, can just as easily be used, if needed) we remove clusters that correspond to the grip-related signals with radial basis function (RBF) network as previously described. Cross-correlation is then used to measure the delays between the sensors in order to remove signals that have relatively large absolute differential delays.

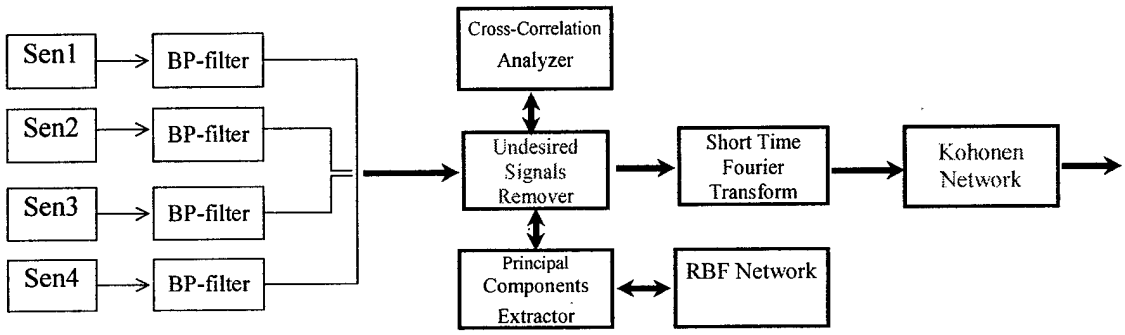

Figure 4.27 Proposed system for acoustic emission clustering.

E.3.2.1 Delay Estimation for the Multi-Sensor Data

Based on the configuration Fig. 4.23, crack-related signals should arrive at all four sensors within about 2-5 microseconds, while grip signals arrive at sensors 1 and 2 earlier, or later, depending on the grip generating the event, than arrival at sensors 3 and 4 by a larger time period, on the order of 10-15 microseconds.

Figure 4.28 shows the estimated differential delays between the signals received at 3 pairs of sensors. The estimated delay is based on the location of the maximum of the cross-correlation between the signals of the two sensors. The intuition behind this method is that, for a pure delay model of propagation, two data sequences from the same source will have the maximum cross-correlation when the delay between these two data sequences is compensated. Only normalized cross-correlation values above a set threshold are utilized as candidate locators for the delay. Ideally, a high threshold, say 0.8, is desired. However, the propagation effects discussed earlier have prompted us to employ threshold values as low as 0.4 for this method, substantially increasing the possibility of large estimation error. In selecting the events based on differential delay between, say sensors 1 and 2, we declare those with delays greater than 10 usec as grip-related.

E.3.2.2 STFT and the Kohonen Network

Although we have applied several methods to remove most of the non-crack signals, some grip and noise-related events still remain. Because we do not have a precise model for crack-related signals, clustering based on a neural network seems to be an appropriate method for our case. Since the data is not presented with a set of input-output pairs, we cannot use a supervised method. Hence we use the Kohonen network, because it is an unsupervised method, in which the network is presented with only the input samples, and samples are grouped into classes which are self-similar. Therefore, in the last stage of the proposed system, a 4×4 Kohonen network was used. The training set was composed of 500 128-

dimensional vectors of the short-time Fourier transforms STFTs of the signals, randomly chosen from the rest of the signals of Sensor 1, which were called potentially crack-related signals. Because of the limited number of the available training vectors, we used them repeatedly during the training phase. The test set consists of the signals of all four sensors, with the training set excluded. Figure 4.29 shows which event mapped to which neuron. Since crack-related signals have different time-frequency features compared to grip and noise-related signals, we expect crack-related signals to be mapped to special neurons. Our results show that almost all the AE signals mapped to the neurons 4-6. Figure 4.30 shows two samples of crack-related signals detected by Kohonen network.

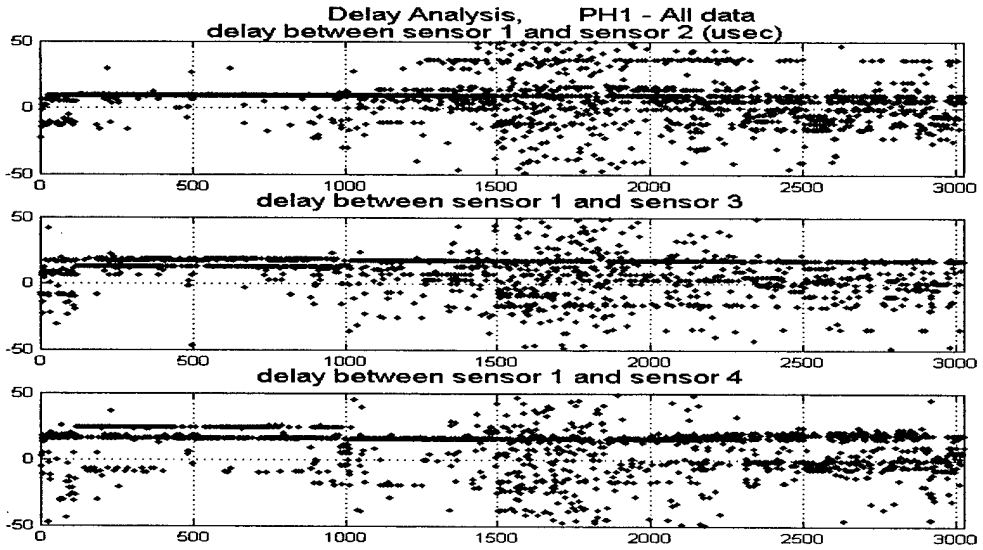

Figure 4.28 Delays between pairs of sensors for all 3027 events, PH1. (a) Sensors 1 and 2. (b) Sensors 1 and 3 (c) Sensors 1 and 4.

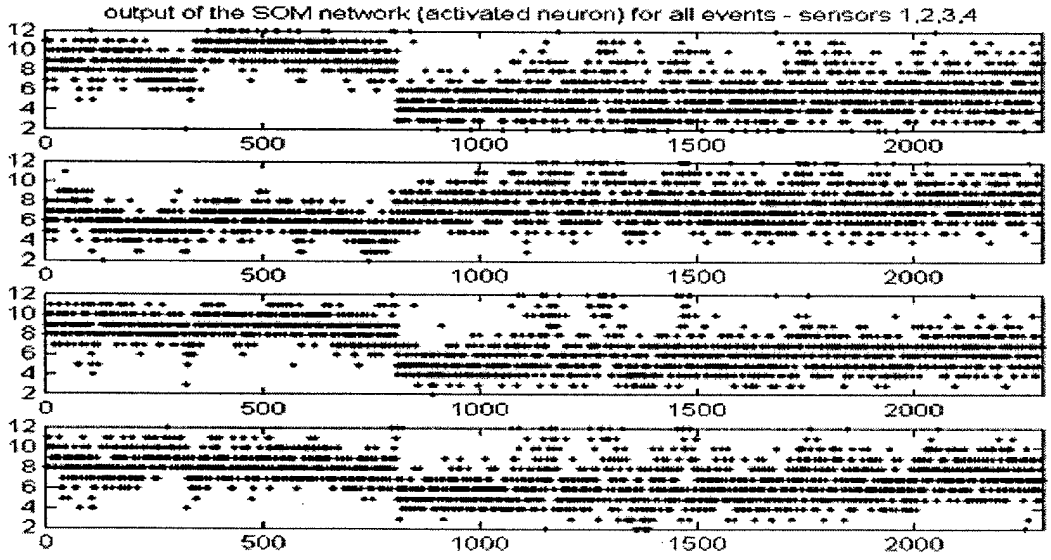

Figure 4.29 Output of the Kohonen network to all potentially crack-related signals.

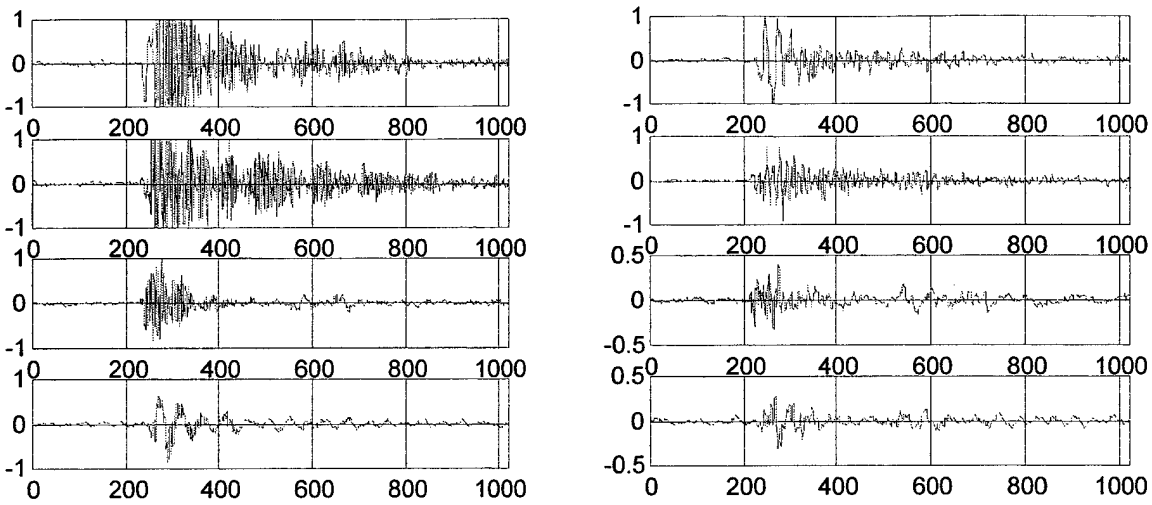

Figure 4.30 Two samples of crack-related signals detected by the Kohonen network.

E.3.3 *Event Classification Based on Signal Subspace Projections*

The previous approach assumed a clustering mechanism based on PCs that did not use a-priori information about the AE signal subspace (or equivalently the interference subspace). Suppose that one is able to characterize the AE signal subspace based on the principal eigenvectors of the covariance matrix of an ensemble of the AE signals, or to characterize the interference subspace based on the principal eigenvectors of an ensemble of interfering signals (see subsections **A.2** and **B**). Several possibilities may allow such characterization:

- The high correlation between successive events during a jump in the event count over an appropriate time window may be used as an indicator of a group of potential well-developed AE events, to be used in estimating the signal subspace.
- The events prior to the possibility of any measurable crack-related ones may be used to estimate the interference subspace.
- Methods such as the one described in the previous section may be used in one experiment to find AE signal candidates, leading to an estimate of the signal subspace to be used in other similar experiments.

Once the signal subspace has been estimated, we can make a normalized projection of the received signals onto this subspace. The norm of this projection is a measure of the closeness of the received signal to the signal subspace. In this case a norm of 1 is a perfect fit for the signal. Thus, the norms above a preset threshold (this can be averaged among several sensors, if available) classify the event as a crack-related AE. The alternative (complementary approach) is to project the measured signals onto the interference subspace. In this case, norms below a threshold are indicators of the presence of crack-generated AE signals.

In the following example, we use a signal subspace of dimension 5, i.e. the first 5 principal vectors span the assumed signal subspace. In Figure 4.31 (4.32), we use the estimated signal subspace for experiment PH1 (PH2) to project all the signals from experiment PH1(PH2) onto. Notice the effective separation of the signals (cluster with higher values of the projections) and interference. More importantly, Figure 4.33 shows the same indicator, when signals from PH1 are projected onto the signal subspace of PH2. Even the use of information obtained from a one experiment to classify the events of a different, but similar experiment seems to hold promise.

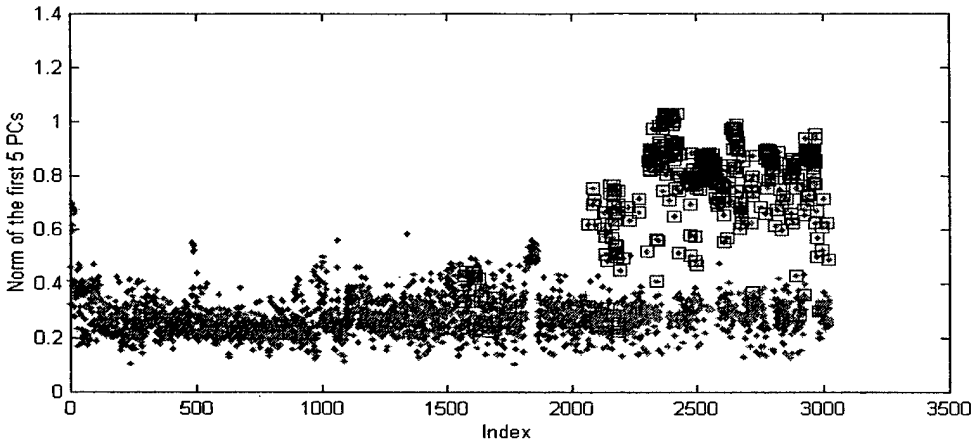

Figure 4.31 Norms of the projections of AE and non-AE signals of PH1 on the PH1 signals subspace of dimension 5.

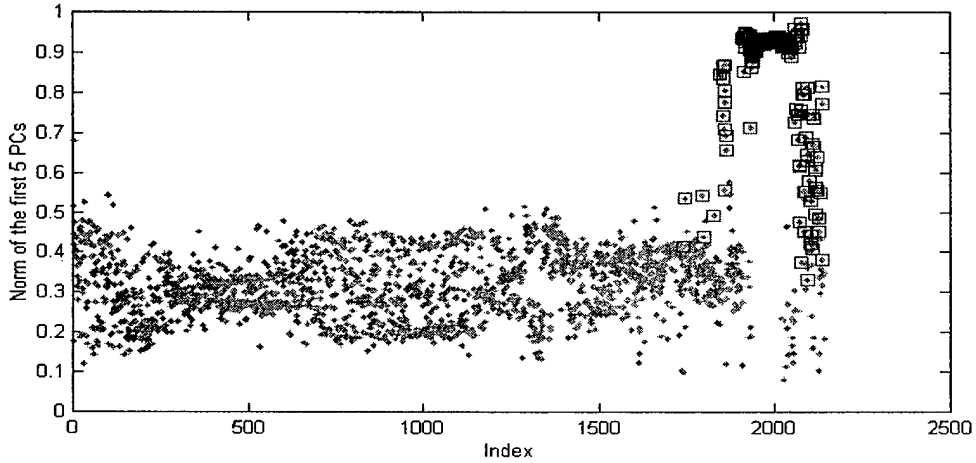

Figure 4.32 Norms of the projections of AE and non-AE signals of PH2 on the PH2 signal subspace of dimension 5.

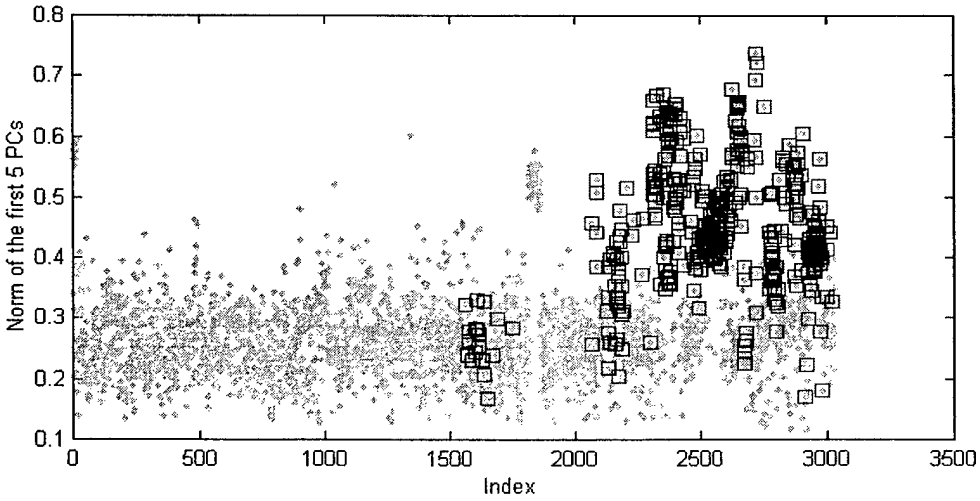

Figure 4.33 Norms of the projections of AE and non-AE signals of PH1 on the PH2 signal subspace of dimension 5.

E.4 Northwestern Crack Growth Data

Acoustic emission data collected from a crack growth test of heat-treated 4340 steel bars (0.5"x2"x14") with an initial 0.8" long EDM center crack was provided to us by the team of Prof. Daniel from Northwestern [18]. The test was conducted with an R-ratio of 0.1, and nominal maximum stress of 6.92ksi. Data was acquired by a commercial AE system (MISTRAS from Physical Acoustics) with two AE transducers with a central frequency at 150 kHz. The experiment utilized two sensors and other processing procedures to acquire, with very high probability, only AE signals related to the crack, sampled at 1MHz.

This data was analyzed in terms of its energy and frequency distribution, correlation between the events, and PCA. As the results of spectral analysis and correlation analysis are extensively reported in [18] and its references, we only give a few examples of our analysis in this report.

The energy diagram of all 20378 events of B07 versus event number is shown in Fig. 4.34. Except for some events at the beginning and at the end, when the specimen is about to break, the remaining events have approximately the same energy.

Most of the power spectrum is concentrated in the 100-200 kHz range, but there are two frequency components (around 314 and 350 kHz) that were seen in almost all 20378 events. The origin and significance of these frequency components, which for some events are dominant is of interest. Fig. 4.5 shows the frequency peaks versus event number.

The maximum cross-correlation between event number 1000 and all other events for test B07 is shown in Fig 4.7. It is seen that, other than the initial and final stages (before breakage) that there is a high degree of correlation between the signals related to a well-developed crack. This is in accord with the results obtained on the Georgia Tech samples described earlier.

The PCs of groups of the events were also analyzed. In this case the 20378 events were divided into groups of 2000 events each with the principal components for each group computed separately. The second principal component versus the first principal component of the 11-groups are shown in Fig. 4.35. Two different clusters, which are seen in the each figure, are located in a roughly circular arrangement, indicating, for the most part very similar signals which may be related only through a delay (phase shift). In the last two figures, while the specimen is breaking, some high-energy events have been generated, resulting in a change in the shape of the clusters. Furthermore, the central cluster in events 1-2000 is related to the initial stage of the experiment that contains signals with low correlation with most of the data set. Also, the later stages clearly indicate an evolving signal characteristic leading to the last stage before breakage.

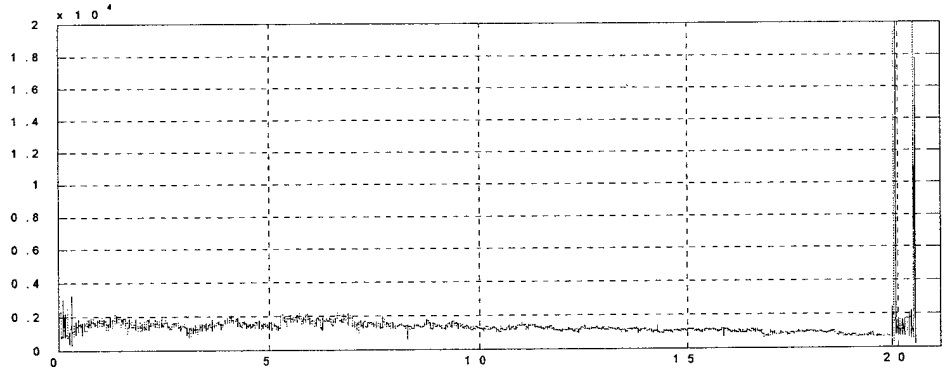

Figure 4.34 Diagram of Energy for all 20378 events in B07.

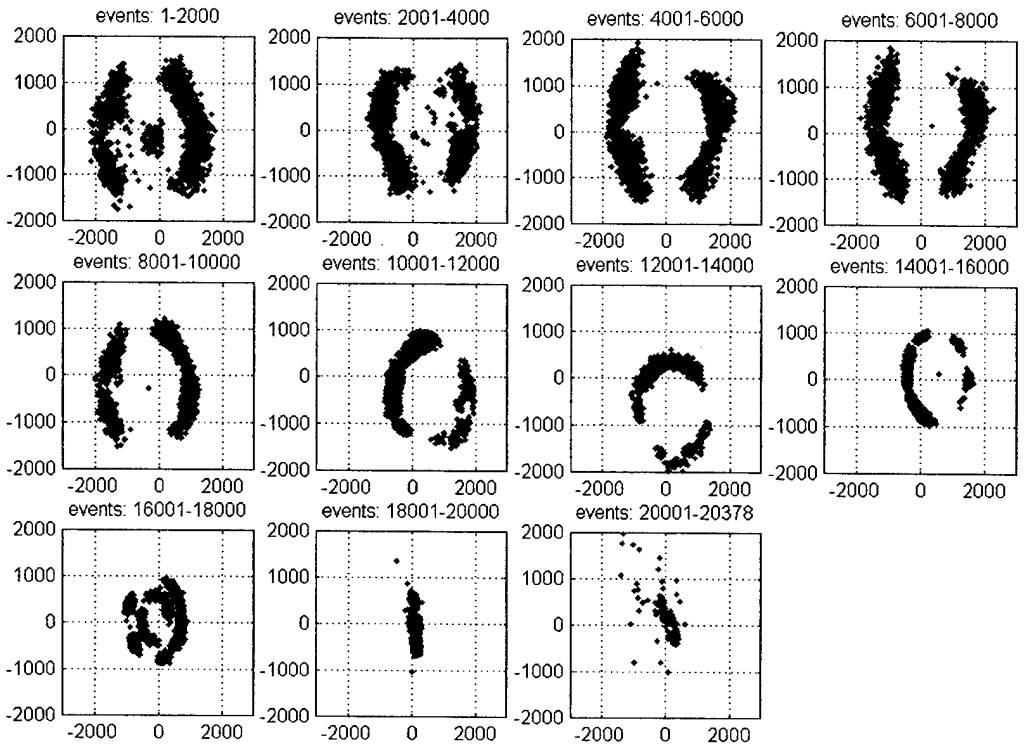

Figure 4.35 Second principal component versus first principal component for test B07.

REFERENCES

Bold numbers in brackets indicate ***MURI publications.***

1. C. Scruby, "An introduction to acoustic emission," J. Phys. E: Scientific Instrumentations, Vol. 20, pp. 946-953, 1987.

2. C. Scala, J. McCardle and S. Bowles, "Acoustic emission monitoring of a fatigue test of an F/A-18 bulkhead", Journal of Acoustic Emission, Vol.10, no.3/4, pp. 49-60, 1992.

[3.] K. Buckley, D. West, G. Venkatesan, and M. Kaveh, "Detection and characterization of cracks for failure monitoring and diagnostics," Proc. of the International Conference on Acoustics, Speech and Signal Processing (ICASSP 96), Vol. 5, pp. 2738-2741, Atlanta, GA, May 7-10, 1996.

[4.] G. T. Venkatesan, D. West, K. M. Buckley, A. Tewfik and M. Kaveh, "Automatic fault monitoring using acoustic emissions," Proc. of the International Conference on Acoustics, Speech and Signal Processing (ICASSP 97), Vol. 3, pp. 1893-1896, Munich, Germany, April 21-24, 1997.

[5.] G. T. Venkatesan, M. Kaveh, A. Tewfik and K. M. Buckley, "Blind identification of single-input, multiple-output pole-zero systems," Proc. of the International Conference on Acoustics, Speech and Signal Processing (ICASSP 98), Vol. 4, pp. 2117-2120, Seattle, WA, May 12-15, 1998.

[6.] G. T. Venkatesan, L. Tong, M. Kaveh, A. Tewfik and K. M. Buckley, "A deterministic blind identification technique for SIMO systems of unkown model order," Proc. of the International Conference on Acoustics, Speech and Signal Processing (ICASSP 99), Vol. 4, pp. 1789-1792, Phoenix, AZ, March 15-19, 1999.

[7.] G. T. Venkatesan, D. Zhang, M. Kaveh, A. Tewfik and K. M. Buckley, "Signal processing for fault monitoring suing acoustic emissions," International Journal of Electronics and Communications (AEU), vol. 53, no. 6, 293-392, December, 1999.

[8.] D. Zhang, G. T. Venkatesan, A. Tewfik and M. Kaveh, "Acoustic Emission Transient Detection Based on Linear Model Residuals," Proc. of Ninth IEEE Workshop on Statistical Signal and Array Processing (SSAP98), pp. 188-191, Portland, OR, September 14-16, 1998.

[9.] D. Zhang, G. T. Venkatesan, M. Kaveh, A. Tewfik and K. M. Buckley, "Fault monitoring using acoustic emissions," Proc. SPIE Conference on Sensory Phenomena and Measurement and Instrumentation for Smart Structures and Materials, New Port Beach, March, 1999.

10. D. L. Donoho, "Denoising by soft thresholding," IEEE Trans. on Information Theory, vol. 41, 613-627, 1995.

[11.] P. Andersson, Analysis of helicopter data and acoustic emission detection methods, M.S. Thesis, KTH, Stockholm, Sweden, (Research carried out at the University of Minnesota), 1999.

12. F. Malver, J. Schoess, J. Kooyman, R. Jiracek and J. Volk, "CH-46 Sea Knight flight-test results for the Rotor Acoustic Monitoring System (RAMS)", Honeywell Technology Center, 1997.

[13.] H. Sun, M. Kaveh and A. Tewfik, "Self-organizing map neural network for transient classification in mechanical diagnostics," Proc. IEEE-EURASIP Workshop on Nonlinear Signal and Image Processing, Antalia, Turkey, June, 1998.

[14.] V. Emamian, M. Kaveh, A. H. Tewfik, "Acoustic emission classification for failure prediction due to mechanical fatigue," Proceeding of SPIE conference on Sensory Phenomena and Measurement Instrumentation for Smart Structure and Materials," Vol. 3986, pp. 78-84, New Port Beach, March 6-8, 2000.

[15.] V. Emamian, M. Kaveh, A. H. Tewfik, "Robust clustering of acoustic emission signals using the Kohonen network," Proc. of the International Conference on Acoustics, Speech and Signal Processing (ICASSP 2000), Vol. 6, pp. 3891-3894, Istanbul, Turkey, June 5-9, 2000,

16. T. Kohonen, "The self-organizing map", Proceedings of IEEE, Vol.78, No. 9, pp. 1464-1480, September, 1990.

17. L. Jacobs and J. Jarzynski, "Acoustic Emission and Transmission from Incipient Fatigue Failure, Integrated Diagnostics M-URI Final Report, Section 2.2.3, Georgia Tech, Atlanta, August 2000.

18. I. M. Daniel, "Acoustic Emission Modeling," Integrated Diagnostics M-URI Final Report, Section 2.2.4, Georgia Tech, Atlanta, August 2000.

2.3.5 MODAL PARAMETER EXTRACTION FROM STRUCTURAL DIAGNOSTIC SIGNALS

Co-Investigators: Michael Drexel, Jerry Ginsberg (Georgia Tech)

OVERVIEW

The decomposition of system response into a modal representation is at the core of analytical and experimental techniques for most dynamical systems, ranging from MEMS devices up to prime movers. Indeed, the mathematics of such systems, requiring the solution of eigenvalue problems, is fundamental to most areas of science and engineering. For predictive evaluations of system models, the modal patterns lead to a set of uncoupled ordinary differential equations describing forced response. In a sense, experimental modal analysis is the inverse problem, for there the objective is to use response data to infer the system's equations. Such capability can then be used to identify system parameters, or underlying system features, which then enables one to improve analytical models, alter system design to remedy deleterious phenomena or to monitor structural diagnostic signals.

The direct measurements of response are the raw material from which system parameters must be identified. The focus of the proposed research is the tasks following data acquisition. As will be seen in following sections, numerous algorithms have been developed to extract the modal parameters from this data. Such algorithms constitute the interface between analysis and experiment, for they are based on matching the measured data to canonical solution forms governing linear systems. One categorization of the methods addresses the form of the data that is required by the extraction technique. Frequency domain methods use displacement, velocity, or acceleration amplitudes that can be obtained directly from shaker excitation, or by applying FFT technology to time responses generated by impulse hammer excitation. In contrast, the data for time domain methods consists of digitized time responses that are used directly. The frequency domain methods are generally older and simpler to implement. The time domain methods tend to have greater generality, but there are frequency domain methods that match that generality.

The proposed work aims to implement a frequency domain technique that has the maximum degree of generality, while simultaneously being more accurate than any existing method, and still maintaining the simplicity of the frequency domain techniques. In part, the work will benefit the development of structural models by improving the capability to address systems whose natural frequencies are sufficiently close that they seem to contribute jointly to the complex frequency response, in a phenomenon known as modal coupling. Results provided in later sections suggest that the technique is more robust than existing methods in the presence of noisy data. Another important objective is to provide physically based experimental identification of rotating systems, particularly rotordynamic systems such as gas and water turbines used for power generation. Accurate methods here will lead to reliable techniques for condition-based modeling and model updating based in real-time parameter identification, which would be particularly welcome in view of the extreme cost of taking power generation systems out of service.

OBJECTIVES

The objective of this study is to develop a technique to retrieve the modal parameters of a structure from health monitoring signals in order to detect changes in the dynamic characteristics of a component prior to failure.

Existing modal parameter extraction techniques require an *a priori* guess of the number of significant modes, or degrees of freedom, of the system. An error in that guess can have serious

consequences with respect to the accuracy of the extraction process. If the number of modes is assumed to be less than the true number of modes, then it is impossible for the algorithms to find all of the modes. If the number of modes is assumed to be greater that the true number of modes the algorithms may produce artifical modes, become numerically intensive due to their N^2 nature with respect to the number of operation, and some algorithms become ill-conditioned as the number of assumed modes is increased.

The complexity of the systems encountered in structural health monitoring situations provides an immediate obstacle to existing modal parameter extraction methods. An *a priori* knowledge of the number of significant modes will not be available and the accuracy of the modal parameter estimation will suffer. In order to successfully extract modal parameters from a complex structure, the algorithm will need to determine the number of significant modes contained in diagnostic signals in an automated fashion. In addition, the algorithm needs to be able to extract modal parameters from system such as non-proportionally damped systems and systems with gyroscopic effects.

STATE OF THE ART OF MODAL EXTRACTION TECHNIQUES

From a fundamental viewpoint, the information sought from modal analysis is quite straightforward. The most fundamental properties are the natural frequencies and modal damping ratios that characterize free vibrations. In some cases, these values are sufficient, but it usually is also desirable to identify the individual mode shapes, that is, the proportions between the displacements in each mode. Buried here is a subtle, yet fundamentally important, aspect of extracting the modal parameters that describe a system. Specifically, the number of degrees of freedom contained in the measured data must be ascertained. Some extraction methods require an *a priori* guess, while others attempt to incorporate this question in their overall scheme.

Single degree of freedom methods are the simplest of the modal parameter extraction techniques. Although the measured data contain contributions from several modes, single degree of freedom techniques rely on a description that divorces each mode from its companions.

The simplest single degree of freedom method for extracting modal parameters is the peak-amplitude method [8]. This is typically a single exciter technique from which the amplitude, as a function of frequency, is derived. The natural frequency of the mode is assumed to occur where the amplitude obtains a local maximum. The damping ratio is obtained by considering the bandwidth [8] of the mode, which is defined by the half-power points. The mode shape associated with each natural frequency ω_n can be obtained by simply evaluating each of the amplitude response curves at ω_n. This assumes that the structure was measured sufficiently to provide a clear picture of the displacement at a particular ω_n.

There are several limitations on the results of this method. Increasing damping moves the peak amplitude away from the natural frequency, and the simple relation between the half-power points and the modal damping ratio loses validity. More significantly, increased damping leads to modal coupling, in which resonant peaks merge, thereby removing the notion of identifiable individual modal contributions. From a practical standpoint, the issue of modal coupling is closely tied to the proximity of natural frequencies, because the underlying issue is the extent to which modal features occur in a distinct manner. Despite these drawbacks, the peak-amplitude method is easy to implement, and the errors are relatively small for systems with light damping and widely spaced natural frequencies.

Another method for extracting modal parameters based on a single degree of freedom model is based on the properties of a Nyquist plot of the complex amplitude in the Argand plane, for which frequency is a parameter defining the real and imaginary parts to be plotted. For small damping this curve is approximately a circle. The method, originally developed by Kennedy and Pancu [18],

proposed parameter extraction by assuming that the natural frequency is the frequency at which maximum spacing on the arc occurs for equal frequency increments. Actually, this is the same method as the peak-amplitude except that the frequency response function is plotted in a different space.

Luk and Mitchell [24] describe a method for parameter extraction based on curve fitting a circle to the frequency response function in a least squares error fit. This approach finds the circle's origin and diameter mathematically in lieu of the graphical method described above. Although the circle fitting method is more accurate that the graphical methods, it possesses the same limitations as the peak-amplitude method when system damping is heavy, natural frequencies are closely spaced, or non-proportional damping is present.

Single degree of freedom methods have inherent errors associated with the notion that individual modes can be considered individually. These errors becomes larger for systems with heavy damping, non-proportional damping, or closely spaced natural frequencies. Improving on the single degree of freedom methods implies that the presence of the other modes must be accounted for in the process of modal parameter extraction. This is typically accomplished by solving for all of the modal parameters in a simultaneous manner. Methods that perform modal parameter extraction in this fashion are multiple degree of freedom methods (MDOF).

The eigensystem realization algorithm (ERA) [16], a MDOF method, is derived from a control and systems identification viewpoint and has become a widely accepted approach to the problem of modal parameter extraction. An important aspect of the formulation is the use of a state-space description, in which displacement and velocity are treated independently. The goal of the eigensystem realization algorithm is to identify the underlying system matrices from the measurements. The theoretical details of the ERA method are quite involved. In addition to providing the system's natural frequencies, damping ratios and mode shapes, ERA also provides modal amplitude coherence and modal phase collinearity. These parameters are an attempt to determine the validity of a mode in the presence of noise and uncertainty. This is required because the singular value decomposition invoked in the procedure may produce non-zero singular values for non-existing modes. The calculation of each of these parameters results in a number, represented as a percentage, that if low in value predicts a small chance that the mode is a physically meaningful mode; the opposite is assumed if the value is high. Juang and Suzuki [17] extended the ERA method to extract modal parameters from frequency domain test data, thereby blurring the demarcation between frequency and time domain methods.

Many improvements have been made to the ERA method in order to improve the algorithm's performance with respect to input noise, model order and computational speed. Longman and Juang [23] used an algorithm (ERA-RC) based on Gram-Schmidt orthonormalization to recursively build up the system order instead of utilizing the non-zero singular values from the singular value decomposition. Roemer and Mook [32], [33] developed Enhanced ERA, which introduces an error estimate that is the difference between the ERA prediction of the system's output and the actual data. Also a function is added to the state equations to represent unmodeled dynamics. Both of these terms are placed in a cost function that is minimized with respect to the unmodeled dynamics function. Knowledge of the estimated unmodeled dynamics function allows for an improved data set for ERA, and then a new prediction of the system. Oshman and Mendelboim [28] presented a maximum likelihood technique (ML/ERA) that utilizes ERA and a stochastic adaptive filter/fixed interval smoother in order to find realization for systems whose process or measurement noise are not known. Quan [29] suggested using both impulse response and forced (frequency) response in order to improve ERA's ability to deal with noise.

Despite the efforts to strengthen ERA, difficulties in accurate modal parameter extraction can still arise. Because the model order is unknown, the assumed number of modes is typically overes-

timated, and the irrelevant modes are truncated based on the information provided by the singular value decomposition. Doebling, Alvin, and Peterson [9] investigated the effect of overestimating the system order. They found that the assumption that more data always leads to an improved approximation is false. They showed that as the model order is increased, some of the modes might 'split' into two modes. In addition, the accuracy indicators showed high confidences in both the single and 'split' modes. This means that the ERA error metrics would conclude that both solutions were correct. Thus, increasing model order does not imply convergence to a unique solution, but perhaps to multiple seemingly correct solutions.

Many other modal parameter extraction techniques have been developed over the years. Allenmang (*et al*, [3]) proposed that a common point of view may be found from which many algorithms take on a similar form. This development is presented here in lieu of surveying the multitude of techniques. Table 1 lists the modal parameter extraction techniques considered to be essentially equivalent from the viewpoint of the system dynamics they aim to capture.

Modal Parameter Extraction Techniques	
CEA	Complex Exponential Algorithm
LSCE	Least Squares Complex Exponential
PTD	Polyreference Time Domain
ITD	Ibrahim Time Domain
MRITD	Multiple Reference Ibrahim Time Domain
ERA	Eigensystem Realization Algorithm
PFD	Polyreference Frequency Domain
SFD	Simultaneous Frequency Domain
MRFD	Multi-Reference Frequency Domain
RFP	Rational Fraction Polynomial
OP	Orthogonal Polynomial
CMIF	Complex Mode Indication Function

Table 1: Acronyms and Modal Parameter Extraction Techniques

Similarity of the underlying principals should not be taken to mean that all of the modal parameter extraction techniques will provide the same estimation of the modal parameters. Each method of solution has numerical algorithms associated with it, each of which will provide a different estimation of the modal parameters. For instance, ERA utilizes singular value decomposition in order to approximate the degrees of freedom of the system, and then requires an eigenproblem solver in order to find the eigenvalues and eigenvector of the system. On the other hand, the rational fraction polynomial method requires an explicit assumption about the degrees of freedom for the system, and then solves for the modal parameters by a least squares approach. Obviously the estimation of modal parameters obtained from these algorithms can be different.

The most critical aspect of multiple degree of freedom methods is the determination of the number of modes contained in the system. This assumed number directly determines the number of modal frequencies that will be found. If the model number is assumed to be smaller than the true number of modes in the system, the number of modes found by the algorithm will be truncated. The number of truncated modes will be the number of true modes less the number of assumed modes. On the other hand, if the number of modes is assumed larger that the true number of modes, then there is the possibility of the creation of artificial modes or numerical instability. An example of the creation of artificial modes was given above, where the ERA algorithm suffered

from mode splitting. An example of numerical instability arises from the ill-conditioned matrices caused by high order polynomials in the rational polynomial methods. In the present state of any of these algorithms, it is difficult to determine if the choice of modal order is an underestimation or an overestimation of the true number of modes. Most algorithms provide an error metric that compares the measured data to the predicted value calculated from assumed solution evaluated with the modal parameters found by the algorithm. The magnitude of the error is then used to gauge the success of the extraction process. This, however, can be misleading as to whether or not the number of modes and the modal parameters are a match to the measured system. It is possible for the incorrect modal parameters to have a small error. In other words, a small error estimate does not directly imply that the modal parameters are the actual modes of the system; it merely implies that the modal parameters that were found correspond well to the measured data. This leaves the assessment of the appropriate number of modes contained in the system as a primary source of error.

The MDOF methods, like single degree of freedom methods, suffer from the problems of heavy damping, closely spaced natural frequencies, and measurement noise. Each increases the difficulty of extracting accurate modal parameters.

ACHIEVEMENTS

Development of Undamped Mode Isolation

Mode isolation has been formulated as a frequency domain technique. The data is taken to be a set of complex displacement amplitudes as a function of drive frequency, corresponding to application of a single harmonic generalized force, $Q_P = \mathrm{Re}\{F_p\, e^{i\omega t}\}$. The following will explain how the algorithm extracts the natural frequencies, modal damping ratios, and modal amplitudes, and therefore the number of degrees of freedom associated with the data set, from data describing the frequency dependence of a single complex displacement amplitude Y_j. In practice, the process would be applied sequentially to the data set for all generalized coordinates. Parameters extracted from analysis of each generalized coordinate then yield an ensemble estimate, in order to lessen the potential effects of reduced modal participation factors and enhanced errors in any specific generalized coordinate.

The first step is to examine the displacement (or acceleration) data for a single generalized coordinate Y_j. If the system response consists of a superposition of undamped modal contributions, then

$$Y_j(\omega) = \sum_{k=1}^{N} A_{jk} \frac{(\omega_k^2 - \omega^2) - i2\zeta_k\omega_k\omega}{(\omega_k^2 - \omega^2)^2 + (2\zeta_k\omega_k\omega)^2} \tag{1}$$

Note that the succession in which modes are isolated is based on the dominance of their contributions within the processed data; this is the basis for assignment of the mode number k. The objective in the first iteration through the data is to obtain values of the natural frequencies, modal damping ratios, and modal amplitudes with which to initiate the second iteration. Subsequent iterations repeat the pattern of the second.

The first iteration begins by seeking evidence of the mode that gives the largest contribution to the overall $Y_j(\omega)$ data set. Such evidence can be the most visible peak exhibited by $|Y_j(\omega)|$ or the sharpest transition in the phase angle $\arg(Y_j(\omega))$. Such characteristics are used to estimate the first mode's natural frequency ω_1, modal damping ratio ζ_1, and modal amplitude A_{j1}. This operation is much like the single degree of freedom methods, in that concepts such as a circle

fit to a Nyquist plot maybe used to estimate the modal parameters of the most dominant mode contributing to the frequency response functions.

The second step in the first iteration is the place where mode isolation diverges from current techniques. In order to bring the next mode into dominance, the contribution of the estimated mode to the frequency response function is subtracted from the measured data. To illustrate the general process for the first iteration, let $Y_j^{(n)}(\omega)$ denote the residual of $Y_j(\omega)$ in the first iteration after the contributions of modes 1 to N have been subtracted. It follows that

$$\begin{aligned} Y_j^{(0)}(\omega) &= Y_j(\omega) \\ Y_j^{(n)}(\omega) &= Y_j^{(n-1)}(\omega) - A_{jn}\frac{(\omega_n^2-\omega^2)-i2\zeta_n\omega_n\omega}{(\omega_n^2-\omega^2)^2+(2\zeta_n\omega_n\omega)^2} \end{aligned} \tag{2}$$

At each step in the first iteration, estimates of ω_n, ζ_n and A_{jn} are obtained from $Y_j^{(n-1)}(\omega)$ by the same procedures as those used to obtain preliminary estimates of the first mode's parameters.

The first iteration ends when there are no highlights in the residual frequency response functions. (This condition will be evident in the example that follows.) At this stage estimates of ω_k, ζ_k and A_{jk} have been obtained for each identified mode. The number of modes, N, described by the data is estimated as the number of steps required to reduce the residual $Y_j^N(\omega)$ to noise.

The second and following iterations are intended to isolate each mode and improve the estimates of the modal parameters. The concept is that any mode may be isolated by using the current estimates for the modal properties. These estimates are used to subtract the contribution of the other modes. Let $X_j^{(n)}(\omega)$ denote the $Y_j(\omega)$ data at a specified iteration step from which the estimated contributions of all except mode n have been subtracted.

$$X_j^{(n)}(\omega) = Y_j(\omega) - \sum_{\substack{j=1 \\ j\neq n}}^{N} A_{jk}\frac{(\omega_k^2-\omega^2)-i2\zeta_k\omega_k\omega}{(\omega_k^2-\omega^2)^2+(2\zeta_k\omega_k\omega)^2} \tag{3}$$

In this expression A_{jk}, ω_k, and ζ_k are the current values, which are known from previous iterations and previous steps in the current iteration. The $X^{(n)}(\omega)$ data is used to obtain improved estimates for ω_n, ζ_n and A_{jn}. The procedure uses a nonlinear least squares, described in the next section. The sequence of steps in which any iteration are performed is based on the largeness of $Y_j(\omega_n)$ or the current residual at a particular step. An iteration progresses sequentially through the higher modes, until all modal parameters have been updated. Additional iterations repeat the steps of the second, until convergence criteria for the ω_n, ζ_n, and A_{jn} parameters are met.

It should be noted that the preceding description is based on using the value of N identified in the preliminary iteration. However, at the end of an iteration, the last residual $X_j^{(N+1)}(\omega)$ has all of the estimated modal properties subtracted out. If this residual indicates that coherent data remains, then the value of N would need to be increased. In that case the steps described by Eq. (2) may be implemented with $Y_j^{(N)}(\omega) = X_j^{(N+1)}(\omega)$ in order to obtain preliminary estimates for any additional modal properties.

Parameter Identification

A crucial aspect of the mode isolation algorithm is the identification of the ω_k and ζ_k values corresponding to the residual data. In the first pass such data is the successive data set X_k obtained from subtracting lower modes. In the second pass the residuals X^k obtained by subtracting current estimates of the other modes. The complex displacement of the k^{th} generalized coordinate when ω

is close to the natural frequency of the mode under consideration is

$$Y_j^k(\omega) \approx A_{jk} \frac{(\omega_k^2 - \omega^2) - i2\zeta_k\omega_k\omega}{(\omega_k^2 - \omega^2)^2 + (2\zeta_k\omega_k\omega)^2} \tag{4}$$

where A_{jk} is an amplitude factor, ω_k is the natural frequency and ζ_k is the damping ratio of the mode. The selection of several points can be used to form an overdetermined system, from which the modal parameters A_{jk}, ω_k and ζ_k can be obtained.

The solution of the overdetermined system requires a nonlinear least squares [5], [10] approach, which leads to

$$\{D\} = [Z]\{\Delta P\} \tag{5}$$

where $\{D\}$ is the error vector formed between the measured data and the assumed solution. The matrix $[Z]$ is the Jacobian of $Y_j^k(\omega)$ with respect to the variables ω_k, ζ_k, A_{jk}, and $\{\Delta P\}$ is a vector of the incremental variables ΔA_{jk}, $\Delta\omega_k$ and $\Delta\zeta_k$.

The solution of Eq. (5) proceeds by premultiplying the equation by $[Z]^T$, then the vector $\{\Delta P\}$ can be solved for in terms of the Jacobian $[Z]$ and the error vector by inverting $[Z]^T[Z]$. This gives

$$\{\Delta P\} = ([Z]^T[Z])^{-1}[Z]^T\{D\} \tag{6}$$

The incremental vector $\{\Delta P\}$ is used to update the vector of modal parameters $\{P\}_m$ giving an improved estimation of the modal parameters, according to

$$\{P\}_{m+1} = \{P\}_m + \{\Delta P\} \tag{7}$$

The process iterates until convergence criteria are met.

The nonlinear least squares method for solving overdetermined systems requires that initial values for the modal parameters be obtained in order to begin the iteration process. The initial values for the vector $\{P\}$ could be obtained by utilizing the peak-amplitude [8] or the Kennedy and Pancu [18] methods. In the mode isolation algorithm the initial value of ω_k is defined as the value of ω where the imaginary part of the frequency response function reaches a global maximum so that

$$\max(\text{imag}(Y_j(\omega))) \Rightarrow \omega_k \tag{8}$$

where $Y_j(\omega)$ is the frequency response data evaluated at the j^{th} generalized coordinate. The initial value of ζ_k is found by utilizing the definition of the half-power points ω_2 and ω_1 and the above approximation of ω_k so that

$$\zeta_k = \frac{\omega_2 - \omega_1}{2\omega_k} \tag{9}$$

Finally the estimation of A_{jk} is

$$A_{jk} = 2\zeta_k\omega_k^2(\max(\text{imag}(Y_j(\omega)))) \tag{10}$$

The complete extraction of the modal parameters requires an estimation of the eigenvectors, as well as the eigenvalues. Comparing Eq. (4) to Eq. (1) implies that the coefficients of each isolated mode must correspond to one of the coefficients in the series of complex displacement functions, resulting in

$$A_{jk} = \Phi_{jk}\Phi_{pk}F_p \tag{11}$$

where Φ_{jk} is the jk^{th} element of the modal matrix. Because A_{jk} and F_p are known, the eigenvector elements may be determined by setting $j = p$, and rewriting Eq. (11), which gives

$$\Phi_{pk} = \left[\frac{|A_{pk}|}{F_p}\right]^{\frac{1}{2}} \tag{12}$$

The absolute value of A_{pk} implies that Φ_{pk} is assumed to be positive. The other elements of the modal transformation matrix may be determined by

$$\Phi_{jk} = \Phi_{pk}\frac{A_{jk}}{|A_{pk}|} \tag{13}$$

The modal transformation matrix $[\Phi_{jk}]$ completes the relationships required to describe the solution vector of generalized coordinates in terms of the modal parameters.

Numerical Example of Undamped Mode Isolation Algorithm

As an example of the mode isolation algorithm, a comparison will be made to the ERA and Enhanced ERA methods using a numerical example given by Roemer and Mook [32], [33]. Their example utilized a four degree of freedom, discretized model of a cantilever wing, which originally was used by Meirovitch [25]. The mass, damping and stiffness matrices are given by

$$[M] = \begin{bmatrix} 1 & 0 & 0 & 0 \\ 0 & 1 & 0 & 0 \\ 0 & 0 & 1 & 0 \\ 0 & 0 & 0 & 1 \end{bmatrix} \quad [C] = \begin{bmatrix} 0.3 & 0 & 0 & 0 \\ 0 & 0.3 & 0 & 0 \\ 0 & 0 & 0.3 & 0 \\ 0 & 0 & 0 & 0.3 \end{bmatrix} \quad [K] = \begin{bmatrix} 10 & -5 & 0 & 0 \\ -5 & 10 & -5 & 0 \\ 0 & -5 & 10 & -5 \\ 0 & 0 & -5 & 10 \end{bmatrix} \tag{14}$$

An exact solution of this system, which is proportionally damped, can be found by solving the associated eigenproblem. The simulated frequency response function has a Gaussian white noise, approximately 10% of the signal amplitude, added to the exact frequency response function. In addition to the noise, the modal parameter extraction is further complicated by the large (approximately 15%) damping ratios. Figures 3.5 and 5 provide a graphic illustration of the progress

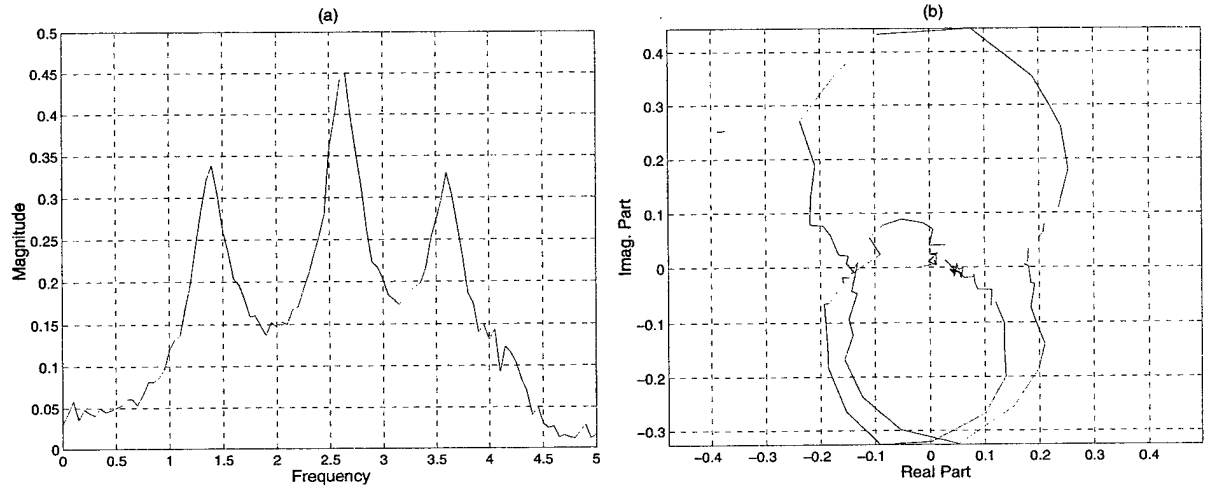

Figure 1: Frequency Response Data $Y_4(\omega)$: (a) Magnitude verses Frequency, (b) Nyquist Plot

through the first iteration. Figure 3.5a shows magnitude of the original data for the fourth generalized coordinate of the system, given by Eq. 14, as a function of drive frequency ω. Figure 3.5b is a Nyquist plot of $Y_4^0(\omega)$ corresponding to the original measured data $Y_4(\omega)$. Figure 2 shows $Y_4^1(\omega)$ as depicted by Eq. (2) after the most dominant mode has been subtracted from the data in Figure 3.5b. Figure 3 depicts $Y_4^2(\omega)$, which is the residual after the two modes dominate modes have been subtracted. The process continues until the state in Figure 5 is attained. At this stage, only noise remains, indicating that no new modes can be estimated.

The first iteration has found an estimate for all of the modes present in the data. This estimation, however, has not addressed the modal coupling because the least squares fit ignored the presence of the other modes. Hence, each estimate is contaminated by the other displacement contributions. The second iteration addresses this matter.

The second iteration begins by subtracting the second and higher modal displacements identified in the first pass from the measured data according to Eq. (3). The nonlinear least squares solution on this isolated mode provides an improved estimate of ω_1, ζ_1 and A_{14}. The isolated mode $X_4^1(\omega)$ is shown in Figure 6. The new estimate of ω_1, ζ_1 and A_{14} and the current values of the other modes are utilized in forming the residual $X_4^2(\omega)$ as described by Eq. (3). The isolated mode $X_4^2(\omega)$ is shown in Figure 7. The algorithm continues to isolate each mode in the manner described above, which completes the second pass through the data. Figure 8 and 9 show the isolated modes $X_4^3(\omega)$ and $X_4^4(\omega)$, respectively.

Additional passes through the data, in the manner of the second pass, continue until the rate of change per iteration of the incremental variables $\Delta\omega_k$, $\Delta\zeta_k$, and ΔA_{jk}, in the nonlinear least squares algorithm, are below 1e-3.

After convergent estimates for the ω_k, ζ_k, and A_{4k} parameters were obtained from $Y_4(\omega)$, the frequency response data, $Y_1(\omega)$, $Y_2(\omega)$, and $Y_3(\omega)$ corresponding to the other generalized coordinates were subjected the same treatment. The modal parameters identified from each frequency response function were averaged to form ensemble estimations of ω_k and ζ_k. In addition, the estimates of

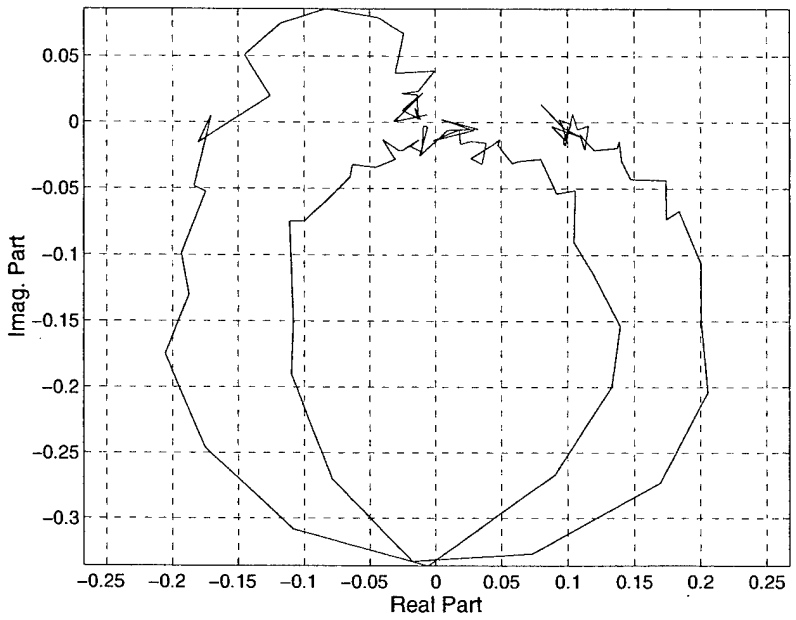

Figure 2: First step in first iteration yields $Y_4^1(\omega)$

Exact solution	ERA	Enhanced ERA	Mode Isolation	Mode Isol. (20%)
-0.150 ± 1.374i	-0.176 ± 1.372i	-0.161 ± 1.387i	-0.151 ± 1.374i	-0.150 ± 1.375i
-0.150 ± 2.624i	-0.171 ± 2.663i	-0.176 ± 2.636i	-0.150 ± 2.624i	-0.151 ± 2.624i
-0.150 ± 3.615i	-15.93 ± 0.000i	-0.281 ± 3.795i	-0.150 ± 3.615i	-0.148 ± 3.616i
-0.150 ± 4.250i	-0.464 ± 4.039i	-0.299 ± 4.324i	-0.150 ± 4.251i	-0.155 ± 4.250i

Table 2: Comparison of ERA and Enhanced ERA to Mode Isolation eigenvalues for a four degree of freedom system.

A_{jk} extracted from each frequency response function are used directly to compute the elements of the eigenvectors.

Table 2 shows the average eigenvalues obtained from ten individual simulations using different seeds for the random number generator for noise. In terms of the properties of undamped modes, the magnitude of a complex eigenvalue's imaginary part is the damped natural frequency, while the real part is the negative product of the modal damping ratio and the natural frequency. Examination of the tabulation shows that ERA found four modes. However, one of the eigenvalues has only a real part, corresponding to an overdamped mode. Another eigenvalue has over 100% relative error in the estimation of the real part. The Enhanced ERA algorithm is able to find four meaningful modes from the data. The damped natural frequency reflects the improvement of the Enhanced ERA algorithm over the standard implementation of ERA. All of the damped natural frequencies are meaningful and have relative errors below 5%. However, the relative error in the real parts of two of the eigenvalues still approaches 100% error.

Mode isolation results for the eigenvalues were obtained by averaging values identified from the

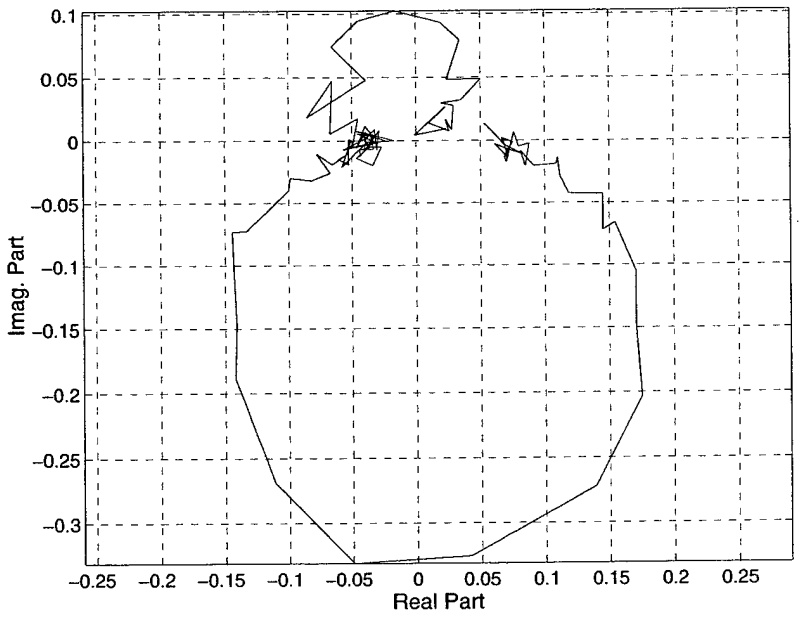

Figure 3: Second step in first iteration: $Y_4^2(\omega)$

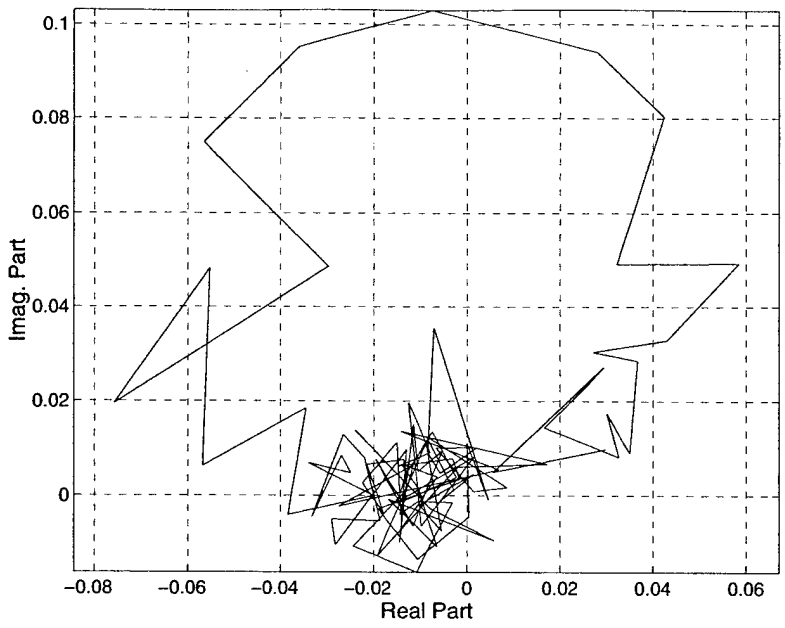

Figure 4: Third step in first iteration: $Y_4^3(\omega)$

frequency response data for each generalized coordinate. Table 2 shows that mode isolation is more accurate than Enhanced ERA with respect to extraction of the damped natural frequencies. It is substantially better in obtaining damping ratios. As a further illustration of the merits of mode isolation, the last column of Table 2 shows the mode isolation algorithm's performance when the

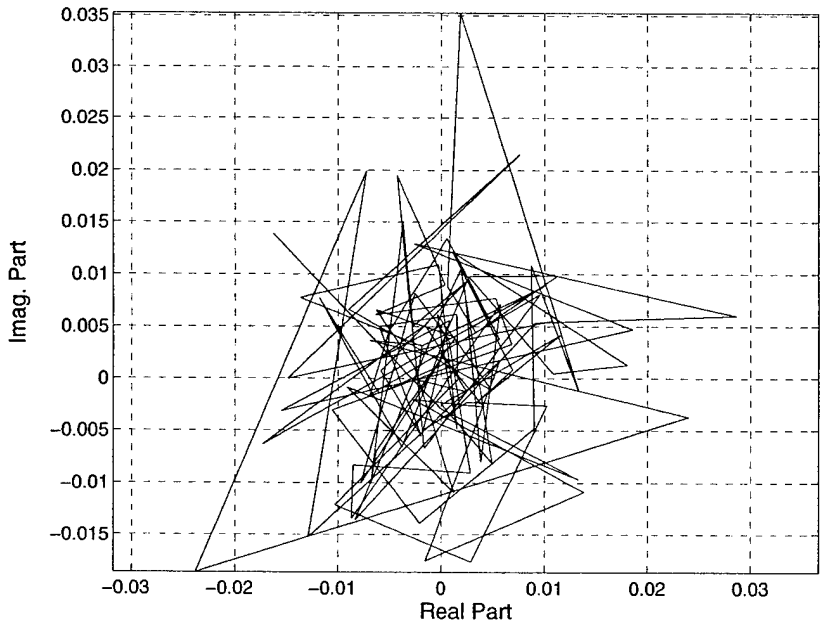

Figure 5: Noise residual $Y_4^4(\omega)$ after fourth step in first iteration

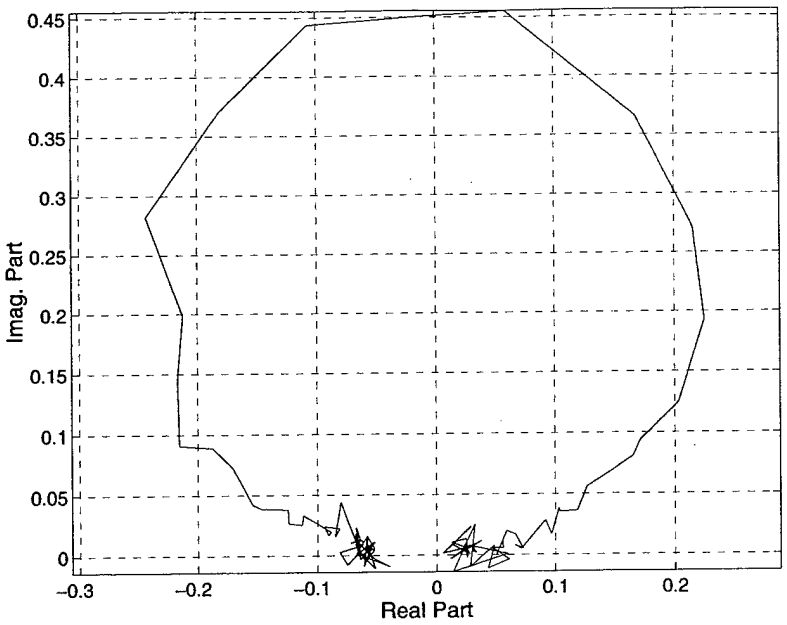

Figure 6: First step in second iteration: X_4^1

white noise is raised to approximately 20% of the signal amplitude. The mode isolation method still is more accurate than Enhanced ERA, even though the parameters were extracted from a signal containing twice the noise of that for Enhanced ERA.

Table 3 compares the extracted eigenvectors from the simulated data for the ERA, Enhanced

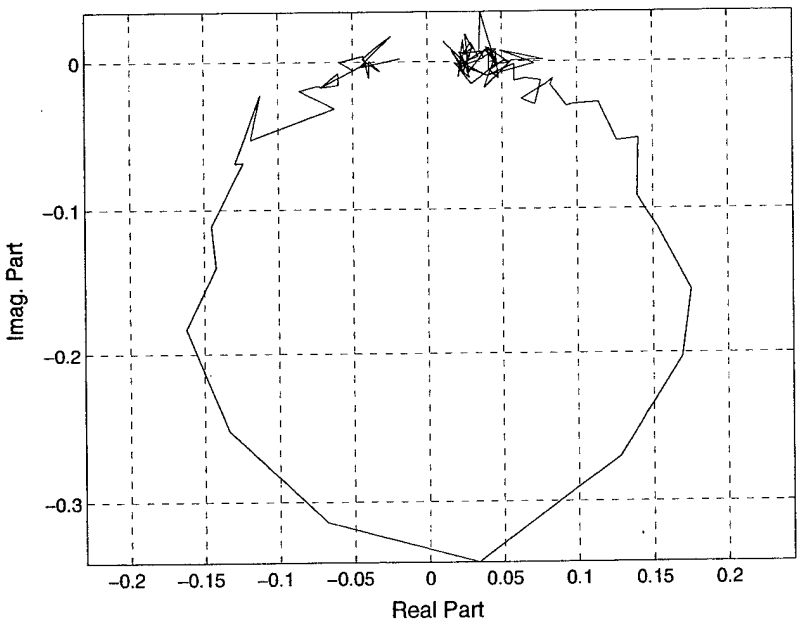

Figure 7: Second step in second iteration: X_4^2

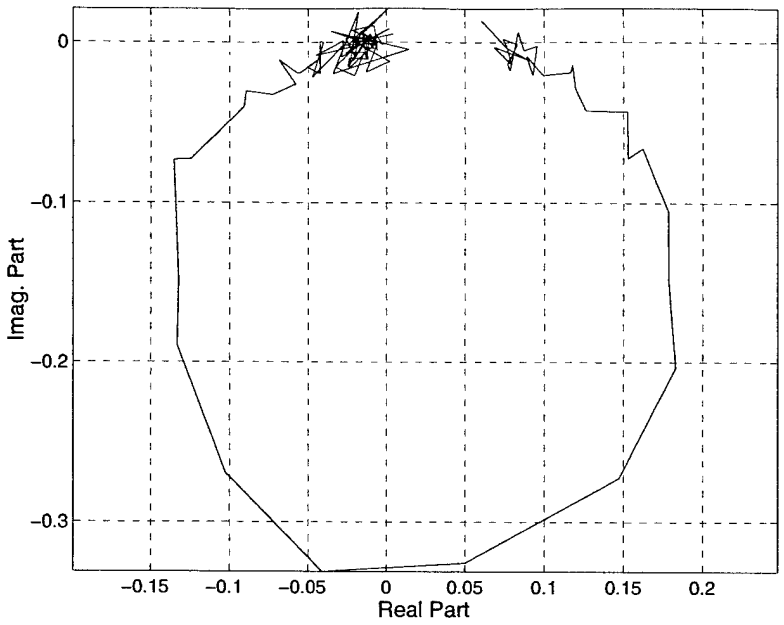

Figure 8: Third step in second iteration: X_4^3

ERA, and mode isolation algorithms. The ERA algorithm fails to extract the third mode correctly. The exact eigenvector is characterized by positive and negative values, whereas the extracted eigenvector reports only positive values. This is not a surprising outcome because of the failure of the ERA algorithm to extract four meaningful eigenvalues. As was the case for eigenvalues, Enhanced

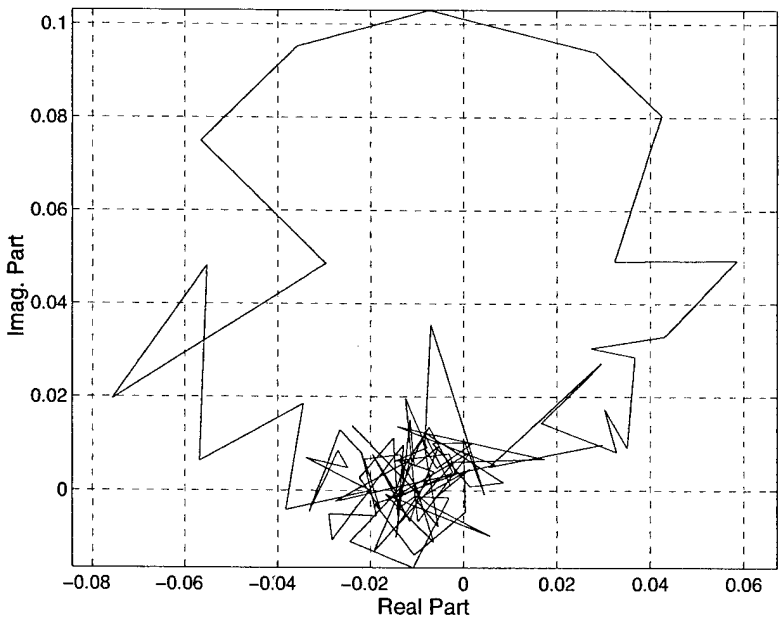

Figure 9: Fourth step in second iteration: X_4^4

Mode Num.	Exact solution	ERA	Enhanced ERA	Mode Isol.	Mode Isol.(20%)
	0.3717	0.4012	0.3705	0.3715	0.3681
mode 1	0.6015	0.5743	0.6098	0.5979	0.6027
	0.6015	0.5912	0.6005	0.6004	0.6022
	0.3717	0.3992	0.3891	0.3782	0.3666
	-0.6015	-0.5945	-0.5685	-0.6021	-0.6024
mode 2	-0.3717	-0.3622	-0.3810	-0.3696	-0.3827
	0.3717	0.4039	0.3711	0.3675	0.3695
	0.6015	0.6069	0.6395	0.6075	0.5936
	0.6015	0.2087	0.5645	0.6000	0.5992
mode 3	-0.3717	0.2532	-0.4193	-0.3641	-0.3846
	-0.3717	0.1717	-0.3496	-0.3739	-0.3962
	0.6015	0.3515	0.6312	0.6082	0.6047
	-0.3717	-0.0751	-0.3223	-0.3773	-0.3811
mode 4	0.6015	0.4508	0.6001	0.5930	0.5881
	-0.6015	-0.7844	-0.7101	-0.5922	-0.6008
	0.3717	0.6279	0.4541	0.3667	0.3408

Table 3: Mode Shape comparison of ERA, Enhanced ERA and Mode Isolation

ERA shows an improvement over ERA by providing four meaningful eigenvectors. Calculation of an average relative error between Enhanced ERA's extracted values and the exact values reveals an error of 6.5%. The mode isolation algorithm yields better results than Enhanced ERA for the case where the simulated data is corrupted with 10% white noise, with an average relative error of 0.95%. The last column of Table 3 shows the mode isolation algorithm's performance when the white noise is raised to 20% of the signal amplitude. The relative error is 2.0%, which is much less that what Enhanced ERA obtained at half this noise level.

Systems with Gyroscopic Effects and General Damping

The present state of the mode isolation method assumes that the system can be described by the equations of motion whose form is

$$[M]\ \{\ddot{q}\} + [C]\ \{\dot{q}\} + [K]\ \{q\} = \{Q\} \tag{15}$$

where $[M]$, $[C]$ and $[K]$ are the mass, damping and stiffness matrices, respectively. The undamped modes solution of these equations, however, is not without underlying assumptions. An undamped modal solution implies that the solution is a sum of several terms of the form given in Eq. (4). This assumed solution is only valid for systems with light damping or for systems with proportional damping, which places limitation on the matrix $[C]$. Proportional damping implies that $[C]$ is of the form given in the previous example, where all of the off diagonal elements are zero. Light damping approximation is, in general, considered appropriate if the off diagonal elements in $[C]$ are at least an order of magnitude smaller than the diagonal elements.

Many systems of interest do not contain a damping matrix of the form described above. In fact, very few realistic systems are proportionally damped, and it is difficult to determine when the light damping approximation is applicable. Gyroscopic systems increase the complexity of the problem due to the skew-symmetric nature of the matrix associated with these types of systems.

Fortunately a state-space formulation is available that provides an exact solution to these types of equations.

Defining $[G]$ and $[E]$ as the gyroscopic inertial and centripetal inertial matrices, respectively, Eq. (15) can be converted to state space form [14],

$$[S]\{\dot{x}\} - [R]\{x\} = \{Q'\} \tag{16}$$

where $\{x\}$ consists of the generalized coordinates stacked above the generalized velocities, $\{Q'\}$ is formed from the generalized forces,

$$\{x\} = \begin{Bmatrix} \{q\} \\ \{\dot{q}\} \end{Bmatrix} \quad \{Q'\} = \begin{Bmatrix} \{0\} \\ \{Q\} \end{Bmatrix} \tag{17}$$

and $[R]$ and $[S]$ are

$$[S] = \begin{bmatrix} -[K] & [0] \\ [0] & [M] \end{bmatrix} \quad [R] = \begin{bmatrix} [0] & -[K] \\ [-[K]+[E]] & [-[C]-[G]] \end{bmatrix} \tag{18}$$

It is important to notice that $[R]$ is not symmetric as it was in the case for undamped modal analysis. The matrix $[S]$ on the other hand, is symmetric as it would be in the case of undamped modal analysis.

The homogeneous solution of the state-space equations is obtained by substituting $\{x\} = \{\phi\}e^{\lambda t}$ into Eq. (16), resulting in the generalized and adjoint eigenvalue problems [15]

$$[[R] - \lambda_n[S]]\{\psi_n\} = \{0\} \quad [[R]^T - \lambda_j[S]]\{\phi_j\} = \{0\} \tag{19}$$

where λ_n and $\{\psi_n\}$ are one of the $2N$ damped mode eigenvalues and eigenvectors, respectively, where as λ_j and $\{\phi_j\}$ are one of the $2N$ adjoint eigenvalues and eigenvectors, respectively.

The eigenvectors $\{\psi_n\}$ and $\{\phi_j\}$ may be biorthonormalized so that the modal properties for the damped modes give

$$\begin{aligned} \{\Phi_j\}^T[S]\{\Psi_n\} &= \delta_{jn} \\ \{\Phi_j\}^T[R]\{\Psi_n\} &= \lambda_n\delta_{jn} \end{aligned} \tag{20}$$

Because $[S]$ and $[R]$ are real, the eigenvalues are either real or occur as complex conjugate pairs, and the eigenvectors are also complex conjugates. The orthogonality properties satisfied by the biorthonormalized modal matrix $[\Psi] = [\{\Psi_1\}\ldots\{\Psi_{2N}\}]$ is

$$[\Phi]^T[S][\Psi] = [I], \quad [\Phi]^T[R][\Psi] = [\lambda] \tag{21}$$

where $[\lambda]$ is a diagonal array of sequenced eigenvalues. The state-space modal transformation is

$$\{x\} = [\Psi]\{\xi\} = \sum_{n=1}^{2N}\{\Psi_n\}\xi_n \tag{22}$$

where the ξ_n are a set of $2N$ damped modal coordinates. Uncoupled equations for the modal coordinates are obtained by substituting Eq. (22) into Eq. (16) and premultiplying by the transpose of complex conjugate of the normalized adjoint modal matrix, which leads to

$$\dot{\xi}_n - \lambda_n\xi_n = \{\Phi_n\}^T\begin{Bmatrix} \{0\} \\ \{Q\} \end{Bmatrix}, \quad n = 1\ldots 2N \tag{23}$$

Representing harmonic excitation by $\{Q\} = \{B\}e^{i\omega t}$ and substituting this expression into Eq. (23) gives

$$\dot{\xi}_n - \lambda_n \xi_n = \{\Phi_n\}^T \begin{Bmatrix} \{0\} \\ \{B\} \end{Bmatrix} e^{i\omega t} \tag{24}$$

whose solutions are

$$\xi_n = \frac{\{\Phi_n\}^T \begin{Bmatrix} \{0\} \\ \{B\} \end{Bmatrix}}{(i\omega - \lambda_n)} e^{i\omega t} \tag{25}$$

Substitution of Eq. (25) into Eq. (22) results in the solution vector $\{x\}$. The jth component of this vector is

$$x_j = \mathrm{Re}\left\{ \left[\sum_{n=1}^{2N} \frac{\Psi_{jn}\{\Phi_n\}^T \begin{Bmatrix} \{0\} \\ \{B\} \end{Bmatrix}}{(i\omega - \lambda_n)} \right] e^{i\omega t} \right\} \tag{26}$$

Eq. (26) is now in the same form as Eq. (1) and represents the appropriate mode function for extraction of the modal parameters of systems with non-proportional damping or gyroscopic effects.

In the case that $[C]$ is symmetric, but not diagonal, Eq. (16) results in a generalized eigenproblem whose adjoint eigenproblem does not add new information. The eigenproblem solution results in one set of eigenvector instead of the two sets shown in the development above. The damped modes without gyroscopic effects can be be recovered by replacing $\{\Phi\}$ with $\{\Psi\}$. This shows that the gyroscopic development encompasses the symmetric damped modes solution.

Development of State Space Mode Isolation

The state space formulation of the mode isolation algorithm allows for systems that contain gyroscopic effects and generalized damping. The abstractions required to extend the algorithm's ability to address these issues only involves a change in the modal description of the system while the fundamental nature of the algorithm remains the same as the undamped formulation. This allows for a direct substitution of the state space modal description into the procedure described in undamped mode isolation development.

As with the undamped formulation, the data is taken to be a set of complex displacement amplitudes as a function of drive frequency, corresponding to application of a single harmonic generalized force $Q_P = \mathrm{Re}\{F_p\, e^{i\omega t}\}$. The complex displacement in terms of the state space formulation is given by the bracketed term in Eq. (26). The natural frequency ω_k and damping ratio ζ_k of the k^{th} mode are implicitly contained in the complex eigenvalue λ_k. Rewriting this expression explicitly in terms of ω_k and ζ_k gives

$$Y_j(\omega) = \sum_{k=1}^{N} 2F_p \frac{A^1_{jk}\zeta_k\omega_k(\omega_k^2 + \omega^2) - A^2_{jk}\omega_k(1-\zeta_k^2)^{\frac{1}{2}}(\omega_k^2 - \omega^2)}{(\omega_k^2 - \omega^2)^2 + (2\zeta_k\omega_k\omega)^2} + \frac{i\,2F_p\left[A^1_{jk}\omega\omega_k^2((1-2\zeta_k^2) - \omega^2) + A^2_{jk}2\omega\zeta_k\omega_k^2(1-\zeta_k^2)^{\frac{1}{2}}\right]}{(\omega_k^2 - \omega^2)^2 + (2\zeta_k\omega_k\omega)^2} \tag{27}$$

where ω_k and ζ_k are the natural frequency and damping ratio associated with the k^{th} mode. A^1_{jk} and A^2_{jk} are modal amplitudes and F_p is the amplitude of the harmonic forcing function. Notice

that the number of modes contained in Eq. (27) is N instead of the $2N$ modes contained in Eq. (26). This is because Eq. (26) is composed of N modes and N complex conjugates of the first N modes, whereas Eq. (27) depicts the result of combining the complex conjugate relationships contained in the modal series.

The first iteration through the data is the same as the procedure described by the undamped modal formulation. The first iteration begins by seeking evidence of the mode that gives the largest contribution to the overall $Y_j(\omega)$ data set. Characteristics from the complex displacement response curve are used to estimate the first mode's natural frequency ω_1, modal damping ratio ζ_1, and modal amplitudes A^1_{j1} and A^2_{j1}. In order to bring the next mode into dominance, the contribution of the estimated mode to the frequency response function is subtracted from the measured data. The general process for the first iteration, let $Y^{(n)}_j(\omega)$ denote the residual of $Y_j(\omega)$ in the first iteration after the contributions of modes 1 to N have been subtracted is given by

$$Y^{(n)}_j(\omega) = Y^{(n-1)}_j(\omega) - 2F_p \frac{A^1_{jk}\zeta_k\omega_k(\omega_k^2+\omega^2) - A^2_{jk}\omega_k(1-\zeta_k^2)^{\frac{1}{2}}(\omega_k^2-\omega^2)}{(\omega_k^2-\omega^2)^2+(2\zeta_k\omega_k\omega)^2} + \frac{i\,2F_p\left[A^1_{jk}\omega\omega_k^2((1-2\zeta_k^2)-\omega^2) + A^2_{jk}2\omega\zeta_k\omega_k^2(1-\zeta_k^2)^{\frac{1}{2}}\right]}{(\omega_k^2-\omega^2)^2+(2\zeta_k\omega_k\omega)^2} \quad (28)$$

At each step in the first iteration, estimates of ω_n, ζ_n A^1_{j1} and A^2_{j1} are obtained from $Y^{(n-1)}_j(\omega)$ by the same procedures as those used to obtain preliminary estimates of the first mode's parameters.

The first iteration ends when there are no highlights in the residual frequency response functions. At this stage estimates of ω_k, ζ_k, A^1_{jk}, and A^2_{jk} have been obtained for each identified mode. The number of modes, N, described by the data is estimated as the number of steps required to reduce the residual $Y^N_j(\omega)$ to noise.

The second and following iterations are intended to isolate each mode and improve the estimates of the modal parameters. The concept is that any mode may be isolated by using the current estimates for the modal properties. These estimates are used to subtract the contribution of the other modes. Let $X^{(n)}_j(\omega)$ denote the $Y_j(\omega)$ data at a specified iteration step from which the estimated contributions of all except mode n have been subtracted.

$$X^{(n)}_j(\omega) = Y_j(\omega) - \sum_{\substack{j=1\\ j\neq n}}^{N} 2F_p \frac{A^1_{jk}\zeta_k\omega_k(\omega_k^2+\omega^2) - A^2_{jk}\omega_k(1-\zeta_k^2)^{\frac{1}{2}}(\omega_k^2-\omega^2)}{(\omega_k^2-\omega^2)^2+(2\zeta_k\omega_k\omega)^2} + \frac{i\,2F_p\left[A^1_{jk}\omega\omega_k^2((1-2\zeta_k^2)-\omega^2) + A^2_{jk}2\omega\zeta_k\omega_k^2(1-\zeta_k^2)^{\frac{1}{2}}\right]}{(\omega_k^2-\omega^2)^2+(2\zeta_k\omega_k\omega)^2} \quad (29)$$

In this expression A^1_{jk}, A^2_{jk}, ω_k, and ζ_k are the current values, which are known from previous iterations and previous steps in the current iteration. The $X^{(n)}(\omega)$ data is used to obtain improved estimates for ω_n, ζ_n, A^1_{jn}, and A^2_{jn}. The sequence of steps in which any iteration are performed is based on the largeness of $Y_j(\omega_n)$ or the current residual at a particular step. An iteration progresses sequentially through the higher modes, until all modal parameters have been updated. Additional iterations repeat the steps of the second, until convergence criteria for ω_n, ζ_n, A^1_{jn}, and A^2_{jn} are met.

Parameter Identification

The above section describes how the mode isolation algorithm constructs data sets that are critical to the identification of the modal parameters ω_k, ζ_k, A^1_{jk}, and A^2_{jk}. In the first iteration such data is the successive data set Y^k_j obtained from subtracting lower modes. In the second pass the residuals X^k_j are obtained by subtracting current estimates of the other modes. It remains, however, to develop the manner in which the modal parameters are extracted from the data when using the state space modal formulation.

The complex displacement of the k^{th} generalized coordinate when ω is close to the natural frequency of the mode under consideration is

$$Y_j(\omega) \approx 2F_p \frac{A^1_{jk}\zeta_k\omega_k(\omega_k^2+\omega^2) - A^2_{jk}\omega_k(1-\zeta_k^2)^{\frac{1}{2}}(\omega_k^2-\omega^2)}{(\omega_k^2-\omega^2)^2+(2\zeta_k\omega_k\omega)^2} + \frac{i\,2F_p\left[A^1_{jk}\omega\omega_k^2((1-2\zeta_k^2)-\omega^2) + A^2_{jk}2\omega\zeta_k\omega_k^2(1-\zeta_k^2)^{\frac{1}{2}}\right]}{(\omega_k^2-\omega^2)^2+(2\zeta_k\omega_k\omega)^2} \tag{30}$$

where A^1_{jk}, A^2_{jk}, ω_k, and ζ_k are the sought after variables. The selection of several points can be used to form an overdetermined system, from which the modal parameters A_{jk}, ω_k and ζ_k can be obtained. The procedure for a nonlinear least squares method of solution is described previously.

The nonlinear least squares method for solving overdetermined systems requires that initial values for the modal parameters be obtained in order to begin the iteration process. The initial value of ω_k is defined as the value of ω where the imaginary part of the frequency response function reaches a global maximum, which is given by Eq. (8).

Because the state space formulation is required to identify the modal parameters in the presences of arbitrary damping, the initial value of ζ_k is found by a direct calculation instead of utilizing the definition of the half-power points which is based on a light damping approximation.

Defining $Y_r = \text{Re}\{Y_j(\omega)|_{\omega_k}\}$ and $Y_i = \text{Im}\{Y_j(\omega)|_{\omega_k}\}$ to be the real and imaginary values of the complex displacement data $Y_j(\omega)$ evaluated at the natural frequency ω_k, respectively, an expression may be obtained in which ζ_k is raised powers of even order. Defining $\alpha = \zeta_k^2$, the expression in quadratic form, such as

$$\alpha = \frac{-B \pm (B^2-4AC)^{\frac{1}{2}}}{2A} \tag{31}$$

where

$$\begin{aligned} A &= 8\omega_k^4\omega^2(\omega^2Y_r^2 - \omega^2Y_i^2 + 2\omega_k^2Y_i^2) \\ B &= 4\omega_k^2Y_i^2(\omega_k^6 - 3\omega_k^4\omega^2 + 3\omega_k^2\omega^4 - \omega^6) \\ C &= -\frac{1}{2}(\omega_k^2-\omega^2)^4(Y_r^2+Y_i^2) \end{aligned} \tag{32}$$

Y_r, Y_i, and ω_k are known quantities and ω is arbitrary. Because ζ_k is defined to be a positive quantity, the positive root of Eq. (31) gives an approximation for $\zeta_k = \alpha^{1/2}$.

The approximations of ω_k, ζ_k and the definitions of Y_r and Y_i leads to the estimations of A^1_{jk} and A^2_{jk} given by

$$\begin{aligned} A^1_{jk} &= \frac{\zeta_k\omega_kY_r}{A_k} \\ A^2_{jk} &= \frac{\zeta_k\omega_kY_r}{A_k(1-\zeta_k^2)^{\frac{1}{2}}}(Y_i + \zeta Y_r) \end{aligned} \tag{33}$$

The modal amplitudes A^1_{jk} and A^2_{jk} contain all of the information required to extract eigenvectors. If $[R]$ is not symmetric the completion of the eigenproblem solution is based on the modal matrix $[\Psi]$ and the adjoint modal matrix $[\Phi]$. However, if $[R]$ is symmetric, which is the case for systems without gyroscopic effects, the eigenvectors in the modal matrix $[R]$ and the eigenvalues completely describe the modal solution of the system. The discussion of eigenvector extraction address only the case of symmetric $[R]$.

Because A^1_{jk}, A^2_{jk} and F_p are known, the eigenvector elements may be determined by setting $j = p$ which gives

$$\Psi_{pk} = (A^1_{pk} + iA^2_{pk})^{\frac{1}{2}} \tag{34}$$

The other elements of the modal transformation matrix may be determined by

$$\Psi_{jk} = \frac{(A^1_{jk} + iA^2_{jk})}{\Psi_{pk}} \tag{35}$$

The above expressions provides an $N \times N$ submatrix of the modal transformation matrix $[\Psi]$. The upper $N \times N$ submatrix corresponding to the matrix extracted by the algorithm can be calculated from the definition of an eigenvector. Let $\{\psi_n\}$ be an eigenvector corresponding to the eigenvalue λ_n. Partitioning the eigenvector into a pair of stacked vectors $\{u_n\}$ and $\{v_n\}$ and substituting into Eq. (19) gives

$$\left[\begin{bmatrix} -[K] & [0] \\ [0] & [M] \end{bmatrix} - \lambda_n \begin{bmatrix} [0] & -[K] \\ [-[K]+[E]] & [-[C]-[G]] \end{bmatrix}\right] \begin{Bmatrix} \{u_n\} \\ \{v_n\} \end{Bmatrix} = \{0\} \tag{36}$$

The upper set of equations in Eq. (36) provides an equation involving the vectors $\{u_n\}$ and $\{v_n\}$ given as

$$-[K]\{v_n\} + \lambda_n [K]\{u_n\} = \{0\} \tag{37}$$

Because $[K]$ is positive definite, then $[K]^{-1}$ exists and Eq. (37) becomes

$$\lambda_n \{u_n\} = \{v_n\} \tag{38}$$

The relationship between $\{u_n\}$ and $\{v_n\}$ allows the construction of the upper submatrix, resulting in a $2N \times N$ matrix of eigenvector elements. The remaining elements of the modal matrix are found from the knowledge that the eigenvectors in $[\Psi]$ occur in complex conjugate pairs. Taking the complex conjugate of the existing eigenvector elements contained in the $2N \times N$ submatrix and appending the results to this matrix provides the complete set of elements for the modal transformation matrix $[\Psi]$.

Numerical Example of State Space Mode Isolation

An example of the state space formulation of the mode isolation algorithm will utilize a continuous system consisting of a cantilever beam and three spring-mass-damper systems attached to the beam. The placement of the spring-mass-damper systems along the length of the beam at $x_1 = L/2$, $x_2 = 3L/4$ $x_3 = L$ as shown by the location x_j in Figure 10. The substructure parameters are defined such that the stiffnesses are the same, the fixed-base natural frequencies increase linearly, and the fixed-base critical damping ratios are constant. Thus, the jth spring-mass-damper system is described by $k_j = \sigma m_0 \Omega_0^2$, $\Omega_j = \Omega_0(0.8j + 0.6N - 1.4)/(N-1)$, $\Omega_j = (k_j/m_j)^{1/2}$ and

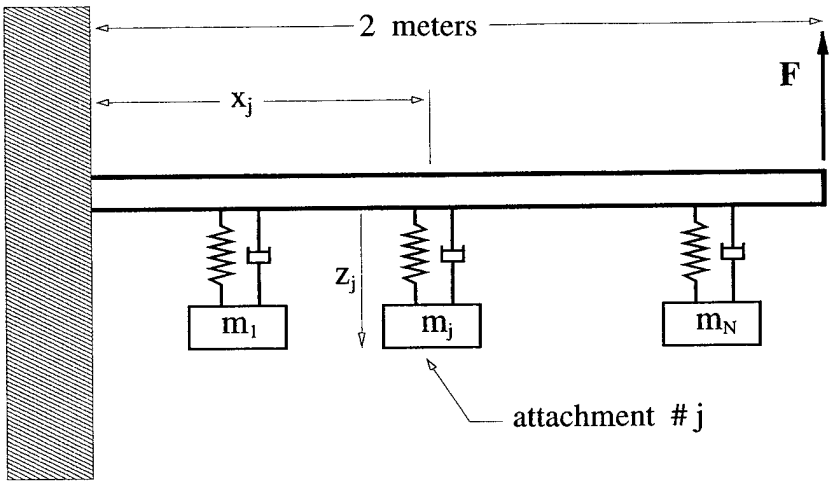

Figure 10: Continuous System Model

$\zeta = c_j/2(k_j m_j)^{1/2}$, where $\Omega_0 = 65.3594$, which is the natural frequency of the cantilever beam without the three oscillators. The factor σ allows for scaling the attached springs stiffness relative to the master structure and ζ is the critical damping ratio for the attached dampers. Additional parameters required to describe the beam are: modulus of elasticity $E = 2.07 \times 10^{11}$ Pa, density $\rho = 7800$ kg/m^2, second moment of area $I = 3.125 \times 10^{-7}$ m^4, cross sectional area $A = 0.0015$ m^2 and the beam length $L = 2$ meters.

The beam displacement shall be represented as a Ritz series whose basis functions are the normalized beam modes of the isolated cantilever beam [25]

$$\begin{aligned}\Psi_j(x) =& C_j(\cos(\alpha_j x) - \cosh(\alpha_j x)) + \\ & C_j\left[\frac{(\sin(\alpha_j L) - \sinh(\alpha_j L)}{(\cos(\alpha_j L) + \cosh(\alpha_j L)}\right](\sin(\alpha_j x) - \sinh(\alpha_j x))\end{aligned} \tag{39}$$

where the α_j's are the solutions to the characteristic equation

$$\cos(\alpha_j L)\cosh(\alpha_j L) = -1 \tag{40}$$

The constant C_j is obtained by setting the associated modal mass to unity,

$$\int_0^L \rho A \Psi_j \Psi_k \, dx = \begin{cases} 1 & \text{if } j = k \\ 0 & \text{if } j \neq k \end{cases} \tag{41}$$

The cantilever beam modes are used as basis functions for a Ritz series representation [41] of the displacement of the beam,

$$w(x,t) = \sum_{j=1}^{J} \Psi_j(x) q_j(t) \tag{42}$$

where J is the number of terms in the Ritz series. This series is substituted into the expressions for Lagrange's equations of motion.

The kinetic and potential energies of the system in Figure 10 are

$$T = \frac{1}{2}\int_0^L \rho A \dot{w}(x,t)^2\,dx + \frac{1}{2}\sum_{j=1}^{N} m_j \dot{z}_j{}^2$$
$$= \frac{1}{2}\sum_{j=1}^{J}\sum_{k=1}^{J}\left(\int_0^L \rho A \Psi_j \Psi_k\,dx\right)\dot{q}_j\dot{q}_k + \frac{1}{2}\sum_{j=1}^{N} m_j \dot{z}_j{}^2$$

$$V = \frac{1}{2}\int_0^L EI\left(\frac{\partial^2 w}{\partial x^2}\right)^2 dx + \frac{1}{2}\sum_{s=1}^{N} k_s(w(x_s,t) - z_s)^2$$
$$= \frac{1}{2}\sum_{j=1}^{J}\sum_{k=1}^{J}\left[\int_0^L EI\frac{d^2\Psi_j}{dx^2}\frac{d^2\Psi_k}{dx^2}\,dx + \sum_{s=1}^{N} k_s \Psi_j(x_s)\Psi_k(x_s)\right] q_j q_k -$$
$$\sum_{s=1}^{N}\sum_{k}^{J} k_s \Psi_k(x_s) q_k z_s + \frac{1}{2}\sum_{s=1}^{N} k_s z_s^2$$

The Rayleigh dissipation function is defined as

$$D = \frac{1}{2}\sum_{s=1}^{N} c_s(\dot{w}(x,t) - \dot{z}_s)^2$$
$$= \frac{1}{2}\sum_{s=1}^{N} c_s\left[\sum_{j=1}^{J}\sum_{k=1}^{J}\Psi_j(x_s)\Psi_k(x_s)\dot{q}_j\dot{q}_k\right] -$$
$$\sum_{s=1}^{N}\sum_{k=1}^{J} c_s \Psi_k(x_s)\dot{q}_k\dot{z}_s + \frac{1}{2}\sum_{s=1}^{N} c_s \dot{z}_s{}^2$$

and the generalized forces are

$$\hat{Q}_j = F\Psi_j(x_f) \tag{43}$$

This representation of T, V and D as quadratic sums leads to a standard form for the linear equations of motions as given in Eq. (16). Because of the orthogonality properties of the normalized beam mode functions, the matrices $[M]$, $[C]$, $[K]$, $\{Q\}$ and $\{q\}$ are defined as

$$[M] = \begin{bmatrix} [\delta_{ij}] & [0] \\ [0]^T & [\delta_{rs} m_s] \end{bmatrix}$$
$$[C] = \begin{bmatrix} \left[\sum_{s=1}^{N} c_s \Psi_i(x_s)\Psi_j(x_s)\right] & [-c_s\Psi_j(x_s)] \\ [-c_s\Psi_j(x_s)]^T & [\delta_{rs}c_s] \end{bmatrix} \tag{44}$$
$$[K] = \begin{bmatrix} \left[\delta_{ij}\omega_j^2 + \sum_{s=1}^{N} k_s \Psi_i(x_s)\Psi_j(x_s)\right] & [-k_s\Psi_j(x_s)] \\ [-k_s\Psi_j(x_s)]^T & [\delta_{rs}k_s] \end{bmatrix}$$

and

$$\{\hat{q}\} = \begin{Bmatrix} \{q_j\} \\ \{z\} \end{Bmatrix} \quad \{Q\} = \begin{Bmatrix} \{\hat{Q}_j\} \\ \{0\} \end{Bmatrix} \tag{45}$$

where $i, j = 1, 2, \ldots J$ and $r, s = 1, 2, \ldots N$.

The equations governing the generalized coordinates for the system have the standard form of a linear vibratory system with non-proportional damping. Analysis using the modes of the damped system leads to analytical expressions for the steady state response without approximating the effects of damping.

The equations are converted to state space form as shown in Eq. (16) and $\{x\}$ consists of the generalized coordinates stacked above the generalized velocities, $\{Q'\}$ is formed from the generalized forces, depicted in Eq. (17). $[R]$ and $[S]$ are defined as given in Eq. (18). Because $[R]$ and $[S]$ are symmetric, the modal analysis is carried out in the same manner as the undamped modes.

The homogeneous solution of the state-space equations is obtained by substituting $\{x\} = \{\phi\}e^{\lambda t}$ into Eq. (15), resulting in the symmetric generalized eigenvalue problem

$$[[R] - \lambda_n[S]]\{\phi_n\} = \{0\} \tag{46}$$

where λ_n and $\{\phi_n\}$ are one of the $2(J+N)$ eigenvalues and eigenvectors, respectively, of Eq. (46). The eigenvectors from this state-space formulation are the damped modes. Because the damping matrix $[C]$ is non-negative, the eigenvalues may be negative and real, or else occur as pairs of complex conjugates with negative real parts.

The modal orthogonality properties for the damped modes give

$$\begin{aligned} \{\phi_j\}^T [S]\{\phi_n\} &= \nu_n \delta_{jn} \\ \{\phi_j\}^T [R]\{\phi_n\} &= \lambda_n \nu_n \delta_{jn} \end{aligned} \tag{47}$$

where ν_n is the complex modal mass. By setting $\nu_n = 1$, a set of normalized damped modes may be defined as

$$\{\Phi_n\} = \frac{\{\phi_n\}}{(\{\phi_n\}^T [S]\{\phi_n\})^{1/2}} \tag{48}$$

For the system parameters in the present analysis, the eigenvalues occur as complex conjugate pairs, and the modes are also complex conjugates. The orthogonality properties satisfied by the normal modal matrix $[\Phi] = [\{\Phi_1\} \ldots \{\Phi_{2(J+N)}\}]$ are

$$[\Phi]^T[S][\Phi] = [I], \quad [\Phi]^T[R][\Phi] = [\lambda] \tag{49}$$

where $[\lambda]$ is a diagonal array of sequenced eigenvalues. The state-space modal transformation is

$$\{x\} = [\Phi]\{\xi\} = \sum_{n=1}^{2(J+N)} \{\Phi_n\}\xi_n \tag{50}$$

where ξ_n are a set of $2(J+N)$ damped modal coordinates. Uncoupled equations for the modal coordinates are obtained by substituting Eq. (22) into Eq. (15) and premultiplying by the transpose of the normal modal matrix, which leads to

$$\dot{\xi}_n - \lambda_n \xi_n = \{\Phi\}^T \begin{Bmatrix} \{0\} \\ \{Q\} \end{Bmatrix}, \quad n = 1 \ldots 2(J+N) \tag{51}$$

Harmonic excitation is represented by $\{Q\} = \{B\}e^{i\omega t}$. Substitution of this expression into Eq. (23) gives

$$\dot{\xi}_n - \lambda_n \xi_n = \{\Phi\}^T \begin{Bmatrix} \{0\} \\ \{B\} \end{Bmatrix} e^{i\omega t} \tag{52}$$

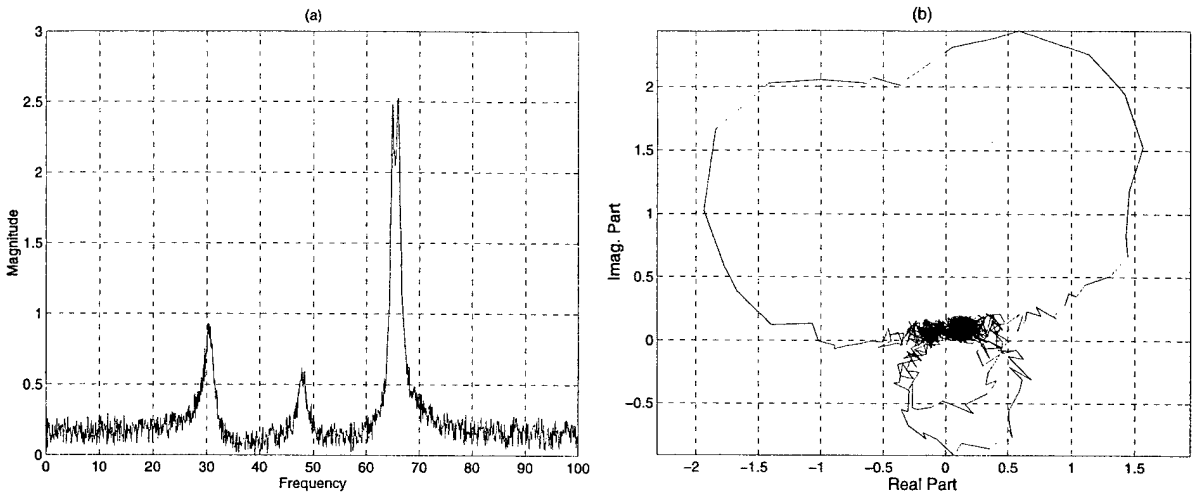

Figure 11: Frequency Response Data $Y(\omega)$: (a) Magnitude verses Frequency, (b) Nyquist Plot

whose solutions are

$$\xi_n = \frac{\{\Phi_n\}^T \begin{Bmatrix} \{0\} \\ \{B\} \end{Bmatrix}}{(i\omega - \lambda_n)} e^{i\omega t} \tag{53}$$

The response in modal coordinates is transformed into the response with respect to physical coordinates q_j by forming the upper partition of Eq. (22). Further, the q_j are related to the beam displacement by the Ritz series in Eq.(42).

As in the case of the undamped mode isolation formulation, an exact solution of this system can be found by solving the associated eigenproblem. The simulated frequency response function

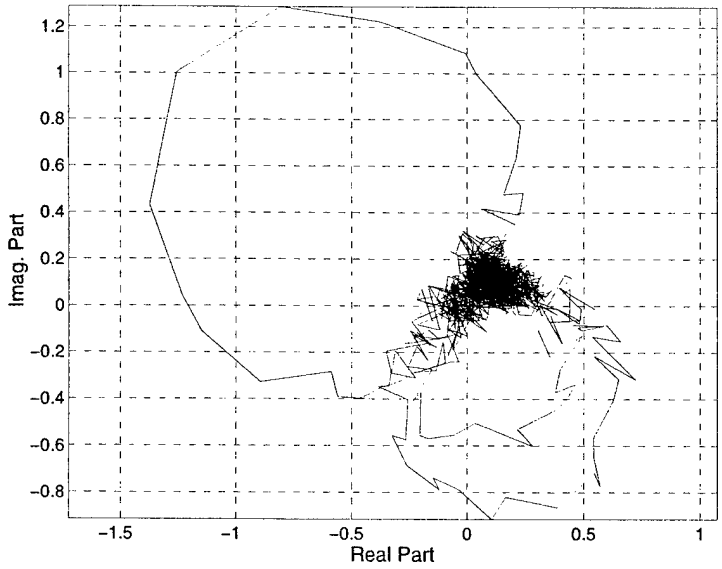

Figure 12: First step in first iteration yields $Y_4^1(\omega)$

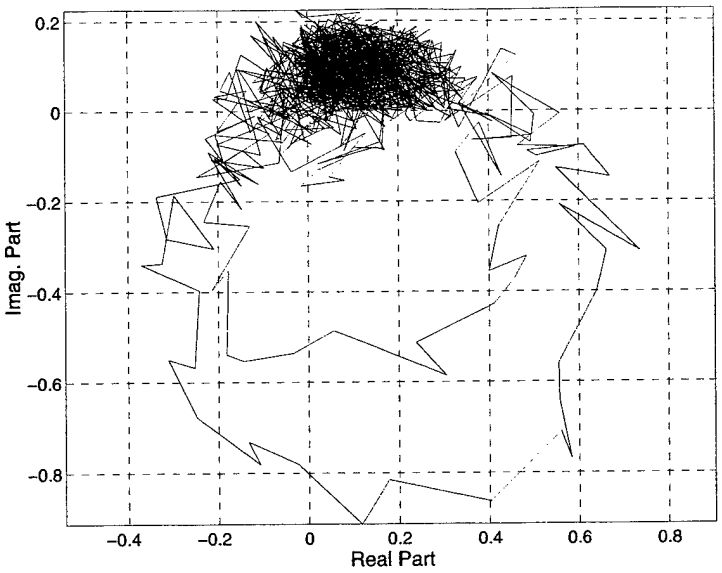

Figure 13: Second step in first iteration: $Y_4^2(\omega)$

has a Gaussian white noise of two levels of approximately 10% and 20% of the signal amplitude added to the exact frequency response function. Figure 11a and Figure 11b show the corresponding data set on which the damped mode isolation algorithm will be tested. The data corresponds to a system with one beam mode and three attached oscillators for a total of four modes. Two features that are present in this data set complicate the extraction process. The first two modes apparent in the data are not well excited and are heavily contaminated with noise. The last two modes show heavy overlap of their modal contributions resulting in an amplitude that shows little evidence of

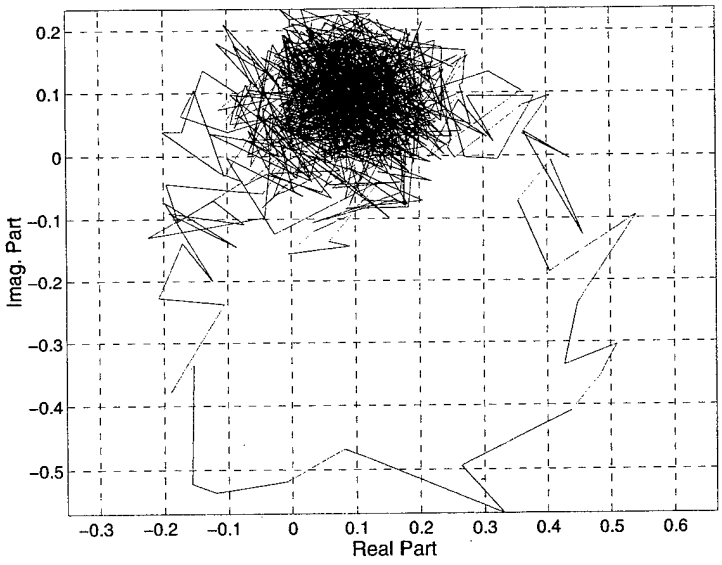

Figure 14: Third step in first iteration: $Y_4^3(\omega)$

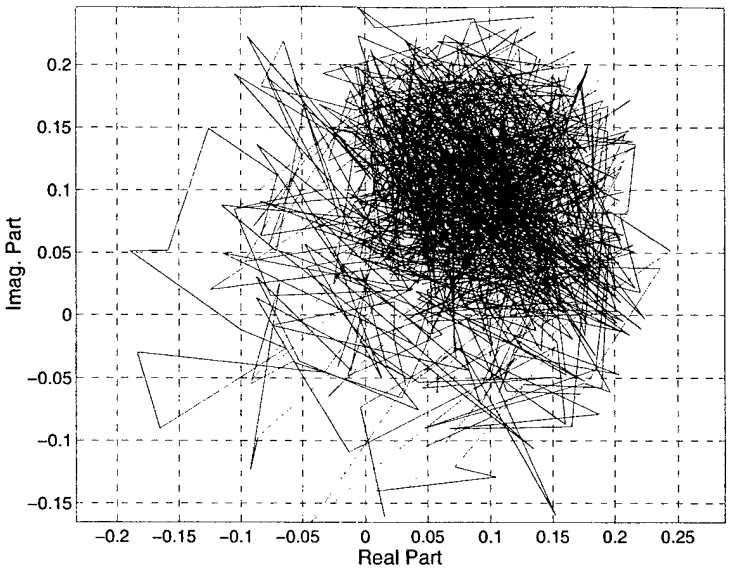

Figure 15: Noise residual $Y_4^4(\omega)$ after fourth step in first iteration

two modes occupying the region.

Figures 11 through 15 provide a graphic illustration of the progress through the first iteration. Figure 11a shows magnitude of the original data for the fourth generalized coordinate of the system, given by Eq. 45, as a function of drive frequency ω. Figure 11b is a Nyquist plot of $Y_4^0(\omega)$ corresponding to the original measured data $Y_4(\omega)$. Figure 12 shows $Y_4^1(\omega)$ as depicted by Eq. (28) after the most dominant mode has been subtracted from the data in Figure 11b. Figure 13 depicts $Y_4^2(\omega)$, which is the residual after the two modes dominate modes have been subtracted. The process continues until the state in Figure 15 is attained. At this stage, only noise remains, indicating that no new modes can be estimated.

Exact solution	Mode Isolation (10%)	Mode Isolation (20%)
-0.7496 ± 30.5454i	-0.7118 ± 30.5142i	-0.6258 ± 30.4497i
-0.7488 ± 48.0244i	-0.6574 ± 47.9972i	-0.6599 ± 47.9773i
-0.3120 ± 64.9089i	-0.3012 ± 64.9241i	-0.3087 ± 64.9401i
-0.4393 ± 65.9895i	-0.4535 ± 65.9877i	-0.4764 ± 65.9875i

Table 4: Comparison of Exact and Identified Eigenvalues

Table 4 compares the exact solution of the eigenproblem with the estimations obtained by the mode isolation algorithm for noise levels of approximately 10% and 20% of the response amplitude. The middle column shows the mode isolation algorithm's performance with respect to 10% noise. It is clear that the algorithm is able to find the four modes. The real part of the eigenvalues, which reflects the damping of the system, has a average relative of 6.0%. The modes located at the lower frequencies cause the majority of the relative error because they are heavily contaminated with noise. The imaginary part of the eigenvalues, reflecting the frequency of oscillation, have an average relative error of less than 1%. The last column of Table 4 shows the modal parameter identification when the noise leve is raised to approximately 20% of the signal amplitude. In this

case the average relative error of the real part of the eigenvalues is 9.5%, but the imaginary part average relative error remains less than 1%.

SUMMARY AND CONCLUSIONS

The mode isolation algorithm does not require an *a priori* knowledge of the number of significant modes contained in the data. This relieves the user from guessing the system's degrees of freedom or, in the case of ERA and its descendants, from specifying the dimensions of the Hankel matrix. The benefit of the mode isolation's recursive search strategy was presented in a numerical example, in which, the ERA algorithm was unable to detect four meaningful modes because of the presence of noise in the data. This implies that the singular value decomposition, on which ERA depends, produced several non-zero values instead of the four that correspond to actual modes. This caused the algorithm to produce artificial modes and large errors in the other modes. The Enhanced ERA algorithm showed an improvement over ERA in regards to the ability to detect all four modes, and to provide reasonable estimates of the damped natural frequencies and eigenvectors. However, Enhanced ERA still displayed large errors in the extraction of the real part of the eigenvalues. The mode isolation algorithm was able to detect all four modes, to achieve excellent estimations of all natural frequencies, damping ratios, and eigenvectors, and to do so in an automated fashion. The mode isolation algorithm continued to provide excellent estimations of the eigenvalues and eigenvectors even though the noise was roughly double the level that ERA and Enhanced ERA were subjected. This suggests that the method is more accurate than ERA and Enhanced ERA. Its merit becomes even more evident in the presents of substantial noise. A potential criticism of the example selected for the undamped mode isolation formulation is that the example addressed a system with proportional damping, so that the modal coordinates are not coupled by damping. Such a property might seem to favor the undamped formulation. However, both versions of ERA also are based on dynamic response models that exactly fit the system (in the absence of noise), and neither of them performed as well in the test.

The state space formulation shows that the mode isolation algorithm is not limited to fitting response data to an undamped modal structure. This new formulation replaces the undamped framework with a state-space modal description that is valid for gyroscopic and heavily damped structures. The numerical example of the state-spaced algorithm, composed of a cantilever beam with multiple attached oscillators, reflects the algorithm's performance on a more realistic structure. As in the case of the undamped formulation, the state-space mode isolation algorithm shows the ability to extract the correct number of modes in an automated fashion, in the presents of noisy data, and closely spaced modes.

An important aspect of the algorithm is the simplicity and versatility of the approach. Changing the modal structure only requires that the nonlinear least squares parameter identification be altered, commensurate with the new modal structure.

FUTURE RESEARCH

The mode isolation algorithm provides a robust methodology of identifying the modal parameters of a system from measured complex frequency response data. This information, however, does not directly reflect the general health of a structure. Relationships are required to connect the dynamics of the structure described by the modal parameters to the failure modes of the structure described by mechanics. Many structures endure modal testing as a normal course of the development cycle, but few, if any, of these tests are conducted in a destructive manner. A standard modal test does provide a state of optimal structural health which can be used as a baseline for

extracting a nominal set of modal parameters. The cost of a destructive modal test would be prohibitive, causing predictive modeling solutions to be sought. The Finite Element Method (FEM) is a well developed concept that is able to relate the failure modes of a structure to the structure's dynamic characteristics in terms of modal parameters in a predictive and cost effective manner. This allows the failure modes of a structure to be mapped as functions of modal parameters and in turn, limits can be set to indicate when the modal parameters report the onset of failure. In other words, the modal parameters can be used to infer the health of a structure by tracing the progress of the parameters from a nominal state to a failure state by utilizing the failure predictions given by FEM. In order to assess the validity of combining mode isolation with FEM in the condition monitoring process, experimental investigations must be constructed in which failure modes and modal parameters are measured simultaneously. Then the experimental results and the mode isolation/FEM algorithms can be evaluated for the desired predictive capabilities.

Because there are multiple modal parameters required to describe each mode, it is logical to inquire whether the parameters are equally sensitive to the failure modes of the structure. The appropriate modal parameter or parameters to trace as a function of failure mode may vary depending on the type of structure being considered. The relationships between the modal parameters and failure modes need to be investigated in hopes of finding a modal parameter that is globally sensitive to the failure modes of an arbitrary structure.

The present state of the mode isolation algorithm is a frequency domain method of modal parameter identification. This implies that the complex displacement function is a function of drive frequency over a sufficient bandwidth to explicitly capture all of the modes of interest. This broad frequency sweep is required by the algorithm in order to provide information for characterizing the modes contained in the data. Systems that are perturb by random excitations do not contain sufficient frequency content to allow for the characterization of a mode in the manner currently used by the algorithm. In order to allow for random excitation of the structure, the modal framework needs to be developed in terms of a random forcing function instead of the present harmonic function. In addition, new indicators are required to locate and provide initial value estimations of the modes contained in the data.

M-URI PUBLICATIONS

Drexel, M. V., Ginsberg, J. H., "Mode Isolation: A New Algorithm for Modal Parameter Extraction", J. Acoust. Soc. Am., (submitted).

References

[1] Allemang, R. J., 1983, *Experimental Modal Analysis*, Winter Annual Meeting, ASME Nov. 13-18, Boston, MA.

[2] Allemang, R. J., Brown, 1987, *Modal Parameter Estimation*, Experimental Modal Analysis and Dynamic Component Synthesis, USAF Technical Report Contract No. F33615-83-C-3218, AFWAL-TR-87-3096, Vol. 3

[3] Allemang, R. J., Brown, D. L., Fladung, W., 1994, *Modal Parameter Estimations: A Unified Matrix Polynomial Approach*, Proceedings of the 12th International Modal Analysis Conference, Honolulu, HA.

[4] Brown, D. L., Allemang, J. R., Zimmerman, R. D., Mergeay, M., 1979, *Parameter Estimation Techniques for Modal Analysis*, SAE Paper No. 790221, SAE Transactions, Vol. 88.

[5] Chapra, S. C., Canale, R. P., 1988, *Numerical Methods for Engineers*, McGraw-Hill, NY.

[6] Coppolino, R. N., 1981, *A Simultaneous Frequency Domain Technique for Estimation of Modal Parameters from Measured Data*, SAE Paper No. 811046, SAE Transactions.

[7] Craig, R. R., Kurdila, A. J., Kim, H. M., 1990, *State-Space Formulation of Multi-Shaker Modal Analysis*, Journal of Analytical and Experimental Modal Analysis, Vol. 5, No. 3.

[8] de Silva, C. W., 1983, *Dynamic Testing and Seismic Qualification Practice*, Heath, Lexington, KY.

[9] Doebling, S. W., Alvin, K. F., Peterson, L. D., 1994, *Limitations of State-Space System Identification Algorithms for Structures with High Modal Density*, Proceedings of the 12th International Modal Analysis Conference, Honolulu, HA.

[10] Draper, N. R., Smith, H., 1998, *Applied Regression Analysis*, Wiley and Sons, NY.

[11] Ebersbach, P., Irretier, H., 1989, *On the Application of Modal Parameter Estimation Using Frequency Domain Algorithms*, Journal of Analytical and Experimental Modal Analysis, Vol. 4, No. 4.

[12] Fukuzono, K., 1986, *Investigation of Multiple-Reference Ibrahim Time Domain Modal Parameter Estimation Technique*, M. S. Thesis, Dept. of Mechanical and Industrial Engineering, University of Cincinnati.

[13] Ibrahim, S. R., Mikulcik, E. C., 1977, *A Method for the Direct Identification of Vibration Parameters from the Free Response*, Shock and Vibration Bulletin, Vol. 47, Part 4.

[14] Inman, D. J., 1996, *Engineering Vibration*, Prentice-Hall, NJ.

[15] Jei, Y. G., Lee, C. W., 1993, *Modal Characteristics of Asymmetrical Rotor-Bearing Systems*, J. of Sound and Vibration, Vol. 162, No. 2.

[16] Juang, J. N., Pappa, R. S., 1985, *An Eigensystem Realization Algorithm for Modal Parameter Identification and Model Reduction*, J. of Guidance, Control, and Dynamics, Vol. 8, No. 5.

[17] Juang, J. N., Suzuki, H., 1988, *An Eigensystem Realization Algorithm in Frequency Domain for Modal Parameter Identification*, J. of Vibration, Stress, and Reliability in Design, Vol. 110.

[18] Kennedy C. C., Panu C. D. P., 1947, *Use of Vectors in Vibration Measurement and Analysis*, J. of Aeronautical Sciences, Vol. 14, No. 11.

[19] Lembregets, F., Leuridan, J. L., Van Brussel, H., 1989, *Frequency Domain Direct Parameter Identification for Modal Analysis: State Space Formulation*, Mechanical Systems and Signal Processing, Vol. 4, No. 1.

[20] Leonard, F., 1988, *ZMODAL: A New Modal Identification Technique*, Journal of Analytical and Experimental Modal Analysis, Vol. 3, No. 2.

[21] Leuridan, J., 1984, *Some Direct Parameter Model Identification Methods Applicable for Multiple Input Modal Analysis*, Doctoral Dissertation, University of Cincinnati.

[22] Lin, A. C. Y., Tsuei, Y. G., 1989, *The Prediction of Substructure and System Modes by the Extended Complex Mode Indication Function*, J. of Vibrations and Acoustics, ASME, Vol. 120, No. 2.

[23] Longman, R. W., Juang, J. N., 1989, *Recursive Form of the Eigensystem Realization Algorithm for System Identification*, J. of Guidance, Control, and Dynamics, Vol. 12, No. 5.

[24] Luk, Y. W., Mitchell, L. D., 1983, *System Identification via Modal Analysis*, Winter Annual Meeting, ASME Nov. 13-18, Boston, MA.

[25] Meirovitch, L., 1975, *Elements of Vibrational Analysis*, McGraw-Hill, Inc., NY.

[26] Mitchell, L. D., 1988, *A Perspective view of Modal Analysis*, 6th International Modal Analysis Conference, Vol. 2. HP Conference for Automotive and Related Industries, Detroit, MI.

[27] Natke, H. G., 1984, *Updating Computational Models in the Frequency Domain Based on Measured Data: A Survey*, Probabilistic Engineering Mechanics, Vol. 3, No. 1.

[28] Oshman, Y., Mendelboim, T., 1994, *Maximum likelihood Identification and Realization of Stochastic Systems*, J. of Guidance, Control, and Dynamics, Vol. 17, No. 4.

[29] Quan, R., 1994, *System Identification Using Frequency Scanning and the Eigensystem Realization Algorithm*, J. of Guidance, Control, and Dynamics, Vol. 17, No. 4.

[30] Richardson, M., Forenti, D. L., 1982, *Parameter Estimation from Frequency Response Measurement Using Rational Fraction Polynomials*, Proceedings, International Modal Analysis Conference, Society of Experimental Mechanics.

[31] Richardson, M. H., 1978, *Measurement and Analysis of the Dynamics of Mechanical Structures*, HP Conference for Automotive and Related Industries, Detroit, MI.

[32] Roemer, M. J., Mook, D. J., 1989, *An Enhanced Mode Shape Identification Algorithm*, AIAA Paper 89-1245, Proceedings of the 30th AIAA SDM Conference.

[33] Roemer, M. J., Mook, D. J., 1990, *Enhanced Realization/Identification of Physical Modes*, J. of Aerospace Engineering, Vol. 3, No. 2.

[34] Roemer, M. J., Mook, D. J., 1990, *A Robust Algorithm for System Realization/Identification*, J. of the Astronautical Sciences, Vol. 38, No. 2.

[35] Shih, C. Y., 1989, *Investigation of Numerical Conditioning in the Frequency Domain Modal Parameter Estimation Methods*, Doctoral Dissertation, University of Cincinnati.

[36] Shih, Y. C., Eman, K. F., Wu, S. M., 1989, *Experimental Complex Modal Analysis of Machine Tool Structures*, J. of Eng. for Industry, ASME, Vol. 111, No. 2.

[37] Van der Auweraer, H., Snoeys, R., Leuridan, J. M., 1986, *A Global Frequency Domain Modal Parameter Estimation Technique for Mini-computers*, ASME Journal of Vibration, Acoustics, Stress, and Reliability in Design.

[38] Vold, H., Kundrat, J., Rocklin, T., Russell, R., 1982, *A Multi-Input Modal Estimation Algorithm for Mini-computers*, SAE Transactions, Vol. 91, No. 1.

[39] Vold, H., Rocklin, T., 1982, *The Numerical Implementation of a Multi-Input Modal Estimation Algorithm for Mini-computers*, Proceedings, International Modal Analysis Conference, Society of Experimental Mechanics.

[40] Vold, H., 1986, *Orthogonal Polynomials in the Polyreference Method*, Proceedings, International Seminar on Modal Analysis, Katholieke University of Leuven, Belgium.

[41] Weinstock, R., 1974, *Calculus of Variations*, Dover Publications, NY.

[42] Zhang, L., Kanda, H., Brown, D. L., Allemang, R. J., 1985, *A Polyreference Frequency Domain Method for Modal Parameter Identification*, ASME Paper No. 85-DET-106.

3. TECHNOLOGY TRANSFER

A pivotal objective of the Integrated Diagnostics program is to accommodate academia's commitment to explore and discover, with the end-user's need to develop and improve. To expedite the transfer of knowledge obtained from academic research, information has been disseminated through a variety of means including publications, monthly updates, meeting presentations and the educational process.

3.1 PUBLICATIONS

Faculty and staff have been encouraged to publish their findings in such archival materials as publications, meeting transactions and books. Current abstracting and computer search activities make such resources quite valuable to the world at large. Manuscripts from *Integrated Diagnostic* activity are listed below.

▪ REFEREED JOURNAL (76)

Anderson, W., Jarzynski, J., and Salant, R. F., "Condition Monitoring of Mechanical Seals: Detection of Film Collapse using Reflected Ultrasonic Waves," IMechE J. of Mechanical Engineering Sciences, 1999 (in press).

Anderson, W., Salant, R. and Jarzynski, J., "Ultrasonic Detection of Lubricating Film Collapse in Mechanical Seals," Tribology Transactions, Vol. 42, 1999, pp. 801-806.

Bahr, D. F., Robach, J., Wright, J. S., Francis, L. F., and Gerberich, W. W., "Mechanical Properties of PZT Thin Films for MEMS Applications," Mater. Sci. and Eng. A, A259, 1998, pp. 126-131.

Beadle, B. and Jarzynski, J., "Measurement of the Speed and Attenuation of Extensional Waves in Optical Fibers," Journal of Optical Engineering, 2000 (submitted).

Bennett, V.P. and McDowell, D.L., "Crystal plasticity analysis of microstructurally small surface cracks in ductile polycrystals," Engineering Fracture Mechanics, 2000 (to be submitted).

Bennett, V.P. and McDowell, D.L., "Crystal plasticity analysis of microstructurally small surface fatigue cracks in ductile polycrystal," Fatigue and Fracture of Engineering Materials and Structures, 2000 (to be submitted).

Bennett, V.P. and McDowell, D.L., "Polycrystal Orientation Distribution Effects on Cyclic Microslip," International journal of Fatigue, 2000 (to be submitted).

Cho, C.R. and Francis, L.F., "Electromechanical Properties and Acoustic Response of Integrated PZT Films," Journal of Materials Science Letters, (accepted).

Cho, C.R., Drinkwater, D. E., Francis, L. F., and Polla, D. L., "Properties of Nb-doped Lead Scandium Niobate Titanate Thin Films Prepared by a Sol-Gel Method," Materials Letters, Vol. 38, 1999, pp. 136-140.

Cho, C.R., Francis, L. F., and Polla, D. L., "Ferroelectric Properties of Sol-Gel Deposited $Pb(Zr,Ti)O_3/LaNiO_3$ Thin Films on Single Crystal Substrates," Materials Letters, Vol. 38, 1999, pp. 125-130.

Cho, C.R., Francis, L.F. and Jang, M-S., "Piezoelectric Properties and Acoustic Wave Detection of $Pb(Zr_{0.52}Ti_{0.48})O_3$ Thin Films for Microelectromechanical Systems Sensor, Jpn. Journal Applied Phys., Vol. 38, 1999, pp. L751-L754.

Daniel, I.M., Luo, J.-J. and Sifniotopulos, C.G., "Monitoring of Fatigue Crack Growth in Metals with Acoustic Emission," The Engineering Science of Structures, ed. by Jay Shen, Illinois Institute of Tech, 2000, pp. 27-46.

Daniel, I. M., Luo, J.-J., Sifniotopoulos, C. G., and Chun, H.-J., "Acoustic Emission Monitoring of Fatigue Damage in Metals," Nondestructive Testing and Evaluation, Vol. 14, 1998, pp. 71-87.

Dayan, J., Zou, M. and Green, I., "Sensitivity Analysis for the Design and Operation of a Noncontacting Mechanical Face Seal," Journal of Mechanical Engineering Sciences (IMechE), 1999 (accepted).

Dayan, J., Zou, M. and Green, I., "Contact Elimination in Mechanical Face Seals Using Active Control," IEEE Transactions on Control Systems Technology, 2000 (to be published).

Drexel, M. and Ginsberg, J., "Mode Isolation: a New Algorithm for Modal Parameter Identification," Journal of the Acoustical Society of America, 2000 (submitted).

Eisenhardt, C., Jacobs, J.J. and Qu, J., "Application of Laser Ultrasonics to Develop Dispersion Curves for Elastic Plates," Journal of Applied Mechanics, Vol. 66, No. 4, 1999, pp. 1043-1045.

Francis, L. F. and Wright, J. S., "Effect of Solution Processing on PZT Thin Films Prepared by a Hybrid MOD Solution Deposition Route," Journal of Electroceramics, 1998 (submitted).

Gosz, M. and Moran, B., "An Interaction Energy Integral Method for Computation of mixed-Mode stress Intensity Factors Along Non-Planar Crack Fronts," Engineering Fracture Mechanics, 2000 (submitted)

Hamm, R. W. and Johnson, W. S., "A Unification of Small and Large Crack Growth Laws," Journal Fatigue and Fracture of Engineering Materials and Structures, 22, 1999, pp. 711-722.

Hamm, R. W., Jin, O. and Johnson, W. S., "Microstructural Influences on the Growth of Small Fatigue Cracks in Ti-6Al-4V," Journal Fatigue and Fracture of Engineering Materials and Structures, 1999 (submitted).

Hamm, R. W., Jin, O. and Johnson, W. S., "Small Crack Growth Behavior in Ti-6Al-4V and the Microstructural Influence" Metallurgical and Materials Transactions, 1998 (submitted).

Hamm, R. W. and Johnson, W. S., "Survey of the State of the Art in Small Crack Research," Journal of Testing and Evaluation, Vol. 26, No. 3, March 1998, pp. 168-175.

Heller, K., Jacobs, L.J. and Qu, J., "Characterization of Adhesive Bond Properties Using Lamb Waves," NDT & E Intl., 2000 (submitted).

Hurlebaus, S., Jacobs, L. J., and Jarzynski, J., "Laser Techniques to Characterize the Effect of Geometry on Acoustic Emission Signals," Nondestructive Testing and Evaluation, Vol. 14, 1998, pp. 21-37.

Jin, O., Hamm, R.W. and Johnson, W.S., "Small Crack Growth Behavior in Ti-6A1-4V and the Microstructural Influence," Journal Fatigure and Fracture of Engineering Materials and Structures, 2000 (submitted).

Jin, O. and Johnson, W.S., "Small Crack Growth Behavior in PH 13-8 Mo Stainless Steel under Saltwater Environment," Met. & Mater. Trans., 2000 (to be submitted).

Kim, J. H., Wang, L., Zurn, S. M., Li, L., Yoon, Y. S., and Polla, D. L., "Fabrication Process of PZT Piezoelectric Cantilever Unimorphs Using Surface Micromachining," Integrated Ferroelectrics, Vol. 15, 1997, pp. 325-332.

Kley, M., Valle, C., Jacobs, L., Qu, J., and Jarzynski, J., "Development of Dispersion Curves for Two-Layered Cylinders using Laser Ultrasonics," J. of the Acoustical Society of America, Vol. 106, 1999, pp. 582-588.

Kromine, A. K., Fomitchov, P. A., Krishnaswamy, S., and Achenbach, J. D., "Laser Ultrasonic Detection of Surface-Breaking Defects: Scanning Laser Source Techniques," Materials Evaluation, Vol. 58, No. 2, 2000, pp. 173-177.

Li, Y., Billington, S., Zhang, C., Kurfess, T., Danyluk, S., and Liang, S., "Adaptive Prognostics for Rolling Element Bearing Condition," Mechanical Systems and Signal Processing, Vol. 13, No.1, 1999, pp. 103-113.

Li, Y., Billington, S., Zhang, C., Kurfess, T., Danyluk, S., and Liang, S., "Dynamic Prediction of Defect Propagation on a Rolling Element Bearing," STLE Tribology Transactions, Vol. 42, No.2, 1999, pp. 385-392.

Li, Y., Kurfess, T.R., and Liang, S.Y., "Stochastic Prognostics for Rolling Element Bearings," Mechanical Systems and Signal Processing, 1999 (in press).

Li, Y., Kurfess, T.R., Danyluk, S., and Liang, S., "Diagnostics and Prognostics of Roller Bearing Defects," IMechE Journal of Mechanical Engineering Sciences, 1999 (in press).

Li, Z. and Berthelot, Y.H., "Propagation of Transient Ultrasound in Thick Annular Waveguides: Modeling, Experiments, and Application to Crack Detection," NDT&E International, Vol. 33, 2000, pp. 225-232.

Li, Z. and Berthelot, Y.H., "Propagation of Transient Ultrasound in a Thick Annulus: Modeling, Experiments and Application to Crack Detection," J. Acoust. Soc. Am., Vol. 104, No. 3, Pt. 2, 1998, p. 1790.

Liu, G., Qu, J. and Jacobs, L., "Effects of Cure State on the Ultrasonic Nonlinear Parameter in Adhesive Joints," Journal of Nondestructive Evaluation, 2000 (submitted).

Liu, G. and Qu, J., "Guided Circumferential Waves in a Circular Annulus," J. Appl. Mech., Vol. 65, 1998, pp. 424-430.

Liu, G. and Qu, J., "Transient Wave Propagation in a Circular Annulus Subjected to Impulse Excitation on Its Outer Surface, " J. Acoust. Soc. Am., Vol. 103, 1998, pp. 1210-1220.

McDowell, D. L., "Damage Mechanics in Metal Fatigue: a Discriminating Perspective," International Journal of Damage Mechanics, ed. D. L. McDowell, Vol. 8, 1999, pp.377-403.

McDowell, D. L., Clayton, J. D., and Bennett, V. P., "Integrated Diagnostic/Prognostic Tools for Small Cracks in Structures, J. Mech. Eng. Sciences, Proc. Inst. Mech. Engrs. Part C, 1999 (to appear).

McDowell, D. L., "Basic Issues in the Mechanics of High Cycle Metal Fatigue," Int. J. Fracture, Vol. 80, 1996, pp. 103-145.

McDowell, D. L., "Mechanics of Small Fatigue Crack Growth in Metals," Intl. J. Fatigue, 1997 (to appear).

McDowell, D. L., "An Engineering Model for Propagation of Small Cracks in Fatigue," Engineering Fracture Mechanics, Vol. 56, No. 3, 1997, pp. 357-377.

McDowell, D. L. and Bennett, V. P., "A Microcrack Growth Law for Multiaxial Fatigue," Fatigue Fract. Engr. Mater. Struct., Vol. 19, No. 7, 1996, pp. 821-837.

Moran, B., Xu, Y., and Achenbach, J., "Limit State Surface Element Method: Application to Fatigue Reliability with NDE Inspections," J. Engr. Mech., Vol. 126, No. 7, 2000, pp. 684-692.

Moser, F., Jacobs, L., and Qu, J., "Application of Finite Element Methods to Study Wave Propagation in Wave Guides," NDT&E International, Vol. 32, 1999, pp. 225-234.

Refereed Journal

Neu, R.W., Pape, J.A., and Swalla, D.R., "Fretting Fatigue Crack Nucleation in High Strength Steels," International Journal of Fatigue, 2000 (submitted).

Niethammer, M., Jacobs, L.J., Qu, J., and Jarzynski, J., "Time-Frequency Representation of Lamb Waves using the Reassigned Spectrogram," Journal of the Acoustical Society of America, Vol. 107, No. 5, 2000, pp. L19-L24. (Acoustics Research Letters Online; http://ojps.aip.org/jasa/).

Niethammer, M., Jacobs, L.J., Qu, J., and Jarzynski, J., "Time-Frequency Representation of Lamb Waves," Journal of the Acoustical Society of America, 2000 (submitted).

Pape, J. A. and Neu, R. W., "Influence of Contact Configuration in Fretting Fatigue Testing," Wear, 225-229, 1999, pp. 1205-1214.

Pape, J.A., Neu, R.W., and Swalla, D.R., "Fretting Fatigue Damage Accumulation in PH 13-8 Mo Stainless Steel," Fatigue and Fracture of Engineering Materials and Structures, 2000 (submitted).

Patel, A. M., Neu, R. W., and Pape, J. A., "Growth of Small Fatigue Cracks in PH 13-8 Mo Stainless Steel," Metallurgical and Materials Transactions A, Vol. 30A, May 1999, pp. 1289-1300.

Polla, D. L. and Francis, L. F., "Processing and Characterization of Piezoelectric Materials and Integration into Microelectromechanical Systems," Annual Reviews of Materials Science, Vol. 23, 1998, pp. 563-597.

Qiu, J. Zhang, C. and Liang, S. Y., "Lifetime Prognostic of Bearing Failure Based on Vibration Analysis and Damage Mechanics," Mechanical Systems and Signal Processing, 1999 (submitted).

Qu, J., Berthelot, Y., and Jacobs, L., "Crack Detection in Thick Annular Components Using Ultrasonic Guided Waves," Journal of Mechanical Engineering Sciences, IMechE, 1999 (in press).

Shi, Z., Jarzynski, J., Bair, S., Hurlebaus, S., and Jacobs, L., "Characterization of Acoustic Emission Signals from Fatigue Fracture," Journal of Mechanical Engineering Sciences, IMechE, 1999 (in press).

Shiroishi, J., Li, Y., Liang, S., Kurfess, T., and Danyluk, S., "Vibration and Acoustic Emission Analysis for Bearing Condition Monitoring," Journal of Brazilian Society of Mechanical Sciences, 1998 (submitted).

Shiroishi, J., Li, Y., Liang, S., Danyluk, S. and Kurfess, T., "Vibration Analysis for Bearing Outer Race Condition Diagnostics," Journal of the Brazilian Soc. of Mechanical Sciences, Vol. 21, No. 3, 1999, pp. 484-492.

Shiroishi, J., Li, Y., Liang, S., Kurfess, T., and Danyluk, S., "Bearing Condition Diagnostics via Multiple Sensors," Mechanical Systems and Signal Processing, Vol. 11, No. 5, 1997, pp. 693-705.

Sukumar, N., Moes, N., Moran, B., and Belytschko, T., "The Extended Finite Element Method for Three-Dimensional Crack Modeling," Intl. Journal for Numerical Methods in Engineering, 1999, (accepted).

Swalla, D.R. and Neu, R.W., "Influence of Coefficient of Friction on Fretting Fatigue Crack Nucleation Prediction," Tribology International, 2000 (submitted).

Valle, C., Niethammer, M., Qu, J. and Jacobs, L.J., "Crack Characterization using Guided Circumferential Waves," Journal of the Acoustical Society of America, 2000 (submitted).

Valle, C., Qu, J., and Jacobs, L., "Guided Circumferential Waves in Layered Cylinders," International Journal of Engineering Science, Vol. 37, 1999, pp. 1369-1387.

Venkatesan, G., Zhang, D., Kaveh, M., Tewfik, A., and Buckley, K., "Signal Processing for Fault Monitoring using Acoustic Emissions," AEU International J. of Electr. Comm., Vol. 53, No. 6, 1999, pp. 333-338.

Wright, J.S. and Francis, L.F., "Effect of Solution Processing on PZT Thin Films Prepared by a Hybrid MOD Solution Deposition Route," Journal of Electroceramics, Vol. 3 No. 3, 1998, pp. 261-268.

Yang, Y., Kurfess, T., Liang, S. and Danyluk, S., "Application of a Specialized Capacitance Probe in Bearing Diagnosis," Wear, 225-229, 1999, pp.1215-1221.

Yang, F., Saxena, A., and Reister, L., "Use of Nanoindentation Technique for Studying Microstructure/Crack Interactions in the Fatigue of 4340 Steel," Metallurgical and Materials Transactions, Vol. 29A, 1998, pp. 3029-3036.

Yang, F. and Saxena, A., "Mechanisms of Fatigue Crack Initiation in Annealed and Quenched and Tempered 4340 Steel," J. Basic Mechanical Sciences (IMechE), 2000 (in press).

Zhang, C., Li, Y., Kurfess, T., Danyluk, S., and Liang, S., "Bearing Diagnostics Negating Operating Condition Effects," International Journal of COMADEM, Vol. 2, No.1, 1999, pp. 23-29.

Zhang, C., Qui, J., Kurfess, T.R., Danyluk, S., and Liang, S.Y., "Impact Dynamics Modeling of Bearing Vibration for Defect Size Estimation," International Journal of COMADEM, 1999 (in press).

Zhang, D., Tewfik, A. H., and Kaveh, M., "Acoustic Emission Transient Detection Based on Linear Model Residuals," IEEE Transactions on Signal Processing, (to be submitted).

Zou, M., Dayan, J., and Green, I., "Dynamic Simulation and Monitoring of a Noncontacting Flexibly Mounted Rotor Mechanical Face Seal," Journal of Mechanical Engineering Sciences (IMechE), 1999 (submitted).

Zou, M. and Green, I., "Parametric Analysis for Contact Control of a Noncontacting Mechanical Face Seal,"Vibration, Noise and Structural Dynamics, 1999 (submitted).

Zou, M., Dayan, J., and Green, I., "Feasibility of Contact Elimination of a Mechanical Face Seal through Clearance Adjustment," ASME Journal of Engineering for Gas Turbine and Power, Vol. 122, July 2000.

Zou, M. and Green I., "Clearance Control of a Mechanical Face Seal," STLE Tribology Transactions, Vol. 42, No. 3, 1999, pp. 535-540.

▪ PROCEEDINGS, CHAPTERS AND TECHNICAL REPORTS (108)

"Integrated Diagnostics-*Monthly Progress Report*," Vol. I, No. 1 thru Vol V, No. 11 Georgia Tech, Atlanta, June 1995 thru May 2000 (50 monthly reports).

"Integrated Diagnostics," N00014-95-1-0539, *M-URI Final Report*, Georgia Tech, Atlanta, 2000 (in press).

"Integrated Diagnostics," June 1998-May 1999 *M-URI Year 4 Annual Performance Report*, Georgia Tech, Atlanta, 1999 (200 pages).

"Integrated Diagnostics," March 1997-May 1998 *M-URI Year 3 Annual Performance Report*, Georgia Tech, Atlanta, 1998 (289 pages).

"Integrated Diagnostics," March 1996-February 1997 M-URI *Year 2 Annual Performance Report*, Georgia Tech, Atlanta, 1997 (285 pages).

"Integrated Diagnostics," March 1995-February 1996 M-URI *Performance Report*, Georgia Tech, Atlanta, 1996.

Achenbach, J. D., "A Portable Laser-Based Ultrasonics System for the Inspection of Aging Aircraft Structures," Proc. First Joint DoD/FAA/NASA Conf. on Aging Aircraft, Ogden, Utah, 1997 (to appear).

Achenbach, J. D., "Laser-Based Ultrasonics for QNDE Applications," Proc. Intl. Conf. on Experimental Mechanics, Singapore, December 1996.

Achenbach, J. D., Moran, B., and Zulfiqar, A., "Techniques and Instrumentation for Structural Diagnostics," Structural Health Monitoring, ed. F.-K. Chang, Technomic Publishing, 1997, pp. 179-190.

Anderson, W. B., Salant, R. F., and Jarzynski, J., "Detection of Lubricating Film Breakdown in Mechanical Seals," Sealing Technology, No. 49, January 1998.

Anderson, W. B., Salant, R. F., and Jarzynski, J., "Detection of Lubricating Film Breakdown in Mechanical Seals," merging Technologies for Machinery Health Monitoring and Prognosis, TRIB-Vol. 7, ed. R. S. Cowan, ASME, 1997, pp. 25-29.

Beadle, B., "Fiber Optic Sensor for Ultrasound," M. S. Thesis, School of Mechanical Engineering, Georgia Tech, Atlanta, 1999.

Bennett, V. and McDowell, D.L. , "Polycrystal Orientation Effects on Microslip and Mixed Mode Behavior of Microstructurally Small Cracks," ASTM STP 1359, Eds. K.J. Miller and D.L. McDowell, 1999, pp. 203-228.

Bennett, V., "A Microscale Study of Small Crack Propagation in Multiaxial Fatigue," Ph.D. Dissertation, G.W.W. School of Mechanical Engineering, Georgia Tech, Atlanta, 1999.

Billington, S., Li, Y., Liang, S., Kurfess, T., and Danyluk, S., "Operating Condition Effects on Rolling Element Bearing Diagnostics," Prognosis of Residual Life of Machinery and Structures, 52nd MFPT Society Meeting, eds. H. Pusey et al., Vibration Institute, 1998, pp. 313-322.

Billington, S., Li, Y., Liang, S., Kurfess, T., and Danyluk, S., "Roller Bearing Defect Detection with Multiple Sensors," Emerging Technologies for Machinery Health Monitoring and Prognosis, TRIB-Vol. 7, ed. R. S. Cowan, ASME, 1997, pp. 31-36.

Buckley, K., Venkatesan, G., West, D., and Kaveh, M., "Detection and Characterization of Cracks for Failure Monitoring and Diagnostics," Proc. ICASSP96, Atlanta, 1996.

Casey, C., "Crack Detection in a Rotordynamic System by Vibration Monitoring," M.S. Thesis, School of Mechanical Engineering, Georgia Tech, Atlanta, August 2000.

Cook, D., "Monitoring Small Fatigue Cracks using Ultrasonic Surface Waves," M.S. Thesis, School of Mechanical Engineering, Georgia Tech, Atlanta, 2000.

Cowan, R. S. and Winer, W. O., "Recent Developments in Health Appraisal and Life Extension of Mechanical Systems," Proc. Korea-USA Tribology Symposium, Seoul, KSTLE, 1995, pp. 17-24.

Cowan, R. S. and Winer, W. O., "Health and Safety Improvement through Tribological Failure Analysis and Prediction," Proc. 10th International Tribology Colloquium, Ostfildern, Germany, January 1996.

Cowan, R. S. and Winer, W. O., "Adding Time to Aging Equipment with an Appropriate Maintenance Methodology," Proc. 7th Nordic Symposium on Tribology, Bergen, Norway, June 1996.

Cowan, R. S. and Winer, W. O., "Emerging Technologies for Machinery Diagnosis and Prognosis," Proc. 10th Intl. Congress and Exhibition- COMADEM, Espoo, Finland, 1997.

Cowan, R. S. and Winer, W. O. (eds.), "Emerging Technologies for Sensing Mechanical Failure," Condition Monitor, No. 137, May 1998, pp. 7-11.

Cowan, R. S. and Winer, W. O., "Emerging Sensor Technologies Tackle Mechanical Failure," Machine Plant & Systems Monitor, May/June 1999, pp. 19-22.

Cowan, R. S. and Winer, W. O., "Engineering Technology for Condition-Based Maintenance," STLE's Lubrication Engineering, July 1999, pp. 43-45.

Cowan, R. S. and Winer, W. O., "Research Developments in Integrated Diagnostics and Prognostics," Structural Health Monitoring 2000, ed. F. -K. Chang, Technomic Publishing, 1999, pp. 237-246.

Cowan, R. S. and Winer, W. O., "Technologies for Machinery Diagnosis and Prognosis," Modern Handbook of Tribology, ed. B. Bhushan, CRC Press, 1999 (in press).

Cowan, R. S. and Winer, W. O., "Condition Monitoring Tools for Tribologists," Proceedings NATO-ASI Conference on the Fundamentals of and Bridging the Gap between Nano and Micro/Macroscale Tribology, ed. B. Bhushan, Kluhwer Press, 2000 (accepted).

Cretegny, L., "Use of Atomic Force Microscopy for Characterizing Damage Evolution during Fatigue," Ph.D. Dissertation, School of Materials Science & Engineering, Georgia Tech, Atlanta, 2000.

Daniel, I. M. and Luo, J.-J., "Analysis of Acoustic Emission Waveforms from Propagating Fatigue Crack," Review of Progress in Quantitative Nondestructive Evaluation, Vol.19, eds. D. O. Thompson & D. E. Chimenti, Plenum Press, Melville, NY, 2000, (submitted).

Daniel, I. M., Luo, J.-J. Sifniotopoulos, C. G., and Chun, H. -J., "Acoustic Emission Monitoring of Fatigue Damage in Metals," Proc. Review of Quantitative NDE, Plenum Press, 16, 1996, pp. 451-458.

Daniel, I. M., Sifniotopoulos, C. G., and Luo, J.-J., "Analysis of Acoustic Emission Output from Propagating Crack," Proc. 1997 Annual Review of QNDE, Vol. 17, eds. D. O. Thompson and D. E. Chimenti, Plenum Press, 1998, pp. 579-586.

Dayan, J., Zou, M., and Green, I., "Contact Elimination in Mechanical Face Seals Using Active Control", Proceedings of the IEEE 7th Mediterranean Conference on Control and Automation Haifa, Israel, 1999, pp. 618-619.

Dayan, J., Zou, M., and Green, I., "Contact Elimination in Mechanical Face Seals using Active Control," accepted for publication to the IEEE Transactions on Control Systems Technology, 2000.

Eisenhardt, C., Jacobs, L. and Qu, J., "Experimental Lamb Wave Spectra of Cracked Plates," Review of Progress in Quantitative Nondestructive Evaluation, Vol.19A, eds. D. O. Thompson & D. E. Chimenti, Plenum Press, 2000, pp. 343-349.

Fomitchov, P., Krishnaswamy, S., and Achenbach, J., "Sagnac Interferometer for Ultrasound Detection on Rough Surfaces," Proc. 8th Intl. Symposium on Nondestructive Characterization of Materials, Boulder, CO, 1997.

Harjani, R., Polla, D. Nair, K. and Zillmer, C., "Data Acquisition and Conversion," Encyclopedia of Electrical and Electronics Engineering, ed. J. Webster, Wiley Interscience, 1999.

Hurlebaus, S., Jacobs, L. J. and Jarzynski, J., "Optical Techniques to Develop Transfer Functions to Remove Geometry Effects from Acoustic Emission Signals," 23rd Annual Review of Progress in Quantitative NDE, eds. D. O. Thompson and D. E. Chimenti, Plenum Press, Vol. 16A, pp. 421-426, 1997.

Jin, O., "The Characterization of Small Fatigue Crack Growth in PH 13-8 Mo Stainless Steel," Ph.D. Dissertation, School of Materials Science & Engineering, Georgia Tech, Atlanta, August 2000.

Kazar, B.M., M.S.E.E. Thesis, "Implementation and Fabrication of Acoustic Emission Sensors," University of Minnesota, Minneapolis, May 2000.

Kim, J, H., Wang, L., Zurn, S. M., Li, L., Yoon, Y. S., and Polla D. L., "Fabrication Process of PZT Piezoelectric Cantilever Unimorphs using Surface Micromachining," Integrated Ferroelectrics, 15, 1997, pp. 325-332.

Kley, M., Valle, C., Jacobs, L., Qu, J. and Jarzynski, J., "Development of Dispersion Relationships for Layered Cylinders using Laser Ultrasonics," Review of Progress in Quantitative NDE, Vol. 18A, eds. D. O. Thompson & D. E. Chimenti, Plenum Press, 1999, pp. 263-268.

Kromine, A. K., Fomitchov, P. A., Krishnaswamy, S., and Achenbach, J. D., "Scanning Laser Source Technique and its Application to Turbine Disk Inspection," Review of Progress in Quantitative Nondestructive Evaluation, Vol.18A, eds. D. O. Thompson & D. E. Chimenti, Plenum Press, 1999, pp. 381-386.

Kromine, A., Fomitchov, P., Krishnaswamy, S. and Achenbach, J.D., "Scanning Laser Source Technique for Detection of Surface-Breaking and Sub-Surface Cracks," Review of Progress in Quantitative Nondestructive Evaluation, Vol. 19A, eds. D.O. Thompson and D.E. Chimenti, AIP, Melville, NY, 2000, pp. 335-342.

Kromine, A., Fomitchov, P., Krishnaswamy, S., Achenbach, J.D., "Applications of Scanning Laser Source Technique for Detection of Surface-Breaking Defects," Proceedings of SPIE, 2000 (submitted).

Li, Y., "Dynamic Prognostics of Rolling Element Bearing Condition," Ph.D. Dissertation, School of Mechanical Engineering, Georgia Tech, Atlanta, 1998.

Li, Y., Billington, S., Kurfess, T., Danyluk, S., and Liang, S., "Dynamic Prognostics of Rolling Element Bearing Condition," Prognosis of Residual Life of Machinery and Structures, 52nd MFPT Society Meeting, eds. H. Pusey et al., Vibration Institute, 1998, pp. 429-430.

Li, Y., Kurfess, T., Danyluk, S., and Liang, S., "Bearing Prognostics Based on Adaptation of Stochastic Defect Growth Model," Proceedings of the 53rd Meeting of the Society of Machinery Failure Prevention Technology, Virginia Beach, VA, 1999, pp.337-347.

Li, Y., Shiroishi, J., Danyluk, S., Kurfess, T. R., and Liang, S. Y., "Bearing Fault Detection via High Frequency Resonance Technique with Adaptive Line Enhancer," Proc. 12th Biennial Conf. on Reliability, Stress Analysis and Failure Prevention, MFPT, 1997, pp. 763-772.

Li, Y., Shiroishi, J., Danyluk, S., Kurfess, T. R., and Liang, S. Y., "Diagnostics of Roller Bearing Defects Based on Vibration and Acoustic Emission," Proc. 10th Intl. Congress-Exhibition, COMADEM, Espoo, Finland, 1997, pp. 256-267.

Li, Z. and Berthelot, Y. H., "Crack Detection in Annular Components by Ultrasonic Guided Waves," Proc. 1997 Annual Review of QNDE, Vol. 17, eds. D. O. Thompson and D. E. Chimenti, Plenum Press, 1998.

Li, Z. and Berthelot, Y., "Crack Detection in Annular Components by Ultrasonic Guided Waves," Proc. of QNDE, 1997 (to appear).

Li, Z. and Berthelot, Y., "Modeling and Experiments on the Propagation of Transient Ultrasound in a Thick Annulus," Review of Progress in Quantitative Nondestructive Evaluation, Vol.18A, eds. D. O. Thompson & D. E. Chimenti, Plenum Press, 1999, pp. 231-238.

Liu, G. and Qu, J., "Guided Transient Waves in a Circular Annulus," Review of Progress in Quantitative NDE, Vol. 16A, eds. D. O. Thompson and D. E. Chimenti, Plenum Press, 1998, pp. 153-160.

Liu, G., Qu, J., Jacobs, L. J. and Li, J., "Characterizing Curing of Adhesive Joints by a Nonlinear Ultrasonic Technique," Review of Progress in Quantitative NDE, eds. D. O. Thompson and D. E. Chimenti, Plenum Press, Vol. 18B, 1999, pp. 2191-2199.

McDowell, D. L. and Bennett, V., Micromechanical Aspects of Small Multiaxial Fatigue Cracks," Proc. 5th Int. Conf. on Biaxial/Multiaxial Fatigue and Fracture, Cracow, Poland, 1997, pp. 325-348.

McDowell, D. L., "A Model for Multiaxial Small Fatigue Crack Growth," Proc. of Engineering Against Fatigue Sheffield, UK, 1997 (to appear).

McDowell, D. L., "A Model for Multiaxial Small Fatigue Crack Growth," Engineering Against Fatigue, eds. J. H. Beynon, M. W. Brown, T. C. Lindley, R. A. Smith, and B. Tomkins, Balkema Press, 1999, pp. 277-285.

McDowell, D. L., "Multiaxial Fatigue Strength," ASM Handbook: Fatigue and Fracture, **19**, ASM, Materials Park, 1996, pp. 263-273.

McDowell, D. L., Neu, R. W., Qu, J., and Saxena, A. "Prognostic Tools for Small Cracks in Structures," Emerging Technologies for Machinery Health Monitoring and Prognosis, TRIB-Vol. 7, ed. R. S. Cowan, ASME, 1997, pp. 1-12.

McDowell, D.L. and Bennett, V., "Micromechanical Aspects of Small Multiaxial Fatigue Cracks," Proc. 5th Intl. Conf. on Biaxial/Multiaxial Fatigue and Fracture, Cracow, Poland, 8-12 Sept. 1997, pp. 325-348.

McDowell, D.L., "A Model for Multiaxial Small Fatigue Crack Growth," Engineering Against Fatigue, eds. J.H. Beynon, M.W. Brown, T.C. Lindley, R.A. Smith and B. Tomkins, Balkema Press, Chapt. 29, 1999, pp. 277-285.

Moran, B., Zulfiqar, A., and Sukumar, N., "On the Direct Integration Method for Fatigue Reliability Calculations," Technical Report, Northwestern, Evanston, July 1996.

Moser, F., Jacobs, L. J., and Qu, J., "Application of Finite Element Methods to Study Transient Wave Propagation in Elastic Wave Guides," Review of Progress in Quantitative NDE, Vol. 16A, eds. D. O. Thompson and D. E. Chimenti, Plenum Press, 1999, pp. 161-167.

Moser, F., Valle, C., Jacobs, L. J., and Qu, J., "Modeling of Guided Waves in Annular Components," Proc. 1998 Annual Review of QNDE, eds. D. O. Thompson and D. E. Chimenti, Plenum Press, 1999 (submitted).

Nair, K. and Harjani, R., "A Telemetry and Interface Circuit for Piezoelectric Circuits," Proc. IEEE International Symposium on Circuits and Systems, Atlanta, 1999.

Nair, K. and Harjani, R., "An Ultra Low Power Transconductance Cell," Proc. IEEE Intl. Conf. on Circuits and Systems, 1997, pp. 217-220.

Neu, R.W., Pape, J.A., and Swalla, D.R., "Methodologies for Linking Nucleation and Propagation Approaches for Predicting Life under Fretting Fatigue," Fretting Fatigue: Current Technology and Practices, ASTM STP 1367, eds. D.W. Hoeppner, V. Chandrasekaran, and C.B. Elliott, ASTM, W. Conshohocken, PA, 2000, pp. 369-388.

Neu, R.W., Swalla, D.R., and Pape, J.A., "Advances in Predicting the Nucleation of Fretting Fatigue Cracks," Proc. of 13th European Conference on Fracture - Fracture Mechanics: Applications & Challenges, San Sebastian, Spain, 2000.

Niethammer, M., "Application of Time Frequency Representations to Characterize Ultrasonic Signals," M. S. Thesis, School of Civil & Environmental Engineering, Georgia Tech, Atlanta, 1999.

Niethammer, M., Jacobs, L.J. and Qu, J., "Application of STFT Techniques to Interpret Ultrasonic Signals," Review of Progress in Quantitative Nondestructive Evaluation, Vol. 19A, eds. D.O. Thompson and D.E. Chimenti, AIP, Melville, NY, 2000, pp. 703-708.

Plummer, J., "Integrated Acoustic Emission Sensor Development," M. S. Thesis, Department of Electrical Engineering, University of Minnesota, Minneapolis, December 1999.

Polla, D. L., and Francis, L. F., "Ferroelectric Thin Films in MEMS Applications," cover article for Materials Research Society Bulletin, July 1996.

Polla, D. L., Francis, L., Robbins, W., and Harjani, R., "MEMS for Integrated Diagnostic Applications," Emerging Technologies for Machinery Health Monitoring and Prognosis, TRIB-Vol. 7, ed. R. S. Cowan, ASME, 1997, pp. 19-24.

Qiu, J., Zhang, J., and Liang, S.Y., "Prognostic of Mechanical Systems Based on Damage Mechanics," Proceedings of Japan-USA Symposium on Flexible Automation, 2000 (submitted).

Qu, J. and Berthelot, Y., "Dispersion of Guided Circumferential Waves in a Circular Annulus," Review of QNDE, 15A, 1996, pp. 169-176.

Qu, J. and Liu, G., "Effect of Residual Stress on Guided Waves in Layered Media," Review of Progress in Quantitative NDE, Vol. 16B, eds. D. O. Thompson and D. E. Chimenti, Plenum Press, 1998, pp. 1635-1642.

Ribadeneira, X., Kurfess, T. R., Billington, S., and Li, Y., "Ball Bearing Diagnostics in Run-to-Failure Lifetime Testing," Proceedings of the 54th Meeting of the Society for Machinery Failure Prevention Technology, Virginia Beach, VA, 2000, pp. 237-246.

Ribadineira, X., "Ball Bearing Diagnosis with Multiple Sensors," M. S. Thesis, School of Mechanical Engineering, Georgia Tech, Atlanta, 1999.

Saxena, A., "Fatigue Crack Growth in Power-Plant Materials and Components," Proc. Fatigue '96, May 1996, pp. 201-212.

Saxena, A., Yang, F. and Cretegny, L., "Use of Atomic Force Microscopy for Studying Fatigue Crack Initiation," Proc. International Conference on Fatigue, Beijing, China, 1999, pp. 2777-2782.

Shi, Z., Bair, S., Jarzynski, J. and Jacobs, L., "Study of Acoustic Emission from Incipient Fatigue Failure," Review of Progress in Quantitative Nondestructive Evaluation, Vol.18A, eds. D. O. Thompson & D. E. Chimenti, Plenum Press, 1999, pp. 395-401.

Shi, Z., Jarzynski, J. and Jacobs, L.J., "Quantitative Acoustic Emission from Fretting Fatigue of PH 13-8 Stainless Steel," Review of Progress in Quantitative Nondestructive Evaluation, Vol. 19A, eds. D.O. Thompson and D.E. Chimenti, AIP, Melville, NY, 2000, pp. 367-373.

Shi, Z., Koutzak, M., Bair, S., Jarzynski, J., and Jacobs, L. J., "Characterization of Acoustic Emission Signals from Fracture Events," Proc. 1997 Annual Review of QNDE, Vol. 17, eds. D. O. Thompson and D. E. Chimenti, Plenum Press, 1998, pp. 565-570.

Shi, Z., Ramalingam, S. and Xue, J., "Eddy Current Micro-sensors for Flaw Imaging and Identification," Proc. of COMADEM 2000, Houston, TX, 2000 (submitted).

Shiroishi, J., Li, Y., Liang, S., Danyluk, S. and Kurfess, T. R., "Vibration Signal Analysis for Bearing Race Damage Diagnostics," Proc. 7th Intl. Conf. on Dynamic Problems in Mechanics, Angra Dos Reis, Brazil, 1997, pp. 187-190.

Sun, H., "Self-Organizing Map Neural Networks for Acoustic Emission Classification," M. S. Thesis, Department of Electrical Engineering, University of Minnesota, Minneapolis, 1999.

Sun, H., Kaveh, M., and Tewfik, A., "Self-Organizing Map Neural Network for Transient Signal Classification in Mechanical Diagnostics," Proc. IEEE Workshop on Nonlinear Signal & Image Processing, ed. E. A. Cetin, Antalya, Turkey, 1999.

Swalla-Michaud, D. R., "Fretting Fatigue Damage Prediction using Multiaxial Fatigue Criteria." M. S. Thesis, School of Mechanical Engineering, Georgia Tech, Atlanta, 1999.

Valle, C., "Guided Circumferential Waves in Annular Structures," Ph.D. Dissertation, School of Mechanical Engineering, Georgia Tech, Atlanta, 1999.

Valle, C., Qu, J. and Jacobs, L.J., "Scattering of Circumferential Waves in a Cracked Annulus," Review of Progress in Quantitative Nondestructive Evaluation, Vol. 19A, eds. D.O. Thompson and D.E. Chimenti, AIP, Melville, NY, 2000, pp. 217-224.

Valle, C., Qu, J., and Jacobs, L. J., "Guided Circumferential Waves in Layered Cylinders," Proc. 1998 Annual Review of QNDE, Vol. 18A, eds. D. O. Thompson and D. E. Chimenti, Plenum Press, 1999, pp. 263-268.

Valle, C., Qu, J., and Jacobs, L. J., "On the Dispersion and Displacement Distribution of Circumferential Waves in Composite Circular Cylinders," Review of Progress in Quantitative Nondestructive Evaluation, Vol.18A, eds. D. O. Thompson & D. E. Chimenti, Plenum Press, 1999, pp. 247-254.

Venkatesan, G. T., Kaveh, M., Tewfik, A. H., and Buckley, K., "Blind Identification of Single-Input Multiple-Output Pole-Zero Systems," Proc. ICASSP 98, 1998 (submitted).

Venkatesan, G. T., Tong, L., Kaveh, M. and Buckley, K., "A Deterministic Blind Identification Technique for SIMO Systems of Unknown Model Order," Proc. ICASSP'99, Vol. 4, 1999, pp. 1789-1792.

Venkatesan, G. T., West, D., Buckley, K. M., Tewfik, A. H., and Kaveh, M., "Automatic Fault Monitoring using Acoustic Emissions," Proc. ICASSP97, Munich, 1997.

Venkatesan, G., "Blind Identification of Single-Input, Multiple-Output Systems," Ph. D. Dissertation, Department of Electrical Engineering, University of Minnesota, Minneapolis, 1998.

Wang, L., Steckenrider, J. S., and Achenbach, J. D., "A Fiber-Based Laser Ultrasonic System for Remote Inspection of Limited Access Components," Review of Progress in Quantitative NDE, eds. D. O. Thompson and D. E. Chimenti, Plenum Press, Vol. 16A, pp. 507-514, 1997.

Williams, T., "Remote Condition Monitoring of Rolling Element Bearings with Natural Crack Development," M.S. Thesis, School of Mechanical Engineering, Georgia Tech, Atlanta, 2000.

Xue, J., "Nondestructive Inspection with Electromagnetic Induction Approach and Eddy Current Micro-sensors," M. S. Thesis, Department of Mechanical Engineering, University of Minnesota, Minneapolis, 1998.

Xue, J., Ramalingam, S., and Shi, Z., "Eddy Current Flaw Imaging Using Micro-Sensor Arrays," Emerging Technologies for Machinery Health Monitoring and Prognosis, TRIB-Vol. 7, ed. R. S. Cowan, ASME, 1997, pp. 13-18.

Zhang, C., Kurfess, T., Danyluk, S., and Liang, S., "Dynamic Modeling of Vibration Signals for Bearing Condition Monitoring," Structural Health Monitoring 2000, ed. F. -K. Chang, Technomic Publishing, 1999, pp. 926-935.

Zhang, D., Venkatesan, G. T., Tewfik, A. H., and Kaveh. M., "Acoustic Emission Transient Detection Based on Linear Model Residuals," Proc. SSAP Workshop, 1998 (submitted).

Zhang, D., Venkatesan, G., Kaveh, M. and Tewfik, M., "Fault Monitoring using Acoustic Emissions," Proc. SPIE Conference on Sensory Phenomena and Measurement Instrumentation for Smart Structures and Materials, Vol. 3670, eds. R. O. Claus and W. B. Spillman, 1999.

Zhang, L., "MEMS Vibration Monitoring Structures," Ph.D. Dissertation, Electrical Engineering, University of Minnesota, Minneapolis, February 2000.

Zheng, L., Xue, J., and Ramalingam, S., "Eddy-Current Micro-sensors for Flaw Imaging: Numerical Simulation and Experimental Evaluation," Monitoring Technology for Condition-Based Maintenance, ed. R. S. Cowan, 96-TRIB-66, ASME, New York, 1997, pp. 25-31.

Zou, M., "Real-Time Monitoring and Control of a Noncontacting Mechanical Face Seal," Ph.D. Dissertation, School of Mechanical Engineering, Georgia Tech, Atlanta, 1998.

3.2 PRESENTATIONS

The process of technology transfer not only involves the recording of information, but also assisting in the understanding of that information and promoting its implications; hence, Integrated Diagnostic activity has been presented at a number of venues as listed below.

▪ INVITED PRESENTATIONS (61)

"Integrated Diagnostics Workshop on Sensors and Signal Processing," Georgia Institute of Technology, Atlanta, GA, February 19, 1999.

Achenbach, J. D., "A Portable Laser-Based Ultrasonics System for the Inspection of Aging Aircraft Structures," *First Joint DoD/FAA/NASA Conf. on Aging Aircraft*, Ogden, Utah, July 8-10, 1997.

Achenbach, J. D., "QNDE in Integrated Diagnostics," 1997 International Mechanical Engineering Congress and Exposition, Dallas, TX, November 16-21, 1997.

Achenbach, J. D., "Laser-Based Ultrasonics for QNDE Applications," *Intl. Conf. on Experimental Mechanics*, Singapore, December 4-6, 1996.

Berthelot, Y. and Qu, J., "Crack Detection in Annular Structures by Ultrasonic Guided Waves," Integrated Diagnostics Forum for Industry & Government, Atlanta, GA, September 14-15, 1999.

Cowan, R. S., "Condition Monitoring Tools for Tribologists, NATO-ASI, Keszthely, Hungary, August 25, 2000.

Cowan, R. S., "Dramatic Reduction of Operation and Maintenance Costs through CBM Technology," 54th Meeting of the Society for Machinery Failure Prevention Technology, Virginia Beach, VA, May 1, 2000.

Cowan, R. S., "New Frontiers in Mechanical System Health Monitoring and Prognosis," 52nd Meeting of the Society for Machinery Failure Prevention Technology, Virginia Beach, VA, March 30-April 3, 1998.

Cowan, R. S., "Integrated Diagnostics," *Condition-based Maintenance (Asset Management) Guideline Workshop*, Oak Ridge National Lab, Oak Ridge, TN, July 29-30, 1997.

Cowan, R. S., "Integrated Diagnostics," *AFOSR/ONR Tribology Program Review*, Englewood, OH, June 24-26, 1997.

Daniel, I., "Acoustic Emission Techniques for Material Damage Characterization," 1999 ASME International Mechanical Engineering Congress & Exposition, Nashville, TN, November 18, 1999.

Daniel, I. M., "Acoustic Emission Modeling for Integrated Diagnostics," Integrated Diagnostics Forum for Industry & Government, Atlanta, GA, September 14-15, 1999.

Daniel, I. M., "Acoustic Emission Modeling," *Material's Society Fatigue and Creep Symposium,* Indianapolis, IN, September 16, 1997.

Daniel, I. M., "Analysis of Acoustic Emission Output from Propagating Crack under Cyclic Tensile Loading," 1997 International Mechanical Engineering Congress and Exposition, Dallas, TX, November 16-21, 1997.

Drexel, M. "Modal Parameter Extraction," Integrated Diagnostics Forum for Industry & Government, Atlanta, GA, September 14-15, 1999.

Emamian, V., Kaveh M. and Tewfik, A., "Acoustic emission classification for failure predication due to mechanical fatigue, SPIE Meeting on Smart Structures and Materials, Newport Beach, CA, March 6-9, 2000.

Emamian, V., Kaveh M. and Tewfik, A., "Robust clustering of acoustic emission signals using the Kohonen network," International Conference on Acoustics, Speech and Signal Processing 2000, Istanbul, Turkey, June 5-9, 2000.

Green, I., "Real-time Monitoring and Controlling of Mechanical Face Seal Behavior," Integrated Diagnostics Forum for Industry & Government, Atlanta, GA, September 14-15, 1999.

Green, I., "Contact Elimination in a Mechanical Face Seal via Active Controls," 10th Annual United Technologies Engineering Conference and Expo, Cromwell, CT, April 21, 1999.

Green, I., "Feasibility of Contact Detection and Elimination in a Mechanical Face Seal," 10th Annual United Technologies Engineering Conference and Expo, Cromwell, CT, April 21, 1999.

Green, I., "Friction Induced Higher Harmonic Oscillations in a Noncontacting FMR Mechanical Face Seal Test Rig," 9th Annual UTC Engineering Conference and Technology Expo, Cromwell, CT, April 22, 1998.

Green, I., "Monitoring, Control and Reduction of Sub or Higher Harmonic Oscillations in Mechanical Face Seals," 9th Annual UTC Engineering Conference and Technology Expo, Cromwell, CT, April 22, 1998.

Green, I., Cowan, R. S., and Winer, W. O., "Integrated Diagnostics for Mechanical Systems," 9th Annual UTC Engineering Conference and Technology Expo, Cromwell, CT, April 22, 1998.

Jacobs, L. and Qu, J., "Crack Detection using Guided Waves," 1999 ASME International Mechanical Engineering Congress & Exposition, Nashville, TN, November 18, 1999.

Jacobs, L. J., "Study of Acoustic Emission from Incipient Fatigue Failure," Integrated Diagnostics Forum for Industry & Government, Atlanta, GA, September 14-15, 1999.

Jacobs, L. J., "Transfer Functions to Remove Geometry Effects from Acoustic Emission Signals," *Intl. Workshop on Materials Research with Advanced Acoustic Emission Techniques*, Max-Planck Society, Rottach-Egern, Germany, October 1996.

Jarzynski, J., "Ultrasonic Technique for Inspection of Bearing Balls," Integrated Diagnostics Forum for Industry & Government, Atlanta, GA, September 14-15, 1999.

Kaveh, M., "Signal Processing for Integrated Diagnostics," Integrated Diagnostics Forum for Industry & Government, Atlanta, GA, September 14-15, 1999.

Kaveh, M., "Mechanical Diagnostics using Acoustic Emissions," Plenary Lecture, SSAP Workshop, Portland, OR, September 1998.

Krishnaswamy, S., Kromine, A. and Achenbach, J. D., "Laser-Based Ultrasonics for Integrated Diagnostics," Integrated Diagnostics Forum for Industry & Government, Atlanta, GA, September 14-15, 1999.

Liang, S., "Adaptive and Probabilistic Prognostics for Condition-Based Maintenance," Integrated Diagnostics Forum for Industry & Government, Atlanta, GA, September 14-15, 1999.

Liang, S.Y., "Dynamic Metrology for Bearing Damage Diagnostics and Prognostics," 1999 ASME International Mechanical Engineering Congress & Exposition, Nashville, TN, November 18, 1999.

McDowell, D.L., Saxena, A., Neu, R.W., Johnson, W.S., and Qu, J. "Integrated Prognostics for Fatigue Damage," 1999 ASME International Mechanical Engineering Congress & Exposition, Nashville, TN, November 18, 1999.

McDowell, D.L., "Structural Fatigue Investigation," Integrated Diagnostics Forum for Industry & Government, Atlanta, GA, September 14-15, 1999.

McDowell, D.L., "A Model for Multiaxial Small Fatigue Crack Growth," *Engng. Against Fatigue,* Univ. Sheffield, UK, March 1997.

McDowell, D. L., "The Mechanics of Small Fatigue Cracks," Lockheed-Martin Corp., Marietta, GA, March 1997.

McDowell, D.L. and Bennett, V., "Micromechanical Aspects of Small Multiaxial Fatigue Cracks," *5th Intl. Conf. on Biaxial/Multiaxial Fatigue and Fracture*, Cracow, Poland, September 8-12, 1997.

Moran, B., "Domain Integrals for Arbitrary Crack Fronts," Aircraft Flight Critical Titanium Alloy Casting Symposium, Boeing Aircraft Company, October 3, 1997.

Neu, R. W., "Fretting Fatigue Projects," General Electric Aircraft Engines, Evandale, OH, June 9, 1999.

Neu, R.W., "Overcoming the Challenges in Predicting the Nucleation of Fretting Fatigue Cracks," Society of Engineering Science, 36th Annual Technical Meeting, Univ. of Texas, Austin, TX, October 25-27, 1999.

Polla, D. L., "Integrated Microsensors for Integrated Diagnostics," Integrated Diagnostics Forum for Industry & Government, Atlanta, GA, September 14-15, 1999.

Polla, D. L., "MEMS Technology and Applications," 1999 International Symposium on VLSI Technology, Systems and Applications, Plenary Session, Taipei, Taiwan, June 1999.

Polla, D. L., Francis, L. F., Drinkwater, D., Robbins, W. P., Harjani, H., Zhang L., Nair, K., Plummer, J., Nam, Y., and Schiller, P., "Piezoelectric MEMS for Integrated Diagnostics," Materials Research Society, San Francisco, CA, March 1999.

Polla, D. L., McGlennen, R. C., and Furcht, L. T., "Biomedical Applications of Ferroelectric MEMS," IEEE Intl. Symposium on Application Ferroelectrics, Monterey, CA, March 1998.

Polla, D. L., "Ferroelectric MEMS," American Physical Society, Los Angles, CA, March 1998.

Polla, D. L., "Integrated Ferroelectric MEMS: Technology Issues and Device Applications," *Proc. 8th International Symposium on Integrated Ferroelectrics*, Phoenix, AZ, March 1996.

Polla, D. L., "Ferroelectric MEMS," *American Vacuum Society/NASA Workshop on Microelectromechanical Systems*, Anaheim, CA, 1995.

Polla, D. L. and Francis, L. F., "Application of Piezoelectric Ceramics in Microelectromechanical Systems,"*7th US-Japan Seminar on Dielectric and Piezoelectric Ceramics*, Tsukuba, Japan, November 1995.

Ramalingam, S., "Eddy Current Microsensors for Flaw Imaging," 1999 ASME International Mechanical Engineering Congress & Exposition, Nashville, TN, November 18, 1999.

Ramalingam, S., "Eddy Current Microsensors for Integrated Diagnostics," Integrated Diagnostics Forum for Industry & Government, Atlanta, GA, September 14-15, 1999.

Salant, R., "Detection of the Precursor to Mechanical Seal Failure in Turbomachinery," Integrated Diagnostics Forum for Industry & Government, Atlanta, GA, September 14-15, 1999.

Salant, R. F., "Detecting Film Breakdown in Mechanical Seals with Ultrasonic Transducers," Laboratory of Seals and Sealing Technology, Technical University of Wroclaw, Wroclaw, Poland, August 25, 1998.

Salant, R. F., "Detection of Mechanical Seal Failure in Turbomachinery," Safematic Oy and VTT Technology Research Center, Espoo, Finland, June 1997.

Salant, R. F., "Integrated Diagnostics," NASA Marshall Space Flight Center, Huntsville, AL, June 25, 1997.

Salant, R.F., Anderson, W. and Jarzynski, J., "Condition Monitoring of Mechanical Seals Using Actively Generated Acoustic Waves," 16th International Conference on Fluid Sealing, BHRG, Brugge, Belgium, September 18-20, 2000.

Saxena, A., "Predicting Remaining Creep-Fatigue Life of Power Plant Components," *9th Intl. Conf. on Fracture*, Sydney, Australia, April 2-6, 1997.

Saxena, A., "Fatigue Crack Growth in Power-Plant Materials and Components," *Fatigue '96 International Conference*, Berlin, Germany, May 1996.

Winer, W. O., "The MultiUniversity Center for Integrated Diagnostics," American Association for Universities (AAU), Cannon House Office Building, Washington, DC, April 29, 1998.

Winer, W. O., "Emerging Technologies for Machinery Diagnosis and Prognosis," *10th Intl. Congress and Exhibition on Condition Monitoring and Diagnostic Engineering Management*, Espoo, Finland, June 9-11, 1997.

Winer, W. O., "Adding Time to Aging Equipment with an Appropriate Maintenance Methodology," *7th Nordic Symposium on Tribology*, Bergen, Norway, June 1996.

Zhang, D., Venkatesan, G., Kaveh, M. and Tewfik, M., "Fault Monitoring using Acoustic Emissions," SPIE Conference on Sensory Phenomena and Measurement Instrumentation for Smart Structures and Materials, Newport Beach, CA, March 1-4, 1999.

▪ CONTRIBUTED PRESENTATIONS (90)

Achenbach, J. D., "A Fiber-Based Laser Ultrasonic System for Remote Inspection of Limited Access Components," *Review of Quantitative NDE*, Brunswick, ME, July 28-August 2, 1996.

Anderson, W., Salant, R. and Jarzynski, J., "Ultrasonic Detection of Lubricating Film Collapse in Mechanical Seals," STLE Annual Meeting, Las Vegas, NV, May 1999.

Anderson, W. B., Salant, R. F., and Jarzynski, J., "Detection of Lubricating Film Breakdown in Mechanical Seals," 1997 Intl. Mechanical Engineering Congress and Exposition, Dallas, TX, November 16-21, 1997.

Beadle, B. and Jarzynski, J., "Fiber-Optic Interferometric Sensor for Ultrasound," 136th Meeting of the Acoustical Society of America, Norfolk, VA, October 12-16, 1998.

Bennett, V. and McDowell, D. L., "Mixed Mode Behavior of Microstructurally Small Fatigue Cracks," ASTM Symposium on Mixed Mode Fatigue and Fracture, Atlanta, GA, May 6-7, 1998.

Berthelot, Y., "Mode Control of Ultrasonic Guided Waves in Thick Cylinders for Crack Detection," *131st Mtg. of the Acoustical Society of America*, Indianapolis, IN, May 16, 1996.

Billington, S., Li, Y., Liang, S., Kurfess, T., and Danyluk, S., "Operating Condition Effects on Rolling Element Bearing Diagnostics," 52nd Meeting of the Society for Machinery Failure Prevention Technology, Virginia Beach, VA, March 30-April 3, 1998.

Billington, S., Li, Y., Liang, S., Kurfess, T., and Danyluk, S., "Roller Bearing Defect Detection with Multiple Sensors," 1997 Intl. Mechanical Engineering Congress and Exposition, Dallas, TX, November 16-21, 1997.

Cho, C. R., Drinkwater, D. E., Francis, L. F., and Polla, D. L., "Solution Deposited $LaNiO_3$ and PZT Thin Films for MEMS Sensor Applications," Annual Meeting of the American Ceramic Society, May 1998.

Cook, D. A. and Berthelot, Y. H., "Detection of fatigue crack initiation and growth in steel specimens from Rayleigh scattering of 5 MHz Rayleigh waves," 138th meeting of the Acoustical Society of America, Columbus, Ohio, November 1999.

Cowan, R. S., "Research Developments in Integrated Diagnostics and Prognostics," 2nd International Workshop on Structural Health Monitoring, Stanford, CA, September 8-10, 1999.

Cowan, R. S., "Research Progress in Integrated Diagnostics," AFOSR-ONR-NSF Tribology Program Review, Islamorda, FL, June 14-18, 1999.

Cowan, R. S., "Integrated Diagnostics," AFOSR-ONR-NSF Tribology Program Review, Annapolis, MD, June 22-25, 1998.

Cowan, R. S., "Integrated Diagnostics," Best Manufacturing Process Center Workshop on Equipment Maintenance, Oak Ridge, TN, October 6-7, 1997.

Cowan, R. S., "Integrated Diagnostics," USAF Inaugural Engine Condition Monitoring Workshop, San Diego, CA, October 21-23, 1997.

Cowan, R. S., "Recent Developments in Health Appraisal and Life Extension of Mechanical Systems,"*1995 Korea-USA Tribology Symposium*, Seoul, Korea, October 1995.

Daniel, I. M., "Acousto-Ultrasonic Technique for Evaluating the Integrity and Strength of Composite Repair Patches for Damaged Aircraft," ASME Conference on Applied Mechanics and Materials, Blacksburg, VA, June 28-30, 1999.

Daniel, I. M., "Analysis of Acoustic Emission Waveforms by a Covariance Method," 26th Annual Review of Progress in Quantitative NDE, Montreal, Quebec, July 25-30, 1999.

Daniel, I., "Acoustic Emission Monitoring of Fatigue Damage in Metals," *Review of Quantitative NDE*, Brunswick, ME, August 1, 1996.

Daniel, I. M., Sifniotopoulos, C. G., and Luo J. -J., "Analysis of AE Output from Propagating Crack," *24th Annual Review of Progress in Quantitative Nondestructive Evaluation*, San Diego, CA, July 1997.

Dayan, J., Zou, M., and Green, I., "Contact Elimination in Mechanical Face Seals Using Active Control," IEEE 7th Mediterranean Conference on Control and Automation (MED99), Haifa, Israel, June 28-30, 1999.

Drinkwater, D. E., Cho, C. R., and Francis, L. F., "PZT-Based MEMS Acoustic Emission Sensors," Annual Meeting of the American Ceramic Society, May 1998.

Eisenhardt, C., Jacobs, L. and Qu, J., "Detection of Cracks in Plates using Guided Waves," 26th Annual Review of Progress in Quantitative NDE, Montreal, Quebec, July 25-30, 1999.

Fomitchov, P. A., Kromine, A., Krishnaswamy, S., and Achenbach, J. D., "Laser-Based Ultrasonics for Crack Detection," Second Joint NASA/FAA/DOD Conference on Aging Aircraft, Williamsburg, VA, August 31-September 4, 1998.

Fomitchov, P., Krishnaswamy, S., and Achenbach, J., "Sagnac Interferometer for Ultrasound Detection on Rough Surfaces," *8th Intl. Symposium on Nondestructive Characterization of Materials*, Boulder, CO, June 1997.

Gardner, B. and Qu, J., "A Numerical Technique to Calculate the Stress Intensity Factors for Cracks with Multiple Kinks," ASTM Symposium on Mixed Mode Fracture, Atlanta, GA, April 6-7, 1998.

Green, I., "Parametric Investigation for Passive and Active Control of a Noncontacting Mechanical Face Seal," STLE Annual Meeting, Las Vegas, NV, May 1999.

Hurlebaus, S., Jacobs, L. and Jarzynski, J., "Transfer Functions to Remove Geometry Effects from AE Signals," *Gordon Conference on Nondestructive Characterization of Materials,* Andover, NH, August 18-23, 1996.

Hurlebaus, S., Jacobs, L. and Jarzynski, J., "Transfer Functions to Remove Geometry Effects from AE Signals," *Review of Quantitative NDE,* Brunswick, ME, July 28-August 2, 1996.

Jacobs, L., Eisenhardt, C., and Qu, J, "Detection of cracks in plates using guided waves," 138th Meeting of the Acoustical Society of America," Columbus, Ohio, November 2, 1999.

Kim, J. H., Wang, L., Li L., Zurn, S., and Polla, D. L., "Device Characteristics of Piezoelectric Cantilever Beam Accelerometers Using Surface Micromachining Process," *Proc. 8th Intl. Symposium on Integrated Ferroelectrics*, Phoenix, AZ, March 1996.

Kley, M., Valle, C., Jacobs, L. J., and Qu, J., "Development of Dispersion Relationships for Layered Cylinders using Laser Ultrasonics," 1998 Review of Progress in Quantitative NDE, Snowbird, UT, July 19-24, 1998.

Kromine, A., Fomitchov, P., Krishnaswamy, S., Achenbach, J.D., "Applications of Scanning Laser Source Technique for Detection of Surface-Breaking Defects," EOS/SPIE Symposium on Applied Photonics, Glasgow, UK, May 22-24, 2000.

Kromine, A., Fomitchov, P., Krishnaswamy, S., Achenbach, J.D., "Detection of Sub-Surface Defects Using Laser Based Technique," 27th Annual Review of Progress in Quantitative Nondestructive Evaluation, Ames, Iowa, July 16-21, 2000.

Kromine, A., Fomitchov, P., Krishnaswamy, S. and Achenbach, J. D., "Scanning Laser Source Technique for Detection of Surface-Breaking and Subsurface Cracks," 26th Annual Review of Progress in Quantitative NDE, Montreal, Quebec, July 25-30, 1999.

Kromine, A., Fomitchov, P. A., Krishnaswamy, S., and Achenbach, J. D., "Scanning Laser Source Technique and Its Application to Turbine Disk Inspection," 1998 Review of Progress in Quantitative NDE, Snowbird, UT, July 19-24, 1998.

Li, Y., Billington, S., Kurfess, T., Danyluk, S., and Liang, S., "Dynamic Prognostics of Rolling Element Bearing Condition," 52nd Meeting of the Society for Machinery Failure Prevention Technology, Virginia Beach, VA, March 30-April 3, 1998.

Li, Y., Kurfess, T., Danyluk, S., and Liang, S., "Bearing Prognostics Based on Adaptation of Stochastic Defect Growth Model," 53rd Meeting of the Society of Machinery Failure Prevention Technology, Virginia Beach, VA, April 22, 1999.

Li, Y., Shiroishi, J., Danyluk, S., Kurfess, T. R., and Liang, S. Y., "Bearing Fault Detection via High Frequency Resonance Technique with Adaptive Line Enhancer," *12th Biennial Conf. on Reliability, Stress Analysis and Failure Prevention,* MFPT, Virginia Beach, VA, April 15-17, 1997.

Li, Y., Shiroishi, J., Danyluk, S., Kurfess, T. R., and Liang, S. Y., "Diagnostics of Roller Bearing Defects Based on Vibration and Acoustic Emission," *10th Intl. Congress, COMADEM,* Espoo, Finland, June 1997.

Li, Z. and Berthelot, Y., "Crack Detection in Annular Components by Guided Ultrasonic Waves," *QNDE '97*, San Diego, CA, July 1997.

Liang, S., "Dynamic Modeling of Vibration Signals for Bearing Condition Monitoring," 2nd International Workshop on Structural Health Monitoring, Stanford, CA, September 8-10, 1999.

Lim, T. H., Kim, J., Wright, J., Li, L., Polla, D. L., and Francis, L., "Direct Depositions of $PbTiO_3$(PT) and PZT on Si/SiO_2 and Si Using Polyimide as a Diffusion Barrier," *Mtg. of the American Physical Society*, St. Louis, MO, March 1996.

Liu, G. and Qu, J., "Guided Wave Propagation in Annulus Components," *Review of Progress in Quantitative Nondestructive Evaluation*, San Diego, CA, July 1997.

Liu, G., Qu, J., and Jacobs, L. J., "Characterizing Adhesive Curing by Nonlinear Ultrasonic Techniques," 1998 Review of Progress in Quantitative NDE, Snowbird, UT, July 19-24, 1998.

McDowell, D.L., "Unresolved Issues in Microstructure-Dependence of High Cycle Fatigue," Workshop on Performance Requirements for the Engineering Diffractometer at the Spallation Neutron Source, Atlanta, GA, January 20, 2000.

McDowell, D. L., "Mechanics of Small Fatigue Crack Growth in Metals," *Engng. Foundation Conf.,* Hyannis, MA, 1996.

McDowell, D. L., Cowan, R. S., and Winer, W. O., "Developing an Integrated Diagnostic System," 1997 International Mechanical Engineering Congress and Exposition, Dallas, TX, November 16-21, 1997.

McDowell, D. L., Neu, R. W., Qu, J., and Saxena, A., "Prognostic Tools for Small Cracks in Structures," 1997 International Mechanical Engineering Congress and Exposition, Dallas, TX, November 16-21, 1997.

Moran, B., "Natural Element Method Workshop on Meshfree Methods," Chicago, IL, June 13, 2000.

Moser, F., Valle, C., Jacobs, L. J., and Qu, J., "Modeling of Guided Waves in Annular Components," *24th Annual Review of Progress in Quantitative Nondestructive Evaluation*, San Diego, CA, July 1997.

Nair, K. and Harjani, R., "A Telemetry and Interface Circuit for Piezoelectric Circuits," IEEE International Symposium on Circuits and Systems, Atlanta, GA, May 30-June 2, 1999.

Neithammer, M., Eisenhardt, C., Jacobs, L., Qu, J., and Jarzynski, J., "Application of Wavelet Transform and STFT Techniques to Interpret Ultrasonic Signals," 26th Annual Review of Progress in Quantitative NDE, Montreal, Quebec, July 25-30, 1999.

Neu, R.W., Swalla, D.R., and Pape, J.A., "Plastic Deformation in Fretting Fatigue: Experiments and Modeling," 20th International Congress of Theoretical and Applied Mechanics (ICTAM), Chicago, IL, August 27 - September 2, 2000.

Neu, R. W., Pape, J. A., and Swalla-Michaud, D. R., "Methodologies for Linking Nucleation and Propagation Approaches for Predicting Life under Fretting Fatigue," 2nd International Symposium on Fretting Fatigue, Salt Lake City, UT, August 30-September 2, 1998.

Pape, J. A. and Neu, R. W., "Influence of Contact Configuration in Fretting Fatigue Testing," 1999 Wear of Materials Conference, Atlanta, GA, April 26-29, 1999.

Pape, J.A., Neu, R.W., and Swalla, D.R., "Fretting Fatigue Damage Accumulation in PH 13-8 Mo Stainless Steel," 1999 ASME International Mechanical Engineering Congress, Nashville, TN, November 15-19, 1999.

Polla, D. L., "Materials Issues in Ferroelectric MEMS," *Am. Vacuum Soc. National Symp.*, October 1996.

Polla, D. L., Buckley, K., Harjani, R., Robbins, W. P., Gerberich, W., Francis, L. F., Mantell, S., Erdman, A., Kaveh, M., and Tewfik, A., "Microsensors for Integrated Diagnostic Applications," 1997 International Mechanical Engineering Congress and Exposition, Dallas, TX, November 16-21, 1997.

Polla, D. L., Francis, L., Robbins, W., and Harjani, R., "MEMS for Integrated Diagnostic Applications," 1997 International Mechanical Engineering Congress and Exposition, Dallas, TX, November 16-21, 1997.

Qu, J., "Using Nonlinear Parameter to Characterize the Curing of Adhesive Joints," 1999 ASME International Mechanical Engineering Congress & Exposition, Nashville, TN, November 15-19, 1999.

Qu, J., "Transverse Matrix Cracking," *ASME Mechanics and Materials Conference*, Baltimore, MD, June 12-14, 1996.

Ramalingam, S., "Eddy-Current Micro-sensors for Flaw Imaging: Numerical Simulation and Experimental Evaluation," *ASME/STLE Tribology Conference,* San Francisco, CA, October 17, 1997.

Ribadeneira, X., Kurfess, T. R., Billington, S., and Li, Y., "Ball Bearing Diagnostics in Run-to-Failure Lifetime Testing," 54th Meeting of the Society for Machinery Failure Prevention Technology, Virginia Beach, VA, May 3, 2000.

Salant, R. F., Anderson, W. and Jarzynski, J., "Condition Monitoring of Mechanical Seals Using Actively Generated Acoustic Waves," 16th International Conference on Fluid Sealing, BHRG, Brugge, Belgium, September 2000.

Saxena, A. and Cretegny, L., "A Model for Predicting the Influence of Microstructure on the J-Resistance Curve," *Workshop on Crack-Tip Micromechanics*, ASTM E-08, St. Louis, MO, May 5-7, 1997.

Saxena, A., Yang, F. and Cretegny, L., "Use of Atomic Force Microscopy for Studying Fatigue Crack Initiation," 7th International Conference on Fatigue, Beijing, China, June 8-12, 1999.

Shi, Z., Jarzynski, J. and Jacobs, L.J., "Study of Acoustic Emission in a Plate using Laser Ultrasonics," 27th Annual Review of Progress in Quantitative NDE, Ames, Iowa, July 16-21, 2000.

Shi, Z., Jarzynski, J. and Jacobs, L.J., "Study of Acoustic Emission in a Plate using Laser Ultrasonics and the Finite Element Method," 139th Meeting Acoustical Society of America, Atlanta, Georgia, May 30-June 3, 2000.

Shi, Z., Jarzynski, J. and Jacobs, L., "Quantitative Acoustic Emission from Fretting Fatigue of PH 13-8 Stainless Steel," 26th Annual Review of Progress in Quantitative NDE, Montreal, Quebec, July 25-30, 1999.

Shi, Z., Bair, S., Jarzynski, J., and Jacobs, L. J., "Study of Acoustic Emission from Incipient Fatigue Failure," 1998 Review of Progress in Quantitative NDE, Snowbird, UT, July 19-24, 1998.

Shi, Z., Bair, S., Jarzynski, J., and Jacobs, L.J., "Acoustic Emission from Incipient Fatigue Failure," 1997 International Mechanical Engineering Congress and Exposition, Dallas, TX, November 16-21, 1997.

Shi, Z., Koutsak, M., Bair, S., Jarzynski, J., and Jacobs, L. J., "Characterization of Acoustic Emission Signals from Fracture Events," *24th Annual Review of Progress in Quantitative Nondestructive Evaluation*, San Diego, CA, July 1997.

Shiroishi, J., Li, Y., Liang, S., Danyluk, S. and Kurfess, T. R., "Vibration Signal Analysis for Bearing Race Damage Diagnostics," *7th Intl. Conf. on Dynamic Problems in Mechanics*, Angra Dos Reis, Brazil, March 1997.

Sun, H., Kaveh, M., and Tewfik, A., "Self-Organizing Map Neural Network for Transient Signal Classification," IEEE Workshop-Nonlinear Signal & Image Processing, Antalya, Turkey, June 20-23, 1999.

Swalla, D.R., Neu, R.W., and Pape, J.A., "Prediction of Fretting Fatigue Damage Using Multiaxial Fatigue Criteria," 1999 ASME Intl. Mechanical Engineering Congress, Nashville, TN, November 15-19, 1999.

Valle, C., Qu, J., and Jacobs, L. J., "Scattering of Circumferential Waves in a Cracked Annulus," 26th Annual Review of Progress in Quantitative NDE, Montreal, Quebec, July 25-30, 1999.

Valle, C., Qu, J., and Jacobs, L. J., "Guided Circumferential Waves in Layered Cylinders," 1998 Review of Progress in Quantitative NDE, Snowbird, UT, July 19-24, 1998.

Valle, C., Qu, J., and Jacobs, L. J., "Guided Circumferential Waves in Layered Cylinders," 13th U. S. National, Congress of Applied Mechanics, Gainesville, FL, June 21-26, 1998.

Venkatesan, G. T., Tong, L., Kaveh, M. and Buckley, K., "A Deterministic Blind Identification Technique for SIMO Systems of Unknown Model Order," ICASSP, Phoenix, AZ, March 15-19, 1999.

Venkatesan, G. T., Kaveh, M., Tewfik, A. H., and Buckley, K., "Blind Identification of Single-Input Multiple-Output Pole-Zero Systems," Proc. Intl. Conf. on Acoustics, Speech and Signal Processing (ICASSP98), Vol. 4, pp. 2117-2120, Seattle, WA, May12-15, 1998.

Winer, W. O., "Health and Safety Improvement through Tribological Failure Analysis and Prediction," *Technische Akademie Esslingen 10th Intl. Tribology Colloquium*, Ostfildern, Germany, January 1996.

Xue, J., Ramalingam, S., and Shi, Z., "Eddy Current Flaw Imaging Using Micro-Sensor Arrays," 1997 International Mechanical Engineering Congress and Exposition, Dallas, TX, November 16-21, 1997.

PRESENTATIONS

Xue, J., Ramalingam, S., and Shi, Z., "Modeling Eddy Current Imaging with Thin Film Micro-Sensors," 1997 International Mechanical Engineering Congress and Exposition, Dallas, TX, November 16-21, 1997.

Zhang, M., Zurn, S.M., Polla, D.L., Nelson, B.J., and Robbins, W.P., "Design, Simulation and Fabrication of a Bridge Structure Microtransducer", 3rd International Conference on Modeling and Simulation of Microsystems, San Diego, CA, March 27-29, 2000.

Zhang, D., Venkatesan, G. T., Tewfik, A. H., and Kaveh. M., "Acoustic Emission Transient Detection Based on Linear Model Residuals," Proc. 9th IEEE Workshop on Statistical Signal and Array Processing (SSAP98), Portland, OR, September 14-16, 1998.

Zou, M. and Green I., "Clearance Control of a Mechanical Face Seal," ASME/STLE Tribology Conference, Toronto, Ontario, October 1998.

Zou, M. and Green, I., "Real-time Condition Monitoring of Mechanical Face Seal," *24th Leeds-Lyon Symposium on Tribology*, London, Imperial College, September 4-6, 1997, 423-430.

Zou, M., Dayan, J., and Green, I., "Feasibility of Contact Elimination of a Mechanical Face Seal through Clearance Adjustment," ASME IGTI Turbo Expo, Indianapolis, IN, June 6-10, 1999.

Zou, M. Dayan, J., and Green, I., "Parametric Analysis for Contact Control of a Noncontacting Mechanical Face Seal," Proceedings of Vibration, Noise and Structural Dynamics, 1999, Venice, Italy, April 28-30.

REPORT DOCUMENTATION PAGE

Form Approved
OMB No. 0704-0188

The public reporting burden for this collection of information is estimated to average 1 hour per response, including the time for reviewing instructions, searching existing data sources, gathering and maintaining the data needed, and completing and reviewing the collection of information. Send comments regarding this burden estimate or any other aspect of this collection of information, including suggestions for reducing the burden, to Department of Defense, Washington Headquarters Services, Directorate for Information Operations and Reports (0704-0188), 1215 Jefferson Davis Highway, Suite 1204, Arlington, VA 22202-4302. Respondents should be aware that notwithstanding any other provision of law, no person shall be subject to any penalty for failing to comply with a collection of information if it does not display a currently valid OMB control number.
PLEASE DO NOT RETURN YOUR FORM TO THE ABOVE ADDRESS.

1. REPORT DATE *(DD-MM-YYYY)*	2. REPORT TYPE	3. DATES COVERED *(From - To)*
31-08-2000	Final	Mar 1995 - Aug 2000

4. TITLE AND SUBTITLE

INTEGRATED DIAGNOSTICS
A DoD Multidisciplinary Research Program of the University Research Initiative

5a. CONTRACT NUMBER

5b. GRANT NUMBER
N00014-95-1-0539

5c. PROGRAM ELEMENT NUMBER

6. AUTHOR(S)

Richard S. Cowan and Ward O. Winer (eds.)

5d. PROJECT NUMBER

5e. TASK NUMBER

5f. WORK UNIT NUMBER

7. PERFORMING ORGANIZATION NAME(S) AND ADDRESS(ES)

Georgia Institute of Technology
MultiUniversity Center for Integrated Predictive Diagnostics
801 Ferst Drive
Atlanta, GA 30332-0405

8. PERFORMING ORGANIZATION REPORT NUMBER

9. SPONSORING/MONITORING AGENCY NAME(S) AND ADDRESS(ES)

Office of Naval Research
800 N. Quincy Street
Arlington, VA 22217-5660

10. SPONSOR/MONITOR'S ACRONYM(S)

11. SPONSOR/MONITOR'S REPORT NUMBER(S)

12. DISTRIBUTION/AVAILABILITY STATEMENT

13. SUPPLEMENTARY NOTES
The information conveyed in this report does not necessarily reflect the position or the policy of the Government, and no official endorsement should be inferred.

14. ABSTRACT This document summarizes performance activity regarding basic research conducted in the area of *Integrated Diagnostics*, a term associated with the technologies and methodologies used to determine how mechanical failures occur, and how they can be detected, predicted and diagnosed in real-time. Objectives, set forth through the Department of Defense Multidisciplinary Research Program of the University Research Initiative (M-URI) have been addressed by faculty and staff from the Georgia Institute of Technology, Northwestern University and the University of Minnesota.

Experiments based on material, load and vibration information from critical rotorcraft components have been conducted so as to collect data of relevance in understanding the mechanisms of failure for use in developing failure models. These models can serve as a guide in the selection and development of sensors to detect faults and pending failures. Effort has been placed on micro-sensor development, and achieving the means to analyze and correlate reliable sensor output for remaining life estimation and operator use. Organizationally, this activity is being accomplished through (13) projects, categorized by three thrust areas.

15. SUBJECT TERMS

Integrated Predictive Diagnostics; Condition-Based Maintenance; Nondestructive Evaluation
Fatigue; Failure Detection; Failure Prediction; Condition Monitoring; Sensors; Direct Sensing.

16. SECURITY CLASSIFICATION OF:			17. LIMITATION OF ABSTRACT	18. NUMBER OF PAGES	19a. NAME OF RESPONSIBLE PERSON
a. REPORT	b. ABSTRACT	c. THIS PAGE			19b. TELEPHONE NUMBER *(Include area code)*
U	U	U	SAR	292	